N°d'ordre : 2014-30

Thèse de l'Université de Lyon
délivrée par l'École Centrale de Lyon
Spécialité : mécanique des milieux fluides

soutenue publiquement le 27 Novembre 2014

par

William RIÉRA

préparée

au Département Aérodynamique Appliquée de l'Onera

&

au Laboratoire de Mécanique des Fluides et d'Acoustique

Evaluation of the ZDES method on an axial compressor: analysis of the effects of upstream wake and throttle on the tip-leakage flow.

École Doctorale de Mécanique, Énergétique, Génie Civil et Acoustique

---

Composition du jury :

JÖRG SEUME	Leibniz Universität, Hannover	*Président du jury*
PASCAL FERRAND	École Centrale de Lyon	*Directeur de thèse de substitution*
PAUL G. TUCKER	University of Cambridge	*Rapporteur*
LIONEL CASTILLON	ONERA, Meudon	*Examinateur*
SÉBASTIEN DECK	ONERA, Meudon	*Examinateur*
XAVIER OTTAVY	École Centrale de Lyon	*Examinateur*
THIERRY OBRECHT	Snecma, Villaroche	*Membre invité*

Acknowledgements/Remerciements

Une thèse n'est pas un diplôme, ni une soutenance, ni un manuscrit, ni des publications et communications dans des congrès. Une thèse est une rencontre. Une rencontre avec un sujet, une infime portion du vaste domaine de la recherche, que l'on s'approprie au fil des ans. Mais c'est surtout une série de rencontres avec des personnes, le long de ces 3 (voire 4...) années passées à éclaircir ce sujet. Je tiens donc à remercier toutes les personnes qui m'ont permis d'aller jusqu'au bout de ce projet.

En tout premier lieu, je voudrais rendre hommage à Francis Lebœuf, mon directeur de thèse, qui nous a quitté tragiquement. Je me souviendrai de lui pour sa grande expérience, son ouverture d'esprit, ses anecdotes sur la Chine... et le fait de sortir toujours motivé après une réunion d'avancement avec lui. Mais ce qui m'a le plus marqué est son optimisme, contagieux...

Je tiens à remercier Pascal Ferrand qui a accepté d'être mon directeur de thèse de substitution, et de m'avoir accompagné lors des derniers mois de thèse.

I would like to thank the jury members, especially Paul G. Tucker, and Pierre Sagaut who have accepted that I defend my thesis and gave me advice to improve it. Ich möchte auch mich bei Jörg Seume, der Jury-Präsident, bedanken.

Ces travaux ont été financé par le Consortium Industrie-Recherche en Turbomachines (CIRT). Je voudrais donc remercier tous les partenaires qui y ont participé.

Du côté de Centrale Lyon, je remercie particulièrement Xavier Ottavy pour les données expérimentales sur CREATE, tous les conseils et le suivi de mes travaux depuis le début. Merci aussi pour ta participation en tant que membre du jury de thèse. Je remercie aussi toute l'équipe du LMFA pour son accueil durant les réunions CIRT et CREATE et surtout pour le mois passé à Ecully lors de la campagne LDA. Notamment, Benoit Paoletti, Isabelle Trébinjac, Antoine Godard, Gilbert Halter, Sébastien Goguey...

Je remercie Snecma, et notamment Michel Dumas qui a suivi mes travaux de thèse depuis le début. Merci aussi à Jacques Riou, encadrant Onera puis encadrant Snecma, tu as toujours gardé un oeil sur mes travaux et relu mes papiers. Merci Thierry Obrecht pour ta relecture du rapport et pour avoir participé au jury de thèse en tant que membre invité.

Plus au sud, je tiens à remercier Turbomeca, en particulier Gilles Leroy et Pierre Biscay.

Cette thèse s'est déroulée principalement à l'Onera de Meudon, dans l'unité "Hélices Hélicoptères Turbomachines" (H2T) du Département Aérodynamique Appliquée. Je remercie Philippe Beaumier de m'avoir accueilli dans l'équipe.

Si je ne devais garder qu'un seul grand, très grand merci, ce serait pour Lionel Castillon. Tu as sû me laisser beaucoup d'autonomie tout en étant un soutien de chaque instant, du premier entretien jusqu'aux dernières corrections. Tu es sûrement la personne la plus pédagogue, humble et brillante que je connaisse. Je n'oublierai jamais les moments passés à discuter ensemble. Merci à toi, tu es le meilleur encadrant qu'on puisse rêver d'avoir, tant techniquement qu'humainement. La deuxième personne qui mérite un énorme merci est Julien Marty. Merci Julien de m'avoir accompagné pendant toutes ces années, de m'avoir prodigué ton expérience de thèse, tes conseils, d'avoir répondu à toutes mes interrogations, de m'avoir soutenu jour après jour. Je n'aurais jamais pu écrire ni présenter ces travaux de thèse sans ton aide. Lionel, Julien, je ne vous remercierai jamais assez pour tout ce que vous avez fait. Cette thèse est en partie la vôtre. Plus que des encadrants, vous êtes des amis.

J'aimerais aussi remercier Sébastien Deck. C'était toujours difficile de trouver un créneau pour te parler Sébastien, mais tu n'hésitais pas à rester tard pour partager ta connaissance et philosopher sur la couche limite, la turbulence et les méthodes numériques. J'ai passé mes Dan grâce à toi et je t'en remercie, oh grand maître de la ZDES!

Je voudrais remercier toutes les autres personnes de Meudon pour ces 3 formidables années en votre compagnie. Vous avez été comme une deuxième famille. Un grand merci Michel, ton dynamisme et nos discussions sur l'univers et le reste me manquent déjà. Faire des calculs c'est bien, mais les post traiter c'est mieux! Voilà pourquoi je voudrais remercier Benoit (post traitement embarqué) et Raphaël (Zeppelin). Sans vous, je n'aurais pas pu montrer tous ces résultats. Merci aussi à Thomas et Philippe, pour votre support avec l'informatique.

Une pensée particulière à la première personne de H2T que j'ai rencontrée alors que je travaillais au DLR, Stéphane, sans qui je n'aurais jamais su l'existence de la thèse. Faut croire que je te suis...

Je voudrais aussi remercier Nabil, toujours présent, même après 20h à l'Onera, ou pour des soirées sur Paris. C'est vraiment un plaisir de continuer à travailler avec toi! Merci à Gilles B. et Antoine F. de l'équipe Turbomachines pour vos avis éclairés sur l'écoulement de jeu et la physique. Merci aussi Antoine D. très cher voisin, je n'oublierai jamais nos discussions, et toutes les fois où tu m'as aidé! Et merci Sophie, pour ton aide dans toutes les tâches administratives, et surtout ta bonne humeur.

Ces années de thèse m'ont permis de partager des moments privilégiés avec des compagnons doctorants. Merci tout d'abord aux anciens: Kader et Simon. Un remerciement particulier pour Gilles J., les séances d'hélico avec Benjamin et toi, les débats sur la turbulence...

Et parce qu'on devient toujours l'ancien de quelqu'un, je voudrais remercier les djeuns! Tout particulièrement le trio Martin "titatitatitututu", Matthieu "anyway" et la pétillante Virginie. Ce fût un plaisir de partager le bureau avec vous!

Sans oublier les doctorants qui sont aussi passés par Meudon (et ceux connus par EChO): Ignacio, Enric, Mehdi, Timothée, Aurélien, Hélène, Romain, Loic, Mickael, Nicolas, Amaury, Andrea, Pierre, Gaelle, Emmanuel, Imane...

Je remercie aussi toutes les personnes que j'ai croisé, au bureau et en dehors et qui m'ont marqué par leur connaissance, leur humour, leur présence...

Pour finir en dehors du cadre de la thèse, je voudrais remercier Jim, Clem, Jon, Flore, Mélo, et Mario. Je remercie mes parents qui ont toujours cru en moi et qui ont tout fait pour que j'aille jusqu'au bout, et ma sœur Virginie! Merci d'être venus le jour J! Et enfin, et surtout, Nathalie, ma fiancée, la femme de ma vie, qui partage tout avec moi depuis tant d'années, des coups durs aux meilleurs moments. Je te remercie d'être là à chaque instant.

"Les pieds sur terre, le cœur avec les hommes, la tête dans les étoiles !"

L'Homme qui en savait trop rien, MH.

Abstract/Résumé

Abstract

The tip-leakage flow in axial compressors is studied with the Zonal Detached Eddy Simulation (ZDES). This study aims at evaluating the capability of hybrid URANS/LES methods to simulate the tip-leakage flow within a realistic axial compressor in order to better understand the involved physics, especially the behaviour of the flow near surge and the effects of stator wakes on the downstream rotor.

Once the ZDES method is chosen, a numerical test bench is defined to simulate the first rotor of the research compressor CREATE. This bench takes into account the unsteady effects of the Inlet Guide Vane (IGV), such as its wake as well as vortices generated at the IGV hub and tip. It is based upon ZDES meshing criteria and is used to evaluate this method compared to classic RANS and URANS approaches. A method validation is carried out up to a spectral analysis compared to experimental data. The ZDES is capable to capture more accurately the intensity and position of the unsteady phenomena encountered in the tip region, especially the tip-leakage vortex. The power spectral densities highlight that this partly originates from a better capture of the energy transfer from large to small structures until their dissipation. The discrepancy between the methods is accentuated as the tip-leakage vortex crosses the shock.

Near the surge line, the interactions between the shock, the tip-leakage vortex, the boundary layer developing on the shroud and the vortex generated by the IGV tip are amplified. The boundary layer on the shroud separates earlier and a local flow inversion occurs. Besides, the tip-leakage vortex widens and is deflected toward the adjacent blade. This strengthens the double leakage.

At the design operating point, the interaction of the IGV tip vortex with the shock and the rotor tip vortex is studied. A vortex flutter is observed as the IGV tip vortex arrives on the rotor blade and stretches the rotor tip vortex. This phenomenon decreases the double leakage.

Keywords : NUMERICAL SIMULATION, RANS, LES, ZDES, TIP LEAKAGE FLOW, AXIAL COMPRESSOR, CREATE, UPSTREAM DISTORTION, TIP LEAKAGE VORTEX, DOUBLE LEAKAGE, WAKE VORTEX INTERACTION, THROTTLE

Résumé

L'écoulement de jeu dans les compresseurs axiaux est étudié à l'aide de la Zonal Detached Eddy Simulation (ZDES). L'objectif consiste à évaluer la capacité de méthodes hybrides URANS/LES à simuler l'écoulement de jeu d'un compresseur axial réaliste afin de mieux comprendre la physique de cet écoulement, notamment son comportement au vannage ainsi que l'effet de sillages venant du stator amont sur le rotor aval.

Après avoir choisi la méthode hybride ZDES, un banc d'essai numérique est défini afin de simuler le premier rotor du compresseur de recherche CREATE. Ce banc a la particularité de pouvoir prendre en compte les effets instationnaires venant de la roue directrice d'entrée (RDE), notamment son sillage ainsi que les tourbillons générés en pied et en tête. Basé sur des critères de maillage ZDES, il est utilisé pour évaluer cette méthode comparativement aux méthodes classiques RANS et URANS. La ZDES est validée par étape jusqu'à une analyse spectrale de l'écoulement de jeu se basant sur des données expérimentales. Elle s'est révélée capable de capturer plus précisément l'intensité et la position des phénomènes instationnaires rencontrés en tête du rotor, notamment le tourbillon de jeu. Les densités spectrales de puissance analysées montrent que cela est dû en partie à une meilleure prise en compte du transfert d'énergie des grandes vers les petites structures de l'écoulement avant leur dissipation. De plus, l'écart entre les approches s'accentue lorsque le tourbillon de jeu traverse le choc en tête.

Proche pompage, les effets d'interaction entre le choc, le tourbillon de jeu, la couche limite carter et le tourbillon venant de la tête de la RDE sont amplifiés. Le décollement de la couche limite carter s'accentue et une inversion locale de l'écoulement est observée. De plus, le tourbillon de jeu s'élargit et est dévié vers la pale adjacente, ce qui intensifie le phénomène de double écoulement de jeu.

L'interaction du tourbillon venant de la tête de la RDE avec le choc et le tourbillon de jeu du rotor est ensuite étudiée au point de dessin. Un battement du tourbillon de jeu est rencontré lors de l'interaction de ce tourbillon avec le tourbillon de tête de la RDE, ce qui diminue le double écoulement de jeu.

Mots clés : SIMULATION NUMERIQUE, RANS, LES, ZDES, ECOULEMENT DE JEU, COMPRESSEUR AXIAL, CREATE, DISTORSION AMONT, TOURBILLON DE JEU, DOUBLE ECOULEMENT DE JEU, INTERACTION SILLAGE TOURBILLON, VANNAGE

Contents

List of Figures

List of Tables

Nomenclature

Symbols

x''	Fluctuation (mass weighted average)
$\overline{x}$	Ensemble average
$\underline{\underline{x}}$	2^{nd} order tensor
$\underline{x}$	Vector - 1^{st} order tensor

Acronyms and abbreviations

BPF	Blade Passing Frequency of the IGV for rotor 1
CERFACS	Centre Européen de Recherche et de Formation Avancées en Calculs Scientifiques
CFD	Computational fluid dynamics
CIRT	Consortium Industrie Recherche en Turbomachine
CREATE	Compresseur de Recherche pour l'Étude des effets Aérodynamiques et TEchnologiques
DES	Detached Eddy Simulation
DNS	Direct Numerical Simulation
elsA	ensemble logiciel de simulation en Aérodynamique
IGV	Inlet Guide Vane
LDA	Laser Doppler Anemometry
LES	Large Eddy Simulation
LE/TE	Leading Edge / Trailing Edge
LMFA	Laboratoire de Mécanique des Fluides et d'Acoustique
ONERA	Office National d'Études et de Recherches Aérospatiales
PS	Pressure Side
Q	Mass flow rate
R1	Rotor 1
RANS	Reynolds Averaged Navier–Stokes
S1	Stator 1
SARC	Spalart-Allmaras turbulence model with curvature correction Spalart and Shur [160]

SA	Turbulence model from Spalart and Allmaras [162]
SS	Suction Side
T	Passage time period of IGV with respect to R1
URANS	Unsteady Reynolds Averaged Navier–Stokes
x^+ , y^+ , z^+	Normalized wall cell dimensions
ZDES	Zonal Detached Eddy Simulation

Introduction

Turbomachines are widely used in many different fields linked to energy conversion. They are built for domestic comfort with mechanical fans or blow-dryers, mass energy conversion in power plants from wind, water or nuclear power and ground, sea or air transportation. The efficiency of these rotating machines and the resulting energy saving is one of the main concern for the users. Among these turbomachines, axial compressors are key elements widely implemented due to their weak energy losses.

Due to structural constraints, there is a gap between the rotating blade tip of these compressor rotors and the casing. This can not be avoided and engineers have to take this element into account while designing new compressors. This tip gap leads to a tip-leakage flow from the pressure side to the suction side of the blade. The interaction of this secondary flow with the main stream, the annulus boundary layer developing on the shroud and the blade wakes leads to penalizing losses and thus a diminished energy efficiency. In order to understand the tip-leakage flow topology and behaviour numerous experimental tests have been carried out since the mid-20^{th} century and the pioneering work of Rains [135] and Herzig et al. [75]. They have identified the tip-leakage flow as one of the major loss generating mechanism in turbomachinery. However, despite the increasing knowledge around this phenomenon, predicting its behaviour for new configurations is a challenge for engineers. The tip-leakage flow is not an isolated mechanism but rather an accumulation of complex flows interacting with one another, for instance the mixing of the tip-leakage flow with wakes and vortices coming from upstream. As a consequence, the tip-leakage flow is rarely accurately simulated and important safety margins have to be set up. Thereby, this reduces the operability range of turbomachines. It is therefore important to understand the behaviour of this tip-leakage flow near surge. Furthermore, this lack of prediction accuracy limits the improvement of flow control devices that could even more decrease the negative impact of the tip-leakage flow on energy efficiency.

In order to take into account the tip-leakage flow while designing new compressors, different methods have been used up to now by engineers. First of all, they have developed empirical models to simulate the tip-leakage flow presence. Different models were proposed based on losses estimation, such as the work of Storer and Cumpsty [165], or with a more simple periodicity assumption, such as the Kirtley's model used by Chima [26]. Some other studies have tried to quantify the blockage effect of the tip clearance flow, such as the work of Khalid et al. [91]. These simplified models only simulate the main effects of the tip-leakage flow on the main flow, that is to say the losses from the mixing of flows of different direction but similar velocity. However their empirical approach, and the numerous hypothesis they are based on, narrows their scope of application to the simplest configurations and only at their design point.

Reynolds Averaged Navier-Stokes simulations (RANS) have the advantage of enabling the flow simulation of compressors even near surge. It is therefore possible to test and develop numerically new architectures before their validation on experimental test-rigs. Nonetheless, classic steady RANS simulations reach their limits when considering unsteady phenomena, such as the hub corner separation and the tip-leakage flow. One can notably cite the recent discussion from Sans et al. [149] with RANS compared to experimental unsteady probes.

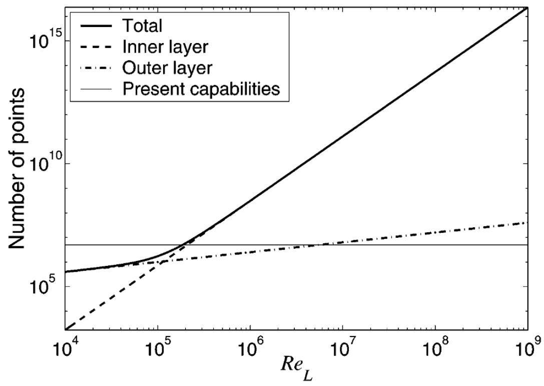

Figure 1 — *Number of grid points required to solve a boundary layer (from Piomelli and Balaras [133]).*

Unsteady RANS (URANS) approaches improved the simulation capability of RANS by adding the time variable. This widens RANS possibility range to the simulation of unsteady flows. Nevertheless, recent studies, in particular the one from Riou [143] or more recently Schoenweitz et al. [150], highlighted the lack of prediction of these simulations.

Direct Numerical Simulation (DNS) would be more likely to simulate the complex flows encountered in turbomachines, but the Reynolds numbers for the simulation of realistic configurations make them impossible for the current processing power. Large Eddy Simulation (LES), which is based on a spatiotemporal filtering of the Navier-Stokes equations, is more adapted than RANS to capture the vortices from the tip-leakage flow as shown by Boudet et al. [13]. In addition it has fewer mesh requirement constraints than DNS. However, its prohibitive cost to simulate high Reynolds number wall-bounded flows limits its actual use to academic low Reynolds number configurations and will not be ready for industrial applications before 2045, as estimated by Spalart [158]. This is one of the major issue of computational fluid dynamics. Most of the flow problems involves walls, and wall-bounded flows are difficult to simulate accurately with DNS or even LES because of the boundary layer mesh requirements which depend on the Reynolds number. Indeed, figure 1 shows the requirements in terms of grid point number to solve the inner and outer layers as a function of the Reynolds number.

This led researchers to consider hybrid methods with LES and RANS to bring the best of both worlds. RANS is used for the high mesh requirement zones, the boundary layers, and LES is used for regions far from walls. The Detached Eddy Simulation (DES) from Spalart et al. [163] is one of these hybrid URANS/LES methods. The transition from RANS to LES is continuous in DES and does not demand any additional constraint on the interface. Thus, this is a global method which is adapted to massively separated flows, especially the tip-leakage flow. Although limitations of the DES method have been emphasized by Spalart et al. [163] as soon as the method was thought, it has brought clear improvements over URANS in many applications [159]. Its main drawback occurs when the method switches from RANS to LES too early in a boundary layer development. When an inadequate mesh is used the method may lead to a modelled stress depletion (MSD). MSD may bring about artificial boundary layer separation, which is unphysical. An improvement of the method is the Delayed DES (DDES) proposed by Spalart et al. [161]. On the one hand, it protects the boundary layer by forcing RANS mode in it, which avoids MSD. On the other hand, as it was shown by Deck [38], DDES may delay too much the separation. This is the case for configurations such as a forward step, where the separation is fixed by the geometry. Other improvements to the DDES are still being developed in order to reach a single model capable to simulate any configuration. Some of these methods have proved to be efficient in the tip-leakage flow simulation as recently presented by Shi and Fu [151]. Nevertheless, as explained by Tyacke et al. [167, 168], the "expectation of producing a single modelling strategy that will work effectively and reliably for all engine zones is unrealistic". That is the reason why Zonal DES (ZDES) was developed by Deck [38]. Zonal Detached Eddy Simulation is a global URANS/LES

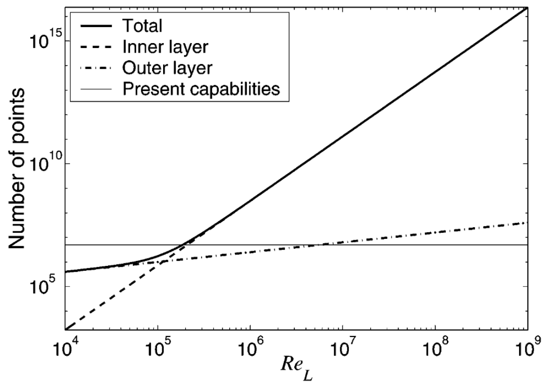

Figure 1 — *Number of grid points required to solve a boundary layer (from Piomelli and Balaras [133]).*

Unsteady RANS (URANS) approaches improved the simulation capability of RANS by adding the time variable. This widens RANS possibility range to the simulation of unsteady flows. Nevertheless, recent studies, in particular the one from Riou [143] or more recently Schoenweitz et al. [150], highlighted the lack of prediction of these simulations.

Direct Numerical Simulation (DNS) would be more likely to simulate the complex flows encountered in turbomachines, but the Reynolds numbers for the simulation of realistic configurations make them impossible for the current processing power. Large Eddy Simulation (LES), which is based on a spatiotemporal filtering of the Navier-Stokes equations, is more adapted than RANS to capture the vortices from the tip-leakage flow as shown by Boudet et al. [13]. In addition it has fewer mesh requirement constraints than DNS. However, its prohibitive cost to simulate high Reynolds number wall-bounded flows limits its actual use to academic low Reynolds number configurations and will not be ready for industrial applications before 2045, as estimated by Spalart [158]. This is one of the major issue of computational fluid dynamics. Most of the flow problems involves walls, and wall-bounded flows are difficult to simulate accurately with DNS or even LES because of the boundary layer mesh requirements which depend on the Reynolds number. Indeed, figure 1 shows the requirements in terms of grid point number to solve the inner and outer layers as a function of the Reynolds number.

This led researchers to consider hybrid methods with LES and RANS to bring the best of both worlds. RANS is used for the high mesh requirement zones, the boundary layers, and LES is used for regions far from walls. The Detached Eddy Simulation (DES) from Spalart et al. [163] is one of these hybrid URANS/LES methods. The transition from RANS to LES is continuous in DES and does not demand any additional constraint on the interface. Thus, this is a global method which is adapted to massively separated flows, especially the tip-leakage flow. Although limitations of the DES method have been emphasized by Spalart et al. [163] as soon as the method was thought, it has brought clear improvements over URANS in many applications [159]. Its main drawback occurs when the method switches from RANS to LES too early in a boundary layer development. When an inadequate mesh is used the method may lead to a modelled stress depletion (MSD). MSD may bring about artificial boundary layer separation, which is unphysical. An improvement of the method is the Delayed DES (DDES) proposed by Spalart et al. [161]. On the one hand, it protects the boundary layer by forcing RANS mode in it, which avoids MSD. On the other hand, as it was shown by Deck [38], DDES may delay too much the separation. This is the case for configurations such as a forward step, where the separation is fixed by the geometry. Other improvements to the DDES are still being developed in order to reach a single model capable to simulate any configuration. Some of these methods have proved to be efficient in the tip-leakage flow simulation as recently presented by Shi and Fu [151]. Nevertheless, as explained by Tyacke et al. [167, 168], the "expectation of producing a single modelling strategy that will work effectively and reliably for all engine zones is unrealistic". That is the reason why Zonal DES (ZDES) was developed by Deck [38]. Zonal Detached Eddy Simulation is a global URANS/LES

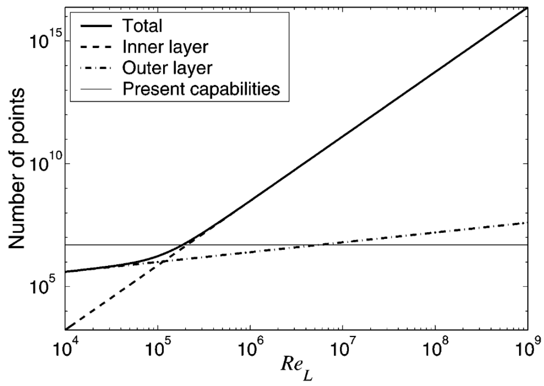

Figure 1 — *Number of grid points required to solve a boundary layer (from Piomelli and Balaras [133]).*

Unsteady RANS (URANS) approaches improved the simulation capability of RANS by adding the time variable. This widens RANS possibility range to the simulation of unsteady flows. Nevertheless, recent studies, in particular the one from Riou [143] or more recently Schoenweitz et al. [150], highlighted the lack of prediction of these simulations.

Direct Numerical Simulation (DNS) would be more likely to simulate the complex flows encountered in turbomachines, but the Reynolds numbers for the simulation of realistic configurations make them impossible for the current processing power. Large Eddy Simulation (LES), which is based on a spatiotemporal filtering of the Navier-Stokes equations, is more adapted than RANS to capture the vortices from the tip-leakage flow as shown by Boudet et al. [13]. In addition it has fewer mesh requirement constraints than DNS. However, its prohibitive cost to simulate high Reynolds number wall-bounded flows limits its actual use to academic low Reynolds number configurations and will not be ready for industrial applications before 2045, as estimated by Spalart [158]. This is one of the major issue of computational fluid dynamics. Most of the flow problems involves walls, and wall-bounded flows are difficult to simulate accurately with DNS or even LES because of the boundary layer mesh requirements which depend on the Reynolds number. Indeed, figure 1 shows the requirements in terms of grid point number to solve the inner and outer layers as a function of the Reynolds number.

This led researchers to consider hybrid methods with LES and RANS to bring the best of both worlds. RANS is used for the high mesh requirement zones, the boundary layers, and LES is used for regions far from walls. The Detached Eddy Simulation (DES) from Spalart et al. [163] is one of these hybrid URANS/LES methods. The transition from RANS to LES is continuous in DES and does not demand any additional constraint on the interface. Thus, this is a global method which is adapted to massively separated flows, especially the tip-leakage flow. Although limitations of the DES method have been emphasized by Spalart et al. [163] as soon as the method was thought, it has brought clear improvements over URANS in many applications [159]. Its main drawback occurs when the method switches from RANS to LES too early in a boundary layer development. When an inadequate mesh is used the method may lead to a modelled stress depletion (MSD). MSD may bring about artificial boundary layer separation, which is unphysical. An improvement of the method is the Delayed DES (DDES) proposed by Spalart et al. [161]. On the one hand, it protects the boundary layer by forcing RANS mode in it, which avoids MSD. On the other hand, as it was shown by Deck [38], DDES may delay too much the separation. This is the case for configurations such as a forward step, where the separation is fixed by the geometry. Other improvements to the DDES are still being developed in order to reach a single model capable to simulate any configuration. Some of these methods have proved to be efficient in the tip-leakage flow simulation as recently presented by Shi and Fu [151]. Nevertheless, as explained by Tyacke et al. [167, 168], the "expectation of producing a single modelling strategy that will work effectively and reliably for all engine zones is unrealistic". That is the reason why Zonal DES (ZDES) was developed by Deck [38]. Zonal Detached Eddy Simulation is a global URANS/LES

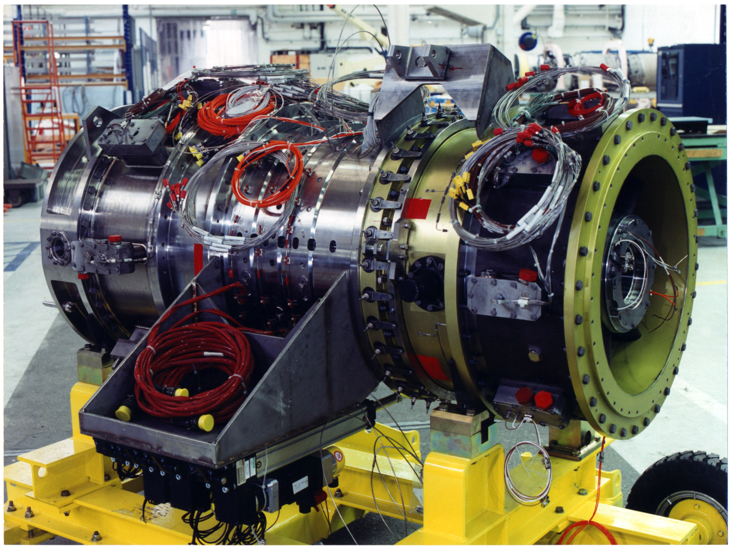

Figure 2 — *The CREATE axial compressor.*

approach like standard DES. Furthermore, it brings a zonal approach so that each flow zone can be solved with the most adapted method. ZDES revealed to be suitable to accurately simulate many different flow configurations, from the simulation of an aircraft [17, 18], to jet [25], base flows [171, 154], and even to the flow control on a missile fin [144]. However, it was not yet evaluated in turbomachinery.

In conclusion, the tools available for the simulation of the tip-leakage flow are numerous. Some are fast and relatively affordable, hence their wide spread in the industry, but their simulation capability is limited for complex flows. By contrast, others are accurate but unfortunately expensive and impossible to use nowadays on realistic configurations due to important computational power requirements. The conception of efficient turbomachines with a wide operability demands to have both an accurate and affordable method. To that purpose, hybrid URANS/LES methods seem to be the best option in the medium term.

This thesis work is carried out so as to appraise what modern advanced numerical methods can bring to the simulation and understanding of the tip-leakage flow. Thus, the present study aims at evaluating the Zonal Detached Eddy Simulation for the simulation of the tip-leakage flow on a realistic configuration and highlighting the physics behind this flow. To that end, the effects of the throttle and the effects of the distortions coming from the Inlet Guide Vane will be considered.

This study is split into three parts.

In a first part, chapter 1 reviews the literature of the tip-leakage flow and the methods to simulate it. Then, chapter 2 explains the techniques based on which the study is conducted along with a description of the experimental test rig.

In a second part, the process consists of the choice of the ZDES as the advanced numerical method, as well as its implementation and evaluation for the simulation of the tip-leakage flow on a realistic axial compressor. In chapter 3, the ZDES is chosen and a numerical test bench is defined. This test bench is built with a view to evaluating the capability of the ZDES method to simulate the tip-leakage flow on the first rotor (R1) of the axial compressor CREATE, presented in figure 2, while taking into account the effects of the Inlet Guide Vane (IGV) and throttle. Being both realistic and well instrumented, CREATE is well suited for code evaluation, and in our case, for the ZDES. One important aspect of this study is that the same numerical test bench, based on ZDES mesh requirements, is then used for the different computations at the design point which are compared. In chapter 4, the capability of the ZDES method to simulate the tip-leakage flow is then evaluated on this numerical test bench following the levels of

grade	level of validation
1	integral forces (lift, drag and pitch)
2	mean aerodynamic field (velocity or pressure profiles)
3	second-order statistics (r.m.s. quantities)
4	one-point spectral analysis (power spectral densities)
5	two-point spectral analysis (correlation, coherence and phase spectra)
6	high-order and time–frequency analysis (time–frequency, bicoherence spectra)

Table 1 — *Validation levels, from Sagaut & Deck [146]*

validation of simulation techniques from Sagaut and Deck [146], detailed in table 1, up to level 4, that is to say one-point spectral analysis. The numerical results are then compared to experimental data from pressure probes and Laser Doppler Anemometry. ZDES is set against URANS so as to understand what distinguishes the two approaches in terms of simulation capability of the tip-leakage flow.

Once the ZDES method is validated, it is then applied to understand the physics of the tip-leakage flow in the third part of the study. In chapter 5, the behaviour of the tip-leakage flow near surge is investigated by analysing two ZDES computations. Two different operating points are compared, one at peak efficiency and one near surge. The configuration near surge is set by adapting the inlet cartography and outlet pressure from the numerical test bench defined at design point in chapter 3. The tip-leakage vortex growth and its influence on the whole tip-leakage flow topology is then analysed.

In chapter 6, the effects of distortions coming from the IGV on the tip-leakage flow are analysed. Two ZDES computations are compared. The first one has a rotating distortion cartography as inlet boundary condition. On the contrary, the same cartography is azimuthally averaged for the second computation. As a consequence, the influence on the tip-leakage flow of the arrival of the IGV distortion, and in particular the IGV tip vortex, stands out in these comparisons. The phenomenon of double tip-leakage flow observed in axial compressors is then discussed.

Finally, the first appendix deals with the influence, in the preliminary study, of the simulated gap size for the Inlet Guide Vane on the flow field used as inlet condition in the numerical test bench, at section 25A. The second appendix presents the influence on the flow field at section 25A of the turbulence model as well as the numerical schemes used in the preliminary study.

First part

Literature, apparatus and techniques

This first part presents a review of the literature concerning the tip-leakage flow and its simulation, the different numerical techniques applied in this study and an overview of the experimental test rig and its instrumentation.

Chapter 1 Literature

Contents

This chapter gives an overview of the literature concerning the tip-leakage flow and the ways to simulate it. Moreover, it presents studies that used the Zonal Detached Eddy Simulation approach in configurations relevant for the simulation of the tip-leakage flow.

1.1 Tip clearance flow physics

This section deals with the physics of the tip-leakage flow within compressor rotors. It does not pretend to be exhaustive but to give an overview of this secondary flow.

1.1.1 Turbomachinery overview

Before presenting the tip-leakage flow physics, one has to consider the turbomachinery field. A turbomachine is a device that transfers energy from or to a fluid, liquid or gas, by the mean of moving blades. Indeed, when the flow impacts a rotating blade, this blade does a positive or negative work on the fluid and therefore changes its stagnation enthalpy (Euler theorem). They can be divided into two categories: the turbines and the compressors. When the energy is extracted from the fluid, the system is called a turbine, such as windmills. By opposition, if the energy is brought to the fluid, the system is a

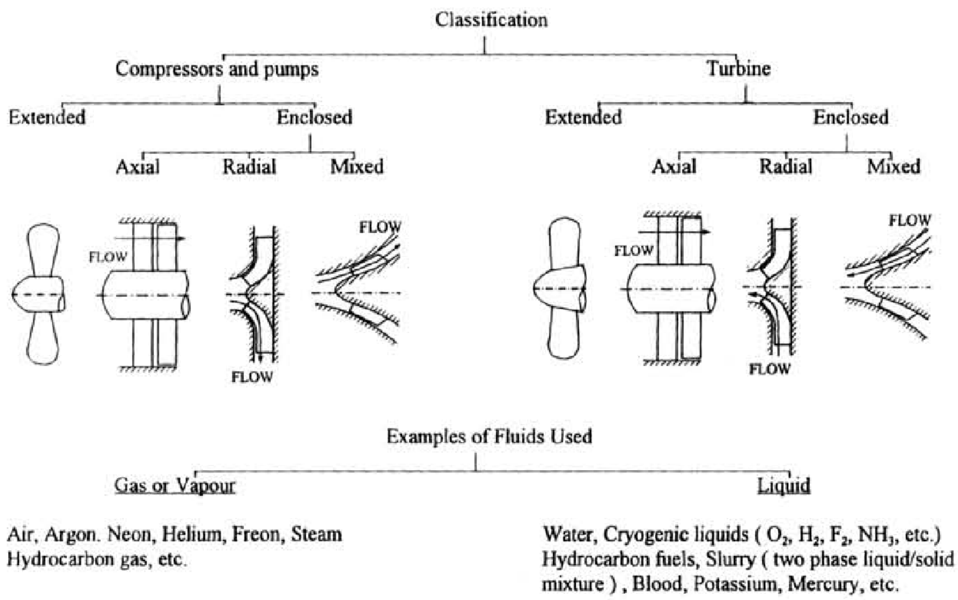

Figure 1.1 — *Classification of turbomachinery (from Lakshminarayana [96]).*

compressor, such as the pumps. The possibilities of turbomachines application are numerous. Therefore they are used in many different configurations linked to energy conversion. Some are *open*, or extended, and thus influence a wide, not quantifiable, area around them. Others are *shrouded*, that is to say, enclosed by a casing.

Depending on the expected service of the machine, that is to say the required pressure ratio and mass flow rate through the cascade, different configurations, presented in figure 1.1, best suit the operating condition. Thereby, depending on how the flow crosses the rotor, the denomination of the machine changes. It is regarded as axial if the through-flow is parallel to the axis of rotation, which is used in high mass flow rate configurations. The machine is considered as radial if the through-flow is perpendicular to the axis of rotation, which is used for compact high pressure ratio configurations. An infinite number of possibilities exists in between, and the resulting machines are then called mixed-flow turbomachines. If a higher pressure ratio is required between the inlet of the machine and its outlet, many rotor stages are mounted in series.

The rotating motion of rotor blades increases the swirl of the fluid. In order to correct the fluid deflection for the next rotor stage, stator blades are implemented in between the stages of rotor blades. This addition of stages increases the complexity of the flow through the turbomachine. For instance, there are interactions between the rotors and the stators that modify the structure of the flow. Besides, the additional stages increase the weight of the compressor. It is however possible to avoid this stator stage with the use of counter rotating rotors. However, this is for the moment only done in few configurations, for instance in Counter Rotating Open Rotors (CROR) or contrafans, due to the higher design constraints it implies.

These two types of blades, rotating for the rotors and steady for the stators lead to two different ways to consider the flow within a turbomachine: with absolute or relative values. As a consequence, there are two frames of reference linked to the stators or rotors. For the rotors, some values in the relative frame of reference differ from the ones in the absolute due to the rotation of the blade. In order to understand this concept, the velocity triangles are used as presented in figure 1.2. The angles defined in the absolute, α, and relative, β, frames of reference are detailed in equation I-1. U is the rotating velocity of the rotor. The velocity V_θ and W_θ are respectively the circumferential velocities in the absolute and relative, or more accurately rotating, frame of reference. The velocities V and W are their meridian counterparts, that is to say, the addition of the axial and radial velocities. The angle between the axial, V_x, and meridian

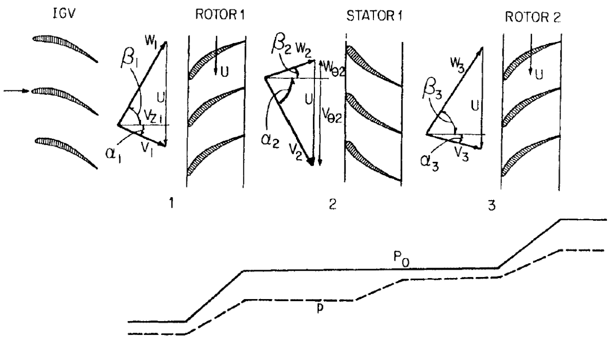

Figure 1.2 — *Velocity triangles in an axial compressor (from Lakshminarayana [96]). The distributions of enthalpy and temperature are similar to the pressure distribution p. The distributions of stagnation enthalpy and temperature are similar to the stagnation pressure distribution P_0.*

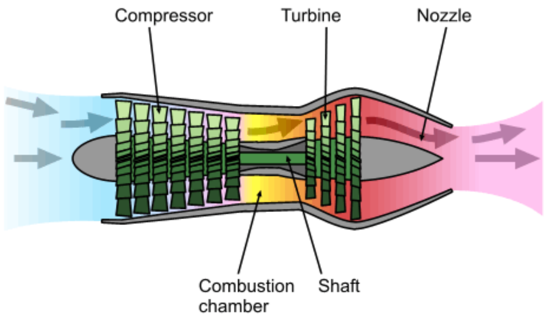

Figure 1.3 — *Axial turbojet engine [51]*

velocity, V_m, is called ϕ, the meridian angle, defined in equation I-2.

$$\alpha = \text{atan}\left(\frac{V_\theta}{V_m}\right) \qquad \beta = \text{atan}\left(\frac{W_\theta}{V_m}\right) \tag{I-1}$$

$$\phi = \text{atan}\left(\frac{V_x}{V_m}\right) \tag{I-2}$$

In aeronautics, turbomachines are used for propulsion systems, such as propellers (open) or turbojet engines (shrouded). In turbojet engines, there are both compressors and turbines as presented in figure 1.3, with many stages. The purpose of the compressor is to transfer the energy from a rotating shaft to the air and thus to rise its pressure. Then, the flow reaches the combustion chamber and is mixed with fuel. It is then burned and therefore its energy increases. The hot fuel-air mix expands and exits the combustion chamber. At the outlet, the turbine extracts a part of the energy of this hot fluid, which decreases its pressure and temperature. This energy is then provided to the compressor through the shaft. Then, the fluid reaches the nozzle, where it is accelerated and given the appropriate direction. Finally, the fluid exits the whole system with a higher pressure and velocity, which produces the thrust necessary for the plane to overcome the drag and therefore to fly.

1.1.2 Operating points

In order to have an efficient energy transfer to the fluid in compressors, the flow must be guided smoothly through the rotor and stator stages of the machine. Moreover, the compressors are very sensitive to the flow angle at the leading edge of the blade. This is the reason why the stators guide the flow

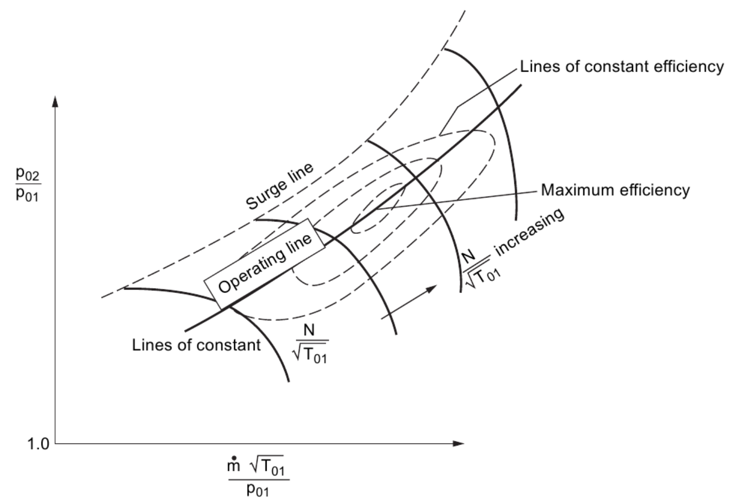

Figure 1.4 — *Performance map of a compressor (from Dixon [45]).*

between the rotor stages so that it reaches the rotor blade with an expected angle, defined in the design step for a good performance of the machine. For a given rotational speed of the shaft, different mass flow rate are possible, which changes the axial component of the velocity and thus the flow angles. Likewise, if the rotational speed changes, the angles change. Therefore, some stators can have a variable stagger to adapt to these different angles. This is often the case for the Inlet Guide Vane (IGV), which is the first stator upstream the first rotor of a compressor.

These different flow configurations define the operating range of the machine, characterized by a performance map, as shown in figure 1.4. It represents the total pressure rise in function of the flow rate.

If the mass flow rate is increased, it reaches a limit due to the inception of a shock downstream of the compressor at its narrowest section. This gives the choke limit in the right part of the map. With the same rotational speed of the shaft, if the mass flow rate is decreased, the operating point moves on an iso speed line. Then, it reaches the position where the efficiency is the highest for this rotational speed, this is the peak efficiency operating point, which is often the design point. With a lower mass flow rate, the efficiency begins to decrease. However, the pressure ratio keeps on increasing. The limiting factor is the amplification of the effects of secondary flows and massive separations. This results in a rotating stall, first near the tip of the channel. It is nevertheless important to keep in mind that in some configurations the instability can be caused by the separation of the flow near the hub. The rotating stall induces a flow blockage at the tip which increases the flow speed at the hub. Then the width of the stall cells increases up to the whole span-width. This massive blockage brings about the surge, that is to say, an axial instability characterized by a low frequency oscillation of the mass flow rate. This phenomenon was studied by de Crécy et al. [32] on the CREATE compressor. At this stage, the energy transferred from the rotor blades to the flow is not sufficient to withstand the strong pressure gradient within the machine. The operating condition where the rotor becomes unstable is the surge limit. Beyond this line, there are strong pressure fluctuations and even an inversion of the flow. These effects are destructive for the turbomachine, thereby engineers define a safety margin, also called surge margin, to avoid that the compressor works beyond this surge line.

As a consequence, it is a necessity in the design of new compressors to know the behaviour of the machine near the surge line. To this end, the numerical simulation is often used to define the performance map of the compressor. It was nevertheless proven that the method retained to carry out these simulations influence the numerical surge limit. Indeed, recent studies with the Reynolds-averaged Navier-Stokes (RANS) approach by Marty et al. [111, 112] have shown a strong dependence of the surge margin to the turbulence model used, as presented in figure 1.5. This comparison is done on the first rotor of

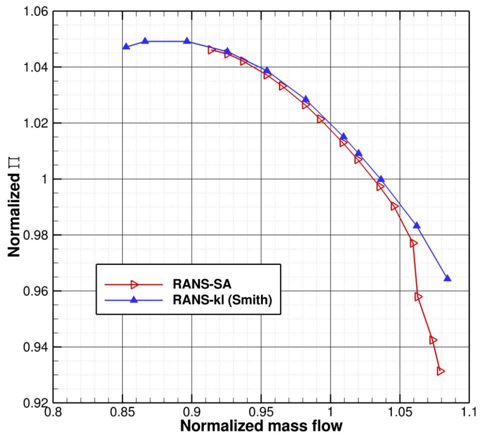

Figure 1.5 — *Surge margin difference between k-l Smith and Spalart-Allmaras turbulence models on the CREATE compressor (Courteously from J. Marty).*

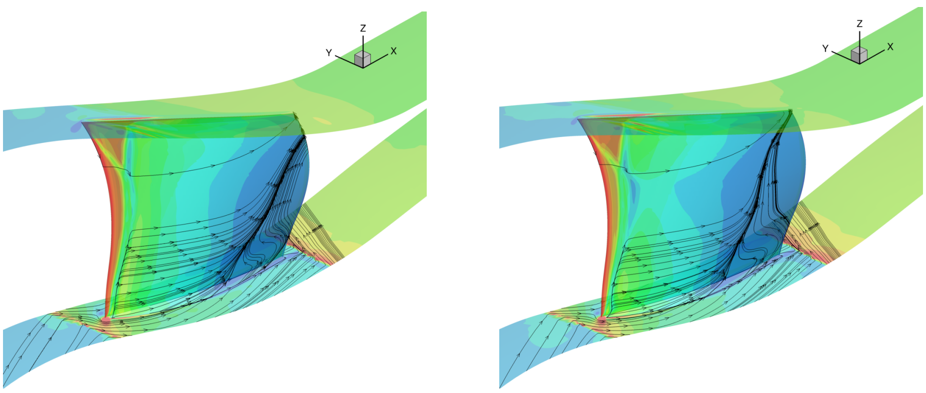

(a) k-l Smith.

(b) Spalart-Allmaras.

Figure 1.6 — *Friction lines on the first rotor of the CREATE compressor near surge (Courteously from J. Marty).*

the CREATE compressor with two turbulence models: the Spalart-Allmaras (RANS-SA) [162] and the k-l model from Smith [156]. This study underlined that the Spalart-Allmaras turbulence model was more unstable than the k-l model from Smith near the surge line. If the Spalart-Allmaras model is used for turbomachinery design, the computed surge margin is then different which leads to a narrower operability range seen by the computation due to the numerical instability. The reason, underscored by Marty, is a more important flow separation at the hub corner with the Spalart-Allmaras turbulence model than with the k-l Smith model, which is not physical and induced by the numerics. This separation difference is visible for computations near surge, in figure 1.6 where the separation line reaches the trailing edge at the blade tip in the Spalart-Allmaras case, contrary to the one with the k-l Smith model. This discrepancy between the methods highlights the difficulty to simulate accurately the secondary flows in the compressor. The tip-leakage flow is one of them.

1.1.3 General principles of the tip-leakage flow

1.1.3.1 A three dimensional flow

In shrouded axial compressors, there is a gap between a rotating blade tip and the annulus wall. The pressure field around a blade implies a pressure gradient between the two sides of the blade. This pressure

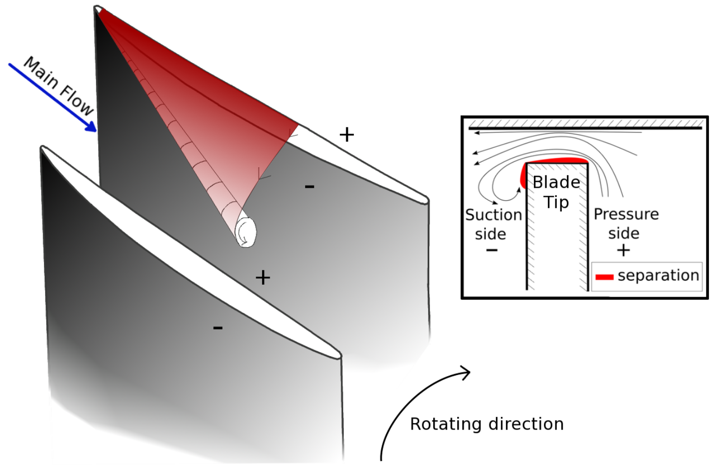

Figure 1.7 — *Inception of the tip-leakage flow and rolling up of the main tip-leakage vortex (Inspired by Lakshminarayana et al. [99]).*

difference leads to a leakage flow from the pressure side to the suction side of the blade, as shown in figure 1.7. The flow then leaks through the clearance following the chordwise pressure distribution. This phenomenon is mainly inviscid as noted by Lakshminarayana and Horlock [97]. Then, it exits the clearance and mixes with the main flow.

The interaction of this secondary flow with the main stream, the annulus boundary layer developing on the shroud and the blade wakes leads to penalizing losses as already mentioned by Herzig et al. [75] in 1954. The shear layer, which stems from the direction difference between the leakage flow and the main stream, is the main loss mechanism in the casing region. By contrast, the non-uniform mixing zone downstream of the blade contributes a little to the whole pressure loss as underlined by Storer and Cumpsty [165]. Therefore designing efficient compressors requires an accurate prediction of the tip-leakage flow and its development.

1.1.3.2 Flow topology near the casing

There are many different configurations of tip-leakage flows depending on the type of turbomachinery. Moreover, the topology in the vicinity of the shroud can be very different.

One of the major encountered phenomenon is the main tip-leakage vortex. When the leakage flow exits the tip gap and mixes with the main flow, it undergoes a loss of circumferential momentum. This results in the rolling up of this jet flow into the main tip-leakage vortex. Nevertheless, in some studies, such rolling up is not experienced, partially or totally. For instance, Furukawa et al. [54] investigated with a RANS simulation a low speed isolated axial compressor rotor with moderate loading and a tip gap height of 1.7% of the chord length. At a low flow rate, they captured a breakdown of the vortex. Nevertheless, downstream of this breakdown, the low streamwise vorticity prevents the flow from rolling up into a vortex again. A case with no rolling up at all was studied by Lakshminarayana et al. [100] on an experimental single stage axial compressor made up of an Inlet Guide Vane (IGV), a rotor and a stator. The tip gap height of the rotor is 2.27% of the chord. The reasons proposed by the authors to explain why the flow did not roll up are that the inlet swirl, high turbulence and high blade loading cause an intense mixing of the leakage jet and therefore prevent the flow from rolling up. In their configuration, the leakage flow high velocity makes it mix rapidly with the main flow. Lakshminarayana et al. [100] underscore that the difference of magnitude and direction of the leakage jet flow and main stream are among the main effects preventing the rolling up. One have to mention here the major importance of the

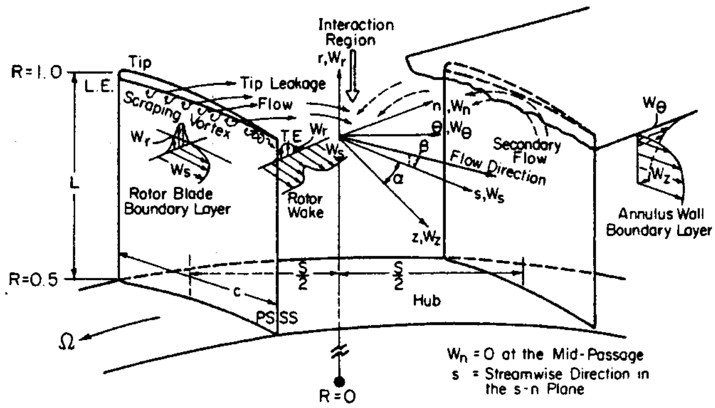

Figure 1.8 — *Secondary flows near the casing (from Lakshminarayana and Ravindranath [98]).*

gap size in the vortex inception, indeed, for the smallest clearances, there is no vortex as shown by Rains [135].

Beyond the fact that there are configurations without rolling up, it is relevant to note that there is a different behaviour of the leakage flow depending on the test case: rotor or linear cascade. Indeed, there are different types of test cases used to analyse the tip-leakage flow. For practical reasons, especially considering the implementation of measuring techniques within the flow field, the test configurations are more or less representative of the real flow occurring in a turbomachine. One of the frequently used test case is the linear cascade. This comprises blades attached to a flat wall. The main advantage is that a wider range of instrumentations can be used on such cases, they can be switched more easily and rapidly to suit different experimental campaigns. In addition, different flow control devices can be evaluated in such facilities, as done by Bae et al. [3]. The variation of the tip gap height is possible without making the rest of the flow field change drastically [87, 88]. Furthermore, linear cascades enable a more accurate control of the flow arriving on the blades, such as the boundary layer thickness or the turbulence characteristics as done by de la Riva et al. [33] and Muthanna and Devenport [122]. These simple configurations are often used for first validations of advanced numerical methods [12]. In order to take into account the relative motion of the rotor blade tip against the endwall, a moving belt facility is often used within the wind tunnel, as in the Virginia Tech cascade wind tunnel [122, 83]. Nonetheless, the flow velocity in the radial direction within real turbomachines is therefore not taken into account with linear cascades. Therefore, there are more realistic test configurations with rotating single or multistages compressors.

In such configurations, the phenomena occurring near the casing are numerous due to the different secondary flows affecting the main axial flow. Besides, the 3D flows near the hub, such as the corner effect, impact on the loads distribution, and thereby change the triangulation at the rotor tip. An overview of the casing secondary flows is given in figure 1.8. There are many interactions between these phenomena, hence the difficulty to capture all of them. For instance, the scraping vortex on the pressure side of the blade has an effect on the flow passing through the tip clearance and thus on the tip-leakage flow inception. The 3D radial flow arriving to the shroud from the pressure side of the blade slows down the tip-leakage vortex migration towards the adjacent blade. The rotor wakes can mix with the tip vortex downstream. Finally, one important and even major interaction is the one with the boundary layers, especially the one developing on the shroud. This seems to be partially responsible for the separation at the casing and the flow blockage as described numerically with a URANS approach by Gourdain and Leboeuf [64] on the CME2 compressor geometry.

These observations are relevant to comprehend the flow structure around the tip gap. However, others have tried to better understand what occurs in the gap itself. Based on experimental observations on a linear cascade, Bindon [11] conceptualized the flow within the gap, as shown in figure 1.9. In this

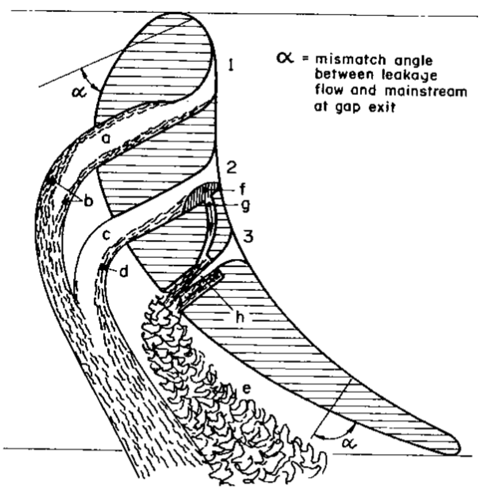

Figure 1.9 — *Conceptual model showing various types of flow active in the tip clearance region (from Bindon [11]).*

conceptual model, Bindon [11] underscores that there is not a single flow pattern leaking through the gap. Instead of a linearly spread leakage, he hypothesized that there are different kinds of channels with and without separation bubbles within the gap. The axial position of these different channels depending on the pressure distribution along the chord, and thus the loading. Kang and Hirsch [87] saw similar channels in the tip gap on a linear cascade with a stationary endwall. With paint-trace visualizations on the endwall, Kang and Hirsch [87] highlighted the flow pattern drawn in the tip clearance, shown in figure 1.10. The skin friction line splits into two branches at a saddle point in front of the leading edge. This results in a horseshoe vortex. The tip-leakage vortex starts to roll-up just downstream the leading edge in the suction side. They pointed out that streamlines in the gap are neither normal to the suction side nor to the camber line, contrary to what was assumed by Rains [135].

1.1.4 Influence of the gap size on the tip-leakage flow

The most important parameter to take into account for the tip-leakage flow is the gap size. As expected, it is the main factor that influences the flow topology at the rotor tip. In order to compare the different configurations, it is then a prerequisite to define a dimensionless value to characterize this parameter. It requires then another length. Two dimensionless terms are built depending on the use of the axial chord or the maximum thickness of the blade tip. They are respectively defined in equations [I-3] and [I-4].

$$\tau = \frac{GapSize}{AxialChord} \tag{I-3}$$

$$\lambda = \frac{GapSize}{MaximumBladeThickness} \tag{I-4}$$

Rains [135] studied experimentally the gap size effects on a rotor at 1750rpm and showed that the leakage flow can be regarded, in a first assumption, as an inviscid phenomenon driven only by the pressure difference for large λ values, and the vortex structure is predominant. In Rains' studied installation, for small ratio between gap size and blade thickness the gap flow was modelled as a channelled flow. For $\lambda = 0.026$ and lower there were no vortex rolling-up. For $\lambda < 0.05$, viscous forces were dominant in the clearance and at $\lambda = 0.1$, the counter pressure effects of the viscosity in the gap were counterbalanced by the lift of the blade. The viscous effects could be neglected for $\lambda >> 0.1$. Finally, beyond

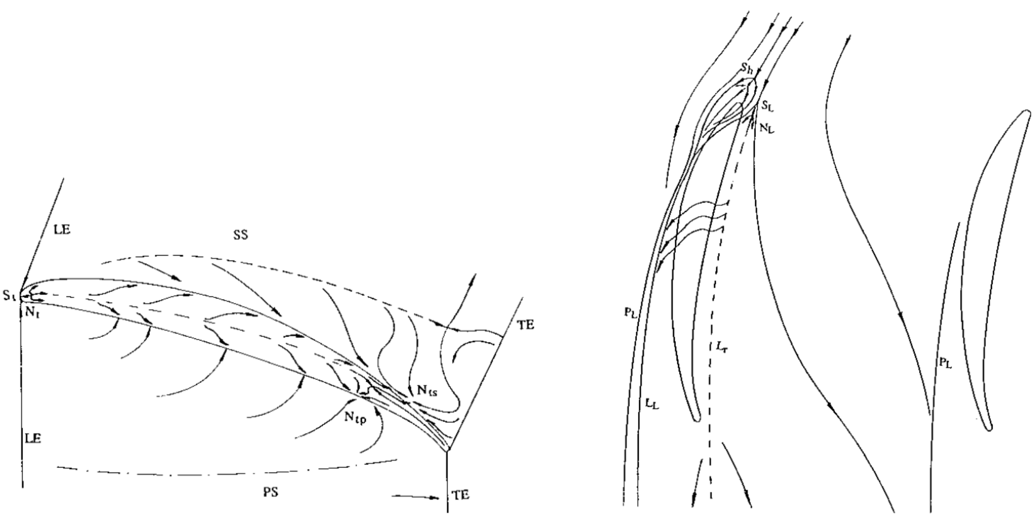

(a) Blade tip. (b) Casing.

Figure 1.10 — *Schematic of flow pattern on the blade tip and on the casing (from Kang and Hirsch [87]).*

$\lambda = 0.167$, a potential flow pressure distribution was established. Rains [135] developed then a model to take into account the tip-leakage flow changes depending on the tip clearance size and based on the number $\lambda^2 \cdot Re \cdot \epsilon$. Re is the Reynolds number based on the free stream velocity and $\epsilon = \frac{\tau}{\lambda}$ is the maximum thickness to chord ratio at the blade tip. He highlighted that viscous forces are predominant for $\lambda^2 \cdot Re \cdot \epsilon < 11$ whilst the inertia forces are predominant for $\lambda^2 \cdot Re \cdot \epsilon > 125$.

More recently, Brion [16] analysed experimentally two configurations: a split wing (NACA0012) configuration generating a vortex pair and the same with a splitter plane. This latter configuration is similar to an isolated fixed linear cascade. The first aim was to study the vortex instability and the influence of the Crow instability [28, 29] which is linked to the interaction between two vortices. Brion [16] observed that for small gaps with $\tau < 2\%$, the flow is nearly perpendicular to the chord which means that it is channelled by the gap and the vortex forms far from the wing and near the hub, which is similar to what Rains saw for small gaps. For $\tau > 2\%$, the vortex remains close to the wing. Thereby, it was shown in the literature that the gap size influences the tip-leakage vortex behaviour. Furthermore, this parameter affects the whole flow topology. For instance, Kang and Hirsch [87, 88] studied the flow field for a linear cascade with 1.0%, 2% and 3.3% gap sizes. The aforementioned horseshoe vortex they detected was only observed for small clearance.

The different flow topologies induced by the different gap sizes imply different losses too. Smith [157] presented experimental data gathered from different studies to understand the effects of the tip gap size. The peak pressure rise for the blade was found to be inversely proportional to the tip gap size τ as presented in figure 1.11. The impact appeared to be 4% of pressure loss for each 1% increase in the dimensionless gap size τ. Bindon [11] analysed the loss in a turbine cascade and highlighted that the loss varies linearly with gap size as shown in figure 1.12. However, there are fundamental differences with and without clearance, and even the smallest gap size changes the loss. He found that the total tip clearance loss is made up of the internal gap loss (39%), the suction corner mixing loss (48%) and endwall/secondary loss (13%) as presented in figure 1.13. Even if these results from Bindon are for turbines, some similarities are found with compressors concerning the tip-leakage flow topology [87], as previously explained.

The main solution found to reduce this negative impact of the leakage flow is to reduce the gap size. This is the reason why abradable material is used on the housing of the compressors used in the industry.

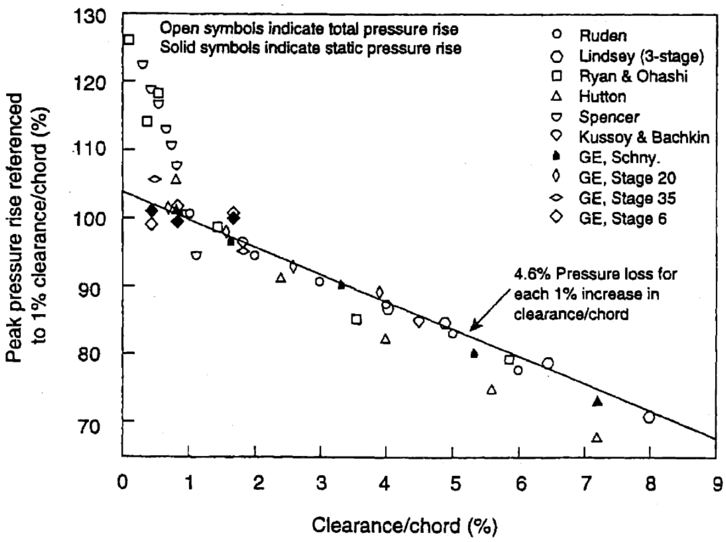

Figure 1.11 — *Effect of tip clearance on peak pressure rise (original data from Smith [157], extracted from Bae [2]).*

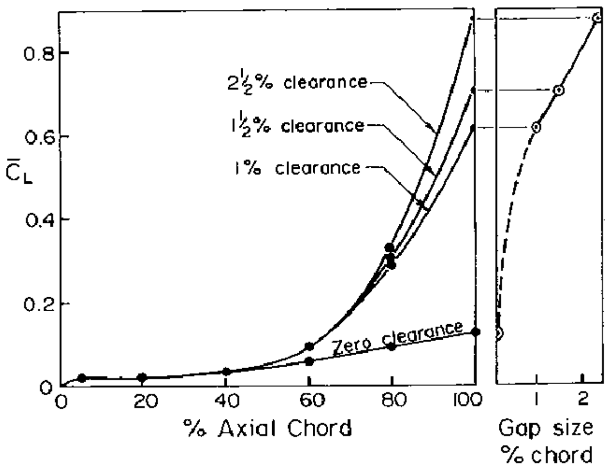

Figure 1.12 — *The growth of total integrated loss coefficient from leading to trailing edge for various values of tip clearance gap size (from Bindon [11]).*

When the rotor rotates, its radial length is increased due to the centrifugal forces. As a consequence, the tip of the blade touches the casing. The resulting friction wears then a part of the abradable material away so that the tip gap size is as small as possible. Another possibility is to reduce the gap size artificially with flow control devices. For instance Bae [2] analysed the effects of synthetic jet actuators located in the tip gap on the vortex flow for a linear cascade. The device reduced the gap size by deflecting the streamline, enhanced the mixing, reduced the influence of the vortex and increased the exit static pressure. Nevertheless, the different flow structure due to the linear cascade prevented to judge the possibilities on a real rotor. Figure 1.14 presents how it could be implemented on a rotor.

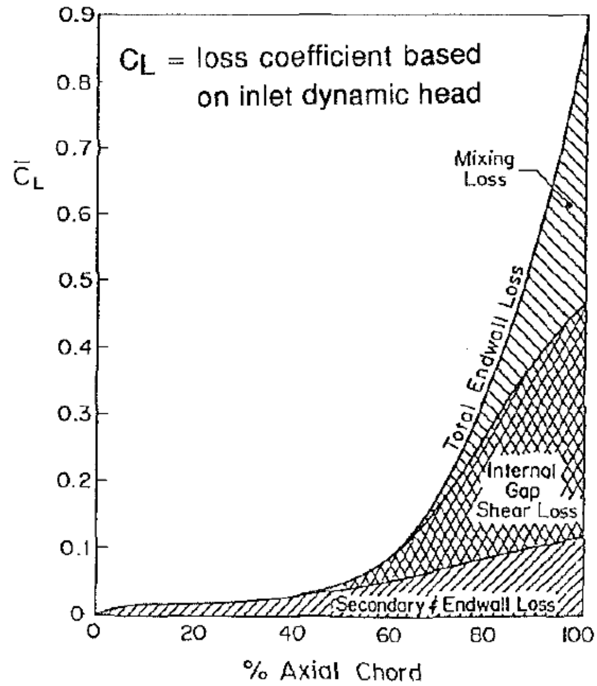

Figure 1.13 — *The growth of tip-leakage loss through a turbine blade passage (Data from Bindon, extracted from Denton [43]).*

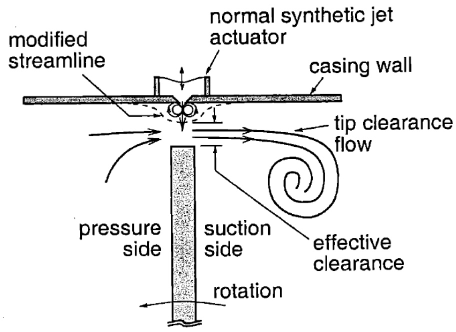

Figure 1.14 — *Illustration of tip-leakage flow rate reduction with a synthetic jet actuator (from Bae [2]).*

Similar control devices are more and more studied, experimentally or numerically, and reveal to give relevant results to improve engine stability. Most of them try to reduce the vortex intensity by making it mix earlier with the main flow. Recently, Geng et al. [58] analysed in URANS an isolated rotor with micro tip flow injection. Upstream of the leading edge, flow was injected to deflect the vortex. These flow injections weakened the tip vortex and improved the stall margin. Similar control devices were evaluated by Marty et al. [113] with blowing upstream and suction downstream of the rotor. Neuhaus and Neise [125] analysed the impact of steady air injection within the gap in different configurations. They emphasized positive effects either on the noise reduction with small injected mass flow rate, or on the performance with high injected mass flow rate. Nevertheless, their results are very case dependent, and the gap size affects them. All these systems can effectively reduce the high loss area induced by the tip vortex. However, they require a non negligible energy amount and are difficult to implement on real compressors. Their suitability is still to be evaluated, hence the numerous recent studies dealing with such control devices. Passive control devices, such as casing treatments, are therefore more adapted to be implemented in real configurations. They change the gap size locally to influence the flow field. One can cite the numerical study of Perrot et al. [131] who added five circumferential grooves as axisymmetric casing treatments. They showed that the fluid leaving the grooves disturbs the leakage flow and limits the vortex spreading. Similarly, Schoenweitz et al. [150] confronted experimental and numerical results of a rotor equipped with axial slot casing treatments within a multistage compressor. In this study, the casing treatments increased the pressure rise down to 60% of radial height by disturbing the tip vortex. Nevertheless, this study illustrated the limitations of classical numerical approaches (URANS) since the velocity gradients were not adequately represented. Castillon and Legras [23] computed the effects of non-circumferential casing treatments with the phase-lag approach. The stall margin was increased although it was underestimated by CFD (RANS simulations). In a different approach, Halbe et al. [72] studied numerically three different tip gap shapes: a divergent/convergent tip clearance, a rounded tip and a classic flat tip. The aim is to modify the flow topology by changing locally the gap size. The difference with casing treatments is that the blade tip is modified here. Furthermore, they studied these configurations with different gap sizes. The tested new configurations presented less sensitivity to gap size variations than the classic flat one. The resulting blade presented better pressure rise too.

Active and passive control devices are being extensively studied to find a way to improve turbomachines. Nevertheless, in order to control these complex flows, it is necessary to get more accurate information on the gap size influence, and especially on the flow in the vicinity of the gap. To this end, Muthanna and Devenport [122] studied a linear cascade mounted in Virginia Tech low speed wind tunnel with a stationary endwall and analysed extensively the flow field for different gap sizes. The axial-chord based Reynolds number of this configuration is about $400,000$. They measured that increasing the gap size by four leads to an increase by three of the vortex circulation. This implies a stronger vortex migrating further downstream. Nonetheless, inside the vortex, the gap size did not affect the turbulence kinetic energy and streamwise velocity levels. The vortex was however larger. This resulted in the same deficit being spread over a larger area. As a consequence, the gradients weakened as the gap size increased. Wenger et al. [173] thoroughly analysed the same experimental case with two-point measurements. They showed that the turbulence in the tip-leakage vortex is highly anisotropic and characterized by elongated eddies. These are inclined at $30°$ to the vortex axis. However, these vortices are not seen in velocity spectra. In order to analyse the vortex inception and more particularly the effects of the pressure field in the vicinity of a tip gap, You et al. [179] used Large Eddy Simulation on this same configuration. This advanced numerical method enabled to investigate what was not investigated experimentally by previous authors. The gap size were 1.53%, 3.06% and 6.11% of the axial chord, and the chord-based Reynolds number is $400,000$. In all these configurations, the tip-leakage vortex dominated the end-wall vortices. As the gap increased, the vortex origin was delayed downstream and the angle between blade chord and vortex core increased. The gap size did not influence drastically this angle in the downstream of the cascade as the vortex path became similar to the blade wakes. Stronger vortices were found in the largest gap configurations. The mechanisms responsible for the vorticity and turbulent kinetic energy

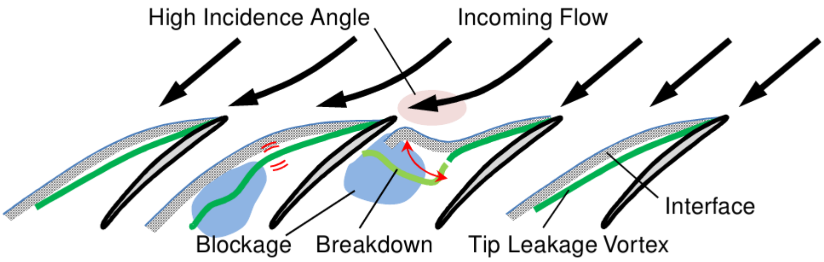

Figure 1.15 — *Illustration of flow mechanism of the disturbance in the large tip clearance case (from Yamada et al. [178]).*

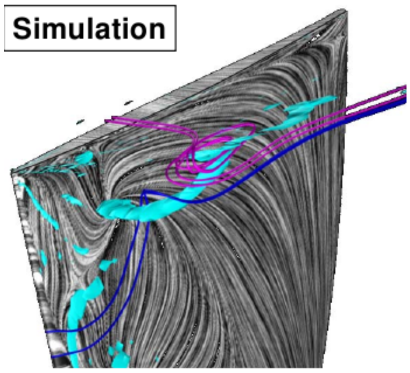

Figure 1.16 — *Illustration of flow mechanism of the disturbance in the small tip clearance case (from Yamada et al. [178]).*

creation were unchanged for the different gap sizes. They concluded that control devices designed for a given gap size can still be effective for different gap sizes as the guidelines for controlling viscous losses are the same. In the most recent studies available in the literature, other advanced numerical methods are used to simulate what is not measured experimentally. For instance, Yamada et al. [178] numerically investigated with a Detached Eddy Simulation an axial compressor configurations with two different τ values: 1% and 3%. They found that the stall inception process differs depending on the clearance size. Indeed, for the large tip clearance case, the stall inception process resulted from the vortex breakdown, as presented in figure 1.15. By contrast, this is a spike-type stall inception in the case with the small gap, as in figure 1.16.

1.1.5 Effects of the relative motion of blade and casing

A parameter that makes the tip-leakage flow more complex than flows occurring on wings [16] is the relative motion of blade and casing that is only encountered in turbomachinery. The high discrepancy between the velocities in the gap region makes this flow more difficult to simulate due to the shear it implies. Indeed, the two frames of reference are very different. The difficulty is increased with multi stage turbomachines. This motion reduces the tip-leakage flow [43] in turbine cases whilst it increases it in compressors. It affects the pressure difference across the blade tip. Moreover, it can lead to scraping vortices developing on the blade tip edge as shown in figure 1.8. In order to understand the influence of this relative motion, linear cascades were equipped with a moving belt. For instance, Wang and Devenport [170] studied the same experimental configuration as Muthanna and Devenport [122] but with a moving endwall. They highlighted that the endwall motion does not change the mechanisms governing the mean flow and turbulence structure of the tip-leakage vortex. The only observed effect is a distortion and displacement of the vortex centre. The magnitude of streamwise mean velocity deficit at the vortex

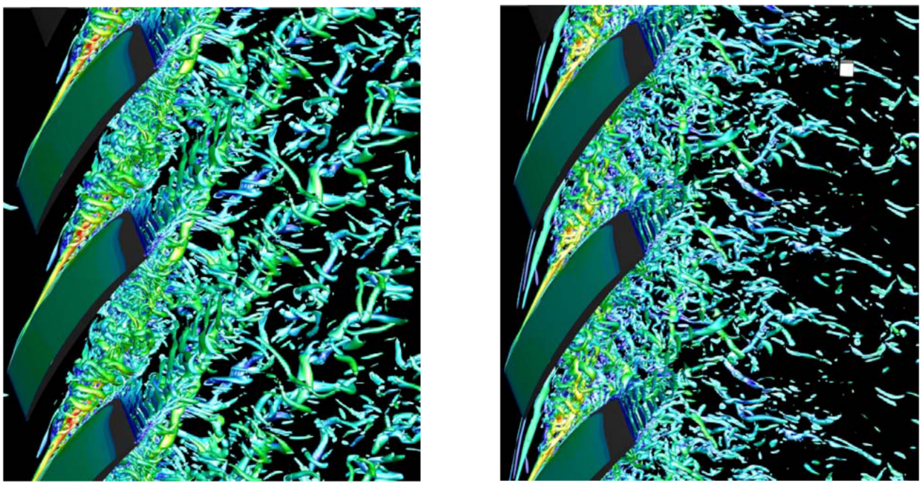

(a) Static end wall.

(b) Moving end wall.

Figure 1.17 — *Q criterium flooded by the longitudinal velocity (from Riou [143]).*

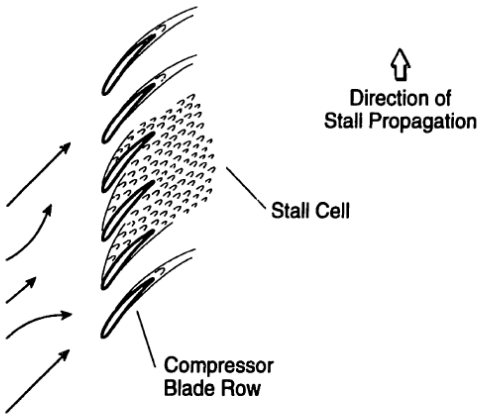

Figure 1.18 — *Physical mechanism of rotating stall (from Hoying [79]).*

centre and its decay downstream are scarcely affected by the moving wall for gap sizes of 0.8%, 1.6% and 3.3% chord. This study confirmed why many fundamental analysis are carried out on linear cascades. The same configuration was numerically investigated with Delayed DES, a first version of Zonal DES and a classic RANS approach by Riou [143]. The purposes were to evaluate the numerical methods and analyse the effects of relative motion Figure 1.17 presents the flow field with ZDES with and without motion. The vortex disrupts earlier with the endwall motion. Moreover, Riou [143] observed a secondary vortex in the moving endwall case. Besides, an elongation of the vortex core is captured too, and it bends towards the neighbouring blade. With no endwall motion, the vortex dilates but remains circular. The steps concerning the inception development and disorganisation of the vortex remains the same in the two cases. Inoue and Furukawa [82] observed similar results, based on various experiments. However, they emphasized that the loss production was considerably smaller with the relative motion than without. Thereby, this highlighted that the loss production is not in proportion to the vortex intensity.

1.1.6 Throttle effect and tip clearance flow

The tip-leakage flow is known to be one of the main instability sources in compressors near surge. This is the reason why its effects are studied in the literature up to the surge.

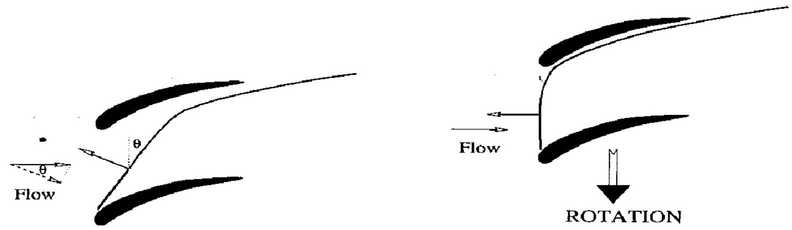

(a) Design point. (b) Near stall.

Figure 1.19 — *Trajectory and induced velocity for the tip clearance vortex at different loading conditions (from Hoying et al. [80]).*

The two main flow instabilities encountered in turbomachinery are rotating stall and surge. The rotating stall is characterized by stalled cells spinning at a lower rotation speed than the rotor (50% to 80% of rotor speed) and occurring when the rotor is overloaded, and mainly with thin blades. These small stalled cells prevent the flow from passing through the channel and thereby reduce the mass flow rate and the pressure ratio of the rotor due to their low axial velocity. This phenomenon is local and covers one or more passages. Emmons et al. [50] proposed a model for its propagation to the adjacent passages which is summarized by Hoying [79] in figure 1.18. The flow blockage generated by a cell forces the incoming fluid to skirt the blocked passage resulting in an under or over deviation of the adjacent blades. Since the blades with a higher incoming flow angle are more likely to present stall, the cells propagate in the opposite direction of the rotor rotation. The cells can be located only near the tip: part-span cell, or extend along the whole span height: full-span cell. There is usually only one full-span cell generated by a spike. These cells turn slower as they become larger. It is important to note that the part-span cell phenomenon can be reversed by increasing slightly the mass flow in the machine. However, the full-span cell phenomenon is more critical and requires more mass flow.

These cells have been and is the subject of numerous studies so as to understand how stall behaves. Furthermore, authors try to find criteria to determine which stage is likely to undergo stall. Hoying [79] highlighted that for tip-critical compressors, as the one they studied numerically, stall inception is a result of the motion of the tip clearance vortex moving upstream the blade passage, as shown in figure 1.19. When the vortex is aligned with the blade leading edge plane, an unstable operating point is reached, which gives rise to the stall. Mailach et al. [108] and März et al. [123] identified two phenomena explaining the onset of a stall cell from this alignment. The first one is that the flow spills into the adjacent passage by skirting the leading edge. This spillage was notably met by Bergner et al. [9] in a transonic compressor. The second one comes from the other side of the blade: the trailing edge. A backflow skirts the trailing edge and impinges the pressure side of the adjacent blade. A part of this flow moves backward to the passage which causes blockage.

In these situations, the leakage flow plays an important role in the stall inception. More accurately, the deflection of this flow is the source of these instabilities. For operating points near the choke limit, the tip-leakage vortex does not impact the adjacent blade because the main flow axial velocity component is far higher than the circumferential velocity of the leakage flow. As the compressor is throttled, the axial component is reduced, and the tip clearance vortex moves upstream. Before reaching the leading edge of the adjacent blade and therefore the criterion from Hoying [79], the vortex impinges the adjacent blade. A part of the tip-leakage flow leaks then through the gap of the neighbouring blade. This phenomenon is called double leakage. Khalid et al. [91] studied the endwall blockage and developed a methodology for quantifying it based on design parameters of axial compressors. This was validated on different numerical and experimental test cases. They have shown that endwall blockage is proportional to clearance height. Nevertheless, the total pressure of the fluid exiting the clearance gap is required to predict the jet leakage angle. Contrary to what was assumed by Storer and Cumpsty [165], the total pressure of the leakage jet is not equal to the free stream total pressure in some configurations, as the ones studied by

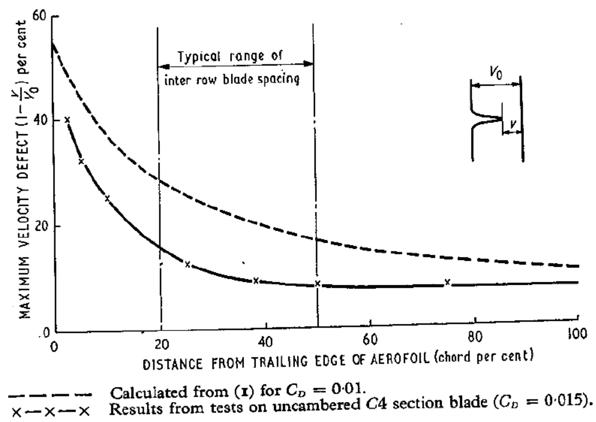

Figure 1.20 — *Variation of maximum velocity defect in wake with distance from trailing edge of blade (from Parker and Watson [129]).*

Khalid et al. [91]. Indeed, they revealed that the double leakage phenomenon reduced the total pressure of the clearance jet which lowered the leakage angle. If this is not taken into account, this leads to important over estimation of the blockage with the developed method. A second error induced by the double leakage is that the fluid leaking over a blade tip did not fully contribute to the related passage's exit plane blockage. Instead, a part of this flow contributes to the adjacent passage's exit plane blockage.

1.1.7 Rotor-stator interaction

In real compressors, the flow field within a rotor passage is influenced by the phenomena coming from upstream and even downstream the rotor blade. These are the rotor-stator interactions. One can especially cite the recent work of Courtiade [27] who studied experimentally these interactions along the different stages of the CREATE compressor. The tip-leakage flow is naturally impacted by these interactions.

1.1.7.1 Influence of upstream phenomena

The flow coming from upstream is the major disturbance source for the tip clearance flow. As previously explained, the direction of the tip-leakage vortex results from the leakage flow and the main flow velocities. If the main flow changes, the vortex direction adjusts itself consequently. This occurs near surge, and when wakes from upstream stators arrive. This latter case is even more complex in multi stages compressors.

Kemp and Sears [89, 90] studied numerical in the 1950s the effects of stator wakes on upstream rotor blades. Despite the strong assumptions which were made, they have shown that the lift value can vary up to 18% of the steady value depending on the axial distance between rows. Parker and Watson [129] analysed the wake profiles behind a cascade of uncambered aerofoil in order to give keys to design compressors with less noise and vibration. They stated that one of the more important characteristics of the wake for these interactions is the maximum velocity defect at its centre which decreases with distance from the trailing edge, as shown in figure 1.20. Beyond a length of 30% of the blade chord behind the blade, the potential flow interaction from upstream blades can be considered as insignificant in comparison with wake interaction.

The wakes impact the tip-leakage vortex periodically and therefore its direction fluctuates. The effects of this interaction was not often studied in the literature.

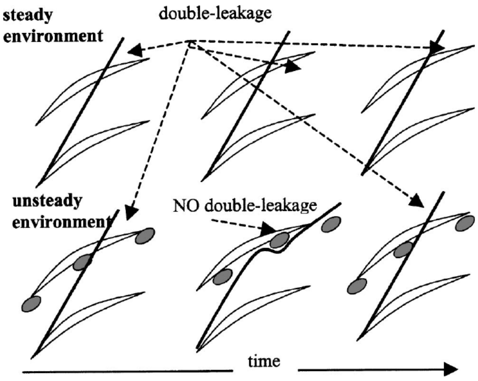

Figure 1.21 — *Fluid scenario to explain the reduction of tip clearance fluid double-leakage and enhancement of performance through pressure pulses (from Sirakov and Tan [155]).*

Sirakov and Tan [155] numerically analysed the last rotor of a three stage low speed axial compressor. They injected an oscillatory upstream stagnation pressure profile at the inlet of the calculation to approximate the effects of stator wakes and investigated how the time-average performance behaves. They highlighted that strong interactions, as presented in figure 1.21, decrease the tip region loss coefficient by up to 40%. The beneficial changes occur only when double-leakage is present. The cause for these observed performance changes is the pressure pulse-tip flow from the wake. Indeed, pressure pulses prevent double-leakage during selected instant of time in a cycle.

Mailach et al. [109] studied experimentally with LDA the flow in the third rotor blade of the four stage Dresden research compressor. In their configuration, the wakes periodically changed the rotor blade loading along with the vortex intensity, the position of maximum clearance mass flow and the vortex orientation. The blockage in the tip region varied with the stator blade passing frequency too. The arrival of stator wakes divides the tip clearance vortices into different segments with varying flow properties. The pairs of counter-rotating vortices within the wakes induce similar pairs of counter rotating vortices as they interact with the tip-leakage vortex, as shown in figure 1.22. Mailach et al. [109] were the first to describe this interaction in detail. More recently, Lange et al. [102] confronted numerical, from URANS and non linear harmonic (NLH) method, and experimental LDA results so as to study the interaction of wakes arriving on rotor in a multi stage compressor. This study aimed at validating the NLH method. They captured a periodical pulsation of the tip clearance vortex originating from the arrival of the incoming wakes. In their configuration, the dominant interaction occurred mainly where the vortex originated, near the leading edge and suction side. The blockage due to the tip-leakage vortex varied radially because the vortex extended radially due to the incoming wakes. This influenced the blockage on the whole span.

There were fewer studies with interaction of vortex from a stator arriving on the rotor blade as it is the case in this thesis work. One can cite the numerical investigation of Kirtley et al. [92] on the influence of the tip-leakage flow on downstream blade rows. Even if this was based on turbine flow, they highlighted that the vortex persisted through the channel and influenced the loading of the second blade. Moreover, the predominant spanwise mixing mechanism was due to this vortical flow in their configuration.

1.1.7.2 Potential effect

On the other side of the rotor domain, there is the potential effect from adjacent stators. Indeed, the physical presence of stators just downstream or upstream the rotor changes the flow field within the rotor passages. This modifies the pressure field on the suction side of the rotor blade following a sine function,

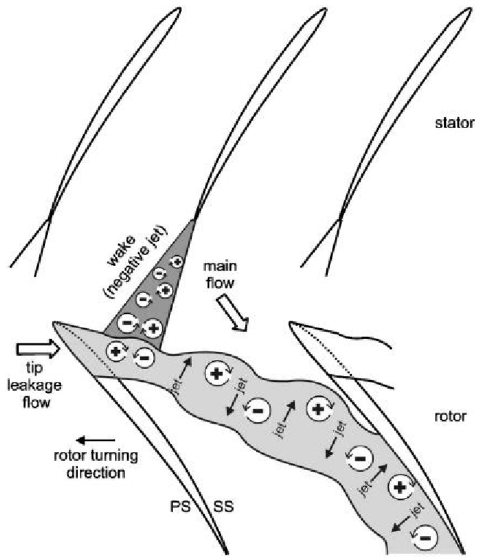

Figure 1.22 — *Schematic of tip clearance vortex influenced by the passing wakes, 2D view, near rotor tip (from Mailach et al. [109]).*

with moments of over and under pressure as shown by Deslot [44]. Graf [66] carried out unsteady rotor-stator simulations to investigate the effects of stator pressure field on upstream rotor performance. They showed that the tip-leakage vortex response to the back-pressure non-uniformity changed the whole rotor end-wall flow field. At the rotor exit, they captured radial and tangential motion of the tip vortex on the order of the blade pitch. Besides, a periodical merge of the tip vortex with the wake of the adjacent rotor blade wake was observed. This resulted in larger flow oscillations downstream.

The potential effect is even more complex in multi stage compressor due to the clocking effect. This comes when two rows have the same blade number. This can be the case for two stators or two rotors. Even if there is a row between these two rows, the influence of one on the other is observed in multi stage compressors, which makes rotor-stator interactions more complex as the number of rows increases. This is a matter of concern in recent studies analysing many rows, as the one of Mailach and Vogeler [107] or Courtiade [27].

1.1.8 Vortex breakdown and vortex/shock interaction

The tip-leakage flow interacts with many different phenomena, such as wakes or boundary layers. Its stability is very dependent on all of these interactions. Besides, the design of compressors at relatively high rotation speed makes the tip-leakage vortex interacts with shocks too. Therefore, vortex breakdown and vortex/shock interactions are studied in the literature [46].

In subsonic rotors, the vortex core can encounter a stagnation point characterized by the local inversion of the tip gap flow. This is known as the vortex breakdown and presented in figure 1.23. Upstream the breakdown point the vortex filament is unaffected. The process is then abrupt and the flow disorganizes rapidly. In transonic compressors, the interaction between passage shock and tip-leakage vortex can result in this vortex breakdown [177]. Peckham and Atkinson [130] first detected it on a highly swept delta wing. Different research studies and analytical theories have emerged since then to explain this phenomenon. This was detected in many different configurations with vortices. Lambourne and Bryer [101] observed that vortex bursting involves a sudden deceleration of the axial flow and an expansion of the vortex around its core. Further downstream, the breakdown of the vortex occurs. In low Reynolds number configurations at least, there is a region of periodic flow in which the axial vortex filament performs a regular whirling motion. This is located between the deceleration area and the turbulent breakdown.

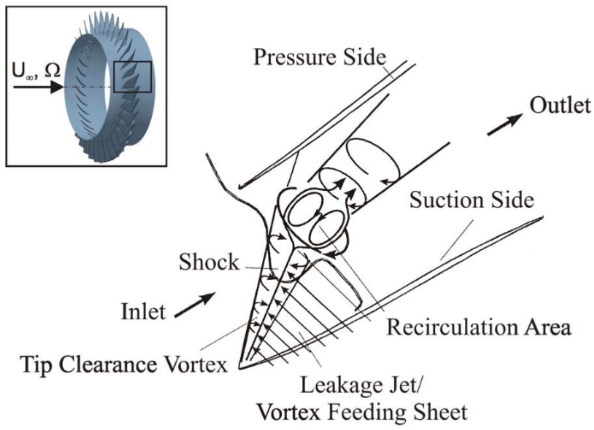

Figure 1.23 — *Shock/tip-leakage vortex interaction (from Hofmann and Ballmann [77]).*

In 1985, Hall [73] summarized the main available analyses and presented the theories [7] behind vortex breakdown in order to explain why there are core bursting in some configurations. Some criteria were developed in the literature to delineate the region where breakdown occurs. For instance, a criterion is based on the fall in the Rossby number [164, 145] defined as the ratio of the axial and circumferential momentum in a vortex. This criterion is applied in some studies such as the recent work of Riou [143] in turbomachinery.

Tip clearance vortex breakdown is considered as a possible cause of stall inception in compressors by many authors such as Hofmann and Ballmann [78, 77]. This seems to be the case mainly in large gap configurations [54]. Indeed, in the small tip clearance cases the aforementioned spike-type stall is predominant. This was recently confirmed by Yamada et al. [178]. They have shown with experimental and DES analyses that the rotating disturbance, in large tip gap cases, appeared intermittently and randomly at near-stall condition. In addition, the compressor did not systematically fall into the stall after the inception of vortex disturbance. Nonetheless, it contributed to the blockage effect near stall.

The interaction of the tip-leakage vortex with a shock in a transonic compressor does not necessarily lead to vortex breakdown as shown by Hah et al. [70]. Nevertheless, the flow field becomes unsteady due to shock oscillations. If the shock is oblique or normal to the vortex, the interaction differs. This interaction seems to depend on the operating point too. Hoeger et al. [76] compared RANS simulations with experimental laser data close to stall, peak efficiency and choke. In their configuration, the vortex core went through the shock without change in cross section at peak efficiency while its cross section increased near stall. However, in all of their studied cases, they highlighted that a steep increase in loss was found in the strong shock-vortex interaction region. Bergner et al. [9] studied experimentally a transonic compressor and highlighted that at peak efficiency, the passage shock was almost normal to the vortex. By contrast, near stall, the shock strength increased because the shock moved upstream which led to an oblique shock/vortex interaction.

The interaction with the shock, the vortex and the boundary layer was studied numerically by Chima [26] and compared to experiments. He highlighted strong interactions between these different flows. Nevertheless, he has shown limitations of the used algebraic turbulence model to compute the flow near the casing, even if the performance predictions were correct. Yamada et al. [177] analysed with RANS and URANS computations the transonic axial compressor known as the Rotor 37 from the NASA. In this configuration, the boundary layer separation on the casing wall and on the blade suction surface emanated from their interaction with the shock wave. Moreover, the same case with no clearance revealed a different position for the separation on the suction surface. This suggested a strong link between these phenomena: boundary layer separation on the suction surface, shock and leakage flow.

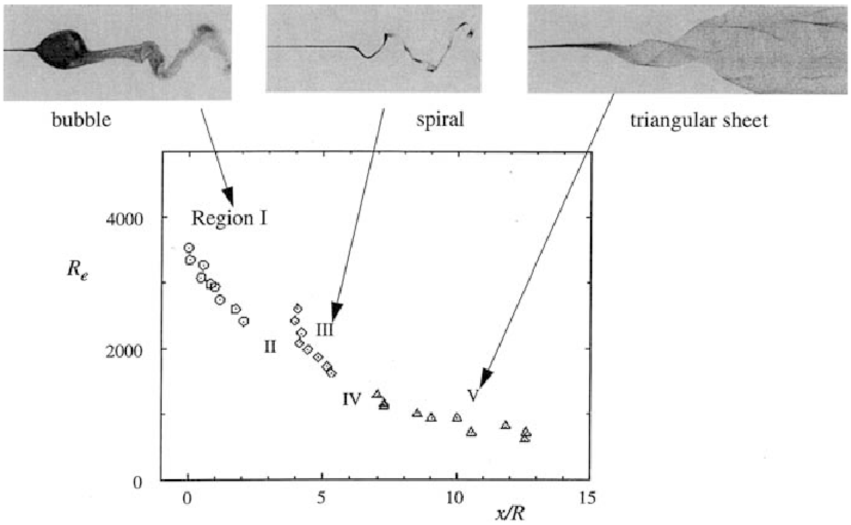

Figure 1.24 — *Vortex breakdown types (from Kurosaka et al. [94]).*

Disturbing the vortex in one of the ways to control it. Some studies tried to increase the mixing, others tried to influence the breakdown. Fundamental analyses are carried out with vortex coming from different form of pipes to analyse more accurately the vortex behaviour and dependence to flow conditions. Kurosaka et al. [94] analysed results from straight tubes and showed that the topology depends on the Reynolds number as shown in figure 1.24. Besides, they underlined that the bubble type or spiral type breakdowns depends highly on the disturbances within the tube. By changing the forcing type inside the tube they could change the spiral type breakdown into a bubble type breakdown and inversely.

1.2 Numerical methods to take the tip clearance flow into account

This section highlights the ways to take the tip-leakage flow into account and aims at giving an overview of the actual possibilities, their advantages and drawbacks.

The first methods used by investigators to evaluate the effects of tip-leakage flows was based on simple models and correlations [96]. First of all, in the 1950s [135], the leakage flow velocity was computed from theoretical and approximated blade pressure distributions. This was mainly used to estimate the loss and efficiency based on correlations from experiments. In the 1960s [97], potential tip vortex models enabled to estimate the drag induced by the leakage flow. These models consisted of two rows of potential tip vortices, one of the row representing the wall effect. These models were then improved to take into account local chordwise effects of the vortex on the pressure distribution or the presence of the vortex core.

Nowadays, models are still used for preliminary designs. For instance, Storer and Cumpsty [165] developed a model to quantify the losses and Khalid et al. [91] a model to evaluate the blockage effect of the tip clearance flows. These models are either simple or very complex. Nevertheless they can not provide accurate predictions. Furthermore, most of them are based on experimental data. Therefore they reach their limits when innovative designs are tested [92].

In the 1970s, the Computational Fluid Dynamics (CFD) provided an adaptable tool suited for new designs. Besides it was then possible to compute what was impossible to measure and led to a better understanding of the leakage flow. Since then, each step in the evolution of computational resources and numerical techniques improved the knowledge of the flow in turbomachinery. Table 1.1 from Spalart [158] summarizes the main CFD approaches available and indicates when they are or will be ready for

Name	Aim	Unsteady	*Re*-dependence	3/2D	Empiricism	Grid	Steps	Ready
2DURANS	Numerical	Yes	Weak	No	Strong	10^5	$10^{3.5}$	1980
3DRANS	Numerical	No	Weak	No	Strong	10^7	10^3	1990
3DURANS	Numerical	Yes	Weak	No	Strong	10^7	$10^{3.5}$	1995
DES	Hybrid	Yes	Weak	Yes	Strong	10^8	10^4	2000
LES	Hybrid	Yes	Weak	Yes	Weak	$10^{11.5}$	$10^{6.7}$	2045
QDNS	Physical	Yes	Strong	Yes	Weak	10^{15}	$10^{7.3}$	2070
DNS	Numerical	Yes	Strong	Yes	None	10^{16}	$10^{7.7}$	2080

Table 1.1 — *Summary of the main strategies to simulate turbulent flows (from Spalart [158])*

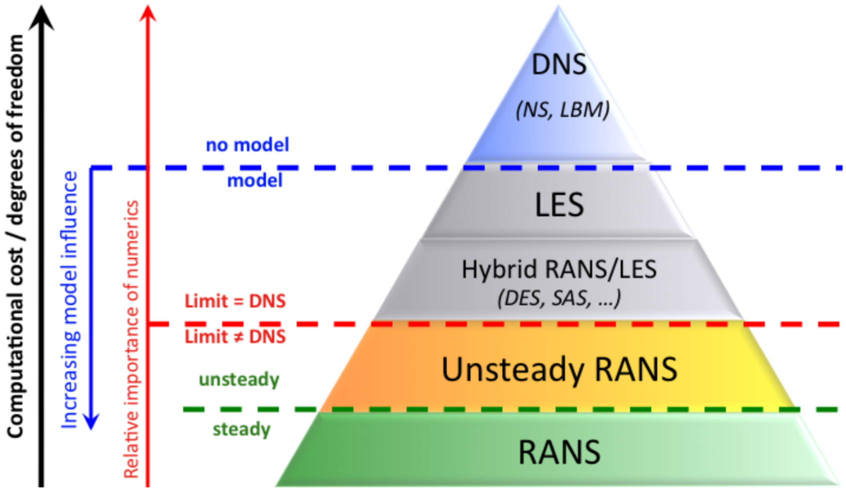

Figure 1.25 — *From RANS to DNS, the possibilities of CFD (from Sagaut et al. [147])*

classic simulations encountered in the industry. Figure 1.25 classifies these approaches depending on their accuracy and dependence on numerics or on models.

The Direct Numerical Simulation (DNS) could solve every time and spatial scales of turbulence and enable the finest description of the tip-leakage flow. However this method is impossible to use for realistic configurations due to the high computational cost it requires. Indeed, the number of nodes depends on the Reynolds number of the case and scales as $Re^{9/4}$ for 3D meshes.

Thereby, DNS is not expected to be used before 2080 [158]. The most recent studies with DNS in turbomachinery are still close to flat plates simulations at low Reynolds. For instance, Wissink [175] and Wissink and Rodi [176] studied the transitional flow in turbine and compressors. Balzer and Fasel [4, 5] studied control devices of a separation bubble in a simple turbine with a Reynolds number of 25000. Such studies inform us accurately on the boundary layer development on curved surfaces. Nevertheless, they are far from being representative of real configurations.

Reynolds-averaged Navier-Stokes (RANS) simulations are widely used in the industry to simulate tip-leakage flows in real configurations at high Reynolds number. With the computational resources available in the 2010, such simulations are possible overnight. This parameter is important for engineers to test new designs. Nevertheless, it is impossible to capture unsteady effects with this method.

The Unsteady RANS (URANS) approach is necessary when investigators try to capture unsteady effects such as rotor-stator interactions [65]. URANS helped discovering and understanding unsteady phenomena encountered in the tip region, such as the vortex rolling-up and its motion. Moreover, it enabled to evaluate the effects of unsteady control devices. However this method revealed not to predict accurately the tip-leakage flow [143] and other complex unsteady flows encountered in turbomachinery [149, 150]. There are nonetheless numerous efforts to improve it by the means of different turbulence models or higher order numerical methods.

Large Eddy Simulation (LES) [14] and Quasi DNS [134] are more adapted to capture the vortices from turbulent flows, as evaluated by some authors, especially in the turbomachinery field [48, 13]. Nevertheless, the simulated configurations are not representative of real rotors, such as linear cascades with low Reynolds number, or are carried out on undersized meshes. Indeed, the prohibitive cost to simulate high Reynolds number wall-bounded flows limits their actual use to academic low Reynolds number configurations [158]. One can cite the work of Moin et al. [121] with one single blade of a linear cascade with moving end-wall and a Reynolds number of 400000. Moin et al. [121] carried out other simulations at Reynolds 10000 to understand the effects of end-wall groove and gap size. In that case, LES enabled to analyse the coherent motion of the vortical structures.

When LES results are confronted to accurate measurements, such as in the configuration from Hah et al. [71], this method can bring relevant informations on the small vortical structures. Hah et al. [71] revealed that the formation of tip clearance vortex was intermittent in this case near stall due to intermittent spillage of the flow around the leading edge. Besides, the interaction between passage shock and tip clearance was studied and compared to PIV measurements.

The LES method is still discussed and "best pratices" to carry out LES computations are regularly proposed by authors [47, 48, 60, 62, 63].

In order to bring the LES capabilities to the industry faster than with full LES, some authors combine the possibilities of RANS to advanced methods. One can cite the study of Borello et al. [12] with a "seamless" hybrid URANS/LES model to simulate the tip-leakage flow. Or more recently the work of Cahuzac [20] with a zonal LES/RANS approach.

	Δx^+	Δy^+	Δz^+
RANS	500	1	1000
DES	200-300	1	200
LES	50	1	15

Table 1.2 — *Mesh requirements for the simulation of wall-bounded flows with RANS, DES and LES methods and low order numerical schemes (adapted from Georgiadis et al. [60], Deck [37] and Sagaut et al. [148])*

One of the most used method in the recent publications is the Detached Eddy Simulation, along with its derivatives, detailled in section 2.2. These methods are more and more used in the recent years since they can give LES-type results far from walls. The main drawback of these methods is their advantage too : the boundary layer resolved in unsteady RANS. This means that the capability near the walls is the one of RANS methods, hence their limitations to study phenomena within the boundary layer. However, this reduces drastically the mesh requirements near for wall bounded flows, as summarized in table 1.2. The new versions of DES-type models were tested recently in turbomachinery. Greschner and Thiele [67] analysed a 2.5D rotor-stator configuration with DDES and IDDES and highlighted clear improvements for wake and boundary layer simulations in IDDES. Gmelin and Thiele [61] compared RANS, DDES and IDDES to capture the separation bubble in a high speed compressor cascade.

Few authors have used DES-type models to study specifically the tip-leakage flow. Yamada et al. [178] analysed with DES the spillage phenomenon of the tip clearance flow near stall. Van Remmings et al. [169] used DDES to compare the influence of numerical periodicity in simulations of the hub leakage flow. To this end they confronted two DDES simulations with one and two simulated channels. They have shown that the computation periodicity influences directly the separated flows and the rotating instabilities. Recently, Shi et al. [152], Shi and Fu [151] used IDDES to analyse the interaction between shock, tip-leakage vortex and the boundary layer.

It is important to keep in mind that these methods are very recent and still being developed and improved. Furthermore, as it is the case for LES computations, DES-type computations requires to follow guidelines and criteria for the meshing step or for the convergence checking. The aforementioned studies seem not to follow such guidelines which leads to coarse meshes for the selected DES-type methods. Besides, these methods are tested in configurations showing the limitations of global RANS/LES approaches, in terms of cost and capability. Tyacke et al. [168] reminds then that "the expectation of producing a single modelling strategy that will work effectively and reliably for all engine zones is unrealistic". This is the reason why zonal approaches were developped.

1.3 ZDES applications

The Zonal Detached Eddy Simulation (ZDES) [38], detailed in section 2.2.4, is one of these zonal approaches. The early versions of this method were tested on numerous configurations that present, in some aspects, similarities with the tip-leakage flow. Indeed, the tip-leakage flow can be considered, in a first approximation, as a combination of the flow encountered on both a backward facing step and a wing. The ZDES method was then applied to the simulation of an aircraft by Brunet and Deck [17], Brunet et al. [18] and high lift aerofoils by Deck [36], Deck and Laraufie [39]. A vortex developing on a missile fin was studied by Riou and Garnier [144] too. Moreover, flows close to a backward facing step were simulated, such as after-body flows by Deck and Thorigny [40], Weiss and Deck [171], Simon et al. [154]. Finally, jet mixing layer were studied by Chauvet et al. [25].

The only case where ZDES was applied to turbomachinery is, to the best knowledge of the author of this work, on the configuration tested by Riou [143], comparing DDES and ZDES. However, this was an early version of the ZDES, and the zonal approach was not used. Despite this early version, Riou [143] highlighted the better capability of this method compared to RANS and even DDES. Indeed, it captured more accurately the velocity distributions corresponding to the tip-leakage vortex position.

1.4 Synthesis of the Literature

This section investigated the existing literature concerning the tip-leakage flow and the physics inherent to this phenomenon. Besides, it reviewed the different simulations methods that have been used to take this flow into account. This highlighted that some realistic configurations were simulated with classic approaches, most of them with RANS or URANS. These methods revealed a lack of capability to simulate accurately the position, direction and intensity of the tip-leakage flow. By contrast, only simple configurations were simulated with advanced approaches due to their requirements in terms of computational resources. There are still few studies that use advanced methods on realistic turbomachinery configurations, and even fewer focussing on the tip-leakage flow. Hybrid approaches based on the URANS and LES methods seems to be encouraging since they bring the LES capability at a fraction of its computational cost for wall-bounded flows. Moreover, the recent ZDES method seems to be capable to simulate many different configurations. Nevertheless, the zonal approach of the ZDES was not yet used in a realistic compressor.

The literature overview revealed that there were no evaluation of what this method can bring to the understanding of the tip-leakage flow in a realistic turbomachinery configuration that takes into account inlet distortions for different operating points, such as near surge. The following thesis work intends to fill this gap.

Chapter 2 Apparatus and Techniques

Contents

This chapter presents the different methods used in this study. In addition, it describes the experimental test bench upon which the study is based.

2.1 Reynolds Averaged Navier-Stokes simulations

Navier-Stokes equations characterize the fundamental principles of laminar and turbulent flows. This open system consists of the mass continuity equation [II-1], the momentum equation [II-2] and the energy equation [II-3], with the time t, the density ρ, the velocity vector $\underline{u}$, the static pressure p, the viscous stress tensor $\underline{\underline{\tau}}$, the heat flux density vector $\underline{q}$ and finally the Identity matrix $\underline{\underline{\mathbb{I}}}$. The gravity is ignored in the momentum equation since only gases are considered. Moreover, as written in equation [II-4], the total energy E comprises the internal energy e as well as the kinetic energy per mass unit.

- Mass continuity equation

$$\frac{\partial \rho}{\partial t} + \text{div}\ (\rho \underline{u}) = 0 \tag{II-1}$$

- Momentum equation

$$\frac{\partial \rho \underline{u}}{\partial t} + \underline{\text{div}}\ (\rho \underline{u} \otimes \underline{u}) = -\underline{\text{grad}}\, p + \underline{\text{div}}\, \underline{\underline{\tau}} \tag{II-2}$$

- Energy equation

$$\frac{\partial \rho E}{\partial t} + \text{div}\ (\rho \underline{u} E) = -\,\text{div}\,\underline{q} + \text{div}\ \left[\underline{u} \cdot \left(\underline{\underline{\tau}} - p\underline{\underline{\mathbb{I}}}\right)\right] \tag{II-3}$$

$$E = e + \frac{1}{2}\underline{u} \cdot \underline{u} \tag{II-4}$$

The resulting system comprises 5 equations for 14 unknowns. This is the reason why it requires further assumptions.

In order to close the equation system, some assumptions are made. The first assumption is that the gas is regarded as a thermally and calorically perfect gas. Furthermore, the specific heat for a constant volume, c_v, and constant pressure, c_p, are considered as constant with a ratio of $\gamma = \frac{c_p}{c_v} = 1.4$, that is to say, the gas is simplified as a diatomic gas. This adds the state equation [II-5] for the pressure to the system, with r, the specific gas constant of the gas (r = 287.058 $J.kg^{-1}.K^{-1}$ for dry air). The internal energy and the enthalpy are then defined by equations [II-6].

$$p = \rho r T \tag{II-5}$$

$$e = c_v T = \frac{1}{\gamma - 1}\frac{p}{\rho} \qquad h = c_p T = \frac{\gamma}{\gamma - 1}\frac{p}{\rho} \tag{II-6}$$

$$\underline{\underline{\tau}} = \lambda\,(\,\text{div}\,\underline{u})\ \underline{\underline{\mathbb{I}}} + 2\mu\underline{\underline{S}} \tag{II-7}$$

For a Newtonian fluid, the viscous stress tensor $\underline{\underline{\tau}}$ is given by equation [II-7], with the dynamic viscosity μ and the second viscosity coefficient λ. The rate of strain tensor $\underline{\underline{S}}$ corresponds to the symmetric part of the velocity gradient tensor. Similarly, the rate of rotation tensor $\underline{\underline{\Omega}}$ is defined for a local rotating velocity of Ω_m. These tensors are then given in equations [II-8].

$$S_{ij} = \frac{1}{2}\left(\frac{\partial u_i}{\partial x_j} + \frac{\partial u_j}{\partial x_i}\right) \qquad \Omega_{ij} = \frac{1}{2}\left(\frac{\partial u_i}{\partial x_j} - \frac{\partial u_j}{\partial x_i}\right) + \varepsilon_{mji}\Omega_m \tag{II-8}$$

The Stokes hypothesis that links the two viscosities, $3\lambda + 2\mu = 0$ gives then equation [II-9].

$$\underline{\underline{\tau}} = 2\mu\left[\underline{\underline{S}} - \frac{1}{3}\,(\,\text{div}\,\underline{u})\ \underline{\underline{\mathbb{I}}}\right] \tag{II-9}$$

In order to evaluate the dynamic viscosity, the Sutherland law, available for the air at moderate temperature, gives the equation [II-10].

$$\mu = \mu_0\sqrt{\frac{T}{T_0}}\frac{1 + \frac{C_0}{T_0}}{1 + \frac{C_0}{T}} \tag{II-10}$$

$$\underline{q} = -K_T\,\underline{\text{grad}}\,T \tag{II-11}$$

$$Pr = \frac{\mu c_p}{K_T} \tag{II-12}$$

Finally, the heat flux density vector derives from the Fourier law, in equation [II-11], and the Prandtl number defined in equation [II-12], regarded as a constant here. In these equations, K_T is the thermal conductivity coefficient.

2.1.1 Averaged Navier-Stokes equations

In order to solve the Navier-Stokes equations, it is necessary to calculate all the spatial and temporal scales of the flow. This is called the Direct Numerical Simulation (DNS). However, this method implies that the computational domain expands up to the largest flow structures and the mesh must be as fine as the smallest turbulent structures where the energy dissipates, also known as the Kolmogorov length scale. Likewise, the computation must take into account the smallest time related to the smallest structures whilst the largest time corresponding to the largest structures must be computed. The ratio between the smallest and largest scales is prohibitive for high Reynolds number wall bounded flows. Indeed, the number of mesh point is about $Re^{\frac{9}{4}}$ and the time range scales in $Re^{\frac{11}{4}}$.

Another possibility, widely used in the industry, is the computation of the averaged equations. This method is called the Reynolds averaged Navier-Stokes (RANS). It was proposed by Reynolds [136] and consists in separating each instantaneous field $f\,(x,t)$ into two fields: an averaged field $\overline{f}$ and a fluctuating field f'. This results in equation [II-13]. This is an ensemble average, that is to say, the mean of the ensemble of the possible independant micro-states f_i. The ensemble average is then given by equation [II-14].

$$f\,(x,t) = \overline{f} + f' \tag{II-13}$$

$$\overline{f} = \lim_{N\to\infty}\left(\frac{1}{N}\sum_{i=1}^{N} f_i\right) \tag{II-14}$$

Assuming that the time over which this average is calculated is longer than the turbulence characteristic time t_{turb}, the ensemble average can be regarded as the time average of equation [II-15].

$$\overline{f}(t) = \lim_{T\to\infty}\frac{1}{2T}\int_{-T}^{T} f(t+\tau)d\tau \tag{II-15}$$

This average operator has the following properties:

$$\begin{array}{rclrclrcl} \overline{f'} &=& 0 & & & & \overline{\dfrac{\partial f}{\partial x}} &=& \dfrac{\partial \overline{f}}{\partial x} \\ \overline{f+g} &=& \overline{f}+\overline{g} & \overline{\alpha f} &=& \alpha\overline{f} \quad \text{for a constant } \alpha & & & \\ \overline{\overline{f}\cdot\overline{g}} &=& \overline{f}\cdot\overline{g} & \overline{f\cdot g} &=& \overline{f}\cdot\overline{g}+\overline{f'\cdot g'} & \overline{\dfrac{\partial f}{\partial t}} &=& \dfrac{\partial \overline{f}}{\partial t} \\ \overline{\overline{f}} &=& \overline{f} & & & & & & \end{array} \tag{II-16}$$

This last property is called idempotence and if equation [II-13] is used, it leads to $\overline{f'} = 0$, this is the reason why the standard deviation of f' is used to quantify the fluctuations.

This ensemble average is then applied to the equations [II-1], [II-2] and [II-3] in the RANS approach. The unsteady RANS approach (URANS) consists in the same average but applied on a time scale relative to the unsteadiness of the average flow field. This gives equation [II-17]. It is based on the strong assumption that the unsteadiness of this average field and the unsteadiness of the fluctuating field are not coupled.

$$\overline{f}(t) = \frac{1}{T}\int_{t-T}^{t} f(s)ds \quad \text{with } T >> t_{turb} \tag{II-17}$$

For compressible flows, the ensemble average is used for the pressure and the density, and a modified version developed by Reynolds [137] and used by Favre [52] is applied to the other quantities following equation [II-18]. The aim is to take into account the density variation while simplifying the equation system. However, the Favre average of the fluctuations is no more equal to 0.

$$f = \tilde{f} + f'' \qquad \tilde{f} = \frac{\overline{\rho f}}{\bar{\rho}} \tag{II-18}$$

By comparison of the instantaneous and averaged momentum equations, a new unknown is revealed: $\overline{\rho \underline{u}'' \otimes \underline{u}''}$. This unknown, called the Reynolds tensor, originates from the average of the non-linear instantaneous terms, and represents the relation between the turbulent and averaged phenomena. The trace of this tensor is twice the turbulent kinetic energy: $\tilde{k} = \frac{1}{2}\widetilde{\underline{u_i}'' \cdot \underline{u_i}''}$. In order to close the equation system, further hypothesis have to be done to characterize this tensor.

2.1.2 Boussinesq eddy viscosity assumption

One of the most used hypothesis is the assumption of eddy viscosity. Boussinesq [15] introduced this concept by analogy with the momentum transfer in Newtonian fluids, and how it can be modelled by a molecular viscosity. This states that the shear is proportional to the deformation as in equation [II-19].

$$-\overline{u'v'} = \nu_t \frac{\partial u}{\partial y} \tag{II-19}$$

This strong assumption means that the turbulence is only a diffusive phenomenon that increases the mixing within the flow. Kolmogorov extended then this equation by linking the Reynolds tensor to the shear stress tensor $\underline{\underline{S}}$ as in equation [II-20]. Nowadays, many RANS models are based on this hypothesis.

$$-\overline{u_i'u_j'} + \frac{2}{3}k\delta_{ij} = 2\nu_t S_{ij} \tag{II-20}$$

2.1.3 Spalart-Allmaras one equation model

In order to determine the eddy viscosity, a transport equation of this value can be used. The Spalart-Allmaras model [162] is a turbulence model with one equation based on the pseudo viscosity equation [II-21].

$$\underbrace{\frac{D\tilde{\nu}}{Dt}}_{Convection} = \underbrace{c_{b1}\tilde{S}\tilde{\nu}}_{Production} + \underbrace{\frac{1}{\sigma}\left[\operatorname{div}\left((\nu+\tilde{\nu})\underline{\operatorname{grad}}\,\tilde{\nu}\right) + c_{b2}(\underline{\operatorname{grad}}\,\tilde{\nu})^2\right]}_{Diffusion} \underbrace{-c_{\omega 1} f_w \left[\frac{\tilde{\nu}}{d_w}\right]^2}_{Destruction} \tag{II-21}$$

Such an equation can not be determined from the Navier-Stokes equations since the Boussinesq equation is only a model. Therefore, Spalart and Allmaras [162] built their model step by step by considering flows with an increasing complexity and by adding corrections to their model at each step. Therefore, this model uses near wall corrections: f_{v1}, f_{v2} and f_w. The pseudo viscosity, $\tilde{\nu}$, is a modification of the eddy viscosity, ν_t, as shown in equation [II-22]. It consists in an adaptation of the eddy viscosity so as to take into account the logarithmic-law region of the boundary layer, as well as the buffer layer and the viscous sublayer. It is based on the assumption of equilibrium between the production, diffusion and destruction terms. As a consequence, $\tilde{\nu} = u_\tau \kappa \cdot y$ in the three areas due to the function

f_{v1}, detailled in equation [II-25]. Moreover, $\nu_t = u_\tau\kappa \cdot y$ in the log layer only. The production term is modified with the use of the pseudo viscosity. The vorticity modulus, S, is adapted with the function f_{v2}, in equation [II-26], so that $\tilde{S}$ behaves like S in the log-law region: $\tilde{S} = u_\tau/\kappa \cdot y$. In the equation [II-21], the destruction term is $-c_{\omega 1} f_w \left[\frac{\tilde{\nu}}{d_w}\right]^2$, with d_w, the wall distance. Finally, the damping function f_w, detailed in equation [II-27] lowers rapidly the pseudo viscosity level in the outer layer. It is important to note here that the distance d_w is one of the key element used in the Detached Eddy Simulation (DES) and Zonal DES as explained in section 2.2.

$$\nu_t = f_{v1}\tilde{\nu} \tag{II-22}$$

$$\tilde{S} = S + \frac{\tilde{\nu}}{\kappa^2 y^2} f_{v2} \tag{II-23}$$

$$\chi = \frac{\tilde{\nu}}{\nu} \tag{II-24}$$

$$f_{v1} = \frac{\chi^3}{\chi^3 + c_{v1}^3} \tag{II-25}$$

$$f_{v2} = 1 - \frac{\chi}{1 + \chi f_{v1}} \tag{II-26}$$

$$f_w = g \cdot [\frac{1 + c_{\omega 3}^6}{g^6 + c_{\omega 3}^6}]^{1/6} \tag{II-27}$$

$$g = r + c_{\omega 2}(r^6 - r) \tag{II-28}$$

$$r = \frac{\tilde{\nu}}{\tilde{S}\kappa^2 {d_w}^2} \tag{II-29}$$

Constant name	Value
c_{b1}	0.1355
c_{b2}	0.622
σ	$\frac{2}{3}$
κ	0.41
$c_{\omega 1}$	$\frac{c_{b1}}{\kappa^2} + \frac{1+c_{b2}}{\sigma}$
$c_{\omega 2}$	0.3
$c_{\omega 3}$	2
c_{v1}	7.1

Table 2.1 — *Values for the Spalart-Allmaras model.*

The Spalart-Allmaras model, described hereinabove, does not take into account the rotation and curvature effects because of the way it was built. Spalart and Shur [160] developed another version, proposed by Dacles-Mariani et al. [30] for another turbulence model, to alleviate this limitation. Its modifies the production term by adding a rotation function, f_{r1}, detailed in equation [II-30].

$$f_{r1}\left(r^*, \tilde{r}\right) = \left(1 + c_{r1}\right) \frac{2r^*}{1 + r^*} \left[1 - c_{r3} \tan^{-1}\left(c_{r2}\tilde{r}\right)\right] - c_{r1} \tag{II-30}$$

By considering the local rotating velocity Ω_m, the dimensionless values r^* and $\tilde{r}$ are then defined by equation [II-31]. This finally leads to equation [II-33], that defines the Spalart-Allmaras model with the curvature correction (SARC).

$$\begin{array}{ll} r^* = \frac{S}{\Omega} & \tilde{r} = \frac{2\Omega_{ik}S_{jk}}{D^4}\left(\frac{DS_{ij}}{Dt} + (\varepsilon_{imn}S_{jn} + \varepsilon_{jmn}S_{in})\,\Omega_m\right) \\ \text{with} & S = \sqrt{2S_{ij}S_{ij}} \qquad \Omega = \sqrt{2\Omega_{ij}\Omega_{ij}} \qquad D = \frac{1}{2}\left(S^2 + \Omega^2\right) \\ \text{and with} & \varepsilon_{ijk} = \frac{(i-j)(j-k)(k-i)}{2} \quad \text{the alternating tensor} \end{array} \tag{II-31}$$

$$c_{r1} = 1 \quad c_{r2} = 12 \quad c_{r3} = 1 \tag{II-32}$$

$$\frac{D\tilde{\nu}}{Dt} = c_{b1}\tilde{S}\boldsymbol{f_{r1}}\tilde{\nu} - c_{w1}f_w\left(\frac{\tilde{\nu}}{d}\right)^2 + \frac{1}{\sigma}\left[\text{div}\left((\nu + \tilde{\nu})\,\underline{\text{grad}}\,\tilde{\nu}\right) + c_{b2}\underline{\text{grad}}\,\tilde{\nu}\cdot\underline{\text{grad}}\,\tilde{\nu}\right] \tag{II-33}$$

2.1.4 Two equations turbulence models

The use of only one equation to characterize the eddy viscosity is not the only method used in turbulence models. It can be defined with more values. Many models implement two equations. Indeed, a simple dimension study on the eddy viscosity term shows that one can use two scales: a velocity and a length. However, they have to be related to the turbulence characteristics to be relevant. The turbulent kinetic energy is often used for the turbulent velocity scale since $u'^2 \sim k$. The second term, for the length scale, differs depending on the model. Among the numerous existing turbulence models based on two equations, the most used are based on the dissipation rate for the kinetic energy ε, a mixing length l and the specific turbulence dissipation ω.

One will give here only an overview of the two models tested in the appendix of this thesis: the $k-\varepsilon$ model from Launder and Sharma [103] and the $k-\omega$ model from Wilcox [174]. Both of them use a transport equation for the turbulent kinetic energy k [II-34], which stems from the trace of the Reynolds tensor.

$$\frac{\partial k}{\partial t} + u_j\frac{\partial k}{\partial x_j} = P_k - \varepsilon + \frac{\partial}{\partial x_l}\left[\left(\nu + \frac{\nu_t}{\sigma_k}\right)\frac{\partial k}{\partial x_l}\right] \tag{II-34}$$

In this equation, σ_k is the Prandtl number, the production term is given by equation [II-35] and the dissipation rate by equation [II-36].

$$P_k = -\overline{u'_i u'_j}\frac{\partial u_i}{\partial x_j} = 2\nu_t S_{ij}S_{ij} \tag{II-35}$$

$$\varepsilon = \nu\overline{\frac{\partial u'_i}{\partial x_j}\frac{\partial u'_i}{\partial x_j}} \tag{II-36}$$

The term ε corresponds to the energy transfer from the large to the smallest scales through the energy cascade of Kolmogorov. The $k-\varepsilon$ model from Launder and Sharma [103] is built on the assumption that the transport equation for ε has the same terms as the transport equation for k with a production term, a convection term, a destruction term and viscous and turbulent dissipations. It was then calibrated to give relevant results on different flow configurations. In order to extend this model to the wall, a low Reynolds version was developed by modifying the dissipation ε term into an isotropic dissipation term $\tilde{\varepsilon}$ that is compatible with the near wall flow regions within the boundary layer.

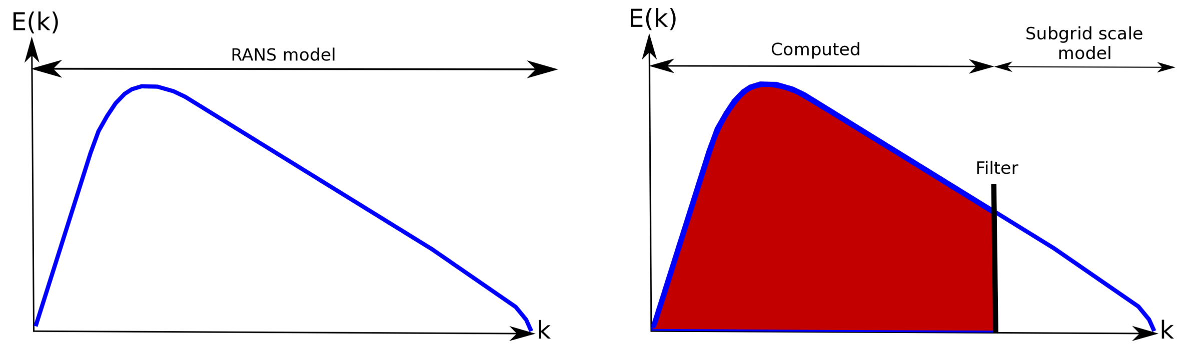

(a) RANS. (b) LES.

Figure 2.1 — *Energy spectra for the repartition of the computed and modeled scales for RANS and LES.*

The $k - \omega$ model from Wilcox [174] uses $\omega \propto \frac{\varepsilon}{k}$ to determine the length scale. This specific turbulence dissipation is defined in the model by equation [II-37]. Its transport equation comes then from the transport equations of k and ε.

$$\omega = \frac{\varepsilon}{\beta^* k} \quad \beta^* = 0,09 \qquad \text{and} \qquad \nu_t = \frac{k}{\omega} \tag{II-37}$$

2.2 Zonal Detached Eddy Simulation

The Zonal Detached Eddy Simulation (ZDES), used in this thesis as the advanced numerical method, is based on the Detached Eddy Simulation (DES), a hybrid model between unsteady RANS and Large Eddy Simulation (LES), as presented in figure 1.25. In order to understand the ZDES model, this section gives an overview of the LES and the main DES versions before detailing the ZDES approach.

2.2.1 Large Eddy Simulation

The Large Eddy Simulation (LES) is different from the aforementioned RANS method. The RANS approaches model the whole turbulent field and are calibrated to give relevant results for the averaged field. However, in cases driven by the turbulence dynamics, with unsteady phenomena, they reach their limits. In order to understand these limitations, it is necessary to understand how the turbulence behaves. The process is called the *energy cascade* and was first thought by Richardson [138] in 1922 and then defined for high Reynolds number isotropic turbulence by Kolmogorov [93] in 1941. The energy is mainly supplied into the turbulent field from the boundary conditions of the domain to the large scales of the flow. Then, the energy is transferred in an inviscid mechanism from the large to the small structures. This zone is the inertial range and is characterized by a constant slope law in $k^{-5/3}$ for the energy distribution, with k the wavenumber. This process is finally limited by the molecular dissipation of the smallest structures when the Kolmogorov scale is reached. This scale depends on the Reynolds number of the flow. The use of the turbulent viscosity in RANS methods aims at modelling the whole cascade. Nevertheless, in real flows, the energy spectrum differs from the theory. For instance, the energy transfer can sometimes be reversed due to the vortex pairing for instance. This phenomenon, called *backscatter*, is not taken into account by these simple RANS models. While the Direct Numerical Simulation (DNS) computes the whole spectral domain, which is impossible with the actual computational resources for high Reynolds number flows, the LES consists in separating the turbulence scales into two domains. The LES computes the large structures and models the smallest ones, as shown in the Fourier space in figure 2.1(b). The scale separation is done through a high-pass filter for the scales, or low-pass filter for the

frequencies. This filtering operation is a convolution in the physical space. The Favre average is then applied to the filtered values as it is for the RANS method. Details on the filtered equations are given by Deardoff [34] who carried out the first LES computations.

It is important to note here that the equations are very similar between the RANS and LES approaches. The main difference is the operator applied: average or filter. As it is the case for the Reynolds averaged equation in the RANS approach, there are some unknowns in the filtered equations. Nevertheless, the filter operator is different from the average operator. One important point is that it is not idempotent. As a consequence, the term $\overline{\underline{u}'' \otimes \underline{u}''}$, appearing in the RANS formulation is different for the LES. Instead of the Reynolds tensor, the LES equation leads to a subgrid scale tensor $\overline{\underline{u}'' \otimes \underline{u}''} - \overline{\underline{u}''} \otimes \overline{\underline{u}''}$. It is then required to model this term to take into account the interactions between the resolved and non resolved scales in LES. One of the main method to close the equation system, and the first one to be historically used, is the Smagorinsky model, defined in equation [II-38], with S the rate of strain, Δ the grid size and C_s the Smagorinsky constant.

$$\nu_{SGS} = (C_S \Delta)^2 \sqrt{2\overline{S_{ij}S_{ij}}} \tag{II-38}$$

2.2.2 The original Detached Eddy Simulation (DES97)

The idea that led to the DES97 is to modify the destruction term of in the equation [II-21] of the Spalart-Allmaras turbulence model so that the RANS model behaves like a LES model in the separated regions of the flow. More precisely, Spalart et al. [163] modified the length scale d_w so that it acts as a LES subgrid scale far from walls. The modification is presented in equation [II-39]. $C_{DES} = 0.65$ is the DES constant and Δ_{max} is the maximum length of the cell, defined in equation [II-40].

$$\tilde{d} = min(d_w, C_{DES}\Delta_{max}) \tag{II-39}$$

$$\Delta_{max} = max\left(\Delta_x, \Delta_y, \Delta_z\right) \tag{II-40}$$

As a consequence, if the wall distance is inferior to $C_{DES}\Delta_{max}$, the model behaves like the RANS formulation. By contrast, far from walls and assuming that for high Reynolds number flows there is a local equilibrium between production and dissipation, $\tilde{\nu}$ in equation [II-21] becomes a Smagorinsky-type subgrid scale viscosity, shown in equation [II-41].

$$\tilde{\nu} \approx \Delta^2 \sqrt{2\overline{S_{ij}S_{ij}}} \tag{II-41}$$

The DES hybrid method computes then the flow field in a LES mode except near the walls, hence a reduced mesh requirement compared to a classic LES. This method is regarded as *global* since there is only one equation for all the configurations. It revealed to give relevant results for various flow computations. Nonetheless, it requires to control precisely the mesh refinement near the wall. Indeed, the area where the method switches continuously from RANS to LES, called "grey zone", depends on the mesh and must be reduced to avoid non-physical separations to occur. The reason is that a refined mesh has a "grey zone" closer to wall. As previously mentioned, the expected behaviour of the DES model is to compute the boundary layer in RANS and the external area in LES. This is the case for coarse meshes. Nevertheless, in configurations with a refined mesh, the LES mode of the DES may be activated in the boundary layer. The grey zone is then located inside the boundary layer.

If the mesh refinement is finer enough to activate the LES mode and too coarse for LES criteria, the turbulence generated by the LES resolution may not be sufficient enough to compensate the drop in the eddy viscosity below the RANS level due to the mode switch. Such configurations induce a phenomenon of drop in the modelled Reynolds stresses, called "Modelled-Stress Depletion" (MSD). This results in an artificial laminarization of the boundary layer. Since a laminar boundary layer is more subject to separation, the MSD may lead to a non physical separation. This phenomenon is known as the "Grid Induced Separation" (GIS). The grey area issue was one of the main concern of Spalart et al. [163] for this original version of the DES. In order to improve the method, different DES versions were then developed.

2.2.3 Delayed Detached Eddy Simulation (DDES)

The Delayed Detached Eddy Simulation is an improvement of the DES97, and is a global approach too. Spalart et al. [161] developed this version so as to overcome the MSD problem and the relating artificial separation (GIS). They implemented a sensor, f_d, defined in equation [II-42] to protect the boundary layer and force the RANS mode in it. The model switches then to the LES mode only outside the boundary layer. The length scale in equation [II-21] differs in the DDES method from the one in the DES97. The equation is given in [II-43].

The DDES improves the capability of DES97, nevertheless, the RANS mode forcing in the boundary layer can lead to a delay in the separation as shown by Chauvet et al. [25] on a jet flow configuration.

$$f_d = 1 - tanh\left[(8 \cdot r_d)^3\right] \tag{II-42}$$

$$\tilde{d} = d_w - f_d max(0, d_w - C_{DES}\Delta_{max}) \tag{II-43}$$

$$r_d = \frac{\nu + \nu_t}{\sqrt{U_{i,j}U_{i,j}}\kappa^2 d_w^2} \tag{II-44}$$

2.2.4 Zonal Detached Eddy Simulation (ZDES)

Some authors, such as Deck [36] or Tyacke et al. [168], reckon that a single model working for all the possible configurations is unrealistic. This is the reason why some zonal hybrid URANS/LES methods are being developed concurrently with the global approaches. The ZDES method is one of these zonal approaches. Actually, the ZDES can be regarded as a global method since it is based on the DES, yet it adds a zonal approach so as to clarify the role of each flow area depending on the flow category it is related to. The method gives the possibility to choose between an unsteady RANS mode (mode = 0), or three different DES modes [38]. The length scale in the transport equation [II-21] is replaced by $\tilde{d}_{ZDES}$, defined in equation [II-45].

$$\tilde{d}_{ZDES} = \begin{cases} d_w & \text{if mode = 0} \\ \tilde{d}^{I}_{DES} & \text{if mode = 1} \\ \tilde{d}^{II}_{DES} & \text{if mode = 2} \\ \tilde{d}^{III}_{DES} & \text{if mode = 3} \end{cases} \tag{II-45}$$

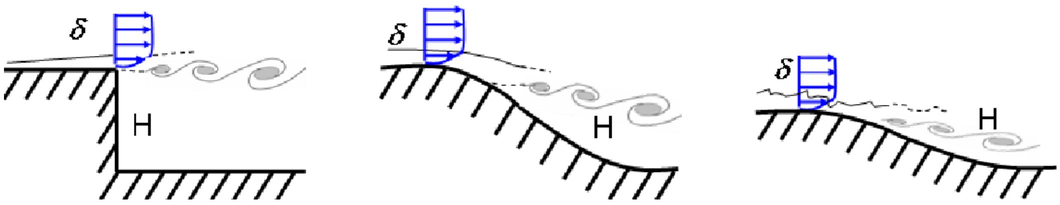

(a) Category I:
separation fixed by the geometry.

(b) Category II:
separation induced by a pressure gradient on a curved surface.

(c) Category III:
separation strongly influenced by the dynamics of the incoming boundary layer.

Figure 2.2 — *Classification of the flow separation types.*

The RANS mode is the standard and recommended [38] ZDES mode and is well adapted to attached flows. The three DES modes correspond to the three main flow categories for separated flows, summarized in figure 2.2.

One can distinguish the following categories and their corresponding ZDES mode:

1. if the separation is fixed by the geometry of the domain boundaries, as seen in figure 2.2(a), the mode 1 is used.
   The resolution in this mode is close to the DES97. The main difference is the use of the length Δ_{vol}, defined in equation [II-51] instead of Δ_{max}, given in equation [II-40] for the subgrid scale. The length for the mode 1 is then explained in equation [II-46].

$$\tilde{d}^{I}_{DES} = min(d_w, C_{DES}\tilde{\Delta}^{I}_{DES}) \qquad \text{(II-46)}$$
$$\tilde{\Delta}^{I}_{DES} = \Delta_{vol}$$

   This change in the length scale aims at reducing the grey zone of the DES97 and therefore switching more rapidly from a RANS to a LES mode. In addition to this length, the damping functions of the LES mode formulation are removed in ZDES mode 1. The asymptotic values are used instead, they are summarized in equation [II-47].

$$f_{v1} = 1 \quad f_{v2} = 0 \quad f_w = 1 \qquad \text{(II-47)}$$

   The purpose is to avoid MSD. Indeed, in regions where the flow is resolved in LES, the eddy viscosity has a low level that can be considered as closeness to the wall by the damping functions. Besides, the production term in equation [II-21] is steeper and does not create LES content artificially. By contrast, the natural unsteadiness within the flow are accelerated.

2. if the separation is fixed by a pressure gradient as seen in figure 2.2(b), mode 2 is chosen. In the same way as the aforementioned DDES, the mode 2 of the ZDES is based on a sensor f_d, shown in equation [II-48] to protect the boundary layer from being resolved in LES. Nevertheless, it adds a threshold, f_{d0}, for this sensor so as to change from a classic DDES mode to another mode in the higher layers of the boundary layer. This latter accelerates the switch from RANS to LES by using a smaller subgrid length scale: Δ_{vol}, shown in equation [II-51], instead of Δ_{max}. The threshold value $f_{d0} = 0.8$ was defined by Riou [142] through computations on flat plates.

$$\tilde{d}_{DES}^{II} = d_w - f_d \cdot max(0, d_w - C_{DES}\tilde{\Delta}_{DES}^{II}) \quad \text{(II-48)}$$

$$\tilde{\Delta}_{DES}^{II} = (0.5 - sign(0.5, f_d - f_{d0})) \times \Delta_{max} + (0.5 + sign(0.5, f_d - f_{d0})) \times \Delta_{vol} \quad \text{(II-49)}$$

$$\text{with } \tilde{\Delta}_{DES}^{II} = \begin{cases} \Delta_{max} & \text{if } f_d < f_{d0} \\ \Delta_{vol} & \text{if } f_d \geq f_{d0} \end{cases} \quad \text{(II-50)}$$

$$\Delta_{vol} = \sqrt[3]{\Delta_x \Delta_y \Delta_z} \quad \text{(II-51)}$$

3. if the separation is strongly dependent on the incoming boundary layer dynamics, as shown in figure 2.2(c), mode 3 can be chosen.
   This mode is a Wall-modelled LES and corresponds to a LES beyond a given distance from the walls, chosen as $d_w^{interface}$. The asymptotic values of the damping functions are forced then. With this method, it is then possible to resolve the boundary layer in LES, however, the requirements in terms of mesh become then the ones for a LES.

$$\tilde{d}_{DES}^{III} = \begin{cases} d_w & \text{if } d_w < d_w^{interface} \\ \tilde{d}_{DES}^{I} & \text{if } d_w \geq d_w^{interface} \end{cases} \quad \text{(II-52)}$$

The ZDES method is still being improved. The last modification in the ZDES concerns the use of a length scale based on the vorticity Δ_ω, instead of Δ_{vol} as described by Deck [38]. This modification applies to mode 2, with Δ_ω a length scale that takes into account the orientation of the vorticity. It was originally proposed by Chauvet et al. [25] in order to improve the performance of the hybrid method for mixing layers by accelerating the switch from RANS to LES in these regions compared to Δ_{vol}. It is available for unstructured grids as explained by Deck [38].

It is important to note that, at the beginning of this thesis work, mode 3 and Δ_ω are not implemented in the *elsA* software and, as a consequence, are not used for this study.

2.3 Numerics

This section deals with the numerical aspects of the simulations that are carried out in this thesis.

2.3.1 The *elsA* software

The solver used in this study is the *elsA* software (ensemble logiciel de simulation en Aérodynamique) from ONERA and co-developed by ONERA and CERFACS. *elsA* is used by numerous manufacturers such as Airbus, Électricité de France, Snecma and Turbomeca, as well as research centers. Its has a wide range of application field, from aircraft to helicopters and, as expected for this study, turbomachinery. A review of its capabilities is given by Cambier et al. [22]. The finite volume method is applied for the discretization of the Navier-Stokes equations on 3D structured meshes with a cell center approach. The Navier-Stokes equations [II-1, II-2 and II-3] can be written under their conservative form as in equation [II-53]. $\underline{W}$ is then the column vector corresponding to the conservative variables, $\underline{F_c}$ for the convective fluxes and $\underline{F_d}$ for the diffusive fluxes.

$$\frac{\partial \underline{W}}{\partial t} + \text{div}\,\left(\underline{F_c} \cdot \underline{F_d}\right) = 0 \tag{II-53}$$

The system [II-53] is integrated on each hexahedric cell *ijk*, which volume is Ω_{ijk}. The numerical fluxes are then evaluated on each of the six faces so as to determine the values for the conservative variables within the cell.

Different methods exist to make the continuous system [II-53] discrete, and compute its solution. An overview of the ones used in the present work is given here.

2.3.2 Time discretization methods

2.3.2.1 The Backward Euler method

The Backward Euler is a time discretization method of order one. It is simple, albeit there is an implicit version. It can be regarded as a part of the Runge-Kutta [95] method with a single-step. It is based on the approximation given in equation [II-54].

With the cell volume Ω_{ijk}, the implicit Backward Euler scheme is then given by equation [II-55].

$$\frac{\partial \underline{W}^n_{ijk}}{\partial t} \approx \frac{\underline{W}^{n+1}_{ijk} - \underline{W}^n_{ijk}}{\Delta t} \tag{II-54}$$

$$\Omega_{ijk} \frac{\underline{W}^{n+1}_{ijk} - \underline{W}^n_{ijk}}{\Delta t} + \sum_{l=1}^{6} (\underline{F_c} - \underline{F_d})^{n+1}_{ijk,l} = 0 \tag{II-55}$$

2.3.2.2 The Gear method

For more accuracy in time in the unsteady calculations, the Gear scheme [56, 57] is used instead of the implicit Backward Euler scheme. Daude [31] carried out LES computations and found this method more efficient than others, such as Dual Time Stepping (DTS), for computations with small time steps, which is the case in this thesis work. This scheme is a backward type too; however, this one is accurate at the second order. Moreover, it is unconditionally stable if the space discretization is stable. It is based on the approximation given in equation [II-56]. The resulting Gear scheme is then given in equation [II-57] for a cell of volume Ω_{ijk}.

$$\frac{\partial \underline{W}^n_{ijk}}{\partial t} \approx \frac{\frac{3}{2}\underline{W}^{n+1}_{ijk} - 2\underline{W}^n_{ijk} + \frac{1}{2}\underline{W}^{n-1}_{ijk}}{\Delta t} \tag{II-56}$$

$$\Omega_{ijk} \frac{\frac{3}{2}\underline{W}^{n+1}_{ijk} - 2\underline{W}^n_{ijk} + \frac{1}{2}\underline{W}^{n-1}_{ijk}}{\Delta t} + \sum_{l=1}^{6} (\underline{F_c} - \underline{F_d})^{n+1}_{ijk,l} = 0 \tag{II-57}$$

The implicit formulation used for the system [II-53] leads to solve a complex matrix system. Therefore, in order to reduce the computational time and memory cost required to solve it, the system is approximated, as detailed in [35]. First, the Jacobian flux matrices ($\frac{\partial F}{\partial W}$) are approximated with a linearisation. Then, the implicit matrix is diagonalized. Finally, a LU factorization of the system, associated with a Newton iterative method, is implemented to simplify the inversion.

2.3.3 Spatial discretization methods

The fluxes in equation [II-53] are still to be discretized. For a simple centred scheme, the convective fluxes at the interface $\Sigma_{1/2}$ and node $\underline{N}_{i+\frac{1}{2}}$ between the cells Ω_i and Ω_{i+1} correspond to the average of the fluxes evaluated at the cell centres as in equation [II-58]. This method is the FDS (Flux Difference Splitting).

$$\underline{\underline{F_c}}(\underline{W}_i, \underline{W}_{i+1}) \cdot \underline{N}_{i+\frac{1}{2}} = \frac{1}{2}[\underline{\underline{F_c}}(\underline{W}_i) + \underline{\underline{F_c}}(\underline{W}_{i+1})] \cdot \underline{N}_{i+\frac{1}{2}} \tag{II-58}$$

Another possibility is based on the fluxes evaluation from the average of the conservative value vectors, as in equation [II-59], also known as the FVS (Flux Vector Splitting).

$$\underline{\underline{F_c}}(\underline{W}_i, \underline{W}_{i+1}) \cdot \underline{N}_{i+\frac{1}{2}} = \underline{\underline{F_c}}(\frac{1}{2}(\underline{W}_i + \underline{W}_{i+1})) \cdot \underline{N}_{i+\frac{1}{2}} \tag{II-59}$$

Jameson et al. [85] added a numerical dissipation $\underline{D}_{i+\frac{1}{2}}$ to equation [II-58] so as to stabilize the scheme and prevent ripples in regions of strong pressure gradients. This dissipation term comprises second and fourth order derivatives of $\underline{W}$ with coefficients depending on the local pressure gradient. The resulting method is then given in equation [II-60].

$$\underline{\underline{F_c}}(\underline{W}_i, \underline{W}_{i+1}) \cdot \underline{N}_{i+\frac{1}{2}} = \frac{1}{2}[\underline{\underline{F_c}}(\underline{W}_i) + \underline{\underline{F_c}}(\underline{W}_{i+1})] \cdot \underline{N}_{i+\frac{1}{2}} - \underline{D}_{i+\frac{1}{2}} \tag{II-60}$$

In order to avoid strong errors where there are no discontinuities, a correction is implemented in these regions only. A discontinuity sensor [84] is then used for the diffusion term $\underline{D}_{i+\frac{1}{2}}$. The resulting scheme is of order 2 excepted in regions with strong pressure gradients where it behaves like a first order scheme. The accuracy of this scheme is weak, nevertheless it is robust and fast, hence its wide use for steady computations.

The FVS schemes are generally more efficient and robust than the FDS ones, although they are less accurate. In order to take the advantages of the two methods, the *Advection Upstream Splitting Method* (AUSM) was developed, originally by Liou and Stephen [106]. This belongs to the FVS family. The AUSM+ improves the original AUSM scheme and brings the accuracy of the FDS schemes in discontinuous areas. The AUSM+P by Edwards and Liou [49] extents the AUSM family to low Mach numbers. It modifies the fluxes discretization of the AUSM+ in regions where the Mach number is lower than 1. This scheme is used in this thesis work for its higher accuracy on a wide range of Mach number as analysed by Mary [116].

The diffusive fluxes $\underline{\underline{F_d}}$ are discretized with a 5 points centred method based on the values in the cells (i-2), (i-1), i, (i+1) and (i+2). First, the values for the conservative variables are computed at the interface $\Sigma_{1/2}$ with an arithmetic average of these values at the centre of the cells on each side of $\Sigma_{1/2}$. Then, the average velocity, temperature and turbulence gradients are evaluated within each cell. Their value at the interface is finally computed with the average of the gradients on each side of $\Sigma_{1/2}$.

2.3.4 The boundary conditions

The computational experiments presented in this thesis work are limited in the spatial domain. The boundary conditions influence directly the computed field as they impose a state to the fluid. Specific conditions are used to compute turbomachinery flows. This section presents the ones applied in this thesis work.

2.3.4.1 Inlet boundary conditions

The boundary condition at the inlet of the domain imposes the stagnation values for the total pressure and enthalpy, as well as the direction of the flow, that is to say the unit velocity vector. Moreover, the turbulent quantities corresponding to the turbulence model are imposed too. For instance, the turbulent kinematic eddy viscosity in the Spalart-Allmaras case. The values are given at the interface of each cell on the domain inlet boundary. This method is usually applied for steady computations, therefore the same values are defined for a given relative height of the channel. The imposed values correspond then to an azimuthal average of the experimental values, or come from a previous computation.

For unsteady computations, upstream unsteady phenomena have to be taken into account in order to have more realistic simulations. This is the reason why a rotating inlet boundary condition was developed by Ngo Boum [126] and successfully applied by Tartousi et al. [166] on a centrifugal compressor. This method consists in taking into account a rotating or translating cartography with the aforementioned values to impose as inlet condition. As a consequence, it is possible to transfer the information related to unsteady phenomena to the flow instead of imposing azimuthally averaged values. This technique is based on a Fourier decomposition of the cartography information. First the cartesian coordinates of the nodes are transformed into cylindrical coordinates. Then the method computes the interpolation coefficients related to the radial direction for each radial line and the curvilinear abscissa of the nodes. The nodes are evenly distributed over the spatial range so that the signal values are distributed with a constant time step. A discrete Fourier transform is then applied to the cartography to extract the coefficients of the Fourier series of the signal. At each time step of the computation, an inverse discrete Fourier transform assembles these coefficients. The signal corresponding to this physical time is then rebuilt for the different values. These values are finally imposed at the interface centres on the inlet boundary.

2.3.4.2 Outlet boundary conditions

The condition of radial equilibrium is a boundary condition used in turbomachinery. It is based on the RANS equations in cylindrical coordinates. Assuming some hypothesis, such as an axial symmetry of the flow ($\frac{\partial}{\partial\theta} = 0$) and no radial velocity ($U_r = 0$), the momentum equation is projected along the radial direction. The result is then the equation [II-61].

$$\frac{\partial p}{\partial r} = \frac{\rho U_\theta^2}{r} + \frac{\partial \tau_{rx}^*}{\partial x} \quad \text{with} \quad \tau_{rx}^* = \mu^* \frac{\partial U_x}{\partial r} \tag{II-61}$$

In this equation, U_x and U_θ are respectively the axial and azimuthal absolute velocities, and r the radial coordinate. The term τ_{rx} corresponds to the shear. Additional hypothesis are available in turbomachinery, such as a plane cross-section for the outlet boundary condition. Moreover, this outlet condition is considered as far enough from the blade row, in practice at least one chord, and restricted by a cylindrical hub and tip. Besides, the shear term is neglected. Assuming that at the radius r_{pivot}, the pressure is p_{pivot}, which is called the pivot pressure, the simplification of the equation [II-61] gives equation [II-62].

$$p(r) = p_{pivot} + \int_{r_{pivot}}^{r} \frac{\rho U_\theta^2}{r} \mathrm{d}r \tag{II-62}$$

This method gives relevant results at the design point in RANS, nevertheless, it may be unstable near surge.

The type 4 throttle law, given in equation [II-63], is often used in RANS near surge because of its enhanced stability. Indeed, compared to the classic pivot pressure with radial equilibrium, this law is more stable when the operating line becomes almost flat near the surge line due to its form in Q^2.

$$p_{pivot} = p_{ref} + \alpha \cdot (\frac{Q(N)}{Q_{ref}})^2 \tag{II-63}$$

2.3.4.3 Wall boundary conditions

The boundary condition that is applied on the interface where the flow should see a wall is an adherence ($U = 0$) condition. The wall can be fixed in the rotor frame of reference or in the stator frame of reference, depending whether it is linked to the rotor, such as the platform wall, or not. Besides, the boundary is considered as adiabatic, that is to say, the flux crossing the interface is null. This approximation is valid in many turbomachinery application since the characteristic time of the turbulence can be regarded as short compared to the characteristic time of thermal diffusion within the material.

Marty et al. [114] shows that this adiabatic condition influences the total temperature distribution near the casing. The influence depends on the method applied to solve the turbulence. Indeed, the total temperature is overestimated in the case of a RANS or URANS method. By contrast, the ZDES method underestimates it. Another possibility is to apply an isothermal boundary condition instead of the adiabatic condition. Nevertheless, it requires an accurate knowledge of the temperature evolution along the machine axis on each wall. This would require to set temperature probes on each wall within the machine. Numerically, an aerothermic coupling is necessary to simulate this evolution. Another drawback is that the use of the entropy as visualization tool to locate the loss area is only available with adiabatic walls, as explained by Denton [43].

2.4 Analysis and validation tools

This section aims at explaining the main analysis methods used for this study. Besides, an explanation of the validation methodology is presented.

2.4.1 Vortex identification

Different methods exist to visualize the vortices in a turbulent flow. One will focus here on the ones retained for the study. First of all, it is important to know that there is no accepted mathematical definition for a vortex [24]. Indeed, a vortex is characterized by an influence area and not by a limited and determined shape, hence the difficulty to visualize it. This is the reason why some methods highlight the effects of the vortex on the flow around it, and not the vortex itself. Another possibility to visualize a vortex is to identify its core. Jeong and Hussain [86] explain that what is considered as a vortex is a coherent structure within a turbulent flow. Therefore some criteria focus on the skeletal structure of a vortex.

The entropy increase is an appropriate method to visualize the flow loss of stagnation pressure as detailed in [43]. In addition, the wall boundary condition used in the study is an adiabatic condition. Thereby, only the entropy creation by irreversibilities contributes significantly to the loss of efficiency. Moreover, Storer and Cumpsty [165] have shown that the principal mechanism of loss caused by the tip leakage flow is the mixing of flows of similar speeds but different direction. As explained in section 1.1, this mixing characterizes the inception of the tip-leakage vortex rolling-up. Besides, the non-uniformity of the clearance flow remaining downstream of the blade contributes a negligible amount to the loss as it mixes out. As a consequence, the visualization of an entropy creation field gives an indication of the tip-leakage vortex location, hence its use in this study.

An important parameter that defines a vortex is the vorticity, Ω. It corresponds to the curl of the velocity, as shown in equations [II-64, II-65 and II-66], with u, v, and w the components of the velocity vector $\underline{V}$, respectively in the x, y and z directions. However, this method can indicate structures that do not correspond to a vortex. Besides, if a vortex changes its orientation, the vorticity may not capture it.

$$\Omega_x = 1/2\,(\partial w/\partial y - \partial v/\partial z) \tag{II-64}$$

$$\Omega_y = 1/2\,(\partial u/\partial z - \partial w/\partial x) \tag{II-65}$$

$$\Omega_z = 1/2\,(\partial v/\partial x - \partial u/\partial y) \tag{II-66}$$

The helicity H is a more valuable method to characterize a vortex. It gives an information on the rotation direction of the vortices: clockwise or counterclockwise. It was defined by Levy et al. [105] as the cosine of the angle between the velocity and the vorticity vectors. It is often normalized for a better understanding of its meaning, as shown in equation [II-67]. Thereby, if the helicity is equal to -1 or 1, the angle between the velocity vector and the vorticity is null or 180°. In other words, these vectors are aligned, which is the case in a vortex core. Another interesting aspect of the normalized helicity is that it gives directly the rotation direction, or direction of swirl of the vortex relative to the streamwise velocity. This criterion is notably used by Furukawa et al. [54] to identify changes in the vortex nature due to a breakdown.

$$H = \underline{\Omega} \cdot \underline{V}/|\underline{\Omega}||\underline{V}| \tag{II-67}$$

In order to capture more accurately the spatial influence domain of the vortex core, it is necessary to apply a criterion capable of appropriately filtering the flow field and make the vortices stand out. Many visualization criteria were developed to reach this purpose and analyse the vortical structures, as listed by Chakraborty et al. [24]. Most of them are based on the velocity gradient analysis, especially the eigenvalues of the velocity gradient tensor, as detailed by Délery [41]. Nevertheless, the effectiveness of some of these methods is weak in highly turbulent flows, and near the walls due to the many small vortices existing in these areas. By contrast, the Q criterion is a way to highlight the main vortical flow structures only. The velocity gradient tensor is split up into a symmetrical part, the shear strain rate, given in equation [II-68], and an anti-symmetrical part, the vorticity tensor, given in equation [II-69]. This leads to $\underline{\underline{\mathrm{grad}}}\,\underline{V} = \underline{\underline{S}} + \underline{\underline{\Omega}}$. The Q criterion, as defined by Hunt et al. [81], is the positive second invariant of the velocity gradient, and is given in equation [II-70]. Q represents then the balance between shear strain rate, $\underline{\underline{S}}$, and vorticity magnitude $\underline{\underline{\Omega}}$. In other words, it represents locations where the rotation dominates the strain. It is a positive scalar. One important advantage of this visualization method is that $Q = 0$ on the walls. Therefore the turbulent structures near the walls do not obstruct the view of the main vortices developing further from the walls.

$$\underline{\underline{S}} = 1/2\,[\underline{\underline{\mathrm{grad}}}\,\underline{V} + (\underline{\underline{\mathrm{grad}}}\,\underline{V})^T] \tag{II-68}$$

$$\underline{\underline{\Omega}} = 1/2\,[\underline{\underline{\mathrm{grad}}}\,\underline{V} - (\underline{\underline{\mathrm{grad}}}\,\underline{V})^T] \tag{II-69}$$

$$Q = 1/2\,[|\underline{\underline{\Omega}}|^2 - |\underline{\underline{S}}|^2] > 0 \tag{II-70}$$

2.4.2 Standard deviation

In order to analyse the unsteadiness within the flow field, the standard deviation is used in this thesis. It measures the average of the discrepancy between the values of a random variable X and the mean value of X. In other words, it represents the dispersion of the values of X around its average, or expected value $E(X)$. It is defined as the square root of the variance $Var(X)$. The König–Huygens theorem [118] is a relation linking the standard deviation to the raw moments $E(X)$ and $E(X^2)$. It is given in equation [II-71]. Thereby, with the average value of X and X^2, it is possible to compute the standard deviation of X.

$$X = \sqrt{Var(X)} = \sqrt{E[X^2] - (E[X])^2} \tag{II-71}$$

2.4.3 Power Spectral Density

Digital signal processing is a vast domain which aims at understanding phenomena based on the analysis of the signals they generate. It is mainly based upon spectral analysis. Indeed, every phenomenon can be represented by a spectrum, that is to say the evolution of a parameter against frequency. The power spectral density (PSD) is one of these possible spectra and represents the flow energy. The estimation of the power spectra is one of the existing methods to understand a phenomenon. The difficulty is to apply the method for a sample of a real signal, which is limited in time [124]. This is the reason why the digital sample does not correspond exactly to the whole analog signal. Therefore, estimates of the statistical parameters of the signal are applied.

These estimates are characterized by three main properties: the bias, the variance and the consistency. The bias is the difference between the expected value of an estimate and its true value. The variance measures the width of the probability density. If bias and variance tend to zero as the sample becomes large, the estimator is regarded as consistent.

The Wiener-Khinchin theorem defines the PSD function, $G_x(f)$, of a signal $x(t)$ as the Fourier transform of the autocorrelation function which is given in equation [II-72] with E[x] the expected value of x. This PSD estimate is called the periodogram.

$$R_{xx}(\tau) = E[x(t)x(t+\tau)] \tag{II-72}$$

The normalized PSD, defined by $\frac{f \cdot G_x(f)}{\sigma^2}$ with σ defined by equation [II-73], gives another information concerning the contribution to the total energy of the different frequencies.

$$\sigma^2 = \int_0^\infty G_x(f)df = \int_0^\infty f \cdot G_x(f)d(log(f)) \tag{II-73}$$

The periodogram is nevertheless an inconsistent estimate of the PSD since its variance does not decrease to 0 for an infinite number of samples. Therefore authors have proposed improved versions.

In order to reduce the variance of the estimate, Bartlett [6] proposed to average independent estimates. The signal is divided into several sections. The PSD is then computed on each of them. Finally, an average of the different PSD is computed. The variance of the method then decreases as the number of sections increases. Unfortunately, the frequency resolution decreases as well and the bias increases.

Another possibility is to reduce the variance of the estimate by smoothing the periodogram. In effect, this is done through a convolution of the periodogram with an appropriate spectral window. In a review of different windows for this smoothing, Harris [74] shows that the window choice affects the detection of harmonic signals. In a recent study, Guénot [68] showed that the Hann window, defined in equation [II-74] is the more appropriate among the classical windows used in the literature.

$$h(t) = \begin{cases} 0.5 - 0.5\cos(2\Pi\frac{t}{T}) & \text{if } t \in [0, T] \\ 0 & \text{otherwise} \end{cases} \tag{II-74}$$

Welch [172] proposed to use the aforementioned improvement methods of Bartlett with a smoothing for each section. Besides, with an eye to enhance the frequency resolution, its method uses an overlap of the sections. Welch suggests then that an overlap of 50% is appropriate to reduce the variance.

The Welch method can be applied to different variables. One of the most common used spectra is the PSD of the velocity. It is notably used to present the cascade of Kolmogorov. The energy spectrum function $E(k)$ scales then in the inertial subrange as the well-known $E(k) = C\varepsilon^{2/3}k^{-5/3}$, with the wavenumber $k = \frac{2\Pi}{l}$ corresponding to the length scale l, the constant C, and the dissipation rate ε. Another possibility is to apply the method to the pressure fluctuations. Nevertheless, the pressure spectrum differs from the one for the velocity. George et al. [59] studied the cross-spectral densities of the pressure analytically. They have shown through decomposition of the turbulence pressure spectrum equation that the spectrum of the turbulent pressure fluctuations in the inertial subrange is made up of three parts that decrease faster than the velocity spectra as frequency increase. First, there is the turbulence-turbulence interaction that scales with a $k^{-7/3}$ slope in the inertial subrange. This interaction is the most likely to be seen in experimental cases with high wavenumbers as described by George et al. [59] who successfully confirmed the theory to various experimental data sets. The two other interactions which occur are turbulence/mean-shear interaction with a $k^{-11/3}$ slope or third moment shear interaction with a k^{-3} slope.

2.4.4 Validation method

An important aspect of this thesis work is the evaluation of an advanced numerical method for turbomachinery applications. As the numerical methods evolve, they are expected to be more accurate in capturing the flow physics. Sagaut and Deck [146] introduce a method of classification of the level of validation of unsteady data from computational fluid dynamics (CFD). These validation levels are summarized in table [2.2]. This starts with the comparison of integral quantities, up to time-frequency analysis. The presented method enables to evaluate the level of trust in a CFD approach.

grade	level of validation
1	integral forces (lift, drag and pitch)
2	mean aerodynamic field (velocity or pressure profiles)
3	second-order statistics (r.m.s. quantities)
4	one-point spectral analysis (power spectral densities)
5	two-point spectral analysis (correlation, coherence and phase spectra)
6	high-order and time–frequency analysis (time–frequency, bicoherence spectra)

Table 2.2 — *Validation levels, from Sagaut and Deck [146]*

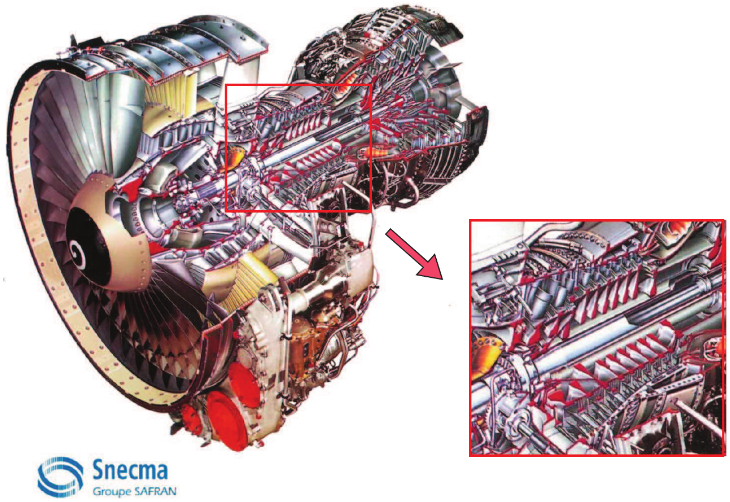

Figure 2.3 — *High pressure bloc in CFM56 jet engine (extracted from Ottavy [127])*

2.5 CREATE

2.5.1 Overview

This section deals with the experimental test bench upon which the study is based.

The simulated axial compressor is CREATE (Compresseur de Recherche pour l'Étude des effets Aérodynamiques et TEchnologiques) [128]. This research compressor was designed by Snecma and is located at the LMFA (Laboratoire de Mécanique des Fluides et d'Acoustique), at the Ecole Centrale de Lyon. It is representative, in terms of geometry and speed, of modern high pressure axial compressors, especially the median-rear block in modern engines, such as turbofans, as shown in figure 2.3. There are two main objectives for the engine company. First, to be able to carry out aerodynamic and mechanical parametric studies on a realistic configuration, and thus optimize the design of future engines. Second, to measure accurately the phenomena occurring in high pressure compressors.

The compressor CREATE is installed within the 2 MW test bench of the LMFA, presented in figure 2.4. This test rig is mounted on a concrete stand uncoupled from the measures room so as to avoid the propagation of vibrations. The test bench works as an open loop as it sucks air from the outside and throws it back. Upstream the compressor, the air coming from the outside is filtered and reaches the settling chamber. There, the total pressure drops to 0.75 bar (74% of the atmospheric pressure) so as to reduce the requirements of the test rig in terms of electric power. Downstream the compressor, a discharge valve enable to step out from a surge state in 0.5s. A butterfly-type valve controls the throttle by reducing the mass flow rate. This mass flow rate is measured at the exit with a Venturi nozzle. The compressor rotation comes from a Jeumont Schneider electric engine of 2.05 MW, which corresponds to the engine power of a high speed train. Along with the gearbox, it enables to reach rotational speeds from 0 to 17000 rpm.

The CREATE compressor comprises $3^{1/2}$ stages, with an inlet guide vane (IGV) and 3 rotor/stator stages. A meridian view is given in figure 2.5. The outer casing diameter is 0.52m and the nominal rotating speed 11543 rpm. The mass flow is then 12.7 $kg.s^{-1}$. The instrumentations installed on CREATE are numerous [27] compared to industrial test rigs. This enables to evaluate more accurately the numerical methods, as it is the case for this study. Furthermore, this compressor aims at analysing the technological effects, improving the flow stability and understanding the mechanisms responsible of the surge inception. In order to ease the measurements on the machine, the axial gap between the rows is increased, the outer-case comprises moving rings with holes for probes, and the spatial periodicity is of

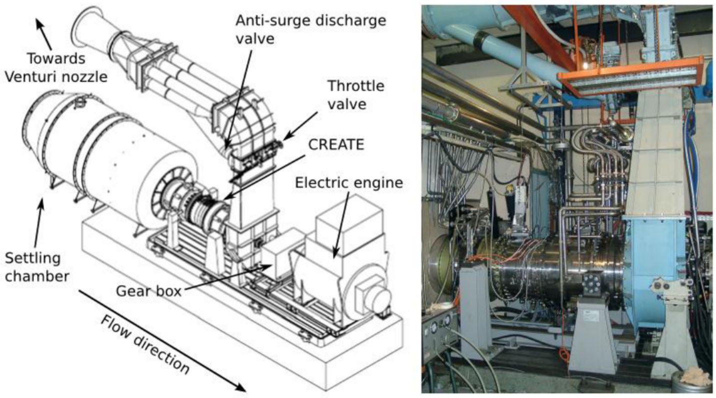

Figure 2.4 — *The CREATE compressor test rig (extracted from Courtiade [27])*

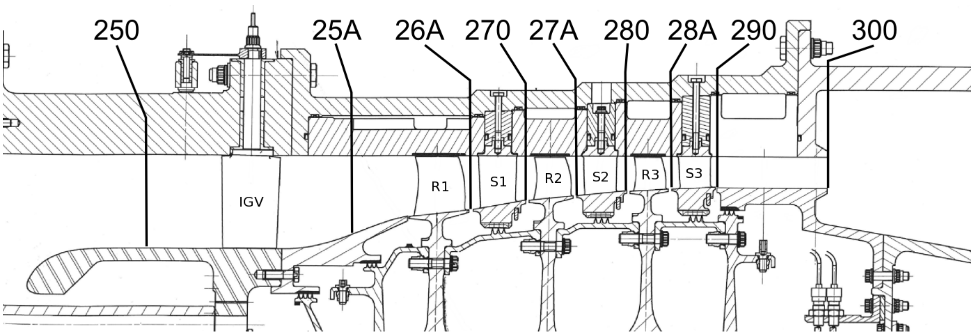

Figure 2.5 — *Meridian view of the CREATE compressor with the location of the axial sections*

$2\Pi/16$ (22.5°). The corresponding blade number for each row is detailed in table 2.3. This thesis work deals with the IGV and the first rotor (R1), hence the spatial periodicity of $2\Pi/32$ (11.25°). However, there are 8 support struts upstream the IGV and downstream the settling chamber on the CREATE compressor test rig, which changes the periodicity if they are taken into account. The IGV is linked to the shroud with a built-in turntable so that its stagger angle can be adapted. Concerning the R1, the inlet Mach number at its tip is 0.92, and the Reynolds number based on the axial chord is of 788000. The dimensionless tip clearances are $\lambda = \frac{GapSize}{MaximumBladeThickness} = 0.23$ and $\tau = \frac{GapSize}{AxialChord} = 1.75$. Based on the Rains criterion [135], the inertia forces are predominant within the gap.

2.5.2 Instrumentation

The aforementioned measurements available on the CREATE compressor are of two types: steady and unsteady. First, there are steady probes that measure the temperature and pressure. Second, there are unsteady measurements synchronized with the rotation of the compressor so that they can measure the same azimuthal position in the same channel at each turn. These measurements are made with unsteady wall static pressure probes, unsteady total pressure probes and Laser Doppler Anemometry (LDA).

The steady measurements are performed at each inter-blade row plane with cobra-type probes. They comprise a thermocouple for the total temperature and four holes for the pressure at the left, front, right and back of the probe. These probes enable to capture the local direction of the flow in the azimuthal

Table 2.3 — *Blade number for the rows*

Row	IGV	R1	S1	R2	S2	R3	S3
Blade number	32	64	96	80	112	80	128

direction. The static pressure is evaluated with the average of the left and right measured pressures. The four measured pressures enable to determine the total pressure that depends on the Mach number and on the direction of the probe. These probes are fixed in the absolute frame of reference and thus capture only the stator influence. The effects from rotors wakes are then averaged. Besides, the integration time of these cobra probes corresponds to the passing period of 20000-30000 channels. As a consequence, the rotor-stator interactions are averaged too.

The unsteady static pressure signals are obtained with unsteady wall probes [19]. The pressure transducers are manufactured by Kulite (XTE-190). They are equipped with a module to compensate the variations of temperature. They are capable to measure the pressure fluctuations up to 145kHz with a spatial discretization of $1mm^2$. The signals are conditioned and then a digital filter is applied to cut off frequencies above 150kHz that could originate from parasites. The digitized signals are finally stored in the data base of the LMFA. The probes are located on the casing at each inter-row plane shown in figure 2.5. Besides, in order to analyse more accurately the flow within a row, such as the tip-leakage flow, removable blocks are placed at the casing where there are the rotors. These blocks contain twelve sensors located at twelve axial positions and four azimuths over 9°. All these probes are used at different operating points on CREATE. A thorough description of this experimental campaign is given by Courtiade [27].

In order to capture unsteady phenomena far from the walls, unsteady total pressure probes, developed by the Von Karman Institute (VKI), are used. Contrary to the steady probes, they have a cylinder shape of 2.5 mm to decrease flow disturbance. Besides, they are built to resist to high temperatures and provide accurate measurements up to 150° and measure pressures up to 250 kHz. Details on these fast-reponse probes are given by Mersinligil et al. [120]. They have been used to measure the pressure in the inter-row planes from section 26A to 290. They have shown good agreement with the steady probes, and within the uncertainties of these methods. For the total pressure measurements, the uncertainties originate from the spatial positioning and the error done during the probe calibration. They are evaluated to 0.1% of the mean steady value [27]. Since measurements with probes are intrusive, the measured values have to be used cautiously, especially near the walls due to the interactions occurring with the boundary layers.

The data extracted from these pressure probes are used in this thesis to carry out power spectral density (PSD) with the Welch method. The frame of reference is different between the computations and the experimental data. Therefore, a change of frame is done before analysing the data. At each axial and radial position, the data are stored depending on their azimuthal position. The acquisition frequency gives the time information. Then, a linear interpolation is used to change the frame of reference, from the experimental one (absolute) to the computational one (rotor frame of reference). The change is based on the rotating velocity of rotor 1 and the radius of the probe location. The PSD is then carried out on the resulting data, in the same reference frame as the computational results.

Contrary to the aforementioned techniques, the Laser Doppler Anemometry (LDA) is a non-intrusive measurement method. It measures the velocity of the flow inside the compressor. This optical technique is based on the analysis of the intersection between two laser beams. Particles of paraffin oil ($1\mu m$) are injected at the inlet of the compressor. They are intended to follow the flow lines along the compressor, hence the choice of light, small particles. An interference volume, characterized by a succession of light and dark fringes, is created by making two coherent laser beams cross where the measurements are required. This volume is ellipsoidal and the spacing d between the fringes depends on the wavelength λ and the angle between the two laser beams θ following the equation [II-75]. When a particle crosses a fringe, it emits a light signal called Doppler burst that is captured by the optical acquisition system. As a result, the captured signal has a frequency corresponding to the passage frequency of the particle, f. By knowing the spatial gap between the fringes, it is then possible to compute the particle velocity, $\underline{V}$ in one direction $\underline{n}$, perpendicular to the fringes, as given in equation [II-76]. The frequency f_b is applied to the signal of one beam through a Bragg cell so as to shift the frequency and therefore add an information on

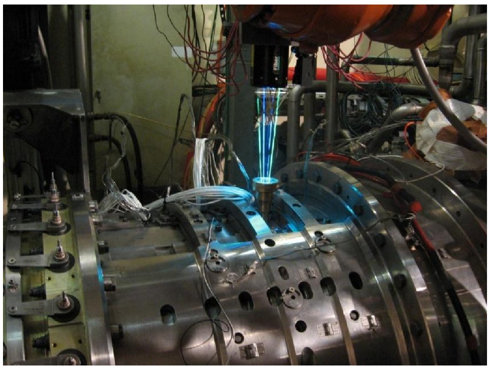

Figure 2.6 — *The four laser beams measuring the axial and circumferential velocities (extracted from Courtiade [27])*

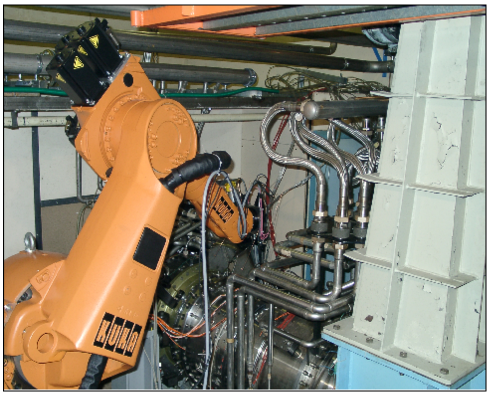

Figure 2.7 — *Robot for the LDA measurements on the CREATE test rig (extracted from Ottavy [127])*

the particle movement to the velocity.

$$d = \frac{\lambda}{2sin(\frac{\theta}{2})} \tag{II-75}$$

$$\underline{V} \cdot \underline{n} = \frac{\lambda}{2sin(\frac{\theta}{2})}(f - f_b) \tag{II-76}$$

This LDA is a statistical technique: the velocity is computed by averaging the velocities of all the particles crossing randomly the fringes. Therefore, it requires a long acquisition time to be able to get a velocity value. Besides, it is more difficult to measure the velocity in regions with few particles, such as the wakes, boundary layers and recirculation areas. In the LDA campaign, the velocity measurements were performed along the compressor from the hub to the tip and over an azimuthal period.

For the experimental test rig located at the LMFA, the LDA method is doubled (LDA-2D) and the four beams focalize on the same volume in order to measure at the same time two components of the velocity: axial and circumferential. Moreover, the optical acquisition device is integrated into the laser head to ease the measurements. Indeed, the laser traverses the compressor casing through a small glass only, as presented in figure 2.6. In order to avoid that oil projections reach this glass, it is located in a hopper extension attached to the portholes. These portholes are implemented in removable blocks mounted on the moving rings. The positioning of this laser head is made with a six axis arm robot, shown in figure 2.7. More details on the LDA technique and the whole acquisition system developed for CREATE are given by Arnaud [1].

The LDA data are used in this thesis for comparison with the computational results. A change of reference frame, similar to the one applied to the pressure probe data, is conducted to be in the same frame as the computations, that is to say the rotor reference frame. The measurements are then stored depending on their azimuthal position in this new frame with a spatial discretization of 200 over $11.25°$ ($2\Pi/32$, the IGV periodicity). The data in each of the 200 spatial domains are then averaged. An adjustment is then required to find the relative azimuthal position between the values from the computations and from the measurements. This shift is based on the blade azimuthal position. The resulting experimental values are then plotted and compared to averaged values from the computations.

Second part

Implementation and evaluation

This second part includes the choice of the advanced numerical method, its implementation in a numerical test bench and its evaluation for the simulation of the tip-leakage flow in the first rotor of the CREATE compressor.

Chapter 3

Numerical test bench definition

Contents

This chapter deals with the choice of the advanced numerical simulation method and the definition of a numerical test bench for its evaluation concerning the tip-leakage flow.

3.1 Choice of the advanced numerical method

Numerical simulations which are regarded as "advanced" at the beginning of this study are numerous. But what is advanced is not necessarily adapted to constraints of research and development, even in the medium term. It is therefore required to choose a method that could surpass the limitations of RANS and even URANS approaches at a reasonable cost for the simulation of realistic configurations.

After methods based on averaged Navier-Stokes equations, LES is the next big step in the field of CFD as seen in chapter 1. This is why it is taken into consideration as the advanced numerical method for the simulation of the tip-leakage flow on the first rotor of the axial compressor CREATE. Indeed, LES has given more accurate results than RANS for the tip-leakage flow simulation [69, 13]. Nevertheless, such results have been highlighted only on very simple test cases, such as the fixed NACA5510 airfoil at low Reynolds number simulated by Boudet et al. [13]. And even on such low Reynolds cases, meshes do not always meet LES requirements for the resolution of turbulent boundary layers. Although some previous studies have been carried out with LES on coarse meshes, this study focusses on evaluating an advanced numerical method following its inherent requirements. The mesh size for the simulation in LES of one channel of the first rotor of CREATE is then estimated. This estimation is based on a RANS solution with a fine mesh so as to find the local friction modulus τ_p. The mesh is then refined to reach the grid sizes in wall unit required for the simulation of wall-bounded flows in LES following recommendations from Sagaut et al. [147]. The resulting mesh comprises 3.2 billion points. This fine mesh can be explained by the high mesh requirements for LES to simulate the anisotropic streaks like structures existing in the turbulent boundary layer. These mesh requirements increase with the Reynolds number. The factor depends on the proportion of the boundary layer to compute [132]. Indeed, if the case is limited to the simulation of the outer-layer the cost in terms of points scales in $Re^{0.6}$, while resolving inner-layer structures rises this cost to $Re^{2.4}$. For the resolution in LES of a turbulent boundary layer with low order numerical schemes, the grid size in wall unit tangential to the flow direction, better known as z^+ is of 15. Its longitudinal counterpart, x^+ , is 50. By comparison, RANS requirements from Deck [37] are respectively of 1000 for z^+ and 500 for x^+ . In other words, a LES type mesh comprises about 660 as many points as a RANS type one. In this case, since the boundary layer is modelled, there is no need to resolve the streaks which reduces the mesh requirements. Higher order numerical schemes, such as the 5^{th} or 7^{th} order, could reduce these requirements and thus reduce the mesh size. Nevertheless, the numerical schemes in *elsA* at the beginning of this study are limited, and no 5^{th} or 7^{th} order scheme is available. Although time-consuming and expensive, this LES computation could be feasible for a single computation. However, above the evaluation of an advanced numerical method, the second objective of this research work is to analyse the effects of the IGV wake distortions and the effects of throttle on the tip-leakage flow. As a consequence, multiple computations are planned to be carried out with the advanced method. Therefore the study framework prevents the use of LES.

Hybrid URANS/LES methods alleviate this cost problem and are more and more present in the literature for the simulation of turbomachinery parts, hence their consideration in this study. Two schools of thought exist concerning these hybrid methods.

The first one is a global hybrid approach. One model is used for all the flow areas with a continuous transition from URANS to LES, such as the DES and DDES. This model aims at being adapted to the widest panel of flow configurations. Zones which are less important have to be treated with the same model which increases the mesh demands. Although rather industry-oriented, their high cost and their non-universality limit their application range.

The second one is a pure zonal approach where URANS and LES regions are distinct. This separates the flow regions according to the method used to resolve them, either URANS or LES. It enables to use the most adapted simulation type in each region at the cost of a more complex implementation. Indeed, the transition zone between RANS and LES in turbulence-driven areas is the main difficulty. This difficulty prevents their widespread use in the industry.

Zonal Detached Eddy Simulation tends to bring the best of both worlds by adding the possibility to use zones, while it is still based on a one-equation model for the entire flow field like standard global approaches. ZDES has three important advantages for this study over other DES like methods. First, it is possible to designate regions resolved only in RANS and thus to reduce the mesh requirements. Second, the different DES modes are adapted to different flow topologies which makes the method flexible. Last but not least, ZDES is still in development and important evolutions are currently being validated, such as mode 3 with wall-resolved LES. This widens the possibility range of what the method can do over the long term. As seen in chapter 1, modes 1 and 2 of the ZDES have been used in production at ONERA for external aerodynamic studies with topologies closed to the ones encountered in the tip-leakage flow. For instance, one can mention the work of Le Pape et al. [104] with ZDES on an airfoil in post-stall condition, or from Deck [38] on a backward facing step. This method is more and more used at ONERA for external aerodynamic flows and has given relevant results. As a consequence, ZDES is an appropriate advanced numerical method to evaluate in turbomachinery for the simulation of tip-leakage flow.

In the next sections of this chapter, the definition of a numerical test case for the ZDES evaluation is detailed.

3.2 Computational domain definition

In this section, the computational domain of the numerical test case is presented.

The CREATE compressor comprises 3.5 stages and this study focusses only on the tip-leakage flow of the first rotor (R1). A full annulus calculation of all the stages for the whole compressor would be anyhow impossible with ZDES mesh requirements. Even in RANS, such a simulation is barely feasible with the current processing powers. A close study was nonetheless carried out by Gourdain [128] in URANS with wall functions following the spatial periodicity of the compressor, in other words $\frac{2\Pi}{16}$ of the 3.5 stages were simulated. Nevertheless, the R1 is between an Inlet Guide Vane (IGV), upstream and the first stator (S1), downstream. Besides, it is important to remember that previous studies on axial compressors, such as the work of Sirakov and Tan [155] or Mailach et al. [109], underscored the strong interactions due to periodical wake arrivals on the tip-leakage flow, hence the importance to take the IGV into account. Another interaction, albeit less important as underlined by Mailach and Vogeler [107], originates from potential effects of downstream blades. In order to reduce the domain size, these potential effects are not taken into account and therefore the S1 is not simulated. This is based on the assumption that concerning the tip-leakage flow, in the R1 of CREATE, potential effects emanating from the S1 are less important than convected wakes from the IGV. This strong assumption will have an impact on the analysis presented in the next chapters.

A second simplification concerns the IGV, which is not simulated. Nevertheless, the wakes coming from the IGV are taken into account through the inlet boundary condition as explained in the next section of this chapter. Without the IGV simulation, first and foremost, there is no rotor-stator boundary condition, which halves the mesh size and avoid the filtering inherent to such boundary conditions. The computations on the R1 are then carried out in the rotor frame of reference. The inlet boundary of the test bench is then set to section 25A of the experimental test rig, located between the IGV and the R1 as presented in figure 2.5. The reason is that measurements are available on the experimental compressor for different operating points at this section. Besides, the possible comparisons with experimental data at section 25A make the numerical test bench more reliable for the evaluation of the method. The outlet boundary condition is based on the hypothesis that the outflow is axisymmetric, hence the location of the outflow surface far from the trailing edge of the R1. Furthermore experimental measurements are available at section 26A, so this section has to be inside the computational domain for validation purposes. Nonetheless, the mesh size is a key element in the domain definition. This is why the outlet boundary of the computational domain is defined at two axial chords downstream the R1.

After the axial restriction, it is compulsory to restrict the azimuthal dimensions of the computational domain too. Since the IGV is taken into account, the periodicity of the IGV-R1 domain is used. Table 2.3 in chapter 2 summarizes the blade number of the different rows on the CREATE compressor. In the area of interest of this study, that is to say the first 1.5 stage of the compressor, and especially the R1, the periodicity is of $\frac{2\Pi}{32}$. This leads to the simulation of two blades of the R1 and one of the IGV. Besides, the computation periodicity influences directly the separated flows and the rotating instabilities as highlighted by Van Remmings et al. [169] in DDES. Thereby, for advanced analysis of the tip-leakage flow, it is relevant to simulate the two channels of the R1.

An important point that has to be mentioned is that even if the periodicity of the group containing the IGV and the R1 is of $\frac{2\Pi}{32}$, the location of the test rig in the test chamber and technological effects upstream remove this periodicity on the measurements. For instance, there are 8 support struts upstream the IGV, that are not taken into account at all for the numerical simulations. These simplifications are classic for the simulations of the axial compressor CREATE, since taking into account every technological effect

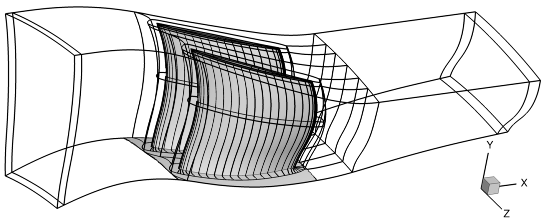

Figure 3.1 — *Computational domain for the different computations on the first rotor of CREATE*

would require to model $360°$ azimuthally of this realistic machine, which is at the time of this study, impossible. This will explain some of the discrepancies between CFD and experimental results. These choices are compromises between the cost of the computation, hence its feasibility, and the expected precision of the computation.

As a consequence, the only blade row to be simulated in this study is the first rotor of CREATE (R1). Moreover, by controlling the inlet and outlet conditions, the differences that stand out from the comparison of the methods originate only from what occurs around the R1, and not from the IGV simulation. The resulting computational domain is thus presented in figure 3.1.

After the definition of the domain boundaries, the next step is the meshing. In order to evaluate the ZDES method compared to the RANS and URANS approaches, the same domain and the same mesh are used for all the computations on the R1. One important aspect of the ZDES method is the possibility to define zones simulated in unsteady RANS. This reduces the mesh size in regions which do not require to be simulated in DES. From this perspective, the area upstream the leading edge of the R1 does not require to be simulated in DES since it is not the main area of interest and is not subject to massive boundary layer separation. Nonetheless, the wakes from the IGV have to be convected with precision, and therefore, a fine RANS mesh is required to avoid too important dissipations upstream the R1. From the leading edge, a DES methodology is applied to solve the tip-leakage flow. The grid suits therefore the ZDES requirements from Deck [37] and Sagaut et al. [147] for the simulation of boundary layers and is based on an O4H mesh topology. The zonal approach affects thereby the mesh refinement: a RANS type mesh upstream of the blade, and a DES type mesh from the LE onward, that is to say, a LES resolution mesh except near the wall.

The cell dimension normal to the wall in wall unit fulfils y^+ of the order of 1 in every zone. However, its wall parallel counterparts differ depending on the zones. Upstream of the R1, x^+ varies between 400 and 500 and z^+ is lower than 100. The closer are the cells from the leading edge of the R1, the finer they are. In the vicinity of the blades, x^+ and z^+ are respectively of the order of 200-300 and 100. In the area of interest, that is to say, the R1 tip clearance, 49 points are used radially to mesh the gap. This gap size is of 1.75% of the axial chord. Finally, downstream of the blades, the mesh is progressively coarsened axially with values up to 1700 for x^+ and 150 for z^+ so as to avoid numerical reflections. The whole mesh is then split into 771 blocks for the computation on 480 cores of the parallel computer Stelvio of ONERA, which is made of SGI Altix ICE 8200EX nodes, comprising Intel Xeon cores. The resulting mesh comprises 88 Million points. The high number of points of this computational domain needs to be put into perspective. Indeed, this is a fine DES type mesh except in the inlet region where the mesh suits RANS requirements. By contrast, a full DES type mesh, required for a DDES simulation for instance, would comprise 128 Million points for the domain. The additional cost would originate from the refinement of the area upstream the R1. This means that in the flow configuration of this study, the zonal approach of the ZDES requires $2/3^{rd}$ of the mesh size of a global DES type approach.

3.3 Specification of the boundary conditions

This section deals with an important part of this study: the definition of the boundary conditions for the numerical test bench. These are essential to ensure that the numerical test bench is as close as possible to the experimental compressor operating point which is analysed. Moreover, the computational domain defined earlier extends from section 25A to two chords axially and over two channels of the R1. This is why the first step is to define the boundary conditions at the inlet, section 25A, and at the outlet.

3.3.1 Domain definition for the preliminary computation

The objective is to get the flow cartography at section 25A for the design point while taking into account the wakes from the IGV. However, experimental data at section 25A are not available throughout the whole radial and azimuthal extensions. Instead, the data are obtained over $10°$ azimuthally. In addition, they extend from 5% to 95% relative height, that is to say, the boundary layers at the hub and tip are not measured. Moreover, it is required to set the flow angles for the inlet boundary condition of the computation on R1. This information is unavailable experimentally for the meridian angle ϕ due to the use of 4 hole probes. Therefore a preliminary computation has to be carried out to extract the flow cartography on $11.25°$ or $\frac{2\Pi}{32}$ azimuthally and all over the radius. For the R1 computations to be at the same operating point corresponding to this flow cartography, it is necessary to know and use the same outlet condition in this preliminary study. Moreover, by taking into account the R1, averaged potential effects from the R1 are expected to be simulated, hence a better agreement with experimental data in particular concerning the pressure. This is why one channel of the IGV and one channel of the R1 are modelled.

The outlet axial position is the same as the one for the computation on the R1 detailed in section 3.2. Experimental data are available at section 250, upstream the IGV, figure 2.5. To this end, the inlet axial position is defined at this section. The junction between the two rows is computed with a standard mixing plane boundary condition located downstream section 25A. The reason is that if the mixing plane is located upstream, the flow cartography would be azimuthally averaged, and in the same way, the variations due to the wakes would not be captured.

The wakes from the IGV are not only subject to the velocity deficit coming from the IGV blade position but also to vortices coming from the IGV blade near the hub and near the casing. Indeed, the IGV geometry is complex since it has a variable stagger and can rotate on its axis to be adapted to the flow conditions. This IGV is structurally linked to the casing through a built-in turntable. A simplification of the geometry for this built-in turntable and another simplification for the IGV hub gap is realized in order not to involve advanced meshing techniques such as the Chimera method used on a similar case by Billonnet et al. [10]. Indeed, a high accuracy in the geometry definition of the IGV is not a prerequisite to the capture of the wakes at section 25A. The capture of the main phenomena only is expected. This is the reason why the simplification presented in figure 3.2 is implemented. The IGV is regarded as a "floating stator" with linear gaps at the hub and tip. For the tip, the gap at the leading edge is of 1.69% of the tip axial chord while it is of 2.64% of the tip axial chord at the trailing edge. For the hub, the gap at the leading edge is of 0.51% of the hub axial chord while it is of 2.95% of the hub axial chord at the trailing edge.

The whole mesh for this preliminary computation is presented in figure 3.3. It respects mesh requirements for a fine RANS computation and thereby comprises 7.3 Million points for one channel of the IGV and one of the R1.

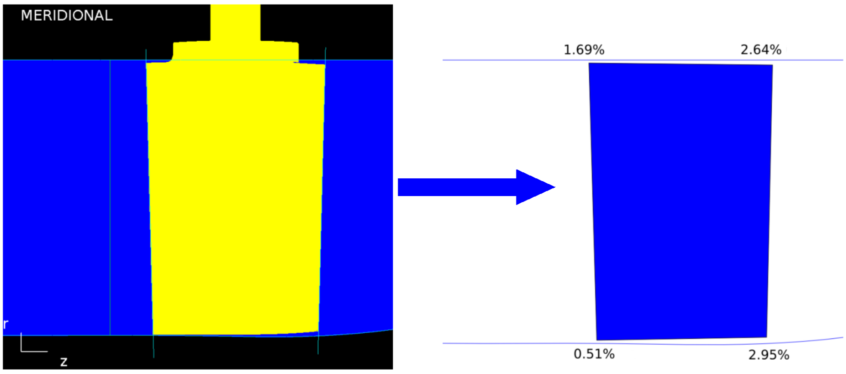

Figure 3.2 — *Simplication of the geometry for the IGV hub and tip gaps with the relative hub and tip gap sizes.*

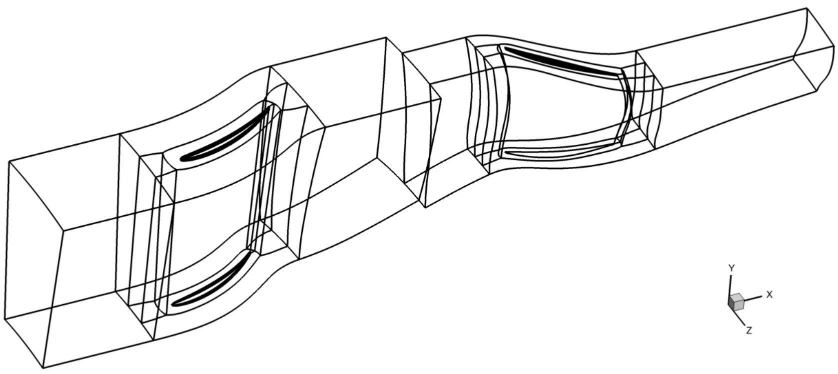

Figure 3.3 — *Computational domain with the IGV and the R1 of CREATE.*

3.3.2 Numerical aspects of the preliminary computation

The preliminary computation is carried out on 64 cores of ONERA's parallel computer with a steady RANS approach. Indeed, this study aims at extracting a steady cartography at section 25A. The one-equation turbulence model of Spalart-Allmaras is used to be consistent with the ZDES method. The spatial integration scheme is the one from Jameson [85] and the implicit Backward-Euler method [95] is applied for time integration.

Concerning the boundary condition upstream, physical values are given at each interface of the section. The physical values are the stagnation pressure, stagnation enthalpy, primitive turbulence quantity of the model and direction of the flow. They originate from radial distributions of experimental probes at section 250, therefore the same value is used for all the cells at each radius. The meridian angle is considered as being constant to zero here since there is no slope at the hub and at the casing around section 250. For the turbulent value $\tilde{\nu}$ of the Spalart-Allmaras model, a simplification is used since there is a strong hypothesis on the fact that there is no turbulence upstream at 250. As a consequence, a negligible value for $\tilde{\nu}$ is chosen. For the outlet boundary condition, the static pressure is specified at the hub and then a simplified radial equilibrium is applied.

3.3.3 Operating point definition

The preliminary study is actually not made up of one computation but many. Their purpose is to extract the flow cartography which corresponds to the design operating point of the experimental data. There are many ways to adapt a computation so that it corresponds to an experimental operating point. However, it is impossible to have a perfect agreement between CFD and experiments. Indeed, the numerical methods are not perfect due to strong assumptions, numerical dissipation, turbulence modelling, inaccurate boundary conditions, technological effects not taken into account or grid density. One possibility is to be as close as possible from the ratio $\frac{\Pi}{Q}$ of the experiment, with Π and Q being respectively the pressure ratio and mass flow rate. Nevertheless, this method, albeit widely used, has an important drawback. Because it is based on a single value only, an accumulation of errors may lead to a working point regarded as pertinent even if it is not the case locally. Besides, it requires an important knowledge of the values which are integrated and averaged to find this single value. In this study, it was decided to proceed in a different way particularly because of the lack of values in the boundary layers. The methodology applied in this study is to find the best agreement for radial distributions at section 25A.

With that in mind, first of all, the pivot pressure at the outlet boundary condition is modified to ensure that the radial distribution of axial momentum obtained at section 25A is in good agreement with the experimental values. The corresponding values for the pivot pressure are normalized by a reference pressure value, Pio, which corresponds to the total pressure at section 250. Figure 3.4(a) shows the axial momentum radial distributions for some of the computed working points in RANS from 0.90 Pio to 0.95 Pio. The black triangles are the probe values for the experimental design point. First of all, one can see that the main effect of a change in the pivot pressure is a shift in the axial momentum values along the radius, from the hub to the tip. Since the area of interest of this study is the tip-leakage flow, a particular attention is paid to the zone near the casing. As a result, the pivot pressure chosen is 0.93 Pio. Indeed, for this value of pivot pressure the axial momentum is in good agreement with the experimental values at mid relative height, and most importantly, the computation captures the correct gradient near the casing. This gradient corresponds to the axial momentum deficit due to the presence of the IGV tip vortex. This IGV tip vortex stems from the gap at the IGV tip which is simulated as linear in the computation, as described earlier, instead of being a built-in turntable. This leads to errors on the characteristics of the IGV tip vortex, especially the flow angles. This error is visible in figure 3.4(b) for the azimuthal angle. It can reach up to 3° near the hub and casing. Moreover, in the range of pivot pressure presented, it does not depend on the outlet pivot pressure. These flow angles influence the blade loading and above

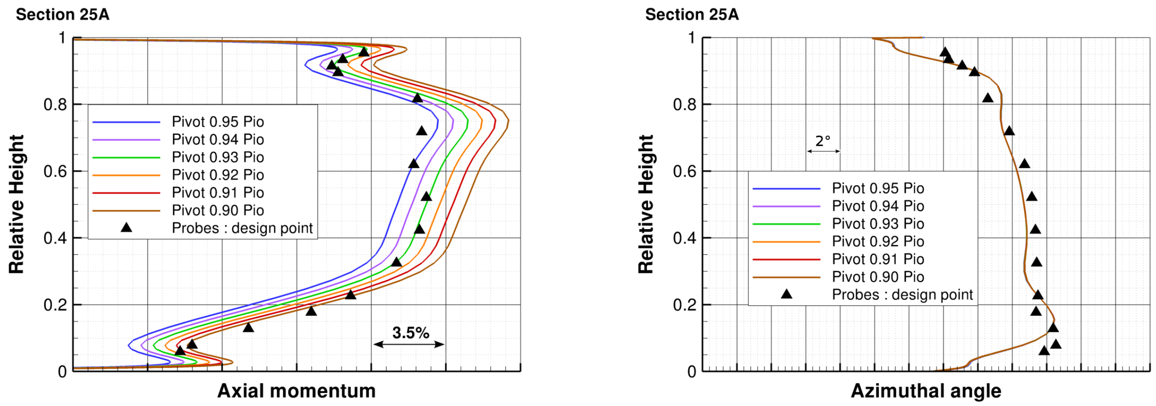

(a) Axial momentum.

(b) Azimuthal angle.

Figure 3.4 — *Radial distribution of time and circumferentially averaged values at section 25A. RANS results on the IGV-R1 domain for different pivot pressures and data from experimental probes at the design point.*

all are extracted directly for the flow cartography. Indeed, they are used for the inlet condition on the computations on the R1. This is the reason why, once the pivot pressure is chosen at 0.93 Pio, another study is carried out to be closer to the experimental values for the flow angles.

In order to reach this goal, different numerical parameters are compared, such as the turbulence model, the spatial discretization scheme and the curvature correction of the Spalart-Allmaras model. Details of these comparisons are explained in appendix B. One will focus here on the two main effects: the impact on the axial momentum and the azimuthal angle. The axial momentum radial distribution at section 25A is presented in figure 3.5(a) for the same outlet pivot pressure chosen earlier, 0.93 Pio, but for different numerical parameters. The reference case uses the Jameson spatial discretization scheme (SA Jameson). Another computation with the AUSM+P scheme is evaluated (SA AUSM+P). Finally, a last one is compared. It is similar to the SA AUSM+P but with the curvature correction for the Spalart-Allmaras scheme [160] (SARC AUSM+P). The AUSM+P versions improve the capture of the gradient at 80% relative height and around 20% relative height. However, near the casing at 90%, the gradient is underestimated. The curvature correction amplifies this trend. This leads to a larger discrepency with the measurements near the hub. Nevertheless, the SARC computation is in better agreement than the SA AUSM+P with the measurements at 90% relative height, that is to say, the IGV tip vortex is better captured. In any case, the discrepancies between the computations at 90% are inferior to 0.7% for the axial momentum.

The real improvements of the AUSM+P scheme are found when comparing the azimuthal angle in figure 3.5(b). The radial position of the inflection around 20% relative height is quite correctly captured with the SA AUSM+P compared to SA Jameson. Moreover, the curvature correction improves even more the prediction capability of the method for the capture of IGV hub vortex width. In other words, the development stage of the hub vortex is captured. Between 80 and 90% relative height, the gradient is in better agreement with the AUSM+P method. The contribution of the AUSM+P is clear near the casing with a 1° improvement of the prevision of the angle value. There is nonetheless few differences between the two computations based on the AUSM+P near the casing. The only prediction variation is an increased angle value above 95% relative height. The lack of measurements so close to the casing however prevents to determine if this inflection is physical or not.

The differences near the casing for the axial momentum are thin and moreover, the angles will be directly used as inlet condition for the R1 computation. So the azimuthal angle is used here to differentiate the methods. In conclusion, the Spalart-Allmaras turbulence model with curvature correction and

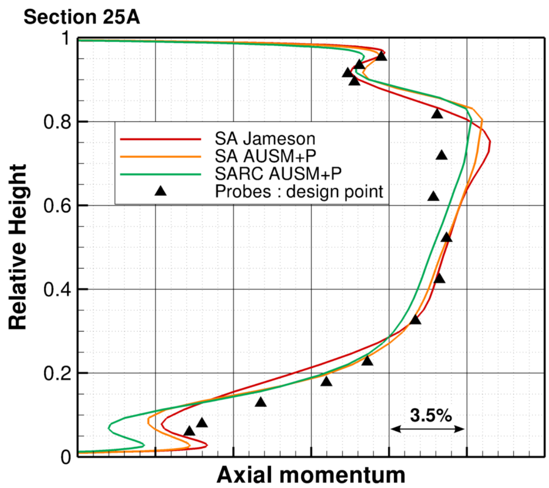

(a) Axial momentum.

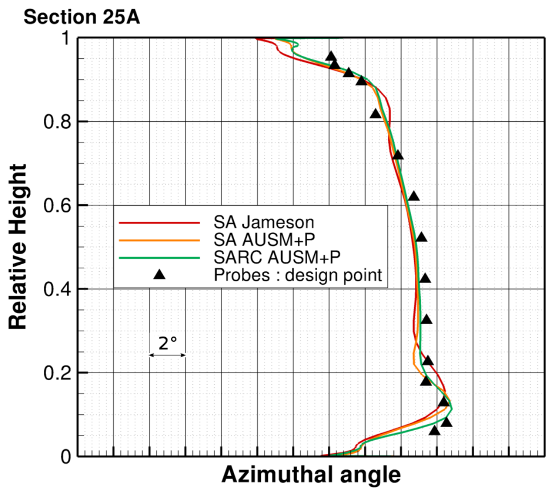

(b) Azimuthal angle.

Figure 3.5 — *Radial distribution of time and circumferentially averaged values at section 25A. RANS results on the IGV-R1 domain for different numerical parameters and data from experimental probes at the design point.*

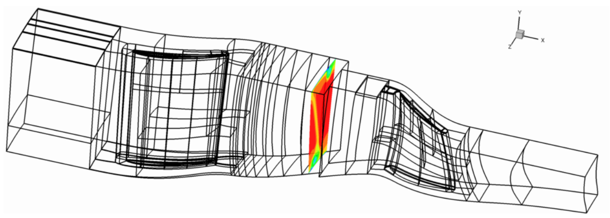

Figure 3.6 — *Position of the extraction plane at section 25A from the preliminary study.*

AUSM+P is finally chosen for its advantages on the simulation of the flow angles. Based on the axial momentum results, Spalart-Allmaras without curvature correction would have been a relevant choice too. A priority is given here to the swirl capture instead of the axial momentum.

The cartography is then extracted at section 25A, shown in figure 3.6, from the computation SARC AUSM+P. Since this cartography results from the choice of the pivot pressure in order to be in good agreement with the experimental probes, the same outlet boundary condition is used for the R1 computations. That is to say, the static pressure 0.93 Pio is specified at the hub of the outlet surface of the R1 computations and then a simplified radial equilibrium is applied, following equation II-62. An important aspect of the study on the R1 is that the same static pressure is used for all of the following computations (RANS, URANS, ZDES with and without the rotating distortion) at the design point.

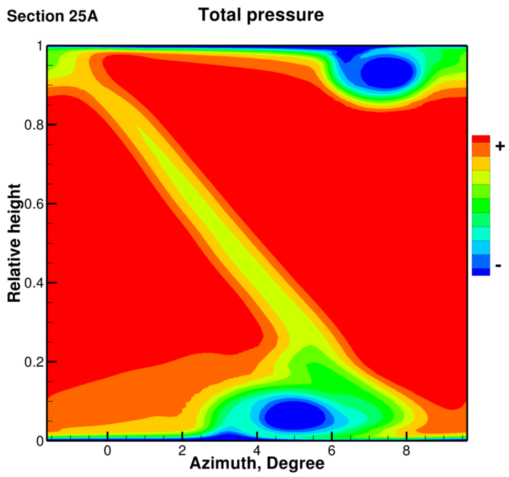

(a) RANS RDE-R1 computation.

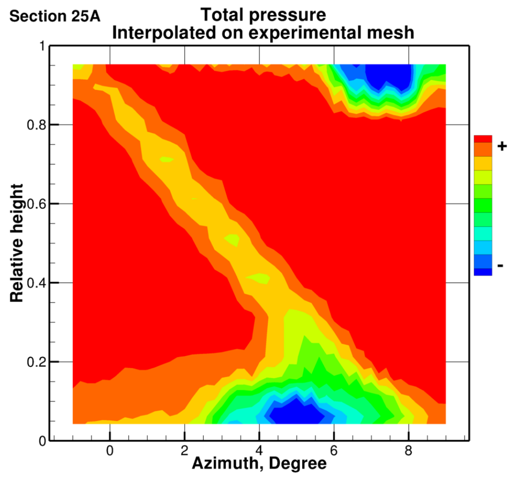

(b) RANS RDE-R1 computation. Interpolated on the experimental mesh.

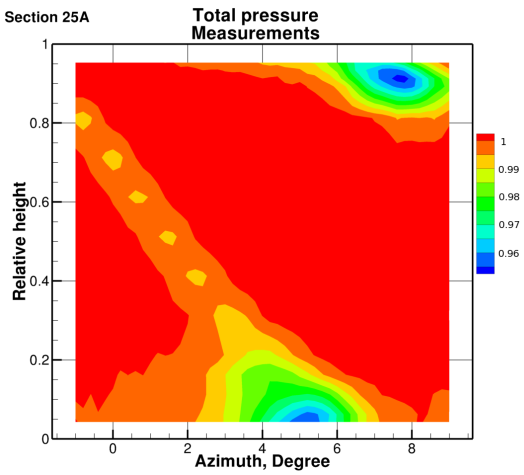

(c) Experimental probes.

Figure 3.7 — *Total pressure cartography at section 25A.*

3.3.4 Inlet cartography definition for the computations on the first rotor

The flow cartography extracted from the chosen configuration in the preliminary study is presented in figure 3.7(a). This 2D map of the total pressure shows that the main phenomena from the IGV are taken into account. Indeed, the hub vortex, azimuth 4-6 and relative height 0-0.1, the tip vortex, azimuth 7-8 and relative height 0.9-1, and finally the main wake diagonally from azimuth 0 and relative height 1 to azimuth 8 and relative height 0, are visible.

In order to ensure these results are due to the flow physics, this cartography is interpolated on the experimental mesh, figure 3.7(b). The map from the experimental probes is presented in figure 3.7(c). The azimuthal position calibration is based on the tip vortex position. While the relative position of the hub and tip vortices from the IGV are correctly captured with the RANS computation, the relative wake position is not. Actually, the problem originates from the azimuthal shift of the vortices with respect to the main wake. This shift results from the simplifications performed on the IGV gap sizes. As detailed in appendix A, the larger the gap, the wider the discrepancy between the main wake and the vortices. Indeed, with a larger gap, the vortices are wider and their axial and azimuthal convection is delayed compared to the main wake. This delay leads to the relative position difference when the wakes reach the section 25A. In addition, the total pressure deficit in the vortices is more important than what it is

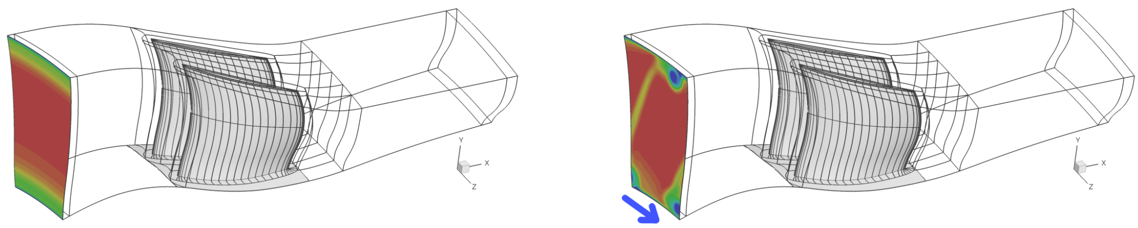

(a) Averaged cartography. (b) Rotating distortion.

Figure 3.8 — *The inlet boundary conditions for the computations on the R1.*

experimentally. Nevertheless, the objective of the preliminary study is fulfilled since the main effects of the IGV are captured.

The inlet boundary conditions for the computations on the R1 are based on this flow cartography at section 25A. Two different inlet boundary conditions are defined for the design operating point. For both conditions, the physical values for stagnation pressure, stagnation enthalpy, direction of the flow and primitive turbulence quantity of the model are given at each cell of the map from the values issued. Since the Spalart-Allmaras model, which is used in the preliminary study, is consistent with the turbulence model used in the ZDES method, the turbulence value, $\rho\tilde{\nu}$, can be directly extracted from the cartography. The difference between the two conditions lies in their steady or unsteady aspects. Indeed, in the first one, the map is azimuthally averaged and then directly applied as inlet condition. The resulting averaged map is visible in figure 3.8(a). By contrast, in the second boundary condition, a specific unsteady boundary condition developed by Ngo Boum [126] is applied. This method has been used on centrifugal compressors by Tartousi et al. [166]. It consists in a rotating distortion from the data of the cartography. The process is summarized below. First of all, the 2D map is interpolated linearly in the azimuthal direction on the inlet mesh surface. Then a second linear interpolation is carried out radially. The points are then uniformly distributed over the azimuthal range. Finally, a decomposition in Fourier series is applied in order to extract the coefficients corresponding to the signal to use as inlet condition. At each time step of the computation, these coefficients are then used for the reconstruction of the distortion for the unsteady inlet boundary condition. The number of harmonics used for the decomposition is chosen to 60 in the study, which follows recommendations from Ngo Boum [126]. This number depends on the mesh size and gradients in the flow cartography. The objective is to avoid the numerical oscillations that could occur with more harmonics while still transferring the thin wakes from the IGV. The criterion is to have a number of harmonics inferior to half of the number of points in the azimuthal direction on the inlet mesh surface. There are 225 azimuthal points on the inlet surface of the mesh presented in section 3.2. Nevertheless, the 60 harmonics are adequate to discretize the IGV main wake, the IGV hub vortex and IGV tip vortex as visible in figure 3.8(b).

At this stage of the study, the inlet and outlet boundary conditions are defined for the computations on the R1. There is still to define the boundary conditions for the other domain boundaries.

3.3.5 Specification of the other boundary conditions

Beyond the inlet and outlet boundary conditions detailed previously, the other boundary conditions are described in this part.

In order to simulate the R1 with accuracy and to be as close as possible from the experimental configuration, the platform positions are taken into account in these computations. Indeed, the walls at the hub have a different velocity whether they are bound to the rotor or not. It is important to note that the computations are achieved in the rotor frame of reference. As a consequence, the corresponding rotating/steady boundaries are presented in figure 3.9 for one channel. Moreover, an adiabatic adherent

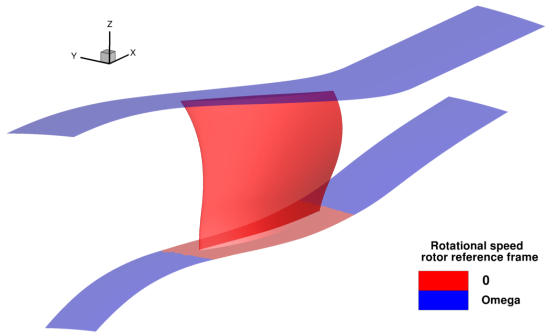

Figure 3.9 — *Wall speed in the rotor reference frame for one channel.*

condition is set for the walls of the computations. This assumes that there is no heat transfer which is probably not the case in the experimental compressor when measurements are taken. Nevertheless, since this condition is still used widely for compressors and, above all, since no temperature data is available on the casing of CREATE, this is the most relevant option for this study.

3.4 Numerical aspects of the test bench

In order to evaluate the advanced numerical method for the simulation of the tip-leakage flow on the CREATE compressor, different computations with the *elsA* [21, 22] software from ONERA are carried out on the numerical domain previously defined. An important aspect of the study is that they are all based on the same grid detailed in the last sections. Moreover, the numerical methods applied on the different computations are chosen to be close one another. The purpose is to avoid influences on the computed flow that could arise from the difference in the applied numerical schemes. The different computations used for the evaluation of the advanced numerical method are explained below.

The first computation is a steady RANS computation which is carried out with a Spalart-Allmaras turbulence model [162]. The Spalart-Allmaras model is chosen because the ZDES version to evaluate is based on it. Moreover all the compared computations are based on it too, therefore the differences between the results do not come from the turbulence model used. For this RANS computation, the spatial discretization scheme of Mary et al. [117] for the inviscid fluxes is based on the second order accurate Advection Upstream Splitting Method for low Mach numbers (AUSM+P), initially developed by Edwards and Liou [49]. A third order limiter is used for fluxes and the convection scheme is discretized to the second order for the turbulent equations. A classic centred formulation is used for the viscous fluxes with a 5 point stencil. The time discretization scheme is the implicit backward-Euler method. The inlet boundary condition is the averaged cartography presented in the previous section.

An unsteady RANS computation (URANS) is compared to the steady one. It is based on the same spatial discretization scheme as the steady one and with the same turbulence model. However, time integration is based on the second order accurate Gear scheme. At each time step, an approximate Newton method based on the LU factorization solves the non-linear problem. The time step is set to $1.6\ 10^{-7}$s which leads to a Courant-Friedrich-Levy number lower than 1 except for the boundary layers. As a consequence, 1000 time steps are necessary to last one IGV passing period. The use of 8 sub-iterations per time-step is required to reach a decay superior to one order of magnitude for the residuals. This criteria is a compromise between accuracy and cost of the computation and takes into account the small time step involved as recommended by [31]. Another difference is the inlet boundary condition. In this case, the rotating distortion is set since the computation is unsteady.

The third computation is the advanced numerical simulation. Time and space integrations schemes, as well as the time step and even the inlet boundary condition are identical to the URANS one. The 8 sub-iterations per time step lead to a decay superior to one order of magnitude for the residuals too. The method is the ZDES developed by ONERA [38] and implemented in *elsA*. It is based on the Spalart-Allmaras RANS model. ZDES enables a zonal approach, detailed in section 2.2.4, compared to the classic DES and therefore the use of models adapted to different flow configurations. The zonal configuration applied in this study is presented in figure 3.10. The upstream domain is defined with RANS mode, that is to say, mode = 0, in red, while DES modes are set to the other zones. Both mode = 1, in blue, and mode = 2, in green and black for the tip gap, are used in the DES part of the ZDES computation. Mode 3 is not used since it was not available in *elsA* at the beginning of this study.

The choice of mode = 0 in the inlet region is due to the will to avoid artificial generation of turbulence for the inlet boundary condition. Indeed, as explained in the previous sections, the value for $\tilde{\nu}$ is extracted from the preliminary study. The results from the preliminary study are validated by a comparison with the experimental data. As a consequence, the value for $\tilde{\nu}$ is reliable contrary to what is imposed with an artificial generation of turbulence, such as the synthetic eddy method (SEM). Besides, mode = 0 is the mode to favour when the boundary layers are attached. Last but not least, mode = 0 decreases the mesh requirements and therefore the mesh size as explained in section 3.2. Thereby, mode = 0 in the inlet region is a relevant choice here.

The choice between modes 1 or 2 of the ZDES is less obvious. These two modes relate to the DES modes of the ZDES method and are very different. First of all, it is important to understand the concepts behind each mode. The mode = 1 of the ZDES is adapted to configurations where the separation is fixed by the geometry and is the standard DES mode. The mode = 2 suits cases where the separation is unknown *a priori* and induced by a pressure gradient on a curved surface. In mode = 2 only, there is a protection of the boundary layer which is computed in RANS mode. This protection avoids the first problem of the hybrid methods: the "grey area", where the method switches from RANS to LES. It is important to underline the fact that modes = 1 and 2 of the ZDES are different from DES97 and DDES. Indeed, the major differences between DES97 and mode = 1 are the following. First the removal of the wall-functions in mode = 1 in order to avoid modelled-stress depletion. Second, a different source term so as to avoid artificial creation of LES content while accelerating the creation of natural one due to natural instabilities. Major differences between DDES and mode = 2 are different subgrid length scales and the addition of a threshold in the boundary layer in order to switch more rapidly from RANS to LES. These differences are of major importance and lead to improvements in the flow simulation as detailed by Deck [38].

Figure 3.10(a) details the zone specification in a blade to blade view. In the present study, mode = 1 is defined in every zone from the axial position of the O mesh of the row. Indeed it is the standard DES mode and LES content is expected in these regions, especially downstream the blade. These regions are not on curved surfaces as the one presented in figure 2.2(b) of section 2.2. Moreover, they are not subject to strong pressure gradient. Around the blades and in the tip gap, mode = 2 is used. The choice of mode = 2 in the vicinity of the blade is direct since it is typically the kind of configuration the method has been developed for. Indeed, the blade is a curved surface with a strong pressure gradient. Nevertheless, the choice of mode = 2 for the tip gap needs to be explained thoroughly. The tip-leakage region is a complex area driven by two main flows. On the one hand the main flow goes in the axial direction, on the other hand the leakage flow goes in the azimuthal direction. If the leakage flow only is considered, as presented in the right part of figure 1.7, it seems natural to use the mode = 1 of the ZDES since the separation is clearly imposed by the geometry. However, this is without taking into account the influence of the main flow on the tip vortex topology, visible in figure 1.7. If mode = 1 is used in the vicinity of the blade tip, the flow on the suction side of the blade could be erroneously computed with a grid induced separation. This would change completely the flow topology computed near the shroud, and therefore lead to important prediction errors concerning the position and direction of the vortex. Thereby, mode = 2 is chosen in order to protect the boundary layer on the suction side of the blade by forcing the RANS mode in it.

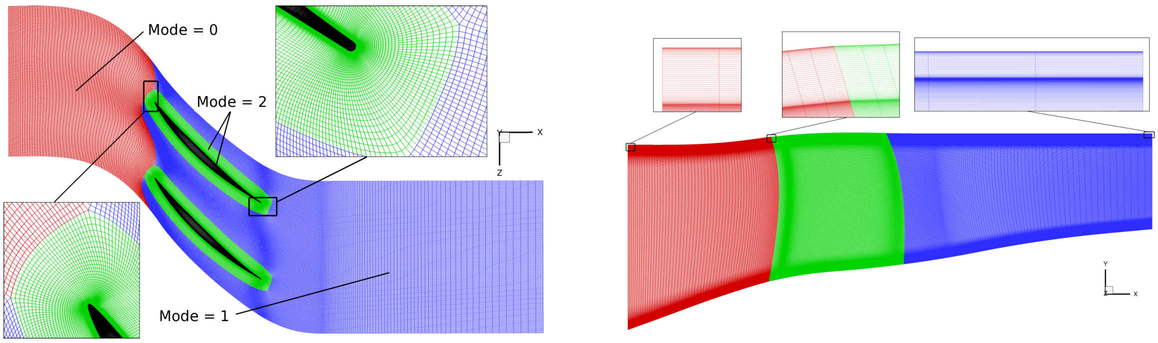

(a) Blade to blade view.

(b) Meridian view.

Figure 3.10 — *Mesh configuration for the different computations on the first rotor of CREATE. Color code for the ZDES method Red: mode = 0. Blue: mode = 1. Green: mode = 2. Black (tip gap mesh): mode = 2.*

3.5 Synthesis

In this chapter, the Zonal Detached Eddy Simulation (ZDES) approach is introduced. Then, a numerical test bench is defined to evaluate this method for the simulation of the tip-leakage flow on a realistic compressor. Hence, two channels of the first rotor (R1) of the axial compressor CREATE are simulated. In order to take into account the influence of the hub vortex, tip vortex and wake from the Inlet Guide Vane (IGV) upstream the R1, a preliminary RANS IGV-R1 study is carried out. The outlet pivot pressure of the computation is adapted to correspond to experimental radial distributions at the design operating point. As a result, a 2D cartography is extracted at section 25A, upstream the R1 and is used for the inlet boundary conditions in the computations on the R1.

With an eye to find out what the ZDES method can bring for the understanding of the tip-leakage flow, different computations are carried out on this numerical test bench: a RANS, an URANS and two ZDES computations. It is important to underline that similar numerical methods are implemented in the different computations. Besides, the same outlet pressure boundary condition is set. Last but not least, the same mesh is used for all the computations on the R1. This grid follows the ZDES mesh requirements with an upstream domain following RANS requirements, and the remainder the DES mesh requirements, that is to say a LES-type mesh except near the walls.

In the next chapter, this numerical test bench will be used for the evaluation of the ZDES method with regards to the simulation of the tip-leakage flow. This approach will be compared to the RANS and URANS computations as well as to experimental data.

Chapter 4

Evaluation of the ZDES

Contents

This chapter deals with the evaluation of the ZDES method for the simulation of the tip-clearance flow. This evaluation is performed on the numerical test bench defined in the previous chapter.

4.1 Validation of the numerical test bench

After the definition of the numerical test bench in the chapter 3, the evaluation of the ZDES approach is addressed. In this section, the different important aspects are discussed: the convergence of the computations, the operating point and finally the modes which were chosen for the ZDES method.

First of all, in order to reduce the cost of the computations, a specific procedure is followed. It consists in reaching convergence of the RANS computation, then using the 3D flow from this RANS computation as initial state for the URANS computation. Finally, when the URANS computation is considered as converged for the mean values, the ZDES computation uses this state as initial state. Thus, the first important step is to check the convergence of the computations.

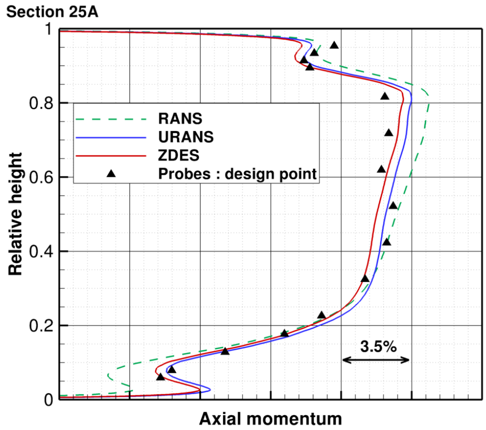

Figure 4.1 — *Radial distribution of axial momentum at section 25A for the computations on R1 with the ZDES type mesh.*

Convergence criteria for the unsteady RANS method and above all LES-type computations are more complex than for the steady RANS approach. Indeed, the main criterion for steady computations is to follow the residual evolution and check global values. Nevertheless, in the case of unsteady approaches, these global values converge faster than localized numerical probes. Even the concept of convergence is not the same because it is impossible to reach a steady value for these probes. In this case, convergence refers to reaching statistical steady state. Besides, the convergence requirement, when spectral analysis is expected, is a limiting factor that leads to increased computational time in order to get reliable data in the phase of "numerical acquisition". This is the reason why the convergence of the computations is checked through stabilization of mean and root-mean-square static pressure over a sliding temporal window containing the last 1000 time steps, that is to say, over one passage of the Inlet Guide Vane (IGV). The pressure is chosen here since it is very sensitive to the phenomena occurring near the tip. This process is performed for different numerical probes located at different positions within the computational domain: upstream the first rotor of CREATE (R1), downstream the R1, between the blades and the most important ones are in the tip gap area where convergence is the most time-consuming to reach. On the one hand, in the RANS case, the final converged state is used for the analysis. On the other hand, the data acquisition for the unsteady computations begins from the iteration regarded as converged with respect to mean and root-mean-square values. The acquisition time is normalized with the passage time period of the IGV with respect to the R1, which is written T henceforth. The computational time for the ZDES computation is around 500000 hours. This comprises the 70 T to reach convergence and the acquisition time. This acquisition time, used for the different analysis thereafter, is of 17 T for the ZDES computation and 18 T for the URANS one. Despite its important computational time, the ZDES computation is as time-consuming as the URANS one in this study. The reason is that the same mesh and the same numerical schemes are used for both computations. Actually, for an URANS computation following only URANS requirements, all the more if no statistical analysis is carried out from the URANS results, the required computational time is lower.

Before analysing thoroughly the computational results, it is important to verify whether the computations are reliable. Two main aspects are discussed in this section. The first one is the numerical operating point with respect to the experimental one. The second one is the validity of the ZDES mode decomposition chosen in this study.

In chapter 3, numerical design point was chosen with an analysis of the radial distribution of the axial momentum at section 25A. This was carried out on a RANS type mesh with one channel of the IGV and the R1. The outlet pivot pressure which defines the operating point was chosen to 0.93 Pio. The same value is used for the boundary condition in the different computations on the R1 test bench, since the outlet axial position is the same. Nevertheless, it is important to verify if this criterion to match the experimental operating point is still relevant. Figure 4.1 represents the radial distribution of axial momentum at section 25A, at the inlet boundary for the numerical test case, for the computations on the R1 and for pneumatic probes. The URANS and ZDES computational data are averaged in time and then in azimuth while the steady data from RANS and pneumatic probes are azimuthally averaged. The averages apply to the acquisition time of the computations defined earlier. Despite the same outlet pivot pressure, the results at the inlet are different. Nevertheless, the discrepancy between the methods is less than 3%, and above all, confirms the choice of the same outlet pivot pressure for the computations on the R1. Indeed, the RANS results are similar to the ones observed in figure 3.5(a) that have led to the choice of the 2D inlet cartography. Notwithstanding these satisfactory results for the RANS computation, the unsteady approaches reveal to be, as expected, better agreement with the experimental probes. This improvement is mainly visible in some regions: near the hub at 5% of relative height, around 80% relative height and finally around 90% of relative height. Unsteady phenomena occur in these regions, such as the hub vortex and the tip vortex, which explains the predominance of unsteady computations. Moreover, along the radius, the unsteady approaches are within 1% of discrepancy with the pneumatic probe data. Nonetheless, the gradients are captured with the three methods, even if it is not with the same accuracy. As a consequence, based on the method retained in the previous chapter for the choice of the numerical operating point, that is to say, the radial distribution of axial momentum, the computations on the numerical test bench can be regarded as reliable.

The next aspect to verify is the validity of the ZDES. To this purpose, different visualizations of the instantaneous flow from the ZDES computation are presented. Figure 4.2(a) represents the instantaneous flow field from the ZDES computation in the vicinity of the blade tip. Three axial planes at sections 22%, 31% and 46% of the blade axial chord (X/C) are coloured by the entropy. Their position along the chord are indicated in figure 4.3. When adiabatic wall conditions are used, zones of entropy creation correspond to zones of loss of stagnation pressure as explained by Denton [43]. In the tip region, these losses stem mainly from the mixing between the clearance jet and the main flow, leading to the tip-leakage vortex. As a result, with the numerical test bench defined in the previous chapter, by observing the entropy field one can observe the tip-leakage vortex.

In addition of the entropy, isolines of the f_d function are overlaid. The f_d function, defined in equation II-42, is a sensor for the boundary layer used in the ZDES. Its value is less than 1 in the boundary layer. It is important to remember that the modes 1 and 2 of the ZDES have a continuous transition from RANS to LES in a zone called "grey area". In mode 2 only, this f_d sensor detects the boundary layer and aims at protecting it by forcing the RANS method in this region. Nevertheless, since this transition is continuous, the location of the transition region between RANS and LES is not accurate. However, the value 0.99 of the f_d sensor, which is represented in the figure, can be used to differentiate the zone regarded as a boundary layer from the outer region within the mode = 2. The other overlaid value, 0.8, of the f_d sensor corresponds to the threshold f_{d0} defined by [142] so as to accelerate the transition from RANS to LES. As a consequence, the information on the f_d values informs us on the method mainly used: RANS or LES.

In addition to this information on the boundary layer in figure 4.2(a), another information is presented in figure 4.2(b) for the same location and time from the ZDES computation. The overlaid f_d values are presented with the instantaneous eddy viscosity field, $viscrapp = \frac{\mu_t}{\mu}$. This is the ratio of the turbulent and laminar viscosity coefficients, and therefore distinguishes the LES zones, which have a low turbulent viscosity from the RANS ones, with a higher value. In fact, its value equals to 0 at the wall, then increases in the boundary layer if resolved in RANS. Then, in the outer region, its value is 0 or a high value depending on whether the turbulence is respectively resolved in LES or RANS. By combining the information from the two figures, it is then possible to check the appropriate behaviour of the method concerning the boundary layer treatment.

First of all, along the chord, the boundary layer developing on the walls is in RANS, which is expected due to the forcing in mode = 2 in these regions in the vicinity of the blade. The boundary

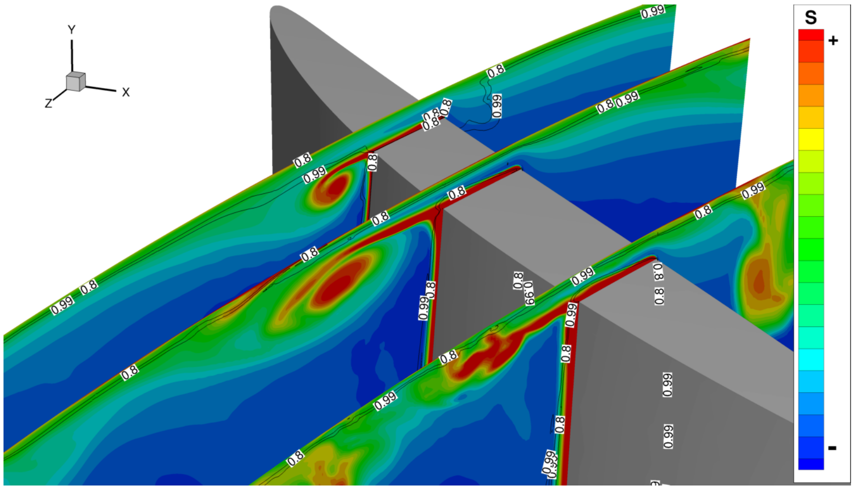

(a) Entropy.

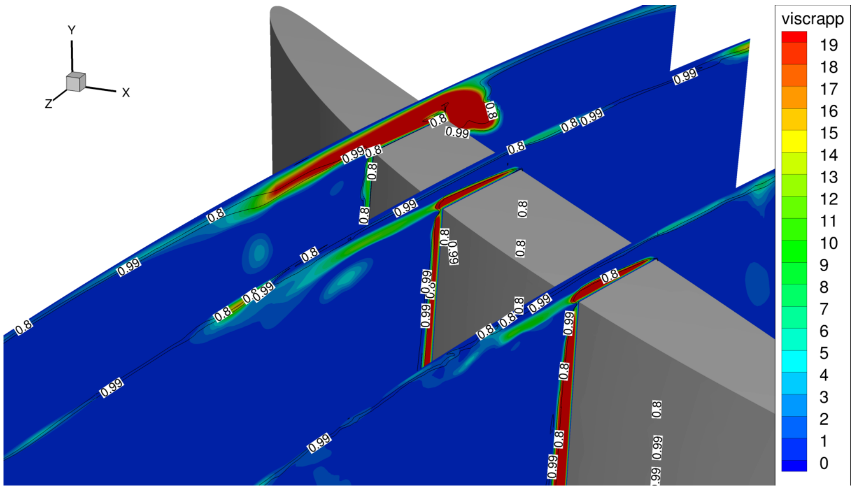

(b) Instantaneous eddy viscosity.

Figure 4.2 — *Entropy and instantaneous eddy viscosity axial planes with isolines of fd sensor. From left to right: sections 22%, 31% and 46% X/C. Tip region from the ZDES computation.*

layer developing on the suction side grows and is still simulated in RANS. Nevertheless, the tip gap zone is more complex due to the two different boundary layers, one for the casing and one for the blade tip. Actually, the whole gap zone is computed with RANS or RANS and LES depending on the axial position. Upstream section 31% X/C, the tip gap is fully resolved in RANS. The reason is the thick boundary layer which comes from the leading edge of the blade and "contaminates" the whole gap. This is even thicker on the edge between the pressure side and the tip, as visible at section 22% X/C. By contrast, from section 33% X/C onward, the tip gap is resolved with both RANS and LES. There is still the RANS mode in the boundary layers due its protection by mode = 2, but between the boundary layer developing on the blade tip and the one developing on the casing, there is a thin zone in LES. The resolution in RANS of the tip gap near the leading edge is a limitation of the RANS/LES approaches based on the DES, but this behaviour was expected. The tip gap size regarding the boundary layer thickness is an important parameter to take into account when DES-type methods are used. Indeed, if the boundary layer is thicker than the gap size, the gap region will be resolved in RANS. This is partly the case in this study, at least near the leading edge. Nevertheless, for the study of the tip-leakage vortex, the computation in LES in the gap is not a prerequisite. This would however be relevant to compute the gap region fully in LES depending on the purpose of the study. For instance, if the dynamics of the boundary layer within the tip gap needs to be captured, mode = 3 is a pertinent choice and could enhance

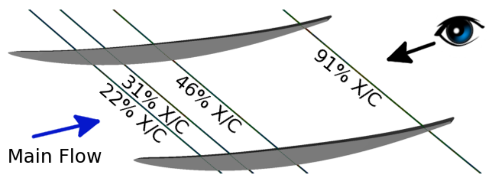

Figure 4.3 — *Position of the visualization sections along the chord.*

the results. Despite this limitation, the formation and development of the tip-leakage vortex is correctly computed in the LES mode of the ZDES. The vortex formation and widening can be seen in figure 4.2(a) on the suction side. Their computation in LES is a positive aspect of using the ZDES method for the simulation of the tip-leakage flow. This behaviour is the one that is expected since the leakage jet flow is clearly a "detached" flow, computed in LES. As a consequence, the ZDES behaves correctly for the simulation of the tip-leakage flow.

Another element concerning the validity of the ZDES is the correct use of mode = 2 in the vicinity of the blade. It was previously demonstrated that in the tip gap, mode = 2 protects the boundary layer and consequently forces the RANS mode. This protection is mainly visible near the leading edge where the boundary layers are thicker, especially on the pressure side at 22% X/C in figure 4.2(a). Nonetheless, this protection is known to have a negative impact on the transition between RANS and LES. This has to be quantified for the study. Indeed, mode = 2 delays this transition, albeit this delay is inferior to the one observed in DDES by Deck [38]. In figure 4.2(b), the suction side in the visible sections highlights different behaviours. In section 22% X/C, the eddy viscosity level is high in the boundary layer emanating from the tip gap and then decreases rapidly when the isoline 0.8 is crossed to be lower than 7 as soon as the isoline 0.99 is reached. At this section, the boundary layer at the tip gap and the one at the casing form only one boundary layer for the ZDES method. The method can not distinguish the two. This confirms that the boundary layer is protected with the mode = 2 close to the blades, and then the outer flow is resolved in LES. However, when mode = 1 is used, refer to figure 3.10(a) for the exact position, the flow is resolved in LES since the mesh suits LES requirements. From section 31% X/C and downstream, the method can distinguish the two boundary layers. As a result, the eddy viscosity field is then closer to the one detailed by Deck [38] obtained on a backward facing step, and similar conclusions can be drawn. One can observe a delay in the switch from RANS to LES. Nevertheless, the eddy viscosity rate drops from over 19 in the tip gap boundary layer to 9 as soon as it is outside the boundary layers from the tip gap and the suction side. This residual eddy viscosity of 9 contaminates the flow until reaches the zone in mode = 1 for section 31% X/C. However, this delay is reduced at section 46% X/C, that is to say, the switch occurs faster downstream. And this is an important point for the simulation of the tip-leakage flow and the main difference with the backward facing step. The eddy viscosity is convected downstream, tangentially to the edge between the tip and suction side. Since the level of eddy viscosity is rather high upstream, at section 22%, it is still high at section 31%. But then, the level decrease and the viscosity field behaves much more like the one in the backward facing step. Thereby, one can say the switch is rapid, even if there is still a delay whatever the axial position.

The same visualizations are presented for the hub region where there is no influence of the tip gap. The section 46% X/C is coloured by the entropy in figure 4.4(a), and by the eddy viscosity in figure 4.4(b). The same f_d isolines are overlaid. On the one hand, the boundary layers developing on the suction side, on the pressure side and near the blades on the hub wall are correctly protected with mode = 2. On the other hand, the boundary layer on the hub wall and far from the blades is not protected. In the unprotected zones, the f_d sensor can not be directly used to identify the boundary layer since it is intrinsic to the mode = 2. Indeed, there is an abrupt reduction of the thickness between the hub wall and the isoline 0.99 for the f_d value when crossing the interface between mode = 1 and mode = 2. Nevertheless, the entropy field between the two blades does not reveal any separation. There is only a thickening of the suction side boundary layer near the hub which is not impacted by the interface between the modes.

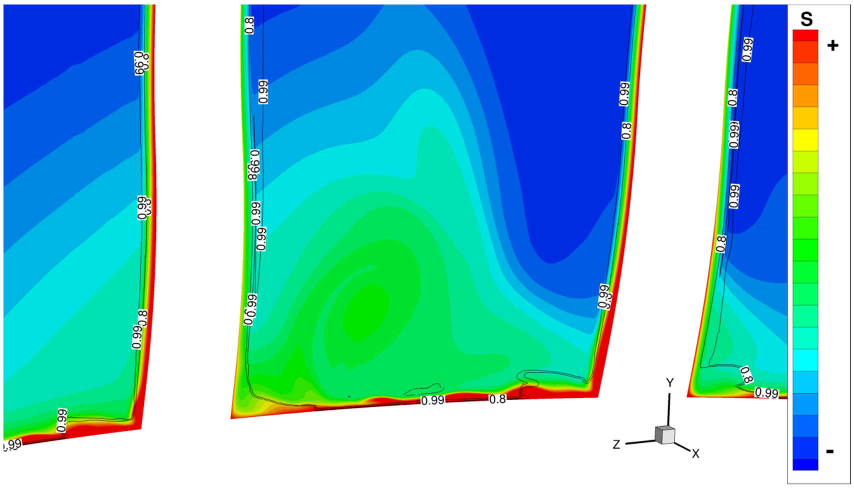

(a) Entropy.

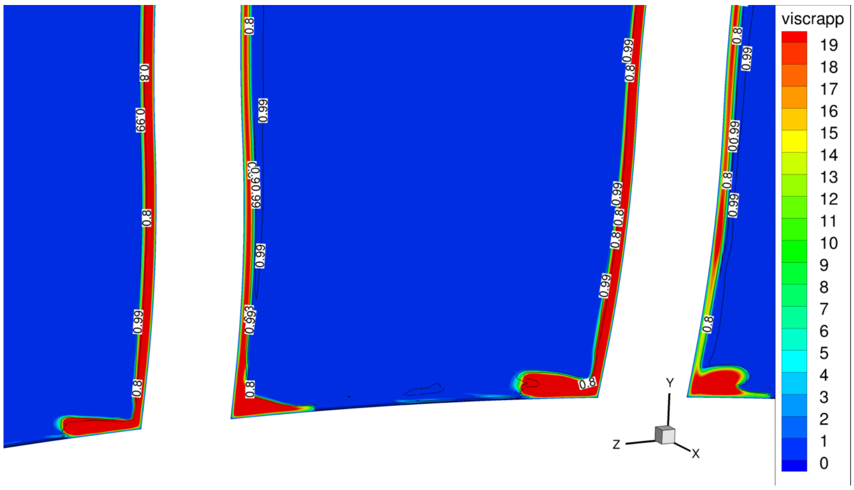

(b) Instantaneous eddy viscosity.

Figure 4.4 — *Entropy and instantaneous eddy viscosity plane at 46% X/C for the ZDES computation with isolines of fd sensor. Hub region.*

Nevertheless, in regions with separation risks, mode = 1 can cause Grid Induced Separation (GIS), hence the importance of mode = 2 in these regions, such as the suction side of the blade. As a consequence, even if mode = 1 is used between the blades, there is no GIS on the hub and the LES computes the flow correctly.

Although there is no GIS on the hub surface, such GIS could occur in the tip region. Indeed, in figure 4.2(a), at section 31% X/C, the boundary layer on the shroud separates. This is near the interface between mode = 1 and mode = 2. The change from mode = 2 to mode = 1 could trigger the separation, hence the necessity to ensure this is a physical phenomenon and that it is not induced by the choices made for the ZDES configuration. Nevertheless, by comparing the normalized helicity field near the tip region at section 31% X/C, one can notice that the separation, in blue in figure 4.5, occurs at the same position in URANS, figure 4.5(a) and in ZDES, figure 4.5(b). Since there is no mode change for the URANS computation, this confirms that the separation is physical or at least, not induced by the chosen configuration for the ZDES method. This separation is a side effect of the momentum loss from the tip-leakage vortex, which makes it roll up as previously underlined on a similar configuration by Gourdain and Leboeuf [64]. This is amplified by the axial momentum loss of incoming wakes as it will be explained in chapter 6.

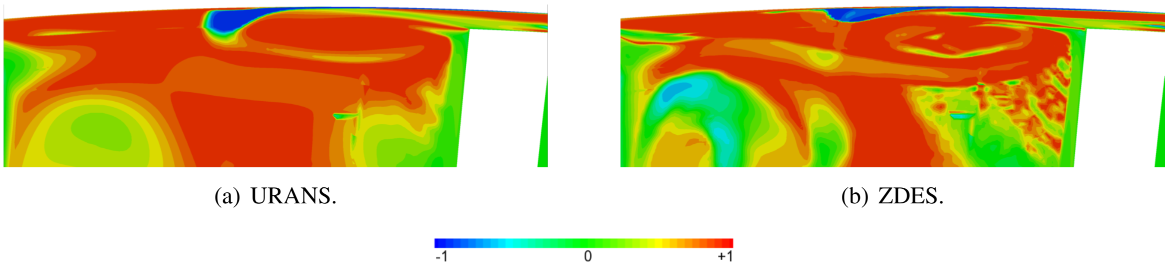

(a) URANS. (b) ZDES.

Figure 4.5 — *Instantaneous normalized helicity at $t = 3T/4$ and section 31% X/C for URANS and ZDES. Boundary layer separation at the casing.*

In conclusion, this section has explained the process for the convergence of the computations and brought out the validity of the numerical test bench concerning the operating point. Besides, the mode configuration for the ZDES has been assessed, which has emphasized the appropriate behaviour of the ZDES modes regarding the tip-leakage flow. In the next sections, an overview of the tip-leakage flow topology will be discussed before focussing on the validation of the ZDES.

4.2 Tip-leakage flow physical analysis

In this section, the tip-leakage flow topology is presented in two steps. On the one hand, the averaged field is detailed, and on the other hand, the evolution of the instantaneous field is assessed. The flow fields in the tip region from the RANS, URANS and ZDES computations are thoroughly compared and discussed.

4.2.1 Time-averaged flow field overview

First of all, it is important to put this study into perspective towards the previous analysis on the tip-leakage flow done in the literature. Two dimensionless criteria are used for the study of tip clearance flow topology. The first one is $\lambda = \frac{GapSize}{MaximumBladeThickness}$, the dimensionless tip clearance size with respect to the maximum blade thickness. In the first rotor of the CREATE compressor, its value is 0.23. Following the analysis from Rains [135], since λ is superior to 0.026, a vortex structure is expected. Moreover, Rains defined then the factor $\lambda^2 \cdot Re \cdot \epsilon$, with Re the Reynolds number based on the free stream velocity, and ϵ the maximum thickness to chord ratio, so as to generalize the tip-leakage flow topologies. For the R1, $\lambda^2 \cdot Re \cdot \epsilon$ is clearly in the domain defined by Rains [135] where the inertia forces are predominant over the viscous forces, mainly due to the high Reynolds number. As a consequence, the topology is mainly driven by the potential flow pressure distribution in the R1 of CREATE. The second criterion is the dimensionless tip clearance size with respect to the axial chord length, $\tau = \frac{GapSize}{AxialChord}$. For the R1, the value for τ is 1.75%. By comparing with the previous experimental studies on different tip clearance sizes from Brion [16], the expected topology with this τ value is a tip-leakage vortex that remains close to the casing while being convected away from the blade suction side.

In order to visualize the tip-leakage flow, an ensemble average is applied on 17 T of the ZDES computation and 18 T of the URANS one. The entropy fields of these averaged computations are presented in figure 4.6 so as to highlight the zones of high losses [43]. Different sections are represented on the same figure : a section at 98% of relative height, and 3 sections at respectively 22%, 31% and 46% of the axial chord. Despite the similar numerical methods implied in the two calculations, and an ensemble average which aims at comparing these two different approaches equally, the development of the tip-leakage vortex differs. Indeed, on the one hand, from the leading edge to section 22% chord, the same entropy field

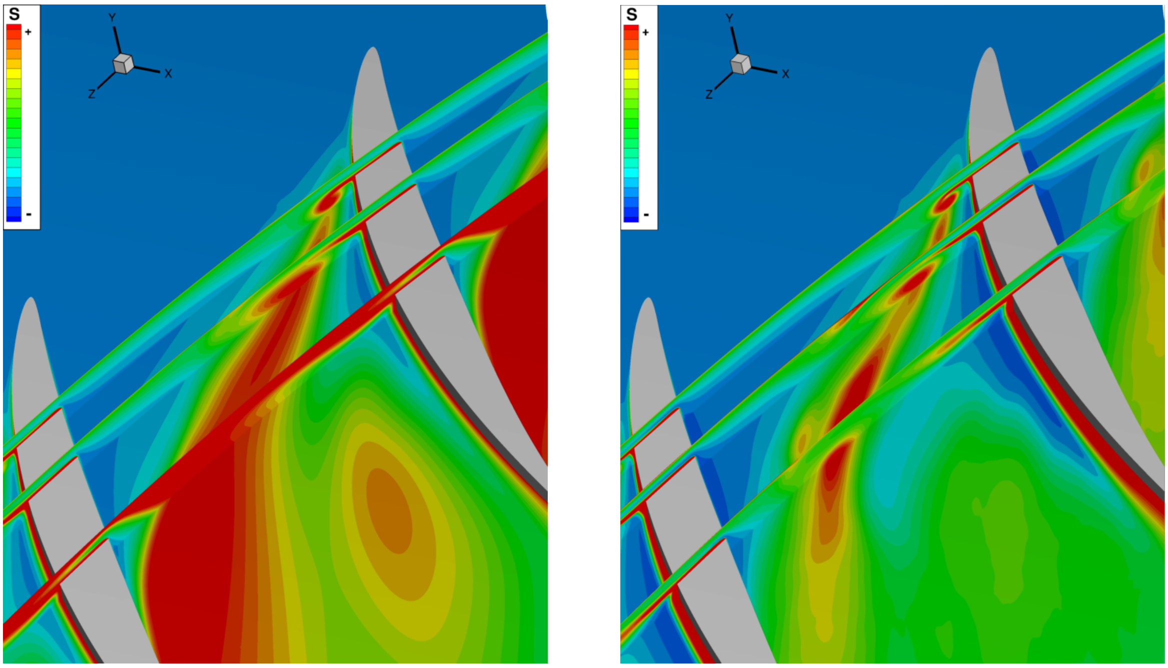

(a) URANS. (b) ZDES.

Figure 4.6 — *Comparison of the time averaged entropy field of URANS and ZDES. Entropy planes at 22%, 31% and 46% chord and 98% relative height.*

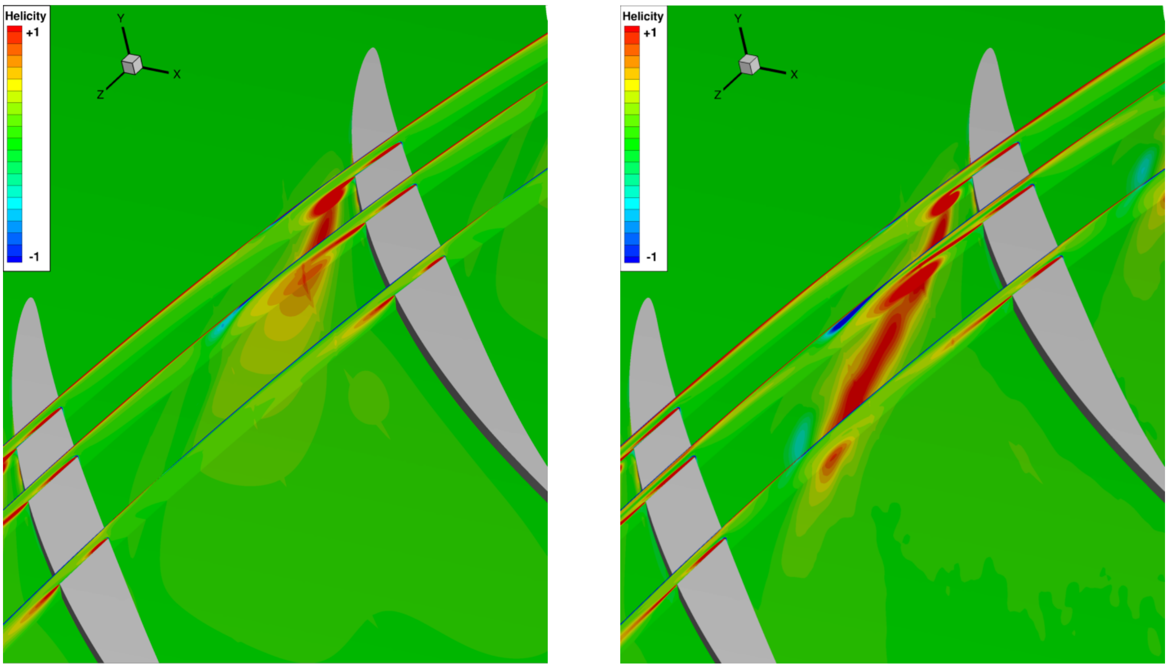

(a) URANS. (b) ZDES.

Figure 4.7 — *Comparison of the time averaged helicity field of URANS and ZDES. Normalized helicity planes at 22%, 31% and 46% chord and 98% relative height.*

is visible for the two computations. The tip-leakage vortex rolls up and then extend azimuthally. On the other hand, from section 31% chord, two different behaviours are captured by the methods. In ZDES, the high entropy zone is concentrated on a thin line following the tip-leakage vortex. By contrast, the high

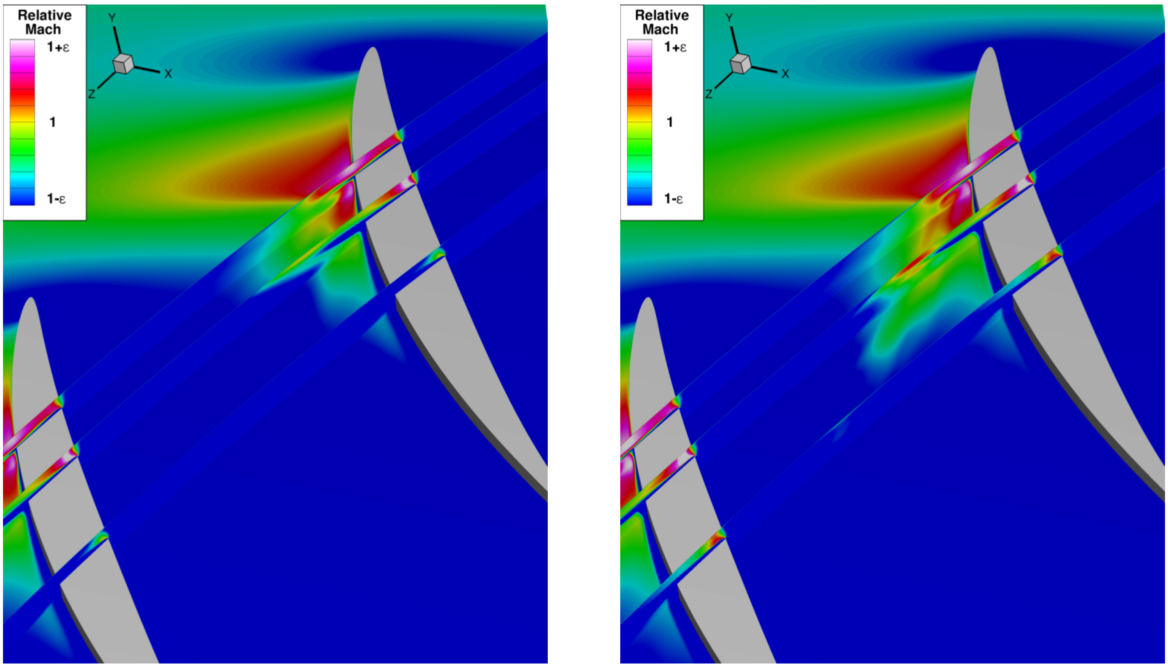

(a) URANS. (b) ZDES.

Figure 4.8 — *Comparison of the time averaged relative Mach number field of URANS and ZDES. Relative Mach number planes at 22%, 31% and 46% chord and 98% relative height.*

entropy zone is wider in URANS. Besides, downstream section 31%, and thus in section 46%, the high entropy zone spreads all over the blade channel up to the adjacent blade. This impacts the boundary layer on the casing in the tip gap of the adjacent blade, and as a consequence, amplifies the contamination. Although the main difference between the methods is underlined by the tip-leakage vortex development, it is not the only one. On the contrary, another difference concerns the development of the boundary layer on the suction side of the blade. In ZDES, the boundary layer becomes thicker as it reaches the trailing edge while it stays relatively thin for the URANS computation.

However, it is difficult to evaluate the exact position of the tip-leakage vortex based only on these entropy fields. Thereby, the same visualizations are presented with the normalized helicity, in figures 4.7(a) and 4.7(b). The normalized helicity shows the rotating direction and the intensity for the vortices, especially the main tip-leakage vortex. This figures indicate the main tip-leakage vortex development in red and the contra-rotative induced vortex near the shroud in blue. The main conclusion arising from the comparison of these two figures is the fast dissipation of the main tip-leakage vortex with the URANS method. Indeed, downstream section 31%, the helicity decreases rapidly up to the levels of the main stream at section 46%. On the contrary, in the ZDES computation, the helicity levels are more important for the main tip-leakage vortex and the induced vortex. Furthermore, the high levels are maintained further downstream and further azimuthally, up to section 46%. Therefore, the main tip-leakage vortex remains coherent beyond section 31% chord. This points out a major difference in the capability of the two methods to capture the vortices, and reveals a major event occurring around sections 22% and 31% chord.

In order to highlight what occurs there, the same visualizations are done with the relative Mach number, in figure 4.8(a) and 4.8(b). The legend is centred around 1. The figures reveal a shock at section 22% near the edge between the tip-gap and the suction side, and close to the casing. This shock position is captured by the two methods, albeit it is more intense in the ZDES case. Besides, the high levels of relative Mach number extend along the vortex core downstream section 31% in the ZDES case. Notwithstanding this difference, the Mach number fields look alike, and thus this confirms the origin

of the differences between the two methods : the behaviour of the tip-leakage flow crossing this shock. The shock is known to trigger high dissipation when a turbulent flow passes through it, even with LES [46]. However, recent studies carried out with hybrid methods, such as the work of Shi [151, 152] with IDDES, lead to the same assessment as the one in this study : the advantages of methods based on LES over the ones based on RANS.

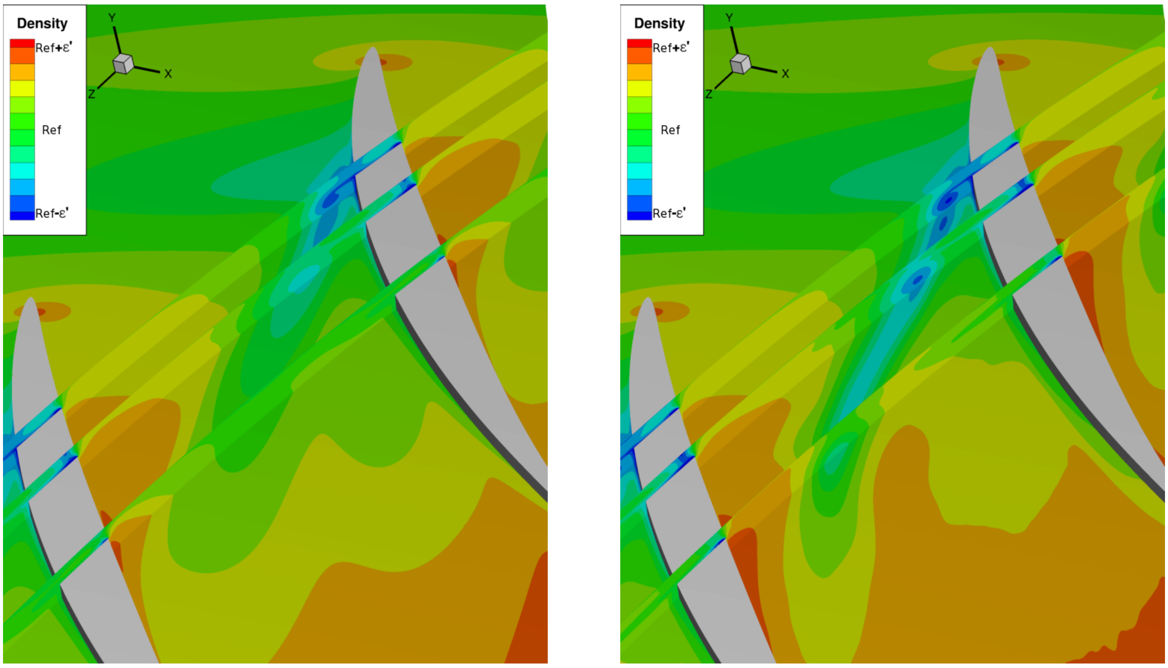

(a) URANS. (b) ZDES.

Figure 4.9 — *Comparison of the time averaged density field of URANS and ZDES. Density planes at 22%, 31% and 46% chord and 98% relative height.* $\epsilon' = 29\%$ *of the density reference value.*

Nevertheless, the shock at the tip of the R1 is not important for the design operating point of CREATE, and can be defined as weak as explained below. This results in some missing effects which occurs for the interaction between a strong shock and the tip-leakage vortex, as observed in the literature with configurations appropriated to analyse the shock/vortex/boundary layer interactions [69, 55, 151]. First of all, the gradients for the Mach number, in figure 4.8, are not important. Besides, there is no sudden drop in the Mach number value after the shock neither a recirculation area [78]. Second, one can analyse the figures 4.9(a) and 4.9(b) which represent the density field centred around a reference value. The presented density ranges from $\pm\epsilon' = 29\%$ of the density reference value. The core of the tip-leakage vortex is defined by a low density and thus it can be tracked by the means of the observation of the lowest density zones. This emphasizes the difference observed through the figures 4.7 with a tip-leakage vortex that extends further in ZDES. However, there is no rapid drop in density level at the shock, contrary to what is observed with strong shocks by Hofmann and Ballmann [77]. A last effect which confirms the weak shock is visible in figures 4.10 with the pressure field centred with $\pm\epsilon'' = 29\%$ of the pressure reference value. In these figures, the gradient for the pressure rise is weak, even at the shock position. As a consequence, the difference between the two methods is triggered by the passage through a weak shock.

Beyond the tip-leakage vortex development, the flow topology within the tip gap is important to understand the tip-leakage flow. First of all, it is important to remember that the ZDES mode used in the tip gap is the mode = 2. That is to say, the boundary layer is protected by the use of the URANS approach in it. As a consequence, this has a direct impact on flow field since the same approach is used near the walls for URANS and ZDES, hence the similar results at the wall. The difference stems from

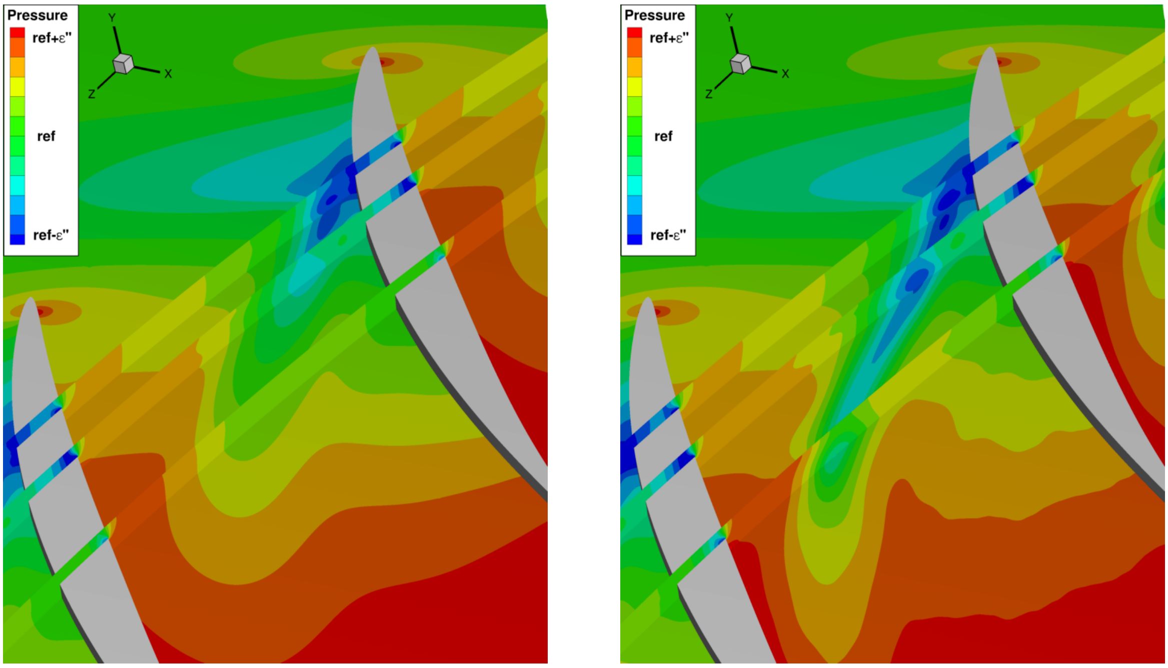

(a) URANS. (b) ZDES.

Figure 4.10 — *Comparison of the time averaged pressure field of URANS and ZDES. Pressure planes at 22%, 31% and 46% chord and 98% relative height.* $\epsilon'' = 29\%$ *of the pressure reference value.*

the flow outside the boundary layer. Figures 4.11(a) and 4.11(b) represent the skin friction lines [41] and friction modulus on the blade tip for the URANS and ZDES computations. Similar friction pattern are observed experimentally by Kang and Hirsch [87]. The separating line originates from the leading edge and then splits into two lines. The two branches diverge. One reaches the pressure side, and the other one the suction side. Contrary to Rains [135], who hypothesized that the tip-leakage flow is two dimensional, and in agreement to results from Kang and Hirsch [87], the friction lines underscore the 3D nature of the tip-leakage flow within the tip gap. Indeed, the friction lines are not normal to the tip blade edges because of the major influence of the axial velocity.

On the suction side of the blade, the friction modulus decreases rapidly at 20% of the chord length. This is due to the shock position seen previously. Indeed, downstream this axial position, the separating line on the blade tip deviates locally from its original axis. This deviation is more important in ZDES and corresponds to the area of low pressure visible in figure 4.10. Figures 4.11(c) and 4.11(d) correspond to the same visualization as for figures 4.11(a) and 4.11(b), excepted that the wall presented is the casing. The deviation of the separating line at the blade tip occurs where the friction modulus at the casing is the highest, in light green in the figure 4.11(d). A detachment node [42] is visible for the two methods, and corresponds to the separation point of the boundary layer at the casing seen in figures 4.6 and 4.7 which was highlighted on a similar configuration by Gourdain and Leboeuf [64]. The position of this detachment node is identical for the URANS and ZDES computations. Moreover, a separating line at the casing follows the tip-leakage vortex and can thus be used to track its axial and azimuthal positions, which proves the similar initial direction taken by the main tip-leakage vortex although computed by two different methods. In the light of figures 4.11, two kinds of skin friction patterns are highlighted depending on the surface considered, the casing or the blade tip. This emphasizes the shear between the two wall flows in the tip gap region and the similarity of the two methods assessed to compute it.

On the contrary, if the whole blade is taken into consideration, the discrepancies between the two methods are accentuated. Figure 4.12 shows the same visualizations for the skin friction lines and friction modulus but with a different view. The suction side of the R1 reveals an important corner effect with

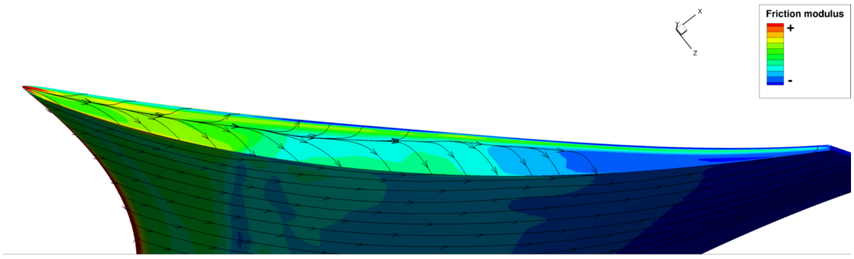

(a) URANS, at the blade tip.

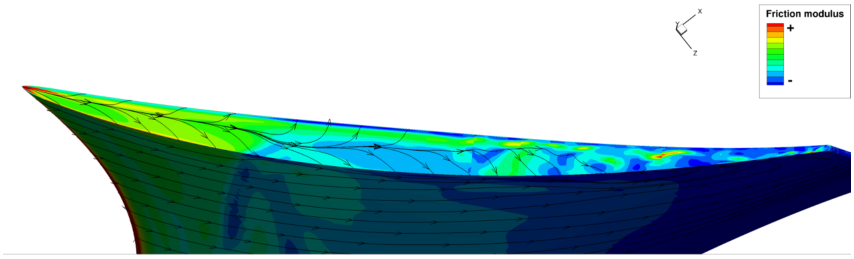

(b) ZDES, at the blade tip.

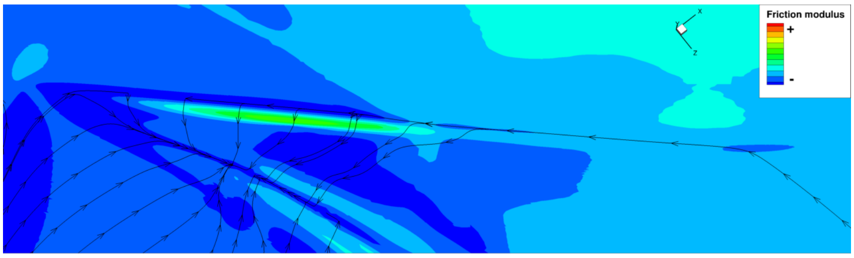

(c) URANS, at the casing.

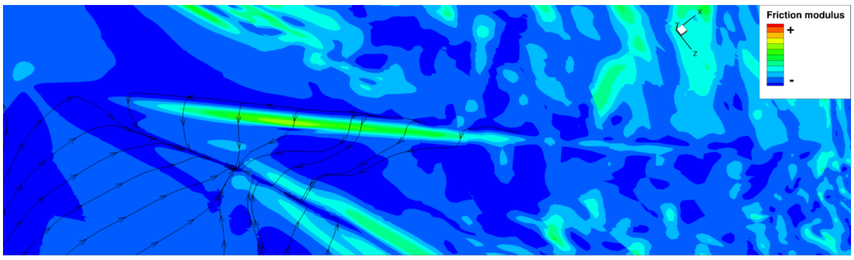

(d) ZDES, at the casing.

Figure 4.11 — *Comparison of the friction lines for the time averaged field of URANS and ZDES at the blade tip and at the casing.*

a separating line going from the mid chord at the hub to 63% of relative height at the trailing edge in URANS. In ZDES, this separating line reaches the trailing edge at 73% of relative height. Therefore the recirculation area is wider in ZDES. This means the separation from the corner effect is more important with the ZDES approach. Besides, this can explain the thickening of the boundary noticed in figure 4.6(b). However, the position of this separating line is already a known drawback of the Spalart-Allmaras turbulence model which tends to over estimate the corner effect as underlined by Marty [112, 111]. For this reason, and since the ZDES method evaluated is based on the Spalart-Allmaras turbulence model, it is coherent to meet this problem with the ZDES too. One will see in section 5.2 that this separating line issue is amplified near the surge. Nevertheless, it is important to emphasize here that, when the friction lines only are considered, the simulation of the corner effect is not drastically changed by the means of the mode = 2 of the ZDES based on Spalart-Allmaras, hence the possible need of mode = 3 or another turbulence model for such simulations.

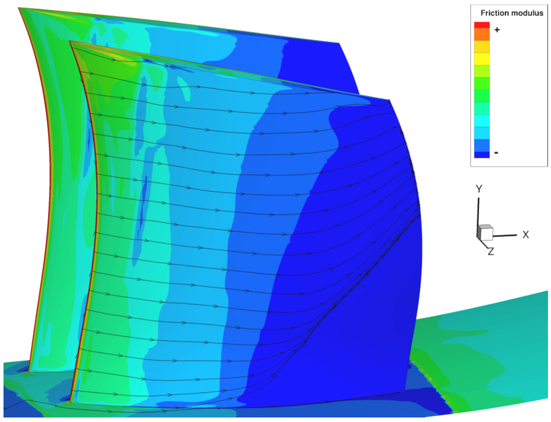

(a) URANS.

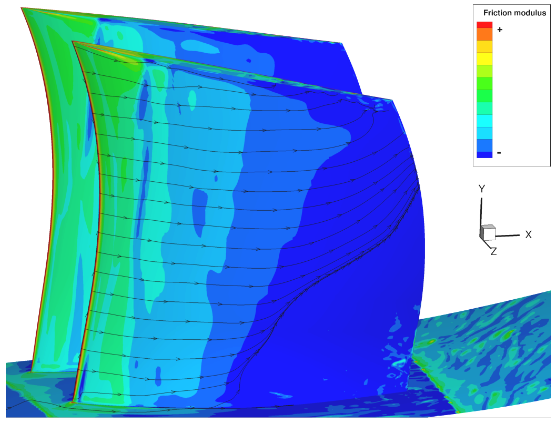

(b) ZDES.

Figure 4.12 — *Comparison of the friction lines for the time averaged field of URANS and ZDES near the hub.*

4.2.2 Flow field snapshots

After the visualization of the time averaged fields, it is important to study the evolution of the instantaneous field for the tip-leakage flow because of its inherent unsteadiness. It must be emphasized that the finest details which are visible by the means of each method are observed here. Indeed, the inherent distinction between the URANS and the ZDES approaches prevents to compare the two methods with exactly the same refinement in terms of flow structures. This is only possible with averaged fields as presented in the previous study. Notwithstanding this restriction, the flow snapshots bring relevant information on the tip clearance flow topology.

Therefore, the iso-surfaces of Q criterion [81], coloured by the normalized helicity [105], along with a plane at 31% X/C filled with the entropy are presented here. Figures 4.13(a), 4.13(c), 4.13(e) and 4.13(g) represent the URANS computation while figures 4.13(b), 4.13(d), 4.13(f) and 4.13(h) show the evolution for the ZDES computation. Four different times are represented in these snapshots: T/4, 2T/4, 3T/4 and T from up to down.

First of all, the richness in terms of vortical structures is the main visible difference between the two methods. The URANS captures only the main vortices as long as they are stable enough. The main tip-leakage vortex and its contra-rotative induced vortex are visible with the two methods, in figure 4.13(a) and 4.13(b). Nevertheless, they extend further downstream in ZDES. This is due to their high unsteadiness from plane 31% X/C onward, which is dissipated by the URANS approach, and as a consequence, not captured.

The ZDES reveals multiple flow patterns similar to the ones suggested by Bindon [11] on a turbine cascade. The tip clearance flow leaks through channels from the pressure to the suction side of the blade. The flow angle depends on the chordwise position and corresponds to the angle observed within the gap in figure 4.11. Secondary tip-leakage vortices, as the one pointed in figure 4.13(f) migrate from the trailing edge toward the leading edge. Then, once close to the main tip-leakage vortex, their direction changes, they roll up around it due to its high rotational momentum. Finally they disrupt. The secondary tip-leakage vortex which is the closest to the main tip-leakage vortex has a specific behaviour. It does not migrate from the trailing edge and the resulting secondary vortex, pointed in figure 4.13(d), always rolls up from the same position as it can be seen in figures 4.13(b), 4.13(d), 4.13(f) and 4.13(h).

A tip-leakage vortex flutter phenomenon is visible in the present configuration, both in URANS and ZDES. The IGV wake and its tip vortex meet periodically the leading edge of the R1 which leads to this flutter. This arrival is highlighted at section 31% X/C in figure 4.13(g). The interaction between the wake

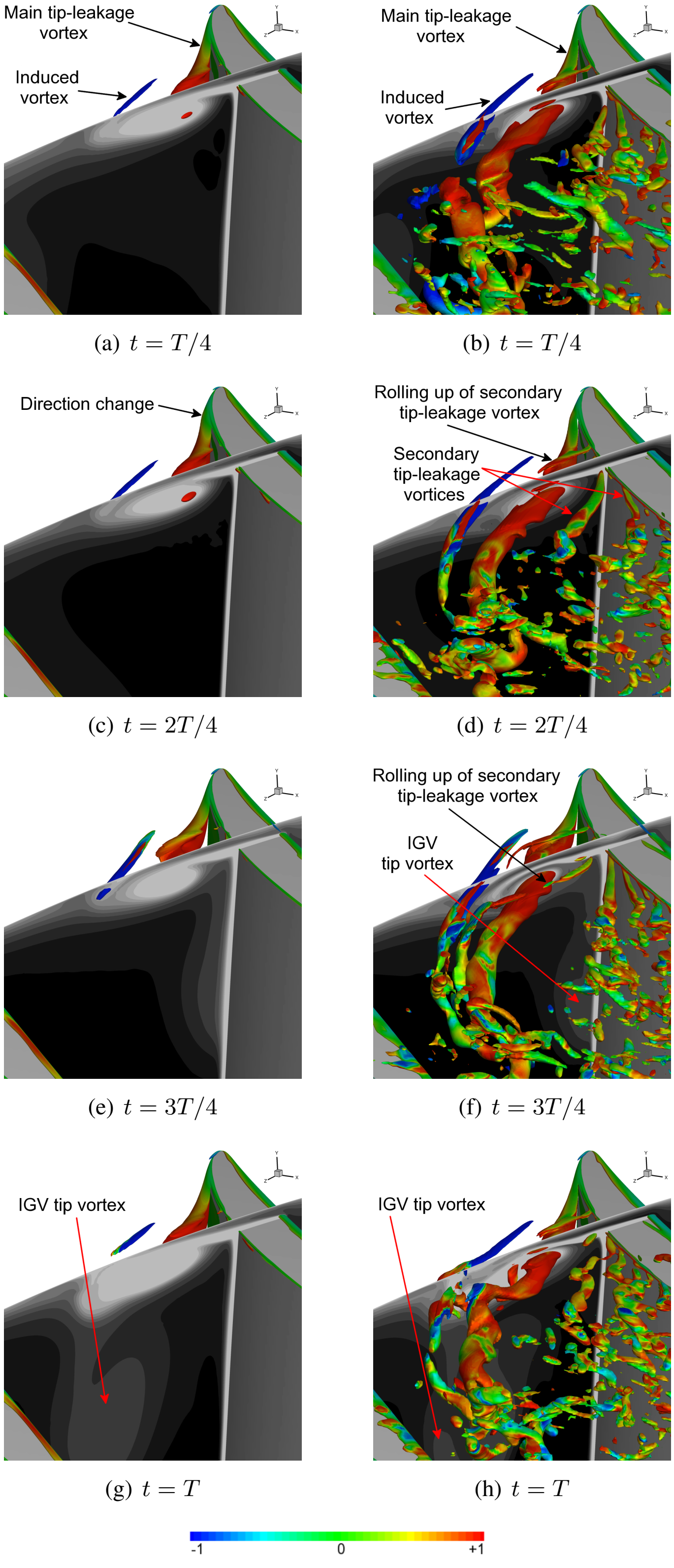

(a) $t = T/4$ (b) $t = T/4$

(c) $t = 2T/4$ (d) $t = 2T/4$

(e) $t = 3T/4$ (f) $t = 3T/4$

(g) $t = T$ (h) $t = T$

Figure 4.13 — *Snapshots of Q criterion iso-surface coloured by the normalized helicity and section 31% X/C filled with the entropy (left: URANS, right: ZDES).*

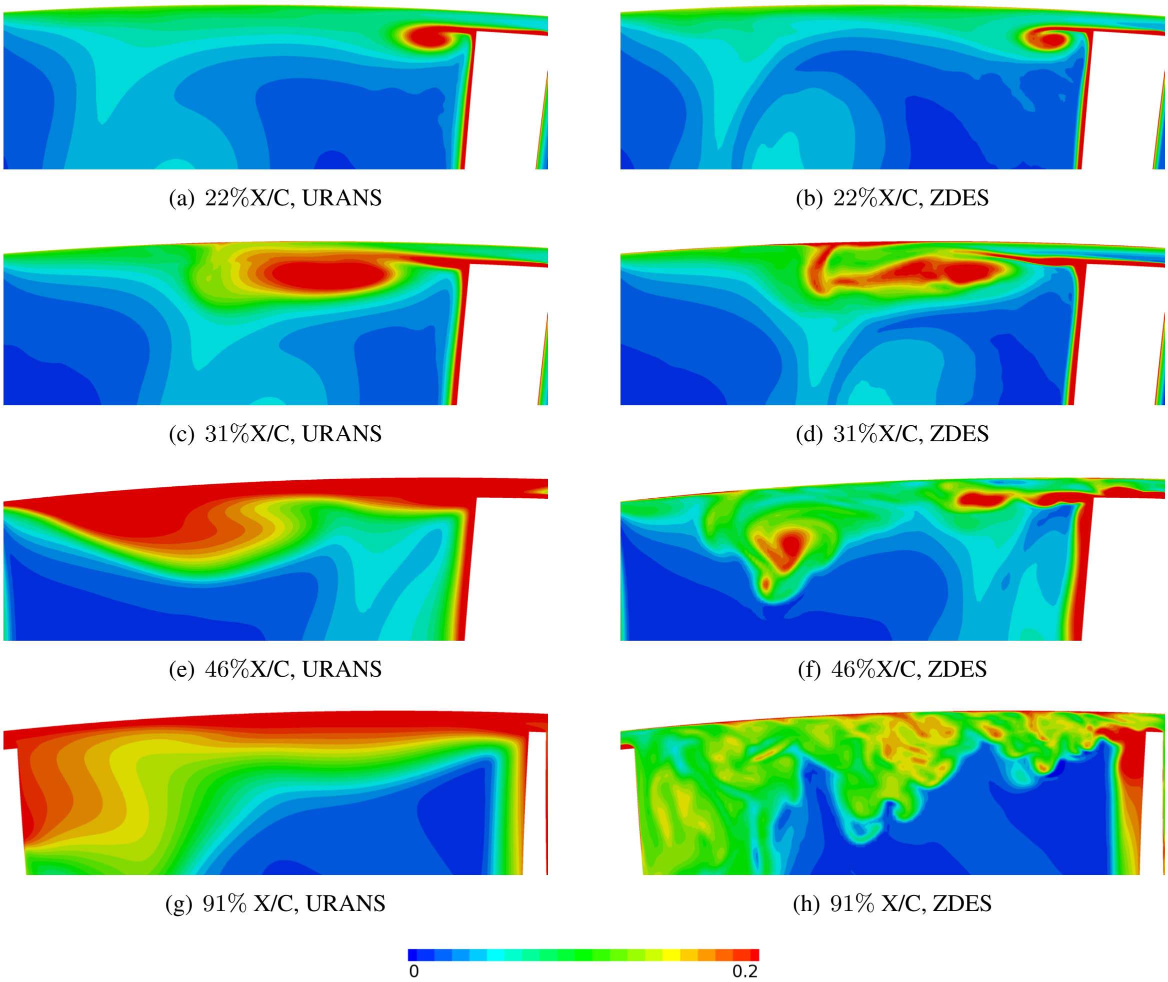

(a) 22%X/C, URANS

(b) 22%X/C, ZDES

(c) 31%X/C, URANS

(d) 31%X/C, ZDES

(e) 46%X/C, URANS

(f) 46%X/C, ZDES

(g) 91% X/C, URANS

(h) 91% X/C, ZDES

Figure 4.14 — *Entropy planes for four different axial positions at t=3T/4 (left: URANS, right: ZDES).*

and the tip clearance flow, hence this flutter, was already experimentally emphasized by Mailach et al. [109], albeit not with an incoming vortex from the stator as it is the case here. Indeed, only a simple wake was simulated. In CREATE, the velocity deficit in the main flow deflects the leakage flow direction as shown in figures 4.13(c) and 4.13(d). As a consequence, the tip-leakage vortex moves away from the suction side of the blade with a period of T and the axial position of its disruption wanders around 31% X/C.

It must be noticed that the tip-leakage vortex evolution along the chord is different depending on the method used as explained with the time averaged fields seen previously. This is illustrated here by the entropy planes at position 22.3%, 31%, 46% and 91% X/C, for a snapshot at t=3T/4 in figure 4.14. Even if the tip-leakage vortex develops at the leading edge, the boundary layers from both the tip of the blade and its suction side supply the tip-leakage vortex along the chord. The resulting tip-leakage vortices are generated at this shared edge between the blade suction side and the blade tip, this from the leading edge to the trailing edge of the blade, figure 4.14(h). In figures 4.14(a) and 4.14(b), the tip-leakage vortex rolls up and its development is as advanced in RANS as in ZDES. From 31% X/C, the topology differs between the two methods. The vortex coming from the IGV tip stretches periodically the tip-leakage vortex azimuthally and accelerates the casing boundary layer separation seen in the time averaged fields. This is clearly shown by figure 4.14(d) that the IGV wake has not an important role in this stretching, contrary to the IGV vortex. The key element here is the velocity deficit which is more important within the IGV tip vortex. The separation at the casing occurs even when this vortex

Case	Normalized mass flow	Normalized R1 total pressure ratio
Pneumatic probes	1.000	1.000
RANS	1.020	1.006
URANS	1.019	1.005
ZDES	1.014	0.992

Table 4.1 — *Mass flow and total pressure ratio for RANS, URANS and ZDES, normalized with the values from the pneumatic probes data.*

does not meet the tip-leakage vortex. However, it separates downstream of 31% X/C when there is no influence of the IGV tip vortex. This boundary layer separation was already referenced on an axial compressor by Gourdain and Leboeuf [64] to explain one of the origins of flow blockage near the casing. With the URANS method, the entropy levels are higher, continuous and azimuthally spread as it can be seen at plane 46% X/C in figure 4.14(e). Thereby, the tip-leakage vortex dissipates earlier with the URANS approach and contaminates the boundary layer up to the adjacent blade near the trailing edge, figure 4.14(g). On the contrary, in ZDES, the entropy field is composed of scattered high entropy spots, in figures 4.14(d), 4.14(f) and 4.14(h), corresponding to the continuity of the tip-leakage vortex and to multiple smaller vortices visible in figure 4.13(f). At 91% X/C, near the trailing edge, the difference is even more pronounced than upstream. Indeed, at this position the main tip-leakage vortex has almost completely turned into smaller vortices with the ZDES approach.

To sum up this section, the analysis of the flow field has highlighted the difference between the two methods in terms of visualization of the tip-leakage flow topology. Upstream section 31% chord, the two approaches give similar results. Nonetheless, beyond this section, the methods differ. The discrepancy stems from the simulation of the shock on the suction side of the blade which results in an important entropy creation in the URANS computation. On the contrary, the entropy creation is localized with the ZDES. These results are not only visible with instantaneous fields but with the averaged field too. That is to say, the use of the ZDES approach gives different results downstream the blade and has an impact on the way the tip-leakage flow is taken into account. It is then necessary to know in what way. Moreover, a question is still pending : is this difference beneficial to the simulation of the tip-leakage flow?

In the next part of this chapter, the ZDES method will be assessed following the levels of validation defined by Sagaut and Deck [146] and summarized in table 2.2. This evaluation will be based on experimental measurements.

4.3 Validation level 1: global values

After the flow visualization of the previous section, which can be regarded as the level 0 of analysis, this section deals with the first level of validation from Sagaut and Deck [146]. It consists in appraising the effects of the choice of the method, either RANS, URANS or ZDES, on the global values of a compressor blade.

For the assessment of these values, one has to reckon with the availability of the experimental measurements in CREATE. Moreover, the restrictions of the study concerning the size of the computational domain prevent the use of data extracted at the rear stages of CREATE, or too far upstream. Thereby, the values which are taken into account correspond to pressure probes in sections 25A and 26A as shown in figure 2.5. These two sections enable the computation of ratios which are consistent with the different computations carried out since they surround the R1 only.

Two values are then computed: the mass flow and the total pressure ratio. They correspond to a dynalpic average [53] of the data available: at each cell for the CFD results and for all the experimental

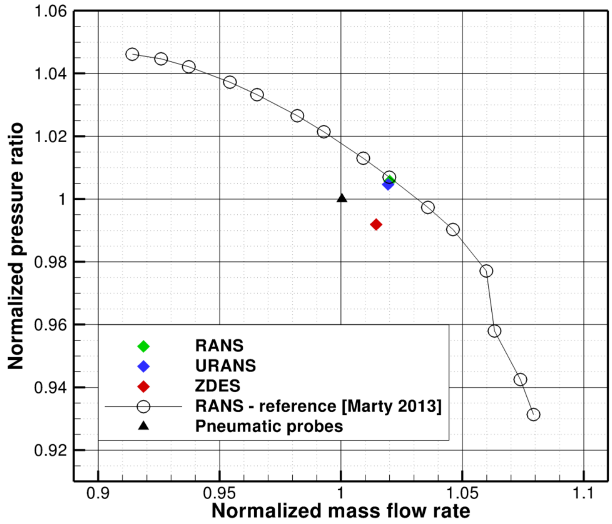

Figure 4.15 — *Pressure ratio versus mass flow rate for RANS, URANS and ZDES, normalized with pneumatic probes data.*

probe values. On the one hand the mass flow average is performed at section 25A, on the other hand, the total pressure ratio corresponds to the ratio of the dynalpic averages at section 25A and 26A. These values are then normalized by the value for the pneumatic probes, and summarized in table 4.1.

First of all, it is important to underscore the fact that the values from pneumatic probes, which are used for reference, have to be considered with caution. Indeed there are important uncertainties for these experimental values since the integration azimuthal period is $9.99°$ instead of $11.25°$ for the R1 periodicity. In addition, and this is the most important uncertainty source, there are no probe values over 95% and below 4% relative height. These zones, near the hub and near the casing are subject to the boundary layer influence and experience a lower total pressure and a lower axial momentum levels. As a consequence, seeing that these values are missing and not totally reliable, using a single value based on integral forces to find the operating point would have led to important errors. This supports the use of the axial momentum radial distribution to define the numerical operating point corresponding to the experimental design point as described in chapter 3. They are nonetheless used as reference here for a better understanding of the computational method effect on the global values.

In order to visualize this effect, the normalized pressure ratio is presented as a function of the normalized mass flow rate in figure 4.15. A reference operating line is given as an example and corresponds to different RANS computations from Marty [113] post processed with the same methodology as the one explained previously. These RANS computations are carried out with elsA 3.4.03 on 48 processors and the averaged inlet cartography from the preliminarily study detailed in chapter 3. The domain is the same as the one for the R1 computation presented in the last chapter, excepted one channel is only modelled. This fine RANS type mesh comprises 4.27 Million points. It is based on a Spalart-Allmaras turbulence model with third order AUSM+P and standard backward Euler. Finally, a radial equilibrium is set as outlet condition with a type 4 valve law, defined in equation II-63. This law is used to define the different working points presented in the figure with circles.

Despite the unsteady aspect of URANS and even the use of a rotating distortion, one can see that its prediction of performance values are close to the ones for RANS. Moreover, the use of a finer grid in this study, based on the ZDES requirements, does not change the operating point when it is compared to the reference RANS cases. All of the computations based on the averaged Navier-Stokes equations overestimate both the pressure ratio and the mass flow rate. Even if similar numerical methods and boundary conditions are used for all the computations of this study, RANS, URANS and ZDES, the global value results differ when considering the ZDES case. Indeed, the ZDES computation overestimates the exper-

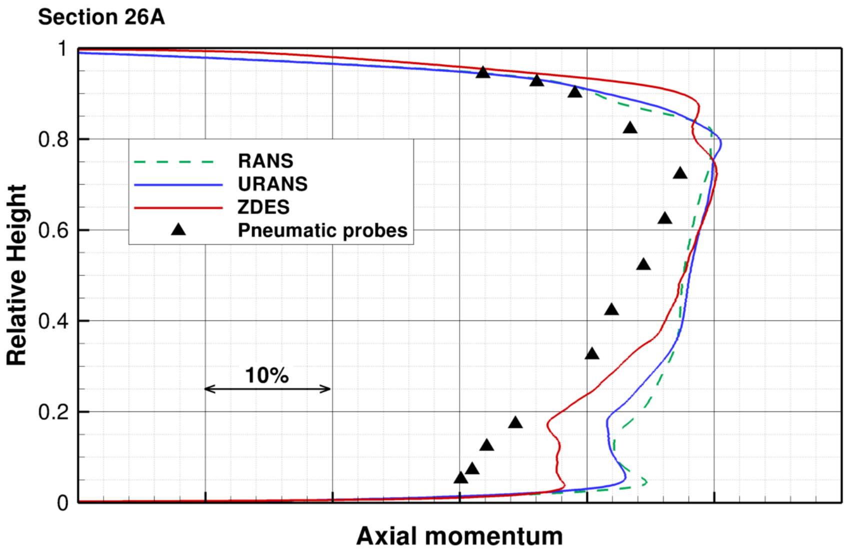

Figure 4.16 — *Radial distribution of time and circumferentially averaged axial momentum at section 26A for RANS, URANS, ZDES and experimental probes.*

imental values for the mass flow like the other computations whilst it underestimates the pressure ratio. The global values shows that the ZDES case is not absolutely in better agreement with the experimental measurements than the RANS or URANS cases. Indeed, the global values for the ZDES are not simply shifted from the RANS values toward the experimental ones. This is more complex and denotes an important change in the flow topology. This discrepancy between the methods can not be justified by just analysing the global values, hence the requirement to move on to the next stage in terms of flow validation.

4.4 Validation level 2: mean aerodynamic field

The second level of validation is the analysis of the mean aerodynamic field. This is performed in this study by the means of radial and azimuthal distributions.

4.4.1 Radial distribution

The radial distributions located downstream the R1, in section 26A, are assessed for the different computations : RANS, URANS and ZDES, and compared to experimental values from probes. The steady data from RANS and pneumatic probes values are azimuthally averaged. The resulting radial distribution of the axial momentum is presented in figure 4.16. As explained previously, the operating point was chosen by the means of the radial distribution of axial momentum at section 25A. Therefore it was previously seen in figure 4.1 that the axial momentum values from the computations are in good agreement with the experimental probe values in section 25A. Notwithstanding this good agreement at section 25A, there are some discrepancies between the methods downstream. Moreover, by crossing the blade passage, the flow changes and the gap between the methods and the probes widens.

The first thing to point out is the overestimation along the whole span of the values from the computations, whatever the method applied. The position for the maximum of axial momentum is correctly located with the ZDES and corresponds to the probe at 72% of relative height. Even if the gradient near the casing is overestimated with all the computations, the ZDES amplifies even more this trend. In fact, this is due to a second local maximum at 87% of relative height. The two maxima, at 72% and 87%

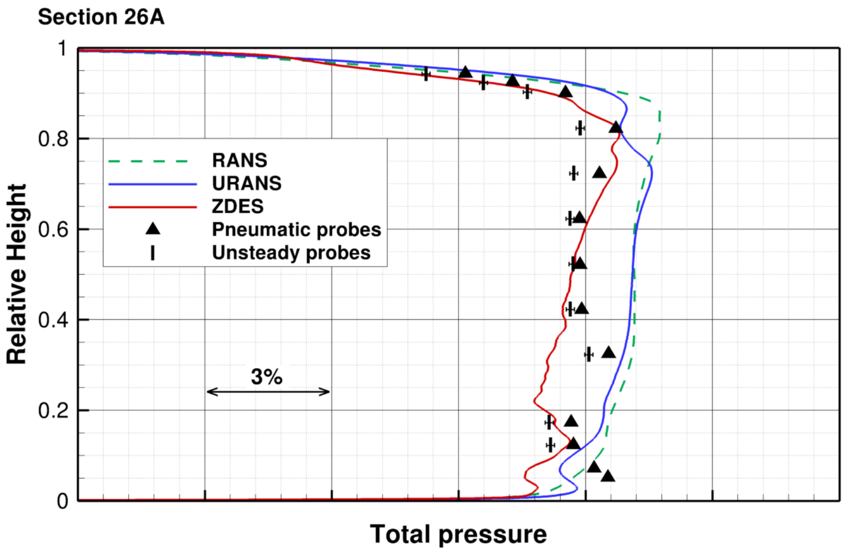

Figure 4.17 — *Radial distribution of time and circumferentially averaged total pressure at section 26A for RANS, URANS, ZDES and experimental probes.*

surround a zone of deficit at 80% which corresponds to the tip-leakage flow from the R1. The probes discretization prevents to be sure if this area is physical or not. Indeed, there is no visible inflection for the values with the probes. Besides, the maximum at 87% is not seen experimentally.

Near the hub, the ZDES is in better agreement with the experimental values, albeit the axial momentum is still overestimated by 5%. There is a discrepancy with the RANS and URANS which have an additional 5% of axial momentum. This is coherent with the global value plotted in figure 4.15. From the hub to the third of the span, the RANS and URANS approaches differ clearly. Below 20% of span, there is a change in the gradient for the unsteady computations with a clear inflection point in CFD. This inflection is located nearer to the hub for the RANS computation. This highlights the location of the corner flow with a change of slope visible around 10% with the probes. However, this increase in the amount of axial momentum near the hub is still overestimated by 5% with the ZDES.

Another interesting value to check is the total pressure. The three computations on R1 are compared with mean experimental results deduced from two different kinds of probes, the pneumatic and the unsteady ones [119]. The unsteady probes and computation data are averaged in time and then in azimuth. The averages apply to the same time domain of 17 T for ZDES and 18 T for URANS as explained in the previous sections. The radial distribution of total pressure at section 26A is plotted in figure 4.17. The averaged unsteady probe symbols comprises the interval with the measure uncertainties which are of 0.1% of the value.

First of all, even if the two experimental data are close at mid span, the gap widens and reaches up to 1% in turbulent regions, such as the tip-leakage flow at 80% relative height. These zones reveal the highest discrepancies between the numerical methods too, and confirm what is observed for the axial momentum. The pressure gradient induced by the secondary flows near casing, from 100% to 85% relative height, is better captured in ZDES than in URANS and RANS which under-estimate it. However, URANS succeeds in capturing the effects on total pressure at 82%, like the ZDES method. Both methods are close to the pneumatic probes value at 82%, albeit still 1% higher than the averaged unsteady probes. This radial position, along with the one at 10% which corresponds to the hub corner effect, is the only one where URANS differs clearly from RANS and gets closer to the ZDES results, indeed, the two RANS methods are similar at mid-span.

It must be noticed that ZDES brings significant improvement over methods based on averaged

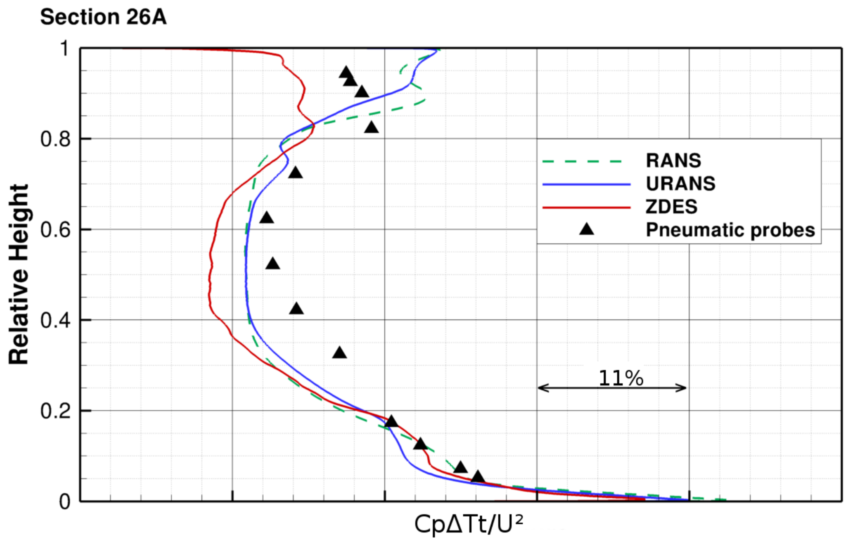

Figure 4.18 — *Radial distribution of time and circumferentially averaged normalized total temperature at section 26A for RANS, URANS, ZDES and experimental probes.*

Navier-Stokes equations for the tip-leakage flow and even at mid span. Nevertheless, at 32% relative height, the computations provide total pressure values which do not match the probes measurements, with an under-estimation of 1% for ZDES and an over estimation of the same order of magnitude for the RANS and URANS methods, depending on the considered probe. A hypothesis for this pressure increase could be that the recirculation from the axial gap upstream from the R1, which can be seen in figure 2.5, modifies the pressure distribution locally at 32% relative height in section 26A. This phenomenon, could not be seen in the configuration set in this paper since no hub recirculation is modelled compared to the configuration studied by Marty and Aupoix [110].

After the axial momentum and the total pressure, another important value informs us on the work of the blade: the total temperature. Figure 4.18 shows the radial distributions at section 26A of the normalized total temperature, $Cp\Delta Tt/U^2$, known as loading coefficient. First, there is a global underestimation of the total temperature value for the computations. This is directly linked to the global overestimation of the axial momentum seen in figure 4.16. This underestimation of the total temperature is amplified for the ZDES which has a value for $Cp\Delta Tt/U^2$ 4% lower than the RANS/URANS cases. Nonetheless, the main difference is visible near the casing where the RANS and URANS computations calculate a $Cp\Delta Tt/U^2$ higher than the probe measurements by 5%. By contrast, the ZDES approach still under predicts the total temperature value which is more consistent with the other values computed below 80% of the span. In order to better understand this difference, a study was carried out by Marty et al. [114] on the same configuration with a different boundary condition at the wall. Marty highlighted that by imposing a temperature, instead of the adiabatic condition, the gradient near the casing can change drastically from the value observed in ZDES to the one in RANS and URANS. Moreover, the boundary condition at the casing wall influences the gradients of temperature above 80% relative height. This is the region where the methods differ here. However, the same adiabatic boundary condition is used for all the computations presented here.

Therefore the difference is due to the method, not the boundary condition. Beyond the absolute value which is directly linked to the operating point, two effects have to be emphasized. The first one is the relative shift between the minimum at mid span and the value near the casing, which is in better agreement with the ZDES. The second one is the inflection point at 82% relative height. This inflection originates from the arrival of the tip-leakage flow. The ZDES captures this inflection. Though the steady RANS captures an inflection, albeit the radial position is overestimated, the unsteady RANS manages to

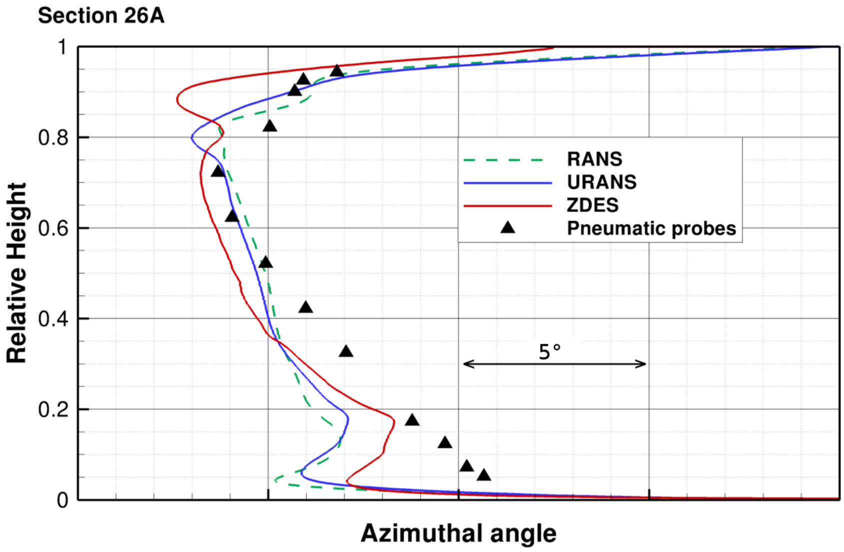

Figure 4.19 — *Radial distribution of time and circumferentially averaged azimuthal angle at section 26A for RANS, URANS, ZDES and experimental probes.*

capture only a light curvature between 90 and 95% and does not capture any inflection. As a consequence, one can see that the ZDES captures more accurately the development stage of the tip-leakage vortex although the operating point of the computation does not match perfectly the experimental one.

The last compared value is the azimuthal angle. The corresponding radial distribution is plotted in figure 4.19. The previous analysis of the axial momentum has shown a work difference between the computations first, and between the computations and the experimental case. This is confirmed by the total temperature distribution. Beyond the main difference with the probes seen along the radius for the different values, there are two zones with different results according to the method used. They are areas where the unsteady aspect of the flow is of major importance: near the casing and near the hub. Moreover, if the angle is changed, the axial momentum changes too. As a result, the same characteristic regions are observed for the axial momentum and the azimuthal angle. The minima of the azimuthal angle are then linked to the maxima of the axial momentum. Indeed, a minimum for the azimuthal angle is encountered at 72% relative height and correctly captured with the ZDES. The ZDES experiences another minimum at 87% which corresponds to the minimum of axial momentum seen in figure 4.16. Even if an inflection can be seen for the probes at 92% relative height, the angle value is clearly underestimated by 2.5° in ZDES. The URANS approach has a similar behaviour but the radial position of its minimum angle is different since it is located at 80%. Besides, there is only one local minimum in URANS contrary to the ZDES. Beyond expectations, the steady RANS reveals to be in better agreement near the casing here.

On the contrary, near the hub, it has the worst results, and the ZDES has the closest angle values to the experimental ones. However, all the computations capture an inflection between 10 and 20% of relative height, which is not measured by the probes. The inflection near the hub is due to the strong corner effect, which is not physical. Many hypothesis can explain this discrepancy with the experimental measurements near the hub. Some are linked to the simplification of the numerical test bench, such as the IGV hub gap modelization, the simplification of the hub surface and platform geometries or the recirculation upstream the R1 which is not taken into account. Other hypothesis are linked to the numerical methods, such as the underlying turbulence model. Indeed, the Spalart-Allmaras model is known for amplifying the separation in turbomachinery as revealed by Marty [112, 111] for the CREATE compressor. The capability of the ZDES to simulate unsteady flows is mainly based on the LES aspect of this method, however, it is important to keep in mind that in the boundary layer, at least with mode = 2, the flow is computed with the unsteady RANS approach. As a consequence, the limitations of the underlying

turbulence model influence directly the ZDES.

Recent studies from Gmelin and Thiele [61] have shown that the prediction of angle and total pressure losses are better in RANS than with DDES or IDDES approaches. In this study, the steady RANS can give locally closer results to the probe values than the URANS or the ZDES approaches. Nevertheless, as it is explained for the total pressure analysis, this method fails, as expected, in capturing the flow physics in zones where the flow is driven by unsteady phenomena, such as the tip-leakage flow. The analysis of radial distributions in this study highlighted a better agreement with the measurements in ZDES than in URANS and RANS. However, the ZDES approach seems to amplify the vortex from the tip clearance with amplitudes not found experimentally. These amplifications are similar to the ones observed in LES by Hah [69] on the Rotor 37. Nevertheless, in the frame of this study, the main issue seems to be the choice of the operating point, and thus, a different load of the blade. This hypothesis will be discussed in chapter 5.

4.4.2 Azimuthal distribution of time averaged velocities

The difference observed previously are located in section 26A, that is to say, downstream the R1. It is important to understand where they come from upstream. As a consequence, and with a view to have a better validation of the flow physics captured, the azimuthal distributions within the blade passage are compared. It is possible to track the development of the tip clearance flow between two blades of the R1 by the means of the Laser Doppler Anemometry (LDA) measurements carried out on the CREATE compressor. An ensemble averaged is applied to the flow field from the unsteady computations with the same time range as for the radial distribution. The flow values are then extracted from the resulting flow field and from the steady RANS computation too. These results are then compared to the available averaged LDA measurements of the axial and circumferential velocities for different axial positions along the blade and at section 26A. Moreover, different radial positions are put forward so as to follow the tip-leakage flow. The corresponding axial positions can be seen in figure 4.3. All the values are normalized by a reference value from the LDA measurements. Since the visualization are represented in the rotor frame of reference, the relative azimuthal position is unknown. Thereby, the relative position between the computations and the experimental values is based on the gradients.

First of all, the flow near the leading edge and near the casing is examined. Figure 4.20(a) represents the normalized axial velocity along the 11.5 degrees of the azimuthal range at 21.7% X/C and 98% of relative height. The plane positions and view direction are detailed in figure 4.3. First of all, one can see that the LDA measurements are not periodical with respect to the IGV blade count. This can be explained by the non periodic configuration of the test rig. For instance, there are 8 support struts upstream the IGV, so the $1/32$ periodicity is only available with the IGV and the first stage. Therefore, the difference between the axial velocities for the LDA is certainly due to this non periodicity. The RANS, URANS and even ZDES computations are similar in terms of axial velocity at this location. They all overestimate the axial velocity. However, this overestimation is minimal at azimuth 3.5 and 9. The discrepancy increases from azimuth 3.5 to 8. This is due to the fact that the axial velocity measured by the LDA drops rapidly above azimuth 6 to the blade.

Figure 4.20(b) shows the same azimuthal distribution for the circumferential velocity. One can see that there are black squares at azimuth 2.5 and 8.5, despite the fact that there is the blade. This stems from errors with the LDA measurements due to reflections on the walls. Nevertheless, the levels of circumferential velocity for the computations are in better with the experimental measurements than for the axial velocity. The circumferential velocity is decreased from azimuth 3.5 to 8. Near the blade, there are small peaks of circumferential velocity, mainly visible in ZDES, albeit perceptible in RANS and URANS too. The LDA only experiences a more pronounced drop in the value up to azimuth 6, and then such peaks.

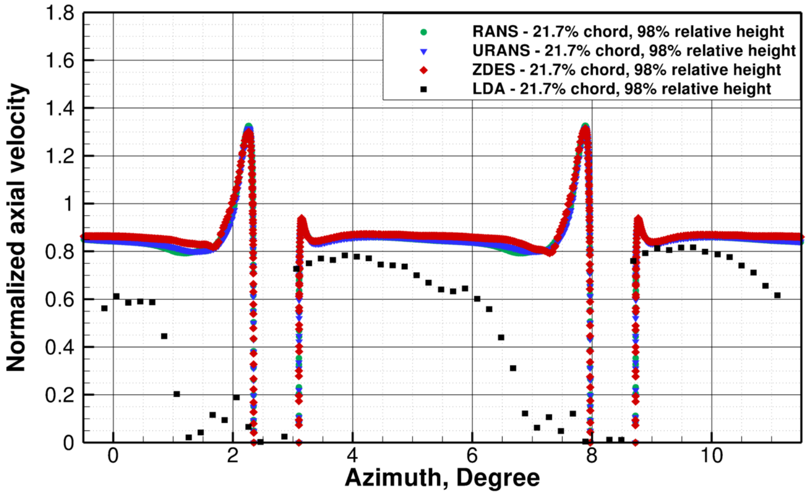

(a) Axial.

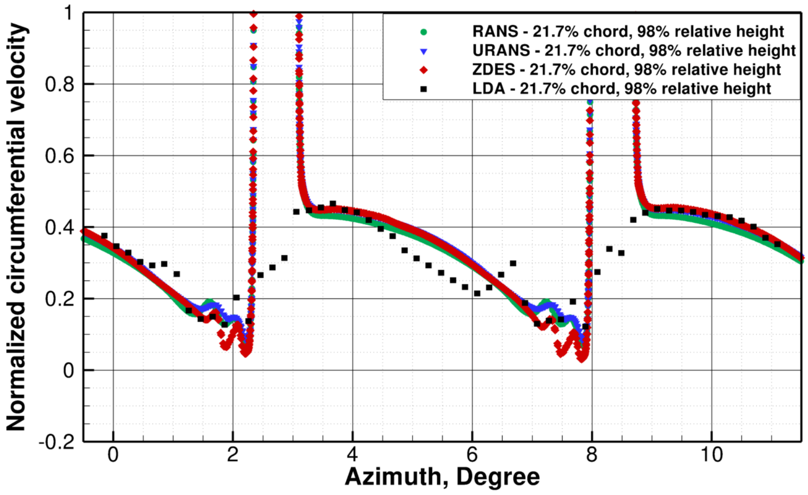

(b) Circumferential.

Figure 4.20 — *Axial and circumferential velocities at 21.7% chord and 98% relative height for RANS, URANS, ZDES and LDA measurements.*

Figure 4.21 shows the same axial and circumferential velocities but at a different position. These azimuthal distributions are located at 44.8% X/C, that is to say, downstream the section 31% where there is the shock as explained previously. The radial position is lower, at 94% of relative height. The computations still overestimate the axial velocity levels, visible in figure 4.21(a), as it was the case upstream. Moreover, the non periodicity of the LDA measurements is amplified here. This is clearly visible at azimuth 3.5 and 9 which have 10% of velocity difference. These positions correspond to the rim of the main tip-leakage vortex. The vortex core is defined by its local minimum of axial velocity. Experimentally, the periodicity of $5.625°$ or $\frac{2\Pi}{64}$ for the R1 is not respected. On the contrary, this is respected for most of the azimuthal positions in the different computations. As a consequence, one can conclude that some important effects, which are not taken into account in the numerical test bench, change the flow structure. This leads to a different shift for the tip-leakage vortex depending on the blade passage considered. The origins of this different behaviour are numerous due the simplifications performed numerically. However, one can reckon that the two main effects are: first the support struts, and second, the potential effects from the first stator (S1) downstream the R1. Notwithstanding the

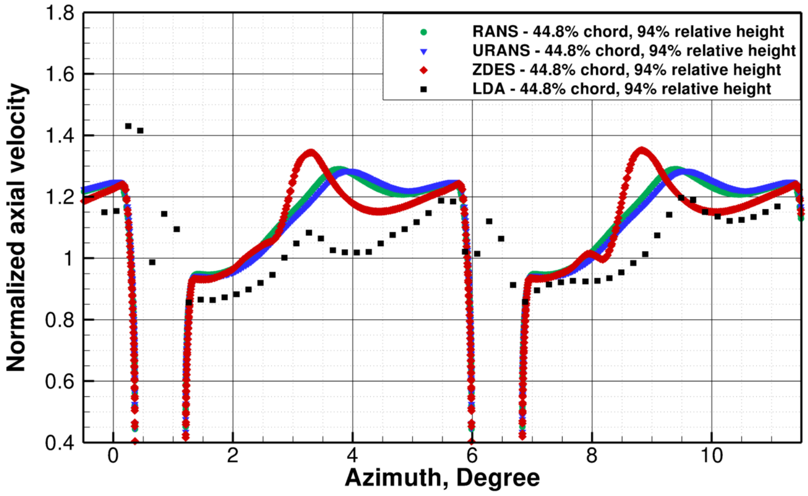

(a) Axial.

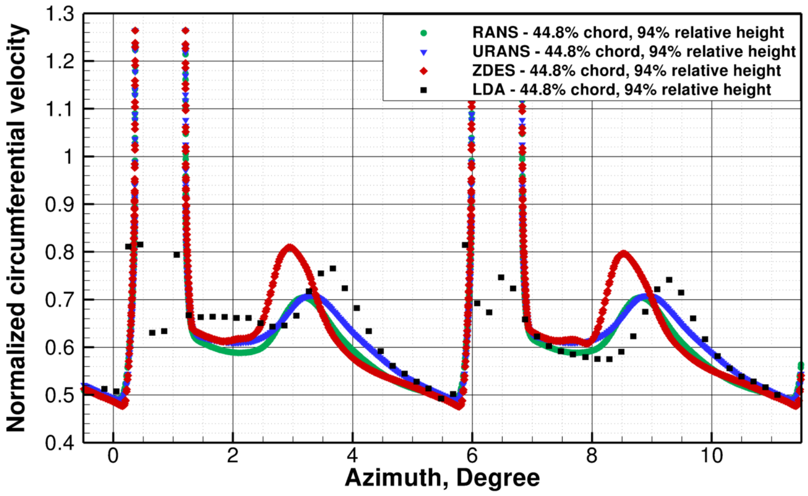

(b) Circumferential.

Figure 4.21 — *Axial and circumferential velocities at 44.8% chord and 94% relative height for RANS, URANS, ZDES and LDA measurements.*

velocity levels that correspond to the tip-leakage flow which are overestimated by the computations, there is a different behaviour at this position between the computations. On the one hand, the levels are better estimated in RANS and URANS, on the other hand, the width of the vortex is in better agreement with the ZDES approach. This widening in RANS and URANS confirms the dissipation observed with the averaged entropy fields in figure 4.6. As the vortex dissipates, it widens.

Another change with the upstream position already analysed is that the sudden drop of axial velocity near the blade, which was observed at 21.7% X/C, does not exist any more. Thereby, the effects seen experimentally at 21.7% X/C near the casing are only located near the leading edge of the blade. At the operating point computed, this phenomenon is captured by none of the compared methods.

The circumferential velocities in figure 4.21(b) do not show the same azimuthal position shift for the experimental data. Therefore this effect influences mainly the axial velocity and corroborates the fact that it is supposed to be linked to erroneous boundary conditions instead of a wrong capture of the tip-leakage flow topology. The same widening and dissipation of the tip-leakage flow are observed in

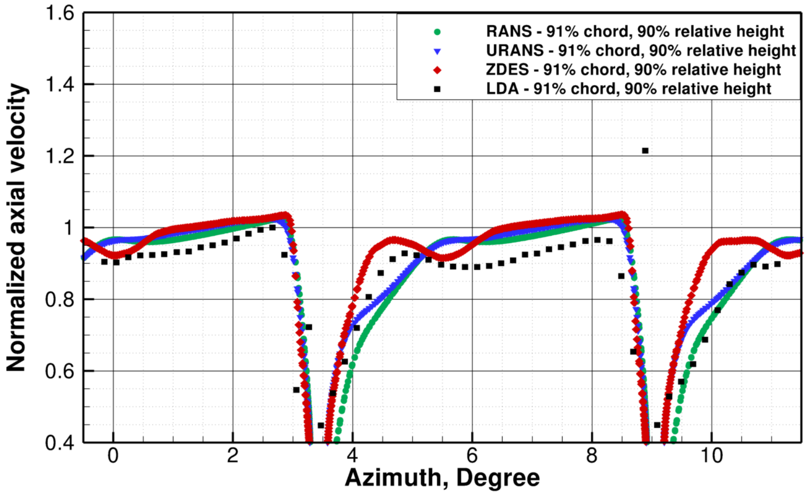

(a) Axial.

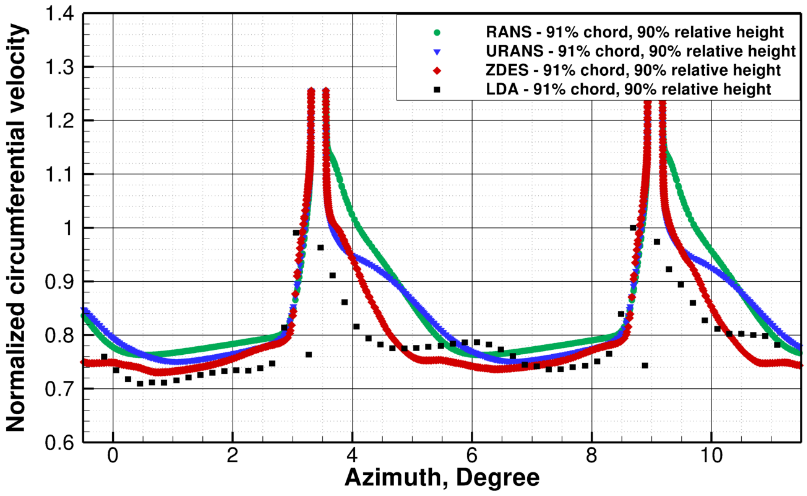

(b) Circumferential.

Figure 4.22 — *Axial and circumferential velocities at 91% chord and 90% relative height for RANS, URANS, ZDES and LDA measurements.*

RANS and URANS. Moreover, its azimuthal position can be more accurately analysed by the means of the circumferential velocity. Thereby, one can notice that its real position is between the one seen by the URANS/RANS approaches and the position captured by the ZDES. As a consequence, this confirms that the two approaches simulate the tip-leakage flow development differently. The deviation of the vortex is different, hence the difference in the azimuthal positions.

In order to confirm this trend, the same visualizations are presented in figure 4.22, near the trailing edge of the blade, at section 91% X/C, and further from the casing, at 90% of relative height. As it was observed in figure 4.7, and 4.13, the main tip-leakage vortex is totally dissipated in URANS and RANS near the trailing edge of the blade. There is no indication of it in figure 4.22(a). By contrast, there is an axial velocity deficit at azimuth 5.5 in ZDES. This position is nonetheless not the one which corresponds to the tip-leakage vortex in the LDA measurements, which is azimuth 6. Besides, its widening is more important in the experiments. By adding the overestimation of the axial velocity seen throughout the passage, this strengthens the hypothesis of a different operating point between the experimental case and

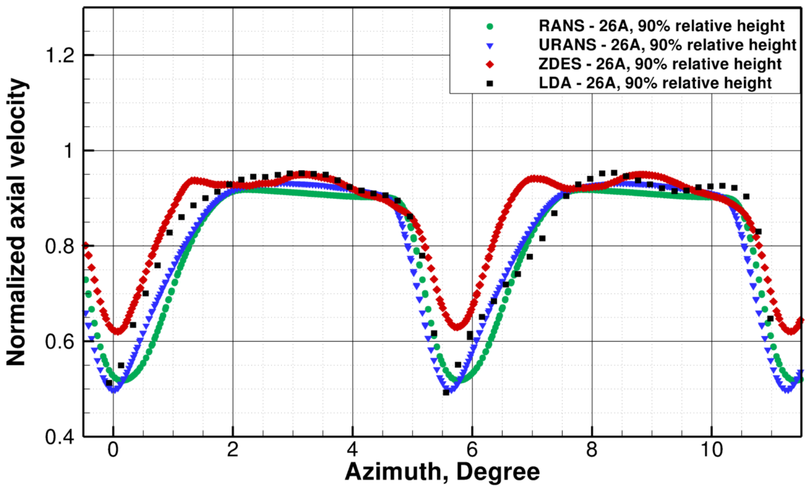

(a) Axial.

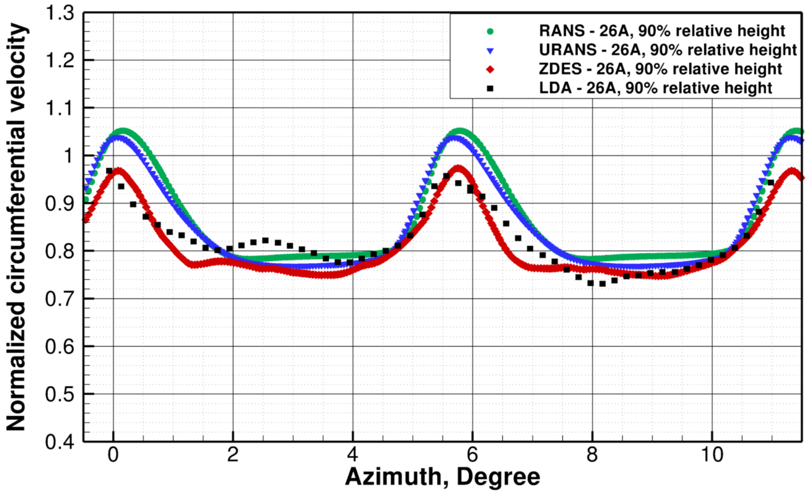

(b) Circumferential.

Figure 4.23 — *Axial and circumferential velocities at section 26A and 90% relative height for RANS, URANS, ZDES and LDA measurements.*

the computations.

The analysis of the circumferential velocity in figure 4.22(b) emphasizes that the ZDES captures more accurately the tip-leakage flow. Indeed, the levels are in better agreement, and the step at azimuth 6 is captured, albeit it is less pronounced than what it is experimentally. This step is not captured by the RANS and URANS approaches. Nevertheless, one has to underscore that between azimuth 6 and 8 the levels are similarly captured by all the methods, albeit the steady RANS overestimates it by 5%.

Finally, the same azimuthal distributions are presented at section 26A in figure 4.23. This section was already analysed by the means of radial distributions. The chosen radial position is 90%. It corresponds to the upper part of the tip-leakage vortex as illustrated by the minimum of azimuthal angle seen in figure 4.19 and local maximum of axial momentum in figure 4.16. The trend observed in the upstream positions is found at section 26A too. This explains the effects observed in the radial distributions. The level discrepancy for the axial velocity between the LDA measurements and the computations diminished gradually in the previous positions. As the flow reaches the section 26A, this discrepancy is almost erased for most of the azimuthal range, as it can be seen in figure 4.23(a). The levels are then similar between the computations. Nevertheless, even if the RANS and URANS methods capture correctly the wake, at azimuth 0 and 5.625, the ZDES approach overestimates the axial velocity within the wake by 10%. The local deficit of axial velocity due to the tip-leakage flow is captured in ZDES and not in URANS. However, the shift between the measurements and the computation is increased here and the lack of periodicity for the LDA measurements is more important than upstream. Indeed, the velocity deficit due to the tip-leakage vortex is at azimuth 9.5 for the LDA and 8 for the ZDES. While there is another zone with a deficit at azimuth 2.5 in the ZDES case, there is nothing clearly visible in LDA at this position. Figure 4.23(b) confirms the better agreement of ZDES with the LDA measurements concerning the circumferential velocity. Even if the tip-leakage vortex is not clearly visible at azimuth 2.5, it is visible for the circumferential velocity. A characteristic step is visible for the LDA and for the ZDES values too at this azimuth. Nevertheless, although such a step is captured by the ZDES at azimuth 8, the footprint of the tip-leakage flow is not visible at this position for the LDA. In summary, the ZDES detects the tip-leakage vortex in the two channels with both the axial and the circumferential velocities. By contrast, the LDA detects its position either on the axial or on the circumferential value, and not both at the same time. This is the reason why it is important to analyse the two components of the velocity for the detection of the tip-leakage vortex.

In conclusion, the ZDES behaves as if the operating point was chosen at a different axial velocity, that is to say, as if the outlet pressure was larger than what it is for the other computations. This behaviour is mainly localized in the regions of unsteadiness: near the tip and near the casing. Thereby, it is correlated to the way the ZDES handles the unsteady flows. Despite this issue concerning the operating point definition, the ZDES conserves the tip-leakage vortex beyond the shock contrary to the RANS and even the URANS approaches that rapidly dissipate it. In the next section, the unsteady aspect will be analysed so as to understand what differentiates the ZDES from the URANS approach in the capture of the unsteady flows.

4.5 Validation level 3: second-order statistics

In this section, the analysis will focus on the unsteadiness within the flow. Therefore, a statistic of second order will be studied. It corresponds to the level 3 in the levels of validation. In order to follow the tip-leakage flow development, and to compare to what was done in the previous section, the same positions are used for the azimuthal distributions presented here. The difference comes from the value which is compared. This time, the standard deviation [118] of the velocities is calculated. This is performed on the same time range as the averages presented previously. No value is displayed for the RANS computation because it is a steady simulation.

First of all, the axial velocity standard deviation is shown for section 21.7% X/C and at 98% relative height in figure 4.24(a). At this position and contrary to what is observed for the axial velocity value in figure 4.20(a), there is already a difference between the URANS and the ZDES approaches. Indeed, the levels of unsteadiness are higher for the ZDES at the azimuthal position 4 to 6. At the azimuthal position 7.5, near the blade, the discrepancy between the methods is the greatest. Contrary to the URANS approach, the values for the ZDES are in good agreement with the measurements. The drop in the measured normalized axial velocity observed in figure 4.20(a) near the blade, and not captured by the computations, coincides with a similar drop in the standard deviation value, from azimuth 6 to 7. This drop in the axial velocity standard deviation is captured by the computations. Besides, there is a sudden increase of the value for the standard deviation near the blade, which corresponds to the area with the peaks in the figure 4.20(a). A similar sudden increase is observed by the computations for the normalized axial velocity, but not measured by the LDA. This time, the LDA detects this increase for the standard deviation value. Notwithstanding the fact that the azimuthal positions of the zones of high unsteadiness

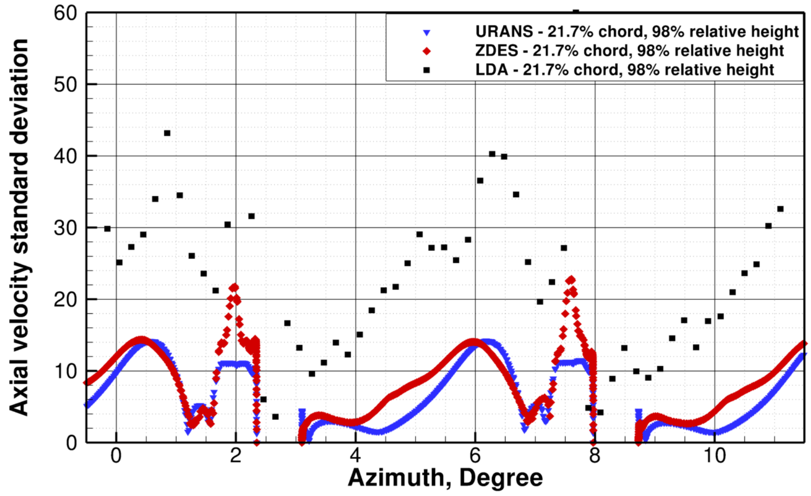

(a) Axial.

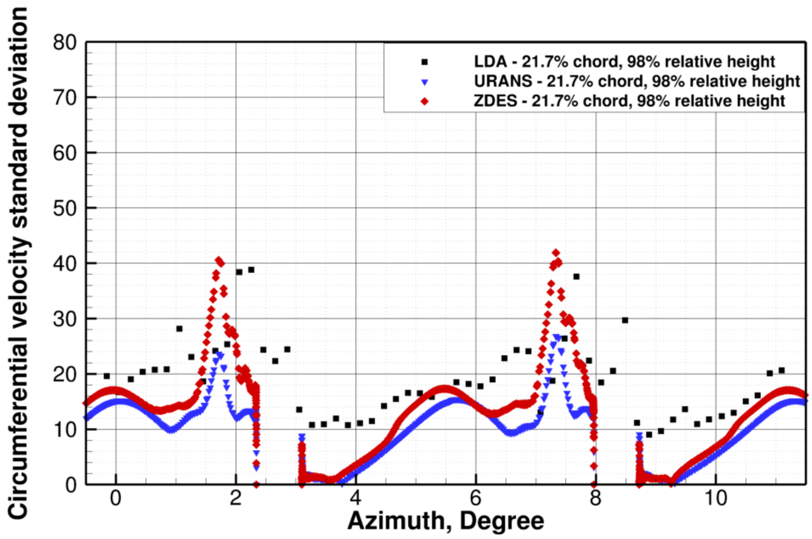

(b) Circumferential.

Figure 4.24 — *Axial and circumferential velocity standard deviations [in $m.s^{-1}$] at 21.7% chord and 98% relative height for RANS, URANS, ZDES and LDA measurements.*

are correctly captured, there is an important underestimation of the standard deviation value for the two computations.

Likewise, the circumferential velocity standard deviation, visible in figure 4.24(b), is underestimated by the computations. In spite of the good agreement for the levels of the normalized circumferential velocity seen in figure 4.20(b), the unsteadiness in the azimuthal direction differs between the computations and the LDA measurements. Indeed, near the pressure side of the blade, at azimuths 3 to 4, it is close to 0 for the computations while it is above $10m.s^{-1}$ for the LDA. The unsteadiness levels for the computations increase in between the blades, up to azimuth 5.5 where it reaches the same levels as the LDA measurements. Then, the levels of the circumferential unsteadiness decrease only for the computations. It only rises again near the suction side of the blade where the levels are in good agreement between the LDA and the computations. At this position, for azimuths 7 to 7.5, there is a peak of unsteadiness corresponding to the position of the main tip-leakage vortex. There is a light improvement for the ZDES with unsteadiness levels closer to the LDA measurements around this peak.

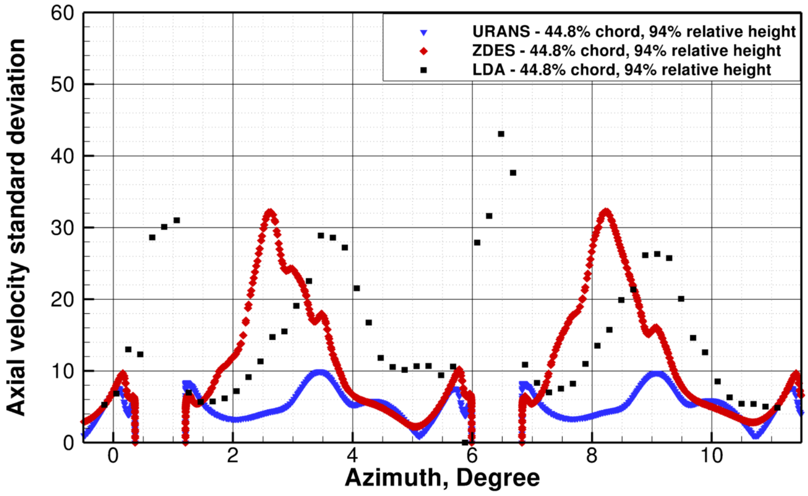

(a) Axial.

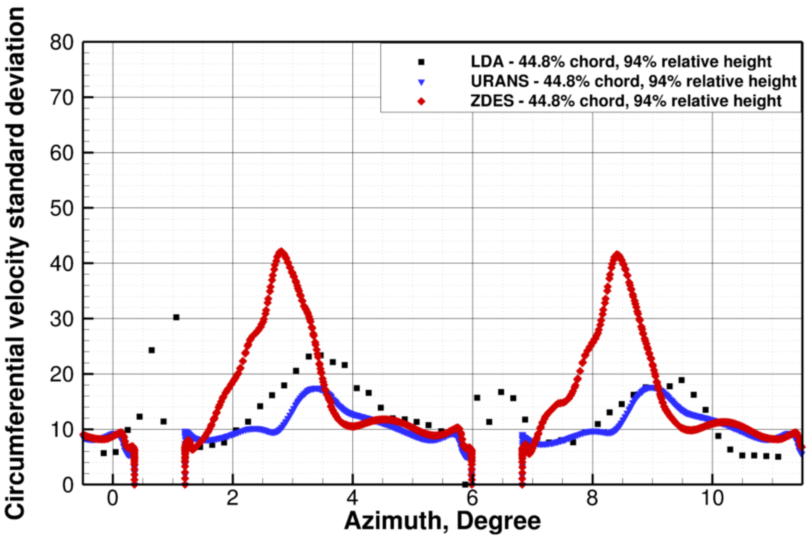

(b) Circumferential.

Figure 4.25 — *Axial and circumferential velocity standard deviations [in $m.s^{-1}$] at 44.8% chord and 94% relative height for RANS, URANS, ZDES and LDA measurements.*

Downstream the shock position, the ZDES capability to capture the axial unsteadiness within the flow outstrips the URANS approach. At the position 44.8% X/C and 94% of relative height, in figure 4.25(a), the levels of axial unsteadiness are correctly captured by the ZDES whereas the URANS barely captures a light unsteady phenomenon. Nevertheless, the azimuthal position has a difference of one degree between the ZDES and the LDA while the position is correct for the URANS. Since the azimuthal position of the tip-leakage vortex is directly correlated to the axial velocity, this confirms the problem of the choice of the operating point for the ZDES. At the same position, the circumferential velocity standard deviation, in figure 4.25(b), highlights an important overestimation for the unsteadiness of the tip-leakage vortex captured by the ZDES which is up to two times higher than what it is experimentally. The same aforementioned position issue is visible for the circumferential velocity standard deviation in ZDES. By contrast, the URANS approach captures correctly the position of the peak at azimuth 3-3.5 and 9. The unsteadiness levels are closer to the ones captured experimentally than what is observed in ZDES. However, there is still an underestimation of the unsteadiness in URANS.

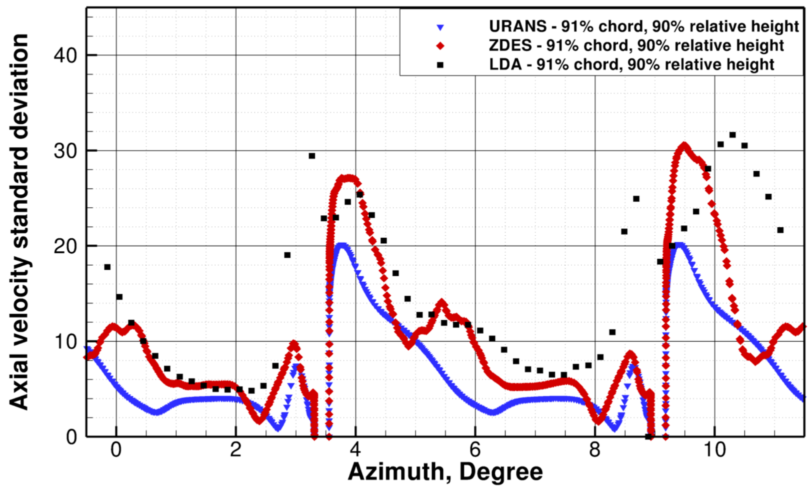

(a) Axial.

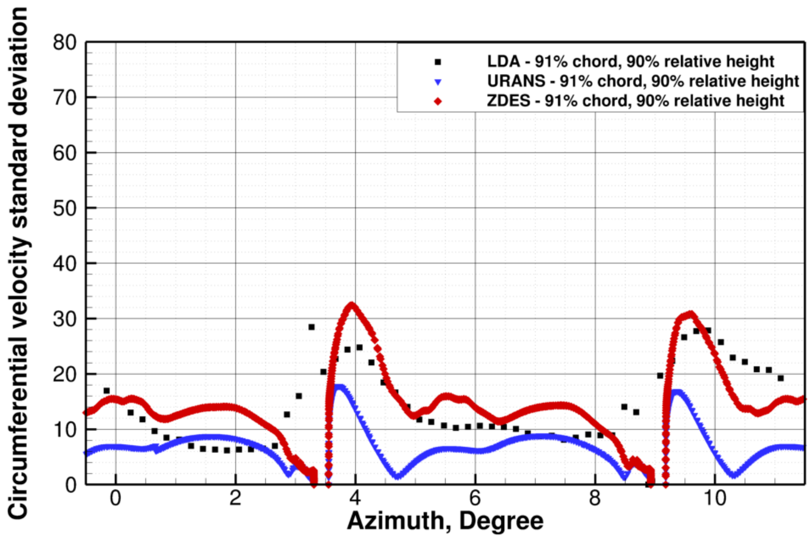

(b) Circumferential.

Figure 4.26 — *Axial and circumferential velocity standard deviations [in $m.s^{-1}$] at 91% chord and 90% relative height for RANS, URANS, ZDES and LDA measurements.*

This trend is confirmed near the trailing edge of the blade, at 91% X/C and 90% of relative height. The axial velocity standard deviation is presented in figure 4.26(a). At this position, the unsteadiness distribution has changed for the computations as well as the measurements. The value is higher near the blade around azimuth 4 and decreases as the azimuth increases up to the other blade. The azimuths 4-6 denote the position of the rim of the main tip-leakage vortex. On the one hand, the intensity and position of this vortex is correctly captured by the ZDES method. On the other hand, the URANS does not capture it at all. Moreover, the levels are lower in URANS with an almost constant 5% discrepancy with the LDA measurements along the azimuth.

Figure 4.26(b) shows similar results for the circumferential velocity standard deviation at the same position. Contrary to what is observed at 44.8% X/C in figure 4.25(b), the ZDES captures unsteadiness levels that suit better the azimuthal distribution observed experimentally than the URANS computation. This confirms that the URANS method underestimates the unsteadiness in both directions downstream the shock position.

The last position to be evaluated is the one corresponding to the upper part of the tip-leakage vortex, in section 26A. Figure 4.27(a) shows the axial velocity standard deviation. The wakes of the R1 are in azimuth 0 and 5.625. Two zones of high unsteadiness in the axial direction are visible on each side of the wake centre, for instance, one at azimuth 5 and one at azimuth 6.5. They have a different level of unsteadiness. This level difference is not captured by the URANS method. Moreover, the URANS computation captures lower levels compared to the LDA measurements. The level difference between the two zones around the wakes is seen by the ZDES, albeit less pronounced than what it is experimentally.

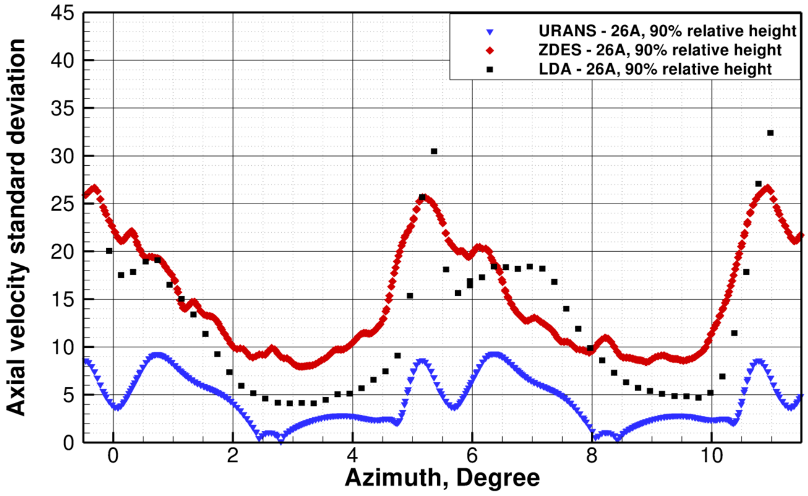

(a) Axial.

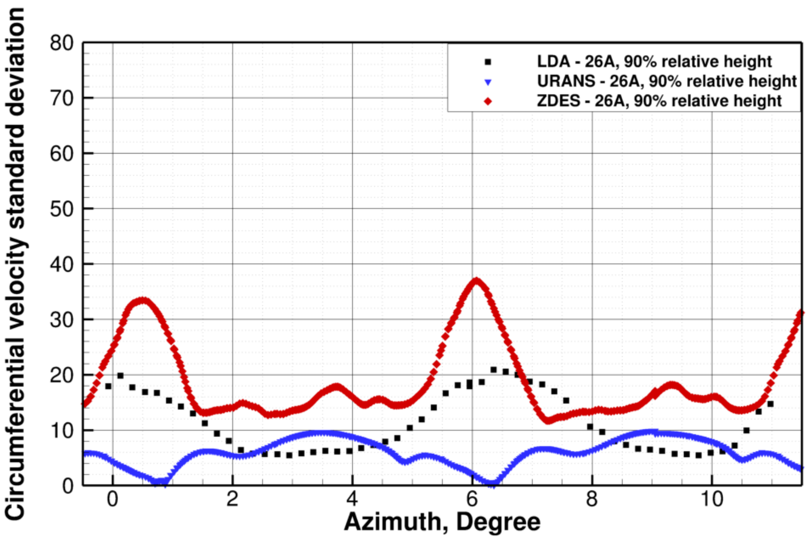

(b) Circumferential.

Figure 4.27 — *Axial and circumferential velocity standard deviations [in $m.s^{-1}$] at section 26A and 90% relative height for RANS, URANS, ZDES and LDA measurements.*

Figure 4.27(b) underlines the difference between the two methods. The circumferential velocity standard deviation is high in ZDES, with values oscillating between 12 and 37 whether there is a wake or not. Conversely, the levels for the URANS method are low and besides, the oscillations have a lower amplitude, from 0 to 10. What is important to notice here, is the level of the LDA measurements. In the zones where there are the wakes, the levels are high and correspond to the peaks seen in the ZDES, albeit the levels in ZDES are almost twice as much as the levels captured experimentally. At these positions,

the URANS method does not experience the unsteadiness of the R1 wakes. By contrast, in between the two wakes, the levels of the LDA are in better agreement with the URANS ones than the levels in ZDES. In other words, the URANS captures only low values of unsteadiness, and as a consequence is in good agreement with the LDA where there is no major phenomenon generating unsteadiness. At this position, and in accordance with what is observed for the normalized velocities in figure 4.23, the tip-leakage vortex is weak and barely visible. Its rim is located at azimuth 2.5 with the step clearly seen in figure 4.23 but it is invisible on the azimuthal distributions of velocity standard deviation for the LDA and for the URANS method. The ZDES tends to conserve the tip-leakage vortex and therefore the unsteadiness of this vortex is still visible in section 26A around azimuth 2.5-3.

In summary, the discrepancy between the LDA measurements and the computations decreases as the flow gets closer to section 26A. This is the case for the normalized velocities too, as seen previously. The low unsteadiness values near the leading edge for the ZDES, and even in the zones captured in LES, originate from the fact that just upstream from the blade, the ZDES behaves like the URANS approach because of the mode = 0. The turbulence generated by the shear of the IGV wake is not fully developed near the leading edge of the R1. Then, the tip-leakage vortex develops and the analysis of the unsteadiness emphasizes the better capability of the ZDES method over the URANS one to capture the unsteady flows. However, the levels for the ZDES results are not in perfect agreement with the LDA measurements. The reason seems to be mainly the operating point since the azimuthal positions of the tip-leakage vortex differ. This confirms the trend seen in the previous analysis of the normalized velocities. Nevertheless, downstream the blade and in between the two wakes of the R1, the ZDES method has higher unsteadiness values than what is observed experimentally by the LDA measurements. The levels of unsteadiness for the wakes are yet correctly captured contrary to the URANS approach. As a consequence, the ZDES method brings improvements over the URANS approach for the simulation of unsteady flows.

In the next section, the fourth level of validation for the ZDES will be discussed with a spectral analysis of the flow.

4.6 Validation level 4: one-point spectral analysis

The fourth level of validation deals with the analysis of the spectra within the flow and its comparison to experimental data. This section intends to evaluate the ZDES approach in the two main regions of concern for this method: in the boundary layer and in the outer flow.

4.6.1 Probe positions

In order to understand how the ZDES behaves in its two different domains for the simulation of unsteady flows, two areas are chosen. The first one is located at 94% of relative height, which is the closest position from the casing and out of the boundary layer with appropriate experimental data from probes. Indeed, the spectral analysis requires unsteady data with a high acquisition frequency. Moreover, the acquisition has to be regular in time and, as a consequence, the LDA measurements are not suitable for this. This is the reason why the spectral study at 94% of relative height is based on the unsteady probes which are available on the CREATE experimental bench. Similar to what is done for the LDA measurements seen previously, a change of frame of reference is applied to the probe data. This induces that the exact relative position between the experimental and numerical probes is approximated. Nonetheless, it enables to carry out all the analysis in the rotor frame of reference which is appropriate to take the tip-leakage vortex and blade wakes into account. The chosen position corresponds to the wake of the R1. The exact azimuthal position for the numerical probe is indicated in figure 4.28 with an instantaneous

entropy plane from the ZDES computation. One can see that this position corresponds to the arrival of the tip-leakage vortex too, albeit it is widened and almost dissipated.

The second area is at the casing of section 26A. The same azimuthal position is chosen so that the difference between the probes comes mainly from their distance to the wall, hence their capture of either the inner boundary layer flow or the outer flow.

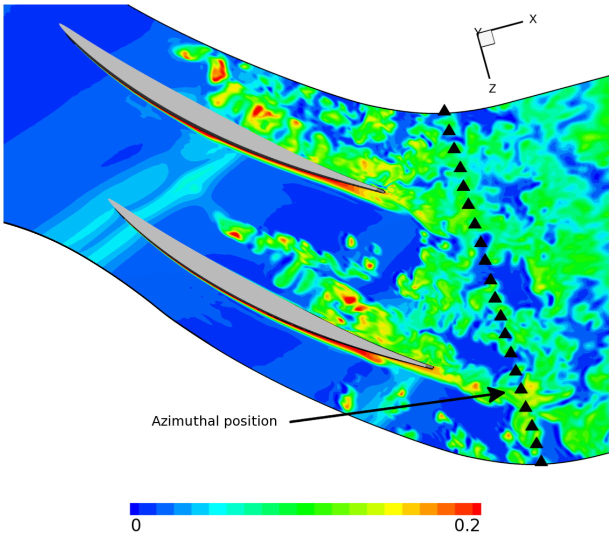

Figure 4.28 — *Probe positions at section 26A. Instantaneous entropy plane at 94% relative height and $t = 3T/4$ from the ZDES computation.*

4.6.2 Power Spectral Density

The spectral analysis is based on the power spectral density (PSD) of the pressure for the aforesaid probes. The PSD is based on the Welch method [172] using an overlap of 50% and ten Hann windows [68] with a linear mean for each. It describes how the root mean squared value of the static pressure is distributed in the frequency spectrum, and thus represents the flow energy. An estimation of the cut-off frequency for the computational results gives $3.2\ 10^5$ Hz. It is based on the cubic root of the cell volume and a characteristic velocity for the turbulent structures defined as $\sqrt{u'^2 + v'^2 + w'^2}$, with u', v' and w' respectively the maximum of the fluctuating velocity in the X, Y and Z directions, as shown in figure 4.28. It is important to keep in mind that the effective cut-off may be at a lower frequency due to the numerous effects that influence it, such as the mesh refinement and the numerical schemes. The value $G_p(f)$ of the static pressure is plotted as a function of the frequency in figure 4.29(a) for the probes at the casing and in figure 4.29(b) for the ones at 94% relative height. For a better understanding, another parameter is displayed : the reduced frequency. It consists in the signal frequency normalized by the IGV blade passing frequency (BPF).

The frequency resolution (FR) is 2000 Hz for the numerical data set arising from a temporal range of 17 T for the ZDES computation and 18 T for the URANS one. This resolution results from the aforementioned minimum number of Hann windows required for the Welch method. By contrast, the resolution for the unsteady probes is of 2 Hz. This is a limiting factor for the comparison of the numerical probes with the experimental ones, especially for the low frequency phenomena. The reason is that the lowest captured frequency is the frequency resolution. Thereby, the phenomena with a characteristic frequency inferior to the frequency resolution of a PSD are not captured. Another effect of the frequency resolution is the level of energy visible in the graphs. Indeed, a small frequency resolution leads to a more

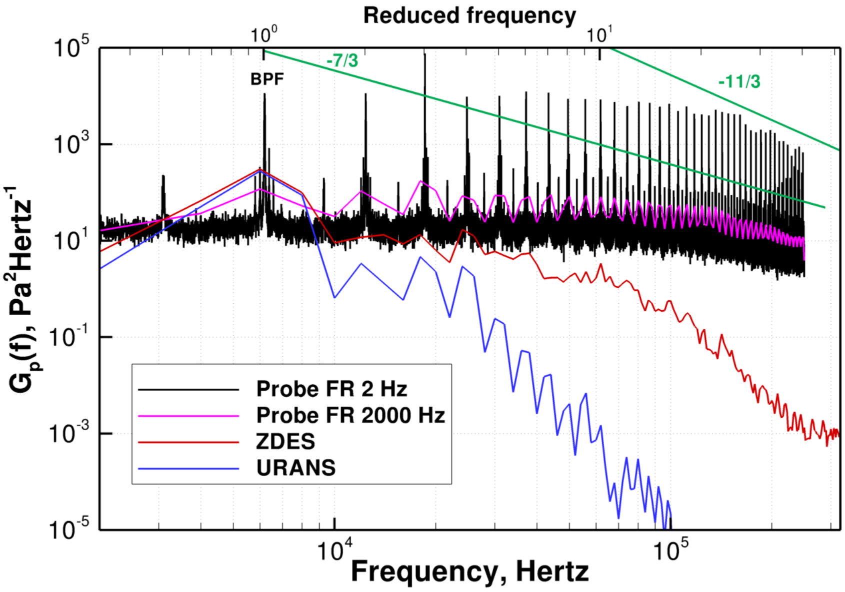

(a) At the casing.

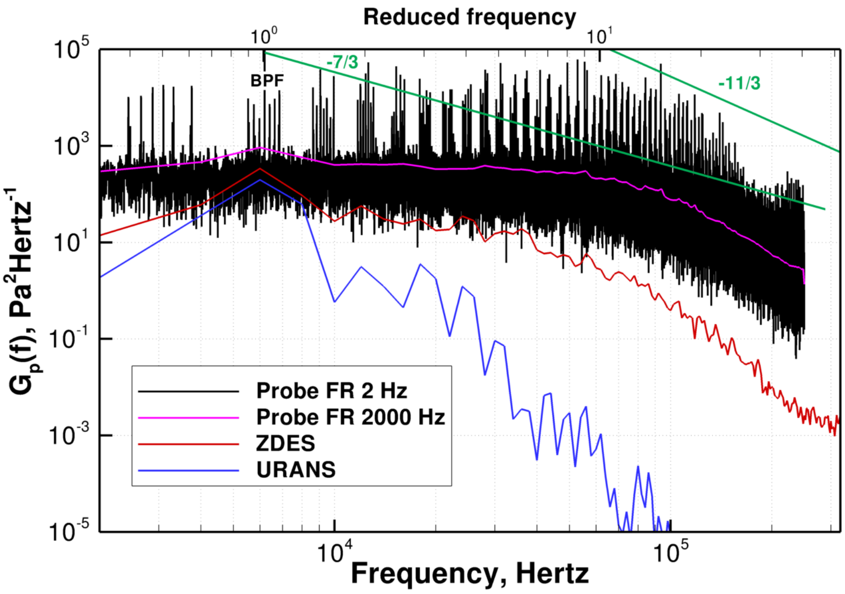

(b) At 94% relative height.

Figure 4.29 — *Power spectral density of pressure at section 26A. URANS, ZDES and experimental unsteady pressure probes (with 2 frequency resolutions).*

accurate capture of the frequency of a phenomenon, denoted by a thin and high peak of energy on the graph. On the contrary, the same phenomenon captured with a higher value for the frequency resolution will result in a wider and shorter peak due to the energy distribution on a wider range of frequency. This effect on the energy level visible is the reason why the PSD for the unsteady probe are displayed with two frequency resolutions. On the one hand, 2 Hz, which is the best available resolution regarding the length of the experimental data set. On the other hand, 2000 Hz, which is the same frequency resolution as the one for the numerical probes from the computations.

One can see in figure 4.29(a) that a low frequency phenomenon is visible for the experimental probe PSD only with the smallest frequency resolution. This phenomenon corresponds to $1/2$ BPF, and is captured neither by the unsteady probe PSD with 2000 Hz of frequency resolution nor by the

computations. Two hypothesis can explain this. First, this phenomenon is related to a flow phenomenon inside the R1 and the limiting frequency resolution prevents the computations from capturing it. Second, this frequency is related to the machine periodicity, and can not be captured by the computations. This second hypothesis is the most plausible. Indeed, the energy level of the BPF is correctly captured by the computations if the corresponding levels are compared with the same frequency resolution. However, from the second harmonic and beyond, the energy levels for the URANS approach drop by one order of magnitude compared to the ZDES levels. The third harmonic, which is the one with the highest energy level, is captured by the two computations with a level similar to the second harmonic. Although its energy level is superior to the BPF level experimentally, it is inferior by two orders of magnitude for the computations. This could originate from the potential effects from the first stator (S1), downstream of the R1 and downstream section 26A. The S1 has 96 blades which coincides with 3 IGV BPF which comprises 32 blades. This is not taken into account numerically since the S1 is not computed in the numerical test bench. As a result, a part of the discrepancy between the experiment and the computations located from the third harmonic of the BPF could be explained by this potential effect. Then, from 4 times the BPF, the discrepancy between the URANS and the ZDES methods increases and the URANS energy value drops off rapidly. Instead of having its energy drop off at the same rate as the URANS method, the ZDES computation keeps energy levels close to the ones for the experimental probes up to the 10^{th} harmonic. Nevertheless, there is an important decrease of the energy levels beyond this harmonic. At the 20^{th} harmonic, the experimental PSD has a slope inflection. The near flat energy level up to the 20^{th} harmonic changes then to a $k^{-7/3}$ slope. When the pressure spectrum is considered for a PSD, the $k^{-7/3}$ slope corresponds to contributions to the pressure fluctuations of the turbulence-turbulence interaction in the inertial subrange. This interaction is the most likely to be seen in experimental cases with high wavenumbers as described by George et al. [59]. Although the levels are higher in ZDES and in better agreement with the probe values than for the URANS approach, the slope is too important beyond the 20^{th} harmonic. Nonetheless, the $k^{-7/3}$ slope can be found from the BPF up to the 20^{th} harmonic. In other words, the turbulence-turbulence interaction seems to occur earlier for the ZDES than what it is experimentally. According to George et al. [59], the two other interactions which can occur are the following. First, the interaction between the turbulence and the mean-shear which is characterized by a $k^{-11/3}$ slope in the inertial subrange. Second, the third moment shear interaction with a k^{-3} slope. None of them are visible on the PSD at the casing.

Figure 4.29(b) shows the same PSD for URANS, ZDES and the unsteady probes but for a different radial position: 94% relative height. The plotted values here still correspond to static pressure data for the computations while total pressure measurements are used for the experimental data. First of all, it must be emphasized that this radial position is out of the boundary layer contrary to the one previously seen. One can see that there is a major difference in the energy levels for the PSD from the experimental probes depending on the radial position. The slope for the highest frequencies tends towards the $k^{-11/3}$. That is to say, at this position, the interaction between the turbulence and the mean-shear is more important than the turbulence-turbulence interaction visible within the boundary layer. Similar to the PSD at the casing, there is a slope inflection around the 20^{th} harmonic of the BPF. Indeed, for frequencies inferior to this inflection point, the spectrum is flat experimentally. Another salient point concerning the experimental data at this position is that the BPF and its harmonics are only distinguishable for the PSD with the frequency resolution of 2 Hz, and no more when configured with 2000 Hz. The reason is that multiple frequencies are found around the peak for the S1 passing frequency detected at the casing. These low frequency phenomena between 2400 and 3700 Hz are evident on the experimental PSD with a frequency resolution of 2 Hz in figure 4.29(b). These frequencies along with their harmonics contaminate the PSD levels. Thereby, it flattens the resulting PSD with a frequency resolution of 2000 Hz, thus it makes the BPF harmonics indiscernible for this resolution. This flat spectrum, which can be regarded as broadband, is not captured by the computations. Moreover, the URANS PSD still has a high dissipation for the highest frequencies.

Concerning the ZDES spectrum, the $k^{-7/3}$ slope, which is visible at the casing, is still noticeable

from 1 BPF to 10 BPF. In fact, the ZDES approach detects only a light decrease in the energy level for the flow field at 94% of relative height compared to the one at the casing. Therefore, the energy levels are in better agreement for the ZDES, albeit the levels are still at two orders of magnitude lower than the experimental PSD values. Nevertheless, what is important here is that the slope is correctly captured with the ZDES approach. The energy decrease is similar to the unsteady probes, even if there is still the issue with the potential effect of the S1. In other words, the interaction between the mean-shear and the turbulence is correctly captured in the ZDES approach contrary to the URANS method.

In summary, the ZDES brings significant improvements for the simulation of the interactions between the mean-shear and the turbulence. This results in energy levels and an energy decrease which are in better agreement with the experimental ones. Some of these enhancements are visible even in the boundary layer, albeit the ZDES behaves like the URANS method there. This behaviour near the wall prevents nonetheless the ZDES from capturing correctly the turbulence-turbulence interactions.

In the next section, one will compare the energy levels between the two unsteady computational methods so as to understand why there is such a difference for the energy levels when the flow arrives at section 26A.

4.7 Analysis of the energy levels along the tip-leakage vortex

In order to understand why there is such a difference for the energy levels between the URANS and the ZDES approaches at section 26A, a spectral analysis is carried out.

4.7.1 Probe positions along the tip-leakage flow

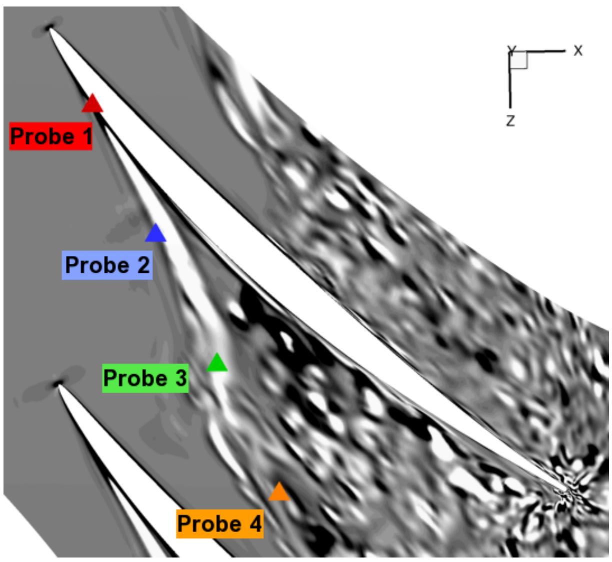

Figure 4.30 — *Probe positions along the main tip-leakage vortex. Instantaneous schlieren at 98% relative height and $T = 3T/4$ from the ZDES computation.*

This analysis aims at understanding how the two methods simulate the tip-leakage vortex development. Thereby, the Power Spectral Density (PSD) function of the static pressure is plotted for four probes within the blade passage. More precisely, they are located at different axial positions along the main tip-leakage vortex core as presented in figure 4.30 with the instantaneous Schlieren at 98% relative height and t=3T/4. The probes 1, in red, and 2, in blue, are located at 11% and 22.5% X/C. The probes

3, in green, and 4, in orange, are located at 33.8% and 45.7% X/C. This means that probes 1 and 2 are upstream the tip-leakage vortex disruption, which occurs after the shock, contrary to probes 3 and 4.

4.7.2 Power Spectral Density along the tip-leakage flow

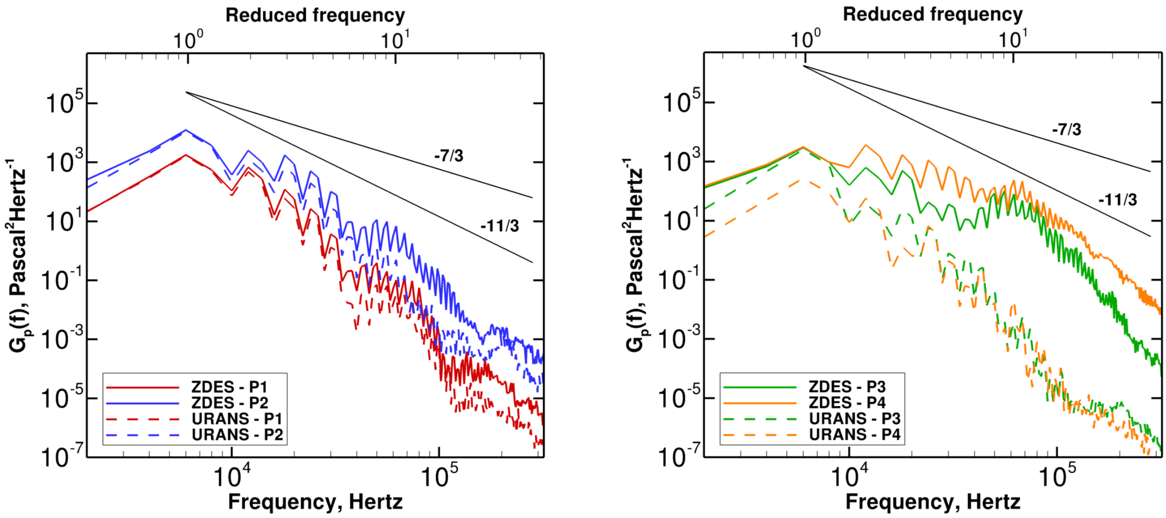

(a) Probes 1 and 2. (b) Probes 3 and 4.

Figure 4.31 — *Power spectral density of static pressure for probes along the main tip-leakage vortex. URANS and ZDES.*

The PSD are based on the Welch method [172] using an overlap of 50% and ten Hann windows with a linear mean for each as in the previous section. The same frequency resolution (FR) of 2000 Hz is chosen for both the computations. The PSD functions are plotted for probes 1 and 2 in figure 4.31(a) and for probes 3 and 4, in figure 4.31(b).

The PSD represents the flow energy. For a thorough knowledge of the energy within the flow, the normalized PSD are used too. They are defined by $\frac{f \cdot G_p(f)}{\sigma^2}$ with σ detailed in equation IV-1. The normalized power spectral density shows the contribution to the total energy of the different frequencies. They are plotted for probes 1 and 2 in figure 4.32(a) and for probes 3 and 4, in figure 4.32(b).

$$\sigma^2 = \int_0^\infty G_p(f)df = \int_0^\infty f \cdot G_p(f)d(log(f)) \qquad \text{(IV-1)}$$

Up to section 31% X/C, the energy level increases for every frequency, low, medium and high, and, above all, for both URANS and ZDES in figure 4.31(a). This characterizes a similar evolution of the tip-leakage flow. In addition, the magnitudes for probe 1 are close until 10^5 Hz, except for one peak at 38000 Hz ; then, they diverge. The frequency from which the two methods differ lowers as the probe is downstream. Indeed, for probe 2, it would be around 56000 Hz. The slope of the PSD changes from a steep one at probe 1 to the $k^{-11/3}$ slope which corresponds to a turbulence/mean-shear interaction. However, the ZDES approach is closer to this slope than the URANS method.

From probe 3 onward, figure 4.31(b), the difference in magnitude is important. At probe 3, the two methods match only at the low frequencies: 6000 and 8000 Hz. And finally, at probe 4, the whole spectrum is lower for the URANS approach. Nevertheless, it must be noticed that the 6000 Hz frequency corresponds to the IGV passage frequency (6156 Hz) regarding the PSD frequency resolution. Its harmonics are captured by both methods, although the magnitudes differ. This is clearly seen with

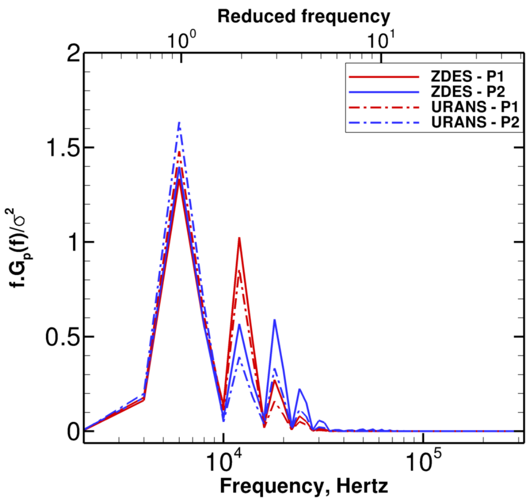

(a) Probes 1 and 2.

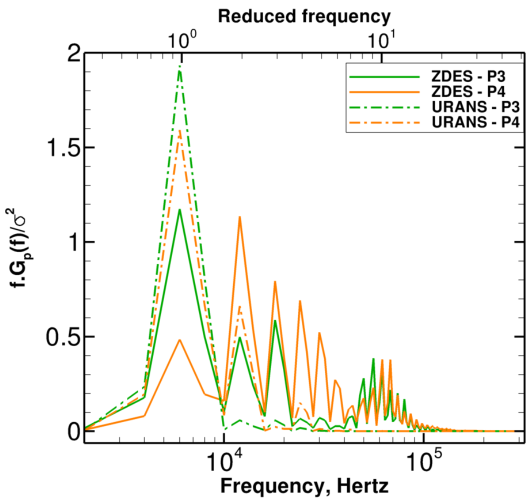

(b) [Probes 3 and 4.

Figure 4.32 — *Normalized power spectral density of static pressure for probes along the main tip-leakage vortex. URANS and ZDES.*

the reduced frequency which corresponds to the flow frequency divided by this IGV passage frequency. These magnitude discrepancies stem from a change in the slope. Although the slope for probes 3 and 4 is similar to the one for probes 1 and 2 for the URANS method, it is distinctly divided into two zones for the ZDES from probe 3 and even more for probe 4. The inflection point is then located around 60000 Hz or 10 BPF. On the one hand, the part of the slope with the highest frequencies is close to the slope observed in URANS but tends to be like the $k^{-11/3}$ slope. It was already the case for probe 2 with the ZDES method, but the trend is confirmed here. On the other hand, the part of the energy spectra with the lowest frequencies is the one that changes rapidly and makes the spectrum broadband at section 26A. The more the considered probe is far from the leading edge of the blade, the more the slope tends to match the $k^{-7/3}$ slope. In other words, the ZDES captures more and more the turbulence-turbulence interaction towards the trailing edge and beyond.

The normalized PSD confirm the aforementioned differences. Figure 4.32(a) shows a similar behaviour for the URANS and ZDES methods while analysing spectra from probes 1 and 2. Nevertheless, the energy contribution of the low frequencies to the whole energy is more important in URANS. This is directly linked to the lack of contribution of the highest frequencies above 30000 Hz or 5 BPF in the URANS case, as highlighted in figures 4.32(a) and 4.32(b). The second harmonic of the BPF has its contribution halved from probe 1 to probe 2, and higher harmonics appear to have more and more contribution to the whole energy. As high frequency phenomena do not have a significant contribution at this development stage of the vortex, the spectral signatures are close between the URANS and the ZDES methods.

From the vortex disruption at 31% X/C, the spectral signature of the two methods differs regarding the energy contribution. Figure 4.32(b) indicates that after the vortex disruption, the energy contribution is focused on the first BPF harmonic in URANS. By contrast, for the ZDES computation, the second and third harmonics have a significant contribution. Moreover, a privileged frequency range of BPF harmonics, around 75000 Hz, is only visible with the ZDES method. This frequency range is then correlated to the arrival of the IGV tip vortex and its important contribution to the whole energy is only triggered after the vortex disruption. However, its energy level is important even upstream section 31% X/C. It is visible around 75000 Hz in figure 4.31(a) for both methods and in figure 4.31(b) only for the ZDES method. Thereby the URANS method dissipates this phenomenon after the shock position contrary to the ZDES method. Besides, its frequency range corresponds to the inflection point for the slopes highlighted in figure 4.31(b), hence its link to the turbulence-turbulence interaction. Therefore, the inception of the effect of the turbulence-turbulence interactions on the total energy of the flow originates from the light shock located at section 31% X/C.

In conclusion, the evolution of the spectra along the tip-leakage vortex corroborates the topology difference between the URANS and ZDES methods which was observed in the previous analysis of this chapter. On the one hand, it is noteworthy to see that there is an energy transfer from the low frequencies to the highest for the ZDES computation. As the main tip-leakage vortex evolves, the ZDES spectrum is broad banded, that is to say, the smallest turbulent structures develop. On the other hand, this behaviour is not present in the URANS computation. In other words, the energy distribution in URANS is concentrated on low frequencies only and as vortices disrupt, the energy is not transferred to smaller vortices. The trend observed along the tip-leakage vortex is confirmed by the validation of level 4 performed downstream the blade at section 26A.

This energy transfer explains the discrepancy between the two methods to simulate small turbulent structures and to accurately predict the evolution of the tip-leakage vortex.

4.8 Synthesis

In this chapter, the ZDES method is validated up to the level 4 of the methodology defined by Sagaut and Deck [146]. This enables to understand the difference between the URANS and the ZDES approach concerning their capability to simulate unsteady flows.

The analysis shows that the capability of the ZDES method is limited in zones where the flow is solved in URANS, such as in the boundary layers. However, this does not prevent the ZDES from giving relevant results for the simulation of the tip clearance flow since the tip-leakage vortex is generated out of the boundary layers.

The discrepancy between the two methods is mainly revealed from section 31% X/C. At this position, there is a light shock on the suction side of the blade. Downstream this section, the URANS dissipates the tip-leakage vortex rapidly whilst the ZDES conserves it.

This difference originates from the capture of the interactions within the flow which differs depending on the method. The ZDES method captures a phenomenon of energy transfer from the large to the smallest structures. In a second step, the energy of the smallest structures is dissipated. By contrast, the URANS method dissipates the energy directly without this energy transfer towards the smallest scales.

An issue concerning the choice of the operating point is emphasized. Even if the same boundary conditions are used for the RANS, URANS and ZDES computations, this study highlights a different behaviour for the capture of unsteady flows with the ZDES. This stems from the difference in the capture of the aforementioned interactions within the flow. This different behaviour causes a change of the operating point for the numerical test bench depending whether the flow is solved in URANS or ZDES. Nevertheless, it is important to ensure that the discrepancy between the ZDES values and the measurements comes from the operating point and is not a lack from the ZDES capabilities. This will be assessed in chapter 5 where the behaviour of the tip-leakage flow near surge will be characterized.

A part of the work detailed in this chapter was presented at the 47th International Symposium of Applied Aerodynamics [139].

Third part

Throttle and inlet distortion effects on the tip-leakage flow

This last part deals with the behaviour of the tip-leakage flow near surge and the effects of the IGV wake on the tip-leakage flow.

Chapter 5 Tip-leakage flow behaviour near surge

Contents

This chapter presents the effects of the operating point on the tip-leakage flow by means of a thorough comparison of two ZDES computations : one at the design point and one near surge.

5.1 Adaptation of the test bench for the operating point near surge

With a view to understand how the tip-leakage flow behaves close to the surge line compared to the design point, the ZDES computation at the design point is set against a ZDES computation near surge. First of all, adapting the numerical test bench defined in chapter 3 is a prerequisite. This adaptation tries to be as close as possible from what was done for the design point and is validated by experimental measurements performed on the CREATE compressor near the surge line. Besides, it complies with the methodology developed in chapter 3.

5.1.1 Preliminary definition of the operating point

In order to be consistent with the test bench at the design point, the same methodology is applied for the operating point near surge. It is then required to define a numerical operating point for the test bench

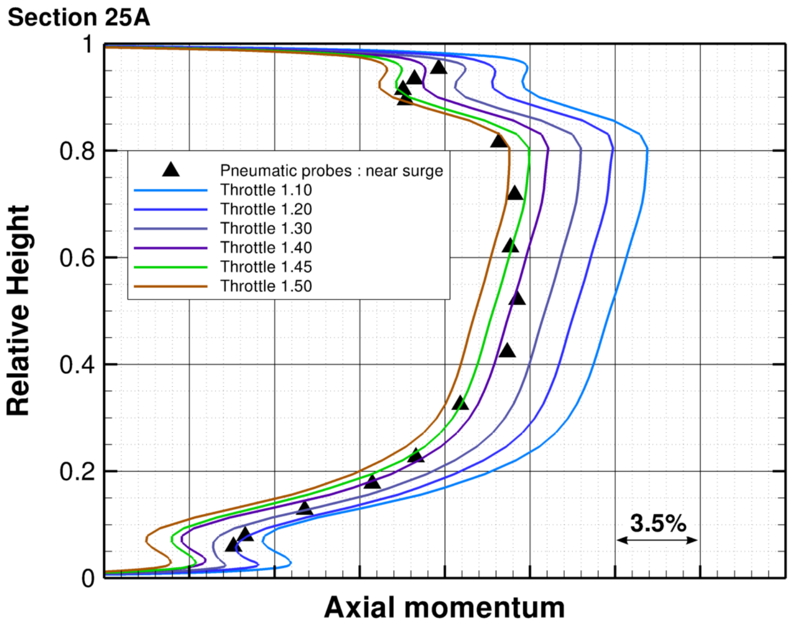

Figure 5.1 — *Radial distribution of time and circumferentially averaged axial momentum at section 25A for different throttle values. RANS computations on the IGV-R1 domain and experimental pressure probes near surge.*

that corresponds to the experimental one.

The domain comprises the Inlet Guide Vane (IGV) and the first rotor of CREATE (R1) and is used for a RANS study to find the inlet and outlet boundary conditions for the computation on the R1 only, like it was done in chapter 3. This RANS computation comprises the same numerical method as well as the same boundary conditions as the one at the design point. For instance, the Spalart-Allmaras turbulence model with curvature correction is used since it revealed to be the most appropriate in the frame of this study. Although the inlet boundary condition for this IGV-R1 computation is the same as for the design point definition, the outlet boundary is modified. Indeed, the classic pivot pressure with the radial equilibrium defined in equation (II-62) is not perfectly adapted for the unstable operating point near the surge. Following the experience on RANS computations at ONERA, the type 4 throttle law, defined in equation (II-63) is applied at the outlet of the domain. A reference massflow and a reference pressure are chosen and fixed. The only varying value is the throttle parameter of the type 4 throttle law: α.

This throttle law is not used in the final ZDES computation, it is only applied in this preliminary RANS study. It is nevertheless important to detail the followed methodology and to explain why it is not retained for the computation on the R1.

Figure 5.1 shows the axial momentum radial distribution at section 25A. Different throttle values are assessed and the resulting axial momentum is compared to the experimental values from steady probes. The chosen operating point corresponds to the throttle 1.45. The reason is that it is in better agreement with the experimental probe values at 90% of relative height, that is to say where the vortex from the IGV is located. Besides, this throttle value leads to an axial momentum similar to the experimental value at mid-span too. The drawback of this point is the underestimation of the axial momentum near the hub. The only throttle value for the outlet boundary condition that matches the probes near the hub is the "throttle 1.2". Nevertheless, this point clearly overestimates the axial momentum from 10% of relative height to the casing. For instance, it captures a value superior by 3.5% to the experimental value where there is the IGV tip vortex. Since the aim of the study is to evaluate the tip clearance flow, the choice favours the better agreement near the casing. This is the reason why the throttle 1.45 is the only relevant

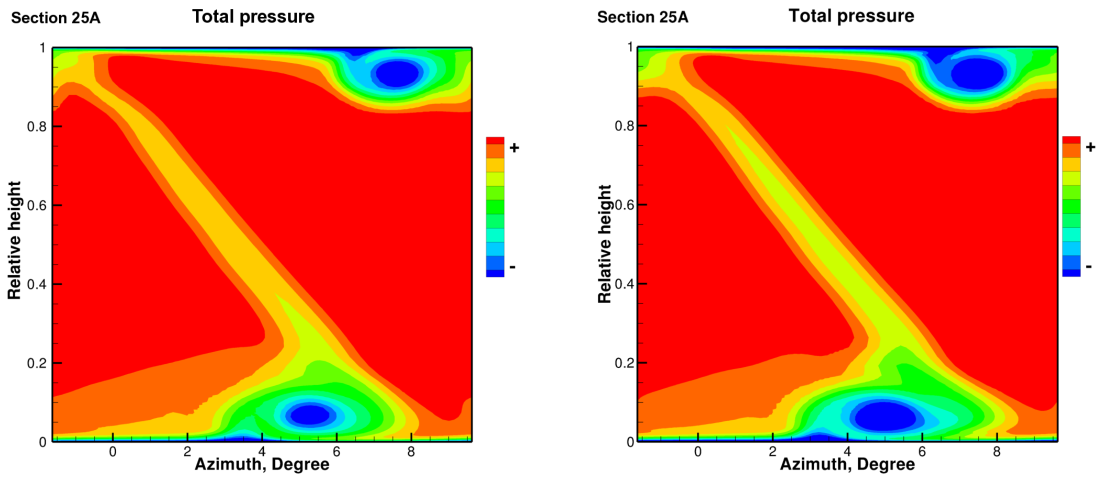

(a) Throttle 1.45. Near surge cartography.

(b) Pivot pressure of 0.93 Pio. Design point cartography.

Figure 5.2 — *Total pressure cartography at section 25A. ZDES computations.*

point for this study and the one retained for the outlet boundary condition.

5.1.2 Inlet cartography definition for the computations on the first rotor near surge

Once the operating point is defined, the flow cartography is extracted at section 25A. The resulting 2D map is then set against the 2D map originating from the design point in the figure 5.2 which shows the total pressure. One can see that the topology of the flows captured is similar between the two operating points. However, the vortices coming from the hub and tip gaps of the IGV are wider at the design point. Besides, they have a lower total pressure in their core. Likewise, the wake is more pronounced at the design point. The azimuthal shift of the tip and hub vortices from the wake position is similar too. That is to say, the vortices development and convection are not drastically changed, despite the change in the axial momentum induced by the change of the operating point.

Notwithstanding these weak differences, it is relevant to use the adapted cartography since the vortex at the tip has changed. This vortex influences the rotor tip-leakage vortex along with the whole flow topology near the casing of the rotor. An insight of this influence was given in chapter 4 and this effect will be further discussed in chapter 6.

5.1.3 Adaptation of the operating point for the computation on the numerical test bench

The same numerical test bench is used for the ZDES computation near surge as the one for the design point. Nonetheless, it is adapted to match the new operating point. Therefore, the unsteady inlet condition known as "rotating distortion" is implemented on the numerical test bench. This time, the rotating distortion is based on the flow cartography near surge previously defined.

The outlet condition is the same type 4 throttle law as the one used for the IGV-R1 preliminary study. The purpose is to be consistent with the methodology followed for the design point. However, the adaptation of the numerical test bench has emphasized a limitation of this throttle law. Indeed, instabilities occur when the type 4 throttle law is used on the numerical test bench defined for this study. It is impossible to achieve a stable operating point, even if the type 4 throttling law was developed originally to avoid instabilities near surge. As far as this issue occurs only with the numerical test bench, which is based on ZDES requirements, and not with the IGV-R1 mesh, the reason seems to be the incompatibility of this boundary with a fine mesh.

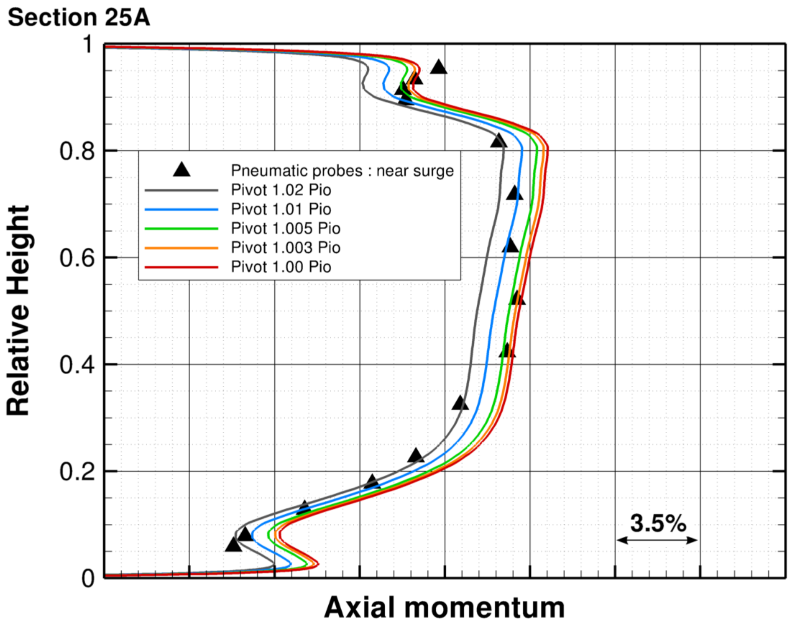

Figure 5.3 — *Radial distribution of time and circumferentially averaged axial momentum at section 25A for different pivot pressure. ZDES computations on the numerical test bench for R1 and experimental pressure probes near surge.*

In order to reach a stable operating point near the surge line, the classic pivot pressure along with the simplified radial equilibrium is tested. Although this boundary condition appears to be not adapted to throttled operating points for RANS studies, it reveals to be suitable in the frame of a ZDES computation. Nevertheless, the operating point has to be defined again with this boundary condition.

First of all, a steady RANS computation is carried out near surge by adapting the pivot pressure. The inlet condition is the "near surge" cartography defined earlier, albeit it is averaged azimuthally like it was done in chapter 3. Once validated with the experimental values, the numerical method is changed to URANS. Moreover, the rotating distortion is implemented with the 2D cartography near surge. When the convergence is sufficiently advanced, that is to say when the global values are stable, the method is changed to ZDES. Then, the final adaptations are performed so that the ZDES computation matches the experimental probe values.

The chosen pivot value is the green line in figure 5.3. It corresponds to a pivot pressure value of 1.005 Pio, with Pio the reference pressure value used in chapter 3. The different radial distributions presented are very close one another due to the small gaps between the pivot pressure value of the order of $1/100^{th}$ of the reference pressure value Pio. A larger range is naturally taken into account in the frame of this study but is not shown here since they are not relevant. In the same way as the choice done in the preliminary study, priority is given here to the value at 90% of relative height which corresponds to the vortex coming from the tip of the IGV. Besides, the 1.005 Pio line is in good agreement with the probes at mid-span.

Convergence is then checked with the same methodology as for the design point: stabilization of mean and root-mean-square static pressure of numerical probes within the flow. Finally, the results over a time range of 21 T are retained for the analysis described thereafter, with T the passage time period of the IGV with respect to the R1.

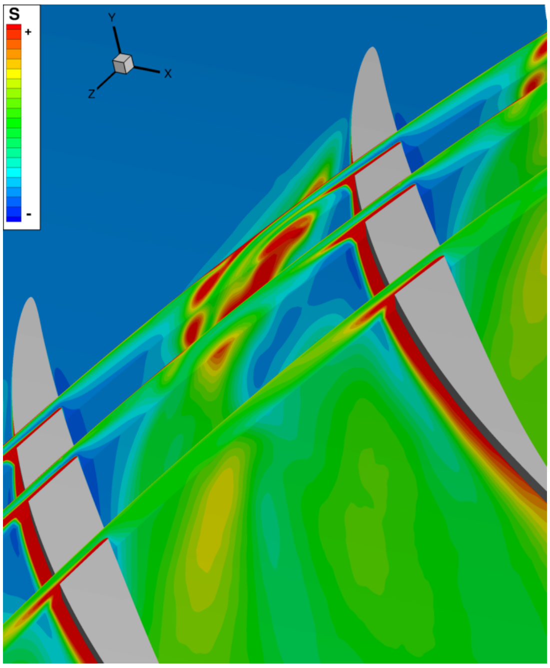

(a) Near surge.

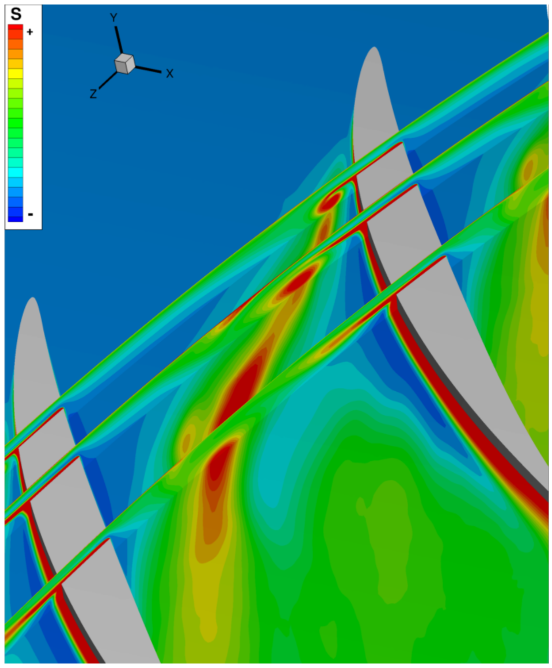

(b) Design point.

Figure 5.4 — *Comparison of the time averaged entropy field for ZDES at two operating points. Entropy planes at 22%, 31% and 46% chord and 98% relative height.*

5.2 Tip-leakage flow visualization

In this section, the flow fields at the two operating points are thoroughly compared and the change in the tip-leakage flow topology discussed.

5.2.1 Time-averaged flow field overview

First of all, the time averaged flow field is presented for the ZDES computations at the design point and near the surge line. Three axial planes at 22, 31 and 46% X/C as well as a plane at 98% of relative height are displayed. The exact position of the axial plane was shown in figure 4.3. Figure 5.4, shows the entropy fields near the casing of the R1 for the two calculations. The high entropy zones highlight the area of high losses[43]. The throttled position, in figure 5.4(a), leads to a widening of the boundary layer developing on the suction side of the blade, even near the leading edge. A widening is found for the whole main tip-leakage vortex too. Actually, the tip-leakage flow topology encountered at the design point exists. Nonetheless, the phenomenon occurs earlier and closer to the leading edge of the blade. This originates from the change in axial momentum for the near surge point. Moreover, there is a deflection toward the adjacent blade of the main tip-leakage vortex along with the whole vortical structures near the casing. Another critical phenomenon is the separation of the boundary layer at the casing. Although such a separation is identified at section 31% X/C for the design point in figure 5.4(b), the separation is already visible at section 22% X/C near surge. Besides, this is massive and leads to a high entropy area going further from the casing wall. However, the high entropy zone related to the tip-leakage flow is localized upstream section 46% X/C, contrary to the design point case.

The normalized helicity, in figure 5.5, shows the intensity as well as the rotating direction of the vortices. This underlines that the main tip-leakage flow is coherent further downstream at the design point. The rotating intensity of the main tip-leakage vortex is concentrated from 10 to 31% X/C near

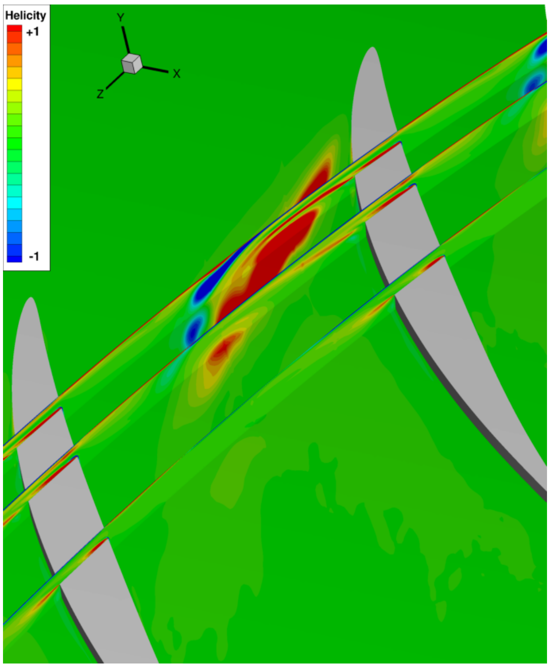

(a) Near surge.

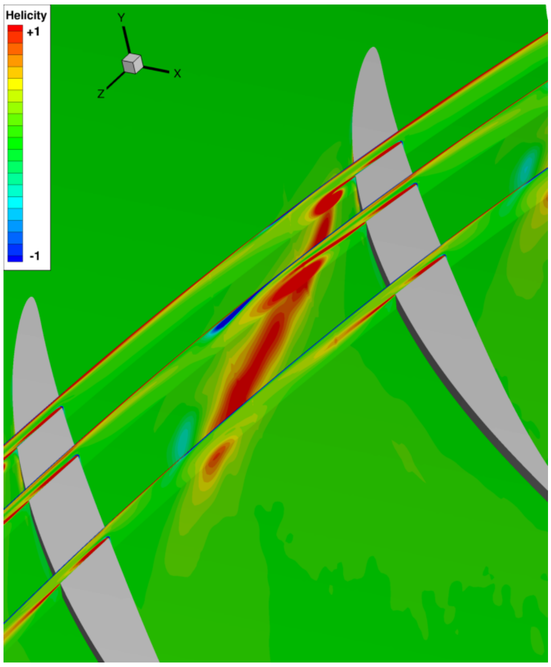

(b) Design point.

Figure 5.5 — *Comparison of the time averaged helicity field for ZDES at two operating points. Normalized helicity planes at 22%, 31% and 46% chord and 98% relative height.*

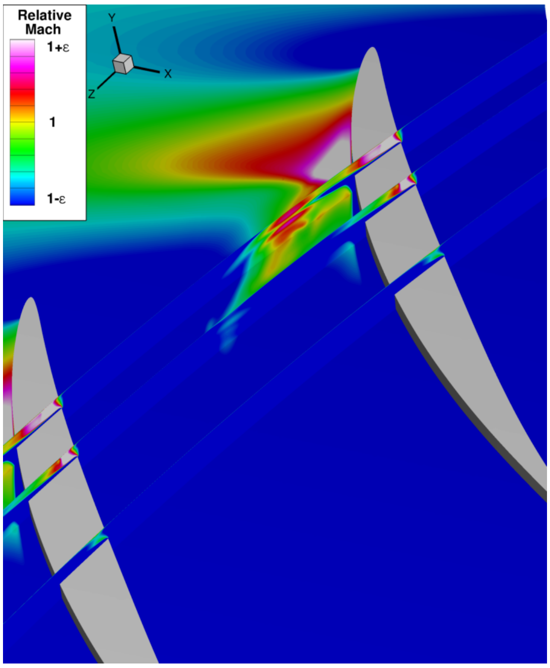

(a) Near surge.

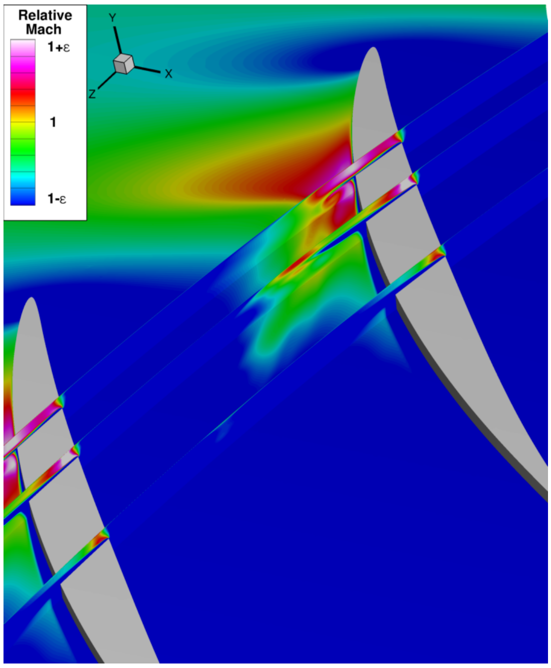

(b) Design point.

Figure 5.6 — *Comparison of the time averaged relative Mach number field for ZDES at two operating points. Relative Mach number planes at 22%, 31% and 46% chord and 98% relative height.*

surge. By contrast, it is still coherent at 46% X/C in figure 5.5(b). Therefore, the tip clearance vortex disrupts earlier at the peak efficiency compared to near surge. Moreover, the counter-rotating induced vortex, in blue in figure 5.5(a) is wider and farther from the casing than at the design operating point.

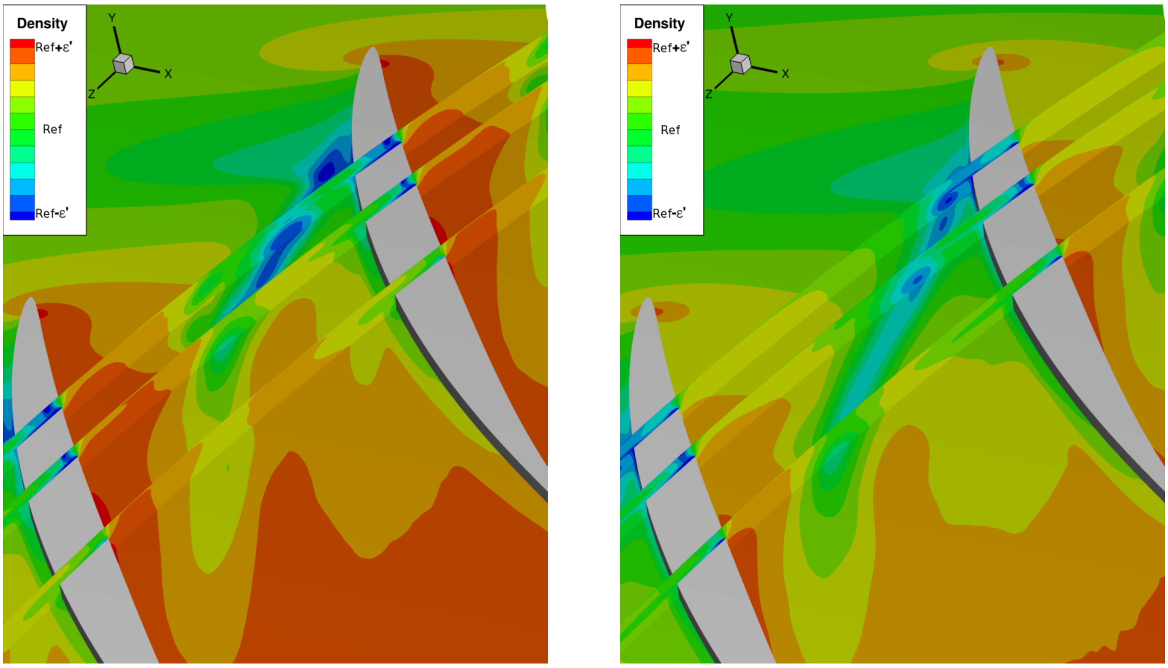

(a) Near surge.

(b) Design point.

Figure 5.7 — *Comparison of the time averaged density field for ZDES at two operating points. Density planes at 22%, 31% and 46% chord and 98% relative height.* $\epsilon' = 29\%$ *of the density reference value.*

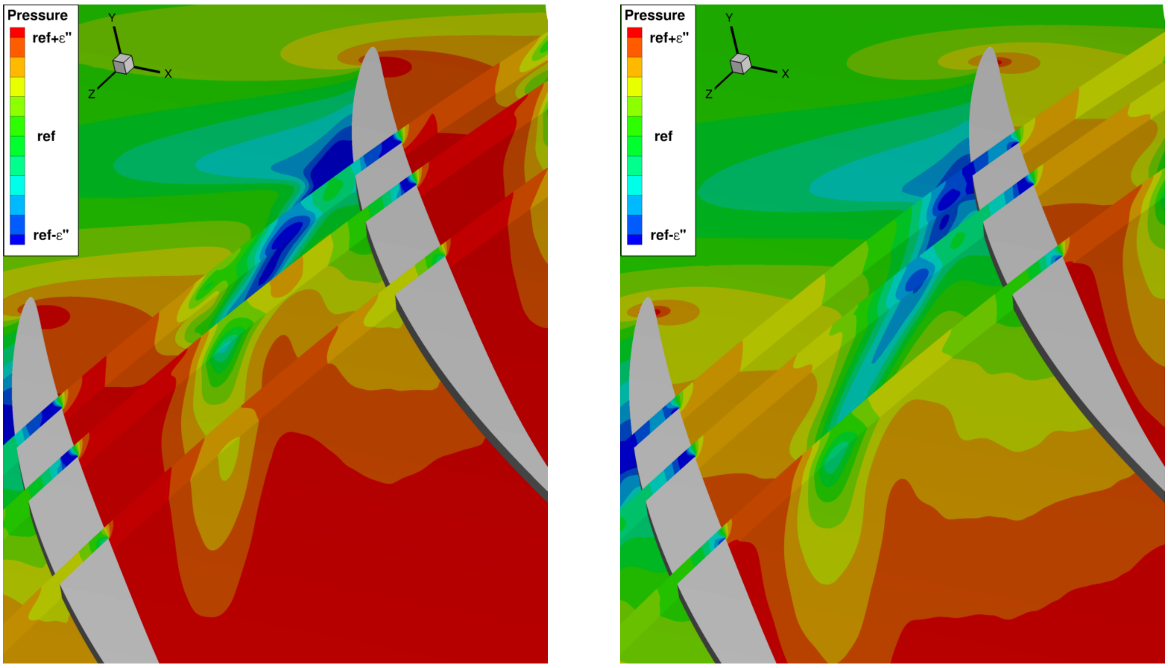

(a) Near surge.

(b) Design point.

Figure 5.8 — *Comparison of the time averaged pressure field for ZDES at two operating points. Pressure planes at 22%, 31% and 46% chord and 98% relative height.* $\epsilon'' = 29\%$ *of the pressure reference value.*

Thereby, this confirms the separation at the casing and the importance of the induced vortex in the boundary layer separation.

The deflection of the tip-leakage flow is easily understood when the velocity triangle are considered.

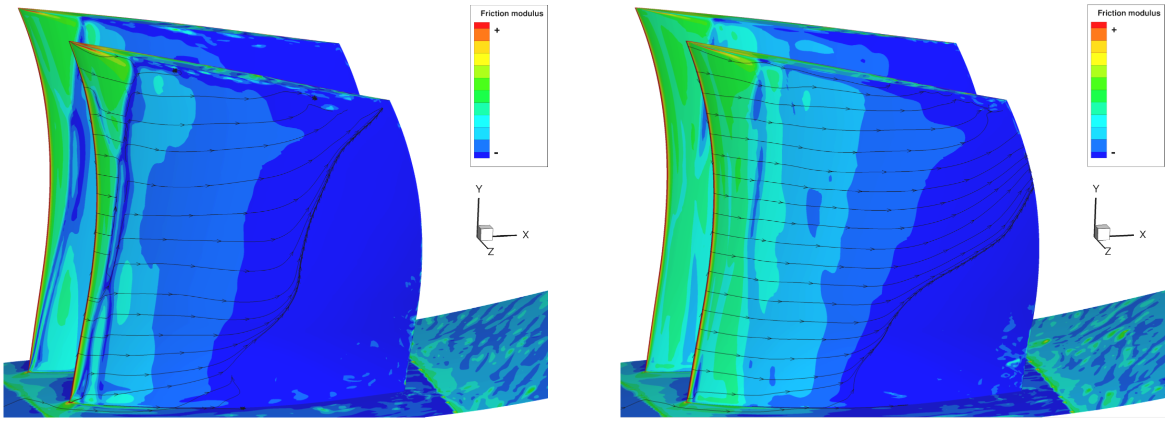

(a) Near surge.

(b) Design point.

Figure 5.9 — *Comparison of the friction lines for the time averaged field for ZDES at two operating points near the hub.*

A decrease of the axial velocity along with the same rotating velocity leads mechanically to an increased angle for the tip-leakage vortex. If the length of the tip-leakage vortex is constant, its disruption occurs earlier axially with a decreased axial velocity. Notwithstanding this effect, there is another phenomenon to be reckoned with: the shock. The analysis of the relative Mach number in figure 5.6 reveals an important difference between the operating points concerning this shock. Indeed, the shock is stronger near surge and the zone of high Mach number is concentrated around the shock which is localized just upstream section 22% X/C. Therefore, it accelerates the vortex disruption. Like the different vortices occurring near the casing, the shock is located closer to the leading edge of the blade near surge. This is coherent with what was observed experimentally by Bergner et al. [9] on a similar configuration.

The effects of the shock are not only visible on the relative Mach number field. Figure 5.7 points out that the drop in the density due to the shock is more important near surge. Although the levels of density are lower near surge at the shock position, near 10% X/C up to just upstream 31% X/C, it must be emphasized that the low density region at 31% X/C, in blue in figure 5.7(b), is not found in figure 5.7(a). Moreover, the density rises again just after section 31%X/C and higher values are found near the trailing edge. In other words, the effects of the shock are localized and centred around its position.

Finally, figure 5.8 corroborates the fact that this is a strong shock compared to the one observed at the design point. Indeed, the gradient is more important near surge. First, there is a rapid decrease of the pressure around 10% X/C with low pressure levels, inferior to the one measured at the same position at the design point. Then, downstream the shock position, there is a rapid rise of the pressure value. Nevertheless, the pressure drop follows the main tip-leakage vortex core, likewise what is noticed with the density.

An interesting effect of the operating point is underscored in figure 5.9, with the skin friction lines [41] and friction modulus at the design point and near the surge line. The area where the friction modulus decreases rapidly near the leading edge is located even closer to this leading edge in the case near surge. The corresponding friction modulus value is inferior too and a distinct line of low friction modulus is emphasized from the tip to the hub of the blade. This line denotes the shock position and its effects throughout the blade height. The friction lines drawn on the suction side of the blade indicate a different behaviour too. The position of the separating line observed at the design point differs. Indeed, it reaches the trailing edge at the tip for the computation near surge. This brings to the fore a massive separation on the suction side for the case near surge. As a consequence, this highlights that the corner effect is amplified near surge. This amplification is however overestimated as already observed for steady RANS computations by Marty et al. [112, 111] and this drawback originates from the Spalart-Allmaras model

upon which the evaluated ZDES method is based.

5.2.2 Flow field snapshots

The effects of the operating point on the flow field are clearly visible when the time averaged fields are regarded, however, it is relevant to observe the consequences on the instantaneous flow field too. Therefore, instantaneous snapshots of the flow near the casing are presented in figure 5.10. Four different times are captured: T/4, 2T/4, 3T/4 and T, from the top figures to the bottom ones. The iso-surfaces of Q criterion [81] are coloured by the normalized helicity [105]. Moreover, the 31% X/C plane is added and filled with the entropy in order to track the arrival of the IGV tip vortex.

First, the deflection of the main tip-leakage flow is confirmed here, as indicated in the figure 5.10(a), even when the IGV tip vortex does not influence the R1 tip-leakage flow angle. Then, in the same figure, the helicity of the main tip-leakage vortex is clearly of a lower level compared to its level in figure 5.10(b). Thereby, the vortex intensity is inferior. As a consequence, it is wider and disturbs earlier in the computation near surge. Secondary tip-leakage vortices are visible in both operating points. They roll-up around the main vortex near surge too. Nonetheless, the stable secondary vortex, indicated in figure 5.10(d) for the design point is located upstream near surge as highlighted in figure 5.10(c). Actually, even without the arrival of the IGV tip vortex, the whole flow topology is shifted toward the leading edge in the near surge case.

Nevertheless, the IGV tip vortex has an influence near surge too. Indeed, the tip-leakage vortex deviates toward the adjacent blade like it is the case at the peak efficiency. Moreover, there is a delay in the arrival of the IGV tip vortex due to the fact that it is wider and thus it is convected at a lower velocity compared to the IGV tip vortex at the design point. This width difference is visible in figure 5.2 and its consequence is detected by comparing figures 5.10(e) and 5.10(f).

Another effect of the change of operating point stems from the shift of the whole vortex topology toward upstream. The phenomena occurring in the tip-leakage flow at the design point are visible upstream. Thereby, the energy transfer from the large eddies to the smaller ones, observed in chapter 4, occurs earlier. This results in a larger amount of visible vortices characterizing the turbulence just upstream plane 31% X/C.

The analysis of the instantaneous entropy planes at a fixed time in figures 5.11 underscores this shift towards upstream for all the phenomena occurring near the casing. In figure 5.11(a), the boundary layer separation is already massive near surge and denoted by a high entropy zone. At this section, this is only the inception of the main tip-leakage vortex roll up. This boundary layer separation occurs only at 31% X/C at the design point. The importance of the boundary layer separation at the casing for the operating point near the surge line confirms the idea of Gourdain and Leboeuf [64] concerning the reasons of the flow blockage near the surge. This major unsteady effect affects the stability of the machine. Besides, at 31% X/C in the near surge case, oscillations are visible in the high entropy zone resulting from the separation of the boundary layer at the blade tip. These oscillations come from unsteady flows arriving in the tip gap, and are only captured at 46% X/C at the design point, as shown in figure 5.11(f). These unsteady phenomena make the boundary layer developing on the casing even more unstable and subject to separation.

However, near the trailing edge, the flow topology between the blades is similar for the two simulated operating points. There is a wide spread area of important entropy throughout the channel. Nevertheless, the high entropy in the boundary layer of the suction side of the blade, experienced in 5.11(h), is missing near surge in figure 5.11(g). Indeed, as it was shown earlier in figure 5.9(a), the predominance of the corner effect near surge leads to a separation of the boundary layer near the trailing edge from the hub to the tip of the blade. By contrast, this separation occurs only up to mid-span for the design point. Finally, the azimuthal shift between the IGV tip vortices for the two operating points, observed previously

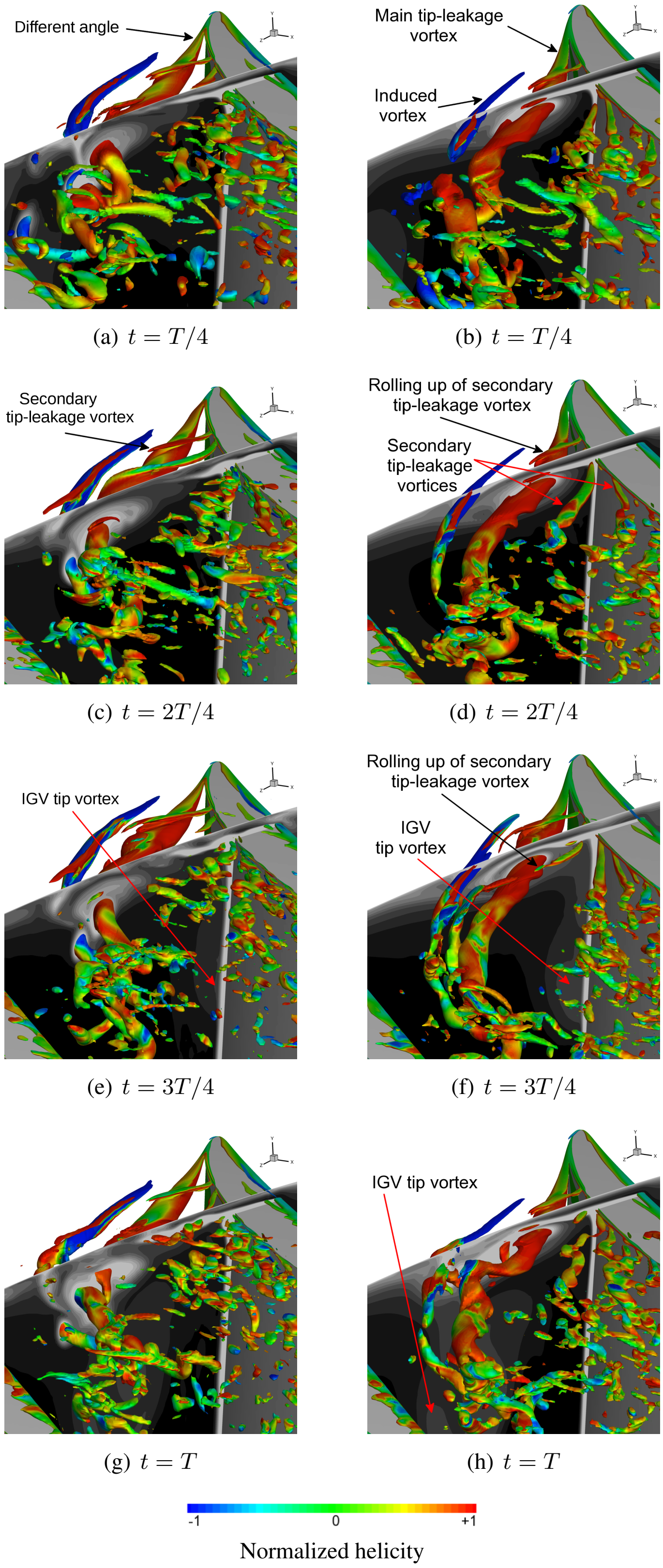

Figure 5.10 — *Snapshots of Q criterion iso-surface coloured by the normalized helicity and section 31% X/C filled with the entropy (left: ZDES near surge, right: ZDES at design point.).*

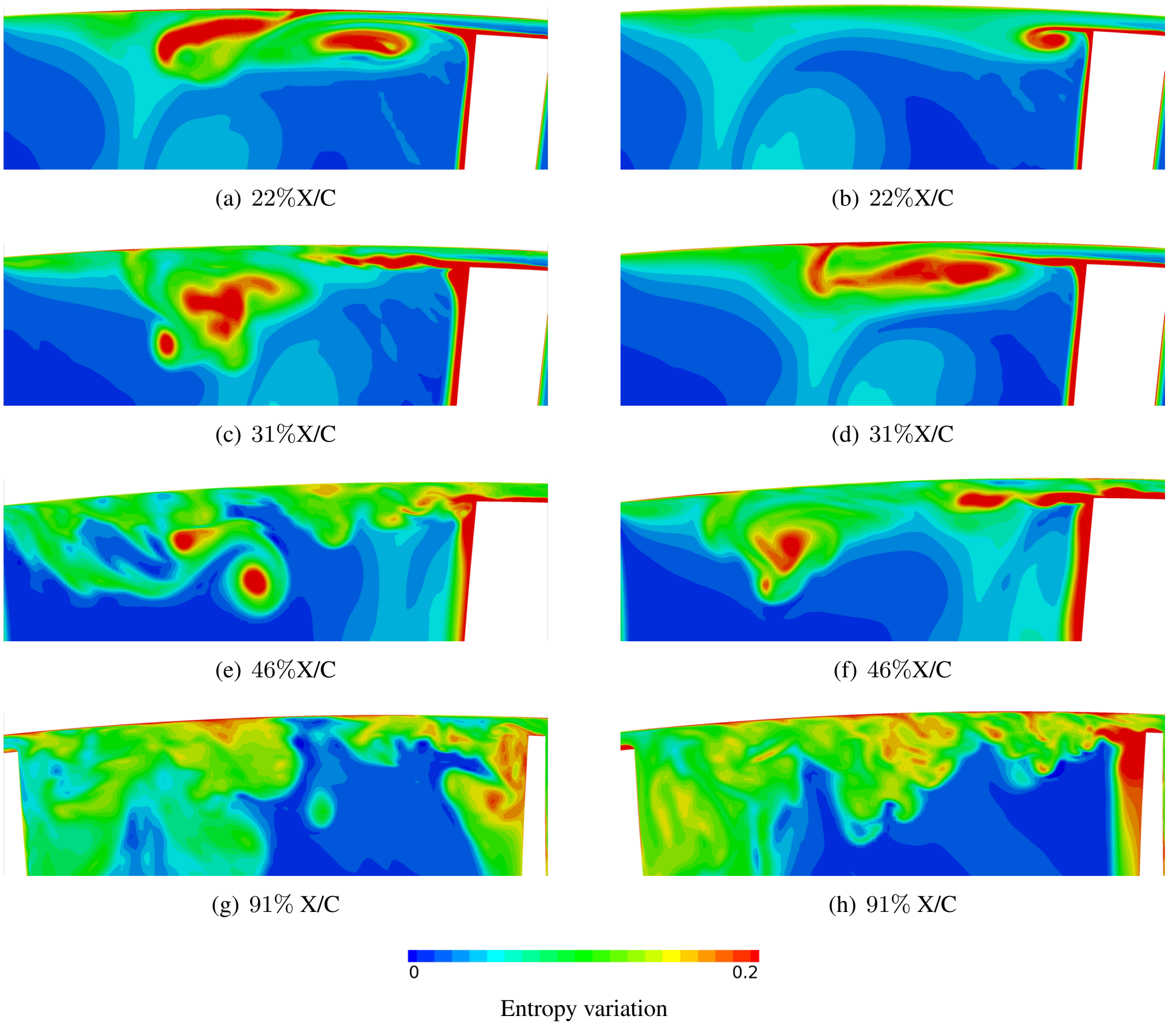

(a) 22%X/C (b) 22%X/C

(c) 31%X/C (d) 31%X/C

(e) 46%X/C (f) 46%X/C

(g) 91% X/C (h) 91% X/C

Figure 5.11 — *Entropy planes for four different axial positions at t=3T/4 (left: ZDES near surge, right: ZDES at design point.).*

with the Q criterion figures, is clearly discernible here by comparing figures 5.11(c) and 5.11(d). This only affects the moment when the IGV tip vortex arrives on the R1 and stretches the tip-leakage vortex azimuthally.

In the next sections, the modifications of the tip-leakage flow when the operating point is close to the surge line will be further discussed with the help of measurements taken on the experimental test bench.

5.3 Effects on performance and 1D distributions

5.3.1 Global values

The first comparison with the experimental data to conduct concerns the global values. The normalized mass flow at section 25A as well as the normalized total pressure ratio between sections 25A and 26A are evaluated for the experiments and the computations. Even if some of the experimental values are missing near the hub and the tip because of the measurement process with the probes, as explained in chapter 4, these global values give an idea of the behaviour of the R1 when the turbomachine gets closer to the surge line. The numerical results along with the experimental ones are summarized in the table

Case	Normalized mass flow	Normalized R1 total pressure ratio
Pneumatic probes - design point	1.000	1.000
Pneumatic probes - near surge	0.927	1.006
ZDES - design point	1.014	0.992
ZDES - near surge	0.948	1.020

Table 5.1 — *Mass flow and total pressure ratio for ZDES at design point and near surge, normalized with the values from the pneumatic probes data at design point.*

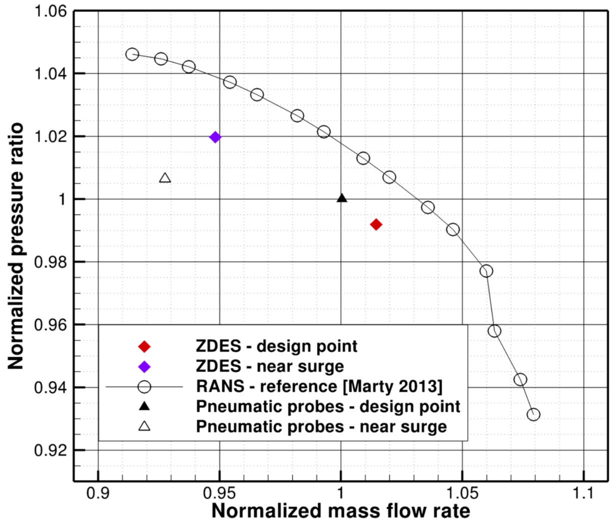

Figure 5.12 — *Pressure ratio versus mass flow rate for ZDES at design point and near surge, normalized with pneumatic probes data at design point.*

5.1. For an easier comparison, they are plotted in figure 5.12 along with the reference computation in RANS from Marty et al. [113]. Details for this reference case are given in chapter 4.

First of all, it must be emphasized that the ZDES underestimates the pressure ratio when it is compared to the reference RANS computations. Therefore, the trend observed in the previous chapter is kept near surge. Nevertheless, and contrary to how it behaves at the design point, the ZDES computation overestimates the pressure ratio compared to experiments. If a line is drawn between the two ZDES computations and the two experimental values, one can distinguish that the slope for the ZDES computations is steeper. However, this slope is similar to the one observed for the reference case, in RANS. Thereby, the same advantage and drawbacks are observed in ZDES as in RANS for this part of the operating line. Notwithstanding the similarity concerning the slopes between the computations, the values are in better agreement in ZDES. This is due to a better capture of the pressure ratio. Moreover, there is still an overestimation by about 2% of the mass flow rate in ZDES near surge, as it is for the design point. This overestimation occurs in spite of the preliminary studies carried out on the IGV-R1 configurations at the design point and near surge that underlined a good agreement of the numerical radial distribution of axial momentum with the probe values at section 25A. This confirms the necessity to rely on radial distributions and not only on global values to choose the appropriate operating point when computations are compared to experiments.

5.3.2 Radial distribution

The radial distributions of different values are plotted at section 26A, which is located downstream R1. Thereby, the phenomena occurring on the blade influence directly these distributions and can be

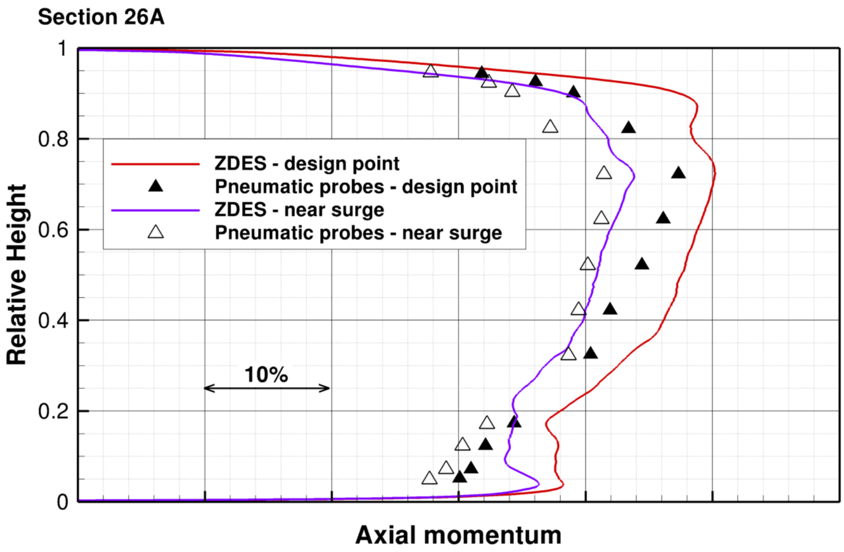

Figure 5.13 — *Radial distribution of time and circumferentially averaged axial momentum at section 26A for ZDES at design point and near surge.*

highlighted.

First of all, the axial momentum is shown in figure 5.13. Even if the choice of the numerical operating points is done through the adaptation of the outlet condition so that the axial momentum is in good agreement with the experimental values upstream the blade, there are major differences downstream the R1. The discrepancy between the two operating points reaches 6% for the computations from 40% to 90% of relative height. By comparison, it is clearly inferior between the two experimental measurements. Nonetheless, experimentally, the zones with the maximum of discrepancy are located at the same radial positions as for the computations. The effect of the flow passing through the blade leads to an overestimation of the axial momentum throughout the radius, in both computations. This amounts up to 3% near the casing near surge, and even 5% at the design point. Moreover, for both calculations, there is a similar overestimation by 5% near the hub.

The ZDES case at the peak efficiency experiences a local deficit at 80% of relative height. This deficit does not exist near surge. In other words, the influence of the tip-leakage vortex on the main flow is decreased near surge at this section. The fact that this deficit is not experienced by the probes confirms what was hypothesized in chapter 4. Indeed, this originates from the choice of the operating point. Although some values from the ZDES near surge are in good agreement with the corresponding experimental measurements, the overall overestimation leads to a ZDES operating point which lies between the two experimental operating points, at least at this axial position.

The total pressure distribution is presented in figure 5.14. For the design point, the steady probe values are plotted along with averaged values from unsteady probes. The symbols for the unsteady probes comprises the interval with the measurement uncertainties. For the near surge point, the steady pressure values are added. First of all, the discrepancy between the values corresponding to the two operating points is different numerically and experimentally. Between the two operating points, in the experiment, there is almost no difference of pressure near the casing. The gap is nonetheless increased to 2% only near the hub. Conversely, there is up to 3% difference between the ZDES computations for the total pressure. This difference is evenly found for the whole radial range, except near the tip. Indeed, at the casing, the gap between the operating points is reduced due to the important gradient between 90% of relative height and the casing wall. However, at these radii the discrepancy is still between 2 and 3%. As a result, one can say that the change in the operating point can be regarded as homogeneous for the computations contrary to what is measured.

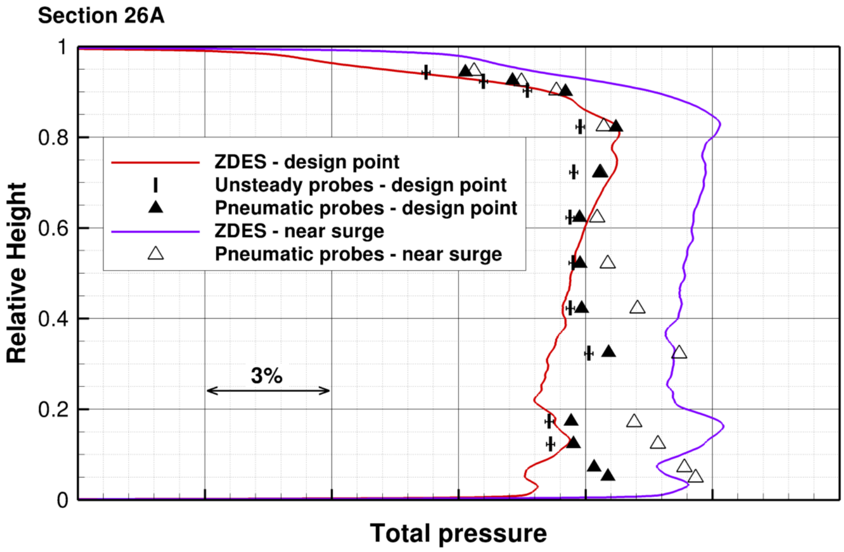

Figure 5.14 — *Radial distribution of time and circumferentially averaged total pressure at section 26A for ZDES at design point and near surge.*

The local overpressure at 10% of relative height experienced at the design point is increased for the point near surge. Besides, it is located further from the hub, at 15% of the span. This denotes an amplified phenomenon near surge which corresponds to the corner effect. This local increase is met experimentally, but at an even greater radius: 30% of relative height.

The analysis of the total temperature radial distribution confirms what is hypothesized in chapter 4. The normalized total temperature, $Cp\Delta Tt/U^2$, or loading coefficient, is plotted in figure 5.15. The underestimation of the total temperature is even in ZDES, compared to the URANS approach. Therefore, the fact that the ZDES underestimates the experimental values at the design point compared to the URANS method originates from an error in the operating point definition for the ZDES. As a consequence, the capability of the ZDES approach is highlighted by comparing the two operating points. Actually, the experimental operating point near surge does not correspond exactly to the one computed. This is the same for the design point. Nevertheless, by changing the outlet boundary condition, that is to say, by changing the outlet pressure, it is possible to be in better agreement with the experimental measurements. The gradient at the tip is correctly captured by the computation near surge. However, some values correspond to the pneumatic probes measurements for the design point and not for the near surge point, for instance, at around 40% of relative height. The overestimation of the total pressure at 15% of relative height, observed in figure 5.14 coincides with a similar overestimation of total temperature observed in figure 5.15 near surge. This phenomenon was less manifest at the design point. This corner effect is then clearly amplified near surge. This strengthens what is observed on the skin friction lines in figure 5.9.

The corner effect results in an increased azimuthal angle around 15% of relative height, as revealed in figure 5.16. Contrary to what is observed with the axial momentum, in figure 5.13, the experimental values are in between the ZDES computation at the design point and the one near surge. Therefore, the choice of the operating point definition with the help of the radial definition of axial momentum is relevant, since it is impossible to be in perfect agreement with all the experimental values at the same time.

Another effect to consider is the underestimation of the azimuthal angle around 90% of relative height, shown in figure 5.16. Even if this exists at the design point, it is almost invisible near surge for the ZDES. The measurements only capture a light deflection at this height but no clear underestimation. Thereby, this corroborates the difference of operating point between the experimental and the numerical

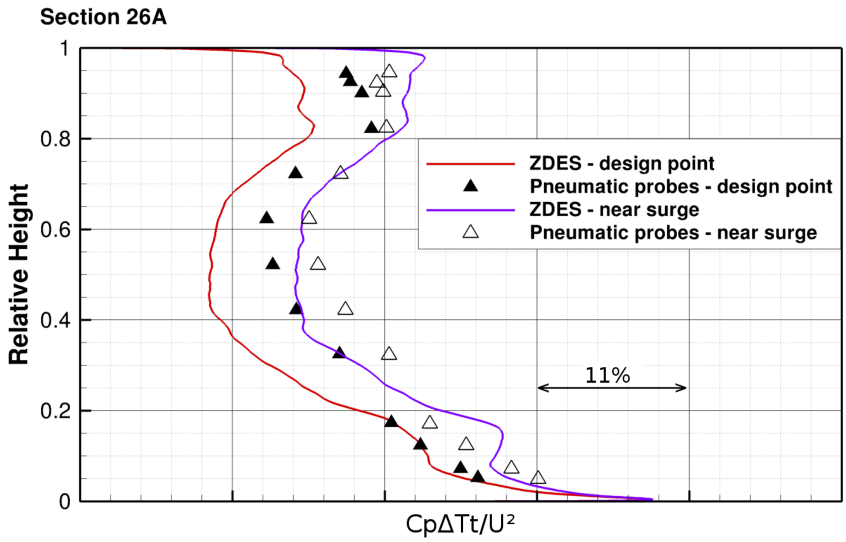

Figure 5.15 — *Radial distribution of time and circumferentially averaged normalized total temperature at section 26A for ZDES at design point and near surge.*

cases at the design point.

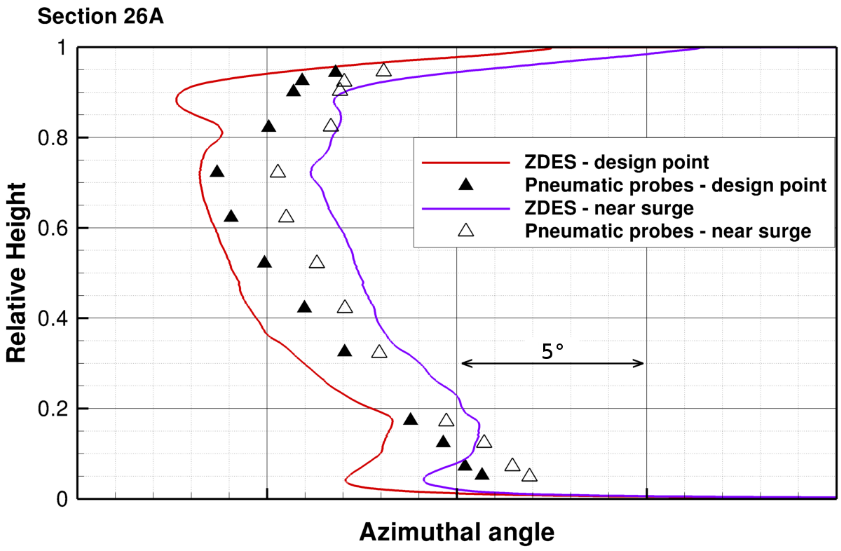

Figure 5.16 — *Radial distribution of time and circumferentially averaged azimuthal angle at section 26A for ZDES at design point and near surge.*

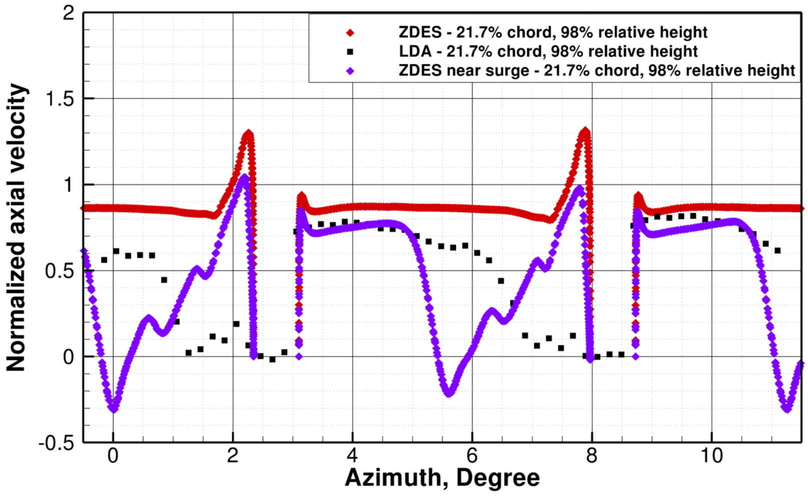

(a) Axial.

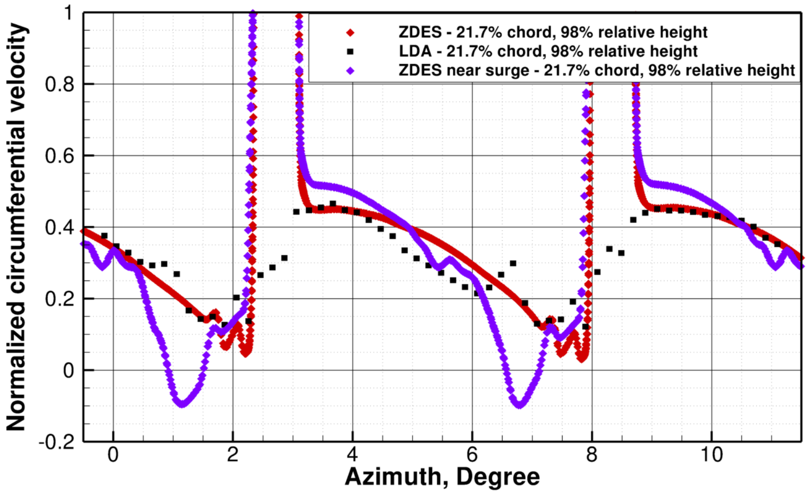

(b) Circumferential.

Figure 5.17 — *Axial and circumferential velocities at 21.7% chord and 98% relative height for ZDES at design point, ZDES near surge and LDA measurements at design point.*

5.3.3 Azimuthal distribution of time averaged velocities

After the visualization of the radial distributions at 26A, the azimuthal distributions of axial and circumferential velocities are taken into account in between two blades of the R1. The purpose is to understand, with the help of the ZDES computation near surge, how the tip-leakage flow behaves when it gets closer to the surge line.

Figure 5.17(a) shows the axial velocity at position 21.7% X/C and 98% of relative height for the two ZDES computations and the experimental values at the design operating point. First of all, the levels of axial velocity are lower near surge. This is expected due to the change of operating point. However, this causes that this new level is in better agreement with the LDA measurements at the design point, at least for a part of the azimuthal range, from azimuth 3 to 5. This confirms what was shown previously in figure 5.13 for the radial distribution of axial momentum at section 26A: the ZDES operating point near surge is close in some aspects to the experimental case at peak efficiency.

The drop in axial velocity near the blade at azimuth 7-8 and encountered in the experiment only for the design point, is visible near the surge in ZDES. This confirms that the position and even presence of this phenomenon is linked to the operating point choice. Indeed, it was not observed, in figure 4.20(a), for the computations regarded as being at the design point because their operating point is not exactly the one of the experiment. This difference can explain that the position of the axial velocity minimum is located at azimuth 5.5 for the ZDES computation near surge whilst it is above azimuth 7 up to the blade position experimentally at the design point. This is coherent with the fact that the numerical operating point near surge for the ZDES is more throttled than the experimental design point as observed in figure 5.14, even if it presents some similarities as explained previously with the radial distributions. Besides, this minimum of axial velocity corresponds actually to an inversion of the flow numerically. This denotes the inception of the whole flow inversion characterising the surge. However, the LDA values are only given for the design point at this position and one can not be sure that this occurs experimentally near surge. The azimuthal position of this phenomenon reveals that it is directly linked to the separation of the boundary layer at the casing underlined previously and clearly visible in figures 5.5(a) and 5.11(a). This separation roots from the momentum deficit of the tip-leakage flow, and generates the induced vortex. A similar separation is captured at the design point with the ZDES method. This one rolls up into the induced vortex pointed in figure 5.10(b). Nevertheless, this separation is located downstream, around 31% X/C and does not lead to such a flow inversion.

The circumferential velocity, plotted in figure 5.17(b), has higher levels near the blade near surge, at azimuth 3-3.5, and lower on the other side of the passage. The local inversion of the axial velocity observed at azimuth 5.5 in figure 5.17(a) corresponds to a small local fluctuation in the circumferential velocity value. The main difference is witnessed around azimuth 7, that is to say near the blade. The value decreases rapidly and then there is an inversion of the circumferential velocity too. By contrast, the value at the design point stays always positive, albeit close to 0. This is both a side effect of the shock, since it is located just upstream this axial position, and directly linked to the tip-leakage vortex. Therefore, this denotes the impact of the interaction between the main tip-leakage vortex and the shock on the flow structure, and its consequences that may lead to the surge.

One will now see how the tip-leakage flow develops downstream. First, the azimuthal distributions of the axial velocities at 44.8% X/C and 94% of relative height are plotted in figure 5.18(a). Once more, the levels for the axial velocity of the ZDES near surge are in good agreement with the LDA measurements at the design point. The values are nonetheless lower. This means that a ZDES computation with an outlet pressure in between the ones for the two presented ZDES calculations could be in better agreement with these LDA measurements.

Notwithstanding the capability of the method to capture the tip-leakage vortex velocity level, one can see that there is always a difference between the two channels. As explained in chapter 4, the numerous simplifications done for the numerical test bench prevent the ZDES method, as well as the other tested methods, from capturing this difference. Therefore, this is not a limitation of the method but a limitation of the test case that does not take into account the first stator (S1) downstream, the support struts upstream the Inlet Guide Vane (IGV), and other technological effects existing on the real machine.

Even if the axial velocities are in good agreement between the experimental values at the design point from the LDA measurements, the operating point difference is mainly visible when the circumferential velocity is considered, as presented in figure 5.18(b). The discrepancy is amplified here compared to near the leading edge. Two opposite effects have to be underlined. On the one hand, the levels of the LDA circumferential velocity are close to the ones captured by the ZDES at the design point. On the other hand, the azimuthal position of the tip-leakage vortex experienced by the LDA corresponds to the position seen by the ZDES near surge. Thereby, none of the ZDES computations presented reflect exactly the tip-leakage vortex development. As a consequence, an adaptation of the numerical operating point would not improve drastically the results for the circumferential velocities, albeit a compromise between close levels along with an approximated position could be found.

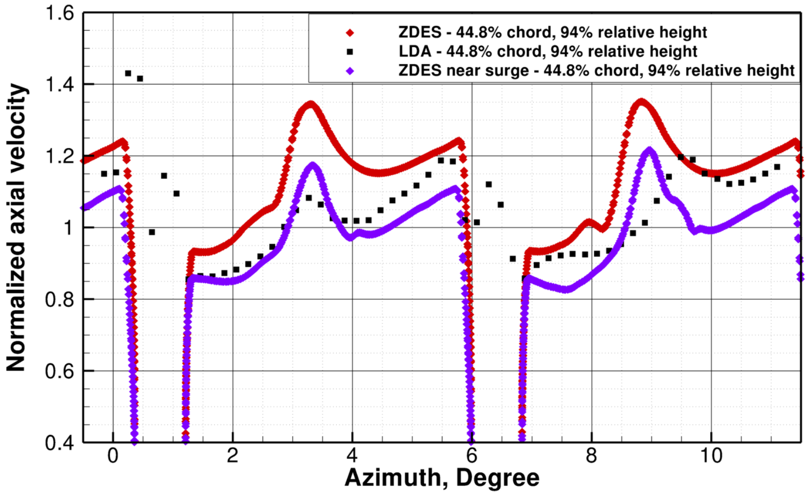

(a) Axial.

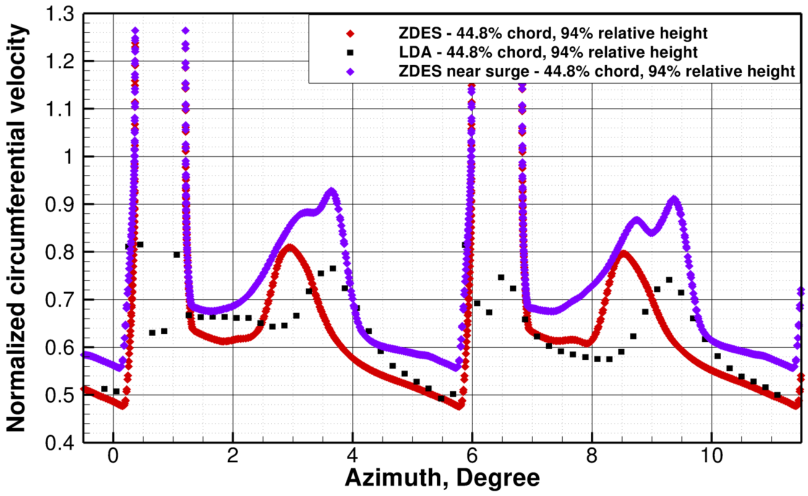

(b) Circumferential.

Figure 5.18 — *Axial and circumferential velocities at 44.8% chord and 94% relative height for ZDES at design point, ZDES near surge and LDA measurements at design point.*

Near from the trailing edge of the blade, at 91% X/C and 90% of relative height, the tip-leakage vortex widens near surge as highlighted in figure 5.19(a) for the axial velocity. The local minimum axial velocity corresponds to azimuth 5.5 for the ZDES at the design point and azimuth 6.5 near surge. By comparison, the LDA measurements experience this minimum at azimuth 6. Besides, it is important to emphasize that the azimuthal span is correctly captured by the ZDES. Therefore, the trend captured in ZDES for the velocity levels and the azimuthal position of the tip-leakage vortex is relevant and in good agreement with the LDA measurements.

The circumferential velocity at this position is shown in figure 5.19(b), and highlights two main effects of the operating point near surge.

The first one is the fact that contrary to what is observed in figure 5.18(b) at 44.8% X/C, the effects of the tip-leakage vortex on the circumferential velocity are invisible for the ZDES near surge. By contrast, a local increase is captured by the ZDES at the design point at azimuth 5.5, and measured by the LDA at azimuth 6. Therefore, the tip-leakage vortex seems almost dissipated near surge at this position if the

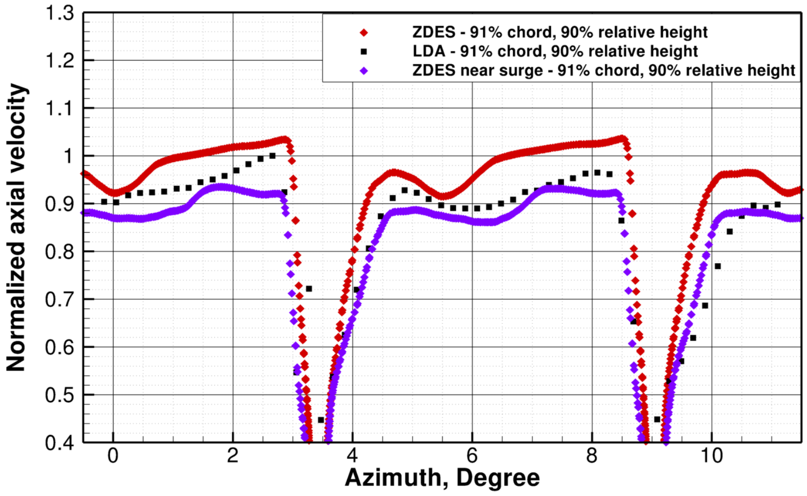

(a) Axial.

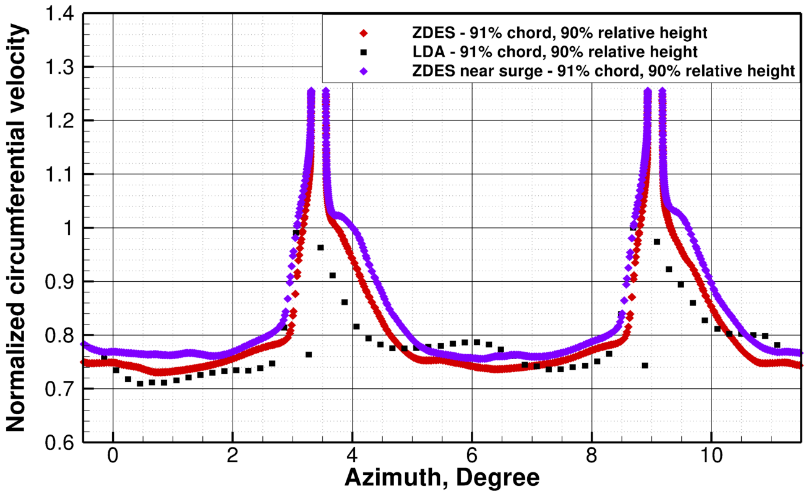

(b) Circumferential.

Figure 5.19 — *Axial and circumferential velocities at 91% chord and 90% relative height for ZDES at design point, ZDES near surge and LDA measurements at design point.*

circumferential velocity is considered only. Indeed, the footprint of the tip-leakage vortex is mainly seen with the axial velocity at this position.

The second phenomenon to be reckoned with is the local increase in the circumferential velocity near the blade at azimuth 4. This is the characteristic of an increased double leakage, and will be more clearly identified in chapter 6. The tip-leakage flow of one blade reaches the adjacent blade and passes through its tip gap which leads to what is called double leakage. Near the surge, the clearance flow bends toward the adjacent blade and reaches it more upstream compared to the design operating point. As a result, it amplifies the double leakage.

The final position assessed is section 26A, where LDA measurements are available at the design point and near surge. The azimuthal distribution of axial velocity is plotted in figure 5.20(a). First of all, one can see that the measurements capture only a small discrepancy inferior to 5% for the axial velocities between the two operating points. By contrast, with the ZDES method, the values near surge are 10% lower than at the design point. Nonetheless, the difference between the two experimental operating

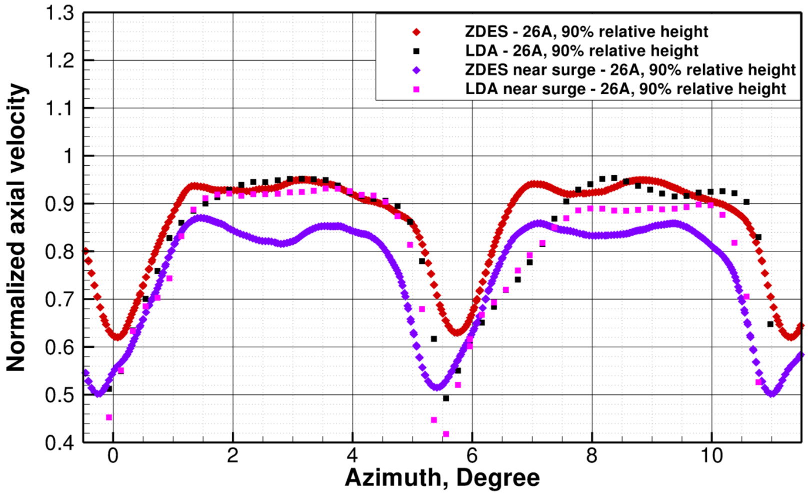

(a) Axial.

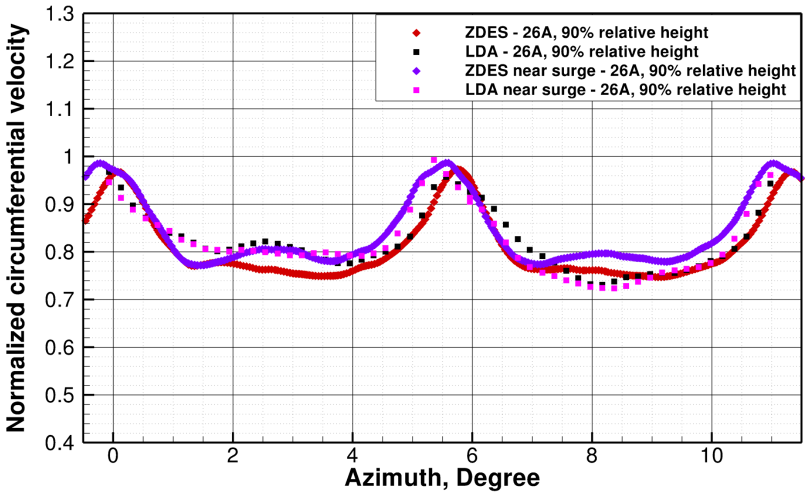

(b) Circumferential.

Figure 5.20 — *Axial and circumferential velocities at section 26A and 90% relative height for ZDES at design point, ZDES near surge and LDA measurements both at design point and near surge.*

points changes depending on the considered channel. Indeed, the ZDES results are in better agreement with the LDA measurements in the channel located from azimuth 5.5 to 11 than in the one located from azimuth 0 to 5. The R1 wake positions are not localized at the same azimuthal positions between the ZDES computations whereas they are at the same azimuth for the two axial velocity distributions from the experimental operating points. On the one hand, the levels for the ZDES at the design point are in good agreement with the experimental values, however the wake positions and width are erroneous. On the other hand, the wake positions and width are more accurately simulated with the ZDES near surge, nevertheless, the velocity levels are underestimated. These effects are similar to the ones observed at 44.8%X/C in figure 5.18(b) for the circumferential velocity. This strengthens the issue concerning the definition of an appropriate operating point when computations are set against experimental values.

Finally, the circumferential velocity at section 26A is plotted in figure 5.20(b). The levels are similar within the compared computations and experiments. The only difference between the two LDA measurements comes from a shift by about 0.3 degrees in the position of the wakes. Nonetheless, the

high circumferential velocity areas corresponding to the wakes are accurately located by both ZDES methods. Indeed, the width and the position of the wake is correctly located at around azimuth 5.3 near surge and 5.6 at the design point for both the LDA and the measurements. Nevertheless, the ZDES near surge is more accurate for the capture of the wake width than the ZDES at the design point. The values around azimuth 2.5, which correspond to the tip-leakage vortex, are in better agreement with the LDA for the ZDES near surge. In the other channel, around azimuth 8, the LDA measurements does not see the tip-leakage vortex contrary to the computations. This is linked to the aforementioned non-periodicity of the real test bench.

5.3.4 Azimuthal distribution of the velocity standard deviations

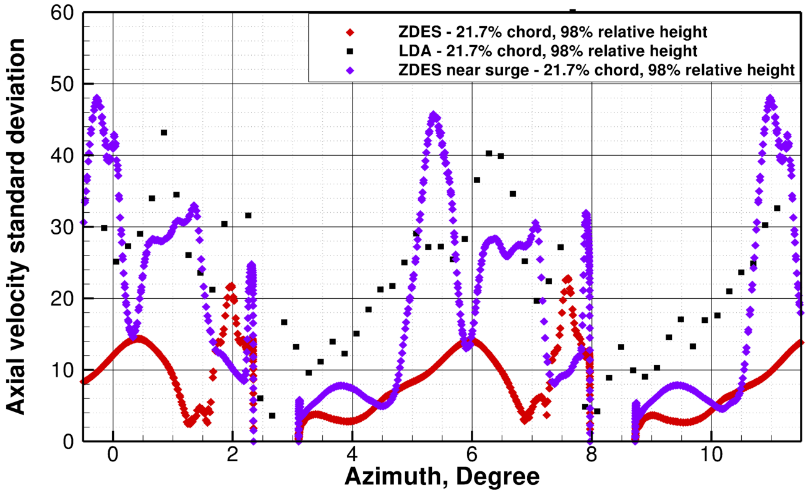

(a) Axial.

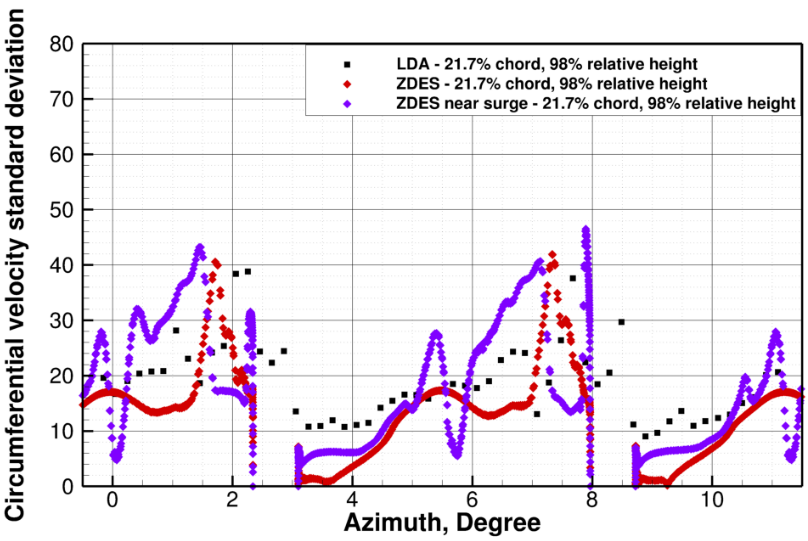

(b) Circumferential.

Figure 5.21 — *Axial and circumferential velocity standard deviations [in $m.s^{-1}$] at 21.7% chord and 98% relative height for ZDES at design point, ZDES near surge and LDA measurements at design point.*

In order to understand the evolution of unsteady phenomena near surge, the standard deviation of the velocities is analysed hereinbelow.

First of all, the axial velocity standard deviation is plotted near the leading edge, at 21.7% X/C and 98% of relative height in figure 5.21(a). The levels measured by the LDA at the design point reach $40m.s^{-1}$. As it was underscored in chapter 4, the ZDES values are twice as small as the experimental ones. Nevertheless, the ZDES computation near surge captures high levels up to $48m.s^{-1}$ and thus it is in better agreement with the measurements. This confirms that the low levels experienced by the ZDES at the design point originate only from a difference in the operating point. Despite the similar levels between the LDA and the ZDES, the azimuthal positions of the captured phenomena differ. Indeed, the maximum is located at azimuth 6.5 experimentally while it is at azimuth 5.3 for the ZDES near surge. That is to say, with the ZDES near surge, it is further from the blade located at azimuth 8. This maximum of axial unsteadiness corresponds to the flow inversion highlighted by figure 4.20(a). More accurately, this is the separation of the boundary layer developing on the shroud. The high unsteadiness level means that this flow is unstable axially. Besides, the area from azimuth 5.3 up to the azimuth 8, where there is the blade, has important levels of unsteadiness, leading to the boundary layer separation. This confirms what was hypothesised when the figure 5.11(a) was analysed. This unsteady flow has an unstable axial position, hence its influence on the instabilities leading to the surge.

The circumferential velocity is plotted for the same position in figure 5.21(b). It reveals that the unsteadiness linked to the boundary layer separation at the casing is important in the azimuthal direction too. The same topology is found for the circumferential values as for the axial values. Indeed, there is a peak around azimuth 5.3 preceded by a sudden drop in the unsteadiness at azimuth 5.7. This area corresponds to the flow inversion observed for the axial velocity in figure 5.17(a).

In summary, the LDA seems to capture a phenomenon which comprises mainly axial unsteadiness while the ZDES near surge experiences high levels of unsteadiness in both axial and azimuthal directions. The ZDES near surge corresponds to an operating point that is more throttled than the design point measured with the LDA, albeit some values correspond at some radial positions as explained previously. Moreover, the ZDES at the design point captures the same unsteadiness levels in the azimuthal direction as the LDA measurements for this phenomenon. Thereby, the separation on the casing seems to be amplified in two steps near the surge line. First, the unsteadiness is mainly axial. Second, the azimuthal unsteadiness is added to the axial one.

The analysis of the flow further downstream brings information on the development of the tip-leakage vortex. The axial velocity standard deviation at 44.8% X/C and 94% of relative height is shown in figure 5.22(a). Near the surge, the levels of axial unsteadiness of the tip-leakage vortex increase and it spreads azimuthally. Indeed, the zone of high unsteadiness widens. This proves that the topology of the tip-leakage vortex is at a more advanced stage of development than at the design point. Besides, the azimuthal position for the maximum of axial unsteadiness coincides with the experimental position at the design point. Notwithstanding this good agreement, the numerical levels are higher by $15m.s^{-1}$ and peaks at $46m.s^{-1}$. Closer to the blade, from azimuth 4, the standard deviation levels drop rapidly to $10m.s^{-1}$ experimentally at the design point. This is twice as much as the ZDES levels there. Furthermore, the ZDES at the design point has its value decrease to $2m.s^{-1}$, which is five times lower than the experimental value for the same operating point. In other words, the ZDES unsteadiness levels are higher than the LDA measurements in areas with unsteady phenomena only.

The same conclusion can be drawn on the basis of the circumferential velocity standard deviation in figure 5.22(b). Indeed, the levels are higher numerically except close to the blade where the level forms a plateau, which denotes a uniform unsteadiness due to the secondary vortices and the related turbulence. The position for the tip-leakage vortex is in better agreement with the LDA measurements at the design point for the ZDES near surge. This strengthens the issue concerning the choice of the operating point.

A phenomenon is only visible with the ZDES near the surge. It consists in a double peak for the circumferential velocity whereas only one peak is experienced by the ZDES method as well as the LDA at the design point. This second zone, which is noticeable in figure 5.22(a) too, corresponds to the

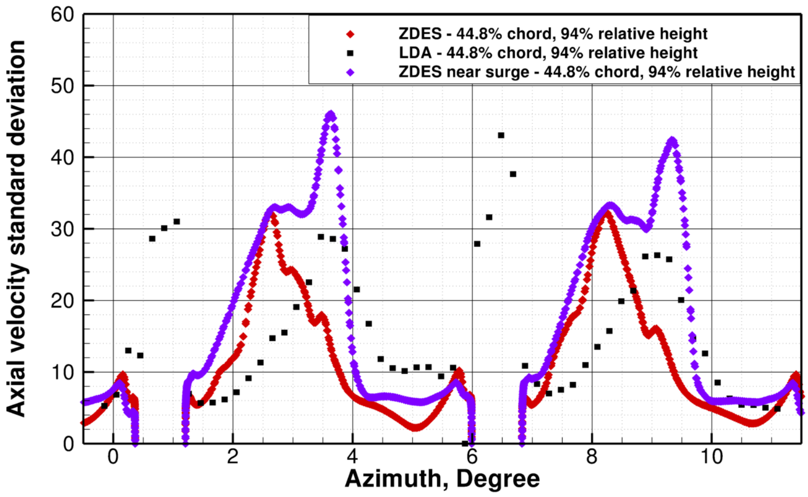

(a) Axial.

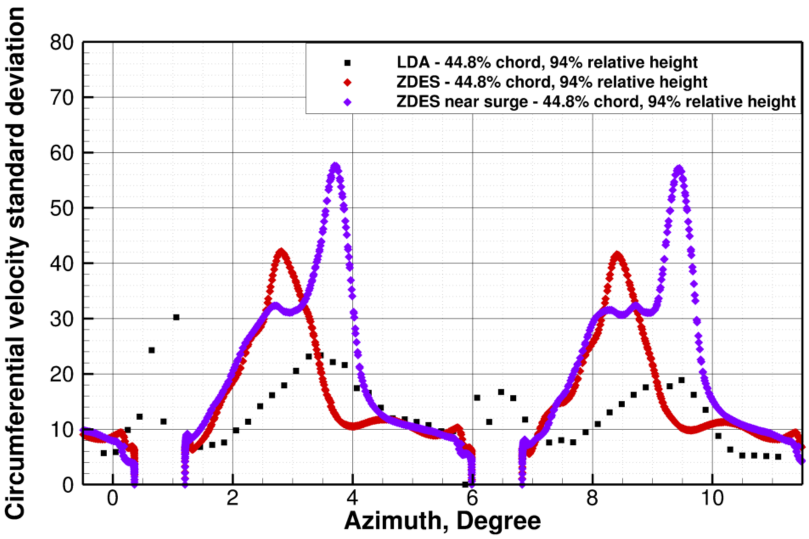

(b) Circumferential.

Figure 5.22 — *Axial and circumferential velocity standard deviations [in $m.s^{-1}$] at 44.8% chord and 94% relative height for ZDES at design point, ZDES near surge and LDA measurements at design point.*

induced vortex that extends further radially from the casing near the surge, due to the boundary layer separation. Since the separation is closer from the leading edge as well as more significant near surge, its influence is captured at 44.8%X/C and 94% of relative height.

Near the trailing edge, at 91% X/C and 90% of relative height, the aforementioned phenomenon of double leakage is clearly highlighted. The axial velocity standard deviation is plotted in figure 5.23(a). At azimuth 4, near the blade, the axial unsteadiness is high with values around $25m.s^{-1}$, whereas the levels of axial velocity standard deviation are between 6 and $14m.s^{-1}$ for the rest of the passage. These values concerns the ZDES near surge. Nonetheless, close levels are captured for the ZDES computation as well as the LDA measurements at the design point. These high unsteadiness levels designate the double leakage phenomenon. At this position, the level of axial unsteadiness near surge is nevertheless lower by $5m.s^{-1}$ compared to the design point.

The position of the tip-leakage vortex rim, located at azimuth 5.5 at the design point for both the nu-

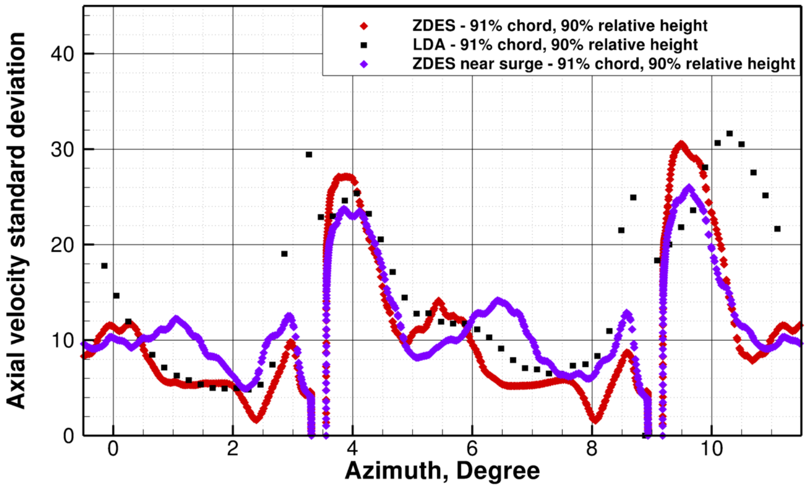

(a) Axial.

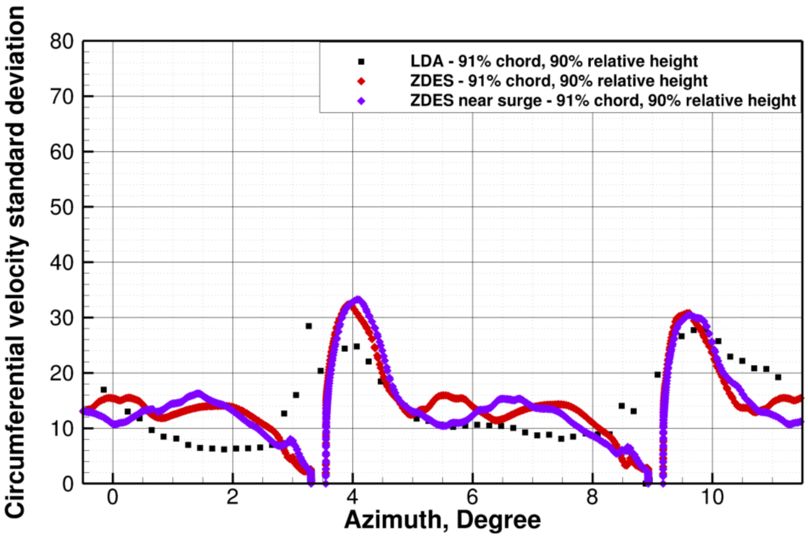

(b) Circumferential.

Figure 5.23 — *Axial and circumferential velocity standard deviations [in $m.s^{-1}$] at 91% chord and 90% relative height for ZDES at design point, ZDES near surge and LDA measurements at design point.*

merical and experimental results, is closer to the blade near surge due to its increased width. Nonetheless, its unsteadiness level is the same as for the design point.

The circumferential velocity standard deviation presented in figure 5.23(b), confirms the double leakage. Although the axial unsteadiness is lower for the double leakage near surge, the levels are similar concerning the circumferential unsteadiness. By contrast, the azimuthal velocity is increased as already seen in figure 5.19(b). Actually, the levels are close throughout the channel. The only exception concerns the position of the peak linked to the rim of the main tip-leakage vortex, as shown at azimuth 6.5 in figure 5.23(b) for the LDA measurements and ZDES near surge. This peak is located at azimuth 5.5 for the ZDES at the design point. This shows that the vortex is wider near surge at this axial position. The ZDES computation near surge is then in better agreement with the LDA measurements, even if this is at the experimental design point.

At section 26A and 90% of relative height, the standard deviation of the velocity is available near

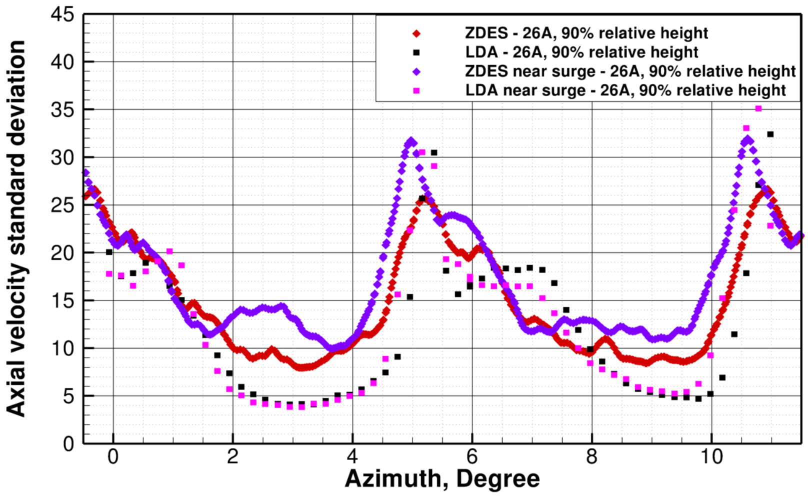

(a) Axial.

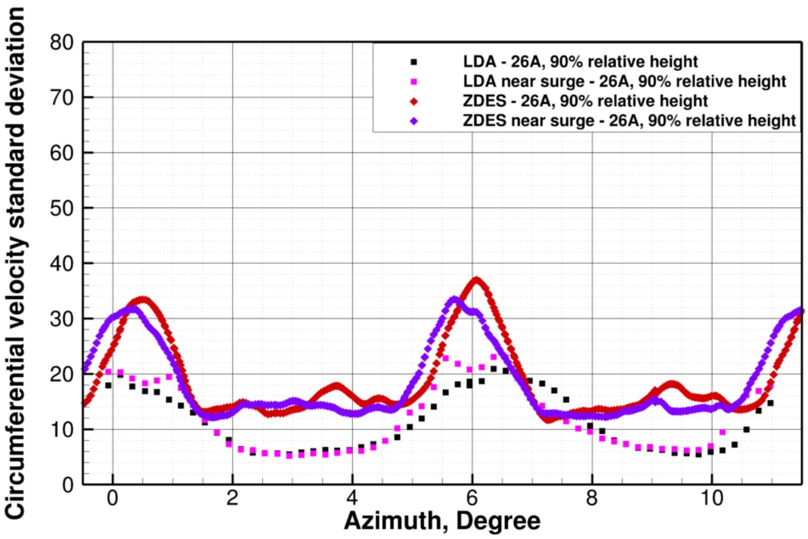

(b) Circumferential.

Figure 5.24 — *Axial and circumferential velocity standard deviations [in $m.s^{-1}$] at section 26A and 90% relative height for ZDES at design point, ZDES near surge and LDA measurements both at design point and near surge.*

surge too. Figure 5.24(a) shows its values for the axial velocity. First, one can see that there is almost no differences between the operating points from the experiments. There is only an azimuthal shift by 0.3 degrees and the maximum level of standard deviation is superior by $3m.s^{-1}$ near surge at azimuth 10.5. This is coherent with the results for the axial velocity seen in figure 5.20(a). Moreover, at the second peak, from azimuth 6 to 7.5, the unsteadiness is higher by 2 $m.s^{-1}$ at the design point than near surge in the experiment. This is the opposite in ZDES for the second maximum peak at azimuth 5.5-6. This shows that some unsteady phenomena occur experimentally and not in the ZDES. This could be explained by potential effects of the stator downstream.

For the computations, at the azimuth 2.5-3 there is a local increase of the unsteadiness due to the tip-leakage vortex. This is clearly amplified near surge with an increase by $5m.s^{-1}$ for the standard deviation. However this is not experienced by the LDA. Actually, the levels captured by the LDA are the same for the two operating points and are twice as small as the values from the ZDES computations.

Therefore, the ZDES overestimates the unsteadiness for the whole domain evenly. This results in high unsteadiness in regions with few measured unsteadiness, such as in between the wakes.

Similar result are found if the circumferential velocity is considered. The corresponding figure is 5.24(b). There is an azimuthal shift by 0.5 degree that differentiates the peaks from the R1, around azimuth 6, depending on the operating point. The same trend is observed with the numerical and experimental data set. However, the ZDES near surge has a lower unsteadiness level for this peak, contrary to what is experienced by the LDA where the unsteadiness is increased by $2m.s^{-1}$. The position of the main tip-leakage vortex is not measured experimentally by none of the operating point. By contrast, the ZDES at the design point experiences a small and localized increase in the unsteadiness at azimuth 3. The operating point change near the surge line makes the ZDES results closer to what is observed experimentally. Indeed, the vortex is no more captured around azimuth 3.5 while there is still a small peak in the other channel, at azimuth 9. This proves that the standard deviation is a sensitive value and above all that the vortex is almost dissipated here near the surge. This effect originates from the more advanced development stage of the vortex near surge, as seen previously.

In the next section, the unsteadiness near surge will be appraised with an evaluation of the flow energy.

5.4 Spectral analysis

With a view to evaluate the energy difference near surge, a spectral analysis is carried out at section 26A with the help of Power Spectral Densities (PSD). Two zones are investigated. The first one is located at the casing while the second one is situated at 94% of relative height. They are at the same azimuthal position, in the wake of the R1 and presented in figure 4.28. The probes at this azimuthal position are influenced by the main tip-leakage vortex arrival because of its width. The parameters concerning the PSD are presented in chapter 4, section 4.6 for the experimental values as well as the ZDES at the design point. The PSD for the ZDES near surge is based on the same configuration, however, the time range extends over 21 T. Its frequency resolution (FR) is nonetheless the same as the PSD from the ZDES at the design point: 2000 Hz. In addition, the PSD from the experimental probes near surge are plotted. They correspond to the same parameters as the ones for the design point. The experimental results are presented for the same frequency resolution as the computations: 2000 Hz.

First of all, the PSD for the numerical and experimental probes at the casing is presented in figure 5.25(a). The first noticeable impact of the operating point near surge on the computed flow in the boundary layer is that the energy level decreases drastically for the frequencies above 4000 Hz, which corresponds to 6 times the Blade Passing Frequency of the IGV for the R1 (BPF). Therefore, the dissipation seems to be higher near surge. This is coherent with what was observed previously in this chapter. Moreover, the part of the PSD with a slope in $k^{-7/3}$ is reduced, hence a weaker influence of the turbulence-turbulence interaction [59]. By contrast, the experimental PSD near surge reveal a higher energy level, with a wider energy range compared to the case at the design point. This is the opposite trend of what is observed with the ZDES approach for the highest frequencies. A part of this discrepancy could originate from the aforementioned difference in the operating point between the experimental and numerical cases near surge. Indeed, the wakes are not localized at the same azimuthal positions with different operating points. However, as shown earlier, the trend differs in the standard deviation at section 26A too. This could stem from the influence of potential effects from the stator 1, not taken into account numerically, that increase the unsteadiness and thus the energy level of the flow at this position.

Another relevant difference comes from the energy level of the third BPF harmonic. Indeed, it has a higher energy level than the second harmonic, contrary to what is experienced by the ZDES at the design point and in agreement with what is measured by the experimental probes at the two operating points. This strengthens the fact that the ZDES near surge is close to the measurements from the experimental

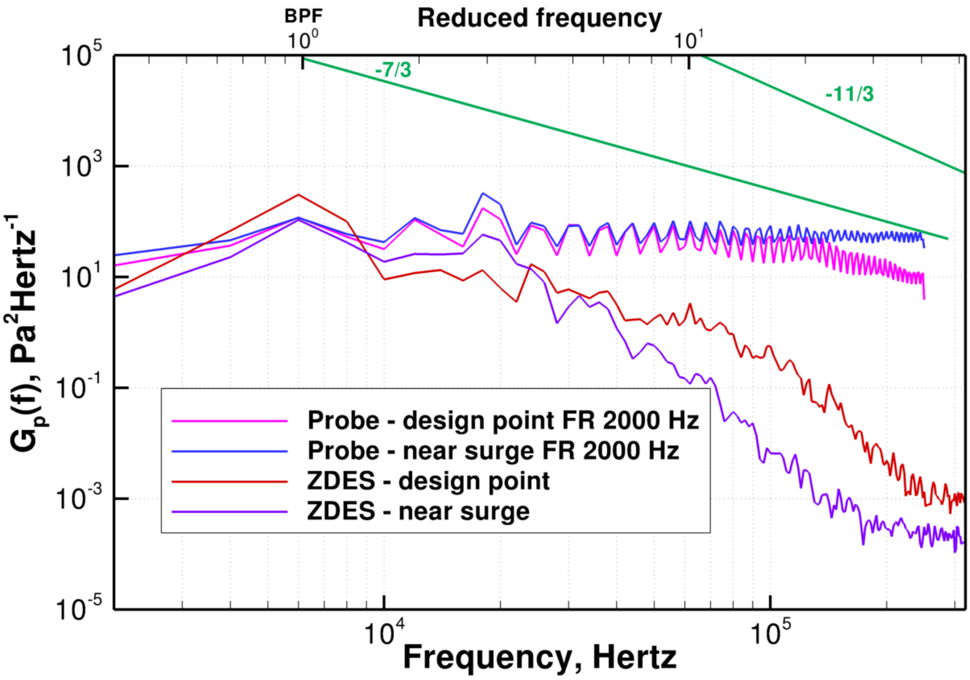

(a) At the casing.

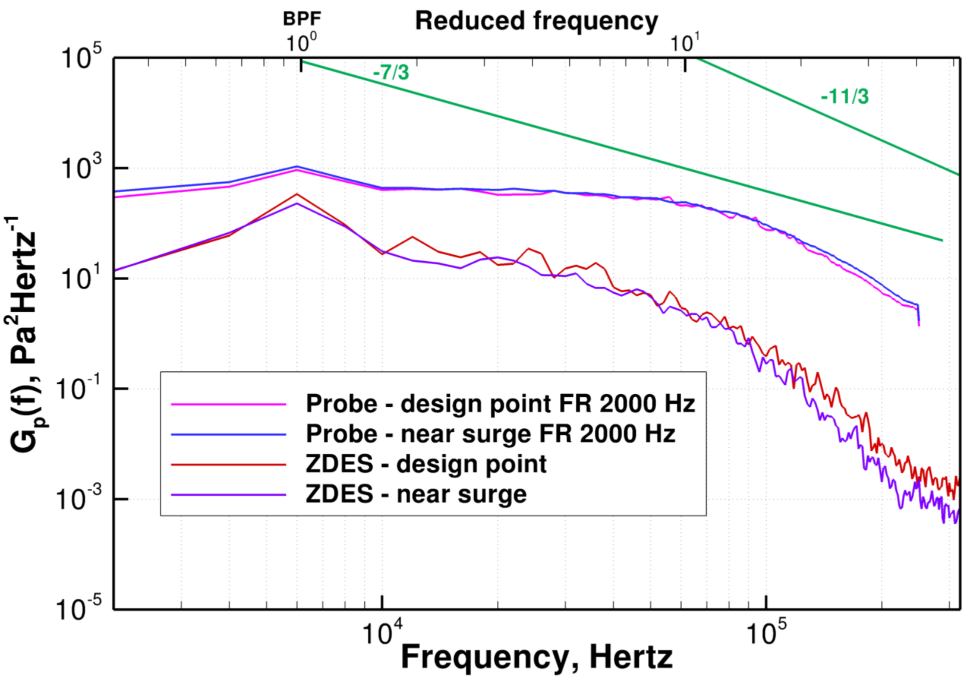

(b) At 94% relative height.

Figure 5.25 — *Power spectral density of pressure at section 26A. ZDES at the design point, ZDES near surge and experimental unsteady pressure probes at the design point.*

design point, at least for some values as shown previously in this chapter. As a result, this proves that the higher energy of the third BPF harmonic comes not only from the potential effect from the first stator (S1) downstream the R1, as it was hypothesized in chapter 4. Otherwise, it would not be captured numerically. Another effect, certainly linked to the surge, seems to participate, along with the potential effect from the S1, to this high energy.

The standard deviation of the axial and circumferential velocities at 90% of relative height have previously demonstrated that there is a higher unsteadiness near the surge line. The difference is nonetheless only concentrated on the wake positions. Before analysing the data at 94% of relative height, it must be emphasized that the plotted values correspond here to static pressure data for the computations while total pressure measurements are used for the experimental data. The PSD from the computations within the wake at 94% of relative height, presented in figure 5.25(b), shows a lower energy for the highest frequencies. Nevertheless, the discrepancy between the operating points is clearly inferior to what is observed at the casing. Besides, the energy for the BPF is lower near surge with the ZDES approach. Therefore, the difference seems to originate mainly from the lower energy levels of the harmonics of the BPF than from a higher dissipation rate. Nevertheless, it was previously revealed that there is an important variation of the energy levels for the highest frequencies at the casing. Even if the analysis of the PSD near surge underlines that there are few differences at 94% relative height, the difference of energy level is still visible for the smallest structures. The experimental probes confirm that the two operating points have similar energy levels too with discrepancies appearing only in the highest frequencies. However, the energy level is slightly higher near surge, and as it was observed at the casing, this is the opposite for the ZDES. This trend difference could come from the potential effects from the stator 1, not taken into account numerically.

In order to understand the effects noticed with the ZDES approach, it is important to remind that the spectral analysis carried out in chapter 4 focussed attention on the energy evolution along the main tip-leakage vortex and put the emphasis on the energy transfer toward the smallest structures. Since the energy levels are lower for the highest frequencies near surge, this demonstrates that the differences highlighted previously for the computation near surge do not come only from a more advanced development stage of the main tip-leakage vortex. Otherwise, the energy levels would be higher for the highest frequencies, and this is the opposite. It was shown in chapter 4 that the slope at the highest frequencies tends to become the $k^{-11/3}$ slope [59] which characterises the interaction between the turbulence and the mean-shear. The inflection point on the graph which denotes the beginning of this slope is located between 10 and 20 BPF for the ZDES computations. From this point onward, the differences between the two operating points increases, whereas the energy levels are similar for lower frequencies. Thereby, near the surge, the interaction between the mean-shear and the turbulence decreases in ZDES. Based on the different levels of analysis carried out in this chapter, the most probable hypothesis to explain this phenomenon is that the main tip-leakage vortex is less coherent near surge at this position, since it is at a more advanced development stage, and thus the mean shear interacts less with the turbulent field.

5.5 Synthesis

In this chapter, the ZDES method is used in order to better understand the effects of the operating point on the tip-leakage flow. To this end, the numerical test bench defined in chapter 3 is adapted to another operating point, near the surge line. Then, a comparison is conducted between the two ZDES computations at the two operating points, as well as experimental measurements.

First of all, it shows that, near the surge line, the tip-leakage vortex gets closer to the pressure side of the adjacent blade. Moreover, it becomes rapidly wider and thus disrupts earlier than at the design operating point. Thereby, the whole topology of the tip-leakage vortex, detailed in chapter 4, occurs more upstream. Besides, since the flow angle increases and the tip-leakage vortex reaches the adjacent blade at a more upstream position, the phenomenon of double leakage is amplified.

Near the surge line, the shock becomes stronger and its effects on the whole flow topology are more intense. Therefore, a massive separation of the boundary layer developing on the shroud occurs. Then it rolls up into the induced vortex that turns in the opposite direction of the main tip-leakage vortex. The separation originates from the axial momentum deficit of the tip-leakage flow when it mixes with the main flow. Where the boundary layer separates, there is a local inversion of the flow, characterized by a high unsteadiness. The unsteadiness seems to come in two steps: first only axially, then axially and azimuthally. This unstable phenomenon could be the inception of the surge. Likewise, downstream the blade, the flow comprises a higher unsteadiness near the surge. Despite this higher unsteadiness, the energy within the flow is lower than at the peak efficiency. This seems to stem from the tip-leakage vortex, which is no more coherent downstream, and therefore interacts less with the turbulent field.

Finally, the analysis presented here corroborates the hypothesis established in chapter 4. Indeed, the difference between the ZDES and the URANS/RANS methods concerning the observed vortex deviation originates from the operating point choice. As a consequence, the trend captured by the ZDES for the vortex topology is in better agreement with the measurements than the URANS and RANS approaches, and thus strengthens the validation of the method.

In the next chapter, the effects of the incoming wakes from the IGV, at the design point, will be characterized with the help of the ZDES method.

Chapter 6

Influence of the IGV wakes on the rotor tip-leakage flow

Contents

This chapter presents the influence of the inlet condition on the tip clearance flow. Two different ZDES computations are compared. A rotating distortion map of the flow cartography is set as inlet condition for the first ZDES computation whilst an azimuthally averaged inlet condition is used for the second one. This uncouples the effects of the inlet guide vane wake from the behaviour inherent to the rotor tip-leakage vortex.

6.1 Overview of the compared computations

6.1.1 Description of the methodology

The aim of this chapter is to evaluate the influence of the inlet condition on the tip-leakage vortex at the design operating point. For this purpose, two different inlet conditions are used: a rotating distortion map and a steady averaged map. They are detailed in chapter 3 and shown in figure 3.8. Both are based on the same initial cartography. The reference ZDES case, that is to say, the one with the rotating distortion, was evaluated in chapter 4. It is set against another ZDES computation with this steady averaged map as inlet condition.

The first inlet condition consists in a rotating distortion map, whose method was used for centrifugal

Case	Normalized mass flow	Normalized R1 total pressure ratio
Pneumatic probes	1.000	1.000
ZDES with rotating distortion	1.014	0.992
ZDES with averaged cartography	1.012	0.987

Table 6.1 — *Mass flow and total pressure ratio for ZDES with averaged cartography and with rotating distortion, normalized with the values from the pneumatic probes data.*

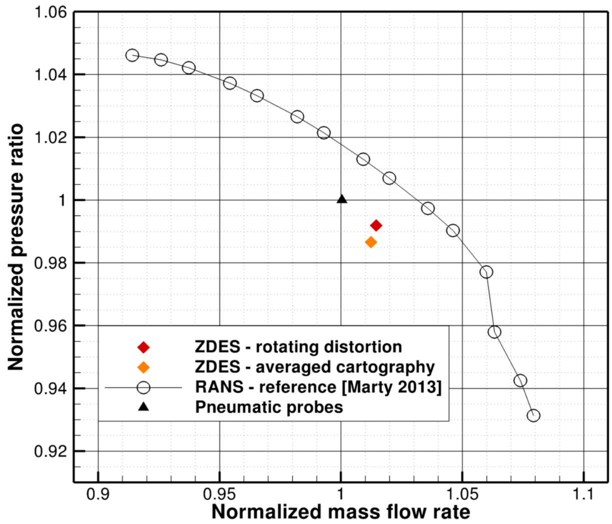

Figure 6.1 — *Pressure ratio versus mass flow rate for ZDES with averaged cartography and with rotating distortion, normalized with pneumatic probes data.*

compressor by Tartousi et al. [166], based on a Fourier decomposition with 60 harmonics, of the two dimensional cartography of the flow. The aim is to capture accurately the phenomena arriving at section 25A from the Inlet Guide Vane (IGV): the IGV wake, the IGV hub vortex and last but not least, the IGV tip vortex. The physical values for stagnation pressure, stagnation enthalpy, primitive turbulence quantity of the model, and direction of the flow are given at each interface of the map. Therefore, with this rotating boundary condition, the unsteady distortion effects induced by the IGV are modelled in the simulation of the flow within the first rotor (R1) of the CREATE compressor. The second one consists in the same two dimensional cartography but azimuthally averaged. There is neither distortion nor rotating inlet map in this case. For each radius, the same physical values are given at each cell of the map. This is the only difference between the two compared ZDES computations. Indeed, the same outlet boundary condition is used for both ZDES computations to comply with the methodology established in chapter 3. Likewise, the same methodology is applied to both the computations to check the convergence. The time range retained for the different analysis of this chapter is 17 T for the ZDES with the averaged cartography, which is the same number of iteration as for the ZDES computation with the rotating distortion.

The fact that the only difference between the computations comes from the inlet condition enables to uncouple the phenomena inherent to the tip-leakage flow from the effects of the IGV wakes on this flow.

6.1.2 The effects on the global values

First of all, table 6.1 summarizes the mass flow at section 25A and the total pressure ratio, between sections 25A and 26A, for the two ZDES fields as well as the experimental values from pneumatic pressure probes. These values are plotted in figure 6.1 for an easier assessment, along with a reference

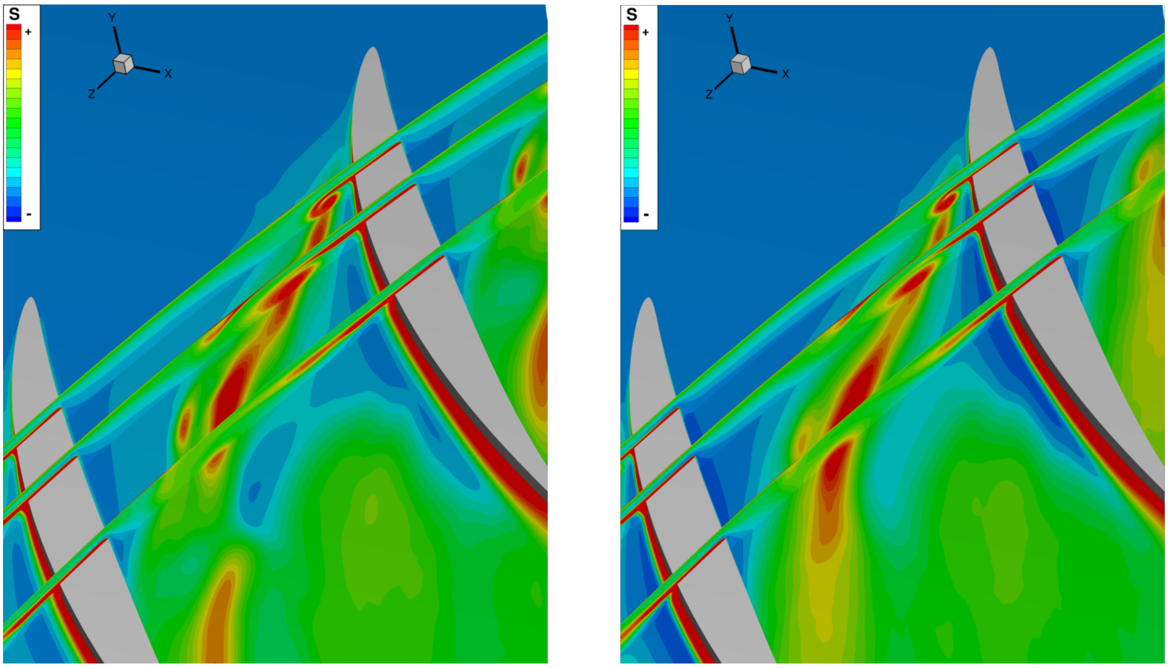

(a) With the averaged cartography.　(b) With the rotating distortion.

Figure 6.2 — *Comparison of the time averaged entropy field for ZDES with different inlet conditions. Entropy planes at 22%, 31% and 46% chord and 98% relative height.*

computation in RANS from Marty et al. [113], that uses the same aforementioned averaged cartography. Details for this reference case are given in chapter 4.

One can see that two effects are clearly visible. First, there is a drop in the pressure ratio for the case with the averaged cartography. Second, it leads to a lower mass flow rate. Thereby, if the IGV wakes are not taken into account numerically, the computational results move away from the experimental values with a lower pressure ratio. Nonetheless, the fact that the mass flow rate decreases tends to be in better agreement with the experiment, but only for the mass flow. Indeed, the resulting numerical operating point is obviously further from the experimental one.

This highlights the positive effect of the IGV wakes on the performance of the R1. It is then necessary to understand how it can affect it, and thus a thorough analysis of the flow field will be carried out in the next section.

6.2 Flow visualization

6.2.1 Time-averaged flow field overview

First of all, the time averaged field is compared between the two computations. The ensemble average is carried out on the aforementioned 17 T.

Different entropy planes at position 22%, 31% and 46% X/C and another one at 98% of relative height are presented in figure 6.2. It is important to remember that the difference in direction between the main flow and the leakage flow leads to a shear layer with high entropy [165]. Moreover, high entropy zones locate regions of high loss as explained by Denton [43]. As a consequence, this visualisation represents the loss and suits an analysis of the tip-leakage vortex. First, at 46% X/C, the high entropy coming from the blade tip contaminates the flow field further azimuthally. This is just a small effect of the

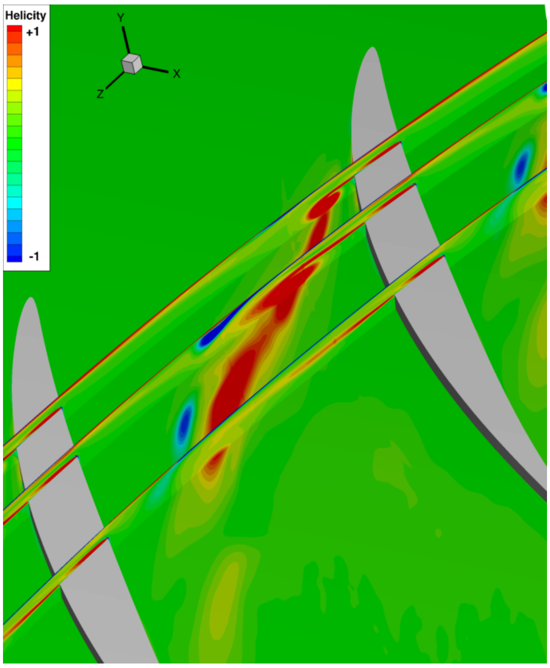

(a) With the averaged cartography.

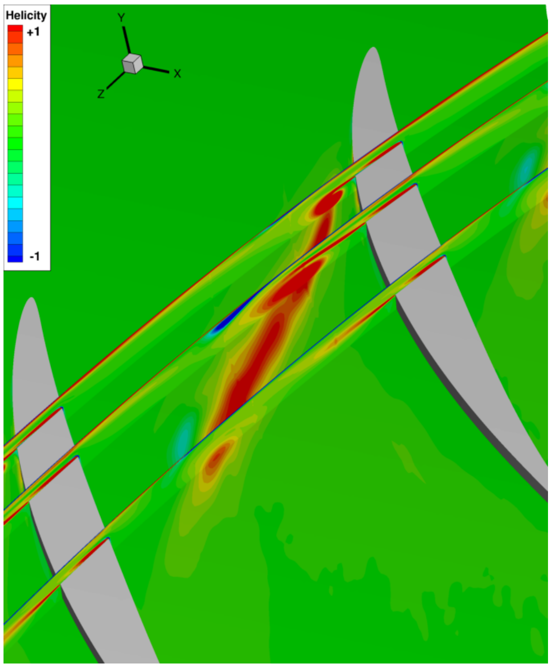

(b) With the rotating distortion.

Figure 6.3 — *Comparison of the time averaged helicity field for ZDES with different inlet conditions. Normalized helicity planes at 22%, 31% and 46% chord and 98% relative height.*

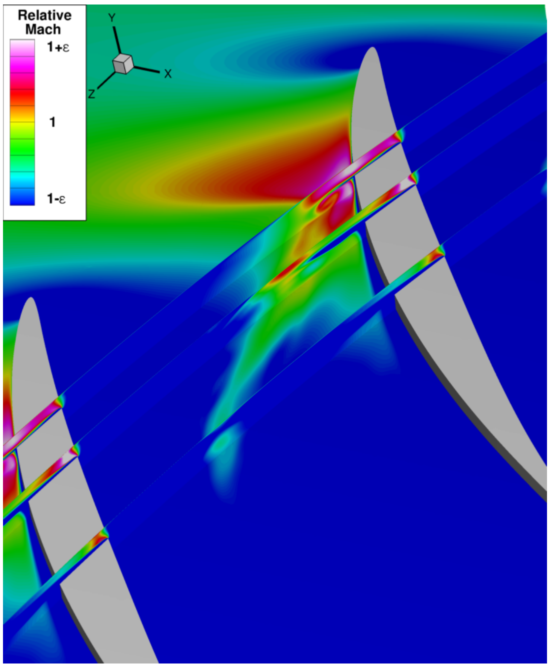

(a) With the averaged cartography.

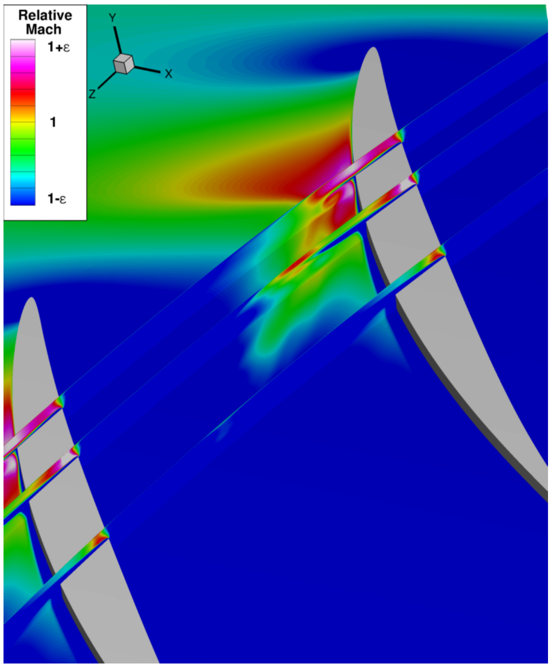

(b) With the rotating distortion.

Figure 6.4 — *Comparison of the time averaged relative Mach number field for ZDES with different inlet conditions. Relative Mach number planes at 22%, 31% and 46% chord and 98% relative height.*

averaged inlet condition, since the whole vortical topology extends azimuthally. Indeed, one can see that the zone of high entropy characterizing the main tip-leakage vortex is slightly wider with the averaged map too. Moreover, this high entropy zone elongates less without the wakes. As a result, the dissipation

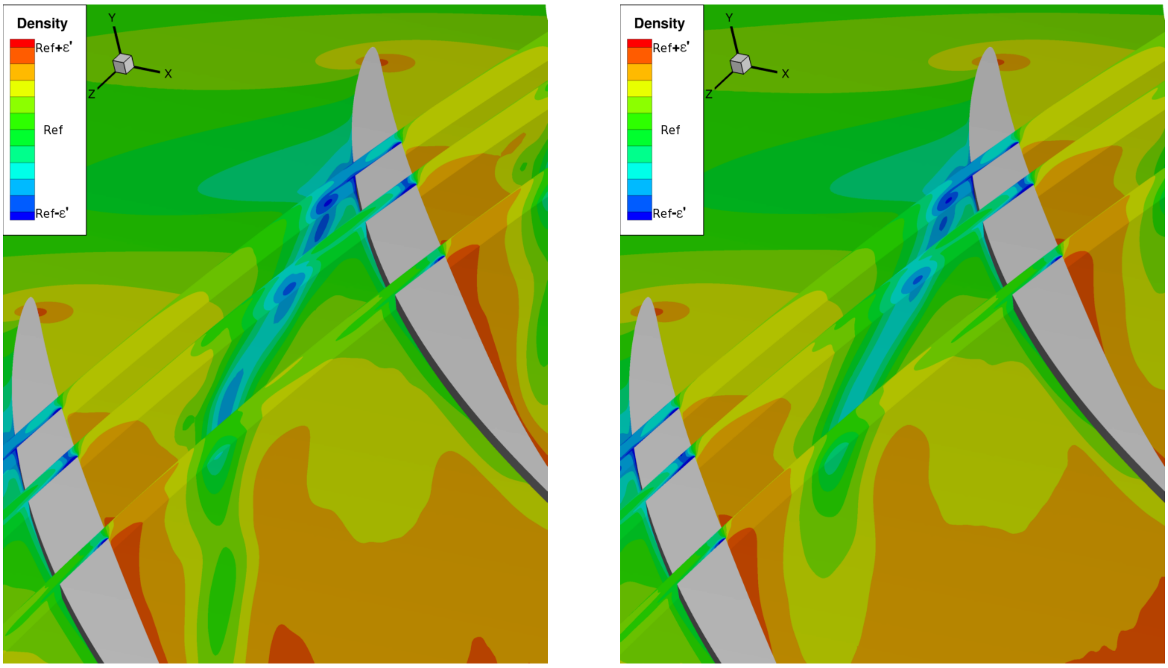

(a) With the averaged cartography.

(b) With the rotating distortion.

Figure 6.5 — *Comparison of the time averaged density field for ZDES with different inlet conditions. Density planes at 22%, 31% and 46% chord and 98% relative height.* $\epsilon' = 29\%$ *of the density reference value.*

rate is mainly focussed near the shock. Nevertheless, a second high entropy area is distinguishable near the pressure side of the adjacent blade in the case with the averaged cartography. Actually, this vortex extends further downstream without the IGV wakes, and then dissipates as it gets closer to the adjacent blade.

The same planes are shown in figure 6.3 for the normalized helicity. The main tip-leakage vortex as well as the induced vortex exhibit a higher rotating intensity highlighted by important zones with a normalized helicity value close to ± 1. Another distinctive effect lies in the amplification of the boundary layer separation at the casing, visible at 31% X/C in figure 6.3(a). Thereby, the effect of the induced vortex is more visible, in blue between the section 31 and 46% X/C in the plane at 98% of relative height. The second zone of high entropy near the pressure side of the adjacent blade is marked by a higher helicity too, albeit less pronounced than the levels upstream section 46% X/C. This clearly strengthens that there is a vortex near the pressure side of the adjacent blade.

Figure 6.4 underscores that the averaged cartography influences the shock on the time averaged field. Indeed, the area with a relative Mach number over 1 is wider. This means that the IGV wakes decrease the shock intensity, at least in average. Besides, a zone of high Mach number, albeit not above 1, extends further downstream along the main tip-leakage vortex up to the section at 46% X/C. This corroborates the fact that the main tip-leakage vortex is more coherent without the wakes.

The analysis of the density field, in figure 6.5 confirms this enhanced coherence of the vortex. The zone of lower density within the vortex core reaches the adjacent blade, whereas the density increases earlier downstream in the case with the IGV wakes. Contrary to the change in operating point detailed in chapter 5, and as expected, the shock does not change drastically without the wakes. The influence of the inlet condition on the shock intensity is nevertheless perceivable, albeit limited.

The pressure field, presented in figure 6.6, validates that the gradients on the time averaged pressure field are similar with or without the arrival of the IGV wakes. Around the shock, there is nothing that

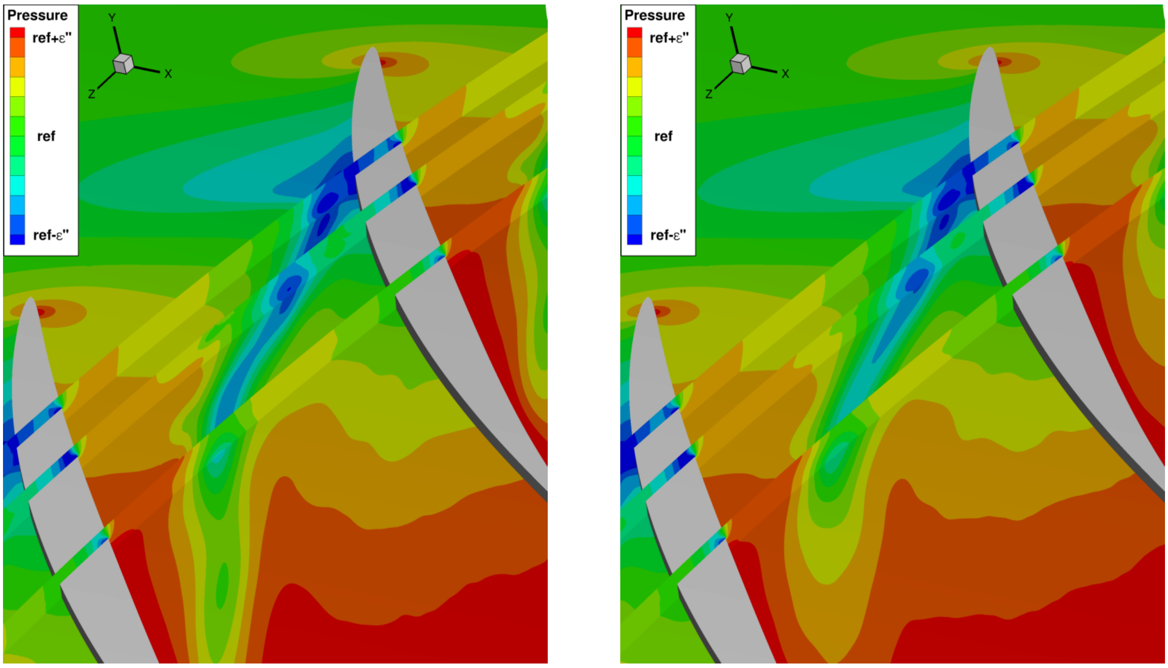

(a) With the averaged cartography.

(b) With the rotating distortion.

Figure 6.6 — *Comparison of the time averaged pressure field for ZDES with different inlet conditions. Pressure planes at 22%, 31% and 46% chord and 98% relative height. $\epsilon'' = 29\%$ of the pressure reference value.*

distinguishes the two computations contrary to what is observed with the relative Mach number in figure 6.4. The only difference lies in the azimuthal and axial extensions of the main tip-leakage vortex, in the same way as what is seen in the density field. Indeed, with the averaged cartography, the vortex core is still perceptible up to section 46% X/C with a low pressure. Besides, a low pressure zone extends further downstream. It is characterized by a lower pressure than for the case with the IGV wakes. Moreover, it is narrower, thus the vortex is more spatially concentrated on a small area. This narrowness indicates a lower dissipation for the vortex, which coincides with the entropy levels seen in figure 6.2.

6.2.2 Flow field snapshots

In order to better understand what occurs within the tip-leakage flow due to the arrival of the IGV wakes, which is an unsteady phenomenon, the instantaneous flow is analysed hereinbelow.

First of all, figure 6.7 shows the vortex topology of the tip-leakage flow as a function of time for the two ZDES computations, with and without the arrival of the IGV wakes. The Q criterion [81] iso-surfaces coloured by the normalized helicity [105] reveals the different vortices and their rotating direction. The entropy plane at 31% X/C, in black and white, underlines the arrival of the wakes. It is important to emphasize that the differences between these two computations comes only from the inlet condition, and whether it takes into account the periodic arrival of the IGV wakes or not. Four different times are shown in these snapshots: T/4, 2T/4, 3T/4 and T.

First of all, the main effect of the inlet condition to emphasize is that the whole vortex topology remains spatially stable with the averaged cartography. Indeed, the case with the rotating distortion captures a vortex flutter phenomenon. The IGV wake and its tip vortex, visible in figure 3.7(a), interacts periodically with the leading edge of R1 which leads to this flutter. Its arrival at section 31% X/C is highlighted in figure 6.7(h). The interaction between the wake and the tip clearance flow, hence this

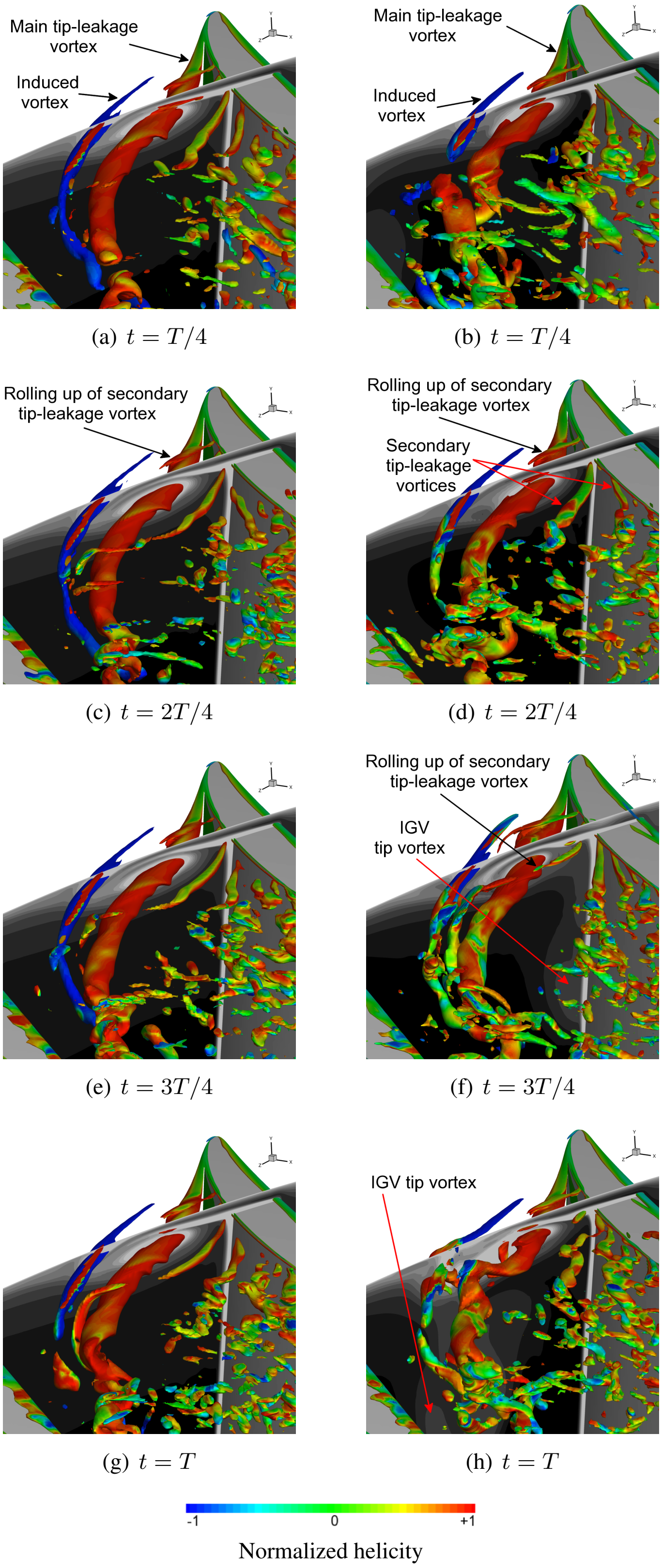

(a) $t = T/4$ (b) $t = T/4$

(c) $t = 2T/4$ (d) $t = 2T/4$

(e) $t = 3T/4$ (f) $t = 3T/4$

(g) $t = T$ (h) $t = T$

Figure 6.7 — *Snapshots of Q criterion iso-surface coloured by the normalized helicity and section 31% X/C filled with the entropy (left: with averaged cartography, right: with rotating distortion).*

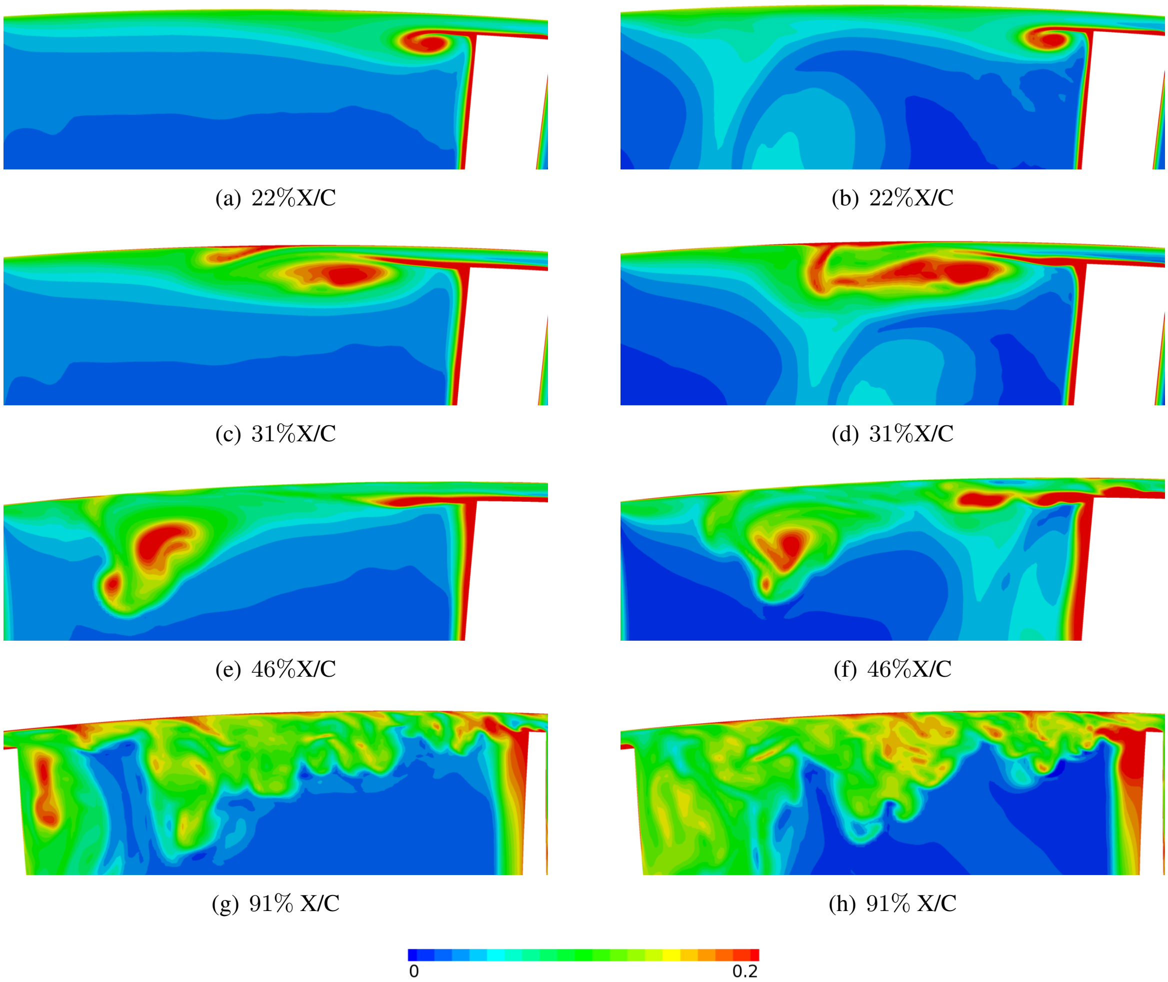

(a) 22%X/C (b) 22%X/C

(c) 31%X/C (d) 31%X/C

(e) 46%X/C (f) 46%X/C

(g) 91% X/C (h) 91% X/C

Entropy variation

Figure 6.8 — *Entropy planes for four different axial positions at t=3T/4 (left: with averaged cartography, right: with rotating distortion).*

flutter, was already experimentally emphasized in [109], albeit not with an incoming vortex from the stator as it is the case here. In the studied configuration, the IGV tip vortex induces this flutter. The IGV wake, which arrives on the rotor leading edge too has a weak contribution to this phenomenon. The velocity deficit of the main flow deflects the leakage flow direction, from the rotor tip-leakage vortex inception, visible in figure 6.7(d). As a consequence, the rotor tip-leakage vortex moves away from the suction side of the blade with a period of T and it disrupts earlier. The disruption position wanders around 31% X/C. One can see, as already highlighted in chapter 4, that secondary tip-leakage vortices, as the one pointed in figure 6.7(f) migrate from the trailing edge toward the leading edge. This migration originates from this momentum deficit too and is only experienced in the case of the ZDES with the rotating distortion.

Without the arrival of the IGV tip vortex, the rotor vortex topology is at the same development stage as for the case with rotating distortion before its disruption caused by the IGV tip vortex. The closer the origin location of a vortex is from the leading edge, the more stable the vortex. Therefore, the main rotor tip-leakage vortex position remains stable and the induced vortex behaves similarly. There is no direction change in this case. Furthermore, these two vortices have an helicity level increased in absolute value compared to the ZDES with the rotating distortion. This confirms what was seen in figure 6.3(a) with the time averaged helicity planes. As a consequence, these vortices extend further downstream and toward the adjacent blade, which increases the effects of the double leakage.

The entropy planes at positions 22.3%, 31%, 46% and 91% X/C are presented in figure 6.8 for the two different ZDES configurations, at a given time t=3T/4. This enables to check the evolution of the tip-leakage vortex along the chord.

At 22% X/C, the entropy field is similar between the two presented cases. The development stage of the main tip-leakage vortex is as advanced with the averaged cartography as with the rotating distortion. Nonetheless, a major difference is revealed : the high entropy of the IGV tip vortex.

From 31% X/C, the topology differs clearly between the two computations. The vortex coming from the IGV tip stretches periodically the rotor tip-leakage vortex azimuthally and accelerates the casing boundary layer separation. This is clearly visible by comparing figures 6.8(c) and 6.8(d). The separation occurs even when the IGV tip vortex does not meet the rotor tip-leakage vortex. Indeed, there is still such a separation for the ZDES case with an averaged map, as shown in figure 6.8(c). However, it separates later downstream in the case without the IGV tip vortex arrival.

It is relevant to remember that this boundary layer separation was already referenced on an axial compressor by Gourdain and Leboeuf [64] to explain one of the origins of flow blockage near the casing. The rotor tip-leakage vortex stretching and therefore its early disruption stems from a combined effect of both the rotation and the velocity deficit implied by the IGV tip vortex, visible in figure 6.8(d). Another consequence of the IGV tip vortex arrival is the thickening of the suction side boundary layer. This periodic thickening is distinguishable in figure 6.8(f). Finally, a last noticeable effect occurs in the tip gap. The IGV tip vortex arrival makes the tip gap boundary layer separate periodically, as shown in figure 6.8(f).

It was shown in section 4.7 that the ZDES approach captures the energy transfer from the large to the small structures contrary to the URANS method. This leads to the noticeable small vortices in figure 6.7. This can be found in the entropy field near the trailing edge. Indeed, it is composed of scattered high entropy spots corresponding to the continuity of the rotor tip-leakage vortex and to the aforesaid multiple smaller vortices. The small structures are more visible with the two ZDES computations at this axial position than upstream since they are related to the turbulent field. However, there is a difference concerning the main rotor tip-leakage vortex, visible by comparing the left side of figures 6.8(g) and 6.8(h). The area of high entropy coincides with the second zone revealed in figure 6.2. This is the main tip-leakage vortex that has almost completely disappeared and turned into smaller vortices for the case with the rotating distortion. By contrast, as it was seen previously in figure 6.7, it is present for the case with the averaged map further than with the rotating distortion. This clearly corroborates that the tip-leakage vortex is still coherent at this position. Therefore it reaches the adjacent blade as shown by figure 6.8(g). This is another factor that confirms the presence of a more pronounced double leakage phenomenon with the averaged map. Indeed, the rotation of the main tip-leakage vortex increases the mass flow inside the tip gap of the adjacent blade, hence the amplified double leakage.

6.3 Radial and azimuthal distributions

Beyond the topological analysis carried out in the last section, it is necessary to appraise the effects of the inlet boundary condition on the tip clearance flow with the help of experimental measurements on the real configuration, that is to say, with the wakes. This is the reason why radial distributions from time and circumferentially averaged data, and azimuthal distributions are compared in this section. Contrary to the previous sections, two additional computations are added in the figures: the RANS and the URANS ones, detailed in chapter 3. The aim is to bring more information on the effects of the inlet condition. Indeed, the steady RANS computation uses the same averaged map as the ZDES computation with the averaged cartography. Moreover, the URANS computation uses the same rotating distortion for the inlet boundary condition as the ZDES with rotating distortion. Thereby, the effects linked to the inlet condition can be more easily identified.

6.3.1 Radial distribution

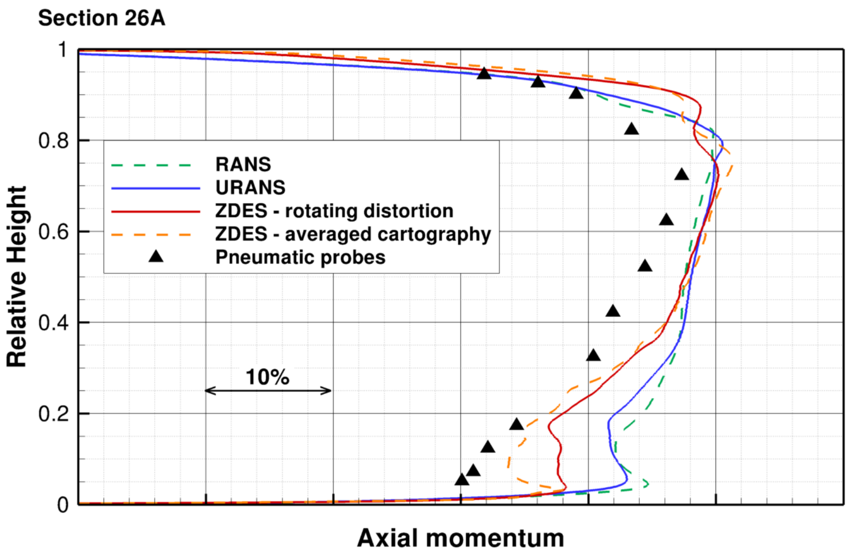

Figure 6.9 — *Radial distribution of time and circumferentially averaged axial momentum at section 26A for RANS, URANS, ZDES with rotating distortion, ZDES with averaged cartography and experimental probes.*

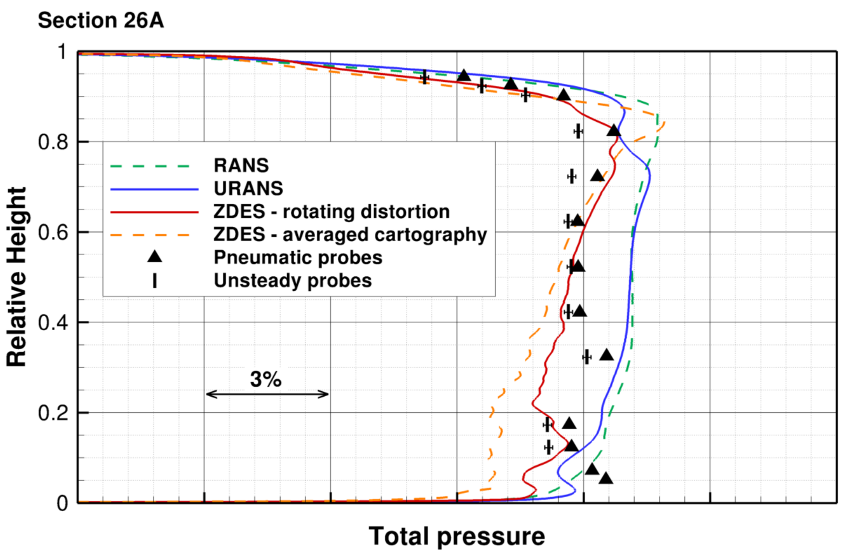

Figure 6.10 — *Radial distribution of time and circumferentially averaged total pressure at section 26A for RANS, URANS, ZDES with rotating distortion, ZDES with averaged cartography and experimental data from steady and unsteady probes.*

First of all, the radial distributions from time and circumferentially averaged data downstream the first rotor (R1), in section 26A, are discussed.

Figure 6.9 shows the radial distribution of the axial momentum for the four computations and experimental values from pneumatic probes. The averaged cartography changes the axial momentum near the hub and near the casing, hence the major influence of the hub and tip vortices from the IGV. On the one hand, at 80% of relative height, the gradients around the local minimum are changed with the averaged map in ZDES. It increases the axial momentum maximum at 75% of relative height by 5%, whilst the other local maximum at 90% of relative height is decreased by the same percentage. On the other hand, from 5 to 20% of relative height, the gradients are transformed from a linear slope with the rotating distortion to a curve with the averaged map. A similar change is experienced from the URANS to the RANS computations. Nevertheless, the axial momentum value drops by 4% in ZDES, whereas it increases slightly and up to 2% in RANS. This has to be put in perspective, since between the RANS and URANS computations there is not only the change in the inlet condition but the major effect of the unsteady approach in URANS too. This unsteady approach makes the value of axial momentum computed near the hub lower, which compensates the drop induced by the use of the averaged cartography.

Though, it is clear that the use of a steady, averaged cartography instead of the unsteady rotating distortion decreases the axial momentum in regions where vortex interactions should occur, in this case at the hub and at the casing. This leads to a change of the global performance as previously shown in figure 6.1.

In figure 6.10, the total pressure radial distribution is plotted. Two different experimental probe values are presented from unsteady and steady probes. The averaged unsteady probe symbols comprise the interval with the measurements uncertainties which are of 0.10%. It is important to remember that even if the probe values are close at mid span, their differences can reach up to 1% in regions of high unsteadiness such as at 85% relative height and near the hub. The secondary flows near the casing lead to a pressure gradient, from 100% to 85% relative height, which is better captured with the ZDES approach, even with the averaged upstream map for the inlet boundary condition. Indeed, the RANS and URANS approaches under-estimate it. A difference in the capture of this radial total pressure gradient denotes a difference in the flow topology near the casing as explained in chapter 4. The computations that take into account the unsteadiness due to the IGV wake, that is to say ZDES with the rotating map and URANS, succeed in capturing the effects on total pressure at 80% and are close to the pneumatic probe value at 80%, albeit still 1% higher than the averaged unsteady probes. The discrepancy near the casing between cases with and without the rotating distortion map derive partly from the presence of the double leakage for the computations with an averaged map. This phenomenon appears with high solidity compressors and is characterized by the leakage flow arriving on the adjacent blade and passing through its tip gap. This phenomenon impacts the loss and may lead to blockage. Sirakov and Tan [155] observed that the interaction between the IGV wake and the tip-leakage flow reduces the double leakage. The presence of a double leakage will be confirmed with the azimuthal distributions in section 6.3.2.

Close results are obtained with the RANS and URANS calculations at mid-span while the two ZDES computations are closer to the probe values. Indeed, there is an overall overestimation of the total pressure for the RANS and URANS computations. Near the hub, the use of an averaged map as inlet condition brings about opposite behaviours for the total pressure, depending on the computational method used. Near 10% relative height, on the one hand, with ZDES, the total pressure is underestimated by 1.5%. On the other hand, with the RANS approach, the total pressure reaches the pneumatic probe value. However, the RANS approach does not capture the hub effect which is visible at 5% relative height with the computations using the rotating distortion. This is only experienced by both the computations with the rotating distortion.

As a consequence, one can assume this hub effect is highly unsteady and arises from the IGV hub vortex. Furthermore, the tip-leakage flow is not only driven by the rotor tip-leakage vortex. Indeed, the IGV tip vortex has a consequence on the rotor tip-leakage vortex development too.

Figure 6.11 presents the radial distribution for the normalized total temperature $Cp\Delta Tt/U^2$, or loading coefficient. Near the hub, between 10 and 15% of relative height, the influence of the inlet condition is perceptible. Indeed, the cases with the averaged map have a value for $Cp\Delta Tt/U^2$ up to 3% higher than with the rotating distortion. This means that the work of the blade differs depending whether there is the IGV hub vortex or not. Above 65% of relative height, the effects of the averaged map are more obvious. The presence of the tip-leakage vortex is clearly observed with the averaged map. Indeed, it amplifies the effects of its presence. For instance, the local maximum of total temperature, in ZDES with

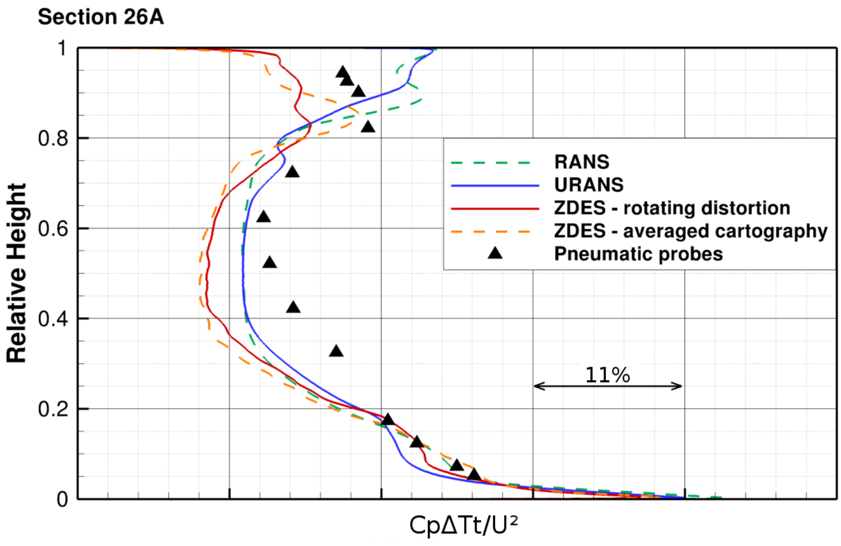

Figure 6.11 — *Radial distribution of time and circumferentially averaged normalized total temperature at section 26A for RANS, URANS, ZDES with rotating distortion, ZDES with averaged cartography and experimental probes.*

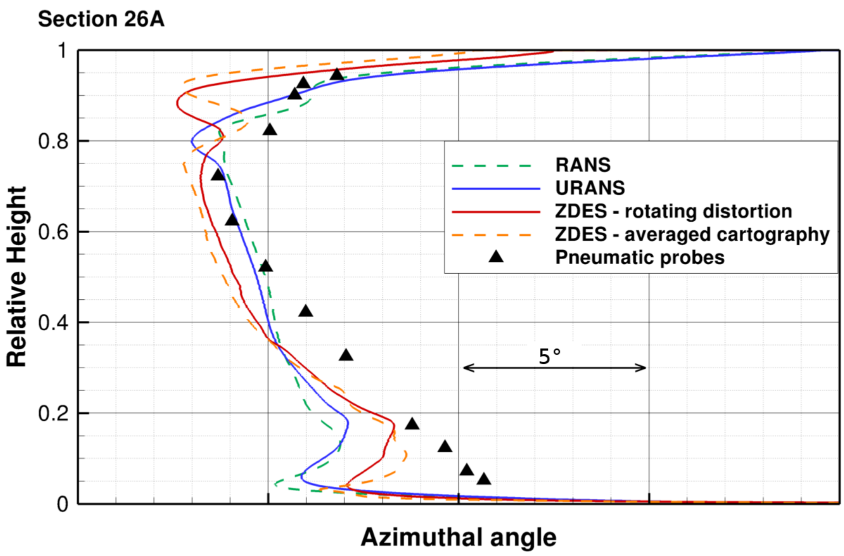

Figure 6.12 — *Radial distribution of time and circumferentially averaged azimuthal angle at section 26A for RANS, URANS, ZDES with rotating distortion, ZDES with averaged cartography and experimental probes.*

the averaged map, corresponds to 0.85% of relative height, which coincides with the maximum for the experimental values. By contrast, this maximum is lower with the rotating distortion. Notwithstanding this apparent advantage of the averaged map for the value at 85% of relative height, the gradient from this radial position to the casing is clearly overestimated. This strengthens the fact the tip-leakage vortex is too coherent with the averaged map compared to what it is in the experiment.

A similar behaviour is captured by the RANS approach. Instead of having just a light curve inflection like in URANS, the use of the averaged cartography enables this steady approach to capture gradients which are in better agreement with the experiments. In other words, the steady RANS approach seems to be more appropriate to simulate the unsteady tip-leakage vortex than the unsteady RANS (URANS) method. This is an unexpected consequence of the use of a less accurate inlet boundary condition.

The azimuthal angle evolution is plotted in figure 6.12. Its analysis near the hub confirms the different angle that leads to a different work for the blade without the IGV wakes, as seen in figure 6.11. In ZDES, the values are closer to the experimental measurements without the IGV wakes. Nonetheless, these values are still clearly underestimated. The reason, as hypothesized in chapter 4 and confirmed in chapter 5 comes mainly from the overestimation of the separation on the suction side generated by the Spalart-Allmaras turbulence model.

At the casing, the angle is still underestimated around 90% of relative height with the averaged map. Besides, the gradients are more pronounced. Therefore, this increases the error due to the operating point explained in chapter 5 and shown in figure 5.16. However, the lack of capability to simulate the tip-leakage vortex for the RANS/URANS approaches prevents the RANS from capturing correctly the gradients. Therefore, even if the gradients for the total temperature are clearly visible in RANS, there is only a light inflection around 90% of relative height for the azimuthal angle.

In conclusion, the impact of the inlet boundary condition is concentrated near the hub and tip, that is to say where the vortices from the hub and tip gaps of the IGV arrive, and there is almost no effect at mid span.

6.3.2 Azimuthal distribution of time averaged velocities

One will focus now on the azimuthal distributions for the axial and circumferential velocities to verify the influence of the IGV tip vortex on the flow at the casing of the R1. The time averaged computational results are compared to averaged measurements performed on the experimental test rig at the design point with a Laser-Doppler-Anemometry (LDA).

First of all, the axial velocity at 21.7% X/C and 98% of relative height is plotted in figure 6.13(a). One can see no major effect of the inlet condition on the averaged flow field. Indeed, even if the lines are not perfectly superposed, the difference is too thin here to be analysed.

The same conclusion can be drawn with the circumferential velocity at the same position. The analysis of figure 6.13(b) underlines the similarity between the computations. This is similar to what is observed for the axial velocity.

As a result, the choice of the inlet condition, averaged or with a rotating distortion, does not change the averaged field near the leading edge. The reason is that the tip-leakage vortex is at a too early stage of development here.

Indeed, at a more downstream position, at 44.8% X/C and 94% of relative height, there is an important difference for the axial velocity profiles, as plotted in figure 6.14(a). With the averaged map in ZDES, the maximum axial velocity value is increased. Besides, the second local maximum is visible in the two channels, contrary to the case with the rotating distortion. As a result, there are two peaks in between the blades for the ZDES with the averaged map. One can see the second captured peak at azimuth 2.5 and 8, whereas it is only experienced at azimuth 8 with the IGV wakes. It is relevant to remember that none of the method based exclusively on the Reynolds averaged Navier-Stokes equations capture it. Moreover, there is almost no difference between the RANS and URANS methods. Once more, this originates from their lack of capability to simulate the tip-leakage vortex. This second maximum is related to the induced vortex that is more coherent without the periodic arrival of the IGV tip vortex.

The circumferential velocity, presented in figure 6.14(b) shows similar results. The peak for the maximum circumferential velocity is higher and narrower without the wakes. This clearly shows that the tip-leakage vortex is intensified compared to the case with the rotating distortion. Nevertheless, there is no second peak for the induced vortex. This proves that it is not as pronounced as the main tip-leakage vortex.

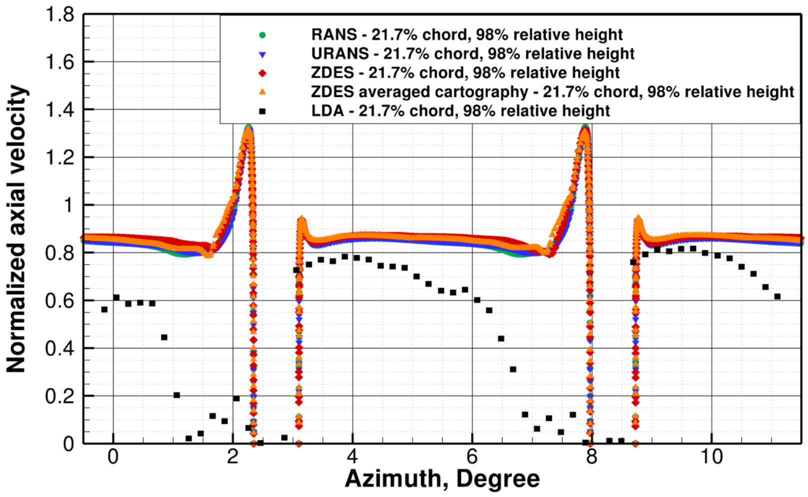

(a) Axial.

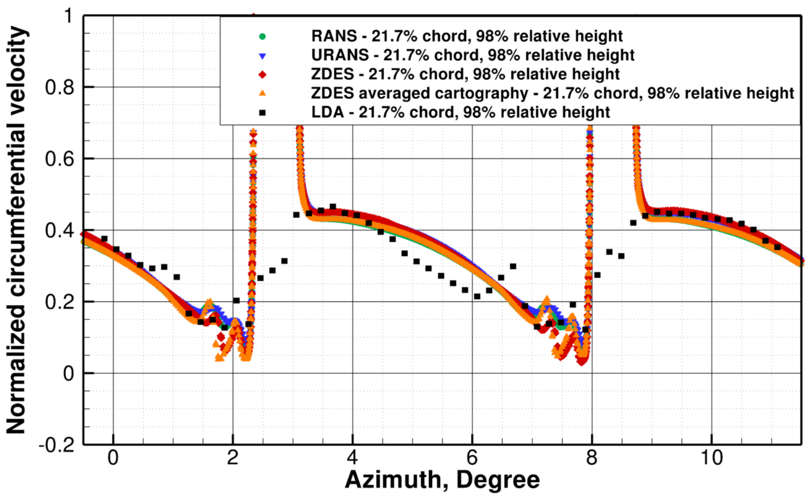

(b) Circumferential.

Figure 6.13 — *Axial and circumferential velocities at 21.7% chord and 98% relative height for RANS, URANS, ZDES with rotating distortion, ZDES with averaged cartography and LDA measurements.*

Near the trailing edge, at 91% X/C and 90% of relative height, the axial velocity, plotted in figure 6.15(a) shows that the influence of the IGV wakes declines downstream. Indeed, the discrepancy decreases between the ZDES computations with or without the periodic arrival of the IGV wakes. Nonetheless, the position of the tip-leakage vortex is more brought out in the case with the averaged map. Therefore, the resulting curve is further from the experimental measurements. Indeed, the vortex is wider experimentally. Moreover, it was proven in chapter 5 that the difference between the experimental values and the ZDES computations originates mainly from a different operating point.

The circumferential velocity, plotted in figure 6.15(b) reveals a major difference, not seen for the axial velocity. The rotating motion of the more coherent main tip-leakage vortex increases the levels of the circumferential velocity near the blade at azimuth 4. As a result, there is a distinctive difference between, on the one hand the computations with the rotating distortion, and on the other hand, the computations with the averaged cartography. This distinction is clearly due to the inlet condition, since two singular behaviours are distinguishable. This is highlighted by the circumferential velocity near the

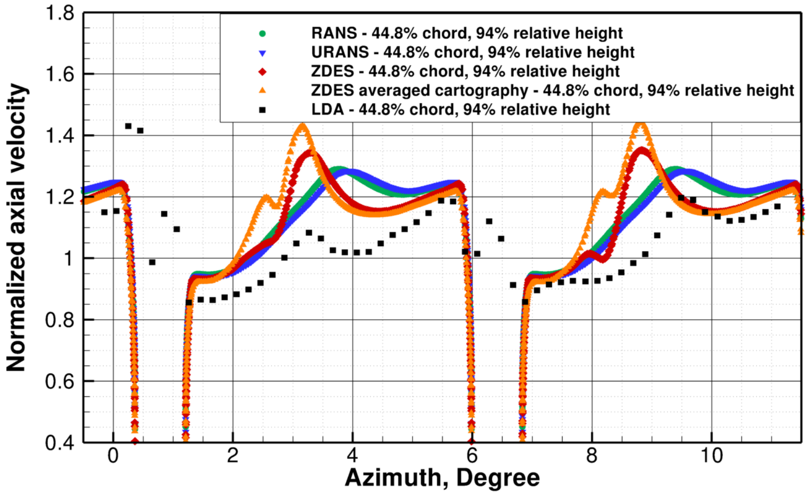

(a) Axial.

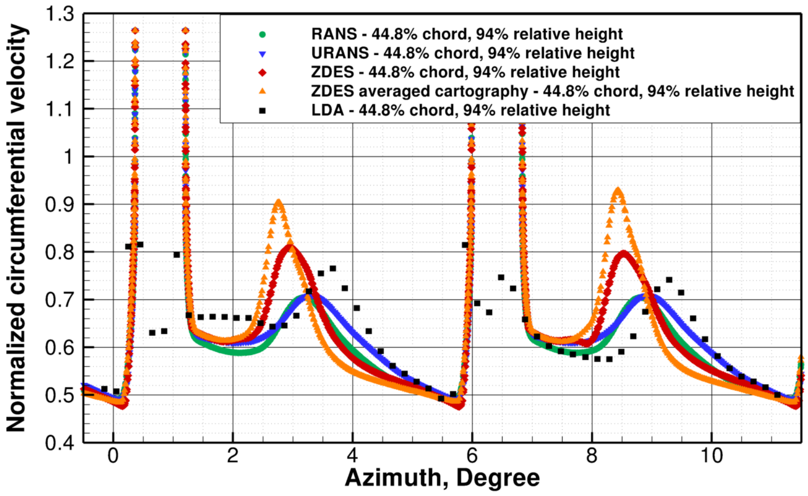

(b) Circumferential.

Figure 6.14 — *Axial and circumferential velocities at 44.8% chord and 94% relative height for RANS, URANS, ZDES with rotating distortion, ZDES with averaged cartography and LDA measurements.*

blade, at azimuth 3.5-4 in the first channel and azimuth 9-9.5 in the second one and thereby corroborates the existence of a more intense double leakage with an averaged map. Indeed, the circumferential velocity is increased compared to the cases with the rotating distortion. The ZDES with an averaged map captures even a positive peak in this zone, corresponding to the increased inlet flow into the tip gap. This increased circumferential flow is perceptible locally at azimuth 3.75 in figure 6.15(b), even for the ZDES computation with the rotating distortion, albeit weaker since the tip-leakage vortex is less coherent. On the other side of the blade, there is a jet flow leading to higher axial velocity values in the averaged map cases, from azimuth 0.5 to 3 and from azimuth 6 to 8.5. This jet flow actually occurs along the chord and causes the secondary tip-leakage vortices, as it was seen in figure 6.7. For the ZDES computation with the averaged map, the increased circumferential velocity value and peak at this azimuth results in a stronger double leakage phenomenon which amplifies this jet flow. In other words, without the unsteadiness from the IGV tip vortex, the rotor tip-leakage vortex would reach the adjacent blade, increase the mass flow within the tip gap and result in secondary tip-leakage vortices with a higher energy. This phenomenon would affect the rotor performances.

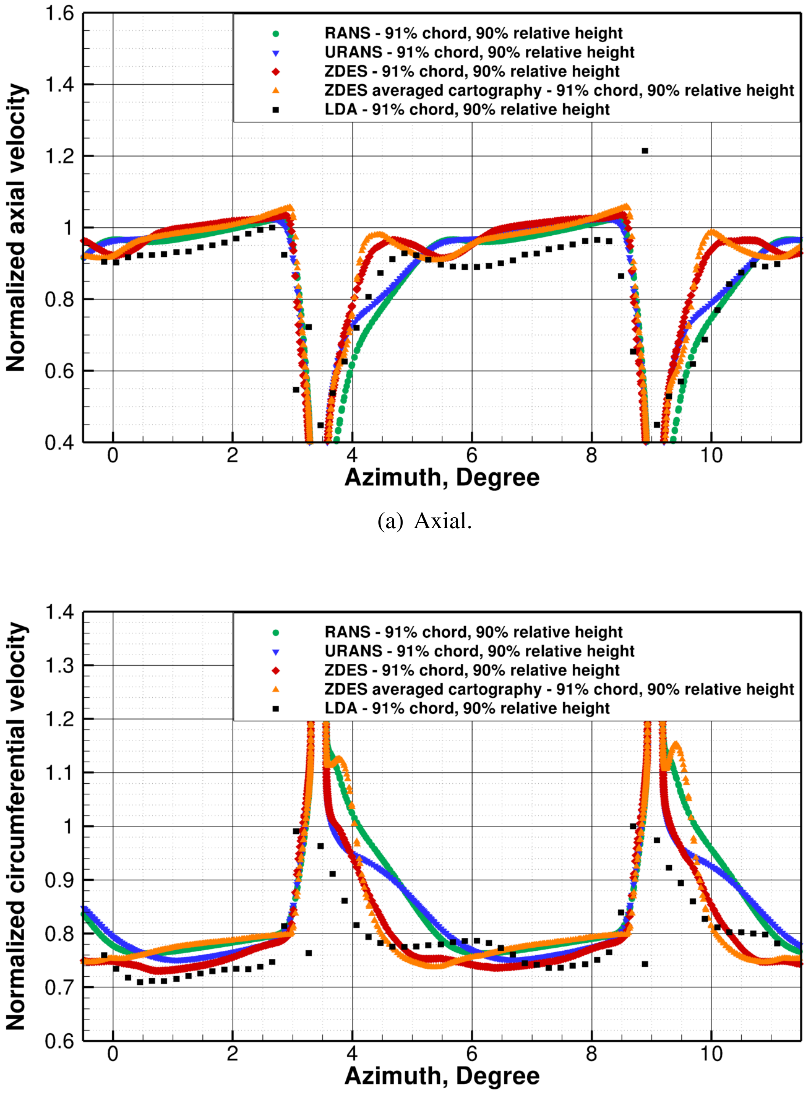

Figure 6.15 — *Axial and circumferential velocities at 91% chord and 90% relative height for RANS, URANS, ZDES with rotating distortion, ZDES with averaged cartography and LDA measurements.*

Finally, the velocities at section 26A and 90% of relative height are compared in order to verify the influence downstream the rotor. Figure 6.16(a) shows the axial velocity. Between the azimuthal positions of the R1 wakes, there is no visible impact from the inlet boundary condition. This is coherent with the trend observed along the chord and especially in figure 6.15(a).

Nevertheless, the IGV wakes influence the wakes from the rotor. Indeed, close to the azimuthal positions of the R1 wakes, the difference can reach up to 5% of the axial velocity value. Moreover, another behaviour can be related to the inlet boundary condition, since it is experienced by both the RANS computation and the ZDES with the averaged map. This behaviour is an azimuthal shift of the R1 wakes as well as a higher velocity within the wakes. There is even a peak within the R1 wakes for the ZDES with the averaged map. This can be explained in the same way as the difference underscored for the different topologies of the tip-leakage flow previously seen. Without the impulsions from the IGV wakes, the rotor wakes are not disturbed. Thereby, they extend further azimuthally. The difference in the velocity value originates from the axial momentum deficit of the IGV wakes. Nonetheless, since the

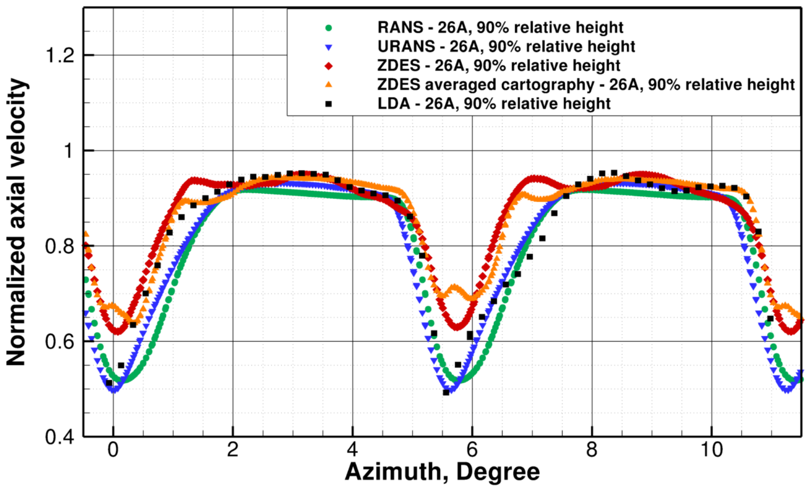

(a) Axial.

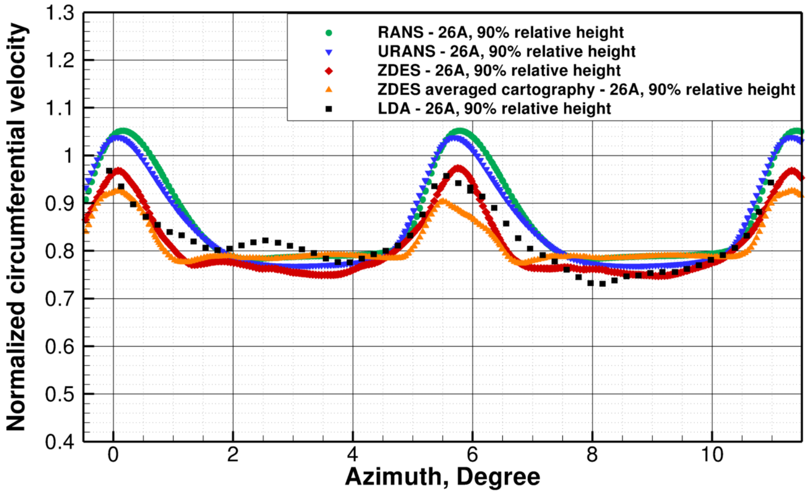

(b) Circumferential.

Figure 6.16 — *Axial and circumferential velocities at section 26A and 90% relative height for RANS, URANS, ZDES with rotating distortion, ZDES with averaged cartography and LDA measurements.*

visualized values are averaged, there could be no difference between the two inlet boundary conditions. Indeed, the inlet averaged boundary condition is based on the same 2D map as the rotating distortion. However, it seems that the complexity of the interaction between the IGV and R1 wakes, as well as between the IGV wakes and the tip-leakage vortex, can not be simplified with the averaged cartography, hence the necessity to take the IGV wakes into account for an accurate simulation.

The circumferential velocity at this position is presented in figure 6.16(b). Its value within the wake is less important in ZDES with the averaged map than with the unsteady inlet condition, contrary to the difference between RANS and URANS. By contrast, its level is uniformly higher in between the wakes contrary to the cases with the rotating distortion. Moreover, the step captured by the reference ZDES computation around azimuth 2, and experienced by the LDA around azimuth 2.5 is not encountered without the IGV wake arrival. Therefore, it seems that the aforementioned increased jet flow with the averaged map influences downstream most of the passage and not only where there is the tip-leakage vortex.

6.3.3 Azimuthal distribution of the velocity standard deviations

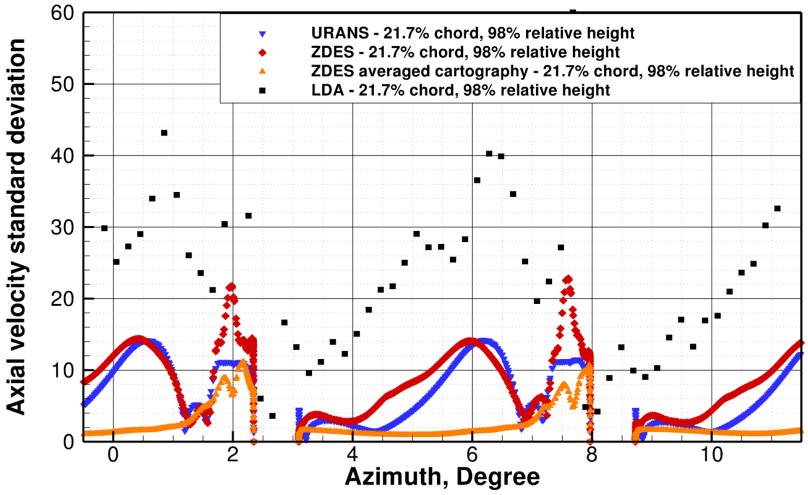

(a) Axial.

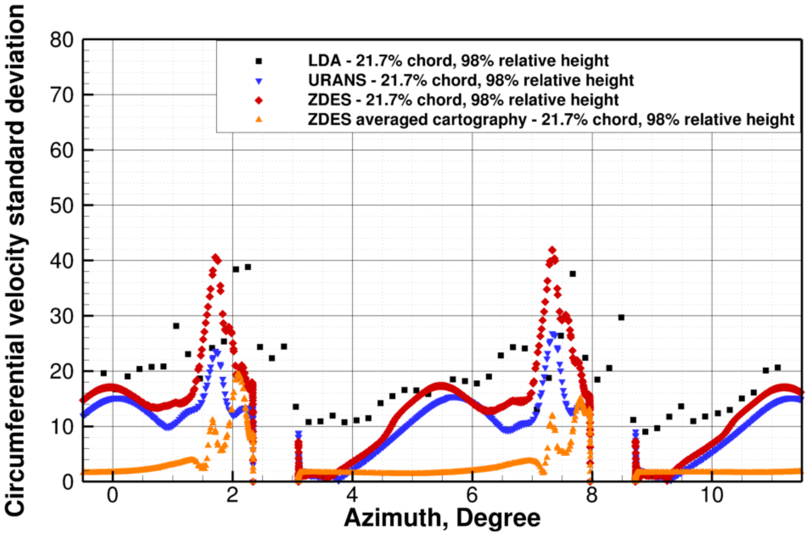

(b) Circumferential.

Figure 6.17 — *Axial and circumferential velocity standard deviations [in $m.s^{-1}$] at 21.7% chord and 98% relative height for URANS, ZDES with rotating distortion, ZDES with averaged cartography and LDA measurements.*

The unsteadiness within the flow is then compared for the same positions with a view to better understand the interactions occurring within the blade passage and downstream. To this end, the azimuthal distributions show the standard deviations of the axial and circumferential velocities. The RANS computation is not displayed within these comparisons, since it is a steady approach.

First of all, the unsteadiness is evaluated near the leading edge of the R1. The axial velocity standard deviation is plotted in figure 6.17(a) for the different azimuthal positions at 21.7% X/C and 98% of relative height. As expected, the case with the averaged cartography has the lower unsteadiness. Nonetheless, the values for the axial unsteadiness are close to $2m.s^{-1}$ from azimuth 4 to azimuth 7. Therefore, there is almost no unsteadiness around azimuth 6 contrary to what is experienced by the LDA, the URANS, and the ZDES with the rotating distortion. As a consequence, the major part of the flow field is stable

without the IGV wakes. However, the unsteadiness rises to reach $10 m.s^{-1}$ at azimuth 8. The area that expends from azimuths 7 to 8 is experienced by the three computations, albeit the unsteadiness is clearly lower with the averaged map. In this zone, the boundary layer on the blade side and the tip-leakage vortex interact, hence this high unsteadiness. Notwithstanding this interaction, the tip-leakage vortex is stable.

The circumferential velocity is shown in figure 6.17(b) for the same position. One can see that there is no unsteadiness in the circumferential direction throughout the whole passage, except close to the blade as it is the case for the axial velocity standard deviation. The unsteadiness levels without the IGV wakes are up to nine times less than with the rotating distortion. This proves that near the leading edge, the instability within the flow close to the shroud originates mainly from the arrival of the IGV tip vortex.

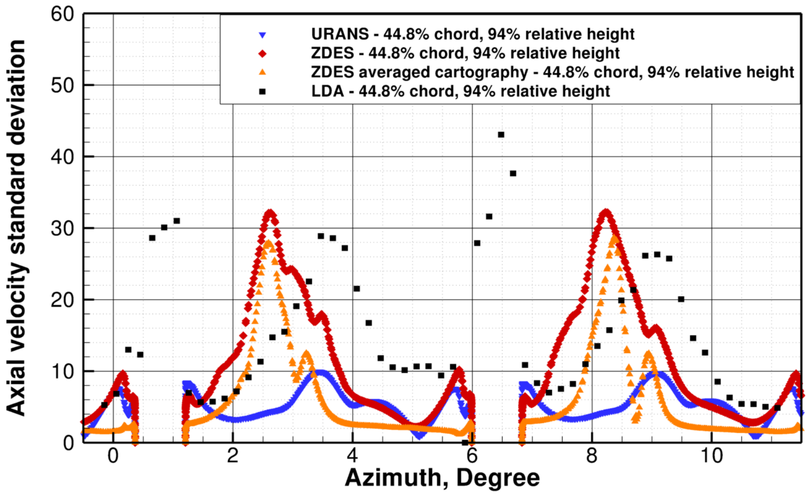

(a) Axial.

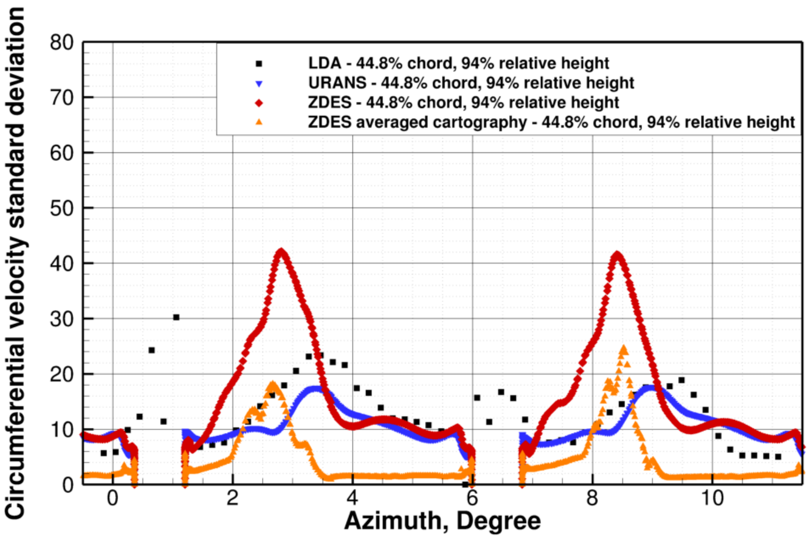

(b) Circumferential.

Figure 6.18 — *Axial and circumferential velocity standard deviations [in $m.s^{-1}$] at 44.8% chord and 94% relative height for URANS, ZDES with rotating distortion, ZDES with averaged cartography and LDA measurements.*

Downstream, at 44.8% X/C and 94% of relative height, the axial velocity standard deviation highlights a more complex pattern, presented in figure 6.18(a). First, without the IGV wakes, the high un-

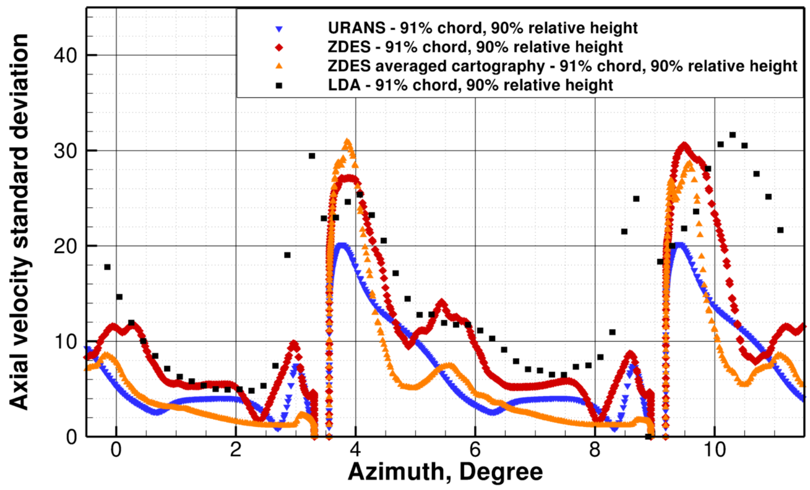

(a) Axial.

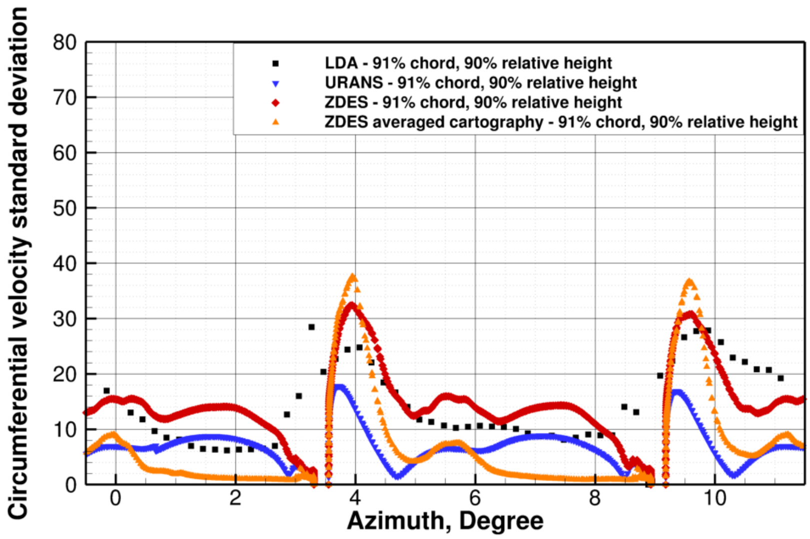

(b) Circumferential.

Figure 6.19 — *Axial and circumferential velocity standard deviations [in $m.s^{-1}$] at 91% chord and 90% relative height for URANS, ZDES with rotating distortion, ZDES with averaged cartography and LDA measurements.*

steadiness area near the blade at azimuth 5.5 is scarcely perceptible contrary to what is seen experimentally and with the two other computations. In the computational cases with the rotating distortion, there is a peak at azimuth 5.5 combined with a rapid and localized drop at azimuth 5. This is not experienced by the LDA that sees a constant and higher value at $10m.s^{-1}$ from azimuths 4.5 to 5.5, that is to say close to the blade. The fact that the experiment captures higher values without this local drop comes from the operating point, as already underlined in chapter 5 in figure 5.22(a).

Second, without the IGV wakes, two peaks are distinguishable. The first one is located at azimuth 2.5, with $28m.s^{-1}$ for its maximum value. The second has a lower unsteadiness value of $12m.s^{-1}$, which shows that it is more stable axially, and is located at azimuth 3.2. They correspond to the main tip-leakage flow and to the induced vortex, or more accurately to the separation of the boundary layer at the casing, visible in figure 6.7(b). Thanks to the averaged cartography, the effects of the vortices stand out from the unsteadiness of the flow. The azimuthal range over which the zone of high unsteadi-

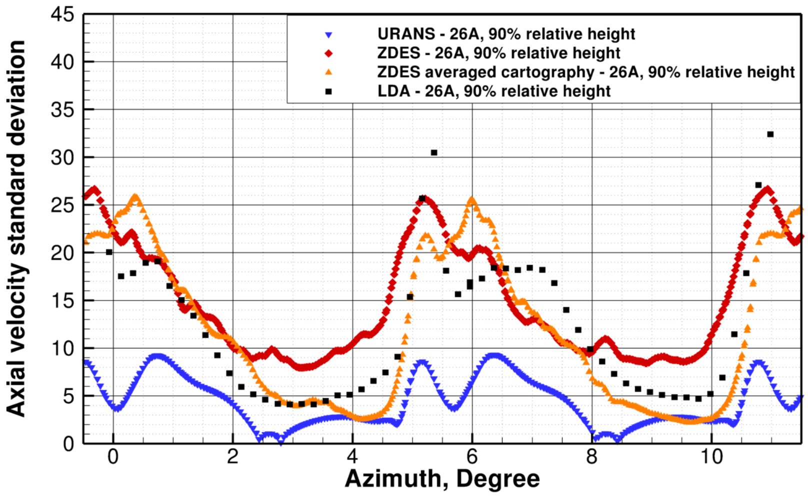

(a) Axial.

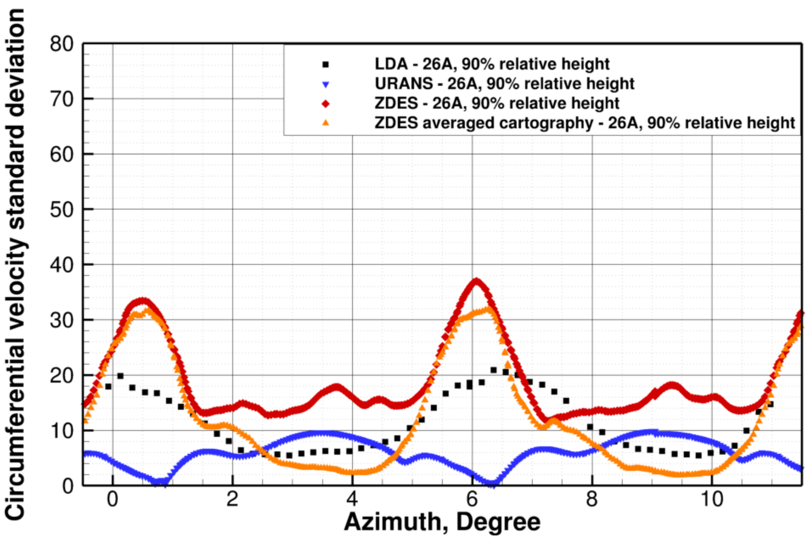

(b) Circumferential.

Figure 6.20 — *Axial and circumferential velocity standard deviations [in $m.s^{-1}$] at section 26A and 90% relative height for URANS, ZDES with rotating distortion, ZDES with averaged cartography and LDA measurements.*

ness spreads is narrower with the averaged map. Besides, this is clearly too narrow compared to the experimental peak. This is expected since there are periodic wakes experimentally. The peak visible on the experimental values is located at a different position : azimuth 3.5. This is due to the difference of operating point underscored in chapter 5. Its value nonetheless corresponds to the one captured by the ZDES computations, either with or without the IGV wakes. The second peak is yet not experienced by the LDA, certainly because of the higher unsteadiness levels throughout the channels.

The circumferential velocity standard deviation, presented in figure 6.18(b) shows the same narrow peak as for the axial velocity standard deviation. Nonetheless, the maximum value is almost halved without the wakes. This proves that the circumferential unsteadiness observed at this axial position comes mainly from the arrival of the wakes from the IGV and their interaction with the flow near the casing. Moreover, the azimuthal position of this peak is more localized, because there is no periodic azimuthal shift due to the arrival of the IGV tip vortex and its stretching of the boundary layer developing

at the casing, as highlighted in figure 6.8. Finally, the boundary layer separation at the casing influences greatly the circumferential unsteadiness at this axial position since the circumferential velocity standard deviation of the case without the IGV wakes has levels close to 0 throughout the channel excepted where there is this separation.

The axial velocity standard deviation is plotted for a position closer to the trailing edge, at 91% X/C and 90% of relative height, in figure 6.19(a). First of all, its value near the blade, from azimuth 8 to 9, is four times less than with the IGV wakes. Therefore, the ZDES with the averaged map does not see the local drop in the unsteadiness at azimuth 8, although the URANS and ZDES case with the rotating distortion experience it. The axial velocity standard deviation value rises only at the position of the tip-leakage vortex, which rim is located at azimuth 5.5. Nonetheless, it still has a lower axial unsteadiness compared to the ZDES with the rotating distortion and the LDA measurements. The URANS approach barely captures it, as already explained in chapter 4. In the vicinity of the blade, at azimuth 4 or 9.625, the unsteadiness levels for the case with the averaged map are close to the ones for the ZDES with the IGV wakes. Depending on the considered channel, the peak value is higher or lower. This shows that there is no impact from the IGV wakes on the axial unsteadiness in the inlet region of the double leakage.

By contrast, the circumferential velocity standard deviation is clearly increased in this region as shown in figure 6.19(b), at azimuths 4 and 9.625. Thereby, the IGV wakes decreases the unsteadiness, as well as the intensity of the double leakage, as shown in figure 6.15(a). Similarly to what is observed with the axial unsteadiness, the only other position with a high circumferential unsteadiness are azimuths 0 and 5.625, in other words, the rim of the tip-leakage vortex.

Further downstream, at section 26A and 90% of relative height for the case with the averaged map, the profiles for the two velocity standard deviations, axially or circumferentially, are close to what is observed experimentally. For instance, the axial component is presented in figure 6.20(a). There are low levels, around $5m.s^{-1}$ in between the wakes from the R1. This is closed to what is experienced by the URANS computation at these location. Therefore, the values for the ZDES with the averaged map are in good agreement with the LDA at azimuths 2.5 to 5. Besides, there is a light azimuthal shift, by 0.5 degrees with the averaged cartography. Finally, the unsteadiness levels within the R1 wakes are the same as for the ZDES case with the IGV wakes, albeit the azimuthal range over which the R1 wakes expand is narrower. Therefore, the unsteadiness becomes in better agreement with the experiments than the reference ZDES computation with the rotating distortion.

Likewise, the circumferential velocity standard deviation plotted in figure 6.20(b) shows the same lower unsteadiness levels in between the R1 wakes. However, there is no azimuthal shift of the peaks corresponding to these wakes. Besides, the values are in better agreement with the LDA measurements for the circumferential unsteadiness in the case with the averaged map.

The analysis of this last axial position corroborates the fact that the vortices simulated with the implemented rotating distortion are too important compared to what occurs experimentally. As a conclusion, this proves that the approximations made to simulate the IGV have an important impact on the flow field, even downstream the rotor.

6.4 Spectral analysis

In this section, spectral analysis are carried out within the flow field in order to understand the impact of the IGV wakes on the energy and to distinguish the effects linked only to the tip-leakage vortex.

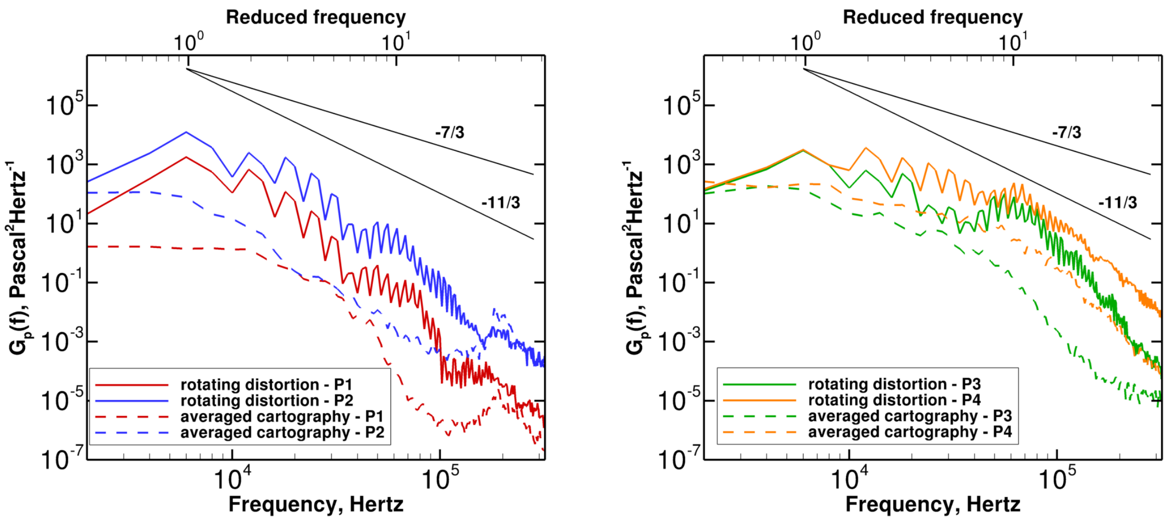

(a) Probes 1 and 2.

(b) [Probes 3 and 4.

Figure 6.21 — *Power spectral density of static pressure for probes along the main tip-leakage vortex. ZDES with the averaged cartography and ZDES with the rotating distortion.*

6.4.1 Influence of the IGV wakes on the energy levels along the tip-leakage vortex

First of all, a spectral analysis is carried out for probes located along the main rotor tip-leakage vortex so as to better understand the physics involved. Only the two ZDES computations at the design point are compared here: the one with the rotating distortion, and the one with the averaged map.

The four probes are located at 98% relative height for different axial positions along the core of the main rotor tip-leakage vortex as presented in chapter 4 in figure 4.30 with the instantaneous Schlieren at 98% relative height and t=3T/4. The probes 1 and 2 are respectively located at 11% and 22.5% X/C. The probes 3 and 4 are located at 33.8% and 45.7% X/C. This means that probes 1 and 2 are upstream the vortex disruption contrary to probes 3 and 4.

The Power Spectral Density (PSD) represents the flow energy distribution. The normalized PSD shows the contribution to the total energy of the different frequencies. Each of them brings a different information on the way the energy is distributed over the frequencies. The PSD functions, $G_p(f)$, are plotted for the probes 1 and 2 in figure 6.21(a) and for 3 and 4, in figure 6.21(b). The normalized PSD functions are plotted for the probes 1 and 2 in figure 6.22(a) and for 3 and 4, in figure 6.22(b).

The main visible difference between the two computations stems from the energy of the IGV tip vortex, which is convected periodically at the IGV Blade Pass Frequency (BPF). Therefore, at the BPF, which is 6156 Hz, and at its harmonics, the whole energy is higher in the case with the rotating distortion as seen in the PSD in figure 6.21. This changes the energy distribution along the frequency bands. Nevertheless, the low frequency phenomena are the limiting factors in the analysis of these computations since the frequency resolution (FR) is 2000 Hz.

The energy level increases for every frequency from probe 1 to probe 2, as highlighted in figure 6.21(a). It arises from the rotor tip-leakage vortex initial development, from a weak jet flow at probe 1 to a full vortex at probe 2. This is the case for both computations. Without the wakes, the slope follows clearly a $k^{-11/3}$ slope at probe 2, which characterizes the interaction between the turbulence and the mean-shear in the inertial subrange [59]. This is distinguishable from the lowest captured frequencies to 20 BPF. However, this interaction does not seem to occur at probe 1 without the IGV wakes, since this slope is not found on the PSD, and the curve can be divided into 3 parts. First, the low frequencies have a lower energy, which is constant up to 2 BPF. Then, the energy level is close to the one for probe

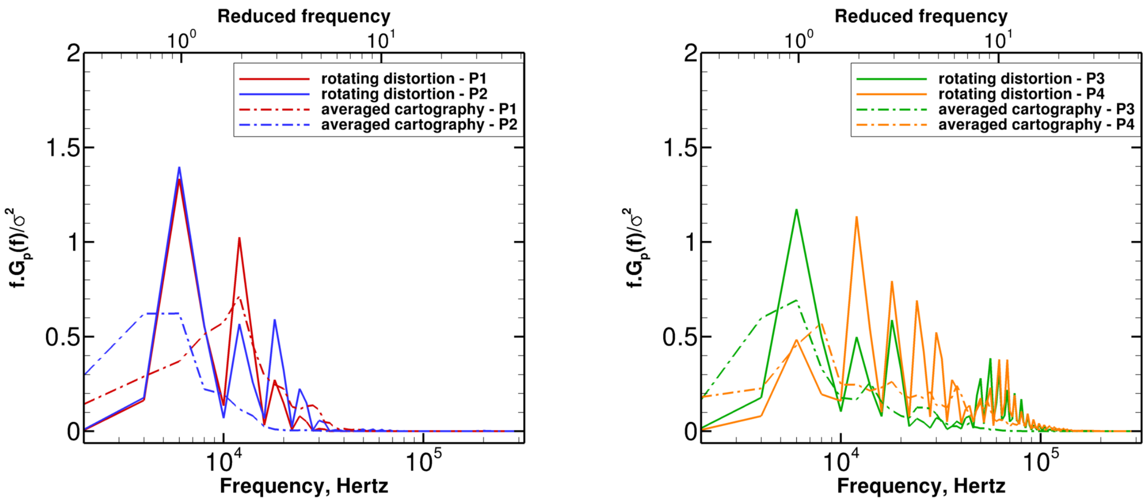

(a) Probes 1 and 2.

(b) [Probes 3 and 4.

Figure 6.22 — *Normalized power spectral density of static pressure for probes along the main tip-leakage vortex. ZDES with the averaged cartography and ZDES with the rotating distortion.*

2 at 4 BPF, which marks the inflection point of the curve. The second part reveals a rapid drop in the energy within the flow from 2 BPF to 20 BPF. In the third part, a high frequency phenomenon stands out for the ZDES with the averaged map. This is almost invisible behind the high energy of the BPF harmonics for the ZDES with the rotating distortion, in figure 6.21(a). This phenomenon, at 200000 Hz, has nevertheless almost no contribution to the whole energy as underlined by figure 6.22(a). Its frequencies are lowered from probe 1 to probe 2 which tends to signify that the size of this phenomenon grows as the main tip-leakage vortex develops.

Another interesting difference between the computations is the local rise in the energy of the BPF harmonics in the 50000 - 100000 Hz frequency range, that occurs only for the case with the rotating distortion. Nevertheless, the contribution from these frequencies to the whole energy is limited upstream section 31% X/C as shown in figure 6.22(a).

For the computation with the rotating distortion, the second harmonic of the BPF has its energy contribution almost halved between probe 1 and probe 2 as plotted in figure 6.22(a). Higher harmonics supersede its contribution. The first harmonic has however the main contribution to the whole energy near the casing before the vortex disruption. With an averaged map, the energy focuses on the low frequencies, as seen in figure 6.22(a). Indeed, probe 1 has its main contribution around the second BPF harmonic, which can be explained by the lack of frequency resolution regarding the contribution spread around 10000 Hz. Then, probe 2 has its main energy contribution between 4000 Hz and 6000 Hz, and the BPF does not contribute to the whole energy. This is expected, since there is no wake arrival.

A different energy distribution is then observed downstream the section 31% X/C. The passage from probe 2 to probe 3, that is to say, through the section where the vortex disrupts, has mainly an effect on the high frequencies between 50000 Hz and 100000 Hz for the computation with the rotating distortion. There is no such local increase for the case with the averaged map. By contrast, the energy transfer to the high frequencies is more evenly distributed. So, there seems to be a privileged frequency range for the BPF harmonics, around 75000 Hz or around 10 BPF, linked to the periodic arrival of the IGV tip vortex. Figure 6.22(b) proves that this frequency range has not only a high energy but contributes greatly to the whole energy spectrum downstream section 31% X/C. Furthermore, its contribution to the whole energy appears only after the vortex disruption even if it was already detected in the PSD upstream near 75000 Hz in figure 6.21(a). Finally, the BPF contribution almost halves between probe 3 and probe 4, as shown in figure 6.22(b). The contribution to the whole energy from low frequencies is then more superseded by higher frequencies, greater than 40000 Hz, and centred around 10 BPF, than before the vortex disruption with a major supply from BPF harmonics of high order. This confirms the high influence of the IGV tip vortex on the rotor tip-leakage vortex disruption and emphasizes the energy linked to the interaction between these two vortices.

Without taking into account this phenomenon at 10 BPF, from probe 3 to probe 4, the energy is increased only for the high frequencies, as shown in figure 6.21(b). These high frequency phenomena may originate from all the smaller vortices seen with the Q criterion in figure 6.7: the ones generated as the main rotor tip-leakage vortex scatters, the secondary tip-leakage vortices and finally the turbulence. Moreover, it was seen in chapter 4 that this increase roots from the energy transfer towards the smallest structures and captured by the ZDES approach. Therefore, this is similarly experienced by the two ZDES computations.

6.4.2 Influence of the IGV wakes on the energy levels downstream

A final spectral analysis is carried out at section 26A, that is to say, downstream the R1. Two radial positions are appraised: at the casing and at 94% of relative height. The same azimuthal position is chosen to be within the wake of the R1 and at the rim of the tip-leakage vortex. This exact position is explained in chapter 4 in figure 4.28. The PSD from experimental unsteady probes are used as reference with two frequency resolution values: 2 Hz and 2000 Hz. The latter value is the same frequency resolution as for the computations.

First of all, the PSD for the probes at the casing, so in the boundary layer, are plotted in figure 6.23(a). In the case with the averaged cartography, as expected, the energy of the BPF and its harmonics is not captured. Therefore, the energy of the flow is lower. Nevertheless, one can see that the discrepancy is localized in the left part of the spectra. The use of an averaged map instead of the rotating distortion results in a major change in the energy for low frequencies only. Indeed, the spectrum is almost flat up to 30000 Hz without the IGV wakes, hence a lower energy level. By contrast, the BPF, as well as its first harmonics stand out in the ZDES case with the rotating distortion. However, the energy levels for the highest captured frequencies are the same with or without the IGV wakes. This confirms that the ZDES is not able to correctly capture the energy levels of the highest frequencies within the boundary layer, as shown in chapter 4.

Figure 6.23(b) shows the PSD at 94% of relative height, that is to say, outside the boundary layer. It must be emphasized that the plotted values for 94% relative height correspond to static pressure data for the computations while total pressure measurements are used for the experimental data. The spectra from the computations are close to the ones at the casing. However, at this position, some relevant discrepancies between the two presented ZDES cases have to be highlighted.

First, and contrary to the casing, there is a difference for the highest frequencies greater than 200000 Hz or 30 BPF. Indeed, the energy levels for these frequencies are lower with the averaged map. This is coherent with the trend noticed along the vortex, in figures 6.21(a) and 6.21(b). This corroborates that the ZDES approach is more capable to simulate the complex flows in its LES region than in its URANS region, since it captures this difference here.

The second important point is denoted by the peak around 3 BPF or 20000 Hz with the averaged map. The exact frequency is unknown due to the limitations of the frequency resolution for the ZDES computations. Nonetheless, this underlines that there is a phenomenon linked to the tip-leakage flow topology associated to these frequencies. Moreover, it was shown in chapter 5 in figure 5.25(a) that this phenomenon has its energy increase near surge. Thereby, this analysis proves that it exists at the design point too, and is not correlated to the IGV wakes. Therefore, this is should be an effect inherent to the tip-leakage flow.

The third point to notice is the similarity with the experimental curve for the case with the averaged map. Indeed, the experimental PSD with 2000 Hz as frequency resolution has few pronounced peaks. Notwithstanding the difference of about 2.5 orders of magnitude, that is almost constant throughout the frequencies, the spectrum of the experimental probe is close to the spectrum for the ZDES with the averaged map. This corroborates the fact that the IGV gaps, approximated in the preliminary study, are too important and overestimate the effects of the IGV tip vortex and IGV hub vortex. Besides, this confirms that the ZDES approach captures correctly the trend of the energy spectra, at least when the flow is computed in the LES zone of the method.

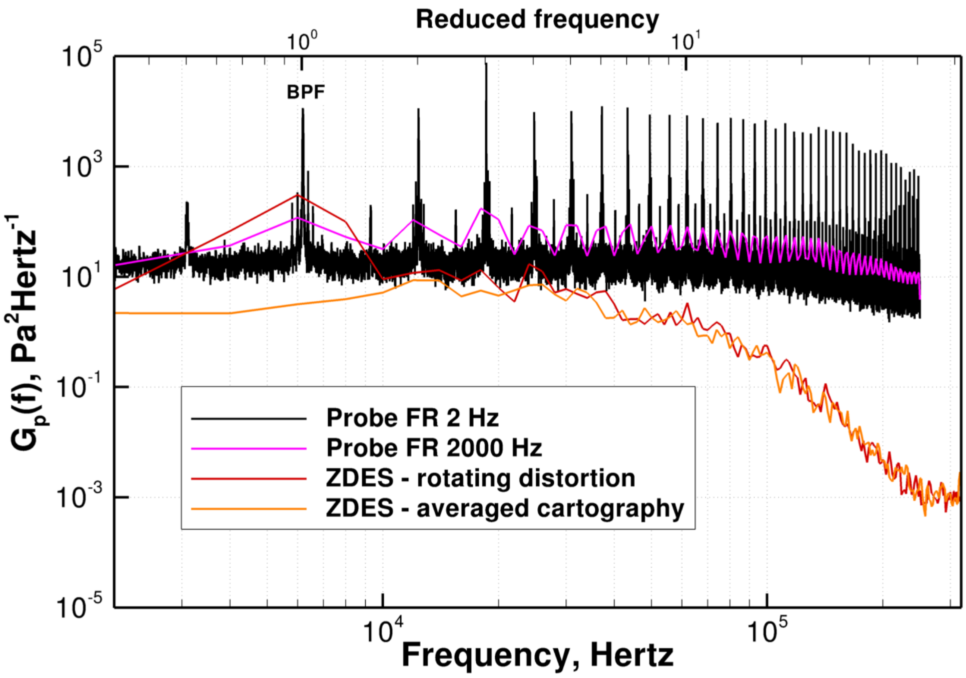

(a) At the casing.

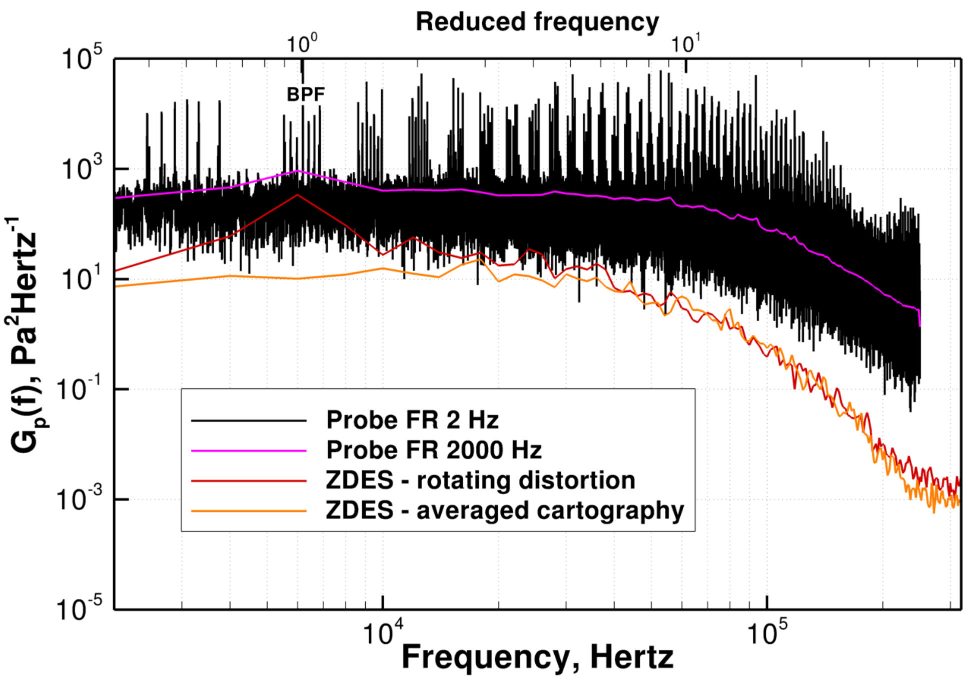

(b) At 94% relative height.

Figure 6.23 — *Power spectral density of pressure at section 26A. ZDES with averaged cartography, ZDES with rotating distortion and data from unsteady probes.*

6.5 Synthesis

In this chapter, the effects of the IGV wakes on the tip-leakage flow is assessed through a comparison of two ZDES computations with two different inlet conditions: one with a rotating distortion and one with the same cartography but azimuthally averaged.

The periodic arrival of the rotating distortions from the IGV wakes changes the performance of the rotor. Indeed, it increases the pressure ratio as well as the mass flow rate in the R1. The effects are mainly localized near the hub and the casing because the IGV hub and tip vortices have the main impact on the flow field. By comparison, the classic IGV wake only impulses a frequency, and has a weak influence on the flow at mid span. The preponderance of the hub and tip vortices from the IGV is due to their strong interactions with the phenomena occurring around the R1 blade, respectively the corner effect and the tip-leakage flow. The main noticed interaction near the shroud is a flutter phenomenon of the main tip-leakage vortex. This originates from the periodic arrival of the IGV tip vortex that stretches the tip-leakage vortex. Moreover, the secondary tip-leakage vortices migrate from the trailing edge toward the leading edge of the blade because of the deficit of axial momentum within the IGV tip vortex. Then, once close to the main rotor tip-leakage vortex, their direction changes and they roll up around it. This behaviour is not experienced with the averaged map, and the position of the secondary vortices remains stable.

When the unsteady effects of the IGV are not taken into account, the topology of the flow near the casing differs. The tip-leakage vortex is still coherent near the pressure side of the adjacent blade, since it is not disrupted by the IGV tip vortex. Thereby, its rotation increases the mass flow rate inside the gap of the adjacent blade. This amplifies the phenomenon of double leakage. Moreover, the fact that the tip-leakage vortex is more coherent and has a higher rotating momentum leads to a more important separation of the boundary layer developing at the casing. This two phenomena increase the pressure losses within the blade and thus decreases the pressure ratio for the rotor. As a result, this changes the computed operating point.

The arrival of the IGV wakes also influences the flow downstream, albeit the effects are less pronounced than within the blade passage. The IGV wakes interact with the wakes from the R1. As a consequence, the R1 wakes are shifted azimuthally.

The analysis of the unsteadiness within the flow highlights that, with the rotating distortion, there is an overestimation of the effects of the vortices from the IGV, which corroborates what was seen in chapter 3. Therefore, a part of the discrepancies observed between the ZDES computation with the rotating distortion and the LDA measurements originates from the approximations made to define the inlet boundary condition. This is supported by a spectral analysis at section 26A. As a consequence, the capability of the ZDES approach to simulate the complex flows encountered in axial turbomachines is confirmed.

Finally, the spectral analysis along the main tip-leakage vortex underlines that the interaction between the IGV wakes and the tip-leakage vortex influences the energy levels downstream the vortex disruption. This comes not only from the higher energy due to the wakes. Indeed, this is indicated by privileged BPF harmonics around 10 BPF that have an important contribution to the whole energy of the flow after the disruption.

A part of the analysis detailed in this chapter was presented at the ASME Turbo Expo 2013 [140] and is the subject of an article in the Journal of Turbomachinery [141].

Conclusion and outlook

Conclusion

This study consisted in appraising what modern advanced numerical methods can bring for a more accurate simulation of the tip-leakage flow in axial compressors. This purpose is then divided into two main objectives. The first one is the choice and validation of an advanced numerical method for the simulation of the tip-leakage flow in a realistic configuration. The second objective is the use of this method to understand the flow physics near the casing for a rotor, especially the effects of the Inlet Guide Vane (IGV) and throttle on the tip-leakage flow.

First of all, a review of the literature was conducted in chapter 1. It highlighted the impact of the tip-leakage flow on the stability and performance of compressors. Besides, it underlined the advantages and drawbacks of the existing methods used to take this flow into account when designing new turbomachines. Finally, it presented some of the configurations, close to the tip-leakage flow, upon which the ZDES approach was already applied.

Then, chapter 2 introduced the methods involved in this study to carry out the different numerical simulations. Moreover, it gave an overview of the experimental test bench: CREATE.

In chapter 3, the Zonal Detached Eddy Simulation approach (ZDES) was chosen to compute the flow in the first rotor (R1) of the axial compressor CREATE for its beneficial capability/cost ratio in the simulation of external flows. However, it was not yet used in turbomachinery. Therefore, in order to evaluate the capability of the method for the simulation of the tip-leakage flow, a numerical test bench was defined. With an eye to simulate the effects of the incoming wakes from the IGV, the inlet boundary condition was a rotating cartography of the flow, extracted from a preliminary study in RANS. The effects of the main IGV wake, as well as the IGV tip vortex and the IGV hub vortex, were taken into account by this boundary condition. The numerical test case followed the mesh requirements for a ZDES computation. Indeed, the area upstream the blade had a fine RANS type mesh, and the zone from the leading edge to the outlet had a DES-type mesh, that is to say, a LES-type mesh except on the walls.

An important aspect of this study was that the same numerical test case was used for all the presented computations on the R1, with similar numerical methods for time and space discretization. Moreover, the same value was used for the pivot pressure at the outlet boundary condition. This pivot pressure was defined so that the radial distribution of the axial momentum from the computations match the experimental values. As a consequence, the main difference between the computations was the chosen approach: a steady RANS, an unsteady RANS (URANS) and the ZDES method. Nonetheless, the RANS computation used an azimuthally averaged map of the rotating cartography applied to the URANS and ZDES computations.

These different computations were compared in chapter 4. The results were assessed with the help of experimental measurements conducted on the experimental compressor. The ZDES method was then validated from the level 1 up to the level 4 of the methodology defined by Sagaut and Deck [146], that is to say, up to a spectral analysis. It highlighted that the limitation of the ZDES approach originates mainly from the RANS model it is based on in the boundary layer. Nevertheless, this did not prevent the ZDES method from correctly capturing the different phenomena occurring near the casing, such as the interaction between the light shock and the tip-leakage vortex, the separation of the boundary layer at the casing, or the secondary tip-leakage vortices. The ZDES method captured more accurately the position as well as the intensity of the vortices, especially the main tip-leakage vortex, than the RANS and even the URANS approaches. A spectral analysis carried out underscored that the better capability of the ZDES approach mainly stems from the fact that, downstream the vortex disruption induced by the shock, it correctly transferred the energy from the large structures to the smallest ones. Then, the dissipation occurred in a second step. By contrast, the URANS approach dissipated rapidly the large structures downstream the shock. This energy transfer difference came from erroneous interactions between the large vortices and the turbulence in URANS, contrary to the ZDES. A side effect of this different behaviour was that the numerical operating points computed by the RANS and URANS approaches, that were close to one another, differed from the operating point experienced by the ZDES method.

Above the validation of the ZDES method in turbomachinery, this study emphasized two difficulties, linked to the boundary conditions, which are amplified with the use of this advanced numerical method. The first difficulty is the choice of the right operating point when computations are set against experiments. Indeed, the differences between the URANS and ZDES approaches, for the simulation of the unsteady phenomena encountered near the casing, led to a different operating point even if all the boundary conditions were identical. As expected, the effects of secondary flows within the turbomachine changed with the operating point. The second difficulty comes from the influence of the incoming distortions. The approximations made for the IGV hub and tip gaps led to amplified interactions of the resulting vortices with the phenomena occurring in the vicinity of the rotor, such as the tip-leakage vortex, the boundary layer separation at the casing, the R1 wakes or the corner effect. These interactions are underestimated in URANS, not in ZDES. Since the ZDES captured more accurately the secondary flows, it was more sensitive to all these changes than the URANS or RANS approaches.

These two difficulties have led to errors in the simulations carried out in this study. Nevertheless, the observed discrepancies with the experimental values are mainly due to the definition of the numerical test bench and are not attributable to the ZDES method. Therefore, all the different analysis carried out in this thesis instruct us on the good capability of the ZDES method to simulate unsteady flows in the axial turbomachines, such as the tip-leakage flow.

Once the ZDES approach was validated, it was used to appraise the effects of the throttle on the tip-leakage flow. In chapter 5, the numerical test bench was adapted to be representative of an operating point near the surge line. The inlet rotating distortion and the outlet pivot pressure were changed consequently. This was done in an iterative process that required the convergence of the averaged flow field in ZDES for each modification of the pivot pressure. Thereby, a ZDES computation near surge was carried out and then set against the ZDES at the design point. This confirmed that most of the discrepancies observed in chapter 4 between the ZDES and the experiment came from the definition of the operating point. In addition, this comparison highlighted that the tip-leakage vortex extended azimuthally and became wider near surge. Actually, this stemmed from the fact that the whole vortex topology near the casing was shifted upstream. Besides, some important phenomena were amplified near surge. For instance, the shock became stronger and its consequences on the flow field were more pronounced than at the design point. Moreover, the separation of the boundary layer developing on the shroud became massive, and the induced vortex more intense. This even led to a local inversion of the flow and disturbed the stability of the vortices. This inversion could lead to a blockage of the flow and could be the inception of the surge.

The last evaluated effect was the impact of the IGV wakes on the tip-leakage flow, presented in chapter 6. With a view to uncouple the influence of the IGV wakes and the phenomena inherent to the tip-leakage flow, two ZDES computations at the design point were compared. The first one was the ZDES with the rotating distortion as inlet boundary condition. The second one used the azimuthally averaged cartography, already implemented in the steady RANS computation. Thereby, the four computations at the design point could be compared, and the effects of the boundary condition stood out from this analysis. The main observed phenomenon was the interaction between the tip-leakage vortex and the IGV tip vortex. This IGV tip vortex stretched azimuthally the vortices near the casing of the R1 and led to the flutter of the tip-leakage vortex. Besides, when the axial momentum deficit of the IGV tip vortex reached periodically the R1, the positions of the secondary vortices migrated from the trailing edge of the blade towards upstream. Then, they rolled up around the main tip-leakage vortex and dissipated. Without the IGV wakes, the main tip-leakage vortex stayed more coherent up to the adjacent blade. Its rotation amplified the phenomenon of double leakage near the trailing edge. Another consequence of this enhanced coherence was the separation of the boundary layer at the casing that was more important. These two main effects led to poor performances of the rotor without the periodic arrival of the IGV wakes. Finally, this study confirmed that the rotating distortion defined in chapter 3 overestimated the effects of the IGV tip and hub vortices, because of the approximation made. Therefore, some of the discrepancies observed throughout this thesis between the ZDES computation with the rotating distortion and the experimental measurements rooted from the approximations made in the inlet boundary condition. This mainly originated from the approximations applied to the geometry of the IGV, with too important hub and tip gaps. This last study corroborated the capability of the ZDES computation to simulate these complex flows.

Outlook

The ZDES approach revealed to capture accurately the tip-leakage flow. Besides, it supplied considerable improvements over the methods based only on averaged Navier-Stokes equations, even for integral values. Nonetheless, the presented computations were carried out on a grid that comprises 88 million points in order to suit the constraints of this advanced numerical method. This is why it can not be widely used in the industry for the design of new turbomachines, at least not until a decade or two. Indeed, the trend in the design departments is to have results overnight, which is impossible in ZDES with the actual computational resources. Nonetheless, this has to be put into perspective, since this method demands less computational than DNS, LES and even some global hybrid URANS/LES methods such as the DDES, thanks to the possibility to use the mode = 0. It brings the capability of LES for detached flows at a lower computational cost. Despite its initial development for external flows, it can be adapted to different configurations thanks to its zonal approach, and this thesis proves it. This is the main strength of the ZDES approach. In a near future, it could be used occasionally when the RANS and URANS approaches fail. However, the understanding of the method as well as its intrinsic limitations is a prerequisite to any ZDES computation. Furthermore, it requires to know the flow *a priori* so as to choose the appropriate mode.

Concerning the ZDES applications, this thesis evaluated the ZDES in an axial compressor rotor. It would be interesting to appraise the method in radial turbomachines, since they are not subject to the same constraints, especially for the meshing.

Moreover, this work underlined that most of the limitations of the ZDES approach relate to the RANS model it is based on. This is appropriate for external flows but shows some drawbacks in turbomachinery, such as the tendency of Spalart-Allmaras to amplify the separation due to the corner effect, as already shown in RANS by Marty et al. [111, 112]. Thereby, it could be interesting to keep the ZDES approach and adapt it to the constraints of turbomachines by changing the RANS model. Such adaptation was already conducted with a k-ω turbulence model in an IDDES approach as explained by Shur et al. [153].

Another limitation of the method is that the boundary layer is always considered as turbulent with the current code. Recent transition model for RANS approaches have shown relevant results. This is the case for the γ-$\overline{Re_{\theta_t}}$ approach from Menter, successfully implemented for the k-ω turbulence model in *elsA* by Benyahia [8]. It would be interesting to evaluate the possibility to use such transition models in ZDES, and not only in mode = 0. Indeed, if it is implemented in the RANS part of mode = 2, this could be beneficial to simulate complex cases seen in low pressure turbines with the separation of the boundary layer, then its transition and finally its reattachment downstream. Such bubbles are difficult to simulate, even with the ZDES, since everything occurs within the boundary layer. Another possibility is the mode = 3 of the ZDES approach, where the boundary layer is treated in LES. This will require a thorough validation in turbomachinery.

Finally, it will be necessary, in the short term, to simulate stages in turbomachinery with advanced numerical methods. This requires high order schemes at the interface between stator and rotor, that are still to be coded.

This thesis highlighted that the tip-leakage flow is driven by complex interactions. Some are beneficial for the performance of the machine, such as the interaction observed between the IGV tip gap and the tip-leakage vortex. However, they tend to decrease the stability of the machine, hence their negative effect on the surge margin. The better comprehension of the way the vortices behave, brought by the ZDES approach, widens the possibility range to control the secondary flows [115] and therefore to improve the operability of the turbomachines. For instance, different control devices could be tested. An impulsed controlled jet, located upstream the leading edge of the blade in the casing, could increase the effects of the IGV wakes by disturbing the tip-leakage vortex at the design point in order to improve the performances of the rotor. This could be done with periodic blowing in the azimuthal direction to stretch the tip-leakage vortex. It is possible to deflect the direction of the vortex so as to decrease the phenomenon of double leakage, through the improvement of the existing control devices, such as casing treatments or upstream constant jets located at the casing. Another possibility lies in the control of the separation position of the boundary layer that develops on the shroud. A suction device could even prevent this separation and thereby limit the flow inversion near surge, hence a better stability of the flow and a wider surge margin.

Appendix A

Influence of the IGV gap size on the flow at section 25A

Contents

This appendix deals with the influence of the approximated gap size for the IGV on the flow cartography at section 25A with a RANS computation.

This thesis has shown that the IGV wakes have an influence on the flow field around the R1 and even downstream. This is mainly due to the hub vortex and the tip vortex generated by the hub and tip gaps modelled for the IGV. This appendix presents the influence of the way the IGV is modelled on the flow field at section 25A, that is to say, where the cartography, used as inlet condition for the numerical test case on the R1, is extracted. To this end, three numerical configurations are defined.

A.1 Description of the compared configurations

First of all, the reference configuration is the one presented in chapter 3, used to define the outlet pivot pressure so that the axial momentum radial distribution corresponds to the one at the experimental design operating point. The outlet pivot pressure is the one finally chosen in that chapter: 0.93 Pio. The turbulence model is the model of Spalart-Allmaras. The numerical methods used are the spatial integration scheme from Jameson and the implicit Backward-Euler for time integration. The spatial domain comprises the IGV and the R1 as describe in the aforementioned chapter. The second configuration is based on the same numerical aspects. Nonetheless, it has a reduced hub gap for the IGV. Indeed, there is still a linear gap modelled, however the height at the leading and trailing edges differ. The leading edge hub gap is reduced from 0.51% to 0.43% of the hub axial chord. The trailing edge hub gap is reduced

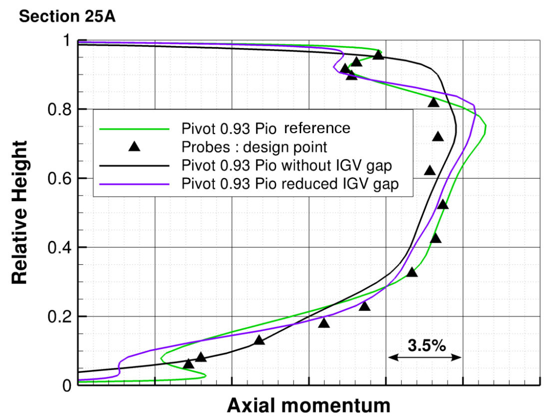

Figure A.1 — *Radial distribution of axial momentum at section 25A for different IGV gaps*

from 2.95% to 1.47% of the hub axial chord. As a result, the gap size is halved and corresponds to a gap configuration smaller than what it is experimentally. The third configuration has neither hub gap nor tip gap for the IGV. These three numerical configurations are compared to the experiment.

A.2 Impact on the radial distributions

First of all, the time and circumferential averaged values are considered through an analysis of the radial distributions at section 25A.

Figure A.1 shows the axial momentum for the three configurations. As expected, the reference configuration is in good agreement with the experimental values from the probes near the hub and near the tip. Indeed, the gradients from the casing down to 80% of relative height are correctly captured, this proves that the IGV tip gap is well taken into account. However, around 70% of relative height, it overestimates the axial momentum value compared to the two other configurations. At this position, the case without any gap tends to be in better agreement. Nevertheless, it does not experience the gradients characterising the IGV tip gap near the casing. This is coherent since this configuration does not model it. Near the hub, this configuration without gap gives relevant results on this averaged radial distribution, since there is no pronounced gradient for the experimental probes. If the configuration with the reduced hub gap is considered, one can clearly observe an underestimation of the axial momentum, both near the hub, and even near the casing. Furthermore, the gradients around 90% of relative height are underestimated too. This proves that a small difference at the hub influences what occurs on the other side of the domain, near the shroud.

The total pressure radial distribution is plotted in figure A.2. Without any gap, the total pressure is clearly overestimated at both hub and tip. By contrast, the configurations with gaps capture a lower total pressure compared to the experimental value. Once more, there is an influence of the modelled hub gap on the flow at the tip, with less pronounced gradients for the IGV tip vortex, around 90% of relative height. The difference is naturally more perceptible near the hub. The gradients are weaker with the reduced hub gap, hence a better agreement with the slope observed experimentally. Nonetheless, there is no shift of the pressure value near the hub toward the value measured by the experimental probe. This highlights two effects. The first one is that the gradient with a "S" form captured by the reference configuration near the hub can be improved by changing the hub gap size. This modifies the vortex width and therefore influences the flow at section 25A. The second noteworthy effect is that the reduced hub gap is not small enough to be in perfect agreement with the experiment. The reduced gap size is nevertheless smaller than the experimental one. Thereby, the total pressure should be higher than what is is experimentally near the hub, and be closer to the configuration with no gap. This shows that the

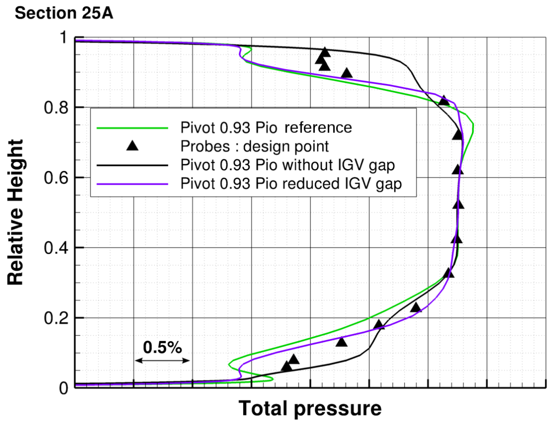

Figure A.2 — *Radial distribution of total pressure at section 25A for different IGV gaps*

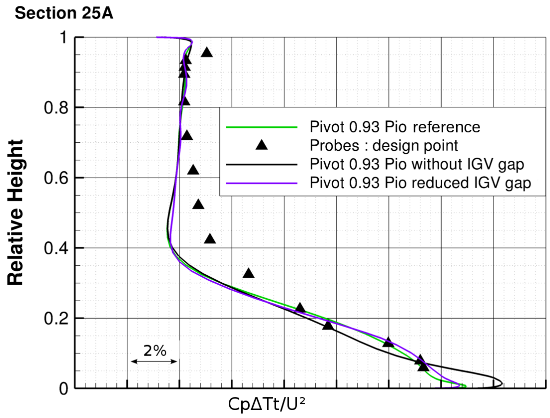

Figure A.3 — *Radial distribution of averaged normalized total temperature at section 25A for different IGV gaps*

Spalart-Allmaras model amplifies the pressure losses. The fact that all the configurations give the same results at mid span strengthens the idea that this drawback of the model is encountered in regions with secondary flows.

Figure A.3 plots the radial distribution of the normalized total temperature, $Cp\Delta Tt/U^2$. There is almost no influence of the gap near the casing, and even at mid span. The simulation of the tip gap influences barely the total temperature. Nevertheless, the figure underlines that even with the smallest hub gap, the simulation is improved compared to the configuration with no gap. However, the gradient around 10% of relative height is captured more accurately in the reference case. This underscores that the corner effect and the hub vortex from the IGV are sensitive to the hub gap size.

The azimuthal angle is plotted in figure A.4. It emphasizes the necessity to take the IGV gaps into account, even with approximations like it is performed in the presented configurations. Indeed, without gap, the angles are overestimated and the gradients not captured at all near the casing and near the hub. This figure reveals that the height corresponding to the gradient of the IGV hub vortex is in better agreement with the experimental measurements in the case of the reduced hub gap. The position of the maximum angle is closer to the hub in this configuration, therefore the curve is similar to what is captured by the probes. By contrast, in the reference case, the angle is underestimated and the position corresponding to the maximum angle value is radial located at a position 5% upper. This highlights that the development stage of the hub vortex, hence its width, is better simulated in the configuration with the reduced gap. However, in this case, the gap size is smaller than what it is in the experiment. This confirms that the numerical schemes and turbulence model used in this study amplify this phenomenon.

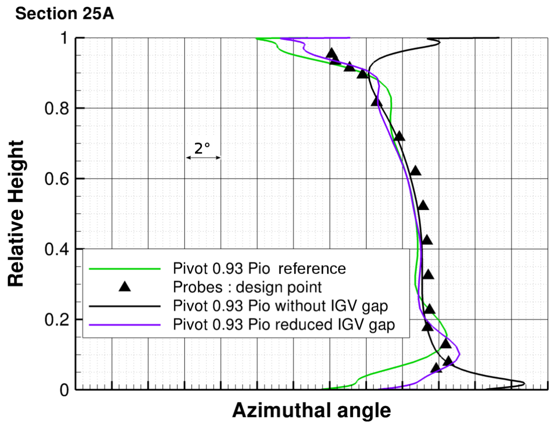

Figure A.4 — *Radial distribution of azimuthal angle at section 25A for different IGV gaps*

A.3 Impact on the captured phenomena in the cartography

This section shows the effects of the IGV gaps on the 2D cartographies of the different configurations. They are presented in figure A.5. The hub gap size influences mainly the azimuthal shift between the IGV hub vortex and the main wake, as visible by comparing the region near 10% of relative height and azimuth 5.5 in figures A.5(a) and A.5(b). This shift originates from the widening of the vortex with a wider gap. Thereby, its azimuthal extension is slower, and there is a delay between the arrival of the main IGV wake and the IGV hub vortex. This phenomenon occurs for the IGV tip vortex too. It results in the IGV tip vortex arriving with an important delay at the leading edge of the R1.

Without gap, some phenomena are experienced too. The cartography captures the IGV main wake and the thickening of the boundary layer on the walls at the hub and casing. Moreover, a corner effect is seen near the hub in figure A.5(c), with a large area of lower total pressure. A similar effect is observed near the tip too. Nevertheless, the effects of the hub and tip vortices are not experienced. It was observed in this thesis that the vortex coming from the IGV tip gap has an important interaction with the tip-leakage vortex of the R1. As a consequence, the simulation of the IGV gaps was necessary in this study in order to accurately capture this interaction.

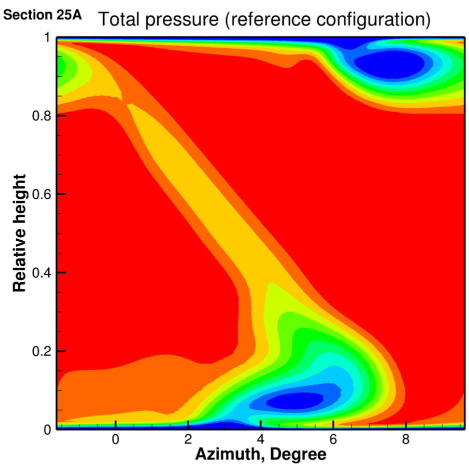

(a) Reference configuration.

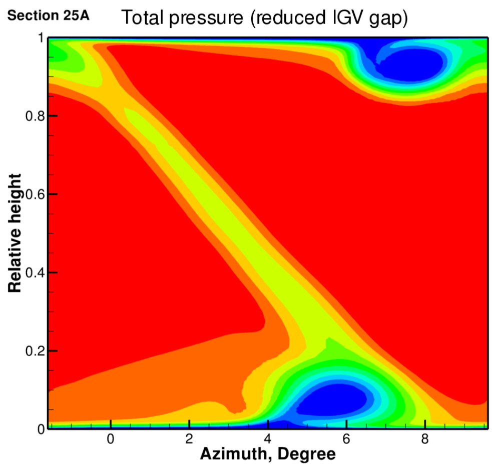

(b) Reduced IGV hub gap configuration.

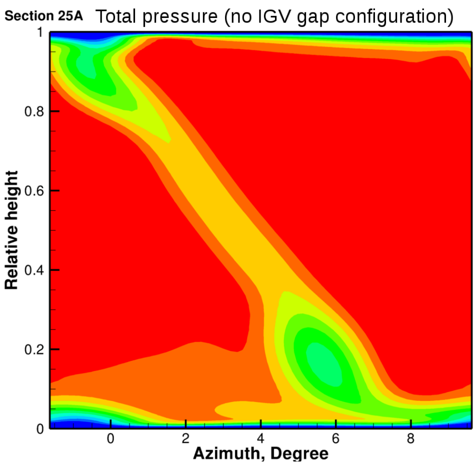

(c) No IGV gap configuration.

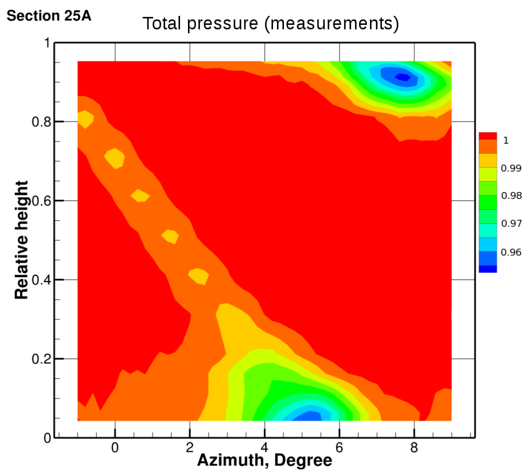

(d) Experimental probes.

Figure A.5 — *Total pressure cartography from the RANS RDE-R1 computations and experimental probes at section 25A. Effects of IGV gaps.*

Appendix B — *Influence of turbulence model and numerical schemes on the flow at section 25A*

Contents

This appendix deals with the effects of the Reynolds-averaged Navier-Stokes model used in the preliminary study presented in chapter 3 on the flow cartography at section 25A.

B.1 Description of the compared configurations

In the frame of this thesis work, different turbulence models and numerical schemes were evaluated in the preliminary study to analyse in what manner this could influence the flow field where the cartography is extracted, that is to say at section 25A. This appendix presents the outcome of this analysis.

All the presented computations are carried out on the same domain that comprises the IGV-R1 computational field with the same boundary conditions as detailed in chapter 3. Furthermore, the numerical time discretization scheme is the implicit Backward-Euler. Different turbulence models are tested with different spatial discretization schemes. They are listed below:

- Spalart-Allmaras (SA) with the Jameson spatial discretization scheme,
- Spalart-Allmaras with the AUSM+P spatial discretization scheme,
- Spalart-Allmaras with curvature correction (SARC) and the AUSM+P spatial discretization scheme,
- k-ω from Wilcox [174] with the AUSM+P spatial discretization scheme,
- k-ϵ from Launder and Sharma [103] and the AUSM+P spatial discretization scheme,

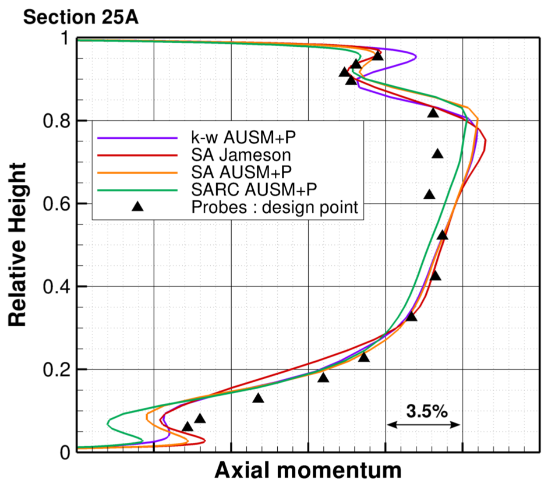

Figure B.1 — *Radial distribution of axial momentum at section 25A for different turbulence models and spatial discretization schemes*

- k-ϵ from Launder and Sharma [103] and the Jameson spatial discretization scheme.

They all converged following the criteria detailed in chapter 3, except both k-ϵ computations. As a consequence they were withdrawn from the following comparison.

B.2 Impact on the radial distributions

The time and circumferential averaged value of axial momentum, total pressure, total temperature, and azimuthal angle are presented below at section 25A.

First of all, figure B.1 shows the radial distribution for the axial momentum. Near the hub, they all underestimate the axial momentum. On the one hand, the AUSM+P scheme tends to increase this discrepancy. On the other hand, it captures more accurately the radial position of the inflection at 80% of relative height. The curvature correction of the Spalart-Allmaras model seems to amplify the effects near the hub. However, it reveals to give relevant results in the area where there is the IGV tip vortex. The k-ω model is the only one to overestimate the axial momentum near the casing. Besides, the captured vortex is further from the casing wall, which shows a major difference in the development stage for the IGV tip vortex with this model. Likewise, near the hub, the gradient with a "S" form captured by all the method is weaker with the k-ω model. As a consequence, it is in better agreement with the measurements.

The total pressure radial distribution is plotted in figure B.2. At mid span, and more accurately from 30% to 80% of relative height, the different computations behave similarly and they all capture the experimental total pressure value. Besides, the deflection at 80% of relative height is correctly experienced by the computations, except the Spalart-Allmaras computation with the Jameson scheme. This computation is the one that underestimates the most the total pressure at the casing, albeit they all underestimate it. This shows the lack of capability of the Jameson scheme to capture the vortex. The k-ω model seems to be the most appropriate to capture both the inflection seen at 90% of relative height and the total pressure level near the casing. As it was observed for the axial momentum, it captures correctly the gradients near the hub.

The normalized total temperature, $Cp\Delta Tt/U^2$, is presented in figure B.3. There is almost no difference between the configurations from 10% of relative height to the casing. The only exception is the area near the hub, where the Spalart-Allmaras computation with the Jameson scheme captures correctly

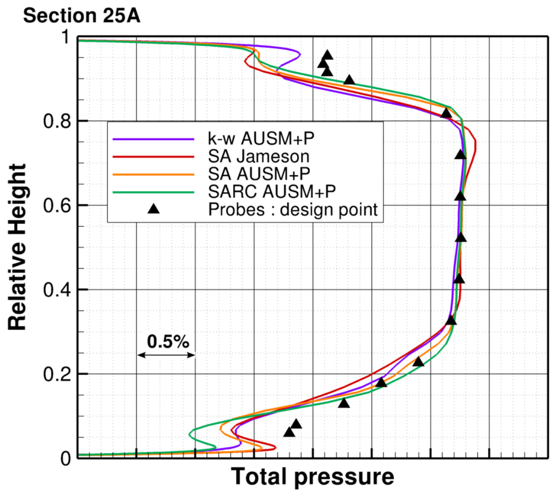

Figure B.2 — *Radial distribution of total pressure at section 25A for different turbulence models and spatial discretization schemes*

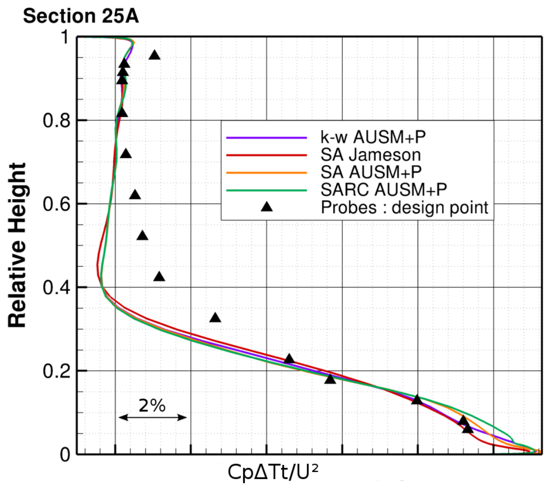

Figure B.3 — *Radial distribution of averaged normalized total temperature at section 25A for different turbulence models and spatial discretization schemes*

the visible inflection. Nevertheless, the other computations experience close results, therefore this is not a key value to consider to appraise the cases.

By contrast, the azimuthal angle, plotted in figure B.4, highlights important discrepancies between the different cases. At the casing, the k-ω model tends to be in better agreement with the experimental values. However, further from the wall, the computations with the Spalart-Allmaras model and the AUSM+P scheme reveal to capture more accurately the inflection induced by the IGV tip vortex, at 90% of relative height. Furthermore, the curvature correction shows better agreement. Moreover, it behaves like the k-ω model above 95% of relative height. Even if all the computations underestimate the angle near the shroud, the Spalart-Allmaras with the Jameson scheme is the configuration with the furthest value from the experiments. Along the span, the results are similar for the methods. Nevertheless, two perceptible effects have to be emphasized. Indeed, two computations stand out from the analysis of this figure. The first one is due to the Jameson scheme, that captures a radial position for the location of the maximum azimuthal angle further from the hub wall compared to the experimental position. This shows that the development stage of the hub vortex is too advanced here. The second is the Spalart-Allmaras with the curvature correction that reveals to be the only one to capture the gradients near the hub for the

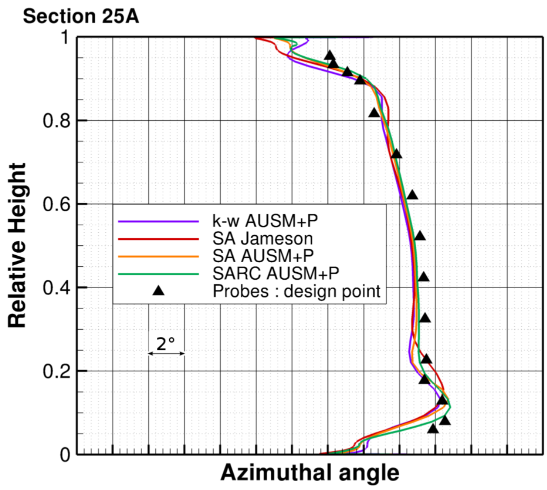

Figure B.4 — *Radial distribution of azimuthal angle at section 25A for different turbulence models and spatial discretization schemes*

azimuthal angle. This is the reason why it was chosen to extract the flow cartography at section 25A, as explained in chapter 3.

Bibliography

[1] D. Arnaud. *Analyse expérimentale des phénomènes instationnaires dans un compresseur multi-étages à forte charge aérodynamique*. PhD thesis, École Centrale de Lyon, 2003.

[2] J. Bae. *Active Control of Tip Clearance Flow in Axial Compressors*. PhD thesis, Massachusetts Institute of Technology, 2001.

[3] J.W. Bae, K.S. Breuer, and C-S. Tan. Active Control of Tip Clearance Flow in Axial Compressors. *Journal of Turbomachinery*, 127:352–362, 2005.

[4] W. Balzer and H.F. Fasel. Direct numerical simulations of laminar separation bubbles on a curved plate: part 1 - simulation setup and uncontrolled flow. In *Proceedings of ASME Turbo Expo 2013: Turbine Technical Conference and Exposition GT2013*, number GT2013-95277, San Antonio, Texas, June 2013.

[5] W. Balzer and H.F. Fasel. Direct numerical simulations of laminar separation bubbles on a curved plate: part 2 - flow control using pulsed vortex generator jets. In *Proceedings of ASME Turbo Expo 2013: Turbine Technical Conference and Exposition GT2013*, number GT2013-95277, San Antonio, Texas, June 2013.

[6] M.S. Bartlett. Periodogram analysis and continuous spectra. *Biometrika*, 37:1–16, 1950. doi: 10.1093/biomet/37.1-2.1.

[7] T.B. Benjamin. Theory of the vortex breakdown phenomenon. *Journal of Fluid Mechanics*, 14: 593–629, 1962. doi: 10.1017/S0022112062001482.

[8] A. Benyahia. *Mise en oeuvre et évaluation d'un modèle de transition à équations de transport pour la simulation d'écoulements en turbomachines*. PhD thesis, Université Toulouse III école doctorale MEGEP, 2012.

[9] J. Bergner, D.K. Hennecke, and C. Hah. Tip-clearance variations of an axial high-speed single-stage transonic compressor. In *17th Symposium on Air Breathing Engines, ISABE, Munich, Germany*, 2005.

[10] G. Billonnet, L. Castillon, J. Riou, G. Leroy, and A. Paillassa. A technological effect modeling on complex turbomachinery applications with an overset grid numerical method. In *Proceedings of the ASME Turbo Expo 2013*, 2013.

[11] J.P. Bindon. The Measurement and Formation of Tip Clearance Loss. *Journal of Turbomachinery*, 111:257–263, 1989. doi: 10.1115/1.3262264.

[12] D. Borello, G. Delibra, K. Hanjalic, and F. Rispoli. Large-eddy simulations of tip leakage and secondary ows in an axial compressor cascade using a near-wall turbulence model. *Journal of Power and Energy*, 223:645–655, 2009. doi: 10.1243/09576509JPE825.

[13] J. Boudet, J. Caro, and M.C. Jacob. Large-eddy simulation of a low-speed tip-clearance flow. In M. Sen, G. Bois, M. Manna, and T. Arts, editors, *9th European Conference on Turbomachinery Fluid Dynamics and Thermodynamics*, pages 147–158, March 2011.

[14] R. Bouffanais. Advances and challenges of applied large-eddy simulation. *Computers & Fluids*, 39:735–738, 2010. doi: 10.1016/j.compïňĆuid.2009.12.003.

[15] M.J. Boussinesq. *Essai sur la théorie des eaux courantes*, volume 23-24. Mémoires Présentés par Divers Savants Étrangers à l'Académie des Sciences, 1877.

[16] V. Brion. *Stabilité des paires de tourbillons contra-rotatifs : application au tourbillon de jeu dans les turbomachines*. PhD thesis, école Polytechnique, 2009.

[17] V. Brunet and S. Deck. Zonal-Detached Eddy Simulation of transonic buffet on a civil aircraft type configuration. In *38th Fluid Dynamics Conference and Exhibit, AIAA, Seattle,Washington*, pages 1–12, 2008.

[18] V. Brunet, P. Molton, H. Bézard, and S. Deck. Advanced Experimental and Numerical Investigations of an Aircraft Powerplant Configuration. In *28th AIAA Applied Aerodynamics Conference, Chicago, Illinois*, number 4814 in 2010, pages 1–11, 2010.

[19] N. Bulot, X. Ottavy, and I. Trébinjac. Unsteady pressure measurements in a high-speed centrifugal compressor. *Journal of Thermal Science*, 19:34–41, 2010. doi: 10.1007/s11630-010-0034-4.

[20] A. Cahuzac. *Aspects cinétiques et acoustiques en simulation numérique des grandes echelles, et application à l'étude du contrôle de l'écoulement de jeu en turbomachines*. PhD thesis, École Centrale de Lyon, July 2012.

[21] L. Cambier and J.P. Veuillot. Status of the elsA CFD Software for Flow Simulation and Multidisciplinary Applications. In *46th AIAA Aerospace Sciences Meeting and Exhibit, Reno, NV*, pages 1–17, January, 7-10 2008.

[22] L. Cambier, S. Heib, and S. Plot. The Onera elsA CFD software: input from research and feedback from industry. *Mechanics & Industry*, 14:159–174, 2013. doi: 10.1051/meca/2013056.

[23] L. Castillon and G. Legras. Overset grid method for simulation of compressors with non-axisymmetric casing treatment. *Journal of Propulsion and Power*, 0:460–465, 2013. doi: 10.2514/1.B34613.

[24] P. Chakraborty, S. Balachandar, and R.J. Adrian. On the relationships between local vortex identication schemes. *Journal of Fluid Mechanics*, 535:189–214, 2005. doi: 10.1017/S0022112005004726.

[25] N. Chauvet, S. Deck, and L. Jacquin. Zonal Detached Eddy Simulation of a Controlled Propulsive Jet. *AIAA Journal*, 45(10):2458–2473, 2007. doi: 10.2514/1.28562.

[26] R.V. Chima. Calculation of Tip Clearance Effects In A Transonic Compressor Rotor. In *International Gas Turbine and Aeroengine Congress and Exhibition No41*, volume 120, pages 131–140, Birmingham, 1998.

[27] N. Courtiade. *Experimental analysis of the unsteady flow and instabilities in a high-speed multi-stage compressor*. PhD thesis, Ecole Centrale de Lyon, 2012.

[28] S.C. Crow. Stability Theory for a Pair of Trailing Vortices. Technical report, Boeing Scientific Research Laboratories, Sep. 1969.

[29] S.C. Crow. Stability Theory for a Pair of Trailing Vortices. *AIAA Journal*, 8:2172–2179, 1970. doi: 10.2514/3.6083.

[30] J. Dacles-Mariani, G.G. Zilliac, J.S. Chow, and P. Bradshaw. Numerical/Experimental Study of a Wingtip Vortex in the Near Field. *AIAA Journal*, 33:1561–1568, 1995. doi: 10.2514/3.12826.

[31] F. Daude. *Méthode d'intégration temporelle implicite pour la simulation des grandes échelles application à la reduction du bruit de cavité*. PhD thesis, Université de Poitiers, Poitiers, 2007.

[32] F. de Crécy, G. Després, G. Ngo Boum, and F. Leboeuf. Study of the aerodynamic instabilities in an axial air compressor using 3d-1d codes coupling approach. In *Proceedings of the 10th European Turbomachinery Conference*, number A079, 2013.

[33] D. de la Riva, W. Devenport, C. Muthanna, and S. Glegg. Behavior of Turbulence Flowing Through a Compressor Cascade. In *AIAA*, volume 42, pages 1302–1313, Jul. 2004.

[34] J. Deardoff. A numerical study of three-dimensional turbulent channel flow at large reynolds numbers. *Journal of Fluid Mechanics*, 41 (2):453–480, 1970. doi: 10.1017/S0022112070000691.

[35] S. Deck. *Simulation numerique des charges laterales instationnaires sur des configurations de lanceur*. PhD thesis, Université d'Orléans, 2002.

[36] S. Deck. Zonal-Detached-Eddy Simulation of the Flow Around a High-Lift Conguration. *AIAA Journal*, 43:2372–2384, 2005. doi: 10.2514/1.16810.

[37] S. Deck. Introduction aux méthodes hybrides RANS/LES. Collège de Polytechnique – Mécanique des Fluides : Simulation des écoulements turbulents, Mar. 2011.

[38] S. Deck. Recent Improvements in the Zonal Detached Eddy Simulation (ZDES) Formulation. *Theoretical and Computational Fluid Dynamics*, 26:523–550, 2012. doi: 10.1007/s00162-011-0240-z.

[39] S. Deck and R. Laraufie. Numerical investigation of the ow dynamics past a three-element aerofoil. *Journal of Fluid Mechanics*, 732:401–444, 2013. doi: 10.1017/jfm.2013.363. Cambridge University Press 2013.

[40] S. Deck and P. Thorigny. Unsteadiness of an axisymmetric separating-reattaching ow : Numerical investigation. *Physics of Fluids*, 19:1–20, 2007. doi: 10.1063/1.2734996.

[41] J. Délery. Décollement en écoulement tridimensionnel et tourbillons. Cours de master.

[42] J. Délery. Separation in three-dimensional steady flows - Part 2: Detachment and attachment separation lines, detachment and attachment separation surfaces. In *Course at the Onera*, 2011.

[43] J.D. Denton. Loss Mechanisms in Turbomachines. *Journal of Turbomachinery*, 115:621–656, 1993. doi: 10.1115/1.2929299.

[44] C. Deslot. *Les interactions rotor-stator en turbine : l'effet potentiel remontant*. PhD thesis, école Centrale de Lyon, 2009.

[45] S.L. Dixon. *Fluid mechanics and thermodynamics of turbomachinery*. Number ISBN : 0-7506-7870-4. Elsevier Butterworth-Heinemann, 2005.

[46] F. Ducros, V. Ferrand, F. Nicoud, C. Weber, D. Darracq, C. Gacherieu, and T. Poinsot. Large-Eddy Simulation of the Shock/Turbulence Interaction. *Journal of Computational Physics*, 152: 517–549, 1999. doi: 10.1006/jcph.1999.6238.

[47] G. Dufour, N. Gourdain, F. Duchaine, O. Vermorel, L.Y.M. Gicquel, JF. Boussuge, and T. Poinsot. Numerical Investigations in Turbomachinery : A State of the Art, Large Eddy Simulation Applications. Technical report, CERFACS, 2009.

[48] S. Eastwood, P. Tucker, H. Xia, and C. Klostermeier. Developing Large Eddy Simulation for Turbomachinery Applications. *Philosophical Transactions of the Royal Society*, 367:2999–3013, 2009. doi: 10.1098/rsta.2008.0281.

[49] J.R. Edwards and M-S. Liou. Low diffusion flux-splitting methods for flows at all speeds. In *AIAA*, volume 1862, pages 261–271, 1997.

[50] H.W. Emmons, C.E. Pearsons, and H.P. Grant. Compressor surge and stall propagation. *Transactions of the ASME*, 77:455–469, 1955.

[51] Emoscopes. Wikimedia commons, CC-BY-SA.

[52] A. Favre. Équations des gaz turbulents compressibles. *Journal de Mécanique*, 4:361–421, 1965.

[53] A. Fourmaux. Unsteady simulation of turbine blade row interactions. Stator clocking effects on the turbine behaviour. In *36th Colloquium of Applied Aerodynamics AAAF, Orléans, France*, 20-22nd Mar. 2000.

[54] M. Furukawa, M. Inoue, K. Saiki, and K. Yamada. The role of tip leakage vortex breakdown in compressor rotor aerodynamics. *Journal of turbomachinery ASME*, 121:469, 1999. doi: 10.1115/1.2841339.

[55] E. Garnier. Stimulated Detached Eddy Simulation of three-dimensional shock/boundary layer interaction. *Shock Waves*, 19:479–486, 2009. doi: 10.1007/s00193-009-0233-7.

[56] C.W. Gear. Algorithm 407: DIFSUB for solution of ordinary differential equations. *Communications of the ACM*, 14:185–190, 1971. doi: 10.1145/362566.362573.

[57] C.W. Gear. Numerical initial value problems in ordinary differential equations. In *Prentice Hall PTR, Upper Saddle River, New Jersey, USA*, 1971.

[58] S. Geng, Z. Hongwu, J. Chen, and W. Huang. Unsteady Tip Clearance Flow Pattern in an Isolated Axial Compressor Rotor with Micro Tip Injection. In *Proceedings of the 8th International Symposium on Experimental and Computational Aerothermodynamics of Internal Flows*, Lyon, July 2007.

[59] W.K. George, P. Beuther, and R.E.A. Arndt. Pressure spectra in turbulent free shear flows. *Journal of Fluid Mechanics*, 148:155–191, 1984. doi: 10.1017/S0022112084002299.

[60] N. Georgiadis, D. Rizzeta, and C. Fureby. Large-Eddy Simulation: Current Capabilities, Recommended Practices, and Future Research. *AIAA Journal*, 48:1772–1784, 2010. doi: 10.2514/1.J050232.

[61] C. Gmelin and F. Thiele. Numerical Analysis of a High Speed Compressor Cascade. In *Proceedings of the 21st ISABE Conference, Busan, Korea*, number ISABE-2013-1115, Sep. 9-13th 2013.

[62] A. Gomar. Simulation Numérique Haute Fidélité d'une Aube de Compresseur Haute Pression. Master's thesis, ISAE-ENSICA, 2010.

[63] A. Gomar, N. Gourdain, and G. Dufour. High-fidelity simulation of the turbulent flow in a transonic axial compressor. In *European Turbomachinery Conference*, 2011.

[64] N. Gourdain and F. Leboeuf. Unsteady Simulation of an Axial Compressor Stage With Casing and Blade Passive Treatments. *Journal of Turbomachinery*, 131:12, 2009. doi: 10.1115/1.2988156.

[65] N. Gourdain, X. Ottavy, and A. Vouillarmet. Experimental and numerical investigation of unsteady flows in a high speed three stages compressor. In *European Turbomachinery Conference*, 2009.

[66] M.B. Graf. *Effects of stator pressure field on upstream rotor performance*. PhD thesis, Massachusetts Institute of Technology, 1996.

[67] B. Greschner and F. Thiele. Wall Modeled LES simulation of Rotor-Stator-Cascade Broadband Noise. In *17th AIAA/CEAS Aeroacoustics Conference*, number 2873, Portland, June, 5-8 2011.

[68] D. Guénot. *Simulation des effets instationnaires à grande échelle dans les écoulements décollés*. PhD thesis, Ecole nationale supérieure de l'aéronautique et de l'espace (Toulouse)., 2004. 2 volumes.

[69] C. Hah. Large Eddy Simulation of Transonic Flow Field in NASA Rotor 37. Technical report, NASA, 2009.

[70] C. Hah, D.C. Rabe, and A.R. Wadia. Role of tip-leakage vortices and passage shock in stall inception in a swept transonic compressor rotor. In *Proceedings of ASME Turbo Expo Power for Land, Sea, and Air*, number GT2004-53867, June, 14-17 2004.

[71] C. Hah, M. Voges, M. Mueller, and H-P. Schiffer. Investigation of unsteady flow behavior in transonic compressor rotors with LES and PIV measurements. In *19th Symposium on Air Breathing Engines, ISABE, Montreal, Canada*, Feb. 2009.

[72] C. Halbe, R.N. Chirantan, A. Pradeep, and B. Roy. Effect of rotor tip shape on the performance of a high hub-to-tip ratio low speed axial compressor. In *Proceedings of the 21st ISABE Conference, Busan, Korea*, number ISABE-2013-1102, Sep. 9-13th 2013.

[73] J.L. Hall. An Introduction to Vortex Breakdown and Vortex Core Bursting. Technical Report NAE-AN-28 NRC NO.24336, National Aeronautical Establishment, Mar. 1985.

[74] F.J. Harris. On the use of windows for harmonic analysis with Discrete Fourier Transform. In *Proceedings of the IEEE*, volume 66, Jan. 1978. doi: 10.1109/PROC.1978.10837.

[75] H.Z. Herzig, A.G. Hansen, and G.R. Costello. A visualization study of secondary flows in cascades. Technical report, Report 1163-National Advisory Committee for Aeronautics, 1954.

[76] M. Hoeger, G. Fritsch, and D. Bauer. Numerical Simulation of the Shock-Tip Leakage Vortex in a HPC Front Stage. *Journal of Turbomachinery*, 121:456–468, 1999. doi: 10.1115/1.2841338.

[77] W. Hofmann and J. Ballmann. Tip-Vortex Evolution and Shock-Vortex Interaction in a Transonic Turbocompressor at Conditions near Stall. In *Worshop on the "Flow mechanisms in turbocompressors at conditions near stall", DFG-Transfer Project*, RWTH Aachen – University of Technology, D-52056 Aachen, Germany, 24-25th Feb. 2004.

[78] W.H. Hofmann and J. Ballmann. Shock-Vortex Interaction in a Transonic Turbocompressor. *Contributions to the 13th STAB/DGLR Symposium Munich, Germany 2002*, 87:458–466, 2004. doi: 10.1007/978-3-540-39604-8_57.

[79] D.A. Hoying. *Blade Passage Flow Structure Effects on Axial Compressor Rotating Stall Inception*. PhD thesis, Massachusetts Institute of Technology, 1996.

[80] D.A. Hoying, C.S. Tan, H.D. Vo, and E.M. Greitzer. Role of Blade Passage Flow Structures In Axial Compressor Rotating Stall Inception. *Journal of Turbomachinery*, 121:735–742, 1999. doi: 10.1115/1.2836727.

[81] J. C. R. Hunt, A. Wray, and P. Moin. Eddies, stream, and convergence zones in turbulent flows. Technical Report N89-24555, Center for Turbulence Research Report CTR-S88, 1988.

[82] M. Inoue and M. Furukawa. Physics of tip clearance flow in turbomachinery. In *ASME*, number FEDSM2002-31184, 2002.

[83] N. Intaratep. *Formation and Development of the Tip Leakage Vortex in a Simulated Axial Compressor with Unsteady Inflow*. PhD thesis, Virginia Polytechnic Institute and State University, 2006.

[84] A Jameson. Numerical solution of the euler equation for compressible inviscid fluids. Technical report, MAE Report 1643, Princeton University, 1983.

[85] A. Jameson, W. Schmidt, and E. Turkel. Numerical Solution of the Euler Equations by Finite Volume Methods Using Runge-Kutta Time-Stepping Schemes. In *AIAA paper 81-1259*, 1981.

[86] J. Jeong and F. Hussain. On the identification of a vortex. *Journal of Fluid Mechanics*, 285:69–94, 1995. doi: 10.1017/S0022112095000462.

[87] S. Kang and C. Hirsch. Experimental study on the three dimensional flow within a compressor cascade with tip clearance. Part 1 : Velocity and pressure fields. In *ASME*, volume 92-GT-215, pages 1–8, 1992.

[88] S. Kang and C. Hirsch. Experimental study on the three dimensional flow within a compressor cascade with tip clearance. Part 2 : The tip leakage vortex. In *ASME*, volume 92-GT-432, pages 1–7, 1992.

[89] N.H. Kemp and W.R. Sears. Aerodynamic Interference Between Moving Blade Rows. *Journal of the Aeronautical Sciences (Institute of the Aeronautical Sciences)*, 20:585–597, 1953. doi: 10.2514/8.2758.

[90] N.H. Kemp and W.R. Sears. The Unsteady Forces Due to Viscous Wakes in Turbomachines. *Journal of the Aeronautical Sciences (Institute of the Aeronautical Sciences)*, 22(7):478–483, 1955. doi: 10.2514/8.3376.

[91] S.A. Khalid, A.S. Khalsa, I.A. Waitz, C.S. Tan, E.M. Greitzer, N.A. Cumpsty, J.J. Adamczyk, and F.E. Marble. Endwall Blockage in Axial Compressors. *Journal of Turbomachinery*, 121:499–509, 1999. doi: 10.1115/1.2841344.

[92] K.R. Kirtley, T.A. Beach, and J. Adamczyk. Numerical analysis of secondary flow in a two stage turbine. In *Proceedings of the AIAA*, 1990.

[93] A.N. Kolmogorov. The local structure of turbulence in incompressible viscous fluid for very large reynolds numbers. *Proceedings of the USSR Academy of Sciences*, 30:299–303, 1941.

[94] M Kurosaka, M. Kikuchi, K. Hirano, T. Yuge, and H. Inoue. Interchangeability of vortex-breakdown types. *Experiments in Fluids*, 34:77–86, 2003. doi: 10.1007/s00348-002-0535-3.

[95] M.W. Kutta. Beitrag zur näherungsweisen Integration totaler Differentialgleichungen. *Zeitschrift für Mathematik und Physik*, 46:435–453, 1901.

[96] B. Lakshminarayana. *Fluid dynamics and heat transfer of turbomachinery*. Number ISBN: 978-0-471-85546-0. Wiley-interscience, 1996.

[97] B. Lakshminarayana and J.H. Horlock. Tip-clearance flow and losses for an isolated compressor blade. Technical report, Department of Mechanical Engineering, The University of Liverpool, 1962.

[98] B. Lakshminarayana and A. Ravindranath. Interaction of Compressor Rotor Blade Wake With Wall boundary Layer/Vortex in the End-Wall Region. *Journal of Engineering Power*, 104:467, Apr. 1982.

[99] B. Lakshminarayana, R. Davino, and M. Pouagare. Three-Dimensional Flow Field in the Tip Region of a Compressor Rotor Passage. *Transactions of the ASME*, 104:772, Oct. 1982.

[100] B. Lakshminarayana, M. Zaccaria, and B. Marathe. Structure of tip clearance flow in axial flow compressors. In *10th Symposium on Air Breathing Engines, ISABE, Nottingham, UK*, 1991.

[101] N.C. Lambourne and D.W. Bryer. The Bursting of Leading-Edge Vortices - Some Observations and Discussion of the Phenomenon. Technical Report 3282, Ministry of Aviation - Aeronautical Research Council Reports and Memoranda, Apr. 1962.

[102] M. Lange, K. Vogeler, and R. Mailach. Tip and hub clearance vortex development due to rotor-stator-interactions in axial compressors. In *13th International Symposium on Unsteady Aerodynamics, Aeroacoustics and Aeroelasticity of Turbomachines, ISUAAT, Tokyo, Japan*, number 5 in 4, 2012.

[103] B.E. Launder and B.I. Sharma. Application of Energy-Dissipation Model of Turbulence to the Calculation of Flow near a Spinning Disc. Letters in Heat and Mass Transfer, 1:131–138, 1974. *Imperial College of Science and Technology, London, England. Letters in Heat and Mass Transfer*, 11:131–138, 1974. doi: 10.1016/0735-1933(74)90024-4.

[104] A. Le Pape, F. Richez, and S. Deck. Zonal Detached-Eddy Simulation of an Airfoil in Poststall Condition. *AIAA Journal*, 51:1919–1931, 2013. doi: 10.2514/1.J052235.

[105] Y. Levy, D. Degani, and A. Seginer. Graphical visualization of vortical flows by means of helicity. *AIAA Journal*, 28:1347–1352, 1990. doi: 10.2514/3.25224.

[106] M. S. Liou and C. J. Stephen. A new flux splitting scheme 23-39, 1993. *Journal of Computational Physics*, 107:23–39, 1993.

[107] R. Mailach and K. Vogeler. Rotor-Stator Interactions in a Four-Stage Low-Speed Axial Compressor—Part I: Unsteady Profile Pressures and the Effect of Clocking. *Journal of Turbomachinery*, 126:507–518, 2004. doi: 10.1115/1.1791641.

[108] R. Mailach, I. Lehmann, and K. Vogeler. Rotating instabilities in an axial compressor originating from the fluctuating blade tip vortex. *Journal of Turbomachinery*, 123:453–460, 2001. doi: 10.1115/1.1370160.

[109] R. Mailach, I. Lehmann, and K. Vogeler. Periodical unsteady flow within a rotor blade row of an axial compressor-part II : wake-tip clearance vortex interaction. *Journal of turbomachinery ASME*, 130:1–10, 2008. doi: 10.1115/1.2812330.

[110] J. Marty and B. Aupoix. Interaction of shrouded stator flow and main flow and its influence on performances of a three-stage high pressure compressor. *Proceedings of the Institution of Mechanical Engineers Part A: Journal of Power and Energy*, 226:489–50, June 2012. doi: 10.1177/0957650911414322.

[111] J. Marty, B. Aupoix, M. Schvallinger, and V.C. Sharma. Effet de la modélisation de la turbulence en proche pompage dans un compresseur multi-étages. In *AAAF, 43ème Colloque d'Aérodynamique Appliquée, Papier 14, Poitiers, France*, Mar. 10-12 2008.

[112] J. Marty, V. Brion, N. Séverac, N. Lantos, G. Billonnet, and N. Ben Nasr. PR LES-DES pour les turbomachines : rapport annuel T0+24. Technical Report RT 3/18120, Onera - DAAP, 2013.

[113] J. Marty, L. Castillon, J-C. Boniface, S. Burguburu, and A. Godard. Numerical and Experimental Investigations of Flow Control in Axial Compressors. *AerospaceLab Journal*, 6:1–13, 2013. doi: 10.12762/2013.AL06-09.

[114] J. Marty, G. Billonnet, N. Ben Nasr, N. Lantos, and B. Michel. PR LES DES pour les turbomachines : rapport annuel T0+36. Technical Report RT 4/18120 DAAP, Onera, Jan. 2014.

[115] J. Marty, W. Riéra, and L. Castillon. Zonal detached eddy simulation of tip leakage flow control in an axial high pressure compressor. In *Proceedings of the ASME Turbo Expo 2014, Düsseldorf, Germany*, number GT2014-25150, 16-20 June 2014.

[116] I. Mary. *Méthode de Newton approchée pour le calcul d'écoulements instationnaires comportant des zones à très faibles nombres de Mach*. PhD thesis, Université Paris XI, 1999.

[117] I. Mary, P. Sagaut, and M. Deville. An algorithm for low mach number unsteady flows. *Computers & Fluids*, 29:119–147, 2000. doi: 10.1016/S0045-7930(99)00007-9.

[118] Sylvie Méléard. *Introduction à la théorie et au calcul des probabilités*. École Polytechnique, 2010. ISBN 978 – 2 – 7302 – 1575.

[119] M. Mersinligil, J-F. Brouckaert, N. Courtiade, and X. Ottavy. A High Temperature High Bandwidth Fast Response Total Pressure Probe for Measurements in a Multistage Axial Compressor. In *ASME Turbo Expo Power for Land Sea and Air, Vancouver, Canada,*, number 45558 in 2011, pages 1–24, June 6-10 2011.

[120] M. Mersinligil, J-F. Brouckaert, N. Courtiade, and X. Ottavy. A High Temperature High Bandwidth Fast Response Total Pressure Probe for Measurements in a Multistage Axial Compressor. *Journal of Engineering for Gas Turbines and Power*, 134(061601):11, 2012. doi: 10.1115/1.4006061.

[121] P. Moin, M. Wang, D. You, and R. Mittal. Large-Eddy Simulation of Rotor Tip-Clearance Flows: Computational Challenges and Accomplishments. In *IEEE*, 2005.

[122] C. Muthanna and W.J. Devenport. Wake of a Compressor Cascade with Tip Gap. *AIAA Journal*, 42(11):2320, Nov. 2004. doi: 10.2514/1.5270.

[123] J. März, C. Hah, and W. Neise. An experimental and numerical investigation into the mechanisms of rotating instability. *Journal of Turbomachinery*, 126:367–375, 2002. doi: 10.1115/1.1460915.

[124] *Power Spectra Estimation*. National Semiconductor Corporation, 1995.

[125] L. Neuhaus and W. Neise. Active Control to Improve the Aerodynamic Performance and Reduce the Tip Clearance Noise of Axial Turbomachines. In *AIAA Aeroacoustics Conference*, 2005.

[126] G. Ngo Boum. Unsteady rotating or translating user map in subsonic inlet boundary condition injrot. /elsa/ni-07014, ONERA-DSNA, 2008.

[127] X. Ottavy. *CREATE – compresseur pour l'étude des instationnarités et des instabilités*. Laboratoire de mécanique des fluides et d'acoustique, 2012.

[128] X. Ottavy, N. Courtiade, and N. Gourdain. Experimental and Computational Methods for Flow Investigation in High-Speed Multistage Compressor. *Journal of Propulsion and Power*, 28(6): 1141–1155, 2012. doi: 10.2514/1.60562.

[129] R. Parker and J.F. Watson. Interaction Effects between Blade Rows in Turbomachines. In *Proceedings of the Institution of Mechanical Engineers*, volume 186, pages 331–340, 1972. doi: 10.1243/PIME_PROC_1972_186_036_02.

[130] D.H. Peckham and S.A. Atkinson. Preliminary results of low speed wind tunnel tests on a gothic wing with aspect ratio 1.0. Technical report, Aeronautical research council, 1957.

[131] V. Perrot, A. Touyeras, and G. Lucien. Detailed cfd analysis of a grooved casing treatment on an axial subsonic compressor. In *European Turbomachinery Conference*, 2007.

[132] U. Piomelli. Wall-layer models for large-eddy simulations. *Progress in Aerospace Sciences*, 44: 437–446, 2008. doi: 10.1016/j.paerosci.2008.06.001.

[133] U. Piomelli and E. Balaras. Wall-layer Models For Large-Eddy Simulations. *Annu. Rev. Fluid Mech*, 34:349–374, 2002. doi: 0066-4189/02/0115-0349.

[134] M.M. Rai. A direct numerical simulation of turbine rotor-stator interaction. In *39th AIAA Fluid Dynamics Conference*, number 3685, San Antonio, June, 22-25 2009.

[135] D.A. Rains. *Tip Clearance Flows In Axial Compressors and Pumps*. PhD thesis, California Institute of Technology, 1954.

[136] O. Reynolds. An experimental investigation of the circumstances whether the motion of water shall be direct and sinuous, and the law of resistance in parallel channels. *Philosophical Transactions of the Royal Society of London*, 174:935–982, 1883.

[137] O. Reynolds. On the dynamical theory of incompressible viscous fluids and the determination of the criterion. *Philosophical Transactions of the Royal Society of London*, 186:123–164, 1895.

[138] L.F. Richardson. Weather prediction by numerical process (second edition, originally published in 1922). *Cambridge University Press*, 1:14, 2007. ISBN 978-0-521-68044-8 paperback.

[139] W. Riéra, L. Castillon, S. Deck, J. Riou, X. Ottavy, and F. Leboeuf. Zonal Detached Eddy Simulation applied to the tip clearance flow in an axial compressor. In *47th International Symposium of Applied Aerodynamics, Paris, France*, number FP07-2012-riera, Paris, Mar. 2012. 3AF.

[140] W. Riéra, L. Castillon, J. Marty, and F. Leboeuf. Inlet condition effects on the tip clearance flow with Zonal Detached Eddy Simulation. In *Proceedings of ASME Turbo Expo 2013: Turbine Technical Conference and Exposition GT2013*, number GT2013-94187, San Antonio, Texas, June 2013. doi: 10.1115/GT2013-94187.

[141] W. Riéra, L. Castillon, J. Marty, and F. Leboeuf. Inlet condition effects on the tip clearance flow with Zonal Detached Eddy Simulation. *Journal of Turbomachinery*, 136(4)(041018):10, April 2014. doi: 10.1115/1.4025216. Editor : R. Bunker.

[142] J. Riou. *Etude et contrôle du décrochage d'ailes et gouvernes de missile en régime transsonique*. PhD thesis, Université Paris 13, Oct. 2009.

[143] J. Riou. Tip-leakage-flow study using hybrid RANS/LES methods. In *46th Symposium for Applied Aerodynamics, Orléans, France*, pages 1–10, Orleans, Mar. 2011. 3AF.

[144] J. Riou and E. Garnier. Control of Separated Flow over Swept Missile Fin Using Pitching Oscillations. *AIAA Journal*, 49:1819–1822, 2011. doi: 10.2514/1.J051198.

[145] B.A. Robinson, R.M. Barnett, and S. Agrawal. Simple Numerical Criterion for Vortex Breakdown. In *AIAA Aerospace sciences meeting*, volume 32, pages 116–122, 1994.

[146] P. Sagaut and S. Deck. Large eddy simulation for aerodynamics: status and perspectives. *Royal Society*, 367:2849–2860, 2009. doi: 10.1098/rsta.2008.0269.

[147] P. Sagaut, S. Deck, and M. Terracol. *Multiscale and Multiresolution Approaches in Turbulence*. Imperial College Press, 2006. doi: 10.1142/9781860948978.

[148] P. Sagaut, S. Deck, and M. Terracol. *Multiscale and Multiresolution Approaches in Turbulence LES, DES and Hybrid RANS/LES Methods: Applications and Guidelines (2nd Edition)*. Imperial College Press, 2013.

[149] J. Sans, G. Dell'era, J. Desset, and J-F. Brouckaert. Time-resolved measurements of the unsteady flow field in a single stage low pressure axial compressor. In *Proceedings of ASME Turbo Expo 2013: Turbine Technical Conference and Exposition GT2013*, number GT2013-94264, San Antonio, Texas, June 2013.

[150] D. Schoenweitz, M. Voges, G Goinis, and G. Enders. Experimental and numerical examinations of a transonic compressor-stage with casing treatment. In *Proceedings of ASME Turbo Expo 2013: Turbine Technical Conference and Exposition GT2013*, number GT2013-95550, San Antonio, Texas, June 2013.

[151] K. Shi and S. Fu. Study of shock/blade tip leakage vortex/boundary layer interaction in a transonic rotor with iddes method. In *Proceedings of ASME Turbo Expo 2013: Turbine Technical Conference and Exposition GT2013*, number GT2013-95252, San Antonio, Texas, June 2013.

[152] K. Shi, Z. Xiao, H. Chen, and S. Fu. Numerical Study of Tip Leakage Flow of a Transonic Compressor Rotor with IDDES Method. In *Proceedings of the 21st ISABE Conference, Busan, Korea*, number ISABE-2013-1116, Sep. 9-13th 2013.

[153] M. Shur, P. Spalart, K. Strelets, and A. Travin. A hybrid RANS-LES approach with delayed-DES and wall-modelled LES capabilities. *International Journal of Heat and Fluid Flow*, 29: 1638–1649, 2008. doi: 10.1016/j.ijheatfluidflow.2008.07.001.

[154] F. Simon, S. Deck, P. Guillen, and P. Sagaut. Reynolds-Averaged Navier–Stokes/Large-Eddy Simulations of Supersonic Base Flow. *AIAA Journal*, 44(11):2578–2590, Nov. 2006. doi: 10. 2514/1.21366.

[155] T.S. Sirakov and C-S. Tan. Effect of Unsteady Stator Wake—Rotor Double-Leakage Tip Clearance Flow Interaction on Time-Average Compressor Performance. *Journal Of Turbomachinery*, 125:465–474, 2003. doi: 10.1115/1.1574822.

[156] B.R. Smith. A near wall model for the k l two equation turbulence model. In *Proceedings of the 25th Fluid Dynamics Conference*, number 94-2386, Colorado Springs, Colorado, June, 20-23 1994.

[157] L.H.Jr Smith. The effect of tip clearance on the peak pressure rise of axial flow fans and compressors. In *ASME symposium on stall*, pages 149–152. American Society of Mechanical Engineers, 4-5th Dec. 1958.

[158] P. Spalart. Strategies for turbulence modelling and simulations. *International Journal for Heat and Fluid Flow*, 21:252–263, 2000. doi: 10.1016/S0142-727X(00)00007-2.

[159] P. Spalart. Detached-Eddy Simulation. *Annual Review of Fluid Mechanics*, 41: 10.1146/annurev.uid.010908.165130, 2009. doi: 10.1146/annurev.ïňĆuid.010908.165130.

[160] P. Spalart and M. Shur. On the sensitization of Turbulence Models to Rotation and Curvature. *Aerospace Science and Technology*, 5:297–302, 1997. doi: 10.1016/S1270-9638(97)90051-1.

[161] P. Spalart, S. Deck, M. Shur, K. Squires, K. Strelets, and A. Travin. A new version of detached-eddy simulation, resistant to ambiguous grid densities. *Theoretical And Computational Fluid Dynamics*, 20:181–195, 2006. doi: 10.1007/s00162-006-0015-0.

[162] P.R. Spalart and S.R. Allmaras. A one-equation turbulence model for aerodynamic flows. *La Recherche Aérospatiale*, 1:5–21, 1994.

[163] P.R. Spalart, W.H. Jou, M. Strelets, and S.R. Allmaras. Comments on the feasibility of LES for wings, and on a hybrid RANS/LES approach. In L Sakell C Liu, Z Liu, editor, *Advances in DNS/LES*, page 137–47, 1997.

[164] R.E. Spall, T.B. Gatski, and C.E. Grosch. A criterion for vortex breakdown. *Physics of Fluids*, 30:3434, 1987. doi: 10.1063/1.866475.

[165] J.A. Storer and N.A. Cumpsty. An Approximate Analysis And Prediction Method For Tip Clearance Loss In Axial Compressors. In *38th International Gas Turbine And Aeroengine Congress and Exposition, ASME, Cincinnati, Ohio*, number 93-GT-140, pages 648–656, May, 24-27 1993.

[166] H. Tartousi, P. Kulisa, F. Leboeuf, G. Ngo Boum, A. Lefebvre, and A. Yammine. Numerical Investigation of a Turbocharger Centrifugal Compressor: Volute Influence on the Performance of The Compressor. In *European Turbomachinery Conference, Istanbul, Turkey*, pages 1–10, March, 21-25 2011.

[167] J. Tyacke, P. Tucker, R. Jefferson-Loveday, N. Rao Vadlamani, R. Watson, I. Naqavi, and X. Yang. LES for turbines: methodologies, cost and future outlooks. In *Proceedings of ASME Turbo Expo 2013: Turbine Technical Conference and Exposition GT2013*, number GT2013-94416, San Antonio, Texas, June 2013.

[168] J. Tyacke, P. Tucker, R. Jefferson-Loveday, N. Rao Vadlamani, R. Watson, I. Naqavi, and X. Yang. LES for turbines: methodologies, cost and future outlooks. *Journal of Turbomachinery*, Accepted Manuscript(TURBO-13-1148):1–17, 2013. doi: 10.1115/1.4025589.

[169] R. Van Remmings, K. Shi, and F. Thiele. Delayed-Detached Eddy Simulation of Near-Stall Axial Compressor Flow with Varying Passage Numbers. *Progress in Hybrid RANS-LES Modelling*, 117:439–448, 2012. doi: 10.1007/978-3-642-31818-4. Notes on numerical fluid mechanics and multidisciplinary design.

[170] Y. Wang and W.J. Devenport. Wake of a Compressor Cascade with Tip Gap. *AIAA Journal*, 42 (11):2332, Nov. 2004. doi: 10.2514/1.5272.

[171] P-E. Weiss and S. Deck. Control of the antisymmetric mode (m=1) for high Reynolds axisymmetric turbulent separating-reattaching flows. *Physics of Fluids*, 23(095102):1–19, 2011. doi: 10.1063/1.3614481].

[172] P.D. Welch. The Use of Fast Fourier Transform for the Estimation of Power Spectra : A Method Based on Time Averaging Over Short, Modified Periodograms. *IEEE Transactions on audio and electroacoustics*, 2(AU-15):70–73, 1967.

[173] C.W. Wenger, W.J. Devenport, K.S. Wittmer, and C. Muthanna. Wake of a Compressor Cascade with Tip Gap. *AIAA Journal*, 42(11):2341, Nov. 2004.

[174] D.C. Wilcox. Reassessment of the scale-determining equation for advanced turbulence models. *AIAA Journal*, 26(11):1299–1310, 1988. doi: 10.2514/3.10041.

[175] J.G. Wissink. DNS of separating, low reynolds number flow in a turbine cascade with incoming wakes. *International Journal of Heat and Fluid Flow*, 24(4):626 – 635, 2003.

[176] J.G. Wissink and W. Rodi. Direct numerical simulations of transitional flow in turbomachinery. *Journal of Turbomachinery*, 128(4):668–678, 2006.

[177] K. Yamada, K. Funazaki, and M. Furukawa. The behavior of tip clearance flow at near-stall condition in a transonic axial compressor rotor. In *Proceedings of GT2007 ASME Turbo Expo 2007: Power for Land, Sea and Air*, 2007.

[178] K. Yamada, H. Kikuta, M. Furukawa, S. Gunjishima, and Y. Hara. Effects of tip clearance on the stall inception process in an axial compressor rotor. In *Proceedings of ASME Turbo Expo 2013: Turbine Technical Conference and Exposition GT2013*, number GT2013-95479, San Antonio, Texas, June 2013.

[179] D. You, M. Wang, P. Moin, and R. Mittal. Effects of tip-gap size on the tip-leakage flow in a turbomachinery cascade. *Physics of Fluids*, 18:105102, 2006. doi: 10.1063/1.2354544.

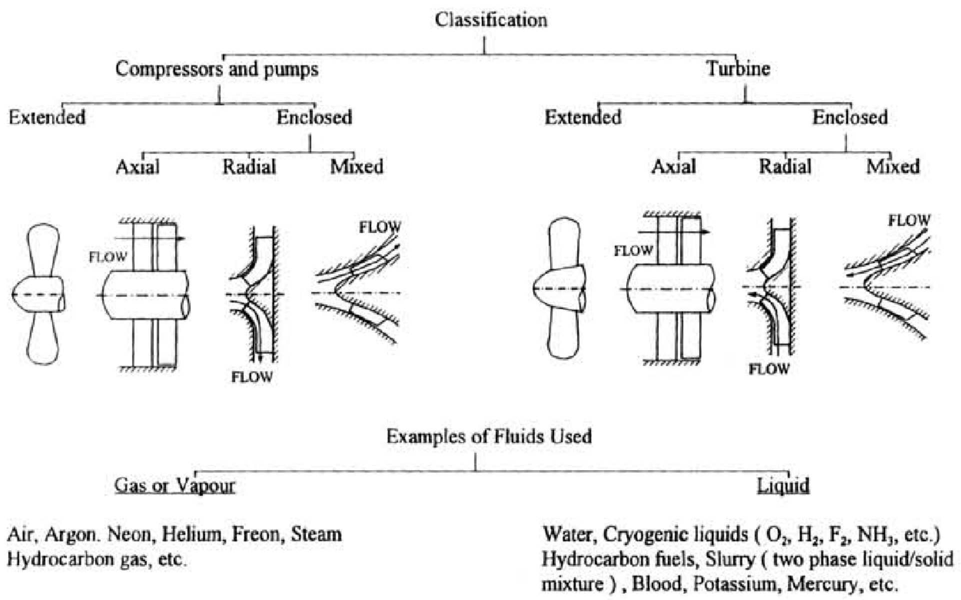

Figure 1.1 — *Classification of turbomachinery (from Lakshminarayana [96]).*

compressor, such as the pumps. The possibilities of turbomachines application are numerous. Therefore they are used in many different configurations linked to energy conversion. Some are *open*, or extended, and thus influence a wide, not quantifiable, area around them. Others are *shrouded*, that is to say, enclosed by a casing.

Depending on the expected service of the machine, that is to say the required pressure ratio and mass flow rate through the cascade, different configurations, presented in figure 1.1, best suit the operating condition. Thereby, depending on how the flow crosses the rotor, the denomination of the machine changes. It is regarded as axial if the through-flow is parallel to the axis of rotation, which is used in high mass flow rate configurations. The machine is considered as radial if the through-flow is perpendicular to the axis of rotation, which is used for compact high pressure ratio configurations. An infinite number of possibilities exists in between, and the resulting machines are then called mixed-flow turbomachines. If a higher pressure ratio is required between the inlet of the machine and its outlet, many rotor stages are mounted in series.

The rotating motion of rotor blades increases the swirl of the fluid. In order to correct the fluid deflection for the next rotor stage, stator blades are implemented in between the stages of rotor blades. This addition of stages increases the complexity of the flow through the turbomachine. For instance, there are interactions between the rotors and the stators that modify the structure of the flow. Besides, the additional stages increase the weight of the compressor. It is however possible to avoid this stator stage with the use of counter rotating rotors. However, this is for the moment only done in few configurations, for instance in Counter Rotating Open Rotors (CROR) or contrafans, due to the higher design constraints it implies.

These two types of blades, rotating for the rotors and steady for the stators lead to two different ways to consider the flow within a turbomachine: with absolute or relative values. As a consequence, there are two frames of reference linked to the stators or rotors. For the rotors, some values in the relative frame of reference differ from the ones in the absolute due to the rotation of the blade. In order to understand this concept, the velocity triangles are used as presented in figure 1.2. The angles defined in the absolute, α, and relative, β, frames of reference are detailed in equation I-1. U is the rotating velocity of the rotor. The velocity V_θ and W_θ are respectively the circumferential velocities in the absolute and relative, or more accurately rotating, frame of reference. The velocities V and W are their meridian counterparts, that is to say, the addition of the axial and radial velocities. The angle between the axial, V_x, and meridian

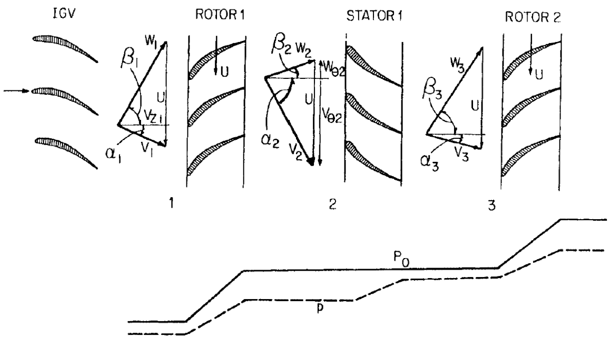

Figure 1.2 — *Velocity triangles in an axial compressor (from Lakshminarayana [96]). The distributions of enthalpy and temperature are similar to the pressure distribution p. The distributions of stagnation enthalpy and temperature are similar to the stagnation pressure distribution P_0.*

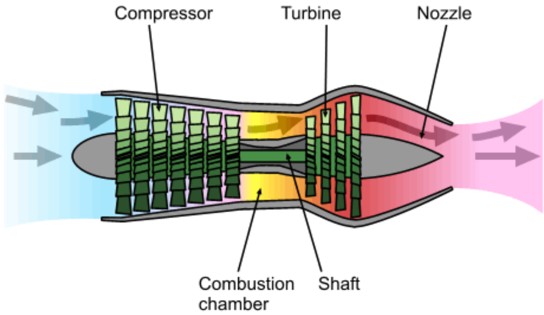

Figure 1.3 — *Axial turbojet engine [51]*

velocity, V_m, is called ϕ, the meridian angle, defined in equation I-2.

$$\alpha = \text{atan}\left(\frac{V_\theta}{V_m}\right) \qquad \beta = \text{atan}\left(\frac{W_\theta}{V_m}\right) \tag{I-1}$$

$$\phi = \text{atan}\left(\frac{V_x}{V_m}\right) \tag{I-2}$$

In aeronautics, turbomachines are used for propulsion systems, such as propellers (open) or turbojet engines (shrouded). In turbojet engines, there are both compressors and turbines as presented in figure 1.3, with many stages. The purpose of the compressor is to transfer the energy from a rotating shaft to the air and thus to rise its pressure. Then, the flow reaches the combustion chamber and is mixed with fuel. It is then burned and therefore its energy increases. The hot fuel-air mix expands and exits the combustion chamber. At the outlet, the turbine extracts a part of the energy of this hot fluid, which decreases its pressure and temperature. This energy is then provided to the compressor through the shaft. Then, the fluid reaches the nozzle, where it is accelerated and given the appropriate direction. Finally, the fluid exits the whole system with a higher pressure and velocity, which produces the thrust necessary for the plane to overcome the drag and therefore to fly.

1.1.2 Operating points

In order to have an efficient energy transfer to the fluid in compressors, the flow must be guided smoothly through the rotor and stator stages of the machine. Moreover, the compressors are very sensitive to the flow angle at the leading edge of the blade. This is the reason why the stators guide the flow

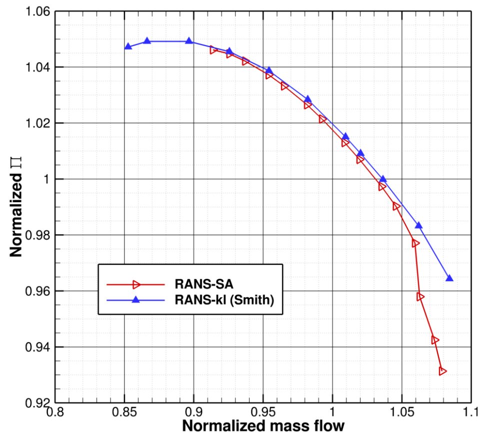

Figure 1.5 — *Surge margin difference between k-l Smith and Spalart-Allmaras turbulence models on the CREATE compressor (Courteously from J. Marty).*

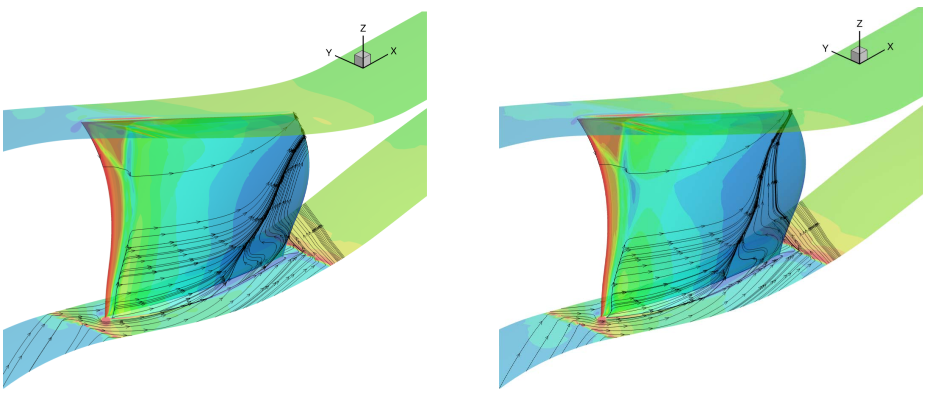

(a) k-l Smith.

(b) Spalart-Allmaras.

Figure 1.6 — *Friction lines on the first rotor of the CREATE compressor near surge (Courteously from J. Marty).*

the CREATE compressor with two turbulence models: the Spalart-Allmaras (RANS-SA) [162] and the k-l model from Smith [156]. This study underlined that the Spalart-Allmaras turbulence model was more unstable than the k-l model from Smith near the surge line. If the Spalart-Allmaras model is used for turbomachinery design, the computed surge margin is then different which leads to a narrower operability range seen by the computation due to the numerical instability. The reason, underscored by Marty, is a more important flow separation at the hub corner with the Spalart-Allmaras turbulence model than with the k-l Smith model, which is not physical and induced by the numerics. This separation difference is visible for computations near surge, in figure 1.6 where the separation line reaches the trailing edge at the blade tip in the Spalart-Allmaras case, contrary to the one with the k-l Smith model. This discrepancy between the methods highlights the difficulty to simulate accurately the secondary flows in the compressor. The tip-leakage flow is one of them.

1.1.3 General principles of the tip-leakage flow

1.1.3.1 A three dimensional flow

In shrouded axial compressors, there is a gap between a rotating blade tip and the annulus wall. The pressure field around a blade implies a pressure gradient between the two sides of the blade. This pressure

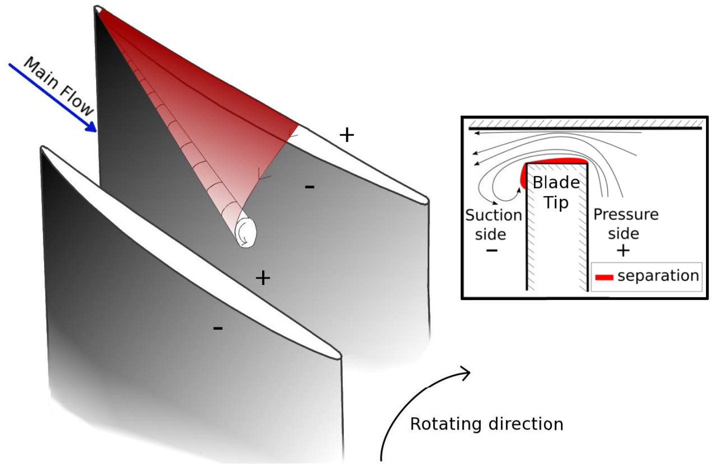

Figure 1.7 — *Inception of the tip-leakage flow and rolling up of the main tip-leakage vortex (Inspired by Lakshminarayana et al. [99]).*

difference leads to a leakage flow from the pressure side to the suction side of the blade, as shown in figure 1.7. The flow then leaks through the clearance following the chordwise pressure distribution. This phenomenon is mainly inviscid as noted by Lakshminarayana and Horlock [97]. Then, it exits the clearance and mixes with the main flow.

The interaction of this secondary flow with the main stream, the annulus boundary layer developing on the shroud and the blade wakes leads to penalizing losses as already mentioned by Herzig et al. [75] in 1954. The shear layer, which stems from the direction difference between the leakage flow and the main stream, is the main loss mechanism in the casing region. By contrast, the non-uniform mixing zone downstream of the blade contributes a little to the whole pressure loss as underlined by Storer and Cumpsty [165]. Therefore designing efficient compressors requires an accurate prediction of the tip-leakage flow and its development.

1.1.3.2 Flow topology near the casing

There are many different configurations of tip-leakage flows depending on the type of turbomachinery. Moreover, the topology in the vicinity of the shroud can be very different.

One of the major encountered phenomenon is the main tip-leakage vortex. When the leakage flow exits the tip gap and mixes with the main flow, it undergoes a loss of circumferential momentum. This results in the rolling up of this jet flow into the main tip-leakage vortex. Nevertheless, in some studies, such rolling up is not experienced, partially or totally. For instance, Furukawa et al. [54] investigated with a RANS simulation a low speed isolated axial compressor rotor with moderate loading and a tip gap height of 1.7% of the chord length. At a low flow rate, they captured a breakdown of the vortex. Nevertheless, downstream of this breakdown, the low streamwise vorticity prevents the flow from rolling up into a vortex again. A case with no rolling up at all was studied by Lakshminarayana et al. [100] on an experimental single stage axial compressor made up of an Inlet Guide Vane (IGV), a rotor and a stator. The tip gap height of the rotor is 2.27% of the chord. The reasons proposed by the authors to explain why the flow did not roll up are that the inlet swirl, high turbulence and high blade loading cause an intense mixing of the leakage jet and therefore prevent the flow from rolling up. In their configuration, the leakage flow high velocity makes it mix rapidly with the main flow. Lakshminarayana et al. [100] underscore that the difference of magnitude and direction of the leakage jet flow and main stream are among the main effects preventing the rolling up. One have to mention here the major importance of the

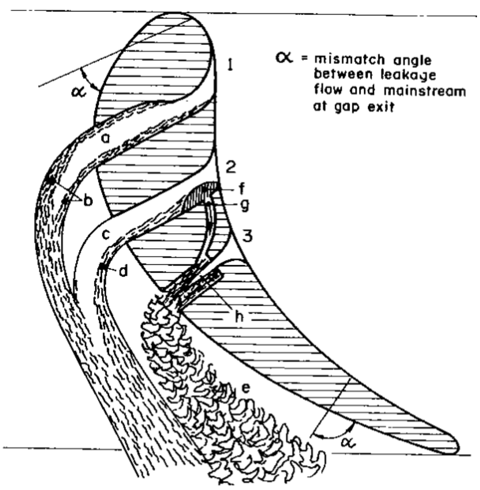

Figure 1.9 — *Conceptual model showing various types of flow active in the tip clearance region (from Bindon [11]).*

conceptual model, Bindon [11] underscores that there is not a single flow pattern leaking through the gap. Instead of a linearly spread leakage, he hypothesized that there are different kinds of channels with and without separation bubbles within the gap. The axial position of these different channels depending on the pressure distribution along the chord, and thus the loading. Kang and Hirsch [87] saw similar channels in the tip gap on a linear cascade with a stationary endwall. With paint-trace visualizations on the endwall, Kang and Hirsch [87] highlighted the flow pattern drawn in the tip clearance, shown in figure 1.10. The skin friction line splits into two branches at a saddle point in front of the leading edge. This results in a horseshoe vortex. The tip-leakage vortex starts to roll-up just downstream the leading edge in the suction side. They pointed out that streamlines in the gap are neither normal to the suction side nor to the camber line, contrary to what was assumed by Rains [135].

1.1.4 Influence of the gap size on the tip-leakage flow

The most important parameter to take into account for the tip-leakage flow is the gap size. As expected, it is the main factor that influences the flow topology at the rotor tip. In order to compare the different configurations, it is then a prerequisite to define a dimensionless value to characterize this parameter. It requires then another length. Two dimensionless terms are built depending on the use of the axial chord or the maximum thickness of the blade tip. They are respectively defined in equations [I-3] and [I-4].

$$\tau = \frac{GapSize}{AxialChord} \tag{I-3}$$

$$\lambda = \frac{GapSize}{MaximumBladeThickness} \tag{I-4}$$

Rains [135] studied experimentally the gap size effects on a rotor at 1750rpm and showed that the leakage flow can be regarded, in a first assumption, as an inviscid phenomenon driven only by the pressure difference for large λ values, and the vortex structure is predominant. In Rains' studied installation, for small ratio between gap size and blade thickness the gap flow was modelled as a channelled flow. For $\lambda = 0.026$ and lower there were no vortex rolling-up. For $\lambda < 0.05$, viscous forces were dominant in the clearance and at $\lambda = 0.1$, the counter pressure effects of the viscosity in the gap were counterbalanced by the lift of the blade. The viscous effects could be neglected for $\lambda >> 0.1$. Finally, beyond

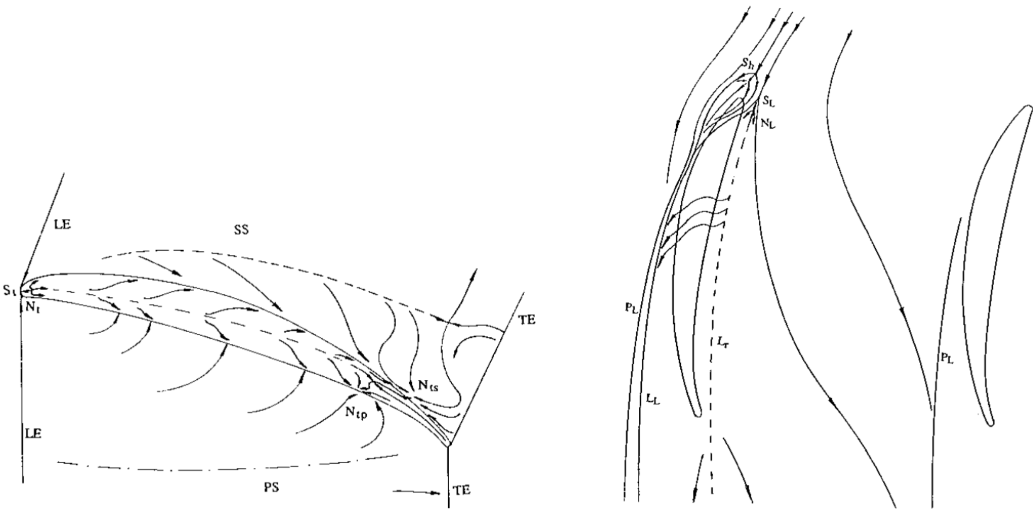

(a) Blade tip. (b) Casing.

Figure 1.10 — *Schematic of flow pattern on the blade tip and on the casing (from Kang and Hirsch [87]).*

$\lambda = 0.167$, a potential flow pressure distribution was established. Rains [135] developed then a model to take into account the tip-leakage flow changes depending on the tip clearance size and based on the number $\lambda^2 \cdot Re \cdot \epsilon$. Re is the Reynolds number based on the free stream velocity and $\epsilon = \frac{\tau}{\lambda}$ is the maximum thickness to chord ratio at the blade tip. He highlighted that viscous forces are predominant for $\lambda^2 \cdot Re \cdot \epsilon < 11$ whilst the inertia forces are predominant for $\lambda^2 \cdot Re \cdot \epsilon > 125$.

More recently, Brion [16] analysed experimentally two configurations: a split wing (NACA0012) configuration generating a vortex pair and the same with a splitter plane. This latter configuration is similar to an isolated fixed linear cascade. The first aim was to study the vortex instability and the influence of the Crow instability [28, 29] which is linked to the interaction between two vortices. Brion [16] observed that for small gaps with $\tau < 2\%$, the flow is nearly perpendicular to the chord which means that it is channelled by the gap and the vortex forms far from the wing and near the hub, which is similar to what Rains saw for small gaps. For $\tau > 2\%$, the vortex remains close to the wing. Thereby, it was shown in the literature that the gap size influences the tip-leakage vortex behaviour. Furthermore, this parameter affects the whole flow topology. For instance, Kang and Hirsch [87, 88] studied the flow field for a linear cascade with 1.0%, 2% and 3.3% gap sizes. The aforementioned horseshoe vortex they detected was only observed for small clearance.

The different flow topologies induced by the different gap sizes imply different losses too. Smith [157] presented experimental data gathered from different studies to understand the effects of the tip gap size. The peak pressure rise for the blade was found to be inversely proportional to the tip gap size τ as presented in figure 1.11. The impact appeared to be 4% of pressure loss for each 1% increase in the dimensionless gap size τ. Bindon [11] analysed the loss in a turbine cascade and highlighted that the loss varies linearly with gap size as shown in figure 1.12. However, there are fundamental differences with and without clearance, and even the smallest gap size changes the loss. He found that the total tip clearance loss is made up of the internal gap loss (39%), the suction corner mixing loss (48%) and endwall/secondary loss (13%) as presented in figure 1.13. Even if these results from Bindon are for turbines, some similarities are found with compressors concerning the tip-leakage flow topology [87], as previously explained.

The main solution found to reduce this negative impact of the leakage flow is to reduce the gap size. This is the reason why abradable material is used on the housing of the compressors used in the industry.

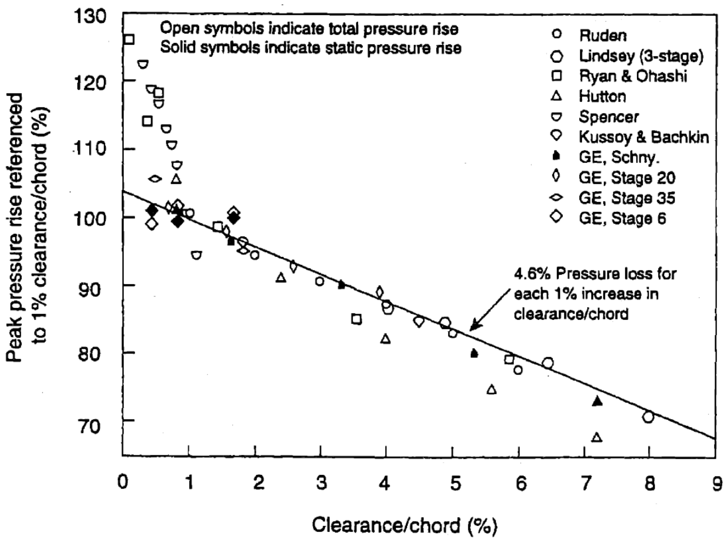

Figure 1.11 — *Effect of tip clearance on peak pressure rise (original data from Smith [157], extracted from Bae [2]).*

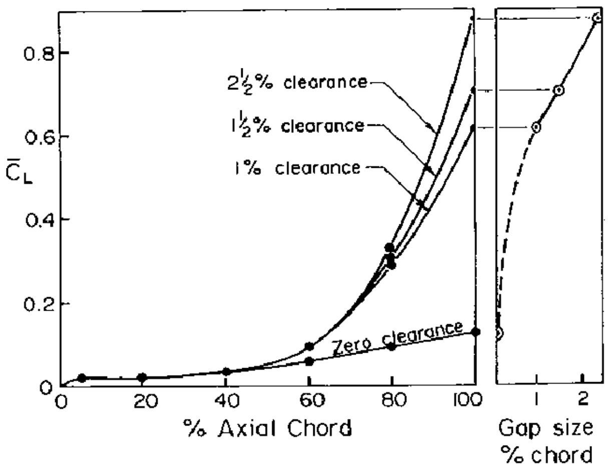

Figure 1.12 — *The growth of total integrated loss coefficient from leading to trailing edge for various values of tip clearance gap size (from Bindon [11]).*

When the rotor rotates, its radial length is increased due to the centrifugal forces. As a consequence, the tip of the blade touches the casing. The resulting friction wears then a part of the abradable material away so that the tip gap size is as small as possible. Another possibility is to reduce the gap size artificially with flow control devices. For instance Bae [2] analysed the effects of synthetic jet actuators located in the tip gap on the vortex flow for a linear cascade. The device reduced the gap size by deflecting the streamline, enhanced the mixing, reduced the influence of the vortex and increased the exit static pressure. Nevertheless, the different flow structure due to the linear cascade prevented to judge the possibilities on a real rotor. Figure 1.14 presents how it could be implemented on a rotor.

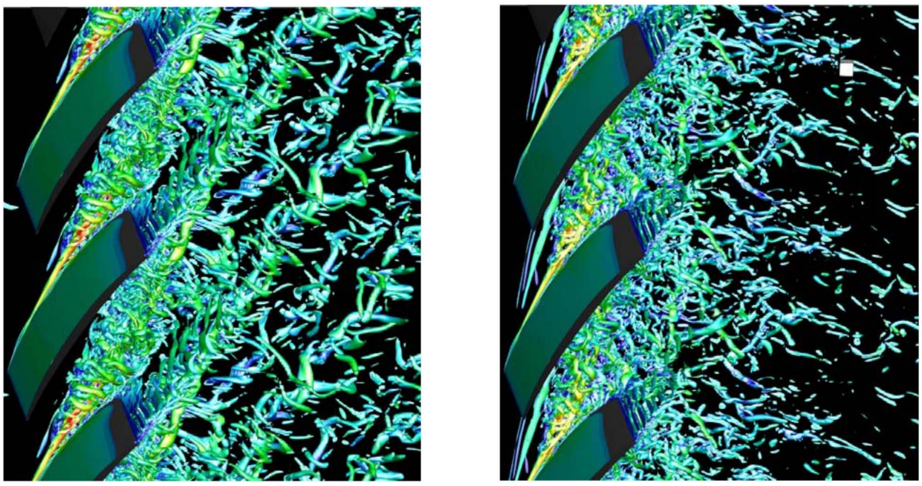

(a) Static end wall. (b) Moving end wall.

Figure 1.17 — *Q criterium flooded by the longitudinal velocity (from Riou [143]).*

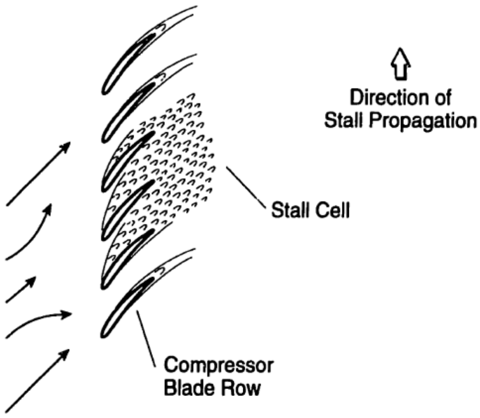

Figure 1.18 — *Physical mechanism of rotating stall (from Hoying [79]).*

centre and its decay downstream are scarcely affected by the moving wall for gap sizes of 0.8%, 1.6% and 3.3% chord. This study confirmed why many fundamental analysis are carried out on linear cascades. The same configuration was numerically investigated with Delayed DES, a first version of Zonal DES and a classic RANS approach by Riou [143]. The purposes were to evaluate the numerical methods and analyse the effects of relative motion Figure 1.17 presents the flow field with ZDES with and without motion. The vortex disrupts earlier with the endwall motion. Moreover, Riou [143] observed a secondary vortex in the moving endwall case. Besides, an elongation of the vortex core is captured too, and it bends towards the neighbouring blade. With no endwall motion, the vortex dilates but remains circular. The steps concerning the inception development and disorganisation of the vortex remains the same in the two cases. Inoue and Furukawa [82] observed similar results, based on various experiments. However, they emphasized that the loss production was considerably smaller with the relative motion than without. Thereby, this highlighted that the loss production is not in proportion to the vortex intensity.

1.1.6 Throttle effect and tip clearance flow

The tip-leakage flow is known to be one of the main instability sources in compressors near surge. This is the reason why its effects are studied in the literature up to the surge.

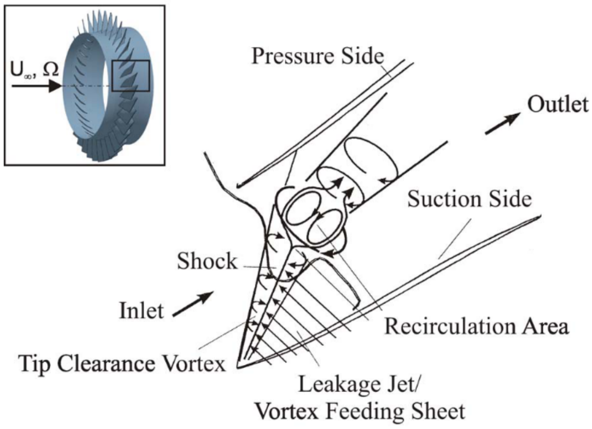

Figure 1.23 — *Shock/tip-leakage vortex interaction (from Hofmann and Ballmann [77]).*

In 1985, Hall [73] summarized the main available analyses and presented the theories [7] behind vortex breakdown in order to explain why there are core bursting in some configurations. Some criteria were developed in the literature to delineate the region where breakdown occurs. For instance, a criterion is based on the fall in the Rossby number [164, 145] defined as the ratio of the axial and circumferential momentum in a vortex. This criterion is applied in some studies such as the recent work of Riou [143] in turbomachinery.

Tip clearance vortex breakdown is considered as a possible cause of stall inception in compressors by many authors such as Hofmann and Ballmann [78, 77]. This seems to be the case mainly in large gap configurations [54]. Indeed, in the small tip clearance cases the aforementioned spike-type stall is predominant. This was recently confirmed by Yamada et al. [178]. They have shown with experimental and DES analyses that the rotating disturbance, in large tip gap cases, appeared intermittently and randomly at near-stall condition. In addition, the compressor did not systematically fall into the stall after the inception of vortex disturbance. Nonetheless, it contributed to the blockage effect near stall.

The interaction of the tip-leakage vortex with a shock in a transonic compressor does not necessarily lead to vortex breakdown as shown by Hah et al. [70]. Nevertheless, the flow field becomes unsteady due to shock oscillations. If the shock is oblique or normal to the vortex, the interaction differs. This interaction seems to depend on the operating point too. Hoeger et al. [76] compared RANS simulations with experimental laser data close to stall, peak efficiency and choke. In their configuration, the vortex core went through the shock without change in cross section at peak efficiency while its cross section increased near stall. However, in all of their studied cases, they highlighted that a steep increase in loss was found in the strong shock-vortex interaction region. Bergner et al. [9] studied experimentally a transonic compressor and highlighted that at peak efficiency, the passage shock was almost normal to the vortex. By contrast, near stall, the shock strength increased because the shock moved upstream which led to an oblique shock/vortex interaction.

The interaction with the shock, the vortex and the boundary layer was studied numerically by Chima [26] and compared to experiments. He highlighted strong interactions between these different flows. Nevertheless, he has shown limitations of the used algebraic turbulence model to compute the flow near the casing, even if the performance predictions were correct. Yamada et al. [177] analysed with RANS and URANS computations the transonic axial compressor known as the Rotor 37 from the NASA. In this configuration, the boundary layer separation on the casing wall and on the blade suction surface emanated from their interaction with the shock wave. Moreover, the same case with no clearance revealed a different position for the separation on the suction surface. This suggested a strong link between these phenomena: boundary layer separation on the suction surface, shock and leakage flow.

Name	Aim	Unsteady	*Re*-dependence	3/2D	Empiricism	Grid	Steps	Ready
2DURANS	Numerical	Yes	Weak	No	Strong	10^5	$10^{3.5}$	1980
3DRANS	Numerical	No	Weak	No	Strong	10^7	10^3	1990
3DURANS	Numerical	Yes	Weak	No	Strong	10^7	$10^{3.5}$	1995
DES	Hybrid	Yes	Weak	Yes	Strong	10^8	10^4	2000
LES	Hybrid	Yes	Weak	Yes	Weak	$10^{11.5}$	$10^{6.7}$	2045
QDNS	Physical	Yes	Strong	Yes	Weak	10^{15}	$10^{7.3}$	2070
DNS	Numerical	Yes	Strong	Yes	None	10^{16}	$10^{7.7}$	2080

Table 1.1 — *Summary of the main strategies to simulate turbulent flows (from Spalart [158])*

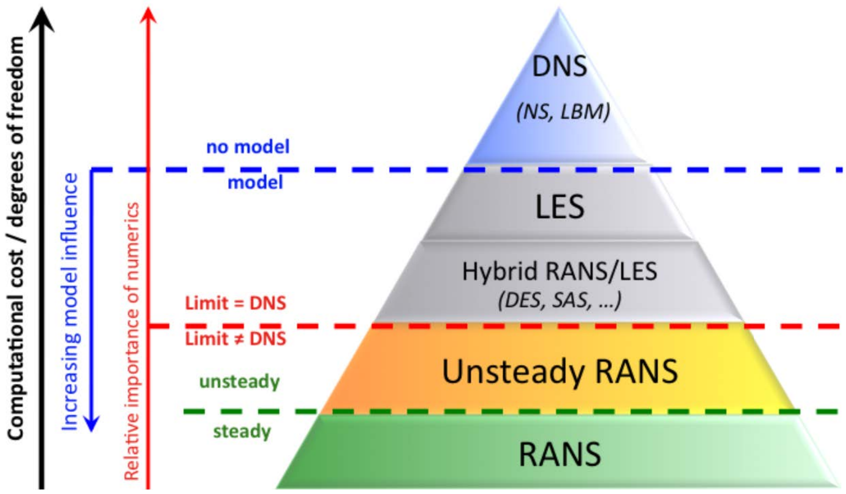

Figure 1.25 — *From RANS to DNS, the possibilities of CFD (from Sagaut et al. [147])*

classic simulations encountered in the industry. Figure 1.25 classifies these approaches depending on their accuracy and dependence on numerics or on models.

The Direct Numerical Simulation (DNS) could solve every time and spatial scales of turbulence and enable the finest description of the tip-leakage flow. However this method is impossible to use for realistic configurations due to the high computational cost it requires. Indeed, the number of nodes depends on the Reynolds number of the case and scales as $Re^{9/4}$ for 3D meshes.

Thereby, DNS is not expected to be used before 2080 [158]. The most recent studies with DNS in turbomachinery are still close to flat plates simulations at low Reynolds. For instance, Wissink [175] and Wissink and Rodi [176] studied the transitional flow in turbine and compressors. Balzer and Fasel [4, 5] studied control devices of a separation bubble in a simple turbine with a Reynolds number of 25000. Such studies inform us accurately on the boundary layer development on curved surfaces. Nevertheless, they are far from being representative of real configurations.

Reynolds-averaged Navier-Stokes (RANS) simulations are widely used in the industry to simulate tip-leakage flows in real configurations at high Reynolds number. With the computational resources available in the 2010, such simulations are possible overnight. This parameter is important for engineers to test new designs. Nevertheless, it is impossible to capture unsteady effects with this method.

The Unsteady RANS (URANS) approach is necessary when investigators try to capture unsteady effects such as rotor-stator interactions [65]. URANS helped discovering and understanding unsteady phenomena encountered in the tip region, such as the vortex rolling-up and its motion. Moreover, it enabled to evaluate the effects of unsteady control devices. However this method revealed not to predict accurately the tip-leakage flow [143] and other complex unsteady flows encountered in turbomachinery [149, 150]. There are nonetheless numerous efforts to improve it by the means of different turbulence models or higher order numerical methods.

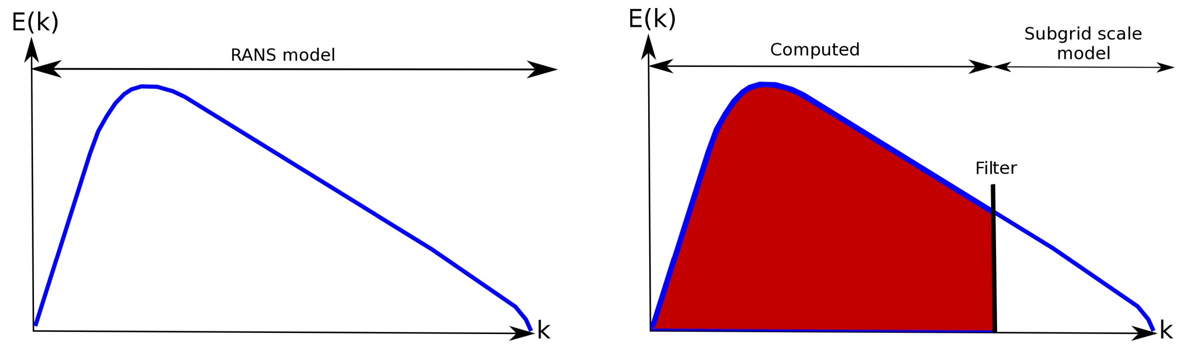

(a) RANS. (b) LES.

Figure 2.1 — *Energy spectra for the repartition of the computed and modeled scales for RANS and LES.*

The $k - \omega$ model from Wilcox [174] uses $\omega \propto \frac{\varepsilon}{k}$ to determine the length scale. This specific turbulence dissipation is defined in the model by equation [II-37]. Its transport equation comes then from the transport equations of k and ε.

$$\omega = \frac{\varepsilon}{\beta^* k} \qquad \beta^* = 0,09 \qquad \text{and} \qquad \nu_t = \frac{k}{\omega} \tag{II-37}$$

2.2 Zonal Detached Eddy Simulation

The Zonal Detached Eddy Simulation (ZDES), used in this thesis as the advanced numerical method, is based on the Detached Eddy Simulation (DES), a hybrid model between unsteady RANS and Large Eddy Simulation (LES), as presented in figure 1.25. In order to understand the ZDES model, this section gives an overview of the LES and the main DES versions before detailing the ZDES approach.

2.2.1 Large Eddy Simulation

The Large Eddy Simulation (LES) is different from the aforementioned RANS method. The RANS approaches model the whole turbulent field and are calibrated to give relevant results for the averaged field. However, in cases driven by the turbulence dynamics, with unsteady phenomena, they reach their limits. In order to understand these limitations, it is necessary to understand how the turbulence behaves. The process is called the *energy cascade* and was first thought by Richardson [138] in 1922 and then defined for high Reynolds number isotropic turbulence by Kolmogorov [93] in 1941. The energy is mainly supplied into the turbulent field from the boundary conditions of the domain to the large scales of the flow. Then, the energy is transferred in an inviscid mechanism from the large to the small structures. This zone is the inertial range and is characterized by a constant slope law in $k^{-5/3}$ for the energy distribution, with k the wavenumber. This process is finally limited by the molecular dissipation of the smallest structures when the Kolmogorov scale is reached. This scale depends on the Reynolds number of the flow. The use of the turbulent viscosity in RANS methods aims at modelling the whole cascade. Nevertheless, in real flows, the energy spectrum differs from the theory. For instance, the energy transfer can sometimes be reversed due to the vortex pairing for instance. This phenomenon, called *backscatter*, is not taken into account by these simple RANS models. While the Direct Numerical Simulation (DNS) computes the whole spectral domain, which is impossible with the actual computational resources for high Reynolds number flows, the LES consists in separating the turbulence scales into two domains. The LES computes the large structures and models the smallest ones, as shown in the Fourier space in figure 2.1(b). The scale separation is done through a high-pass filter for the scales, or low-pass filter for the

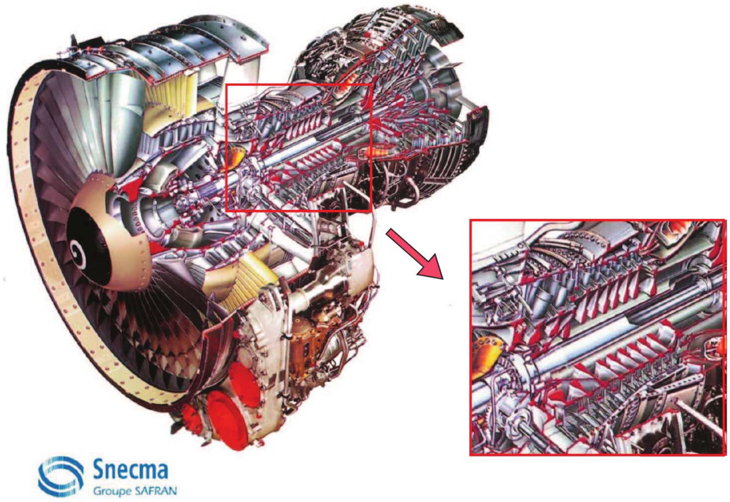

Figure 2.3 — *High pressure bloc in CFM56 jet engine (extracted from Ottavy [127])*

2.5 CREATE

2.5.1 Overview

This section deals with the experimental test bench upon which the study is based.

The simulated axial compressor is CREATE (Compresseur de Recherche pour l'Étude des effets Aérodynamiques et TEchnologiques) [128]. This research compressor was designed by Snecma and is located at the LMFA (Laboratoire de Mécanique des Fluides et d'Acoustique), at the Ecole Centrale de Lyon. It is representative, in terms of geometry and speed, of modern high pressure axial compressors, especially the median-rear block in modern engines, such as turbofans, as shown in figure 2.3. There are two main objectives for the engine company. First, to be able to carry out aerodynamic and mechanical parametric studies on a realistic configuration, and thus optimize the design of future engines. Second, to measure accurately the phenomena occurring in high pressure compressors.

The compressor CREATE is installed within the 2 MW test bench of the LMFA, presented in figure 2.4. This test rig is mounted on a concrete stand uncoupled from the measures room so as to avoid the propagation of vibrations. The test bench works as an open loop as it sucks air from the outside and throws it back. Upstream the compressor, the air coming from the outside is filtered and reaches the settling chamber. There, the total pressure drops to 0.75 bar (74% of the atmospheric pressure) so as to reduce the requirements of the test rig in terms of electric power. Downstream the compressor, a discharge valve enable to step out from a surge state in 0.5s. A butterfly-type valve controls the throttle by reducing the mass flow rate. This mass flow rate is measured at the exit with a Venturi nozzle. The compressor rotation comes from a Jeumont Schneider electric engine of 2.05 MW, which corresponds to the engine power of a high speed train. Along with the gearbox, it enables to reach rotational speeds from 0 to 17000 rpm.

The CREATE compressor comprises $3^{1/2}$ stages, with an inlet guide vane (IGV) and 3 rotor/stator stages. A meridian view is given in figure 2.5. The outer casing diameter is 0.52m and the nominal rotating speed 11543 rpm. The mass flow is then 12.7 $kg.s^{-1}$. The instrumentations installed on CREATE are numerous [27] compared to industrial test rigs. This enables to evaluate more accurately the numerical methods, as it is the case for this study. Furthermore, this compressor aims at analysing the technological effects, improving the flow stability and understanding the mechanisms responsible of the surge inception. In order to ease the measurements on the machine, the axial gap between the rows is increased, the outer-case comprises moving rings with holes for probes, and the spatial periodicity is of

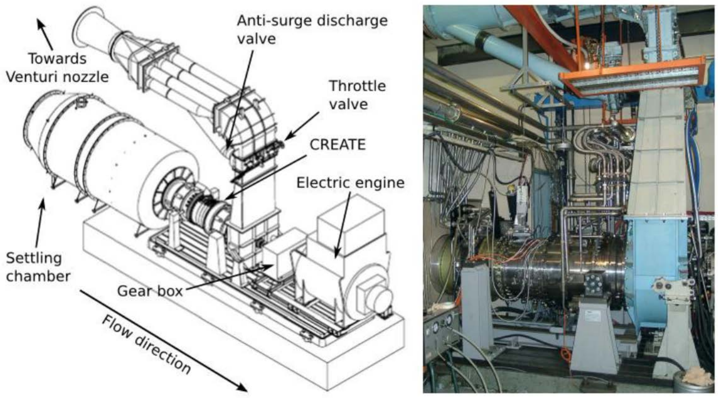

Figure 2.4 — *The CREATE compressor test rig (extracted from Courtiade [27])*

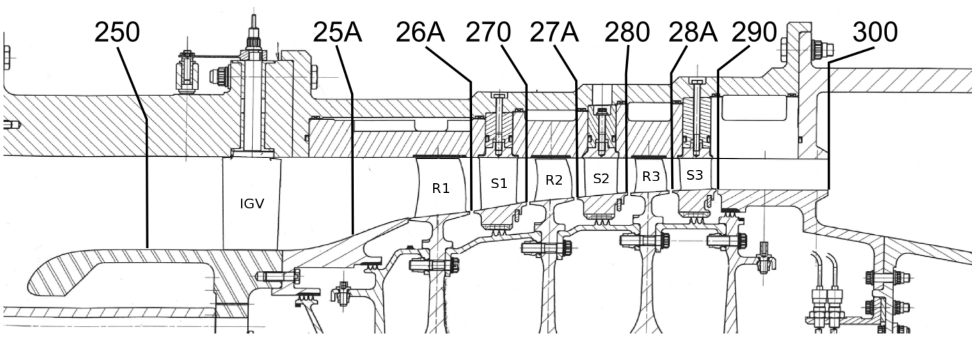

Figure 2.5 — *Meridian view of the CREATE compressor with the location of the axial sections*

$2\Pi/16$ (22.5°). The corresponding blade number for each row is detailed in table 2.3. This thesis work deals with the IGV and the first rotor (R1), hence the spatial periodicity of $2\Pi/32$ (11.25°). However, there are 8 support struts upstream the IGV and downstream the settling chamber on the CREATE compressor test rig, which changes the periodicity if they are taken into account. The IGV is linked to the shroud with a built-in turntable so that its stagger angle can be adapted. Concerning the R1, the inlet Mach number at its tip is 0.92, and the Reynolds number based on the axial chord is of 788000. The dimensionless tip clearances are $\lambda = \frac{GapSize}{MaximumBladeThickness} = 0.23$ and $\tau = \frac{GapSize}{AxialChord} = 1.75$. Based on the Rains criterion [135], the inertia forces are predominant within the gap.

2.5.2 Instrumentation

The aforementioned measurements available on the CREATE compressor are of two types: steady and unsteady. First, there are steady probes that measure the temperature and pressure. Second, there are unsteady measurements synchronized with the rotation of the compressor so that they can measure the same azimuthal position in the same channel at each turn. These measurements are made with unsteady wall static pressure probes, unsteady total pressure probes and Laser Doppler Anemometry (LDA).

The steady measurements are performed at each inter-blade row plane with cobra-type probes. They comprise a thermocouple for the total temperature and four holes for the pressure at the left, front, right and back of the probe. These probes enable to capture the local direction of the flow in the azimuthal

Table 2.3 — *Blade number for the rows*

Row	IGV	R1	S1	R2	S2	R3	S3
Blade number	32	64	96	80	112	80	128

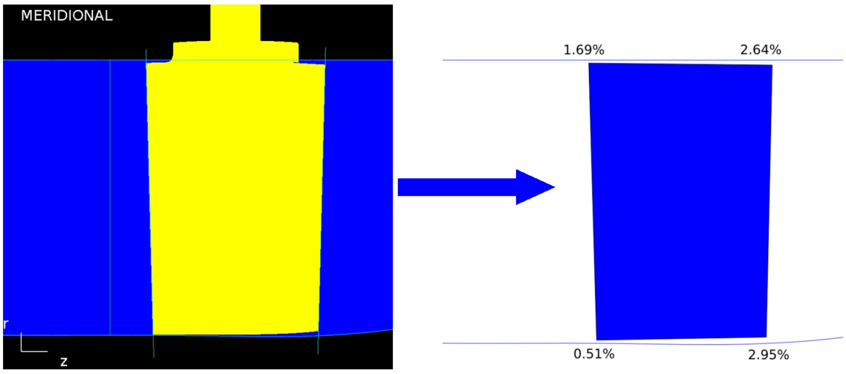

Figure 3.2 — *Simplication of the geometry for the IGV hub and tip gaps with the relative hub and tip gap sizes.*

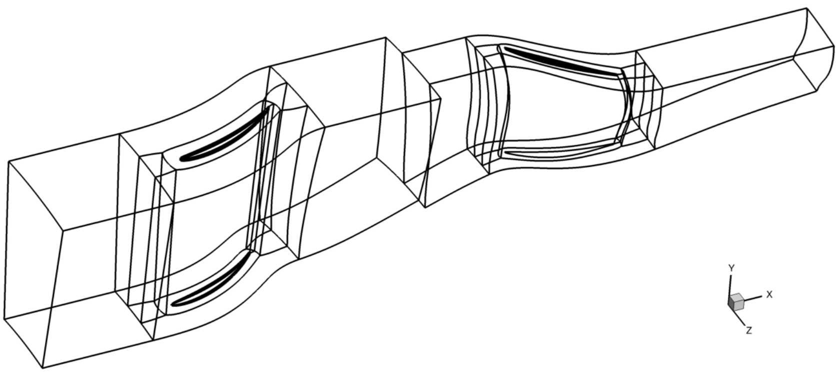

Figure 3.3 — *Computational domain with the IGV and the R1 of CREATE.*

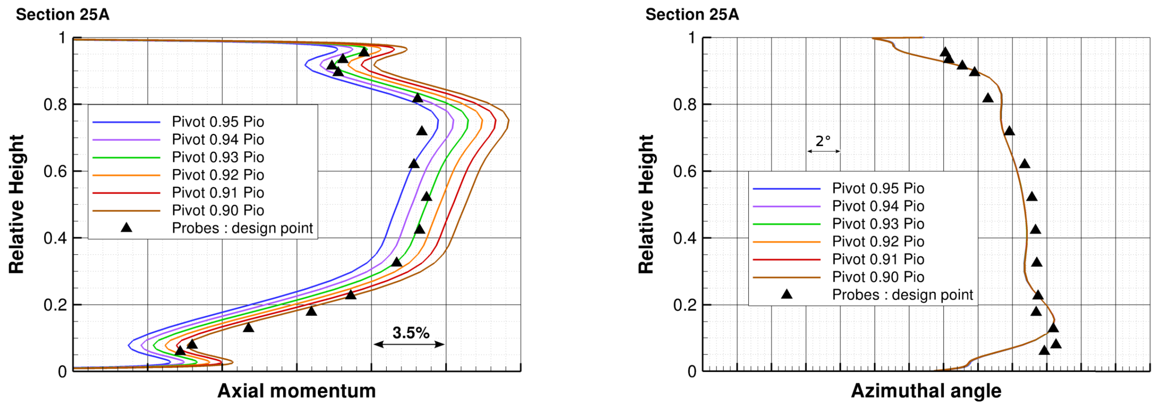

(a) Axial momentum.

(b) Azimuthal angle.

Figure 3.4 — *Radial distribution of time and circumferentially averaged values at section 25A. RANS results on the IGV-R1 domain for different pivot pressures and data from experimental probes at the design point.*

all are extracted directly for the flow cartography. Indeed, they are used for the inlet condition on the computations on the R1. This is the reason why, once the pivot pressure is chosen at 0.93 Pio, another study is carried out to be closer to the experimental values for the flow angles.

In order to reach this goal, different numerical parameters are compared, such as the turbulence model, the spatial discretization scheme and the curvature correction of the Spalart-Allmaras model. Details of these comparisons are explained in appendix B. One will focus here on the two main effects: the impact on the axial momentum and the azimuthal angle. The axial momentum radial distribution at section 25A is presented in figure 3.5(a) for the same outlet pivot pressure chosen earlier, 0.93 Pio, but for different numerical parameters. The reference case uses the Jameson spatial discretization scheme (SA Jameson). Another computation with the AUSM+P scheme is evaluated (SA AUSM+P). Finally, a last one is compared. It is similar to the SA AUSM+P but with the curvature correction for the Spalart-Allmaras scheme [160] (SARC AUSM+P). The AUSM+P versions improve the capture of the gradient at 80% relative height and around 20% relative height. However, near the casing at 90%, the gradient is underestimated. The curvature correction amplifies this trend. This leads to a larger discrepency with the measurements near the hub. Nevertheless, the SARC computation is in better agreement than the SA AUSM+P with the measurements at 90% relative height, that is to say, the IGV tip vortex is better captured. In any case, the discrepancies between the computations at 90% are inferior to 0.7% for the axial momentum.

The real improvements of the AUSM+P scheme are found when comparing the azimuthal angle in figure 3.5(b). The radial position of the inflection around 20% relative height is quite correctly captured with the SA AUSM+P compared to SA Jameson. Moreover, the curvature correction improves even more the prediction capability of the method for the capture of IGV hub vortex width. In other words, the development stage of the hub vortex is captured. Between 80 and 90% relative height, the gradient is in better agreement with the AUSM+P method. The contribution of the AUSM+P is clear near the casing with a 1° improvement of the prevision of the angle value. There is nonetheless few differences between the two computations based on the AUSM+P near the casing. The only prediction variation is an increased angle value above 95% relative height. The lack of measurements so close to the casing however prevents to determine if this inflection is physical or not.

The differences near the casing for the axial momentum are thin and moreover, the angles will be directly used as inlet condition for the R1 computation. So the azimuthal angle is used here to differentiate the methods. In conclusion, the Spalart-Allmaras turbulence model with curvature correction and

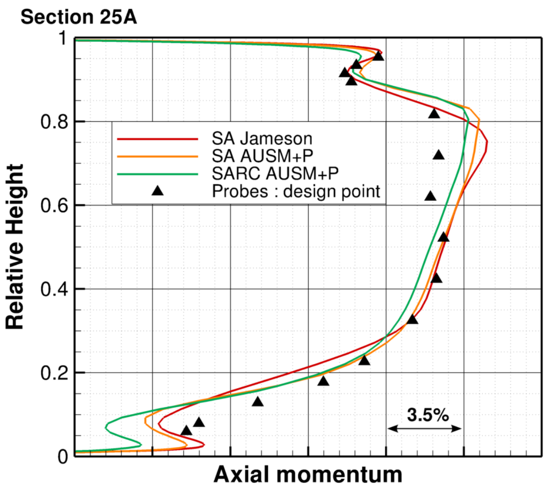

(a) Axial momentum.

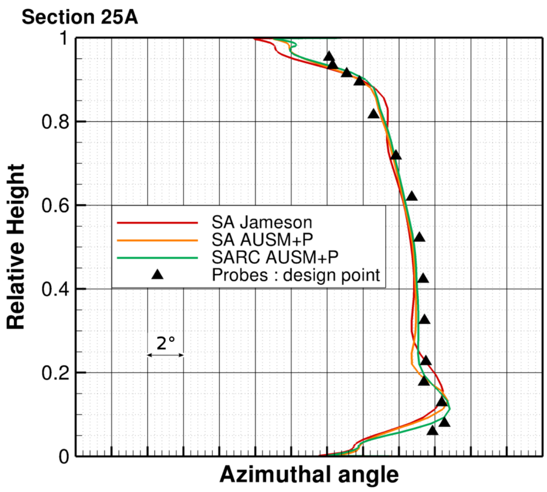

(b) Azimuthal angle.

Figure 3.5 — *Radial distribution of time and circumferentially averaged values at section 25A. RANS results on the IGV-R1 domain for different numerical parameters and data from experimental probes at the design point.*

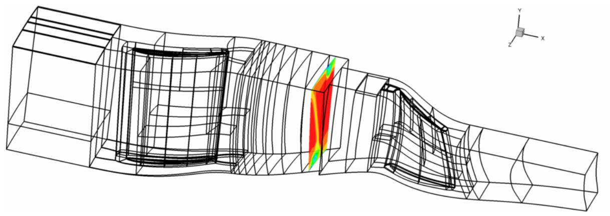

Figure 3.6 — *Position of the extraction plane at section 25A from the preliminary study.*

AUSM+P is finally chosen for its advantages on the simulation of the flow angles. Based on the axial momentum results, Spalart-Allmaras without curvature correction would have been a relevant choice too. A priority is given here to the swirl capture instead of the axial momentum.

The cartography is then extracted at section 25A, shown in figure 3.6, from the computation SARC AUSM+P. Since this cartography results from the choice of the pivot pressure in order to be in good agreement with the experimental probes, the same outlet boundary condition is used for the R1 computations. That is to say, the static pressure 0.93 Pio is specified at the hub of the outlet surface of the R1 computations and then a simplified radial equilibrium is applied, following equation II-62. An important aspect of the study on the R1 is that the same static pressure is used for all of the following computations (RANS, URANS, ZDES with and without the rotating distortion) at the design point.

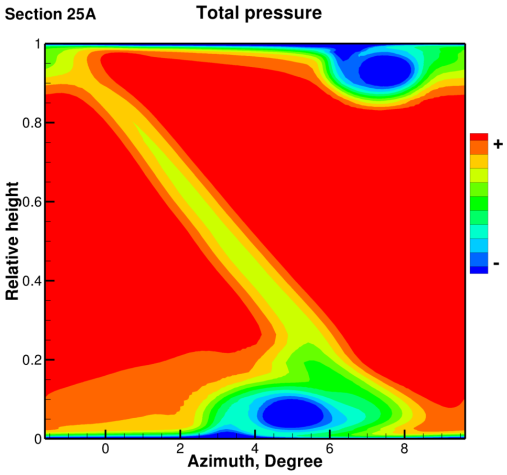

(a) RANS RDE-R1 computation.

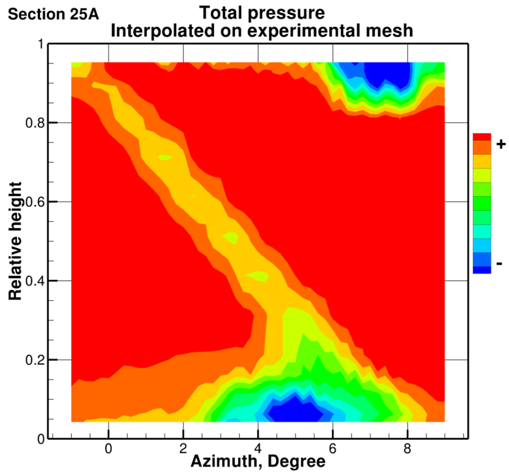

(b) RANS RDE-R1 computation. Interpolated on the experimental mesh.

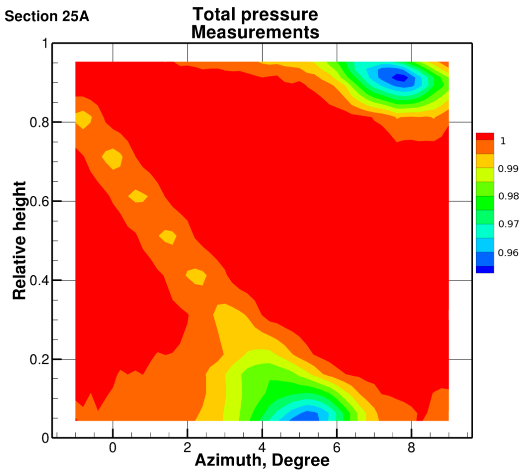

(c) Experimental probes.

Figure 3.7 — *Total pressure cartography at section 25A.*

3.3.4 Inlet cartography definition for the computations on the first rotor

The flow cartography extracted from the chosen configuration in the preliminary study is presented in figure 3.7(a). This 2D map of the total pressure shows that the main phenomena from the IGV are taken into account. Indeed, the hub vortex, azimuth 4-6 and relative height 0-0.1, the tip vortex, azimuth 7-8 and relative height 0.9-1, and finally the main wake diagonally from azimuth 0 and relative height 1 to azimuth 8 and relative height 0, are visible.

In order to ensure these results are due to the flow physics, this cartography is interpolated on the experimental mesh, figure 3.7(b). The map from the experimental probes is presented in figure 3.7(c). The azimuthal position calibration is based on the tip vortex position. While the relative position of the hub and tip vortices from the IGV are correctly captured with the RANS computation, the relative wake position is not. Actually, the problem originates from the azimuthal shift of the vortices with respect to the main wake. This shift results from the simplifications performed on the IGV gap sizes. As detailed in appendix A, the larger the gap, the wider the discrepancy between the main wake and the vortices. Indeed, with a larger gap, the vortices are wider and their axial and azimuthal convection is delayed compared to the main wake. This delay leads to the relative position difference when the wakes reach the section 25A. In addition, the total pressure deficit in the vortices is more important than what it is

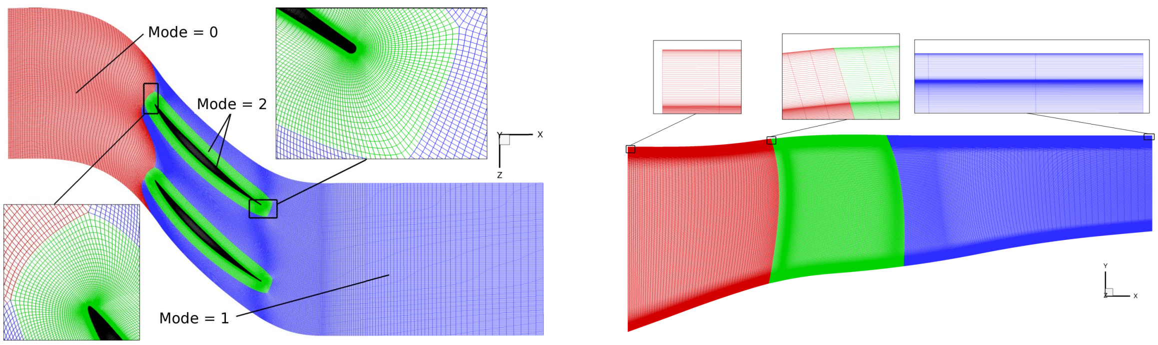

(a) Blade to blade view.

(b) Meridian view.

Figure 3.10 — *Mesh configuration for the different computations on the first rotor of CREATE. Color code for the ZDES method Red: mode = 0. Blue: mode = 1. Green: mode = 2. Black (tip gap mesh): mode = 2.*

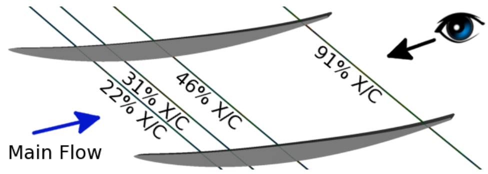

Figure 4.3 — *Position of the visualization sections along the chord.*

the results. Despite this limitation, the formation and development of the tip-leakage vortex is correctly computed in the LES mode of the ZDES. The vortex formation and widening can be seen in figure 4.2(a) on the suction side. Their computation in LES is a positive aspect of using the ZDES method for the simulation of the tip-leakage flow. This behaviour is the one that is expected since the leakage jet flow is clearly a "detached" flow, computed in LES. As a consequence, the ZDES behaves correctly for the simulation of the tip-leakage flow.

Another element concerning the validity of the ZDES is the correct use of mode = 2 in the vicinity of the blade. It was previously demonstrated that in the tip gap, mode = 2 protects the boundary layer and consequently forces the RANS mode. This protection is mainly visible near the leading edge where the boundary layers are thicker, especially on the pressure side at 22% X/C in figure 4.2(a). Nonetheless, this protection is known to have a negative impact on the transition between RANS and LES. This has to be quantified for the study. Indeed, mode = 2 delays this transition, albeit this delay is inferior to the one observed in DDES by Deck [38]. In figure 4.2(b), the suction side in the visible sections highlights different behaviours. In section 22% X/C, the eddy viscosity level is high in the boundary layer emanating from the tip gap and then decreases rapidly when the isoline 0.8 is crossed to be lower than 7 as soon as the isoline 0.99 is reached. At this section, the boundary layer at the tip gap and the one at the casing form only one boundary layer for the ZDES method. The method can not distinguish the two. This confirms that the boundary layer is protected with the mode = 2 close to the blades, and then the outer flow is resolved in LES. However, when mode = 1 is used, refer to figure 3.10(a) for the exact position, the flow is resolved in LES since the mesh suits LES requirements. From section 31% X/C and downstream, the method can distinguish the two boundary layers. As a result, the eddy viscosity field is then closer to the one detailed by Deck [38] obtained on a backward facing step, and similar conclusions can be drawn. One can observe a delay in the switch from RANS to LES. Nevertheless, the eddy viscosity rate drops from over 19 in the tip gap boundary layer to 9 as soon as it is outside the boundary layers from the tip gap and the suction side. This residual eddy viscosity of 9 contaminates the flow until reaches the zone in mode = 1 for section 31% X/C. However, this delay is reduced at section 46% X/C, that is to say, the switch occurs faster downstream. And this is an important point for the simulation of the tip-leakage flow and the main difference with the backward facing step. The eddy viscosity is convected downstream, tangentially to the edge between the tip and suction side. Since the level of eddy viscosity is rather high upstream, at section 22%, it is still high at section 31%. But then, the level decrease and the viscosity field behaves much more like the one in the backward facing step. Thereby, one can say the switch is rapid, even if there is still a delay whatever the axial position.

The same visualizations are presented for the hub region where there is no influence of the tip gap. The section 46% X/C is coloured by the entropy in figure 4.4(a), and by the eddy viscosity in figure 4.4(b). The same f_d isolines are overlaid. On the one hand, the boundary layers developing on the suction side, on the pressure side and near the blades on the hub wall are correctly protected with mode = 2. On the other hand, the boundary layer on the hub wall and far from the blades is not protected. In the unprotected zones, the f_d sensor can not be directly used to identify the boundary layer since it is intrinsic to the mode = 2. Indeed, there is an abrupt reduction of the thickness between the hub wall and the isoline 0.99 for the f_d value when crossing the interface between mode = 1 and mode = 2. Nevertheless, the entropy field between the two blades does not reveal any separation. There is only a thickening of the suction side boundary layer near the hub which is not impacted by the interface between the modes.

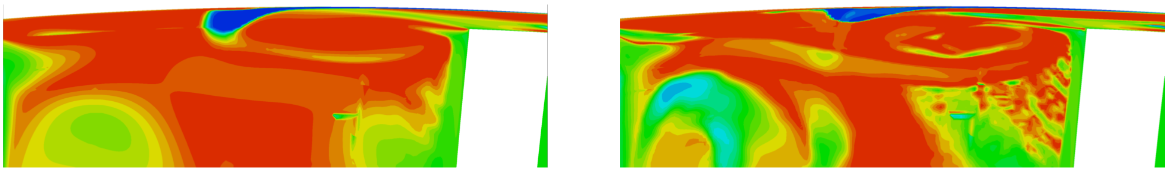

(a) URANS. (b) ZDES.

Normalized helicity

Figure 4.5 — *Instantaneous normalized helicity at $t = 3T/4$ and section 31% X/C for URANS and ZDES. Boundary layer separation at the casing.*

In conclusion, this section has explained the process for the convergence of the computations and brought out the validity of the numerical test bench concerning the operating point. Besides, the mode configuration for the ZDES has been assessed, which has emphasized the appropriate behaviour of the ZDES modes regarding the tip-leakage flow. In the next sections, an overview of the tip-leakage flow topology will be discussed before focussing on the validation of the ZDES.

4.2 Tip-leakage flow physical analysis

In this section, the tip-leakage flow topology is presented in two steps. On the one hand, the averaged field is detailed, and on the other hand, the evolution of the instantaneous field is assessed. The flow fields in the tip region from the RANS, URANS and ZDES computations are thoroughly compared and discussed.

4.2.1 Time-averaged flow field overview

First of all, it is important to put this study into perspective towards the previous analysis on the tip-leakage flow done in the literature. Two dimensionless criteria are used for the study of tip clearance flow topology. The first one is $\lambda = \frac{GapSize}{MaximumBladeThickness}$, the dimensionless tip clearance size with respect to the maximum blade thickness. In the first rotor of the CREATE compressor, its value is 0.23. Following the analysis from Rains [135], since λ is superior to 0.026, a vortex structure is expected. Moreover, Rains defined then the factor $\lambda^2 \cdot Re \cdot \epsilon$, with Re the Reynolds number based on the free stream velocity, and ϵ the maximum thickness to chord ratio, so as to generalize the tip-leakage flow topologies. For the R1, $\lambda^2 \cdot Re \cdot \epsilon$ is clearly in the domain defined by Rains [135] where the inertia forces are predominant over the viscous forces, mainly due to the high Reynolds number. As a consequence, the topology is mainly driven by the potential flow pressure distribution in the R1 of CREATE. The second criterion is the dimensionless tip clearance size with respect to the axial chord length, $\tau = \frac{GapSize}{AxialChord}$. For the R1, the value for τ is 1.75%. By comparing with the previous experimental studies on different tip clearance sizes from Brion [16], the expected topology with this τ value is a tip-leakage vortex that remains close to the casing while being convected away from the blade suction side.

In order to visualize the tip-leakage flow, an ensemble average is applied on 17 T of the ZDES computation and 18 T of the URANS one. The entropy fields of these averaged computations are presented in figure 4.6 so as to highlight the zones of high losses [43]. Different sections are represented on the same figure : a section at 98% of relative height, and 3 sections at respectively 22%, 31% and 46% of the axial chord. Despite the similar numerical methods implied in the two calculations, and an ensemble average which aims at comparing these two different approaches equally, the development of the tip-leakage vortex differs. Indeed, on the one hand, from the leading edge to section 22% chord, the same entropy field

of the differences between the two methods : the behaviour of the tip-leakage flow crossing this shock. The shock is known to trigger high dissipation when a turbulent flow passes through it, even with LES [46]. However, recent studies carried out with hybrid methods, such as the work of Shi [151, 152] with IDDES, lead to the same assessment as the one in this study : the advantages of methods based on LES over the ones based on RANS.

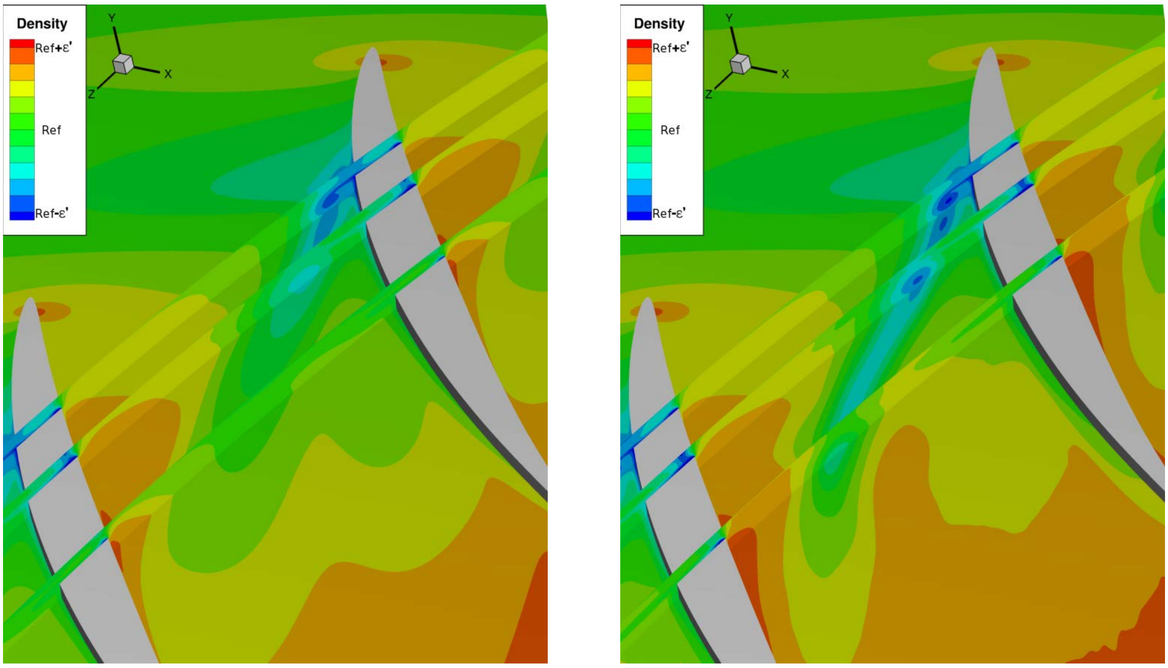

(a) URANS. (b) ZDES.

Figure 4.9 — *Comparison of the time averaged density field of URANS and ZDES. Density planes at 22%, 31% and 46% chord and 98% relative height.* $\epsilon' = 29\%$ *of the density reference value.*

Nevertheless, the shock at the tip of the R1 is not important for the design operating point of CREATE, and can be defined as weak as explained below. This results in some missing effects which occurs for the interaction between a strong shock and the tip-leakage vortex, as observed in the literature with configurations appropriated to analyse the shock/vortex/boundary layer interactions [69, 55, 151]. First of all, the gradients for the Mach number, in figure 4.8, are not important. Besides, there is no sudden drop in the Mach number value after the shock neither a recirculation area [78]. Second, one can analyse the figures 4.9(a) and 4.9(b) which represent the density field centred around a reference value. The presented density ranges from $\pm\epsilon' = 29\%$ of the density reference value. The core of the tip-leakage vortex is defined by a low density and thus it can be tracked by the means of the observation of the lowest density zones. This emphasizes the difference observed through the figures 4.7 with a tip-leakage vortex that extends further in ZDES. However, there is no rapid drop in density level at the shock, contrary to what is observed with strong shocks by Hofmann and Ballmann [77]. A last effect which confirms the weak shock is visible in figures 4.10 with the pressure field centred with $\pm\epsilon'' = 29\%$ of the pressure reference value. In these figures, the gradient for the pressure rise is weak, even at the shock position. As a consequence, the difference between the two methods is triggered by the passage through a weak shock.

Beyond the tip-leakage vortex development, the flow topology within the tip gap is important to understand the tip-leakage flow. First of all, it is important to remember that the ZDES mode used in the tip gap is the mode = 2. That is to say, the boundary layer is protected by the use of the URANS approach in it. As a consequence, this has a direct impact on flow field since the same approach is used near the walls for URANS and ZDES, hence the similar results at the wall. The difference stems from

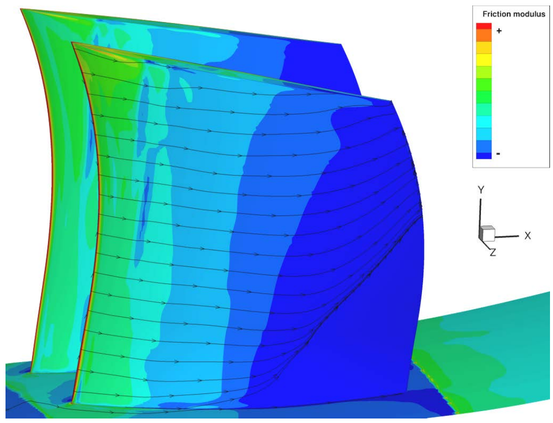

(a) URANS.   (b) ZDES.

Figure 4.12 — *Comparison of the friction lines for the time averaged field of URANS and ZDES near the hub.*

4.2.2 Flow field snapshots

After the visualization of the time averaged fields, it is important to study the evolution of the instantaneous field for the tip-leakage flow because of its inherent unsteadiness. It must be emphasized that the finest details which are visible by the means of each method are observed here. Indeed, the inherent distinction between the URANS and the ZDES approaches prevents to compare the two methods with exactly the same refinement in terms of flow structures. This is only possible with averaged fields as presented in the previous study. Notwithstanding this restriction, the flow snapshots bring relevant information on the tip clearance flow topology.

Therefore, the iso-surfaces of Q criterion [81], coloured by the normalized helicity [105], along with a plane at 31% X/C filled with the entropy are presented here. Figures 4.13(a), 4.13(c), 4.13(e) and 4.13(g) represent the URANS computation while figures 4.13(b), 4.13(d), 4.13(f) and 4.13(h) show the evolution for the ZDES computation. Four different times are represented in these snapshots: T/4, 2T/4, 3T/4 and T from up to down.

First of all, the richness in terms of vortical structures is the main visible difference between the two methods. The URANS captures only the main vortices as long as they are stable enough. The main tip-leakage vortex and its contra-rotative induced vortex are visible with the two methods, in figure 4.13(a) and 4.13(b). Nevertheless, they extend further downstream in ZDES. This is due to their high unsteadiness from plane 31% X/C onward, which is dissipated by the URANS approach, and as a consequence, not captured.

The ZDES reveals multiple flow patterns similar to the ones suggested by Bindon [11] on a turbine cascade. The tip clearance flow leaks through channels from the pressure to the suction side of the blade. The flow angle depends on the chordwise position and corresponds to the angle observed within the gap in figure 4.11. Secondary tip-leakage vortices, as the one pointed in figure 4.13(f) migrate from the trailing edge toward the leading edge. Then, once close to the main tip-leakage vortex, their direction changes, they roll up around it due to its high rotational momentum. Finally they disrupt. The secondary tip-leakage vortex which is the closest to the main tip-leakage vortex has a specific behaviour. It does not migrate from the trailing edge and the resulting secondary vortex, pointed in figure 4.13(d), always rolls up from the same position as it can be seen in figures 4.13(b), 4.13(d), 4.13(f) and 4.13(h).

A tip-leakage vortex flutter phenomenon is visible in the present configuration, both in URANS and ZDES. The IGV wake and its tip vortex meet periodically the leading edge of the R1 which leads to this flutter. This arrival is highlighted at section 31% X/C in figure 4.13(g). The interaction between the wake

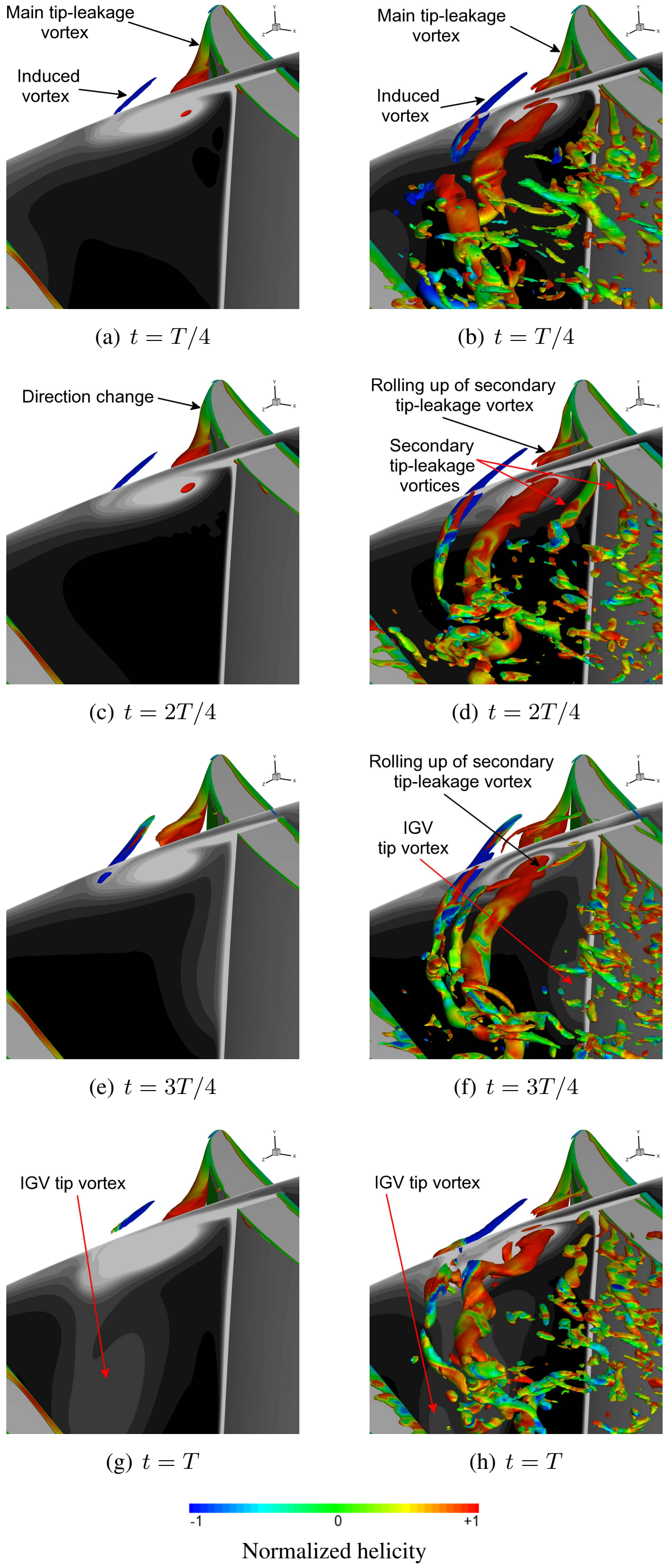

(a) $t = T/4$ (b) $t = T/4$

(c) $t = 2T/4$ (d) $t = 2T/4$

(e) $t = 3T/4$ (f) $t = 3T/4$

(g) $t = T$ (h) $t = T$

Figure 4.13 — *Snapshots of Q criterion iso-surface coloured by the normalized helicity and section 31% X/C filled with the entropy (left: URANS, right: ZDES).*

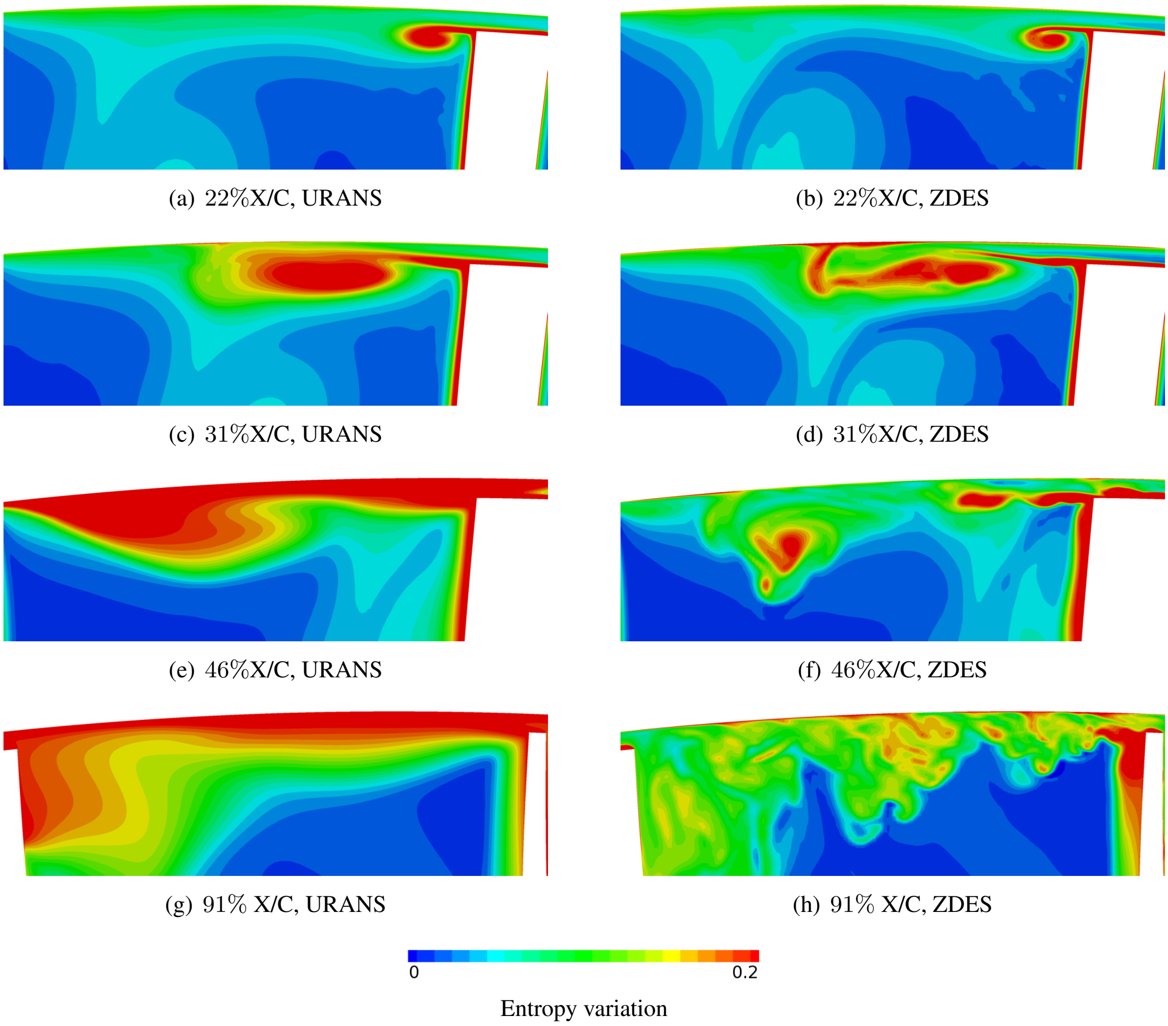

Figure 4.14 — *Entropy planes for four different axial positions at t=3T/4 (left: URANS, right: ZDES).*

and the tip clearance flow, hence this flutter, was already experimentally emphasized by Mailach et al. [109], albeit not with an incoming vortex from the stator as it is the case here. Indeed, only a simple wake was simulated. In CREATE, the velocity deficit in the main flow deflects the leakage flow direction as shown in figures 4.13(c) and 4.13(d). As a consequence, the tip-leakage vortex moves away from the suction side of the blade with a period of T and the axial position of its disruption wanders around 31% X/C.

It must be noticed that the tip-leakage vortex evolution along the chord is different depending on the method used as explained with the time averaged fields seen previously. This is illustrated here by the entropy planes at position 22.3%, 31%, 46% and 91% X/C, for a snapshot at t=3T/4 in figure 4.14. Even if the tip-leakage vortex develops at the leading edge, the boundary layers from both the tip of the blade and its suction side supply the tip-leakage vortex along the chord. The resulting tip-leakage vortices are generated at this shared edge between the blade suction side and the blade tip, this from the leading edge to the trailing edge of the blade, figure 4.14(h). In figures 4.14(a) and 4.14(b), the tip-leakage vortex rolls up and its development is as advanced in RANS as in ZDES. From 31% X/C, the topology differs between the two methods. The vortex coming from the IGV tip stretches periodically the tip-leakage vortex azimuthally and accelerates the casing boundary layer separation seen in the time averaged fields. This is clearly shown by figure 4.14(d) that the IGV wake has not an important role in this stretching, contrary to the IGV vortex. The key element here is the velocity deficit which is more important within the IGV tip vortex. The separation at the casing occurs even when this vortex

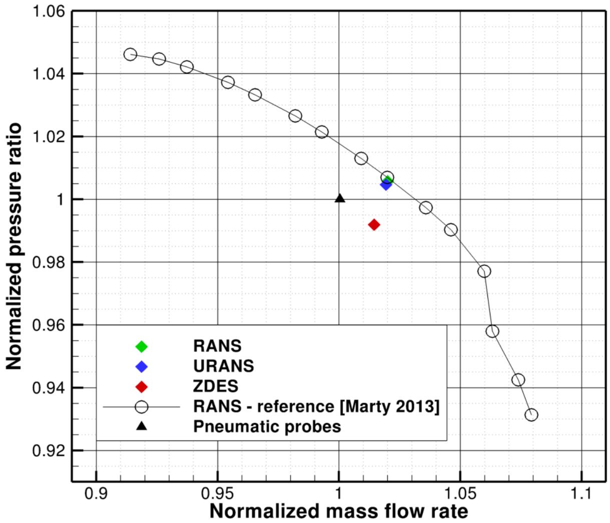

Figure 4.15 — *Pressure ratio versus mass flow rate for RANS, URANS and ZDES, normalized with pneumatic probes data.*

probe values. On the one hand the mass flow average is performed at section 25A, on the other hand, the total pressure ratio corresponds to the ratio of the dynalpic averages at section 25A and 26A. These values are then normalized by the value for the pneumatic probes, and summarized in table 4.1.

First of all, it is important to underscore the fact that the values from pneumatic probes, which are used for reference, have to be considered with caution. Indeed there are important uncertainties for these experimental values since the integration azimuthal period is $9.99°$ instead of $11.25°$ for the R1 periodicity. In addition, and this is the most important uncertainty source, there are no probe values over 95% and below 4% relative height. These zones, near the hub and near the casing are subject to the boundary layer influence and experience a lower total pressure and a lower axial momentum levels. As a consequence, seeing that these values are missing and not totally reliable, using a single value based on integral forces to find the operating point would have led to important errors. This supports the use of the axial momentum radial distribution to define the numerical operating point corresponding to the experimental design point as described in chapter 3. They are nonetheless used as reference here for a better understanding of the computational method effect on the global values.

In order to visualize this effect, the normalized pressure ratio is presented as a function of the normalized mass flow rate in figure 4.15. A reference operating line is given as an example and corresponds to different RANS computations from Marty [113] post processed with the same methodology as the one explained previously. These RANS computations are carried out with elsA 3.4.03 on 48 processors and the averaged inlet cartography from the preliminarily study detailed in chapter 3. The domain is the same as the one for the R1 computation presented in the last chapter, excepted one channel is only modelled. This fine RANS type mesh comprises 4.27 Million points. It is based on a Spalart-Allmaras turbulence model with third order AUSM+P and standard backward Euler. Finally, a radial equilibrium is set as outlet condition with a type 4 valve law, defined in equation II-63. This law is used to define the different working points presented in the figure with circles.

Despite the unsteady aspect of URANS and even the use of a rotating distortion, one can see that its prediction of performance values are close to the ones for RANS. Moreover, the use of a finer grid in this study, based on the ZDES requirements, does not change the operating point when it is compared to the reference RANS cases. All of the computations based on the averaged Navier-Stokes equations overestimate both the pressure ratio and the mass flow rate. Even if similar numerical methods and boundary conditions are used for all the computations of this study, RANS, URANS and ZDES, the global value results differ when considering the ZDES case. Indeed, the ZDES computation overestimates the exper-

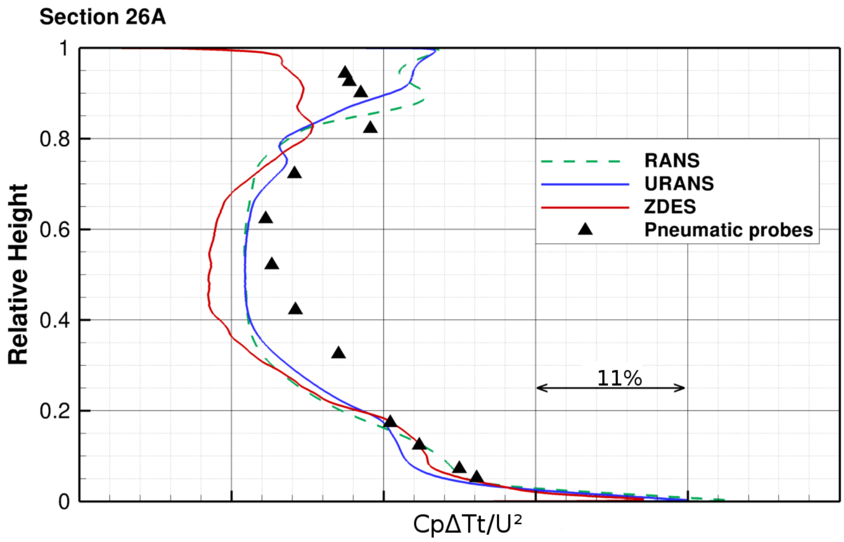

Figure 4.18 — *Radial distribution of time and circumferentially averaged normalized total temperature at section 26A for RANS, URANS, ZDES and experimental probes.*

Navier-Stokes equations for the tip-leakage flow and even at mid span. Nevertheless, at 32% relative height, the computations provide total pressure values which do not match the probes measurements, with an under-estimation of 1% for ZDES and an over estimation of the same order of magnitude for the RANS and URANS methods, depending on the considered probe. A hypothesis for this pressure increase could be that the recirculation from the axial gap upstream from the R1, which can be seen in figure 2.5, modifies the pressure distribution locally at 32% relative height in section 26A. This phenomenon, could not be seen in the configuration set in this paper since no hub recirculation is modelled compared to the configuration studied by Marty and Aupoix [110].

After the axial momentum and the total pressure, another important value informs us on the work of the blade: the total temperature. Figure 4.18 shows the radial distributions at section 26A of the normalized total temperature, $Cp\Delta Tt/U^2$, known as loading coefficient. First, there is a global underestimation of the total temperature value for the computations. This is directly linked to the global overestimation of the axial momentum seen in figure 4.16. This underestimation of the total temperature is amplified for the ZDES which has a value for $Cp\Delta Tt/U^2$ 4% lower than the RANS/URANS cases. Nonetheless, the main difference is visible near the casing where the RANS and URANS computations calculate a $Cp\Delta Tt/U^2$ higher than the probe measurements by 5%. By contrast, the ZDES approach still under predicts the total temperature value which is more consistent with the other values computed below 80% of the span. In order to better understand this difference, a study was carried out by Marty et al. [114] on the same configuration with a different boundary condition at the wall. Marty highlighted that by imposing a temperature, instead of the adiabatic condition, the gradient near the casing can change drastically from the value observed in ZDES to the one in RANS and URANS. Moreover, the boundary condition at the casing wall influences the gradients of temperature above 80% relative height. This is the region where the methods differ here. However, the same adiabatic boundary condition is used for all the computations presented here.

Therefore the difference is due to the method, not the boundary condition. Beyond the absolute value which is directly linked to the operating point, two effects have to be emphasized. The first one is the relative shift between the minimum at mid span and the value near the casing, which is in better agreement with the ZDES. The second one is the inflection point at 82% relative height. This inflection originates from the arrival of the tip-leakage flow. The ZDES captures this inflection. Though the steady RANS captures an inflection, albeit the radial position is overestimated, the unsteady RANS manages to

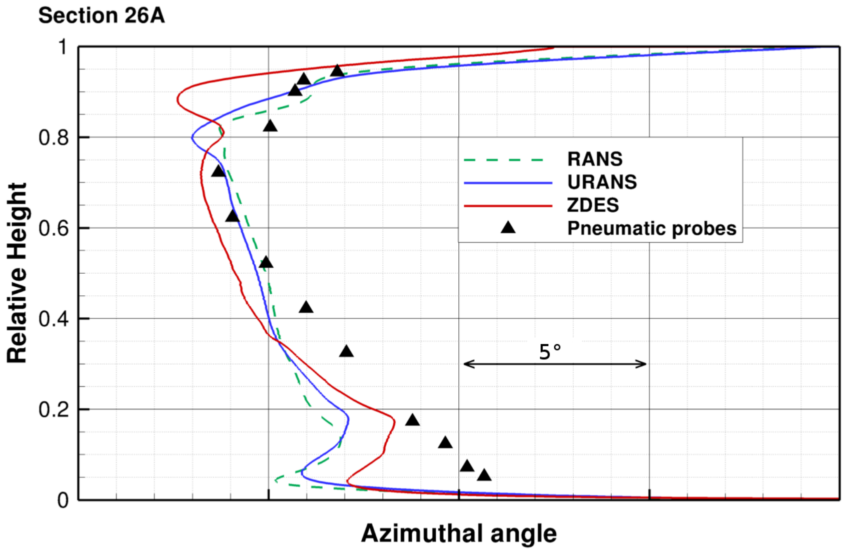

Figure 4.19 — *Radial distribution of time and circumferentially averaged azimuthal angle at section 26A for RANS, URANS, ZDES and experimental probes.*

capture only a light curvature between 90 and 95% and does not capture any inflection. As a consequence, one can see that the ZDES captures more accurately the development stage of the tip-leakage vortex although the operating point of the computation does not match perfectly the experimental one.

The last compared value is the azimuthal angle. The corresponding radial distribution is plotted in figure 4.19. The previous analysis of the axial momentum has shown a work difference between the computations first, and between the computations and the experimental case. This is confirmed by the total temperature distribution. Beyond the main difference with the probes seen along the radius for the different values, there are two zones with different results according to the method used. They are areas where the unsteady aspect of the flow is of major importance: near the casing and near the hub. Moreover, if the angle is changed, the axial momentum changes too. As a result, the same characteristic regions are observed for the axial momentum and the azimuthal angle. The minima of the azimuthal angle are then linked to the maxima of the axial momentum. Indeed, a minimum for the azimuthal angle is encountered at 72% relative height and correctly captured with the ZDES. The ZDES experiences another minimum at 87% which corresponds to the minimum of axial momentum seen in figure 4.16. Even if an inflection can be seen for the probes at 92% relative height, the angle value is clearly underestimated by 2.5° in ZDES. The URANS approach has a similar behaviour but the radial position of its minimum angle is different since it is located at 80%. Besides, there is only one local minimum in URANS contrary to the ZDES. Beyond expectations, the steady RANS reveals to be in better agreement near the casing here.

On the contrary, near the hub, it has the worst results, and the ZDES has the closest angle values to the experimental ones. However, all the computations capture an inflection between 10 and 20% of relative height, which is not measured by the probes. The inflection near the hub is due to the strong corner effect, which is not physical. Many hypothesis can explain this discrepancy with the experimental measurements near the hub. Some are linked to the simplification of the numerical test bench, such as the IGV hub gap modelization, the simplification of the hub surface and platform geometries or the recirculation upstream the R1 which is not taken into account. Other hypothesis are linked to the numerical methods, such as the underlying turbulence model. Indeed, the Spalart-Allmaras model is known for amplifying the separation in turbomachinery as revealed by Marty [112, 111] for the CREATE compressor. The capability of the ZDES to simulate unsteady flows is mainly based on the LES aspect of this method, however, it is important to keep in mind that in the boundary layer, at least with mode = 2, the flow is computed with the unsteady RANS approach. As a consequence, the limitations of the underlying

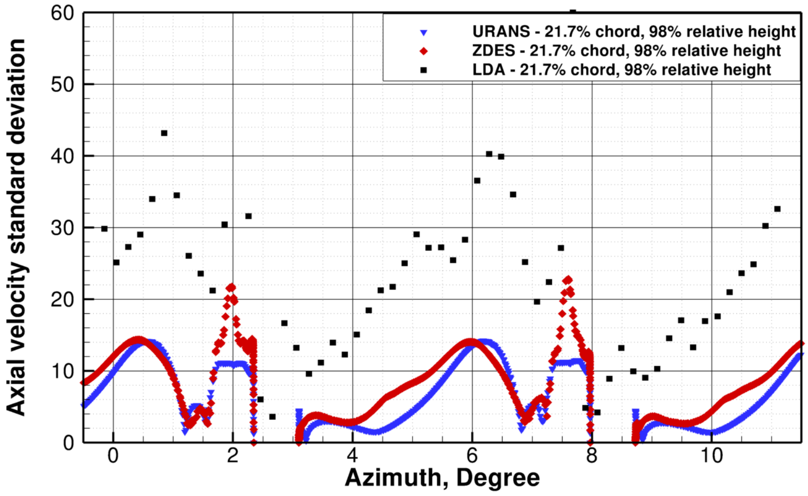

(a) Axial.

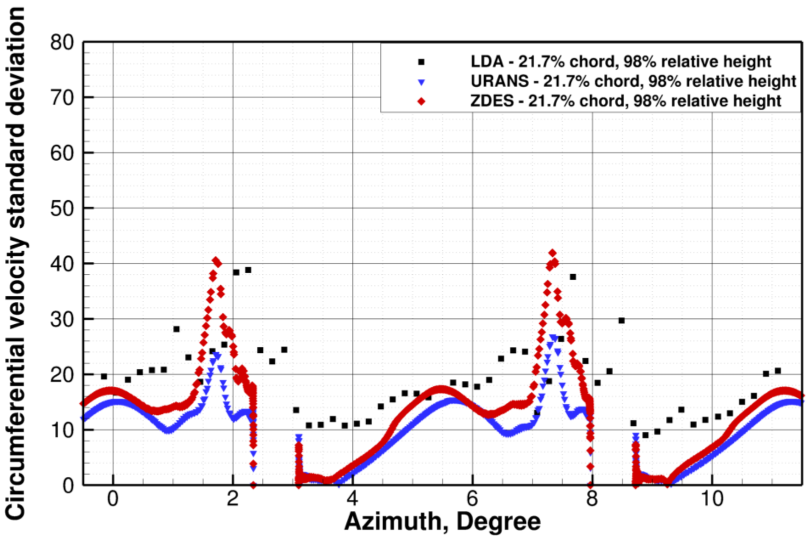

(b) Circumferential.

Figure 4.24 — *Axial and circumferential velocity standard deviations [in $m.s^{-1}$] at 21.7% chord and 98% relative height for RANS, URANS, ZDES and LDA measurements.*

are correctly captured, there is an important underestimation of the standard deviation value for the two computations.

Likewise, the circumferential velocity standard deviation, visible in figure 4.24(b), is underestimated by the computations. In spite of the good agreement for the levels of the normalized circumferential velocity seen in figure 4.20(b), the unsteadiness in the azimuthal direction differs between the computations and the LDA measurements. Indeed, near the pressure side of the blade, at azimuths 3 to 4, it is close to 0 for the computations while it is above $10m.s^{-1}$ for the LDA. The unsteadiness levels for the computations increase in between the blades, up to azimuth 5.5 where it reaches the same levels as the LDA measurements. Then, the levels of the circumferential unsteadiness decrease only for the computations. It only rises again near the suction side of the blade where the levels are in good agreement between the LDA and the computations. At this position, for azimuths 7 to 7.5, there is a peak of unsteadiness corresponding to the position of the main tip-leakage vortex. There is a light improvement for the ZDES with unsteadiness levels closer to the LDA measurements around this peak.

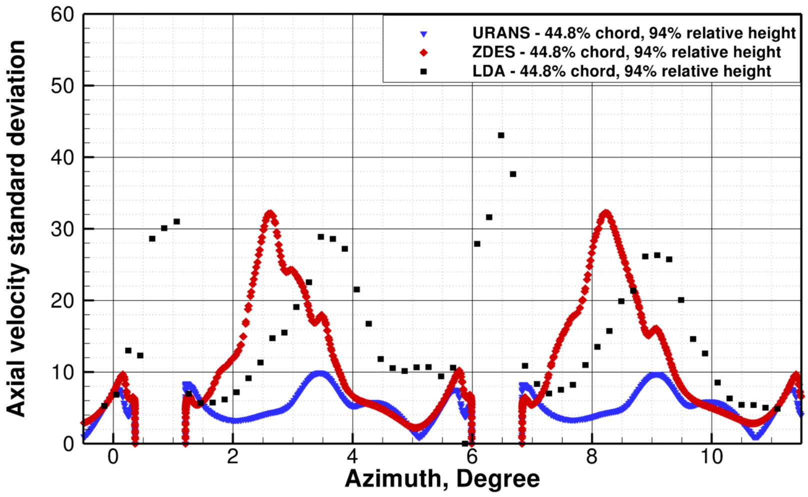

(a) Axial.

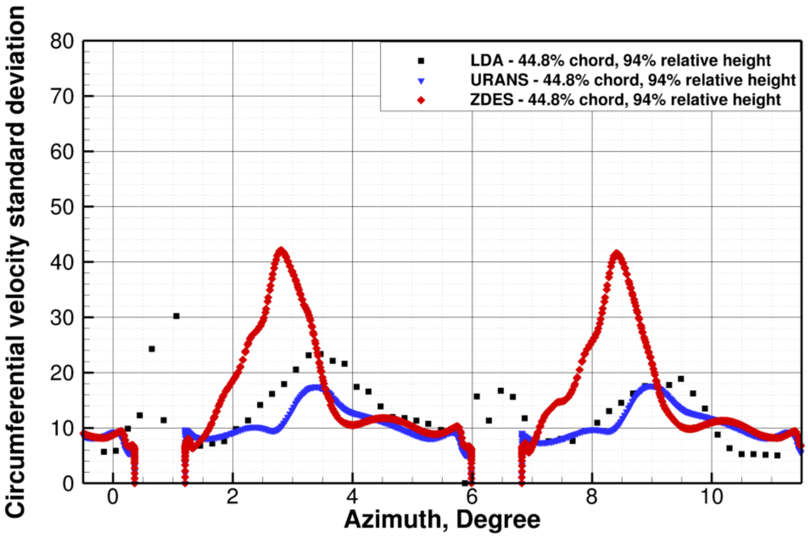

(b) Circumferential.

Figure 4.25 — *Axial and circumferential velocity standard deviations [in $m.s^{-1}$] at 44.8% chord and 94% relative height for RANS, URANS, ZDES and LDA measurements.*

Downstream the shock position, the ZDES capability to capture the axial unsteadiness within the flow outstrips the URANS approach. At the position 44.8% X/C and 94% of relative height, in figure 4.25(a), the levels of axial unsteadiness are correctly captured by the ZDES whereas the URANS barely captures a light unsteady phenomenon. Nevertheless, the azimuthal position has a difference of one degree between the ZDES and the LDA while the position is correct for the URANS. Since the azimuthal position of the tip-leakage vortex is directly correlated to the axial velocity, this confirms the problem of the choice of the operating point for the ZDES. At the same position, the circumferential velocity standard deviation, in figure 4.25(b), highlights an important overestimation for the unsteadiness of the tip-leakage vortex captured by the ZDES which is up to two times higher than what it is experimentally. The same aforementioned position issue is visible for the circumferential velocity standard deviation in ZDES. By contrast, the URANS approach captures correctly the position of the peak at azimuth 3-3.5 and 9. The unsteadiness levels are closer to the ones captured experimentally than what is observed in ZDES. However, there is still an underestimation of the unsteadiness in URANS.

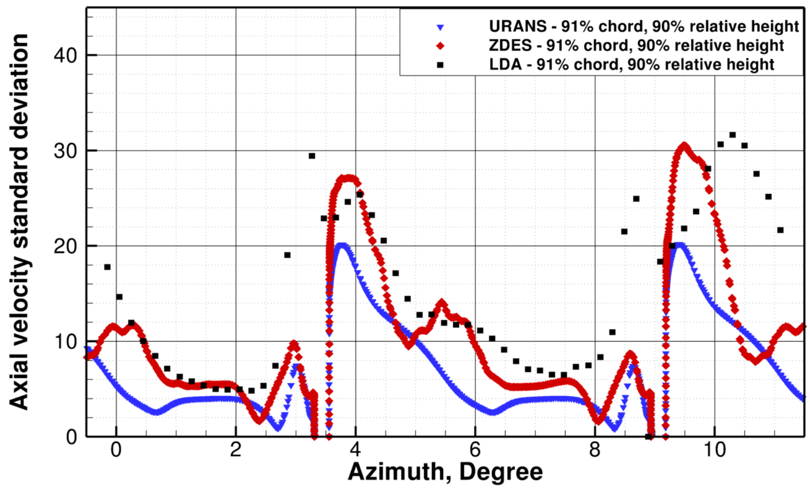

(a) Axial.

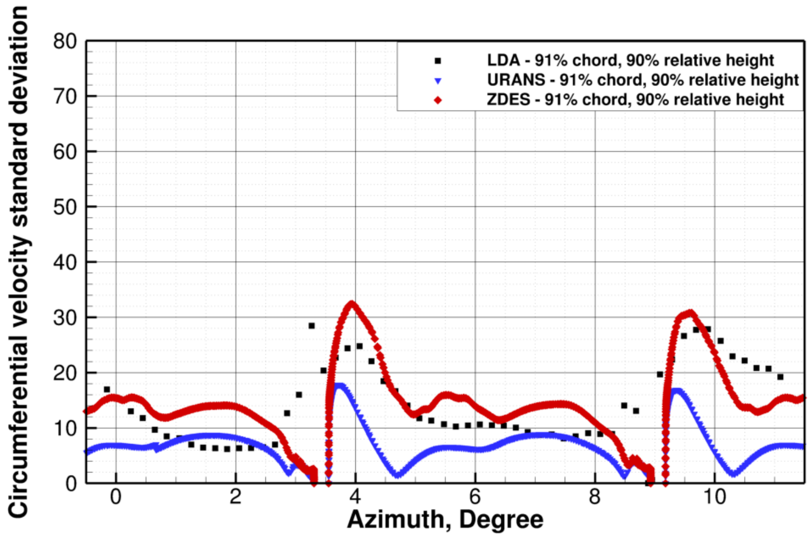

(b) Circumferential.

Figure 4.26 — *Axial and circumferential velocity standard deviations [in $m.s^{-1}$] at 91% chord and 90% relative height for RANS, URANS, ZDES and LDA measurements.*

This trend is confirmed near the trailing edge of the blade, at 91% X/C and 90% of relative height. The axial velocity standard deviation is presented in figure 4.26(a). At this position, the unsteadiness distribution has changed for the computations as well as the measurements. The value is higher near the blade around azimuth 4 and decreases as the azimuth increases up to the other blade. The azimuths 4-6 denote the position of the rim of the main tip-leakage vortex. On the one hand, the intensity and position of this vortex is correctly captured by the ZDES method. On the other hand, the URANS does not capture it at all. Moreover, the levels are lower in URANS with an almost constant 5% discrepancy with the LDA measurements along the azimuth.

Figure 4.26(b) shows similar results for the circumferential velocity standard deviation at the same position. Contrary to what is observed at 44.8% X/C in figure 4.25(b), the ZDES captures unsteadiness levels that suit better the azimuthal distribution observed experimentally than the URANS computation. This confirms that the URANS method underestimates the unsteadiness in both directions downstream the shock position.

The last position to be evaluated is the one corresponding to the upper part of the tip-leakage vortex, in section 26A. Figure 4.27(a) shows the axial velocity standard deviation. The wakes of the R1 are in azimuth 0 and 5.625. Two zones of high unsteadiness in the axial direction are visible on each side of the wake centre, for instance, one at azimuth 5 and one at azimuth 6.5. They have a different level of unsteadiness. This level difference is not captured by the URANS method. Moreover, the URANS computation captures lower levels compared to the LDA measurements. The level difference between the two zones around the wakes is seen by the ZDES, albeit less pronounced than what it is experimentally.

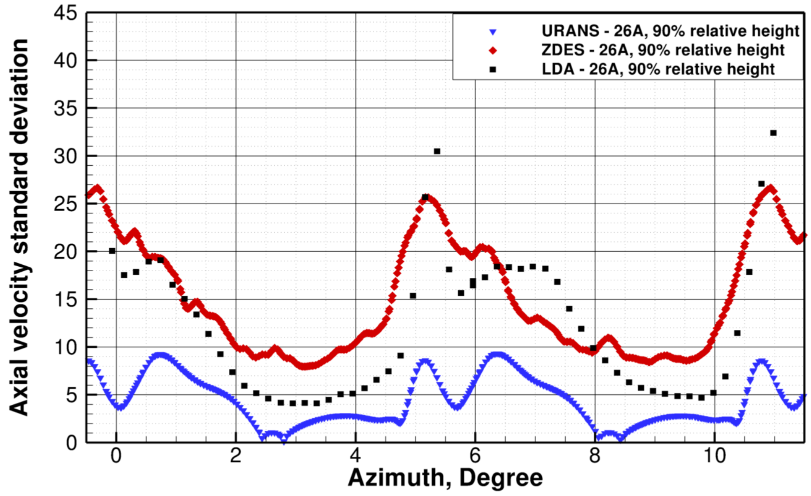

(a) Axial.

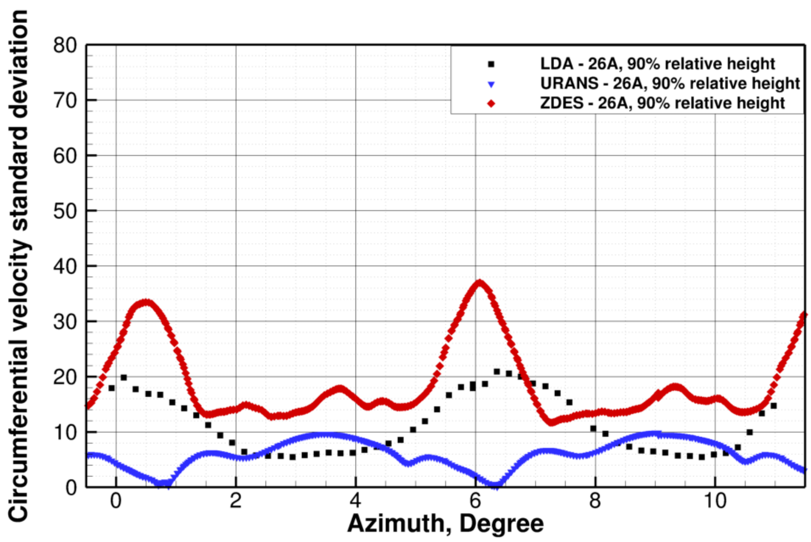

(b) Circumferential.

Figure 4.27 — *Axial and circumferential velocity standard deviations [in $m.s^{-1}$] at section 26A and 90% relative height for RANS, URANS, ZDES and LDA measurements.*

Figure 4.27(b) underlines the difference between the two methods. The circumferential velocity standard deviation is high in ZDES, with values oscillating between 12 and 37 whether there is a wake or not. Conversely, the levels for the URANS method are low and besides, the oscillations have a lower amplitude, from 0 to 10. What is important to notice here, is the level of the LDA measurements. In the zones where there are the wakes, the levels are high and correspond to the peaks seen in the ZDES, albeit the levels in ZDES are almost twice as much as the levels captured experimentally. At these positions,

entropy plane from the ZDES computation. One can see that this position corresponds to the arrival of the tip-leakage vortex too, albeit it is widened and almost dissipated.

The second area is at the casing of section 26A. The same azimuthal position is chosen so that the difference between the probes comes mainly from their distance to the wall, hence their capture of either the inner boundary layer flow or the outer flow.

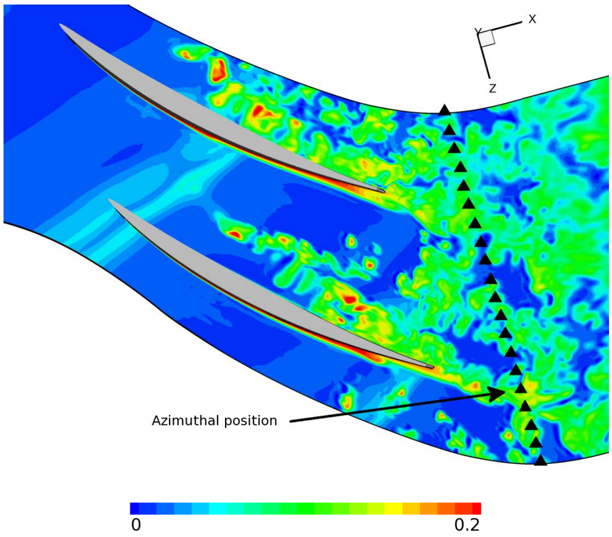

Figure 4.28 — *Probe positions at section 26A. Instantaneous entropy plane at 94% relative height and $t = 3T/4$ from the ZDES computation.*

4.6.2 Power Spectral Density

The spectral analysis is based on the power spectral density (PSD) of the pressure for the aforesaid probes. The PSD is based on the Welch method [172] using an overlap of 50% and ten Hann windows [68] with a linear mean for each. It describes how the root mean squared value of the static pressure is distributed in the frequency spectrum, and thus represents the flow energy. An estimation of the cut-off frequency for the computational results gives $3.2\ 10^5$ Hz. It is based on the cubic root of the cell volume and a characteristic velocity for the turbulent structures defined as $\sqrt{u'^2 + v'^2 + w'^2}$, with u', v' and w' respectively the maximum of the fluctuating velocity in the X, Y and Z directions, as shown in figure 4.28. It is important to keep in mind that the effective cut-off may be at a lower frequency due to the numerous effects that influence it, such as the mesh refinement and the numerical schemes. The value $G_p(f)$ of the static pressure is plotted as a function of the frequency in figure 4.29(a) for the probes at the casing and in figure 4.29(b) for the ones at 94% relative height. For a better understanding, another parameter is displayed : the reduced frequency. It consists in the signal frequency normalized by the IGV blade passing frequency (BPF).

The frequency resolution (FR) is 2000 Hz for the numerical data set arising from a temporal range of 17 T for the ZDES computation and 18 T for the URANS one. This resolution results from the aforementioned minimum number of Hann windows required for the Welch method. By contrast, the resolution for the unsteady probes is of 2 Hz. This is a limiting factor for the comparison of the numerical probes with the experimental ones, especially for the low frequency phenomena. The reason is that the lowest captured frequency is the frequency resolution. Thereby, the phenomena with a characteristic frequency inferior to the frequency resolution of a PSD are not captured. Another effect of the frequency resolution is the level of energy visible in the graphs. Indeed, a small frequency resolution leads to a more

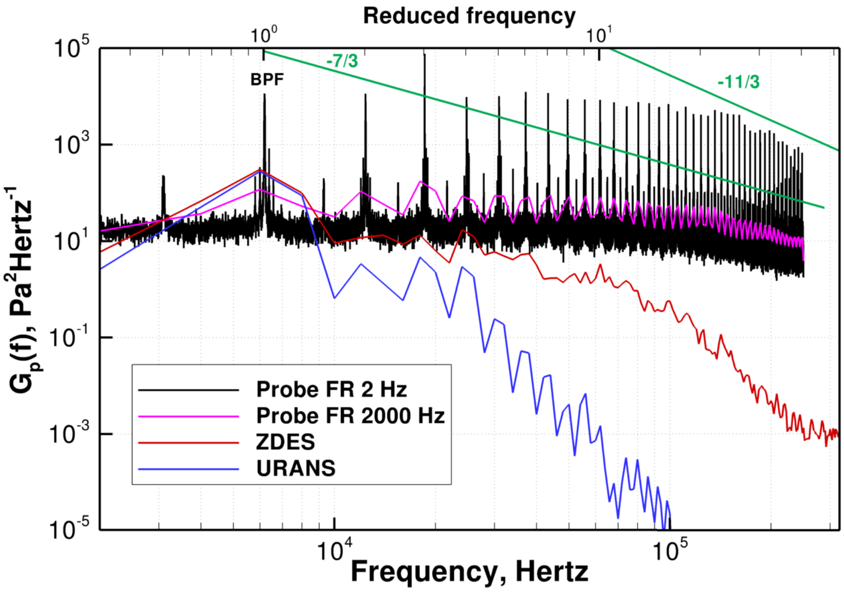

(a) At the casing.

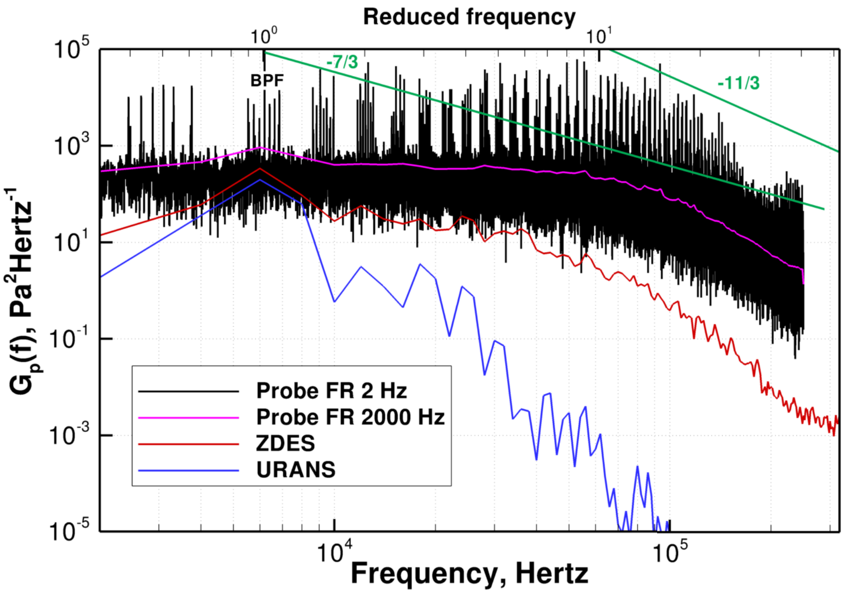

(b) At 94% relative height.

Figure 4.29 — *Power spectral density of pressure at section 26A. URANS, ZDES and experimental unsteady pressure probes (with 2 frequency resolutions).*

accurate capture of the frequency of a phenomenon, denoted by a thin and high peak of energy on the graph. On the contrary, the same phenomenon captured with a higher value for the frequency resolution will result in a wider and shorter peak due to the energy distribution on a wider range of frequency. This effect on the energy level visible is the reason why the PSD for the unsteady probe are displayed with two frequency resolutions. On the one hand, 2 Hz, which is the best available resolution regarding the length of the experimental data set. On the other hand, 2000 Hz, which is the same frequency resolution as the one for the numerical probes from the computations.

One can see in figure 4.29(a) that a low frequency phenomenon is visible for the experimental probe PSD only with the smallest frequency resolution. This phenomenon corresponds to $1/2$ BPF, and is captured neither by the unsteady probe PSD with 2000 Hz of frequency resolution nor by the

from 1 BPF to 10 BPF. In fact, the ZDES approach detects only a light decrease in the energy level for the flow field at 94% of relative height compared to the one at the casing. Therefore, the energy levels are in better agreement for the ZDES, albeit the levels are still at two orders of magnitude lower than the experimental PSD values. Nevertheless, what is important here is that the slope is correctly captured with the ZDES approach. The energy decrease is similar to the unsteady probes, even if there is still the issue with the potential effect of the S1. In other words, the interaction between the mean-shear and the turbulence is correctly captured in the ZDES approach contrary to the URANS method.

In summary, the ZDES brings significant improvements for the simulation of the interactions between the mean-shear and the turbulence. This results in energy levels and an energy decrease which are in better agreement with the experimental ones. Some of these enhancements are visible even in the boundary layer, albeit the ZDES behaves like the URANS method there. This behaviour near the wall prevents nonetheless the ZDES from capturing correctly the turbulence-turbulence interactions.

In the next section, one will compare the energy levels between the two unsteady computational methods so as to understand why there is such a difference for the energy levels when the flow arrives at section 26A.

4.7 Analysis of the energy levels along the tip-leakage vortex

In order to understand why there is such a difference for the energy levels between the URANS and the ZDES approaches at section 26A, a spectral analysis is carried out.

4.7.1 Probe positions along the tip-leakage flow

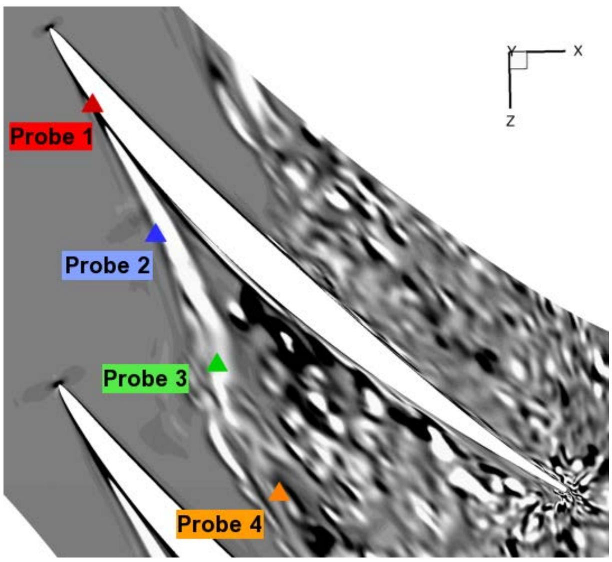

Figure 4.30 — *Probe positions along the main tip-leakage vortex. Instantaneous schlieren at 98% relative height and $T = 3T/4$ from the ZDES computation.*

This analysis aims at understanding how the two methods simulate the tip-leakage vortex development. Thereby, the Power Spectral Density (PSD) function of the static pressure is plotted for four probes within the blade passage. More precisely, they are located at different axial positions along the main tip-leakage vortex core as presented in figure 4.30 with the instantaneous Schlieren at 98% relative height and t=3T/4. The probes 1, in red, and 2, in blue, are located at 11% and 22.5% X/C. The probes

3, in green, and 4, in orange, are located at 33.8% and 45.7% X/C. This means that probes 1 and 2 are upstream the tip-leakage vortex disruption, which occurs after the shock, contrary to probes 3 and 4.

4.7.2 Power Spectral Density along the tip-leakage flow

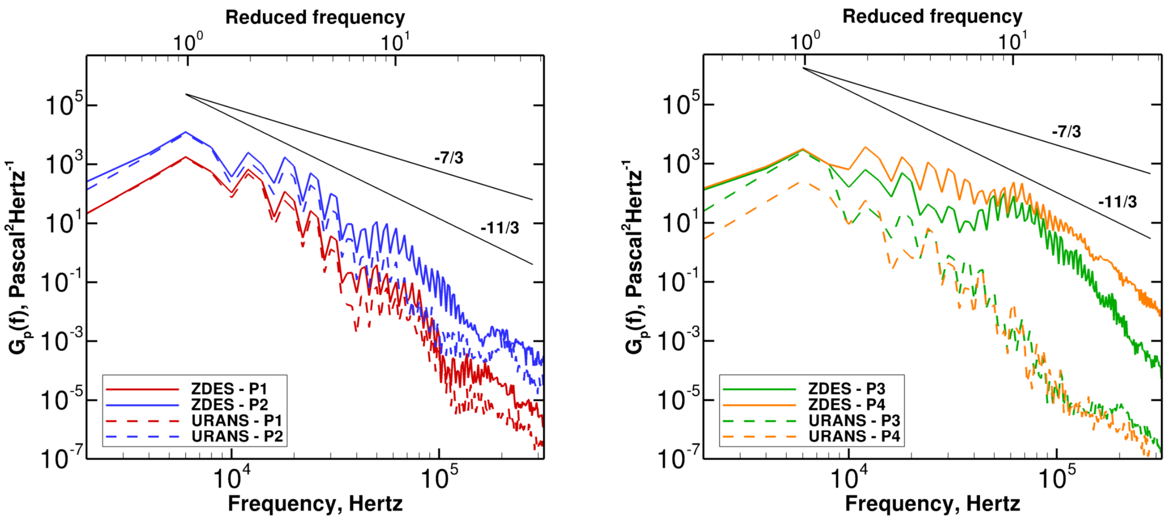

(a) Probes 1 and 2.

(b) Probes 3 and 4.

Figure 4.31 — *Power spectral density of static pressure for probes along the main tip-leakage vortex. URANS and ZDES.*

The PSD are based on the Welch method [172] using an overlap of 50% and ten Hann windows with a linear mean for each as in the previous section. The same frequency resolution (FR) of 2000 Hz is chosen for both the computations. The PSD functions are plotted for probes 1 and 2 in figure 4.31(a) and for probes 3 and 4, in figure 4.31(b).

The PSD represents the flow energy. For a thorough knowledge of the energy within the flow, the normalized PSD are used too. They are defined by $\frac{f \cdot G_p(f)}{\sigma^2}$ with σ detailed in equation IV-1. The normalized power spectral density shows the contribution to the total energy of the different frequencies. They are plotted for probes 1 and 2 in figure 4.32(a) and for probes 3 and 4, in figure 4.32(b).

$$\sigma^2 = \int_0^\infty G_p(f)df = \int_0^\infty f \cdot G_p(f)d(log(f)) \qquad \text{(IV-1)}$$

Up to section 31% X/C, the energy level increases for every frequency, low, medium and high, and, above all, for both URANS and ZDES in figure 4.31(a). This characterizes a similar evolution of the tip-leakage flow. In addition, the magnitudes for probe 1 are close until 10^5 Hz, except for one peak at 38000 Hz ; then, they diverge. The frequency from which the two methods differ lowers as the probe is downstream. Indeed, for probe 2, it would be around 56000 Hz. The slope of the PSD changes from a steep one at probe 1 to the $k^{-11/3}$ slope which corresponds to a turbulence/mean-shear interaction. However, the ZDES approach is closer to this slope than the URANS method.

From probe 3 onward, figure 4.31(b), the difference in magnitude is important. At probe 3, the two methods match only at the low frequencies: 6000 and 8000 Hz. And finally, at probe 4, the whole spectrum is lower for the URANS approach. Nevertheless, it must be noticed that the 6000 Hz frequency corresponds to the IGV passage frequency (6156 Hz) regarding the PSD frequency resolution. Its harmonics are captured by both methods, although the magnitudes differ. This is clearly seen with

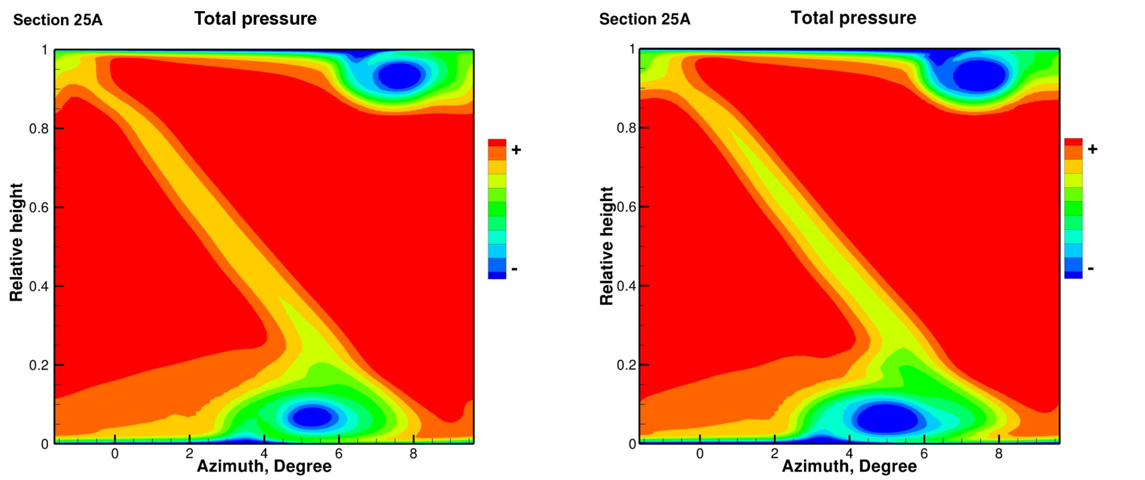

(a) Throttle 1.45. Near surge cartography.

(b) Pivot pressure of 0.93 Pio. Design point cartography.

Figure 5.2 — *Total pressure cartography at section 25A. ZDES computations.*

point for this study and the one retained for the outlet boundary condition.

5.1.2 Inlet cartography definition for the computations on the first rotor near surge

Once the operating point is defined, the flow cartography is extracted at section 25A. The resulting 2D map is then set against the 2D map originating from the design point in the figure 5.2 which shows the total pressure. One can see that the topology of the flows captured is similar between the two operating points. However, the vortices coming from the hub and tip gaps of the IGV are wider at the design point. Besides, they have a lower total pressure in their core. Likewise, the wake is more pronounced at the design point. The azimuthal shift of the tip and hub vortices from the wake position is similar too. That is to say, the vortices development and convection are not drastically changed, despite the change in the axial momentum induced by the change of the operating point.

Notwithstanding these weak differences, it is relevant to use the adapted cartography since the vortex at the tip has changed. This vortex influences the rotor tip-leakage vortex along with the whole flow topology near the casing of the rotor. An insight of this influence was given in chapter 4 and this effect will be further discussed in chapter 6.

5.1.3 Adaptation of the operating point for the computation on the numerical test bench

The same numerical test bench is used for the ZDES computation near surge as the one for the design point. Nonetheless, it is adapted to match the new operating point. Therefore, the unsteady inlet condition known as "rotating distortion" is implemented on the numerical test bench. This time, the rotating distortion is based on the flow cartography near surge previously defined.

The outlet condition is the same type 4 throttle law as the one used for the IGV-R1 preliminary study. The purpose is to be consistent with the methodology followed for the design point. However, the adaptation of the numerical test bench has emphasized a limitation of this throttle law. Indeed, instabilities occur when the type 4 throttle law is used on the numerical test bench defined for this study. It is impossible to achieve a stable operating point, even if the type 4 throttling law was developed originally to avoid instabilities near surge. As far as this issue occurs only with the numerical test bench, which is based on ZDES requirements, and not with the IGV-R1 mesh, the reason seems to be the incompatibility of this boundary with a fine mesh.

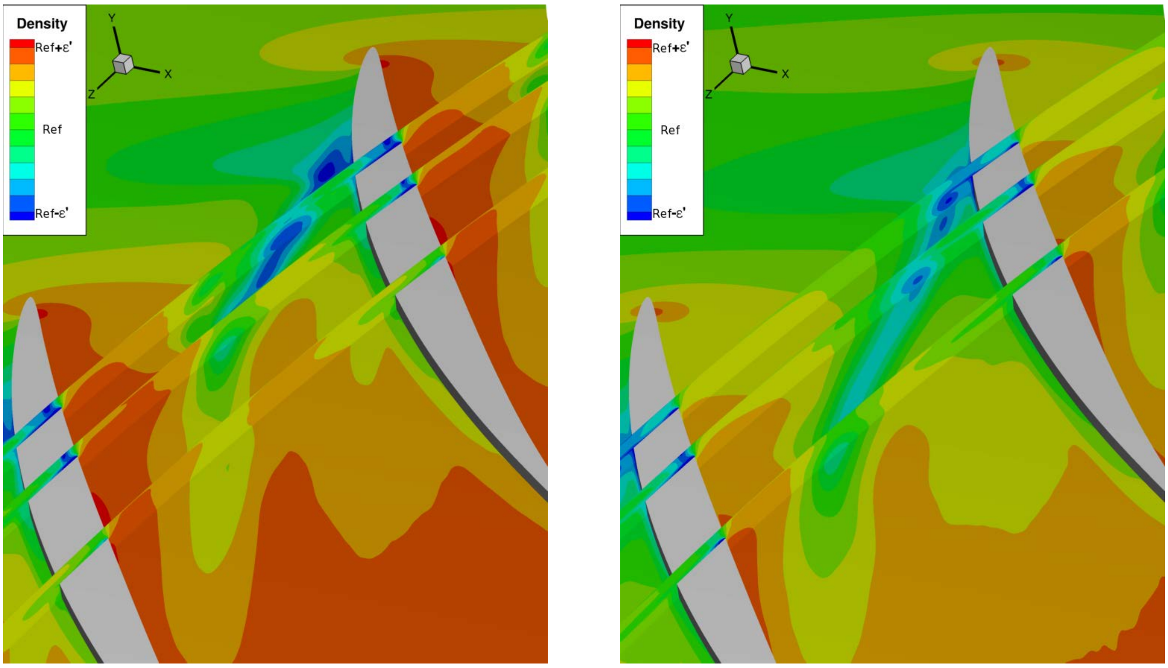

(a) Near surge.

(b) Design point.

Figure 5.7 — *Comparison of the time averaged density field for ZDES at two operating points. Density planes at 22%, 31% and 46% chord and 98% relative height.* $\epsilon' = 29\%$ *of the density reference value.*

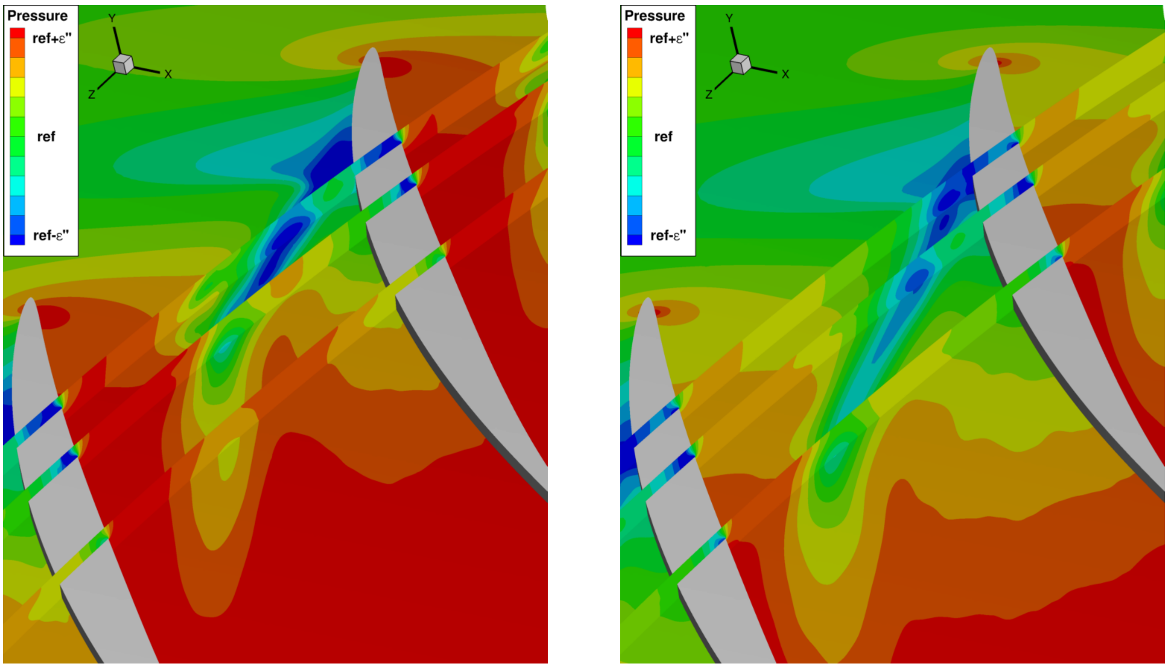

(a) Near surge.

(b) Design point.

Figure 5.8 — *Comparison of the time averaged pressure field for ZDES at two operating points. Pressure planes at 22%, 31% and 46% chord and 98% relative height.* $\epsilon'' = 29\%$ *of the pressure reference value.*

Thereby, this confirms the separation at the casing and the importance of the induced vortex in the boundary layer separation.

The deflection of the tip-leakage flow is easily understood when the velocity triangle are considered.

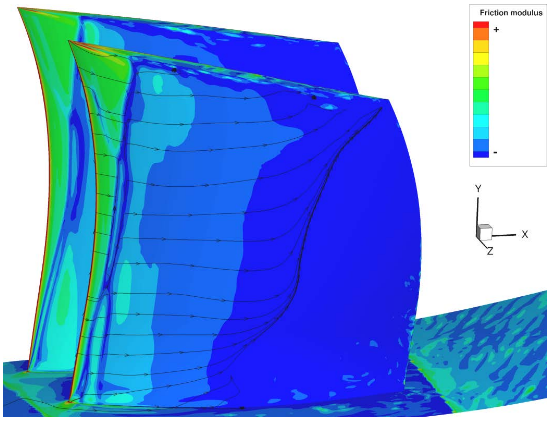

(a) Near surge.

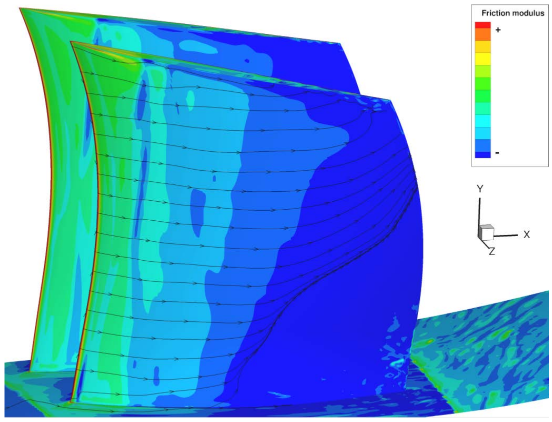

(b) Design point.

Figure 5.9 — *Comparison of the friction lines for the time averaged field for ZDES at two operating points near the hub.*

A decrease of the axial velocity along with the same rotating velocity leads mechanically to an increased angle for the tip-leakage vortex. If the length of the tip-leakage vortex is constant, its disruption occurs earlier axially with a decreased axial velocity. Notwithstanding this effect, there is another phenomenon to be reckoned with: the shock. The analysis of the relative Mach number in figure 5.6 reveals an important difference between the operating points concerning this shock. Indeed, the shock is stronger near surge and the zone of high Mach number is concentrated around the shock which is localized just upstream section 22% X/C. Therefore, it accelerates the vortex disruption. Like the different vortices occurring near the casing, the shock is located closer to the leading edge of the blade near surge. This is coherent with what was observed experimentally by Bergner et al. [9] on a similar configuration.

The effects of the shock are not only visible on the relative Mach number field. Figure 5.7 points out that the drop in the density due to the shock is more important near surge. Although the levels of density are lower near surge at the shock position, near 10% X/C up to just upstream 31% X/C, it must be emphasized that the low density region at 31% X/C, in blue in figure 5.7(b), is not found in figure 5.7(a). Moreover, the density rises again just after section 31%X/C and higher values are found near the trailing edge. In other words, the effects of the shock are localized and centred around its position.

Finally, figure 5.8 corroborates the fact that this is a strong shock compared to the one observed at the design point. Indeed, the gradient is more important near surge. First, there is a rapid decrease of the pressure around 10% X/C with low pressure levels, inferior to the one measured at the same position at the design point. Then, downstream the shock position, there is a rapid rise of the pressure value. Nevertheless, the pressure drop follows the main tip-leakage vortex core, likewise what is noticed with the density.

An interesting effect of the operating point is underscored in figure 5.9, with the skin friction lines [41] and friction modulus at the design point and near the surge line. The area where the friction modulus decreases rapidly near the leading edge is located even closer to this leading edge in the case near surge. The corresponding friction modulus value is inferior too and a distinct line of low friction modulus is emphasized from the tip to the hub of the blade. This line denotes the shock position and its effects throughout the blade height. The friction lines drawn on the suction side of the blade indicate a different behaviour too. The position of the separating line observed at the design point differs. Indeed, it reaches the trailing edge at the tip for the computation near surge. This brings to the fore a massive separation on the suction side for the case near surge. As a consequence, this highlights that the corner effect is amplified near surge. This amplification is however overestimated as already observed for steady RANS computations by Marty et al. [112, 111] and this drawback originates from the Spalart-Allmaras model

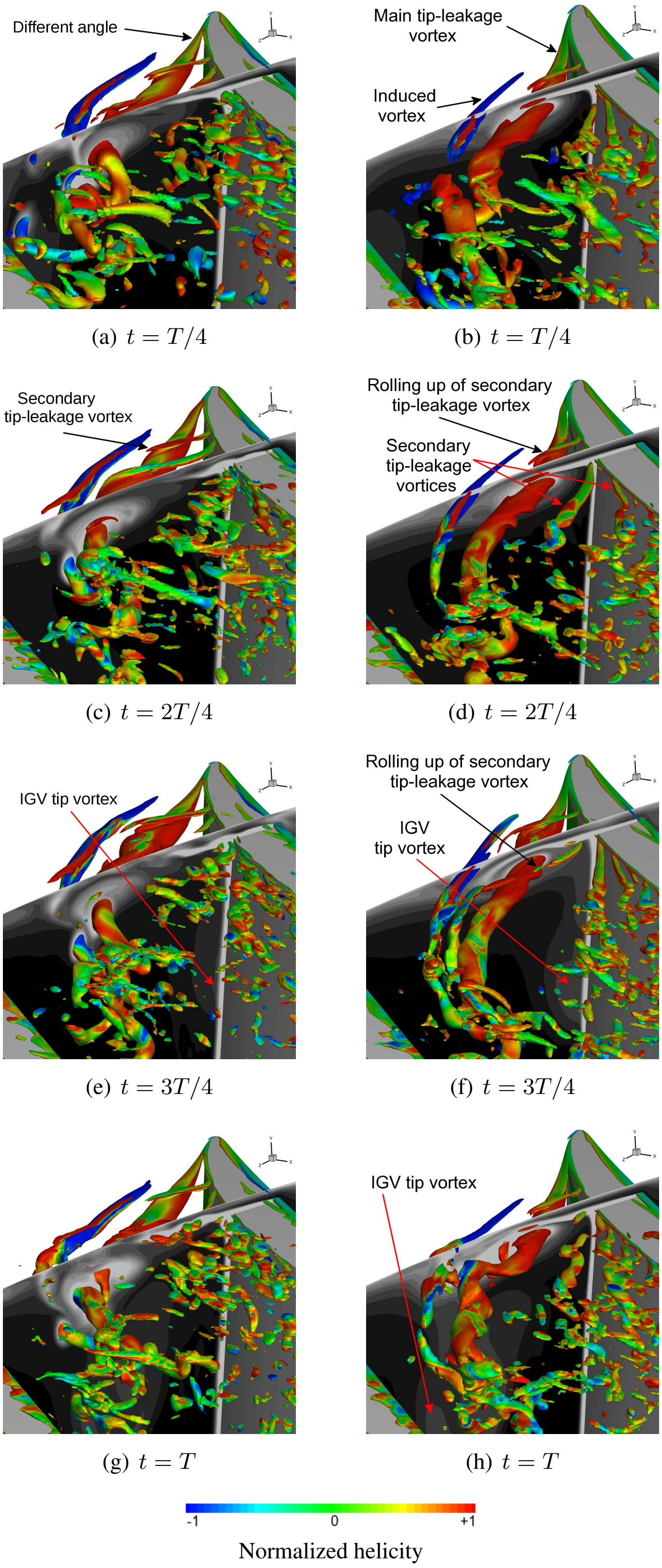

Figure 5.10 — *Snapshots of Q criterion iso-surface coloured by the normalized helicity and section 31% X/C filled with the entropy (left: ZDES near surge, right: ZDES at design point.).*

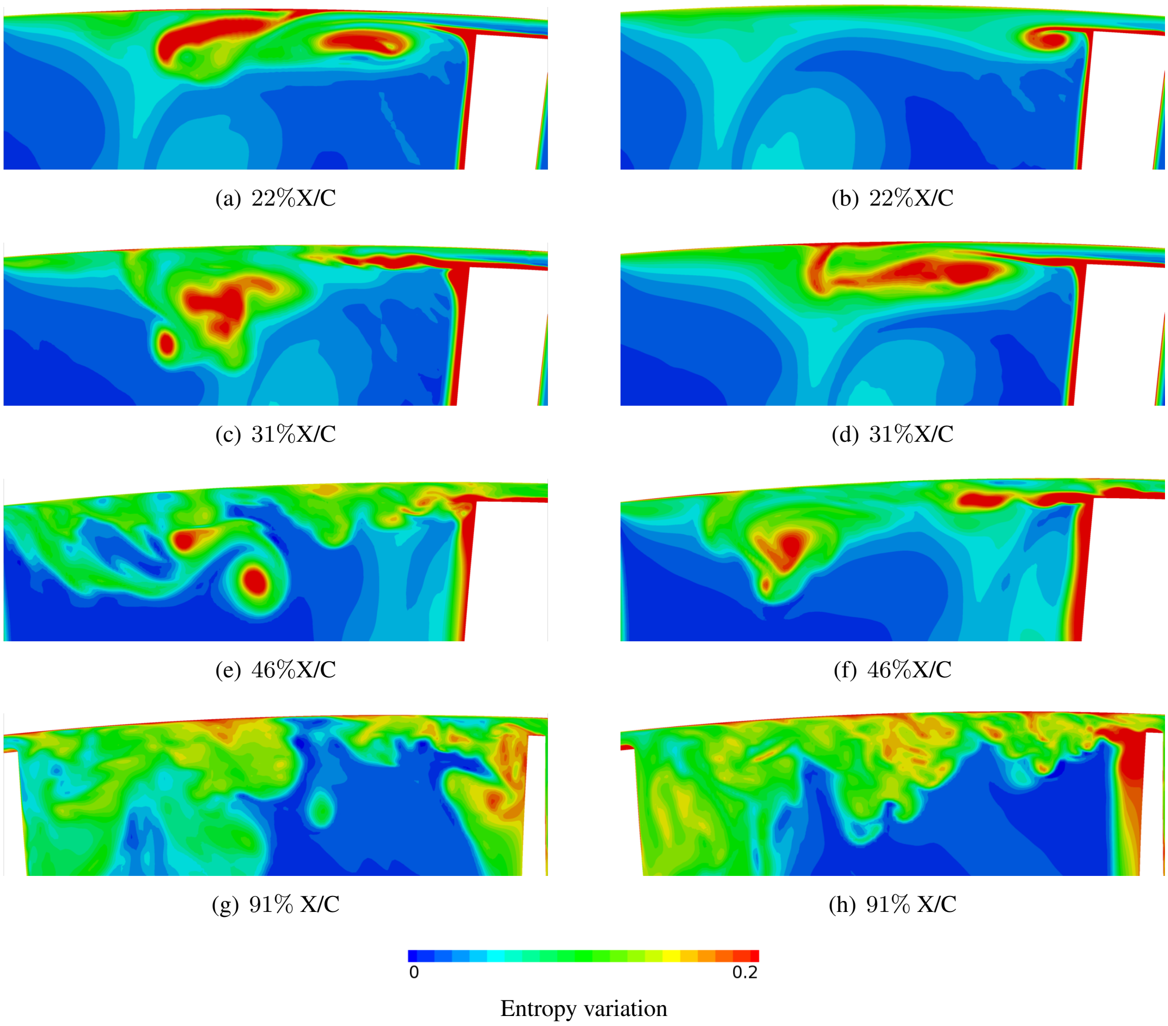

Figure 5.11 — *Entropy planes for four different axial positions at t=3T/4 (left: ZDES near surge, right: ZDES at design point.).*

with the Q criterion figures, is clearly discernible here by comparing figures 5.11(c) and 5.11(d). This only affects the moment when the IGV tip vortex arrives on the R1 and stretches the tip-leakage vortex azimuthally.

In the next sections, the modifications of the tip-leakage flow when the operating point is close to the surge line will be further discussed with the help of measurements taken on the experimental test bench.

5.3 Effects on performance and 1D distributions

5.3.1 Global values

The first comparison with the experimental data to conduct concerns the global values. The normalized mass flow at section 25A as well as the normalized total pressure ratio between sections 25A and 26A are evaluated for the experiments and the computations. Even if some of the experimental values are missing near the hub and the tip because of the measurement process with the probes, as explained in chapter 4, these global values give an idea of the behaviour of the R1 when the turbomachine gets closer to the surge line. The numerical results along with the experimental ones are summarized in the table

Case	Normalized mass flow	Normalized R1 total pressure ratio
Pneumatic probes - design point	1.000	1.000
Pneumatic probes - near surge	0.927	1.006
ZDES - design point	1.014	0.992
ZDES - near surge	0.948	1.020

Table 5.1 — *Mass flow and total pressure ratio for ZDES at design point and near surge, normalized with the values from the pneumatic probes data at design point.*

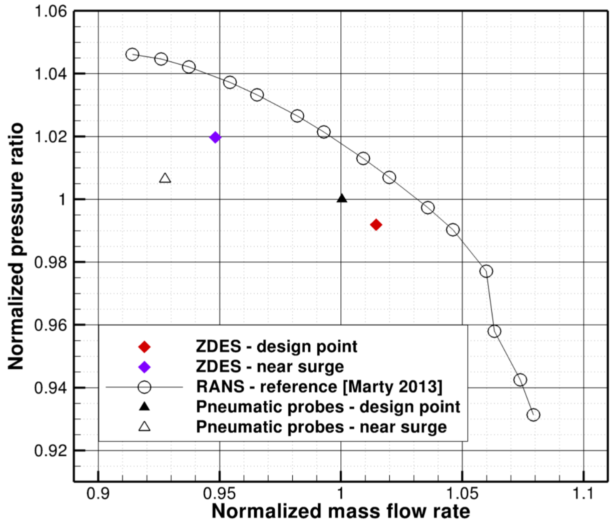

Figure 5.12 — *Pressure ratio versus mass flow rate for ZDES at design point and near surge, normalized with pneumatic probes data at design point.*

5.1. For an easier comparison, they are plotted in figure 5.12 along with the reference computation in RANS from Marty et al. [113]. Details for this reference case are given in chapter 4.

First of all, it must be emphasized that the ZDES underestimates the pressure ratio when it is compared to the reference RANS computations. Therefore, the trend observed in the previous chapter is kept near surge. Nevertheless, and contrary to how it behaves at the design point, the ZDES computation overestimates the pressure ratio compared to experiments. If a line is drawn between the two ZDES computations and the two experimental values, one can distinguish that the slope for the ZDES computations is steeper. However, this slope is similar to the one observed for the reference case, in RANS. Thereby, the same advantage and drawbacks are observed in ZDES as in RANS for this part of the operating line. Notwithstanding the similarity concerning the slopes between the computations, the values are in better agreement in ZDES. This is due to a better capture of the pressure ratio. Moreover, there is still an overestimation by about 2% of the mass flow rate in ZDES near surge, as it is for the design point. This overestimation occurs in spite of the preliminary studies carried out on the IGV-R1 configurations at the design point and near surge that underlined a good agreement of the numerical radial distribution of axial momentum with the probe values at section 25A. This confirms the necessity to rely on radial distributions and not only on global values to choose the appropriate operating point when computations are compared to experiments.

5.3.2 Radial distribution

The radial distributions of different values are plotted at section 26A, which is located downstream R1. Thereby, the phenomena occurring on the blade influence directly these distributions and can be

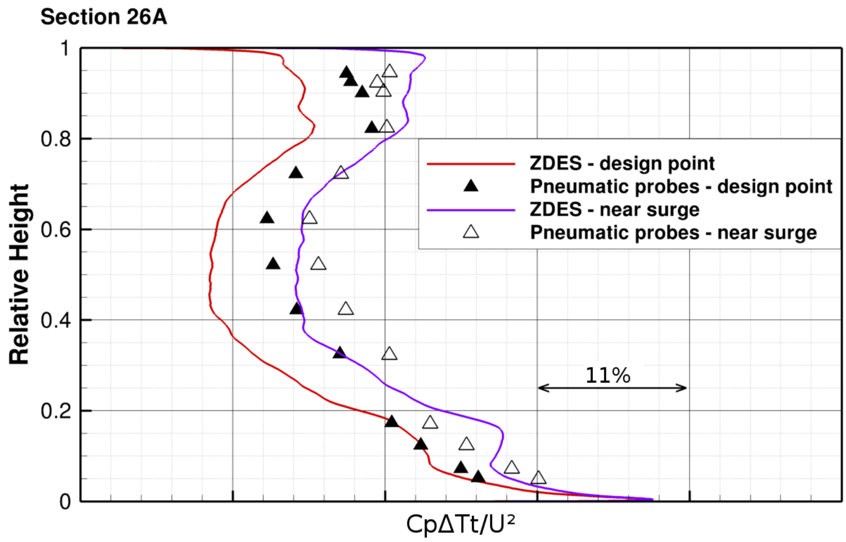

Figure 5.15 — *Radial distribution of time and circumferentially averaged normalized total temperature at section 26A for ZDES at design point and near surge.*

cases at the design point.

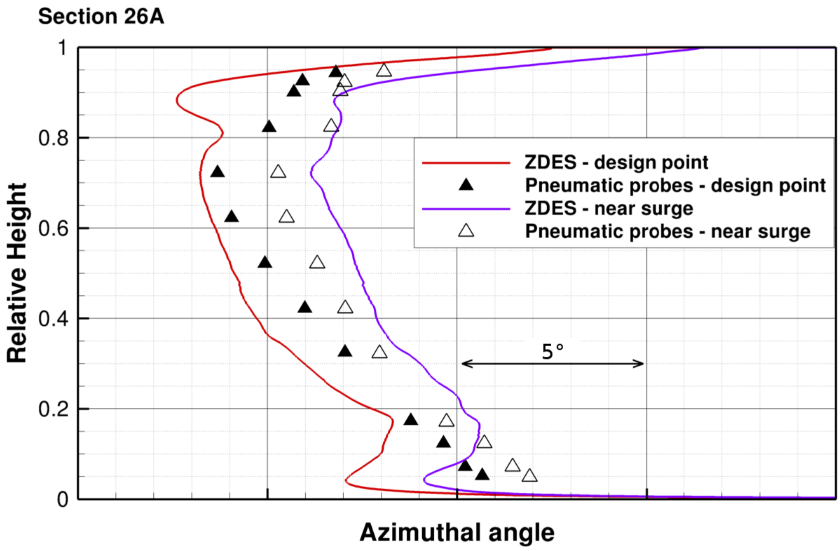

Figure 5.16 — *Radial distribution of time and circumferentially averaged azimuthal angle at section 26A for ZDES at design point and near surge.*

high circumferential velocity areas corresponding to the wakes are accurately located by both ZDES methods. Indeed, the width and the position of the wake is correctly located at around azimuth 5.3 near surge and 5.6 at the design point for both the LDA and the measurements. Nevertheless, the ZDES near surge is more accurate for the capture of the wake width than the ZDES at the design point. The values around azimuth 2.5, which correspond to the tip-leakage vortex, are in better agreement with the LDA for the ZDES near surge. In the other channel, around azimuth 8, the LDA measurements does not see the tip-leakage vortex contrary to the computations. This is linked to the aforementioned non-periodicity of the real test bench.

5.3.4 Azimuthal distribution of the velocity standard deviations

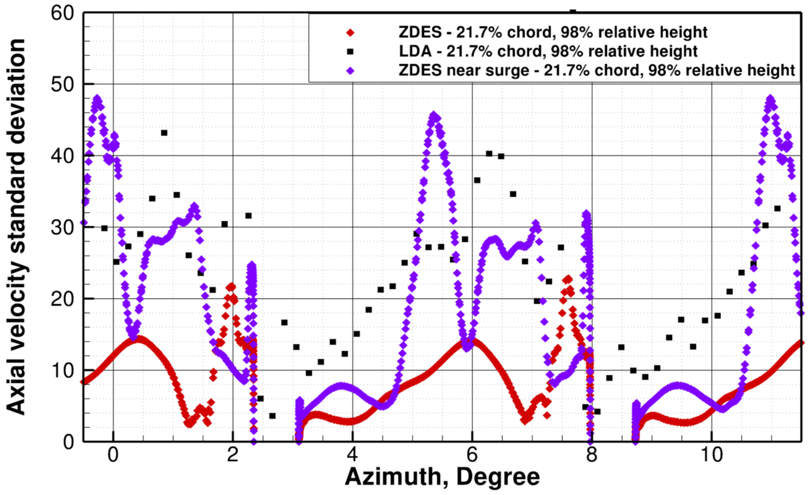

(a) Axial.

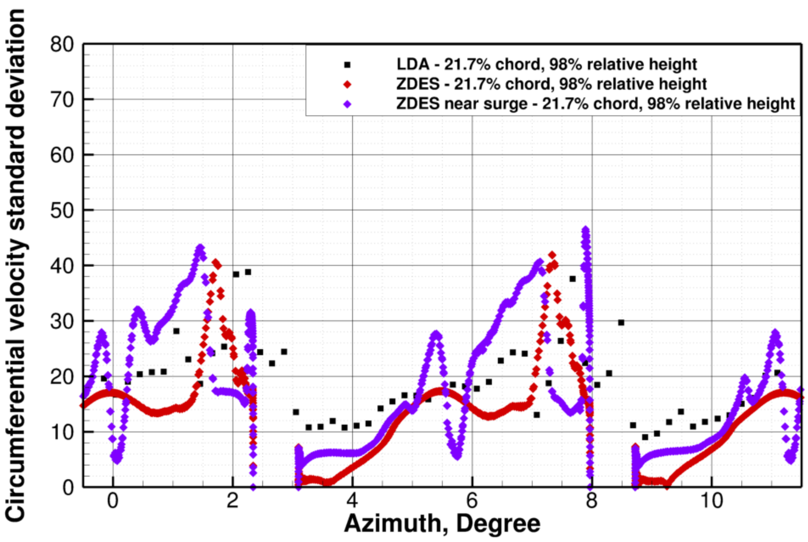

(b) Circumferential.

Figure 5.21 — *Axial and circumferential velocity standard deviations [in $m.s^{-1}$] at 21.7% chord and 98% relative height for ZDES at design point, ZDES near surge and LDA measurements at design point.*

In order to understand the evolution of unsteady phenomena near surge, the standard deviation of the velocities is analysed hereinbelow.

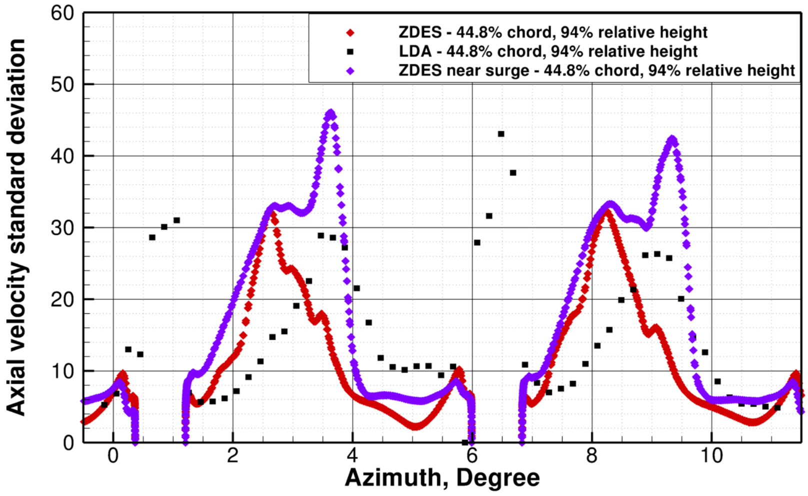

(a) Axial.

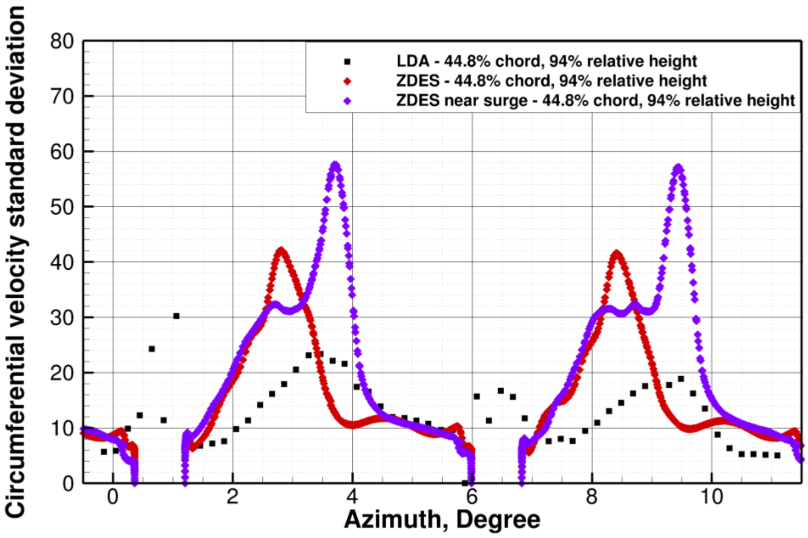

(b) Circumferential.

Figure 5.22 — *Axial and circumferential velocity standard deviations [in $m.s^{-1}$] at 44.8% chord and 94% relative height for ZDES at design point, ZDES near surge and LDA measurements at design point.*

induced vortex that extends further radially from the casing near the surge, due to the boundary layer separation. Since the separation is closer from the leading edge as well as more significant near surge, its influence is captured at 44.8%X/C and 94% of relative height.

Near the trailing edge, at 91% X/C and 90% of relative height, the aforementioned phenomenon of double leakage is clearly highlighted. The axial velocity standard deviation is plotted in figure 5.23(a). At azimuth 4, near the blade, the axial unsteadiness is high with values around $25m.s^{-1}$, whereas the levels of axial velocity standard deviation are between 6 and $14m.s^{-1}$ for the rest of the passage. These values concerns the ZDES near surge. Nonetheless, close levels are captured for the ZDES computation as well as the LDA measurements at the design point. These high unsteadiness levels designate the double leakage phenomenon. At this position, the level of axial unsteadiness near surge is nevertheless lower by $5m.s^{-1}$ compared to the design point.

The position of the tip-leakage vortex rim, located at azimuth 5.5 at the design point for both the nu-

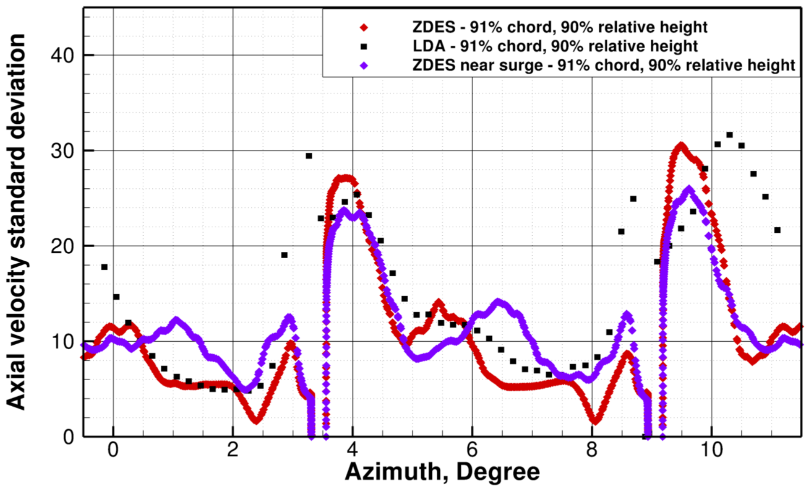

(a) Axial.

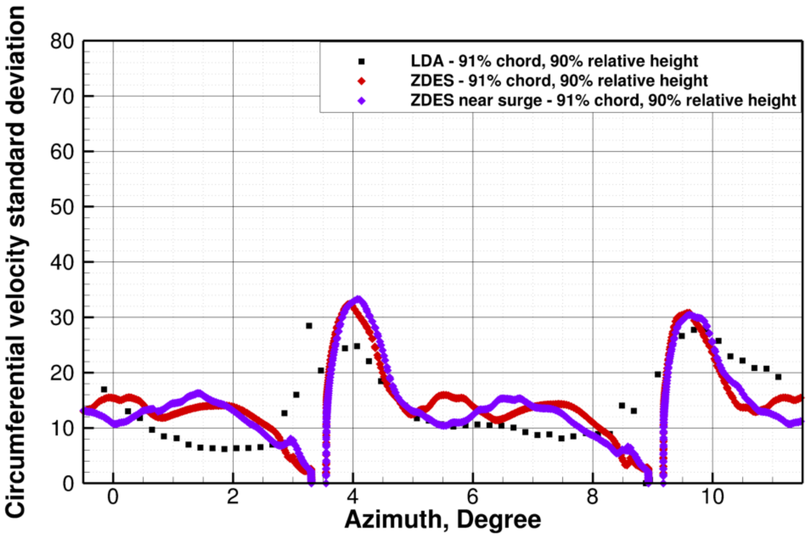

(b) Circumferential.

Figure 5.23 — *Axial and circumferential velocity standard deviations [in $m.s^{-1}$] at 91% chord and 90% relative height for ZDES at design point, ZDES near surge and LDA measurements at design point.*

merical and experimental results, is closer to the blade near surge due to its increased width. Nonetheless, its unsteadiness level is the same as for the design point.

The circumferential velocity standard deviation presented in figure 5.23(b), confirms the double leakage. Although the axial unsteadiness is lower for the double leakage near surge, the levels are similar concerning the circumferential unsteadiness. By contrast, the azimuthal velocity is increased as already seen in figure 5.19(b). Actually, the levels are close throughout the channel. The only exception concerns the position of the peak linked to the rim of the main tip-leakage vortex, as shown at azimuth 6.5 in figure 5.23(b) for the LDA measurements and ZDES near surge. This peak is located at azimuth 5.5 for the ZDES at the design point. This shows that the vortex is wider near surge at this axial position. The ZDES computation near surge is then in better agreement with the LDA measurements, even if this is at the experimental design point.

At section 26A and 90% of relative height, the standard deviation of the velocity is available near

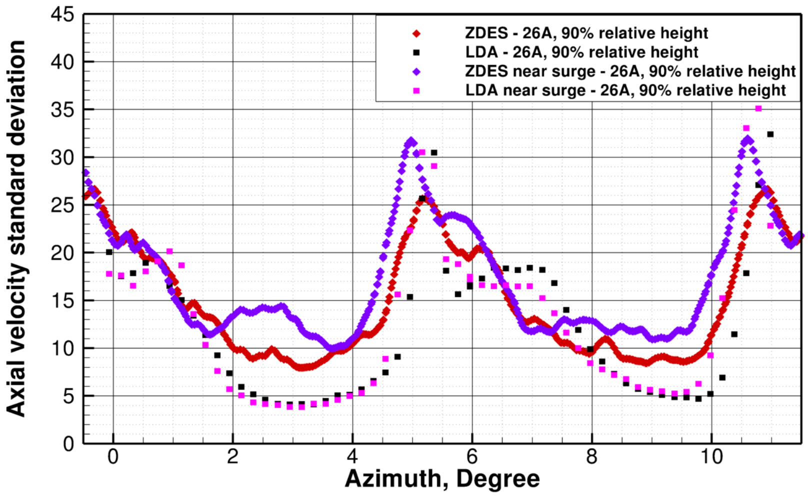

(a) Axial.

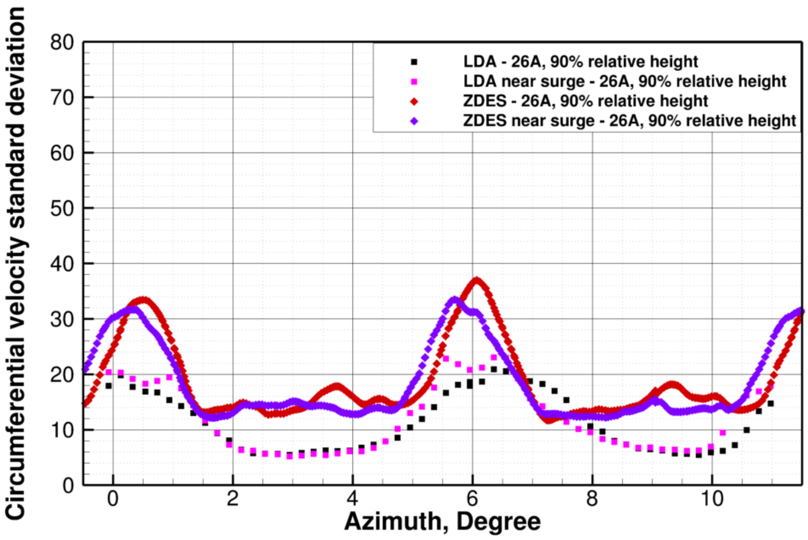

(b) Circumferential.

Figure 5.24 — *Axial and circumferential velocity standard deviations [in $m.s^{-1}$] at section 26A and 90% relative height for ZDES at design point, ZDES near surge and LDA measurements both at design point and near surge.*

surge too. Figure 5.24(a) shows its values for the axial velocity. First, one can see that there is almost no differences between the operating points from the experiments. There is only an azimuthal shift by 0.3 degrees and the maximum level of standard deviation is superior by $3m.s^{-1}$ near surge at azimuth 10.5. This is coherent with the results for the axial velocity seen in figure 5.20(a). Moreover, at the second peak, from azimuth 6 to 7.5, the unsteadiness is higher by 2 $m.s^{-1}$ at the design point than near surge in the experiment. This is the opposite in ZDES for the second maximum peak at azimuth 5.5-6. This shows that some unsteady phenomena occur experimentally and not in the ZDES. This could be explained by potential effects of the stator downstream.

For the computations, at the azimuth 2.5-3 there is a local increase of the unsteadiness due to the tip-leakage vortex. This is clearly amplified near surge with an increase by $5m.s^{-1}$ for the standard deviation. However this is not experienced by the LDA. Actually, the levels captured by the LDA are the same for the two operating points and are twice as small as the values from the ZDES computations.

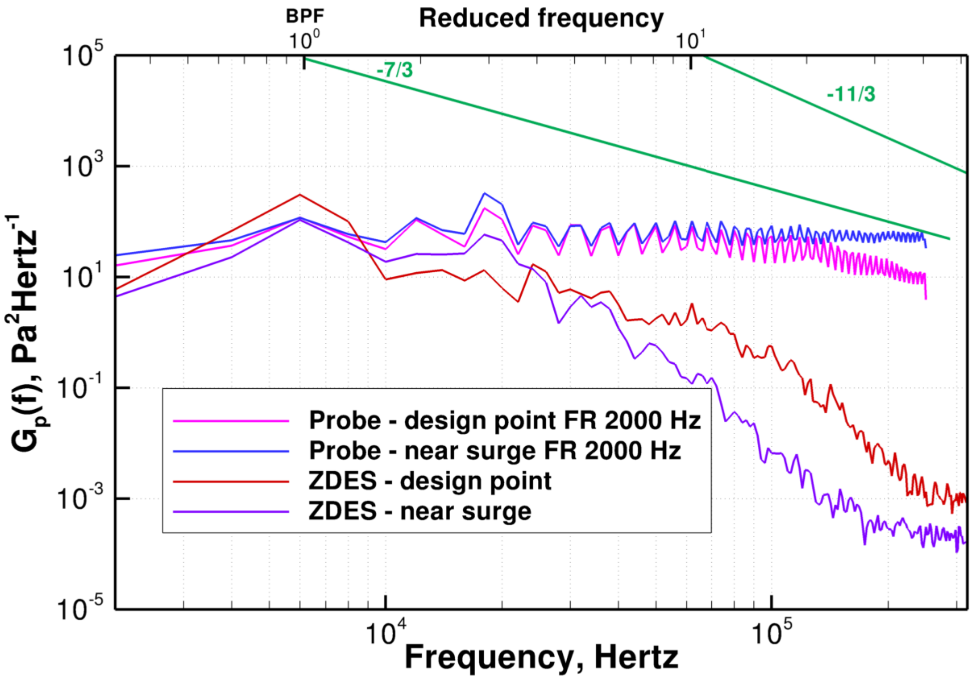

(a) At the casing.

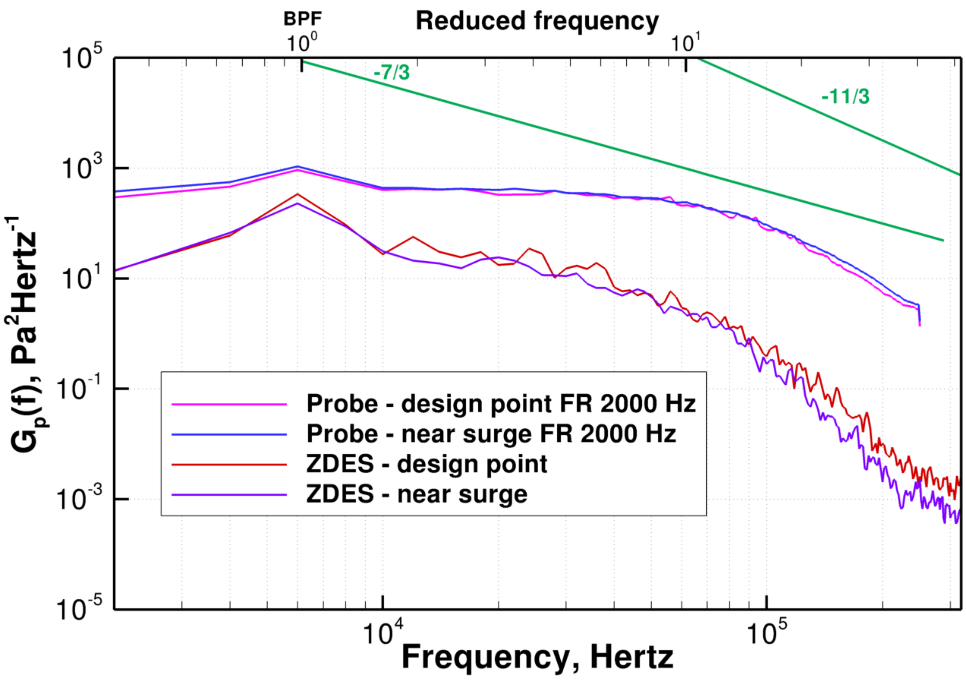

(b) At 94% relative height.

Figure 5.25 — *Power spectral density of pressure at section 26A. ZDES at the design point, ZDES near surge and experimental unsteady pressure probes at the design point.*

design point, at least for some values as shown previously in this chapter. As a result, this proves that the higher energy of the third BPF harmonic comes not only from the potential effect from the first stator (S1) downstream the R1, as it was hypothesized in chapter 4. Otherwise, it would not be captured numerically. Another effect, certainly linked to the surge, seems to participate, along with the potential effect from the S1, to this high energy.

Case	Normalized mass flow	Normalized R1 total pressure ratio
Pneumatic probes	1.000	1.000
ZDES with rotating distortion	1.014	0.992
ZDES with averaged cartography	1.012	0.987

Table 6.1 — *Mass flow and total pressure ratio for ZDES with averaged cartography and with rotating distortion, normalized with the values from the pneumatic probes data.*

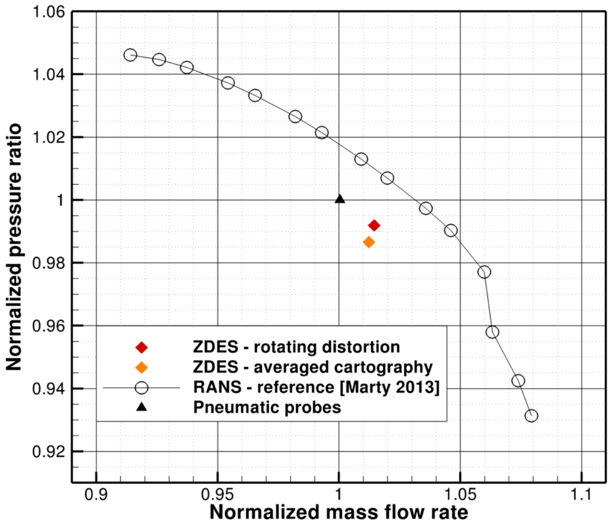

Figure 6.1 — *Pressure ratio versus mass flow rate for ZDES with averaged cartography and with rotating distortion, normalized with pneumatic probes data.*

compressor by Tartousi et al. [166], based on a Fourier decomposition with 60 harmonics, of the two dimensional cartography of the flow. The aim is to capture accurately the phenomena arriving at section 25A from the Inlet Guide Vane (IGV): the IGV wake, the IGV hub vortex and last but not least, the IGV tip vortex. The physical values for stagnation pressure, stagnation enthalpy, primitive turbulence quantity of the model, and direction of the flow are given at each interface of the map. Therefore, with this rotating boundary condition, the unsteady distortion effects induced by the IGV are modelled in the simulation of the flow within the first rotor (R1) of the CREATE compressor. The second one consists in the same two dimensional cartography but azimuthally averaged. There is neither distortion nor rotating inlet map in this case. For each radius, the same physical values are given at each cell of the map. This is the only difference between the two compared ZDES computations. Indeed, the same outlet boundary condition is used for both ZDES computations to comply with the methodology established in chapter 3. Likewise, the same methodology is applied to both the computations to check the convergence. The time range retained for the different analysis of this chapter is 17 T for the ZDES with the averaged cartography, which is the same number of iteration as for the ZDES computation with the rotating distortion.

The fact that the only difference between the computations comes from the inlet condition enables to uncouple the phenomena inherent to the tip-leakage flow from the effects of the IGV wakes on this flow.

6.1.2 The effects on the global values

First of all, table 6.1 summarizes the mass flow at section 25A and the total pressure ratio, between sections 25A and 26A, for the two ZDES fields as well as the experimental values from pneumatic pressure probes. These values are plotted in figure 6.1 for an easier assessment, along with a reference

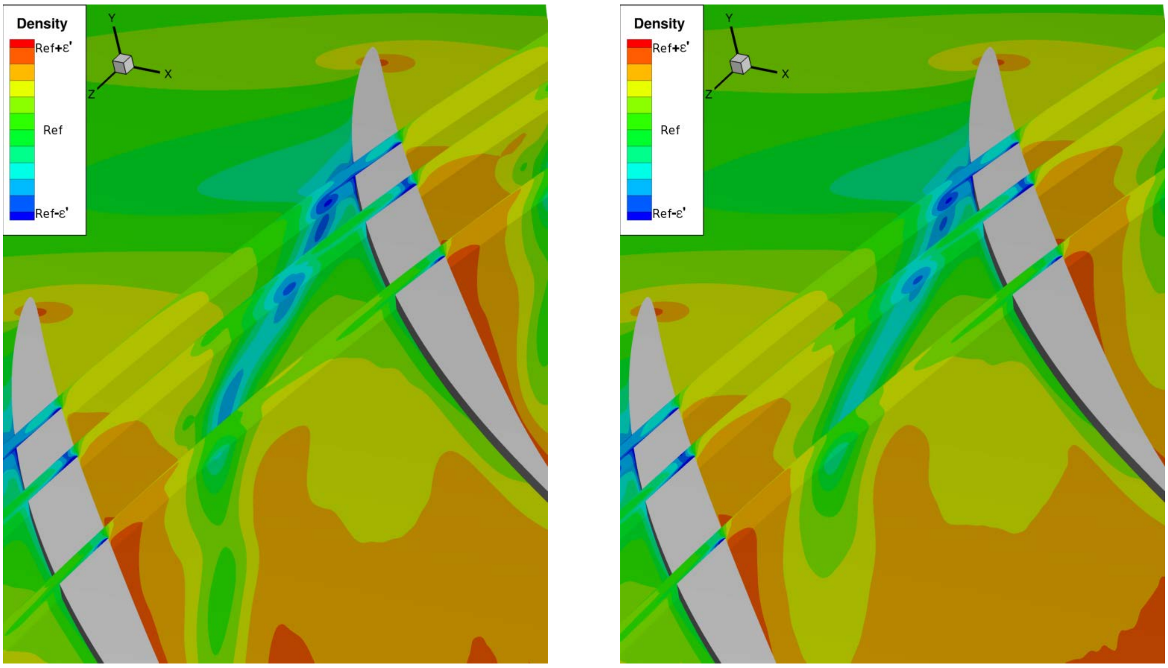

(a) With the averaged cartography.

(b) With the rotating distortion.

Figure 6.5 — *Comparison of the time averaged density field for ZDES with different inlet conditions. Density planes at 22%, 31% and 46% chord and 98% relative height.* $\epsilon' = 29\%$ *of the density reference value.*

rate is mainly focussed near the shock. Nevertheless, a second high entropy area is distinguishable near the pressure side of the adjacent blade in the case with the averaged cartography. Actually, this vortex extends further downstream without the IGV wakes, and then dissipates as it gets closer to the adjacent blade.

The same planes are shown in figure 6.3 for the normalized helicity. The main tip-leakage vortex as well as the induced vortex exhibit a higher rotating intensity highlighted by important zones with a normalized helicity value close to ± 1. Another distinctive effect lies in the amplification of the boundary layer separation at the casing, visible at 31% X/C in figure 6.3(a). Thereby, the effect of the induced vortex is more visible, in blue between the section 31 and 46% X/C in the plane at 98% of relative height. The second zone of high entropy near the pressure side of the adjacent blade is marked by a higher helicity too, albeit less pronounced than the levels upstream section 46% X/C. This clearly strengthens that there is a vortex near the pressure side of the adjacent blade.

Figure 6.4 underscores that the averaged cartography influences the shock on the time averaged field. Indeed, the area with a relative Mach number over 1 is wider. This means that the IGV wakes decrease the shock intensity, at least in average. Besides, a zone of high Mach number, albeit not above 1, extends further downstream along the main tip-leakage vortex up to the section at 46% X/C. This corroborates the fact that the main tip-leakage vortex is more coherent without the wakes.

The analysis of the density field, in figure 6.5 confirms this enhanced coherence of the vortex. The zone of lower density within the vortex core reaches the adjacent blade, whereas the density increases earlier downstream in the case with the IGV wakes. Contrary to the change in operating point detailed in chapter 5, and as expected, the shock does not change drastically without the wakes. The influence of the inlet condition on the shock intensity is nevertheless perceivable, albeit limited.

The pressure field, presented in figure 6.6, validates that the gradients on the time averaged pressure field are similar with or without the arrival of the IGV wakes. Around the shock, there is nothing that

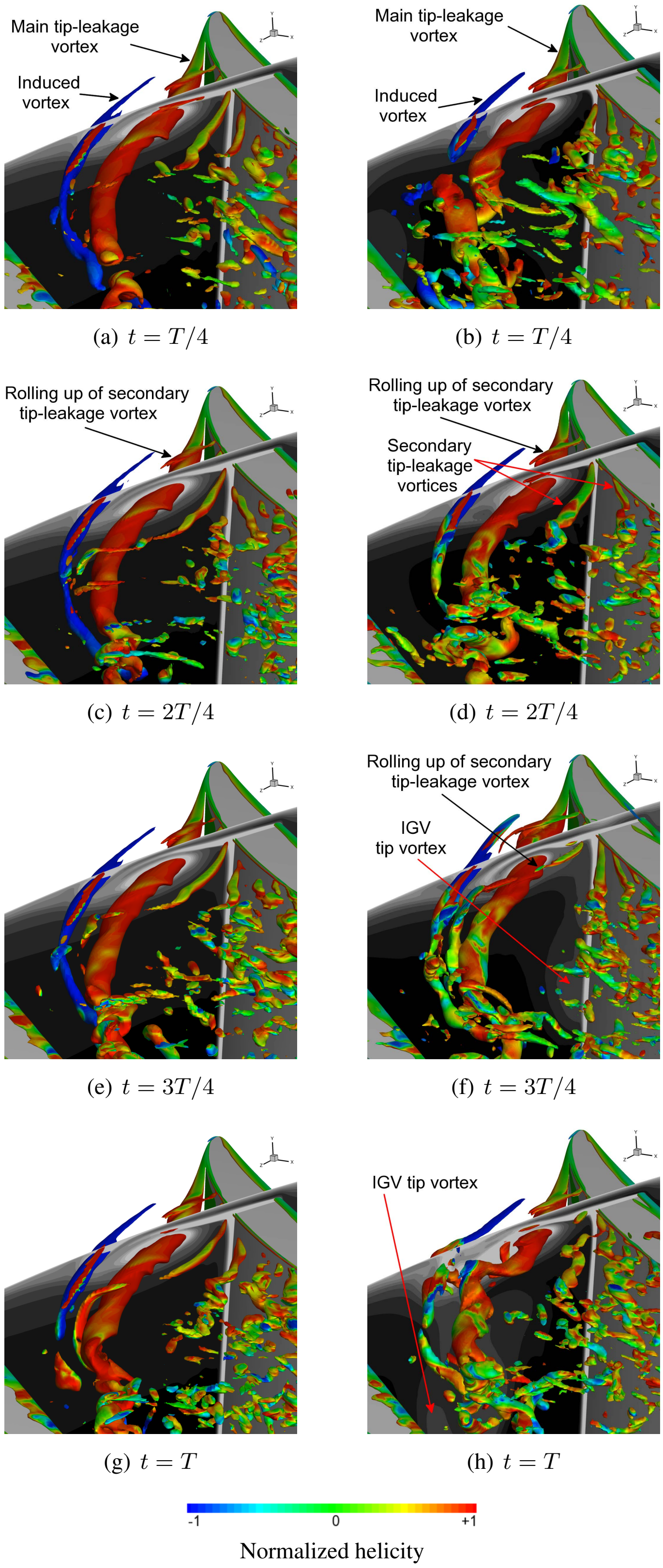

(a) $t = T/4$ (b) $t = T/4$

(c) $t = 2T/4$ (d) $t = 2T/4$

(e) $t = 3T/4$ (f) $t = 3T/4$

(g) $t = T$ (h) $t = T$

Figure 6.7 — *Snapshots of Q criterion iso-surface coloured by the normalized helicity and section 31% X/C filled with the entropy (left: with averaged cartography, right: with rotating distortion).*

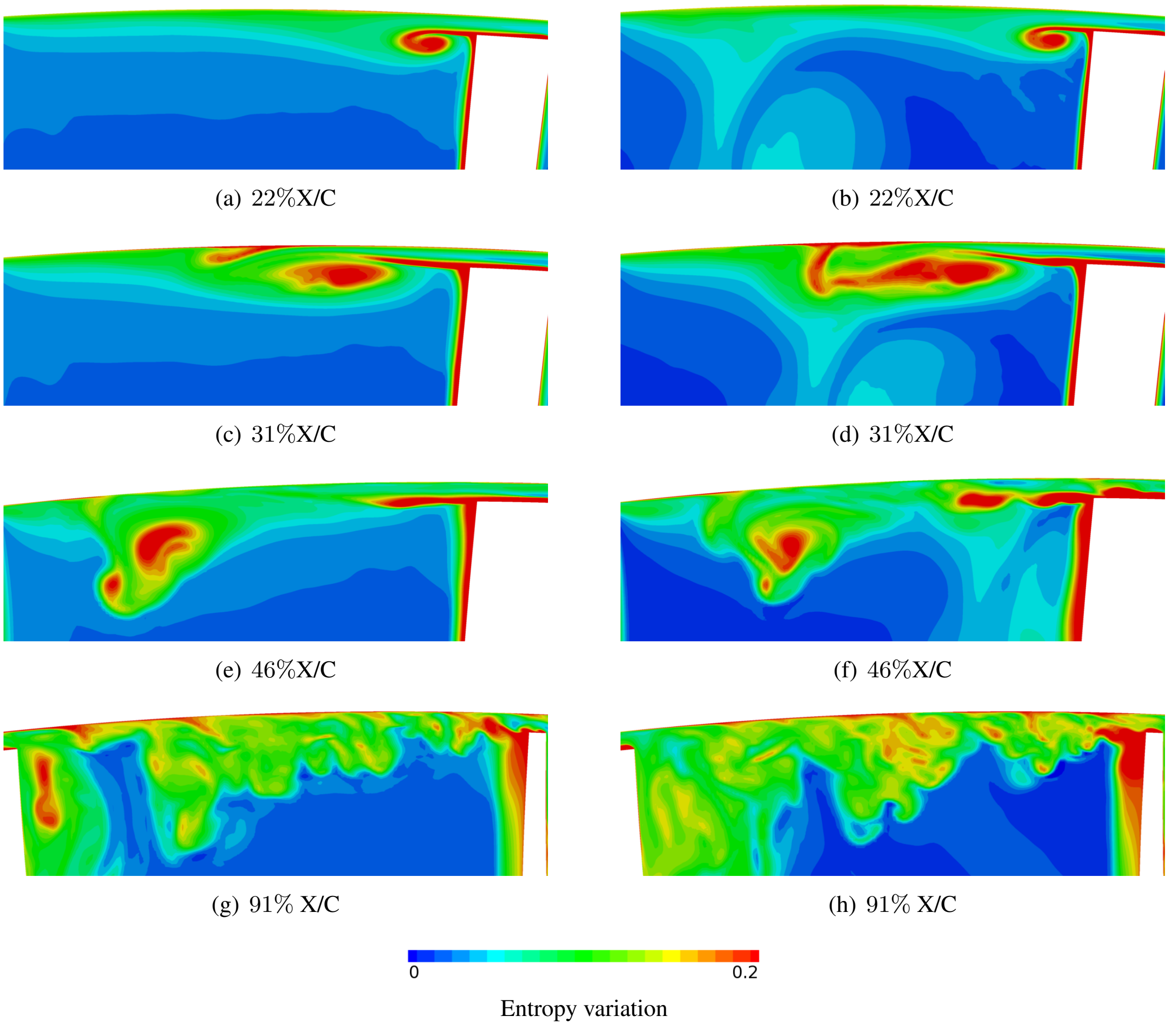

Figure 6.8 — *Entropy planes for four different axial positions at t=3T/4 (left: with averaged cartography, right: with rotating distortion).*

flutter, was already experimentally emphasized in [109], albeit not with an incoming vortex from the stator as it is the case here. In the studied configuration, the IGV tip vortex induces this flutter. The IGV wake, which arrives on the rotor leading edge too has a weak contribution to this phenomenon. The velocity deficit of the main flow deflects the leakage flow direction, from the rotor tip-leakage vortex inception, visible in figure 6.7(d). As a consequence, the rotor tip-leakage vortex moves away from the suction side of the blade with a period of T and it disrupts earlier. The disruption position wanders around 31% X/C. One can see, as already highlighted in chapter 4, that secondary tip-leakage vortices, as the one pointed in figure 6.7(f) migrate from the trailing edge toward the leading edge. This migration originates from this momentum deficit too and is only experienced in the case of the ZDES with the rotating distortion.

Without the arrival of the IGV tip vortex, the rotor vortex topology is at the same development stage as for the case with rotating distortion before its disruption caused by the IGV tip vortex. The closer the origin location of a vortex is from the leading edge, the more stable the vortex. Therefore, the main rotor tip-leakage vortex position remains stable and the induced vortex behaves similarly. There is no direction change in this case. Furthermore, these two vortices have an helicity level increased in absolute value compared to the ZDES with the rotating distortion. This confirms what was seen in figure 6.3(a) with the time averaged helicity planes. As a consequence, these vortices extend further downstream and toward the adjacent blade, which increases the effects of the double leakage.

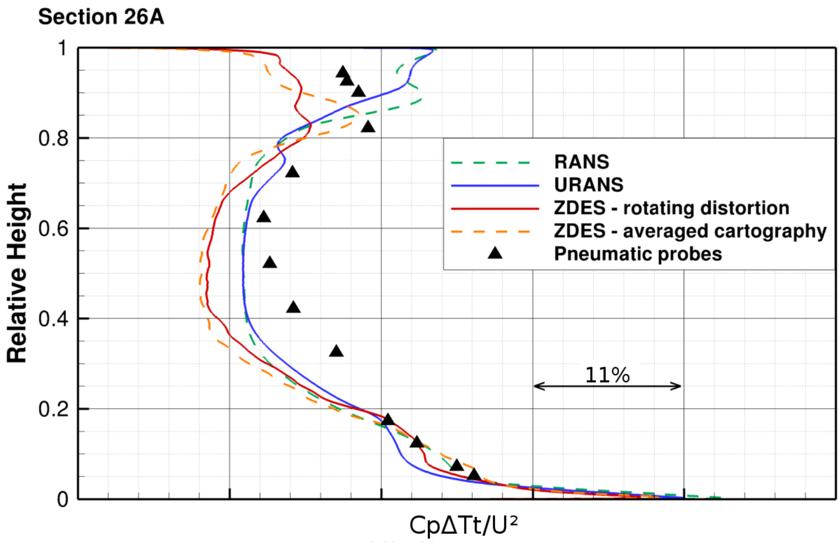

Figure 6.11 — *Radial distribution of time and circumferentially averaged normalized total temperature at section 26A for RANS, URANS, ZDES with rotating distortion, ZDES with averaged cartography and experimental probes.*

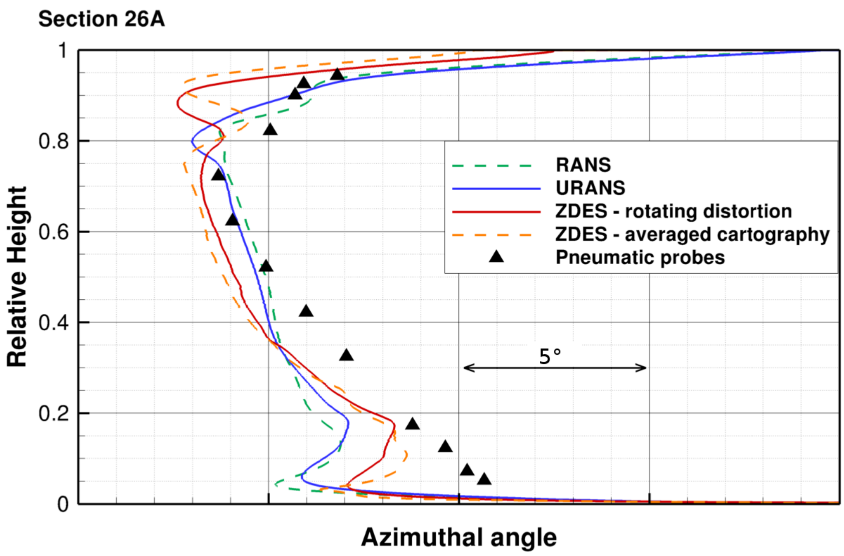

Figure 6.12 — *Radial distribution of time and circumferentially averaged azimuthal angle at section 26A for RANS, URANS, ZDES with rotating distortion, ZDES with averaged cartography and experimental probes.*

the averaged map, corresponds to 0.85% of relative height, which coincides with the maximum for the experimental values. By contrast, this maximum is lower with the rotating distortion. Notwithstanding this apparent advantage of the averaged map for the value at 85% of relative height, the gradient from this radial position to the casing is clearly overestimated. This strengthens the fact the tip-leakage vortex is too coherent with the averaged map compared to what it is in the experiment.

A similar behaviour is captured by the RANS approach. Instead of having just a light curve inflection like in URANS, the use of the averaged cartography enables this steady approach to capture gradients which are in better agreement with the experiments. In other words, the steady RANS approach seems to be more appropriate to simulate the unsteady tip-leakage vortex than the unsteady RANS (URANS) method. This is an unexpected consequence of the use of a less accurate inlet boundary condition.

6.3.3 Azimuthal distribution of the velocity standard deviations

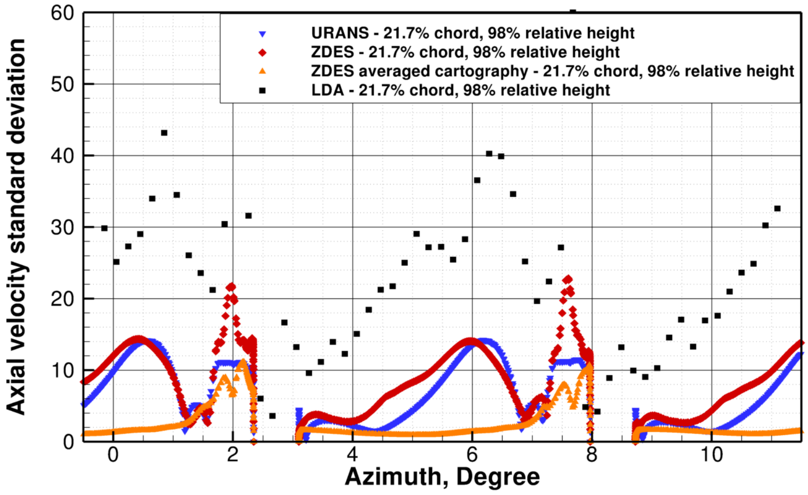

(a) Axial.

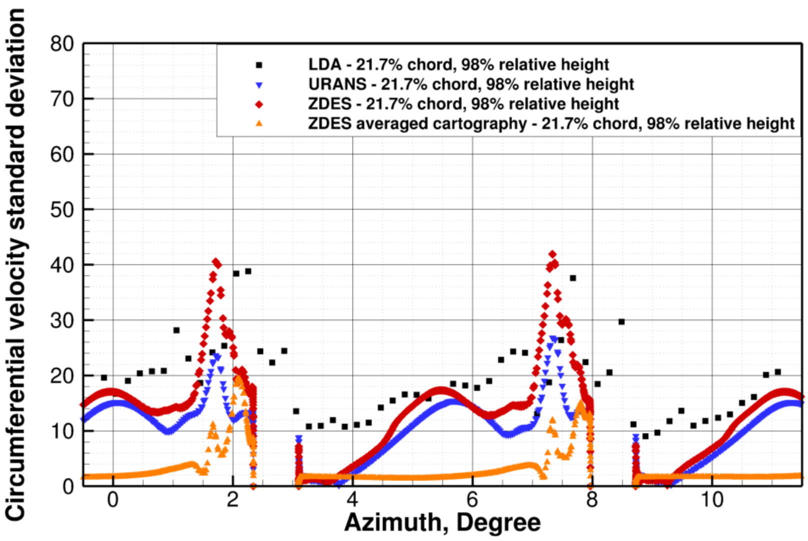

(b) Circumferential.

Figure 6.17 — *Axial and circumferential velocity standard deviations [in $m.s^{-1}$] at 21.7% chord and 98% relative height for URANS, ZDES with rotating distortion, ZDES with averaged cartography and LDA measurements.*

The unsteadiness within the flow is then compared for the same positions with a view to better understand the interactions occurring within the blade passage and downstream. To this end, the azimuthal distributions show the standard deviations of the axial and circumferential velocities. The RANS computation is not displayed within these comparisons, since it is a steady approach.

First of all, the unsteadiness is evaluated near the leading edge of the R1. The axial velocity standard deviation is plotted in figure 6.17(a) for the different azimuthal positions at 21.7% X/C and 98% of relative height. As expected, the case with the averaged cartography has the lower unsteadiness. Nonetheless, the values for the axial unsteadiness are close to $2m.s^{-1}$ from azimuth 4 to azimuth 7. Therefore, there is almost no unsteadiness around azimuth 6 contrary to what is experienced by the LDA, the URANS, and the ZDES with the rotating distortion. As a consequence, the major part of the flow field is stable

without the IGV wakes. However, the unsteadiness rises to reach $10m.s^{-1}$ at azimuth 8. The area that expends from azimuths 7 to 8 is experienced by the three computations, albeit the unsteadiness is clearly lower with the averaged map. In this zone, the boundary layer on the blade side and the tip-leakage vortex interact, hence this high unsteadiness. Notwithstanding this interaction, the tip-leakage vortex is stable.

The circumferential velocity is shown in figure 6.17(b) for the same position. One can see that there is no unsteadiness in the circumferential direction throughout the whole passage, except close to the blade as it is the case for the axial velocity standard deviation. The unsteadiness levels without the IGV wakes are up to nine times less than with the rotating distortion. This proves that near the leading edge, the instability within the flow close to the shroud originates mainly from the arrival of the IGV tip vortex.

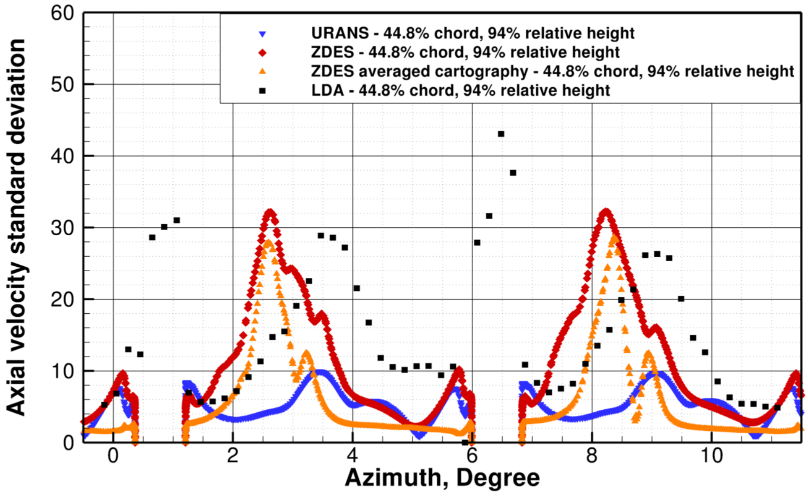

(a) Axial.

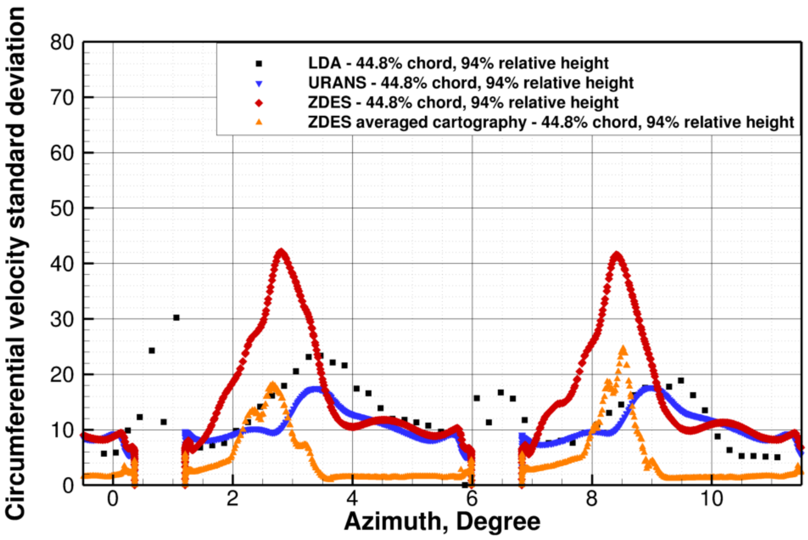

(b) Circumferential.

Figure 6.18 — *Axial and circumferential velocity standard deviations [in $m.s^{-1}$] at 44.8% chord and 94% relative height for URANS, ZDES with rotating distortion, ZDES with averaged cartography and LDA measurements.*

Downstream, at 44.8% X/C and 94% of relative height, the axial velocity standard deviation highlights a more complex pattern, presented in figure 6.18(a). First, without the IGV wakes, the high un-

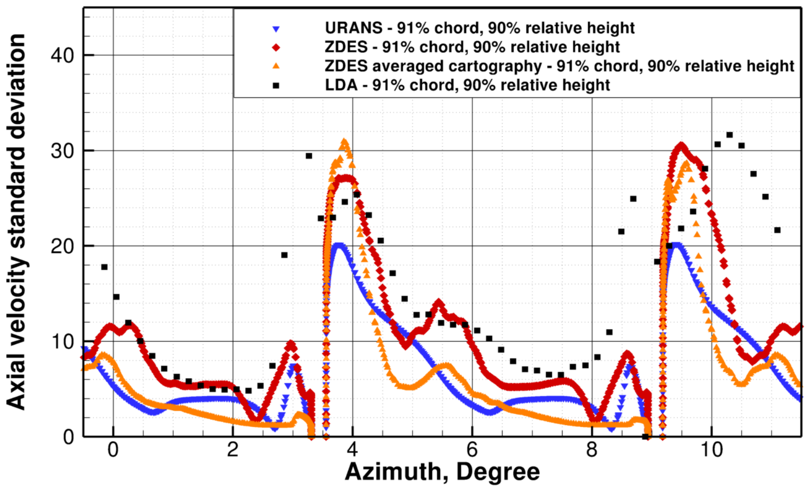

(a) Axial.

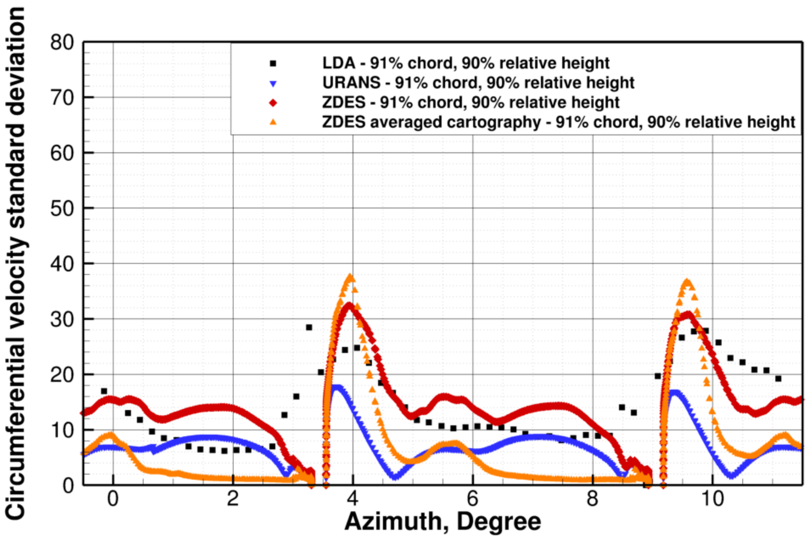

(b) Circumferential.

Figure 6.19 — *Axial and circumferential velocity standard deviations [in $m.s^{-1}$] at 91% chord and 90% relative height for URANS, ZDES with rotating distortion, ZDES with averaged cartography and LDA measurements.*

steadiness area near the blade at azimuth 5.5 is scarcely perceptible contrary to what is seen experimentally and with the two other computations. In the computational cases with the rotating distortion, there is a peak at azimuth 5.5 combined with a rapid and localized drop at azimuth 5. This is not experienced by the LDA that sees a constant and higher value at $10m.s^{-1}$ from azimuths 4.5 to 5.5, that is to say close to the blade. The fact that the experiment captures higher values without this local drop comes from the operating point, as already underlined in chapter 5 in figure 5.22(a).

Second, without the IGV wakes, two peaks are distinguishable. The first one is located at azimuth 2.5, with $28m.s^{-1}$ for its maximum value. The second has a lower unsteadiness value of $12m.s^{-1}$, which shows that it is more stable axially, and is located at azimuth 3.2. They correspond to the main tip-leakage flow and to the induced vortex, or more accurately to the separation of the boundary layer at the casing, visible in figure 6.7(b). Thanks to the averaged cartography, the effects of the vortices stand out from the unsteadiness of the flow. The azimuthal range over which the zone of high unsteadi-

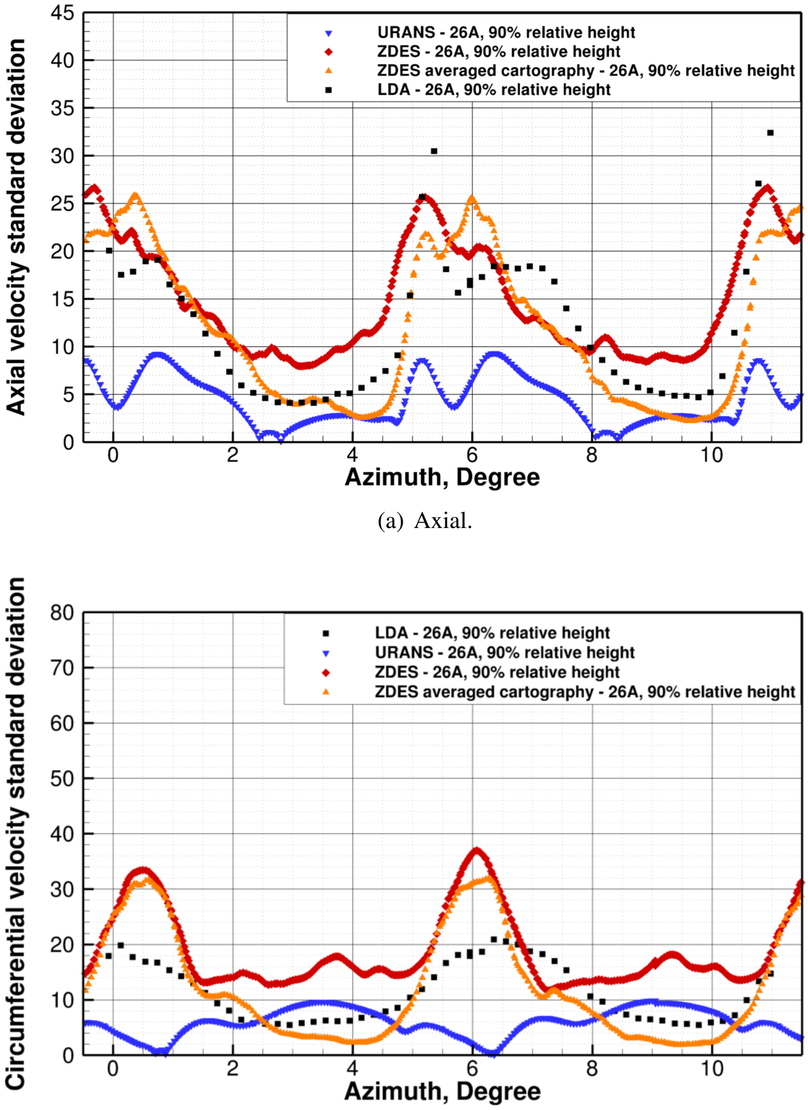

(a) Axial.

(b) Circumferential.

Figure 6.20 — *Axial and circumferential velocity standard deviations [in $m.s^{-1}$] at section 26A and 90% relative height for URANS, ZDES with rotating distortion, ZDES with averaged cartography and LDA measurements.*

ness spreads is narrower with the averaged map. Besides, this is clearly too narrow compared to the experimental peak. This is expected since there are periodic wakes experimentally. The peak visible on the experimental values is located at a different position : azimuth 3.5. This is due to the difference of operating point underscored in chapter 5. Its value nonetheless corresponds to the one captured by the ZDES computations, either with or without the IGV wakes. The second peak is yet not experienced by the LDA, certainly because of the higher unsteadiness levels throughout the channels.

The circumferential velocity standard deviation, presented in figure 6.18(b) shows the same narrow peak as for the axial velocity standard deviation. Nonetheless, the maximum value is almost halved without the wakes. This proves that the circumferential unsteadiness observed at this axial position comes mainly from the arrival of the wakes from the IGV and their interaction with the flow near the casing. Moreover, the azimuthal position of this peak is more localized, because there is no periodic azimuthal shift due to the arrival of the IGV tip vortex and its stretching of the boundary layer developing

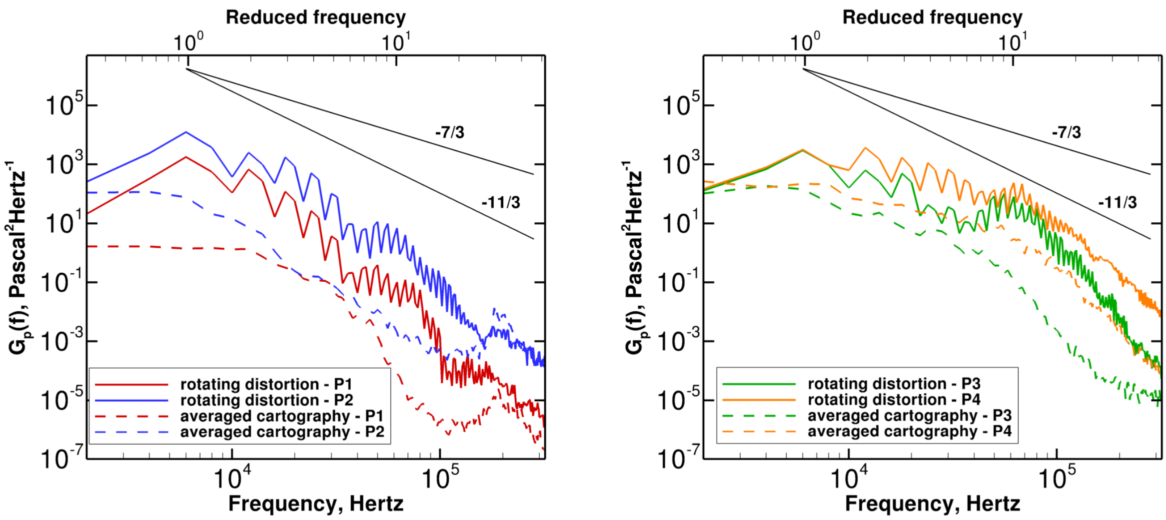

(a) Probes 1 and 2.

(b) [Probes 3 and 4.

Figure 6.21 — *Power spectral density of static pressure for probes along the main tip-leakage vortex. ZDES with the averaged cartography and ZDES with the rotating distortion.*

6.4.1 Influence of the IGV wakes on the energy levels along the tip-leakage vortex

First of all, a spectral analysis is carried out for probes located along the main rotor tip-leakage vortex so as to better understand the physics involved. Only the two ZDES computations at the design point are compared here: the one with the rotating distortion, and the one with the averaged map.

The four probes are located at 98% relative height for different axial positions along the core of the main rotor tip-leakage vortex as presented in chapter 4 in figure 4.30 with the instantaneous Schlieren at 98% relative height and t=3T/4. The probes 1 and 2 are respectively located at 11% and 22.5% X/C. The probes 3 and 4 are located at 33.8% and 45.7% X/C. This means that probes 1 and 2 are upstream the vortex disruption contrary to probes 3 and 4.

The Power Spectral Density (PSD) represents the flow energy distribution. The normalized PSD shows the contribution to the total energy of the different frequencies. Each of them brings a different information on the way the energy is distributed over the frequencies. The PSD functions, $G_p(f)$, are plotted for the probes 1 and 2 in figure 6.21(a) and for 3 and 4, in figure 6.21(b). The normalized PSD functions are plotted for the probes 1 and 2 in figure 6.22(a) and for 3 and 4, in figure 6.22(b).

The main visible difference between the two computations stems from the energy of the IGV tip vortex, which is convected periodically at the IGV Blade Pass Frequency (BPF). Therefore, at the BPF, which is 6156 Hz, and at its harmonics, the whole energy is higher in the case with the rotating distortion as seen in the PSD in figure 6.21. This changes the energy distribution along the frequency bands. Nevertheless, the low frequency phenomena are the limiting factors in the analysis of these computations since the frequency resolution (FR) is 2000 Hz.

The energy level increases for every frequency from probe 1 to probe 2, as highlighted in figure 6.21(a). It arises from the rotor tip-leakage vortex initial development, from a weak jet flow at probe 1 to a full vortex at probe 2. This is the case for both computations. Without the wakes, the slope follows clearly a $k^{-11/3}$ slope at probe 2, which characterizes the interaction between the turbulence and the mean-shear in the inertial subrange [59]. This is distinguishable from the lowest captured frequencies to 20 BPF. However, this interaction does not seem to occur at probe 1 without the IGV wakes, since this slope is not found on the PSD, and the curve can be divided into 3 parts. First, the low frequencies have a lower energy, which is constant up to 2 BPF. Then, the energy level is close to the one for probe

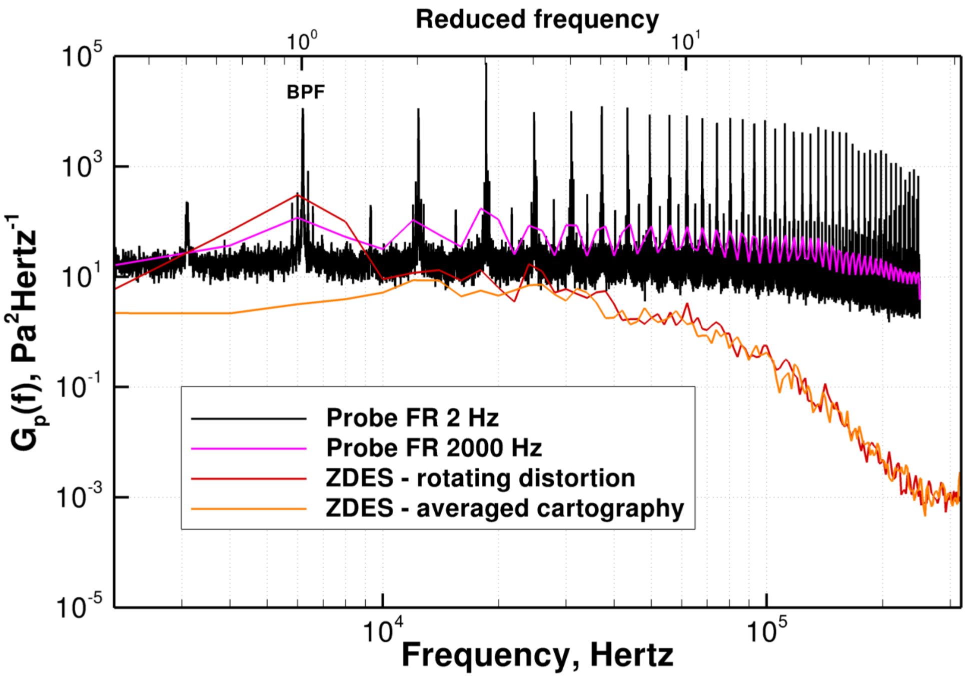

(a) At the casing.

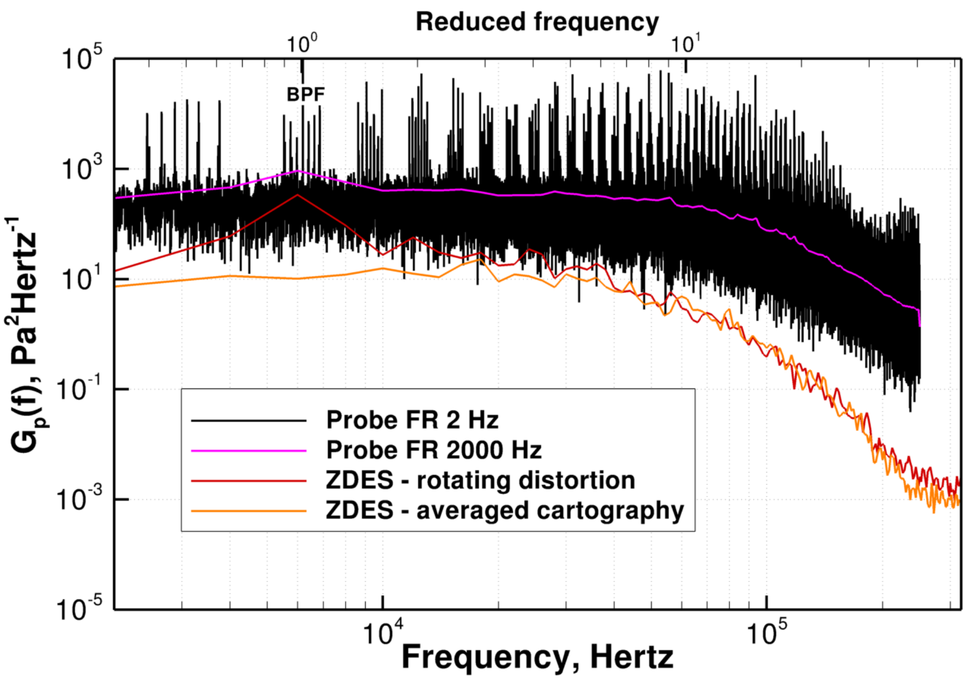

(b) At 94% relative height.

Figure 6.23 — *Power spectral density of pressure at section 26A. ZDES with averaged cartography, ZDES with rotating distortion and data from unsteady probes.*

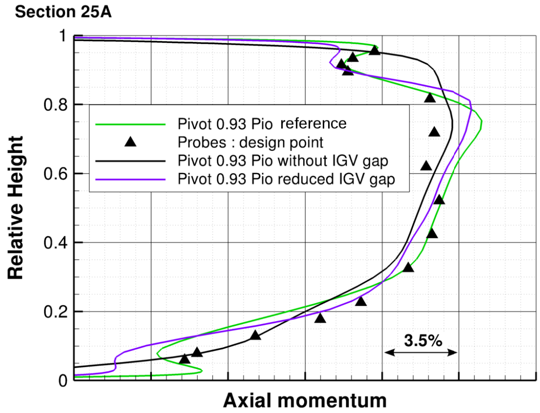

Figure A.1 — *Radial distribution of axial momentum at section 25A for different IGV gaps*

from 2.95% to 1.47% of the hub axial chord. As a result, the gap size is halved and corresponds to a gap configuration smaller than what it is experimentally. The third configuration has neither hub gap nor tip gap for the IGV. These three numerical configurations are compared to the experiment.

A.2 Impact on the radial distributions

First of all, the time and circumferential averaged values are considered through an analysis of the radial distributions at section 25A.

Figure A.1 shows the axial momentum for the three configurations. As expected, the reference configuration is in good agreement with the experimental values from the probes near the hub and near the tip. Indeed, the gradients from the casing down to 80% of relative height are correctly captured, this proves that the IGV tip gap is well taken into account. However, around 70% of relative height, it overestimates the axial momentum value compared to the two other configurations. At this position, the case without any gap tends to be in better agreement. Nevertheless, it does not experience the gradients characterising the IGV tip gap near the casing. This is coherent since this configuration does not model it. Near the hub, this configuration without gap gives relevant results on this averaged radial distribution, since there is no pronounced gradient for the experimental probes. If the configuration with the reduced hub gap is considered, one can clearly observe an underestimation of the axial momentum, both near the hub, and even near the casing. Furthermore, the gradients around 90% of relative height are underestimated too. This proves that a small difference at the hub influences what occurs on the other side of the domain, near the shroud.

The total pressure radial distribution is plotted in figure A.2. Without any gap, the total pressure is clearly overestimated at both hub and tip. By contrast, the configurations with gaps capture a lower total pressure compared to the experimental value. Once more, there is an influence of the modelled hub gap on the flow at the tip, with less pronounced gradients for the IGV tip vortex, around 90% of relative height. The difference is naturally more perceptible near the hub. The gradients are weaker with the reduced hub gap, hence a better agreement with the slope observed experimentally. Nonetheless, there is no shift of the pressure value near the hub toward the value measured by the experimental probe. This highlights two effects. The first one is that the gradient with a "S" form captured by the reference configuration near the hub can be improved by changing the hub gap size. This modifies the vortex width and therefore influences the flow at section 25A. The second noteworthy effect is that the reduced hub gap is not small enough to be in perfect agreement with the experiment. The reduced gap size is nevertheless smaller than the experimental one. Thereby, the total pressure should be higher than what is is experimentally near the hub, and be closer to the configuration with no gap. This shows that the

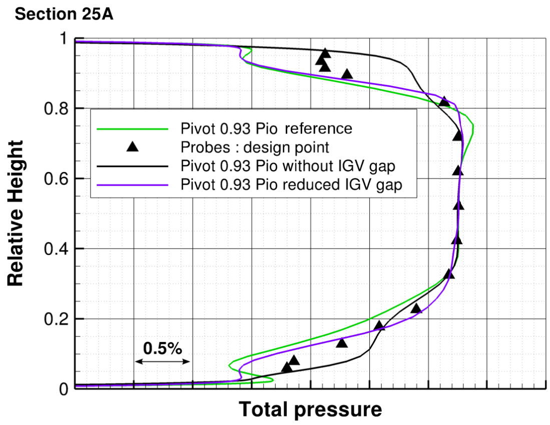

Figure A.2 — *Radial distribution of total pressure at section 25A for different IGV gaps*

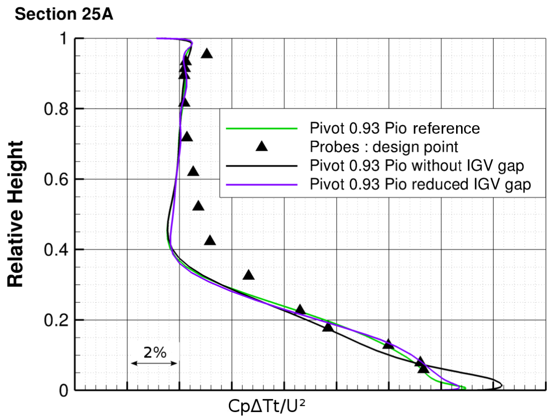

Figure A.3 — *Radial distribution of averaged normalized total temperature at section 25A for different IGV gaps*

Spalart-Allmaras model amplifies the pressure losses. The fact that all the configurations give the same results at mid span strengthens the idea that this drawback of the model is encountered in regions with secondary flows.

Figure A.3 plots the radial distribution of the normalized total temperature, $Cp\Delta Tt/U^2$. There is almost no influence of the gap near the casing, and even at mid span. The simulation of the tip gap influences barely the total temperature. Nevertheless, the figure underlines that even with the smallest hub gap, the simulation is improved compared to the configuration with no gap. However, the gradient around 10% of relative height is captured more accurately in the reference case. This underscores that the corner effect and the hub vortex from the IGV are sensitive to the hub gap size.

The azimuthal angle is plotted in figure A.4. It emphasizes the necessity to take the IGV gaps into account, even with approximations like it is performed in the presented configurations. Indeed, without gap, the angles are overestimated and the gradients not captured at all near the casing and near the hub. This figure reveals that the height corresponding to the gradient of the IGV hub vortex is in better agreement with the experimental measurements in the case of the reduced hub gap. The position of the maximum angle is closer to the hub in this configuration, therefore the curve is similar to what is captured by the probes. By contrast, in the reference case, the angle is underestimated and the position corresponding to the maximum angle value is radial located at a position 5% upper. This highlights that the development stage of the hub vortex, hence its width, is better simulated in the configuration with the reduced gap. However, in this case, the gap size is smaller than what it is in the experiment. This confirms that the numerical schemes and turbulence model used in this study amplify this phenomenon.

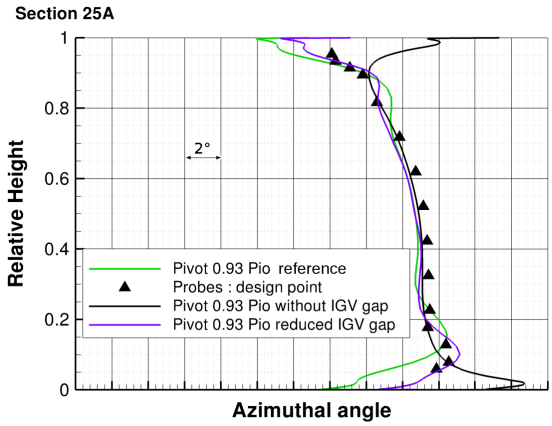

Figure A.4 — *Radial distribution of azimuthal angle at section 25A for different IGV gaps*

A.3 Impact on the captured phenomena in the cartography

This section shows the effects of the IGV gaps on the 2D cartographies of the different configurations. They are presented in figure A.5. The hub gap size influences mainly the azimuthal shift between the IGV hub vortex and the main wake, as visible by comparing the region near 10% of relative height and azimuth 5.5 in figures A.5(a) and A.5(b). This shift originates from the widening of the vortex with a wider gap. Thereby, its azimuthal extension is slower, and there is a delay between the arrival of the main IGV wake and the IGV hub vortex. This phenomenon occurs for the IGV tip vortex too. It results in the IGV tip vortex arriving with an important delay at the leading edge of the R1.

Without gap, some phenomena are experienced too. The cartography captures the IGV main wake and the thickening of the boundary layer on the walls at the hub and casing. Moreover, a corner effect is seen near the hub in figure A.5(c), with a large area of lower total pressure. A similar effect is observed near the tip too. Nevertheless, the effects of the hub and tip vortices are not experienced. It was observed in this thesis that the vortex coming from the IGV tip gap has an important interaction with the tip-leakage vortex of the R1. As a consequence, the simulation of the IGV gaps was necessary in this study in order to accurately capture this interaction.

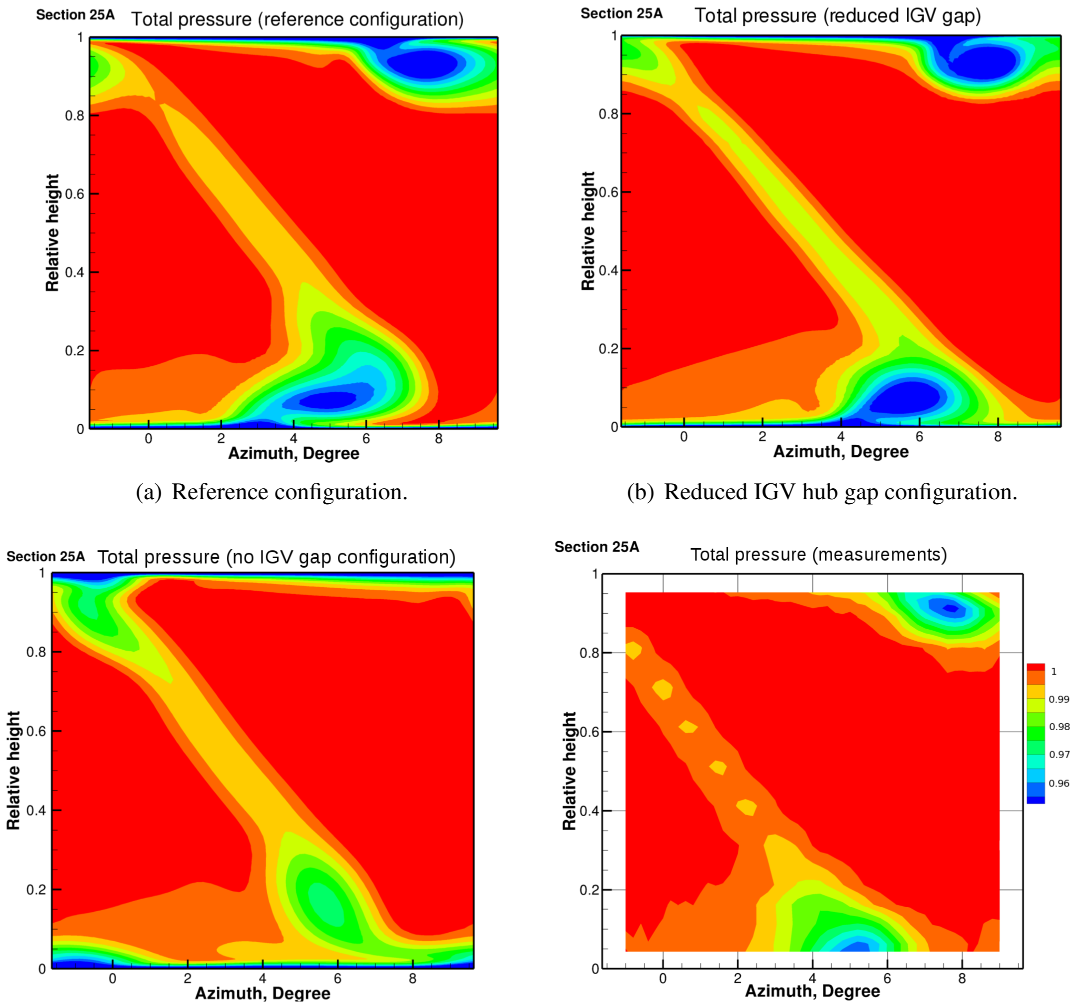

(a) Reference configuration.

(b) Reduced IGV hub gap configuration.

(c) No IGV gap configuration.

(d) Experimental probes.

Figure A.5 — *Total pressure cartography from the RANS RDE-R1 computations and experimental probes at section 25A. Effects of IGV gaps.*

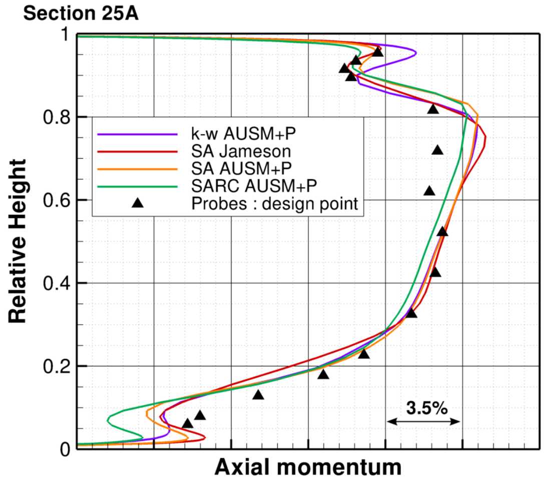

Figure B.1 — *Radial distribution of axial momentum at section 25A for different turbulence models and spatial discretization schemes*

- k-ϵ from Launder and Sharma [103] and the Jameson spatial discretization scheme.

They all converged following the criteria detailed in chapter 3, except both k-ϵ computations. As a consequence they were withdrawn from the following comparison.

B.2 Impact on the radial distributions

The time and circumferential averaged value of axial momentum, total pressure, total temperature, and azimuthal angle are presented below at section 25A.

First of all, figure B.1 shows the radial distribution for the axial momentum. Near the hub, they all underestimate the axial momentum. On the one hand, the AUSM+P scheme tends to increase this discrepancy. On the other hand, it captures more accurately the radial position of the inflection at 80% of relative height. The curvature correction of the Spalart-Allmaras model seems to amplify the effects near the hub. However, it reveals to give relevant results in the area where there is the IGV tip vortex. The k-ω model is the only one to overestimate the axial momentum near the casing. Besides, the captured vortex is further from the casing wall, which shows a major difference in the development stage for the IGV tip vortex with this model. Likewise, near the hub, the gradient with a "S" form captured by all the method is weaker with the k-ω model. As a consequence, it is in better agreement with the measurements.

The total pressure radial distribution is plotted in figure B.2. At mid span, and more accurately from 30% to 80% of relative height, the different computations behave similarly and they all capture the experimental total pressure value. Besides, the deflection at 80% of relative height is correctly experienced by the computations, except the Spalart-Allmaras computation with the Jameson scheme. This computation is the one that underestimates the most the total pressure at the casing, albeit they all underestimate it. This shows the lack of capability of the Jameson scheme to capture the vortex. The k-ω model seems to be the most appropriate to capture both the inflection seen at 90% of relative height and the total pressure level near the casing. As it was observed for the axial momentum, it captures correctly the gradients near the hub.

The normalized total temperature, $Cp\Delta Tt/U^2$, is presented in figure B.3. There is almost no difference between the configurations from 10% of relative height to the casing. The only exception is the area near the hub, where the Spalart-Allmaras computation with the Jameson scheme captures correctly

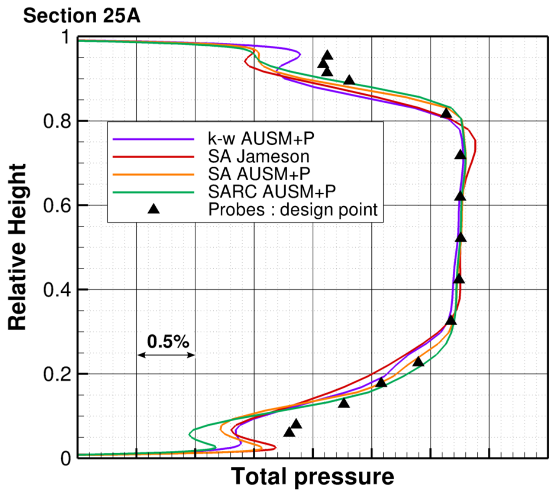

Figure B.2 — *Radial distribution of total pressure at section 25A for different turbulence models and spatial discretization schemes*

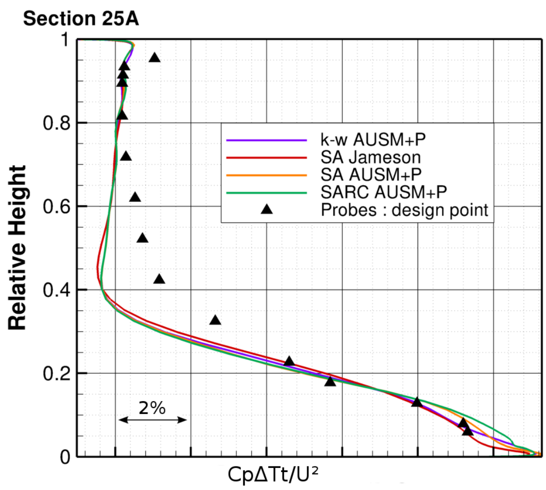

Figure B.3 — *Radial distribution of averaged normalized total temperature at section 25A for different turbulence models and spatial discretization schemes*

the visible inflection. Nevertheless, the other computations experience close results, therefore this is not a key value to consider to appraise the cases.

By contrast, the azimuthal angle, plotted in figure B.4, highlights important discrepancies between the different cases. At the casing, the k-ω model tends to be in better agreement with the experimental values. However, further from the wall, the computations with the Spalart-Allmaras model and the AUSM+P scheme reveal to capture more accurately the inflection induced by the IGV tip vortex, at 90% of relative height. Furthermore, the curvature correction shows better agreement. Moreover, it behaves like the k-ω model above 95% of relative height. Even if all the computations underestimate the angle near the shroud, the Spalart-Allmaras with the Jameson scheme is the configuration with the furthest value from the experiments. Along the span, the results are similar for the methods. Nevertheless, two perceptible effects have to be emphasized. Indeed, two computations stand out from the analysis of this figure. The first one is due to the Jameson scheme, that captures a radial position for the location of the maximum azimuthal angle further from the hub wall compared to the experimental position. This shows that the development stage of the hub vortex is too advanced here. The second is the Spalart-Allmaras with the curvature correction that reveals to be the only one to capture the gradients near the hub for the

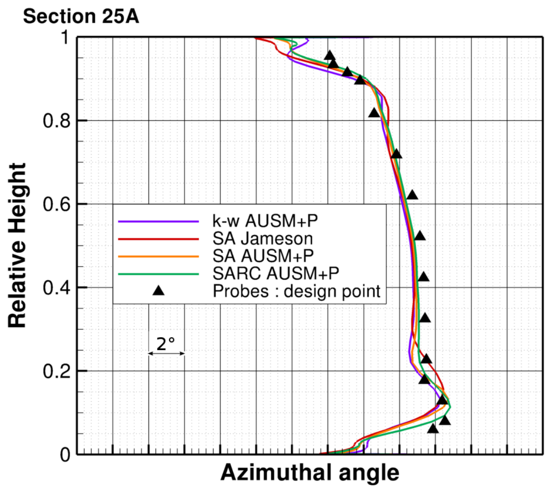

Figure B.4 — *Radial distribution of azimuthal angle at section 25A for different turbulence models and spatial discretization schemes*

azimuthal angle. This is the reason why it was chosen to extract the flow cartography at section 25A, as explained in chapter 3.

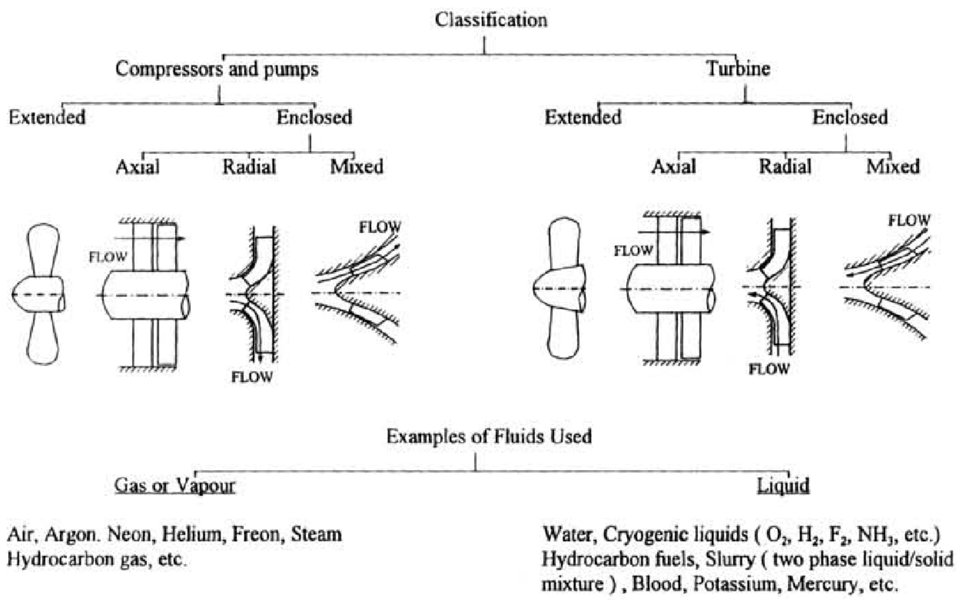

Figure 1.1 — *Classification of turbomachinery (from Lakshminarayana [96]).*

compressor, such as the pumps. The possibilities of turbomachines application are numerous. Therefore they are used in many different configurations linked to energy conversion. Some are *open*, or extended, and thus influence a wide, not quantifiable, area around them. Others are *shrouded*, that is to say, enclosed by a casing.

Depending on the expected service of the machine, that is to say the required pressure ratio and mass flow rate through the cascade, different configurations, presented in figure 1.1, best suit the operating condition. Thereby, depending on how the flow crosses the rotor, the denomination of the machine changes. It is regarded as axial if the through-flow is parallel to the axis of rotation, which is used in high mass flow rate configurations. The machine is considered as radial if the through-flow is perpendicular to the axis of rotation, which is used for compact high pressure ratio configurations. An infinite number of possibilities exists in between, and the resulting machines are then called mixed-flow turbomachines. If a higher pressure ratio is required between the inlet of the machine and its outlet, many rotor stages are mounted in series.

The rotating motion of rotor blades increases the swirl of the fluid. In order to correct the fluid deflection for the next rotor stage, stator blades are implemented in between the stages of rotor blades. This addition of stages increases the complexity of the flow through the turbomachine. For instance, there are interactions between the rotors and the stators that modify the structure of the flow. Besides, the additional stages increase the weight of the compressor. It is however possible to avoid this stator stage with the use of counter rotating rotors. However, this is for the moment only done in few configurations, for instance in Counter Rotating Open Rotors (CROR) or contrafans, due to the higher design constraints it implies.

These two types of blades, rotating for the rotors and steady for the stators lead to two different ways to consider the flow within a turbomachine: with absolute or relative values. As a consequence, there are two frames of reference linked to the stators or rotors. For the rotors, some values in the relative frame of reference differ from the ones in the absolute due to the rotation of the blade. In order to understand this concept, the velocity triangles are used as presented in figure 1.2. The angles defined in the absolute, α, and relative, β, frames of reference are detailed in equation I-1. U is the rotating velocity of the rotor. The velocity V_θ and W_θ are respectively the circumferential velocities in the absolute and relative, or more accurately rotating, frame of reference. The velocities V and W are their meridian counterparts, that is to say, the addition of the axial and radial velocities. The angle between the axial, V_x, and meridian

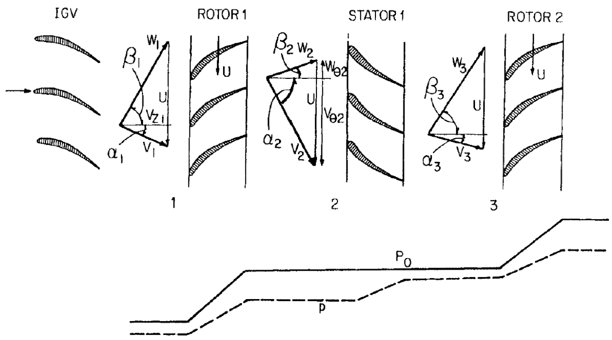

Figure 1.2 — *Velocity triangles in an axial compressor (from Lakshminarayana [96]). The distributions of enthalpy and temperature are similar to the pressure distribution p. The distributions of stagnation enthalpy and temperature are similar to the stagnation pressure distribution P_0.*

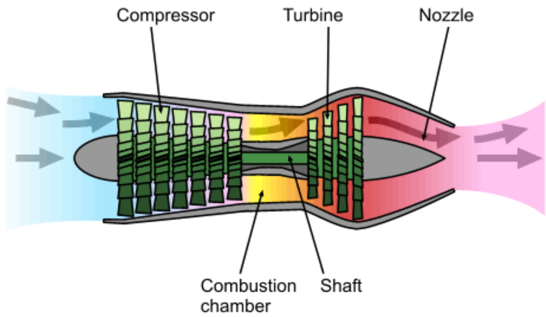

Figure 1.3 — *Axial turbojet engine [51]*

velocity, V_m, is called ϕ, the meridian angle, defined in equation I-2.

$$\alpha = \text{atan}\left(\frac{V_\theta}{V_m}\right) \qquad \beta = \text{atan}\left(\frac{W_\theta}{V_m}\right) \tag{I-1}$$

$$\phi = \text{atan}\left(\frac{V_x}{V_m}\right) \tag{I-2}$$

In aeronautics, turbomachines are used for propulsion systems, such as propellers (open) or turbojet engines (shrouded). In turbojet engines, there are both compressors and turbines as presented in figure 1.3, with many stages. The purpose of the compressor is to transfer the energy from a rotating shaft to the air and thus to rise its pressure. Then, the flow reaches the combustion chamber and is mixed with fuel. It is then burned and therefore its energy increases. The hot fuel-air mix expands and exits the combustion chamber. At the outlet, the turbine extracts a part of the energy of this hot fluid, which decreases its pressure and temperature. This energy is then provided to the compressor through the shaft. Then, the fluid reaches the nozzle, where it is accelerated and given the appropriate direction. Finally, the fluid exits the whole system with a higher pressure and velocity, which produces the thrust necessary for the plane to overcome the drag and therefore to fly.

1.1.2 Operating points

In order to have an efficient energy transfer to the fluid in compressors, the flow must be guided smoothly through the rotor and stator stages of the machine. Moreover, the compressors are very sensitive to the flow angle at the leading edge of the blade. This is the reason why the stators guide the flow

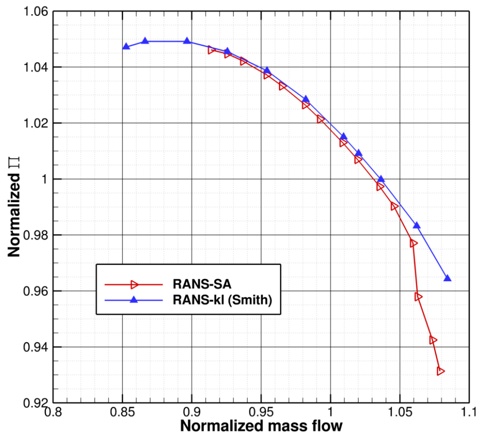

Figure 1.5 — *Surge margin difference between k-l Smith and Spalart-Allmaras turbulence models on the CREATE compressor (Courteously from J. Marty).*

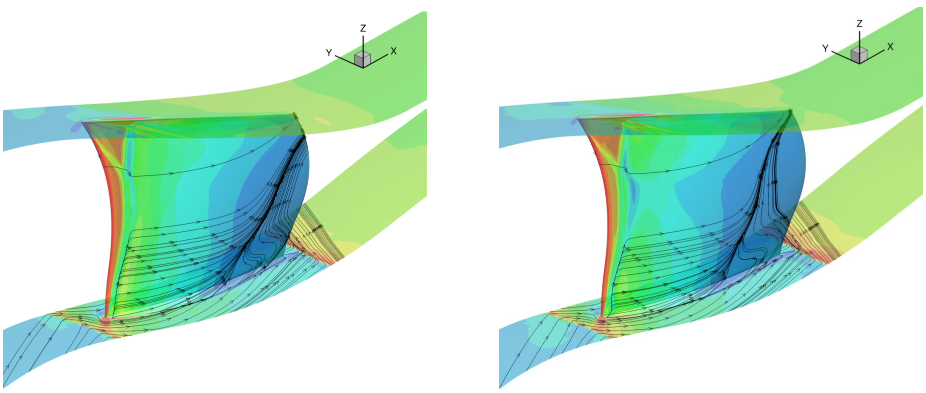

(a) k-l Smith.

(b) Spalart-Allmaras.

Figure 1.6 — *Friction lines on the first rotor of the CREATE compressor near surge (Courteously from J. Marty).*

the CREATE compressor with two turbulence models: the Spalart-Allmaras (RANS-SA) [162] and the k-l model from Smith [156]. This study underlined that the Spalart-Allmaras turbulence model was more unstable than the k-l model from Smith near the surge line. If the Spalart-Allmaras model is used for turbomachinery design, the computed surge margin is then different which leads to a narrower operability range seen by the computation due to the numerical instability. The reason, underscored by Marty, is a more important flow separation at the hub corner with the Spalart-Allmaras turbulence model than with the k-l Smith model, which is not physical and induced by the numerics. This separation difference is visible for computations near surge, in figure 1.6 where the separation line reaches the trailing edge at the blade tip in the Spalart-Allmaras case, contrary to the one with the k-l Smith model. This discrepancy between the methods highlights the difficulty to simulate accurately the secondary flows in the compressor. The tip-leakage flow is one of them.

1.1.3 General principles of the tip-leakage flow

1.1.3.1 A three dimensional flow

In shrouded axial compressors, there is a gap between a rotating blade tip and the annulus wall. The pressure field around a blade implies a pressure gradient between the two sides of the blade. This pressure

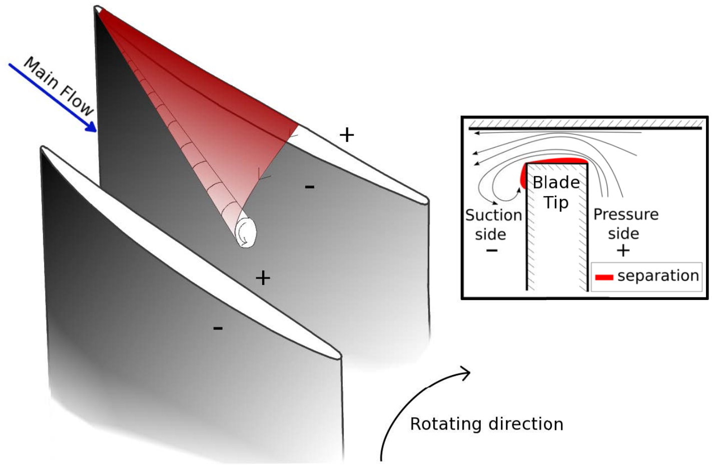

Figure 1.7 — *Inception of the tip-leakage flow and rolling up of the main tip-leakage vortex (Inspired by Lakshminarayana et al. [99]).*

difference leads to a leakage flow from the pressure side to the suction side of the blade, as shown in figure 1.7. The flow then leaks through the clearance following the chordwise pressure distribution. This phenomenon is mainly inviscid as noted by Lakshminarayana and Horlock [97]. Then, it exits the clearance and mixes with the main flow.

The interaction of this secondary flow with the main stream, the annulus boundary layer developing on the shroud and the blade wakes leads to penalizing losses as already mentioned by Herzig et al. [75] in 1954. The shear layer, which stems from the direction difference between the leakage flow and the main stream, is the main loss mechanism in the casing region. By contrast, the non-uniform mixing zone downstream of the blade contributes a little to the whole pressure loss as underlined by Storer and Cumpsty [165]. Therefore designing efficient compressors requires an accurate prediction of the tip-leakage flow and its development.

1.1.3.2 Flow topology near the casing

There are many different configurations of tip-leakage flows depending on the type of turbomachinery. Moreover, the topology in the vicinity of the shroud can be very different.

One of the major encountered phenomenon is the main tip-leakage vortex. When the leakage flow exits the tip gap and mixes with the main flow, it undergoes a loss of circumferential momentum. This results in the rolling up of this jet flow into the main tip-leakage vortex. Nevertheless, in some studies, such rolling up is not experienced, partially or totally. For instance, Furukawa et al. [54] investigated with a RANS simulation a low speed isolated axial compressor rotor with moderate loading and a tip gap height of 1.7% of the chord length. At a low flow rate, they captured a breakdown of the vortex. Nevertheless, downstream of this breakdown, the low streamwise vorticity prevents the flow from rolling up into a vortex again. A case with no rolling up at all was studied by Lakshminarayana et al. [100] on an experimental single stage axial compressor made up of an Inlet Guide Vane (IGV), a rotor and a stator. The tip gap height of the rotor is 2.27% of the chord. The reasons proposed by the authors to explain why the flow did not roll up are that the inlet swirl, high turbulence and high blade loading cause an intense mixing of the leakage jet and therefore prevent the flow from rolling up. In their configuration, the leakage flow high velocity makes it mix rapidly with the main flow. Lakshminarayana et al. [100] underscore that the difference of magnitude and direction of the leakage jet flow and main stream are among the main effects preventing the rolling up. One have to mention here the major importance of the

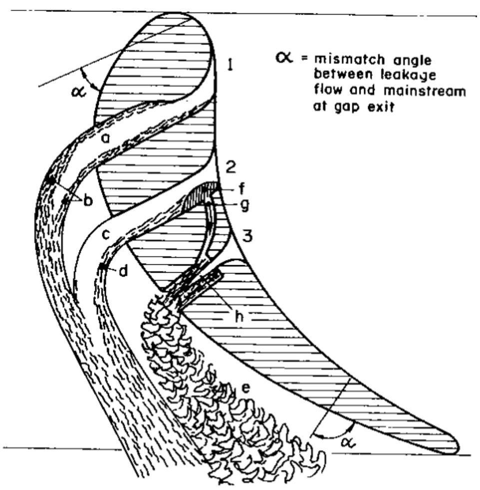

Figure 1.9 — *Conceptual model showing various types of flow active in the tip clearance region (from Bindon [11]).*

conceptual model, Bindon [11] underscores that there is not a single flow pattern leaking through the gap. Instead of a linearly spread leakage, he hypothesized that there are different kinds of channels with and without separation bubbles within the gap. The axial position of these different channels depending on the pressure distribution along the chord, and thus the loading. Kang and Hirsch [87] saw similar channels in the tip gap on a linear cascade with a stationary endwall. With paint-trace visualizations on the endwall, Kang and Hirsch [87] highlighted the flow pattern drawn in the tip clearance, shown in figure 1.10. The skin friction line splits into two branches at a saddle point in front of the leading edge. This results in a horseshoe vortex. The tip-leakage vortex starts to roll-up just downstream the leading edge in the suction side. They pointed out that streamlines in the gap are neither normal to the suction side nor to the camber line, contrary to what was assumed by Rains [135].

1.1.4 Influence of the gap size on the tip-leakage flow

The most important parameter to take into account for the tip-leakage flow is the gap size. As expected, it is the main factor that influences the flow topology at the rotor tip. In order to compare the different configurations, it is then a prerequisite to define a dimensionless value to characterize this parameter. It requires then another length. Two dimensionless terms are built depending on the use of the axial chord or the maximum thickness of the blade tip. They are respectively defined in equations [I-3] and [I-4].

$$\tau = \frac{GapSize}{AxialChord} \tag{I-3}$$

$$\lambda = \frac{GapSize}{MaximumBladeThickness} \tag{I-4}$$

Rains [135] studied experimentally the gap size effects on a rotor at 1750rpm and showed that the leakage flow can be regarded, in a first assumption, as an inviscid phenomenon driven only by the pressure difference for large λ values, and the vortex structure is predominant. In Rains' studied installation, for small ratio between gap size and blade thickness the gap flow was modelled as a channelled flow. For $\lambda = 0.026$ and lower there were no vortex rolling-up. For $\lambda < 0.05$, viscous forces were dominant in the clearance and at $\lambda = 0.1$, the counter pressure effects of the viscosity in the gap were counter-balanced by the lift of the blade. The viscous effects could be neglected for $\lambda >> 0.1$. Finally, beyond

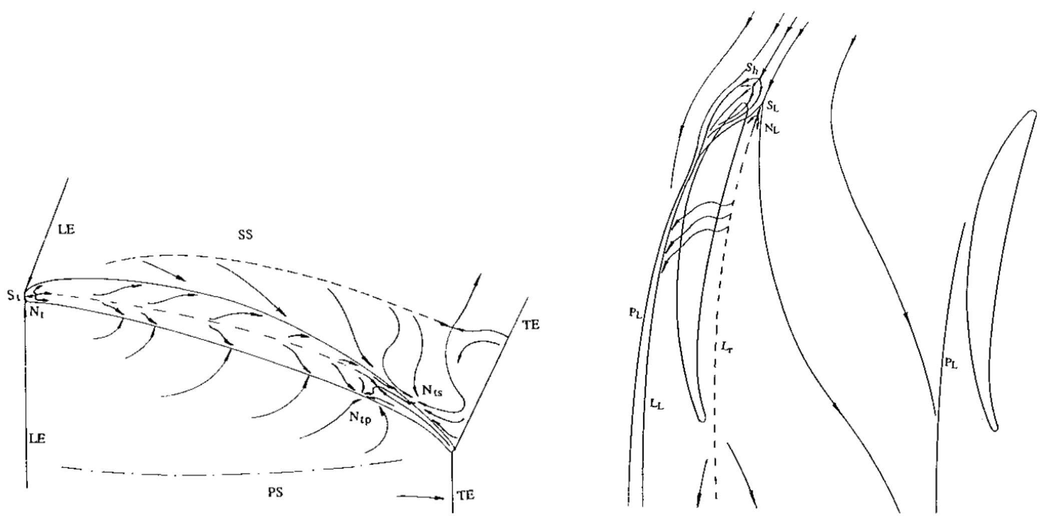

(a) Blade tip. (b) Casing.

Figure 1.10 — *Schematic of flow pattern on the blade tip and on the casing (from Kang and Hirsch [87]).*

$\lambda = 0.167$, a potential flow pressure distribution was established. Rains [135] developed then a model to take into account the tip-leakage flow changes depending on the tip clearance size and based on the number $\lambda^2 \cdot Re \cdot \epsilon$. Re is the Reynolds number based on the free stream velocity and $\epsilon = \frac{\tau}{\lambda}$ is the maximum thickness to chord ratio at the blade tip. He highlighted that viscous forces are predominant for $\lambda^2 \cdot Re \cdot \epsilon < 11$ whilst the inertia forces are predominant for $\lambda^2 \cdot Re \cdot \epsilon > 125$.

More recently, Brion [16] analysed experimentally two configurations: a split wing (NACA0012) configuration generating a vortex pair and the same with a splitter plane. This latter configuration is similar to an isolated fixed linear cascade. The first aim was to study the vortex instability and the influence of the Crow instability [28, 29] which is linked to the interaction between two vortices. Brion [16] observed that for small gaps with $\tau < 2\%$, the flow is nearly perpendicular to the chord which means that it is channelled by the gap and the vortex forms far from the wing and near the hub, which is similar to what Rains saw for small gaps. For $\tau > 2\%$, the vortex remains close to the wing. Thereby, it was shown in the literature that the gap size influences the tip-leakage vortex behaviour. Furthermore, this parameter affects the whole flow topology. For instance, Kang and Hirsch [87, 88] studied the flow field for a linear cascade with 1.0%, 2% and 3.3% gap sizes. The aforementioned horseshoe vortex they detected was only observed for small clearance.

The different flow topologies induced by the different gap sizes imply different losses too. Smith [157] presented experimental data gathered from different studies to understand the effects of the tip gap size. The peak pressure rise for the blade was found to be inversely proportional to the tip gap size τ as presented in figure 1.11. The impact appeared to be 4% of pressure loss for each 1% increase in the dimensionless gap size τ. Bindon [11] analysed the loss in a turbine cascade and highlighted that the loss varies linearly with gap size as shown in figure 1.12. However, there are fundamental differences with and without clearance, and even the smallest gap size changes the loss. He found that the total tip clearance loss is made up of the internal gap loss (39%), the suction corner mixing loss (48%) and endwall/secondary loss (13%) as presented in figure 1.13. Even if these results from Bindon are for turbines, some similarities are found with compressors concerning the tip-leakage flow topology [87], as previously explained.

The main solution found to reduce this negative impact of the leakage flow is to reduce the gap size. This is the reason why abradable material is used on the housing of the compressors used in the industry.

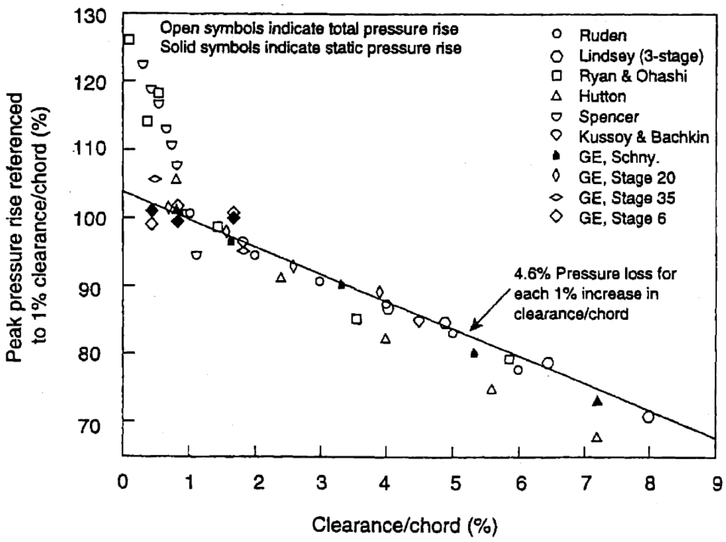

Figure 1.11 — *Effect of tip clearance on peak pressure rise (original data from Smith [157], extracted from Bae [2]).*

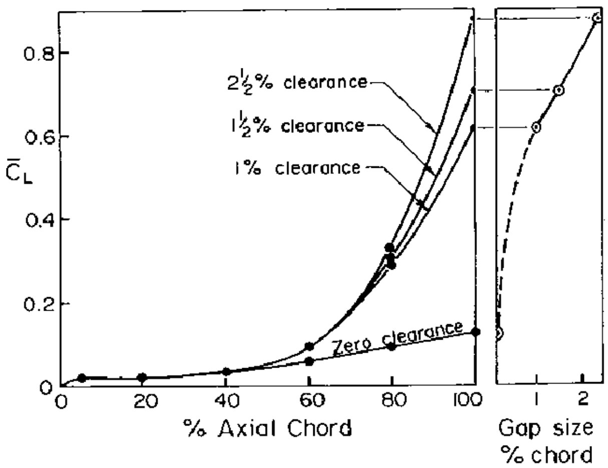

Figure 1.12 — *The growth of total integrated loss coefficient from leading to trailing edge for various values of tip clearance gap size (from Bindon [11]).*

When the rotor rotates, its radial length is increased due to the centrifugal forces. As a consequence, the tip of the blade touches the casing. The resulting friction wears then a part of the abradable material away so that the tip gap size is as small as possible. Another possibility is to reduce the gap size artificially with flow control devices. For instance Bae [2] analysed the effects of synthetic jet actuators located in the tip gap on the vortex flow for a linear cascade. The device reduced the gap size by deflecting the streamline, enhanced the mixing, reduced the influence of the vortex and increased the exit static pressure. Nevertheless, the different flow structure due to the linear cascade prevented to judge the possibilities on a real rotor. Figure 1.14 presents how it could be implemented on a rotor.

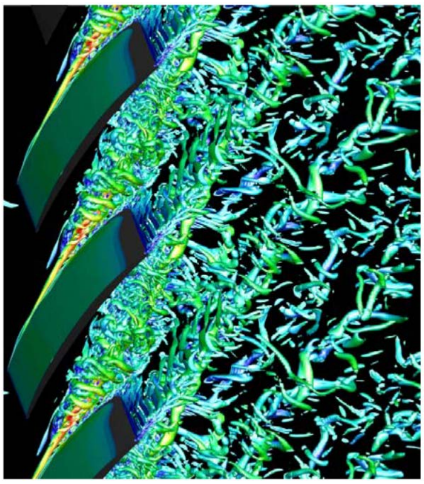

(a) Static end wall.

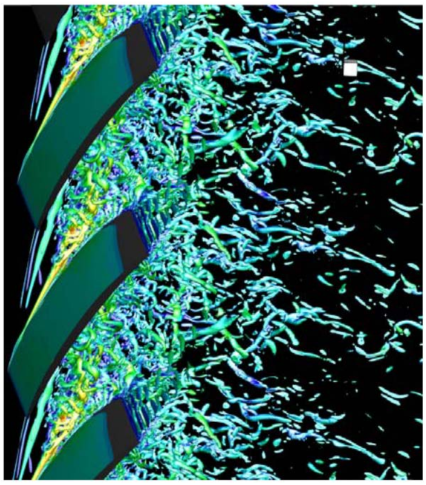

(b) Moving end wall.

Figure 1.17 — *Q criterium flooded by the longitudinal velocity (from Riou [143]).*

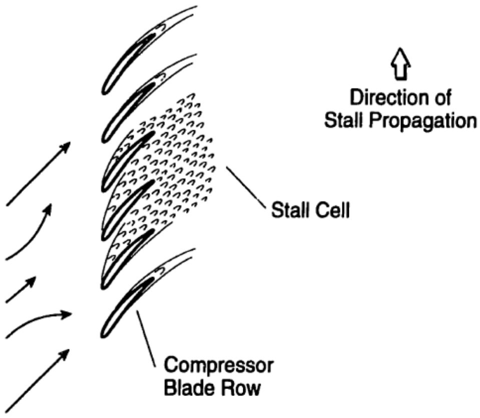

Figure 1.18 — *Physical mechanism of rotating stall (from Hoying [79]).*

centre and its decay downstream are scarcely affected by the moving wall for gap sizes of 0.8%, 1.6% and 3.3% chord. This study confirmed why many fundamental analysis are carried out on linear cascades. The same configuration was numerically investigated with Delayed DES, a first version of Zonal DES and a classic RANS approach by Riou [143]. The purposes were to evaluate the numerical methods and analyse the effects of relative motion Figure 1.17 presents the flow field with ZDES with and without motion. The vortex disrupts earlier with the endwall motion. Moreover, Riou [143] observed a secondary vortex in the moving endwall case. Besides, an elongation of the vortex core is captured too, and it bends towards the neighbouring blade. With no endwall motion, the vortex dilates but remains circular. The steps concerning the inception development and disorganisation of the vortex remains the same in the two cases. Inoue and Furukawa [82] observed similar results, based on various experiments. However, they emphasized that the loss production was considerably smaller with the relative motion than without. Thereby, this highlighted that the loss production is not in proportion to the vortex intensity.

1.1.6 Throttle effect and tip clearance flow

The tip-leakage flow is known to be one of the main instability sources in compressors near surge. This is the reason why its effects are studied in the literature up to the surge.

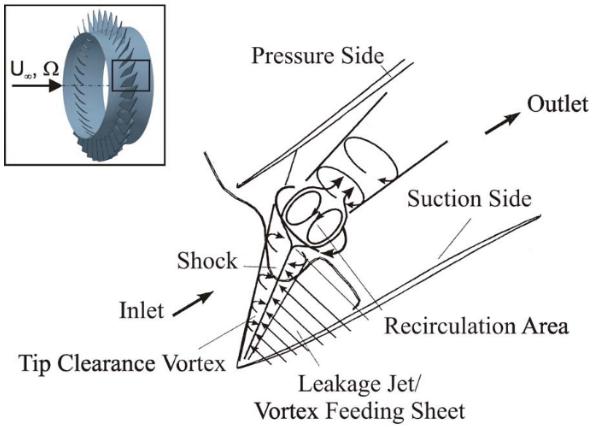

Figure 1.23 — *Shock/tip-leakage vortex interaction (from Hofmann and Ballmann [77]).*

In 1985, Hall [73] summarized the main available analyses and presented the theories [7] behind vortex breakdown in order to explain why there are core bursting in some configurations. Some criteria were developed in the literature to delineate the region where breakdown occurs. For instance, a criterion is based on the fall in the Rossby number [164, 145] defined as the ratio of the axial and circumferential momentum in a vortex. This criterion is applied in some studies such as the recent work of Riou [143] in turbomachinery.

Tip clearance vortex breakdown is considered as a possible cause of stall inception in compressors by many authors such as Hofmann and Ballmann [78, 77]. This seems to be the case mainly in large gap configurations [54]. Indeed, in the small tip clearance cases the aforementioned spike-type stall is predominant. This was recently confirmed by Yamada et al. [178]. They have shown with experimental and DES analyses that the rotating disturbance, in large tip gap cases, appeared intermittently and randomly at near-stall condition. In addition, the compressor did not systematically fall into the stall after the inception of vortex disturbance. Nonetheless, it contributed to the blockage effect near stall.

The interaction of the tip-leakage vortex with a shock in a transonic compressor does not necessarily lead to vortex breakdown as shown by Hah et al. [70]. Nevertheless, the flow field becomes unsteady due to shock oscillations. If the shock is oblique or normal to the vortex, the interaction differs. This interaction seems to depend on the operating point too. Hoeger et al. [76] compared RANS simulations with experimental laser data close to stall, peak efficiency and choke. In their configuration, the vortex core went through the shock without change in cross section at peak efficiency while its cross section increased near stall. However, in all of their studied cases, they highlighted that a steep increase in loss was found in the strong shock-vortex interaction region. Bergner et al. [9] studied experimentally a transonic compressor and highlighted that at peak efficiency, the passage shock was almost normal to the vortex. By contrast, near stall, the shock strength increased because the shock moved upstream which led to an oblique shock/vortex interaction.

The interaction with the shock, the vortex and the boundary layer was studied numerically by Chima [26] and compared to experiments. He highlighted strong interactions between these different flows. Nevertheless, he has shown limitations of the used algebraic turbulence model to compute the flow near the casing, even if the performance predictions were correct. Yamada et al. [177] analysed with RANS and URANS computations the transonic axial compressor known as the Rotor 37 from the NASA. In this configuration, the boundary layer separation on the casing wall and on the blade suction surface emanated from their interaction with the shock wave. Moreover, the same case with no clearance revealed a different position for the separation on the suction surface. This suggested a strong link between these phenomena: boundary layer separation on the suction surface, shock and leakage flow.

Name	Aim	Unsteady	*Re*-dependence	3/2D	Empiricism	Grid	Steps	Ready
2DURANS	Numerical	Yes	Weak	No	Strong	10^5	$10^{3.5}$	1980
3DRANS	Numerical	No	Weak	No	Strong	10^7	10^3	1990
3DURANS	Numerical	Yes	Weak	No	Strong	10^7	$10^{3.5}$	1995
DES	Hybrid	Yes	Weak	Yes	Strong	10^8	10^4	2000
LES	Hybrid	Yes	Weak	Yes	Weak	$10^{11.5}$	$10^{6.7}$	2045
QDNS	Physical	Yes	Strong	Yes	Weak	10^{15}	$10^{7.3}$	2070
DNS	Numerical	Yes	Strong	Yes	None	10^{16}	$10^{7.7}$	2080

Table 1.1 — *Summary of the main strategies to simulate turbulent flows (from Spalart [158])*

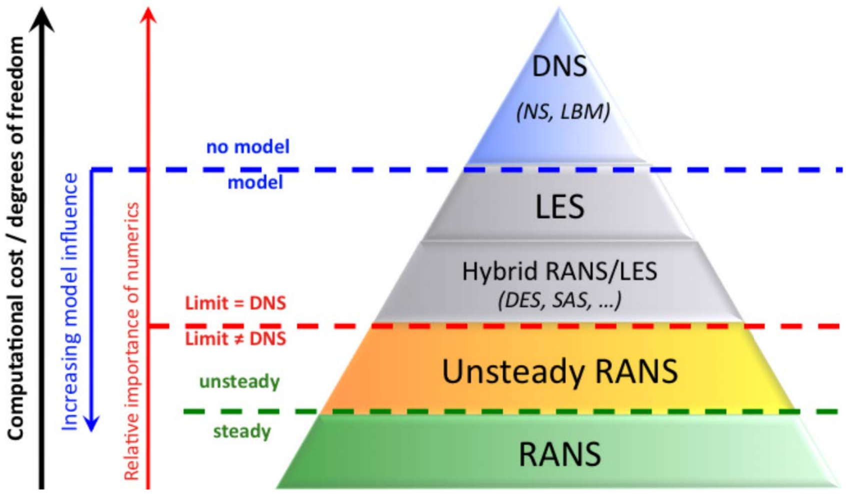

Figure 1.25 — *From RANS to DNS, the possibilities of CFD (from Sagaut et al. [147])*

classic simulations encountered in the industry. Figure 1.25 classifies these approaches depending on their accuracy and dependence on numerics or on models.

The Direct Numerical Simulation (DNS) could solve every time and spatial scales of turbulence and enable the finest description of the tip-leakage flow. However this method is impossible to use for realistic configurations due to the high computational cost it requires. Indeed, the number of nodes depends on the Reynolds number of the case and scales as $Re^{9/4}$ for 3D meshes.

Thereby, DNS is not expected to be used before 2080 [158]. The most recent studies with DNS in turbomachinery are still close to flat plates simulations at low Reynolds. For instance, Wissink [175] and Wissink and Rodi [176] studied the transitional flow in turbine and compressors. Balzer and Fasel [4, 5] studied control devices of a separation bubble in a simple turbine with a Reynolds number of 25000. Such studies inform us accurately on the boundary layer development on curved surfaces. Nevertheless, they are far from being representative of real configurations.

Reynolds-averaged Navier-Stokes (RANS) simulations are widely used in the industry to simulate tip-leakage flows in real configurations at high Reynolds number. With the computational resources available in the 2010, such simulations are possible overnight. This parameter is important for engineers to test new designs. Nevertheless, it is impossible to capture unsteady effects with this method.

The Unsteady RANS (URANS) approach is necessary when investigators try to capture unsteady effects such as rotor-stator interactions [65]. URANS helped discovering and understanding unsteady phenomena encountered in the tip region, such as the vortex rolling-up and its motion. Moreover, it enabled to evaluate the effects of unsteady control devices. However this method revealed not to predict accurately the tip-leakage flow [143] and other complex unsteady flows encountered in turbomachinery [149, 150]. There are nonetheless numerous efforts to improve it by the means of different turbulence models or higher order numerical methods.

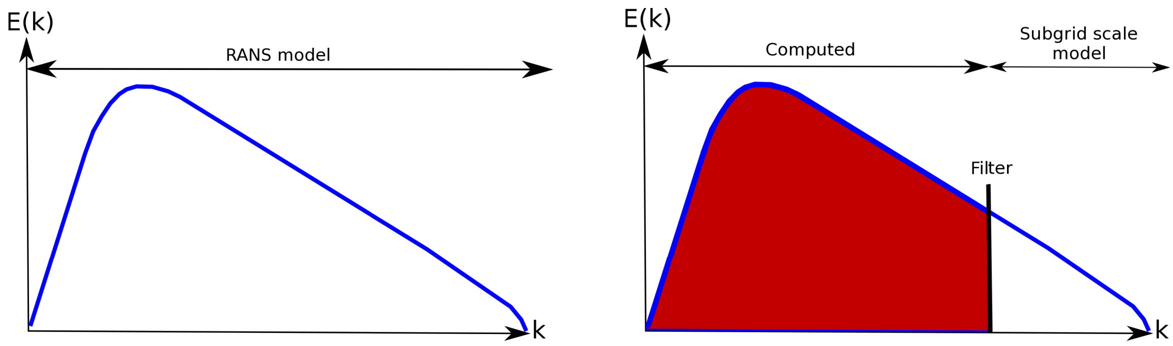

(a) RANS.

(b) LES.

Figure 2.1 — *Energy spectra for the repartition of the computed and modeled scales for RANS and LES.*

The $k-\omega$ model from Wilcox [174] uses $\omega \propto \frac{\varepsilon}{k}$ to determine the length scale. This specific turbulence dissipation is defined in the model by equation [II-37]. Its transport equation comes then from the transport equations of k and ε.

$$\omega = \frac{\varepsilon}{\beta^* k} \quad \beta^* = 0,09 \qquad \text{and} \qquad \nu_t = \frac{k}{\omega} \tag{II-37}$$

2.2 Zonal Detached Eddy Simulation

The Zonal Detached Eddy Simulation (ZDES), used in this thesis as the advanced numerical method, is based on the Detached Eddy Simulation (DES), a hybrid model between unsteady RANS and Large Eddy Simulation (LES), as presented in figure 1.25. In order to understand the ZDES model, this section gives an overview of the LES and the main DES versions before detailing the ZDES approach.

2.2.1 Large Eddy Simulation

The Large Eddy Simulation (LES) is different from the aforementioned RANS method. The RANS approaches model the whole turbulent field and are calibrated to give relevant results for the averaged field. However, in cases driven by the turbulence dynamics, with unsteady phenomena, they reach their limits. In order to understand these limitations, it is necessary to understand how the turbulence behaves. The process is called the *energy cascade* and was first thought by Richardson [138] in 1922 and then defined for high Reynolds number isotropic turbulence by Kolmogorov [93] in 1941. The energy is mainly supplied into the turbulent field from the boundary conditions of the domain to the large scales of the flow. Then, the energy is transferred in an inviscid mechanism from the large to the small structures. This zone is the inertial range and is characterized by a constant slope law in $k^{-5/3}$ for the energy distribution, with k the wavenumber. This process is finally limited by the molecular dissipation of the smallest structures when the Kolmogorov scale is reached. This scale depends on the Reynolds number of the flow. The use of the turbulent viscosity in RANS methods aims at modelling the whole cascade. Nevertheless, in real flows, the energy spectrum differs from the theory. For instance, the energy transfer can sometimes be reversed due to the vortex pairing for instance. This phenomenon, called *backscatter*, is not taken into account by these simple RANS models. While the Direct Numerical Simulation (DNS) computes the whole spectral domain, which is impossible with the actual computational resources for high Reynolds number flows, the LES consists in separating the turbulence scales into two domains. The LES computes the large structures and models the smallest ones, as shown in the Fourier space in figure 2.1(b). The scale separation is done through a high-pass filter for the scales, or low-pass filter for the

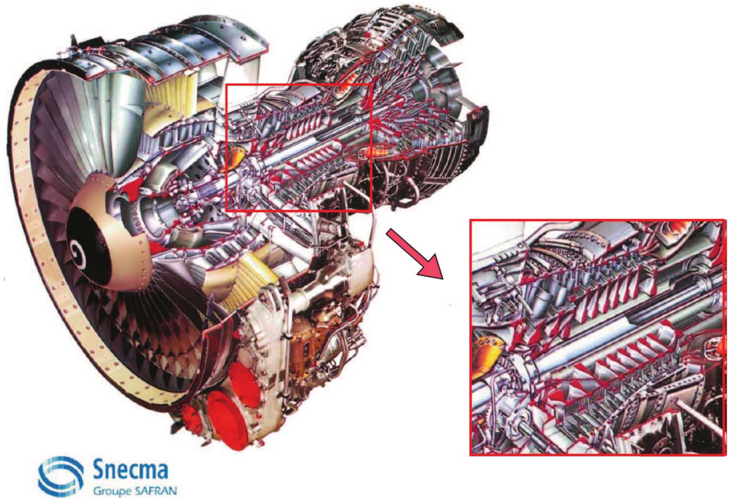

Figure 2.3 — *High pressure bloc in CFM56 jet engine (extracted from Ottavy [127])*

2.5 CREATE

2.5.1 Overview

This section deals with the experimental test bench upon which the study is based.

The simulated axial compressor is CREATE (Compresseur de Recherche pour l'Étude des effets Aérodynamiques et TEchnologiques) [128]. This research compressor was designed by Snecma and is located at the LMFA (Laboratoire de Mécanique des Fluides et d'Acoustique), at the Ecole Centrale de Lyon. It is representative, in terms of geometry and speed, of modern high pressure axial compressors, especially the median-rear block in modern engines, such as turbofans, as shown in figure 2.3. There are two main objectives for the engine company. First, to be able to carry out aerodynamic and mechanical parametric studies on a realistic configuration, and thus optimize the design of future engines. Second, to measure accurately the phenomena occurring in high pressure compressors.

The compressor CREATE is installed within the 2 MW test bench of the LMFA, presented in figure 2.4. This test rig is mounted on a concrete stand uncoupled from the measures room so as to avoid the propagation of vibrations. The test bench works as an open loop as it sucks air from the outside and throws it back. Upstream the compressor, the air coming from the outside is filtered and reaches the settling chamber. There, the total pressure drops to 0.75 bar (74% of the atmospheric pressure) so as to reduce the requirements of the test rig in terms of electric power. Downstream the compressor, a discharge valve enable to step out from a surge state in 0.5s. A butterfly-type valve controls the throttle by reducing the mass flow rate. This mass flow rate is measured at the exit with a Venturi nozzle. The compressor rotation comes from a Jeumont Schneider electric engine of 2.05 MW, which corresponds to the engine power of a high speed train. Along with the gearbox, it enables to reach rotational speeds from 0 to 17000 rpm.

The CREATE compressor comprises $3^{1/2}$ stages, with an inlet guide vane (IGV) and 3 rotor/stator stages. A meridian view is given in figure 2.5. The outer casing diameter is 0.52m and the nominal rotating speed 11543 rpm. The mass flow is then 12.7 $kg.s^{-1}$. The instrumentations installed on CREATE are numerous [27] compared to industrial test rigs. This enables to evaluate more accurately the numerical methods, as it is the case for this study. Furthermore, this compressor aims at analysing the technological effects, improving the flow stability and understanding the mechanisms responsible of the surge inception. In order to ease the measurements on the machine, the axial gap between the rows is increased, the outer-case comprises moving rings with holes for probes, and the spatial periodicity is of

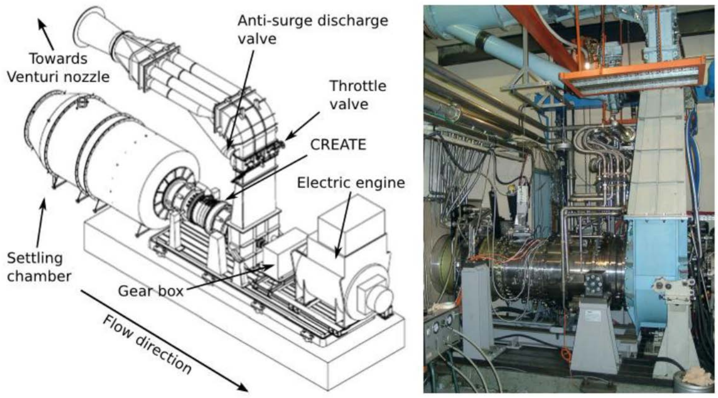

Figure 2.4 — *The CREATE compressor test rig (extracted from Courtiade [27])*

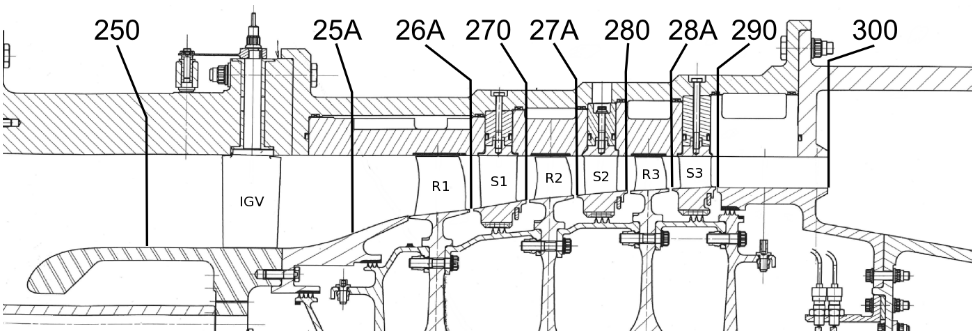

Figure 2.5 — *Meridian view of the CREATE compressor with the location of the axial sections*

$2\Pi/16$ (22.5°). The corresponding blade number for each row is detailed in table 2.3. This thesis work deals with the IGV and the first rotor (R1), hence the spatial periodicity of $2\Pi/32$ (11.25°). However, there are 8 support struts upstream the IGV and downstream the settling chamber on the CREATE compressor test rig, which changes the periodicity if they are taken into account. The IGV is linked to the shroud with a built-in turntable so that its stagger angle can be adapted. Concerning the R1, the inlet Mach number at its tip is 0.92, and the Reynolds number based on the axial chord is of 788000. The dimensionless tip clearances are $\lambda = \frac{GapSize}{MaximumBladeThickness} = 0.23$ and $\tau = \frac{GapSize}{AxialChord} = 1.75$. Based on the Rains criterion [135], the inertia forces are predominant within the gap.

2.5.2 Instrumentation

The aforementioned measurements available on the CREATE compressor are of two types: steady and unsteady. First, there are steady probes that measure the temperature and pressure. Second, there are unsteady measurements synchronized with the rotation of the compressor so that they can measure the same azimuthal position in the same channel at each turn. These measurements are made with unsteady wall static pressure probes, unsteady total pressure probes and Laser Doppler Anemometry (LDA).

The steady measurements are performed at each inter-blade row plane with cobra-type probes. They comprise a thermocouple for the total temperature and four holes for the pressure at the left, front, right and back of the probe. These probes enable to capture the local direction of the flow in the azimuthal

Table 2.3 — *Blade number for the rows*

Row	IGV	R1	S1	R2	S2	R3	S3
Blade number	32	64	96	80	112	80	128

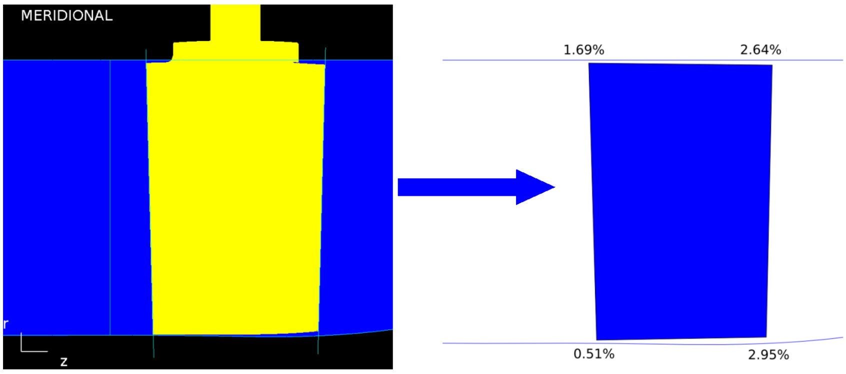

Figure 3.2 — *Simplication of the geometry for the IGV hub and tip gaps with the relative hub and tip gap sizes.*

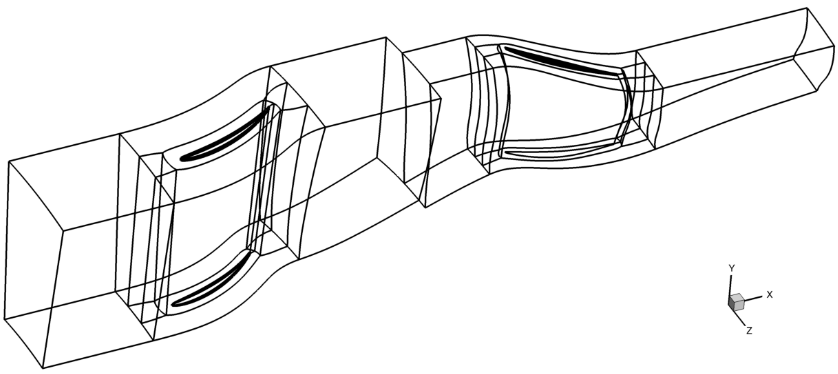

Figure 3.3 — *Computational domain with the IGV and the R1 of CREATE.*

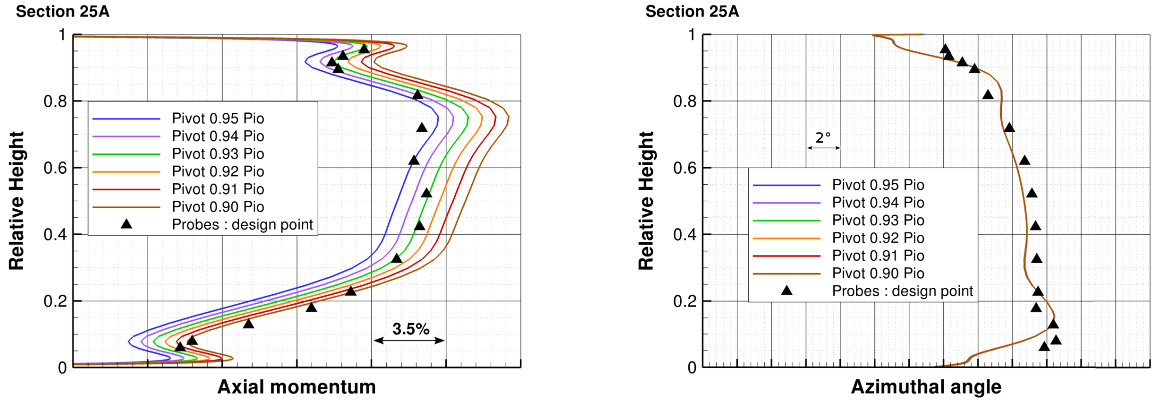

(a) Axial momentum. (b) Azimuthal angle.

Figure 3.4 — *Radial distribution of time and circumferentially averaged values at section 25A. RANS results on the IGV-R1 domain for different pivot pressures and data from experimental probes at the design point.*

all are extracted directly for the flow cartography. Indeed, they are used for the inlet condition on the computations on the R1. This is the reason why, once the pivot pressure is chosen at 0.93 Pio, another study is carried out to be closer to the experimental values for the flow angles.

In order to reach this goal, different numerical parameters are compared, such as the turbulence model, the spatial discretization scheme and the curvature correction of the Spalart-Allmaras model. Details of these comparisons are explained in appendix B. One will focus here on the two main effects: the impact on the axial momentum and the azimuthal angle. The axial momentum radial distribution at section 25A is presented in figure 3.5(a) for the same outlet pivot pressure chosen earlier, 0.93 Pio, but for different numerical parameters. The reference case uses the Jameson spatial discretization scheme (SA Jameson). Another computation with the AUSM+P scheme is evaluated (SA AUSM+P). Finally, a last one is compared. It is similar to the SA AUSM+P but with the curvature correction for the Spalart-Allmaras scheme [160] (SARC AUSM+P). The AUSM+P versions improve the capture of the gradient at 80% relative height and around 20% relative height. However, near the casing at 90%, the gradient is underestimated. The curvature correction amplifies this trend. This leads to a larger discrepency with the measurements near the hub. Nevertheless, the SARC computation is in better agreement than the SA AUSM+P with the measurements at 90% relative height, that is to say, the IGV tip vortex is better captured. In any case, the discrepancies between the computations at 90% are inferior to 0.7% for the axial momentum.

The real improvements of the AUSM+P scheme are found when comparing the azimuthal angle in figure 3.5(b). The radial position of the inflection around 20% relative height is quite correctly captured with the SA AUSM+P compared to SA Jameson. Moreover, the curvature correction improves even more the prediction capability of the method for the capture of IGV hub vortex width. In other words, the development stage of the hub vortex is captured. Between 80 and 90% relative height, the gradient is in better agreement with the AUSM+P method. The contribution of the AUSM+P is clear near the casing with a 1° improvement of the prevision of the angle value. There is nonetheless few differences between the two computations based on the AUSM+P near the casing. The only prediction variation is an increased angle value above 95% relative height. The lack of measurements so close to the casing however prevents to determine if this inflection is physical or not.

The differences near the casing for the axial momentum are thin and moreover, the angles will be directly used as inlet condition for the R1 computation. So the azimuthal angle is used here to differentiate the methods. In conclusion, the Spalart-Allmaras turbulence model with curvature correction and

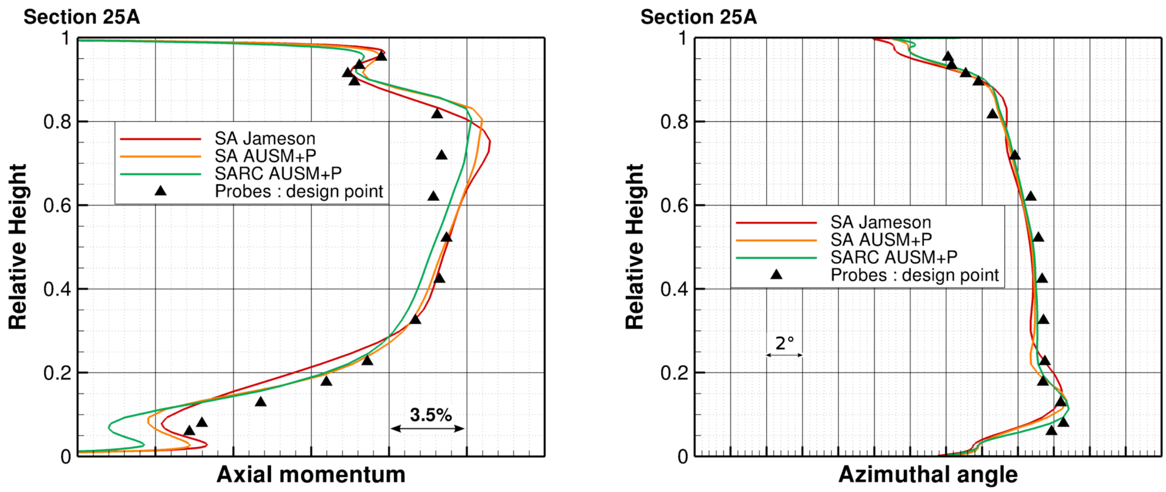

(a) Axial momentum. (b) Azimuthal angle.

Figure 3.5 — *Radial distribution of time and circumferentially averaged values at section 25A. RANS results on the IGV-R1 domain for different numerical parameters and data from experimental probes at the design point.*

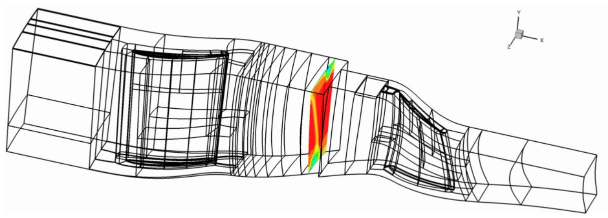

Figure 3.6 — *Position of the extraction plane at section 25A from the preliminary study.*

AUSM+P is finally chosen for its advantages on the simulation of the flow angles. Based on the axial momentum results, Spalart-Allmaras without curvature correction would have been a relevant choice too. A priority is given here to the swirl capture instead of the axial momentum.

The cartography is then extracted at section 25A, shown in figure 3.6, from the computation SARC AUSM+P. Since this cartography results from the choice of the pivot pressure in order to be in good agreement with the experimental probes, the same outlet boundary condition is used for the R1 computations. That is to say, the static pressure 0.93 Pio is specified at the hub of the outlet surface of the R1 computations and then a simplified radial equilibrium is applied, following equation II-62. An important aspect of the study on the R1 is that the same static pressure is used for all of the following computations (RANS, URANS, ZDES with and without the rotating distortion) at the design point.

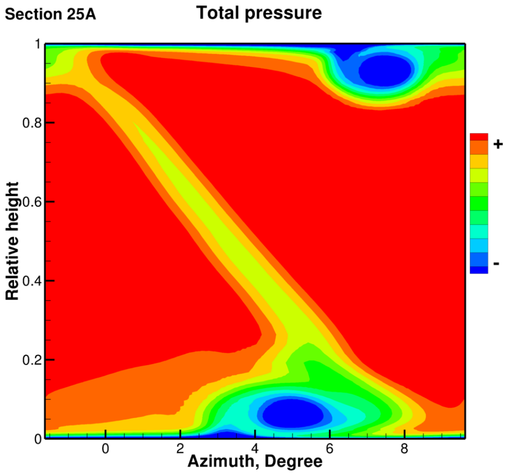

(a) RANS RDE-R1 computation.

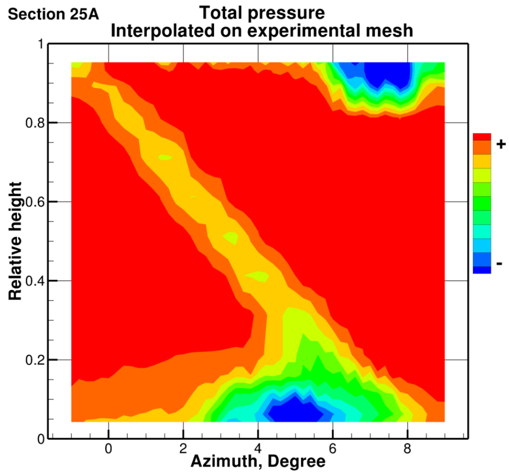

(b) RANS RDE-R1 computation. Interpolated on the experimental mesh.

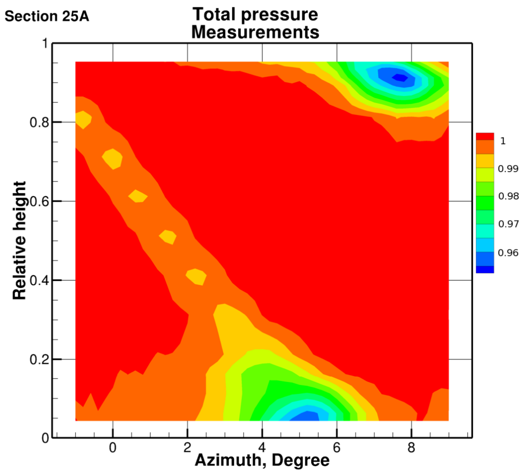

(c) Experimental probes.

Figure 3.7 — *Total pressure cartography at section 25A.*

3.3.4 Inlet cartography definition for the computations on the first rotor

The flow cartography extracted from the chosen configuration in the preliminary study is presented in figure 3.7(a). This 2D map of the total pressure shows that the main phenomena from the IGV are taken into account. Indeed, the hub vortex, azimuth 4-6 and relative height 0-0.1, the tip vortex, azimuth 7-8 and relative height 0.9-1, and finally the main wake diagonally from azimuth 0 and relative height 1 to azimuth 8 and relative height 0, are visible.

In order to ensure these results are due to the flow physics, this cartography is interpolated on the experimental mesh, figure 3.7(b). The map from the experimental probes is presented in figure 3.7(c). The azimuthal position calibration is based on the tip vortex position. While the relative position of the hub and tip vortices from the IGV are correctly captured with the RANS computation, the relative wake position is not. Actually, the problem originates from the azimuthal shift of the vortices with respect to the main wake. This shift results from the simplifications performed on the IGV gap sizes. As detailed in appendix A, the larger the gap, the wider the discrepancy between the main wake and the vortices. Indeed, with a larger gap, the vortices are wider and their axial and azimuthal convection is delayed compared to the main wake. This delay leads to the relative position difference when the wakes reach the section 25A. In addition, the total pressure deficit in the vortices is more important than what it is

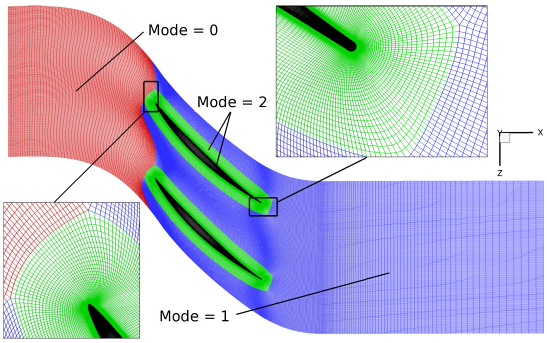

(a) Blade to blade view.

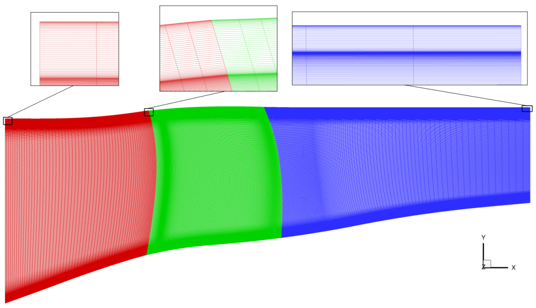

(b) Meridian view.

Figure 3.10 — *Mesh configuration for the different computations on the first rotor of CREATE. Color code for the ZDES method Red: mode = 0. Blue: mode = 1. Green: mode = 2. Black (tip gap mesh): mode = 2.*

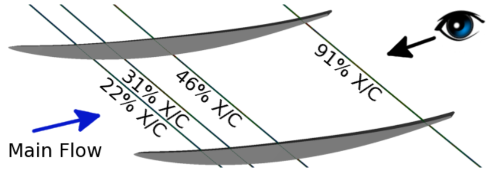

Figure 4.3 — *Position of the visualization sections along the chord.*

the results. Despite this limitation, the formation and development of the tip-leakage vortex is correctly computed in the LES mode of the ZDES. The vortex formation and widening can be seen in figure 4.2(a) on the suction side. Their computation in LES is a positive aspect of using the ZDES method for the simulation of the tip-leakage flow. This behaviour is the one that is expected since the leakage jet flow is clearly a "detached" flow, computed in LES. As a consequence, the ZDES behaves correctly for the simulation of the tip-leakage flow.

Another element concerning the validity of the ZDES is the correct use of mode = 2 in the vicinity of the blade. It was previously demonstrated that in the tip gap, mode = 2 protects the boundary layer and consequently forces the RANS mode. This protection is mainly visible near the leading edge where the boundary layers are thicker, especially on the pressure side at 22% X/C in figure 4.2(a). Nonetheless, this protection is known to have a negative impact on the transition between RANS and LES. This has to be quantified for the study. Indeed, mode = 2 delays this transition, albeit this delay is inferior to the one observed in DDES by Deck [38]. In figure 4.2(b), the suction side in the visible sections highlights different behaviours. In section 22% X/C, the eddy viscosity level is high in the boundary layer emanating from the tip gap and then decreases rapidly when the isoline 0.8 is crossed to be lower than 7 as soon as the isoline 0.99 is reached. At this section, the boundary layer at the tip gap and the one at the casing form only one boundary layer for the ZDES method. The method can not distinguish the two. This confirms that the boundary layer is protected with the mode = 2 close to the blades, and then the outer flow is resolved in LES. However, when mode = 1 is used, refer to figure 3.10(a) for the exact position, the flow is resolved in LES since the mesh suits LES requirements. From section 31% X/C and downstream, the method can distinguish the two boundary layers. As a result, the eddy viscosity field is then closer to the one detailed by Deck [38] obtained on a backward facing step, and similar conclusions can be drawn. One can observe a delay in the switch from RANS to LES. Nevertheless, the eddy viscosity rate drops from over 19 in the tip gap boundary layer to 9 as soon as it is outside the boundary layers from the tip gap and the suction side. This residual eddy viscosity of 9 contaminates the flow until reaches the zone in mode = 1 for section 31% X/C. However, this delay is reduced at section 46% X/C, that is to say, the switch occurs faster downstream. And this is an important point for the simulation of the tip-leakage flow and the main difference with the backward facing step. The eddy viscosity is convected downstream, tangentially to the edge between the tip and suction side. Since the level of eddy viscosity is rather high upstream, at section 22%, it is still high at section 31%. But then, the level decrease and the viscosity field behaves much more like the one in the backward facing step. Thereby, one can say the switch is rapid, even if there is still a delay whatever the axial position.

The same visualizations are presented for the hub region where there is no influence of the tip gap. The section 46% X/C is coloured by the entropy in figure 4.4(a), and by the eddy viscosity in figure 4.4(b). The same f_d isolines are overlaid. On the one hand, the boundary layers developing on the suction side, on the pressure side and near the blades on the hub wall are correctly protected with mode = 2. On the other hand, the boundary layer on the hub wall and far from the blades is not protected. In the unprotected zones, the f_d sensor can not be directly used to identify the boundary layer since it is intrinsic to the mode = 2. Indeed, there is an abrupt reduction of the thickness between the hub wall and the isoline 0.99 for the f_d value when crossing the interface between mode = 1 and mode = 2. Nevertheless, the entropy field between the two blades does not reveal any separation. There is only a thickening of the suction side boundary layer near the hub which is not impacted by the interface between the modes.

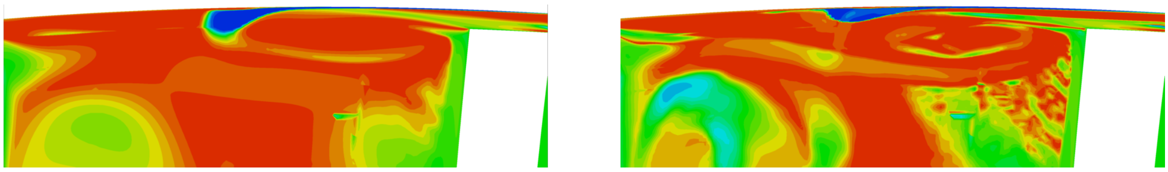

(a) URANS. (b) ZDES.

Normalized helicity

Figure 4.5 — *Instantaneous normalized helicity at $t = 3T/4$ and section 31% X/C for URANS and ZDES. Boundary layer separation at the casing.*

In conclusion, this section has explained the process for the convergence of the computations and brought out the validity of the numerical test bench concerning the operating point. Besides, the mode configuration for the ZDES has been assessed, which has emphasized the appropriate behaviour of the ZDES modes regarding the tip-leakage flow. In the next sections, an overview of the tip-leakage flow topology will be discussed before focussing on the validation of the ZDES.

4.2 Tip-leakage flow physical analysis

In this section, the tip-leakage flow topology is presented in two steps. On the one hand, the averaged field is detailed, and on the other hand, the evolution of the instantaneous field is assessed. The flow fields in the tip region from the RANS, URANS and ZDES computations are thoroughly compared and discussed.

4.2.1 Time-averaged flow field overview

First of all, it is important to put this study into perspective towards the previous analysis on the tip-leakage flow done in the literature. Two dimensionless criteria are used for the study of tip clearance flow topology. The first one is $\lambda = \frac{GapSize}{MaximumBladeThickness}$, the dimensionless tip clearance size with respect to the maximum blade thickness. In the first rotor of the CREATE compressor, its value is 0.23. Following the analysis from Rains [135], since λ is superior to 0.026, a vortex structure is expected. Moreover, Rains defined then the factor $\lambda^2 \cdot Re \cdot \epsilon$, with Re the Reynolds number based on the free stream velocity, and ϵ the maximum thickness to chord ratio, so as to generalize the tip-leakage flow topologies. For the R1, $\lambda^2 \cdot Re \cdot \epsilon$ is clearly in the domain defined by Rains [135] where the inertia forces are predominant over the viscous forces, mainly due to the high Reynolds number. As a consequence, the topology is mainly driven by the potential flow pressure distribution in the R1 of CREATE. The second criterion is the dimensionless tip clearance size with respect to the axial chord length, $\tau = \frac{GapSize}{AxialChord}$. For the R1, the value for τ is 1.75%. By comparing with the previous experimental studies on different tip clearance sizes from Brion [16], the expected topology with this τ value is a tip-leakage vortex that remains close to the casing while being convected away from the blade suction side.

In order to visualize the tip-leakage flow, an ensemble average is applied on 17 T of the ZDES computation and 18 T of the URANS one. The entropy fields of these averaged computations are presented in figure 4.6 so as to highlight the zones of high losses [43]. Different sections are represented on the same figure : a section at 98% of relative height, and 3 sections at respectively 22%, 31% and 46% of the axial chord. Despite the similar numerical methods implied in the two calculations, and an ensemble average which aims at comparing these two different approaches equally, the development of the tip-leakage vortex differs. Indeed, on the one hand, from the leading edge to section 22% chord, the same entropy field

of the differences between the two methods : the behaviour of the tip-leakage flow crossing this shock. The shock is known to trigger high dissipation when a turbulent flow passes through it, even with LES [46]. However, recent studies carried out with hybrid methods, such as the work of Shi [151, 152] with IDDES, lead to the same assessment as the one in this study : the advantages of methods based on LES over the ones based on RANS.

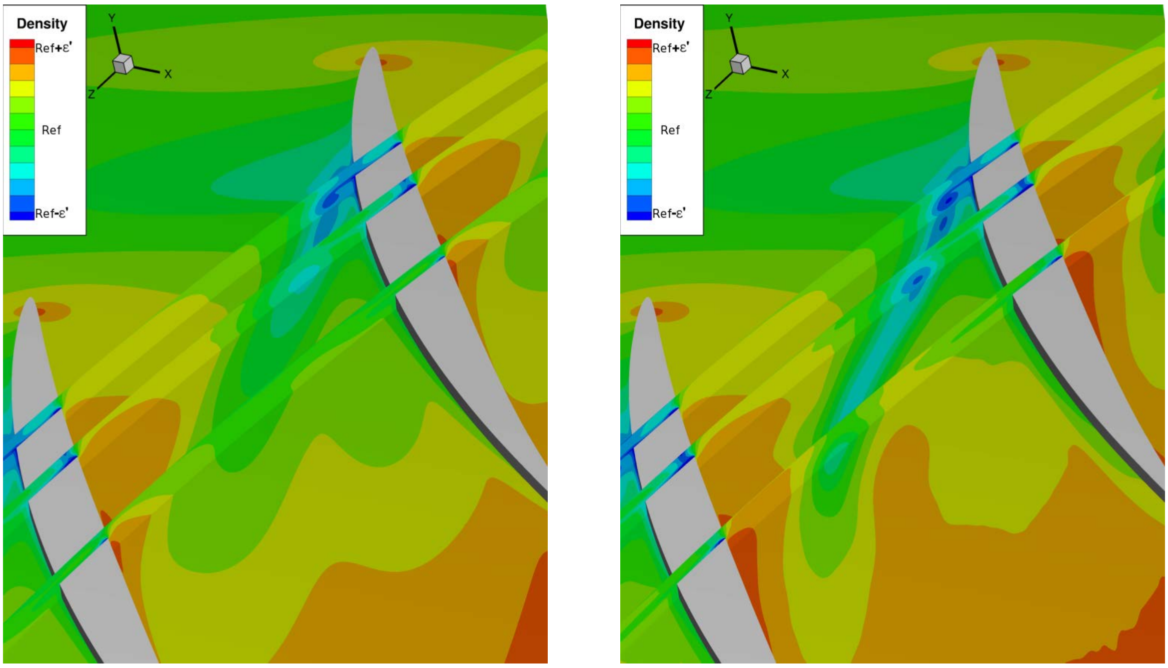

(a) URANS. (b) ZDES.

Figure 4.9 — *Comparison of the time averaged density field of URANS and ZDES. Density planes at 22%, 31% and 46% chord and 98% relative height.* $\epsilon' = 29\%$ *of the density reference value.*

Nevertheless, the shock at the tip of the R1 is not important for the design operating point of CREATE, and can be defined as weak as explained below. This results in some missing effects which occurs for the interaction between a strong shock and the tip-leakage vortex, as observed in the literature with configurations appropriated to analyse the shock/vortex/boundary layer interactions [69, 55, 151]. First of all, the gradients for the Mach number, in figure 4.8, are not important. Besides, there is no sudden drop in the Mach number value after the shock neither a recirculation area [78]. Second, one can analyse the figures 4.9(a) and 4.9(b) which represent the density field centred around a reference value. The presented density ranges from $\pm\epsilon' = 29\%$ of the density reference value. The core of the tip-leakage vortex is defined by a low density and thus it can be tracked by the means of the observation of the lowest density zones. This emphasizes the difference observed through the figures 4.7 with a tip-leakage vortex that extends further in ZDES. However, there is no rapid drop in density level at the shock, contrary to what is observed with strong shocks by Hofmann and Ballmann [77]. A last effect which confirms the weak shock is visible in figures 4.10 with the pressure field centred with $\pm\epsilon'' = 29\%$ of the pressure reference value. In these figures, the gradient for the pressure rise is weak, even at the shock position. As a consequence, the difference between the two methods is triggered by the passage through a weak shock.

Beyond the tip-leakage vortex development, the flow topology within the tip gap is important to understand the tip-leakage flow. First of all, it is important to remember that the ZDES mode used in the tip gap is the mode = 2. That is to say, the boundary layer is protected by the use of the URANS approach in it. As a consequence, this has a direct impact on flow field since the same approach is used near the walls for URANS and ZDES, hence the similar results at the wall. The difference stems from

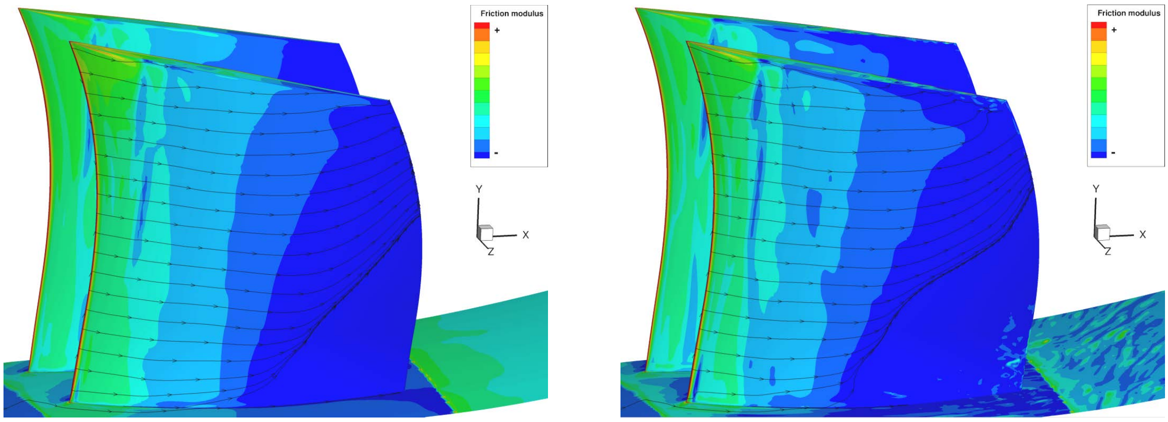

(a) URANS. (b) ZDES.

Figure 4.12 — *Comparison of the friction lines for the time averaged field of URANS and ZDES near the hub.*

4.2.2 Flow field snapshots

After the visualization of the time averaged fields, it is important to study the evolution of the instantaneous field for the tip-leakage flow because of its inherent unsteadiness. It must be emphasized that the finest details which are visible by the means of each method are observed here. Indeed, the inherent distinction between the URANS and the ZDES approaches prevents to compare the two methods with exactly the same refinement in terms of flow structures. This is only possible with averaged fields as presented in the previous study. Notwithstanding this restriction, the flow snapshots bring relevant information on the tip clearance flow topology.

Therefore, the iso-surfaces of Q criterion [81], coloured by the normalized helicity [105], along with a plane at 31% X/C filled with the entropy are presented here. Figures 4.13(a), 4.13(c), 4.13(e) and 4.13(g) represent the URANS computation while figures 4.13(b), 4.13(d), 4.13(f) and 4.13(h) show the evolution for the ZDES computation. Four different times are represented in these snapshots: T/4, 2T/4, 3T/4 and T from up to down.

First of all, the richness in terms of vortical structures is the main visible difference between the two methods. The URANS captures only the main vortices as long as they are stable enough. The main tip-leakage vortex and its contra-rotative induced vortex are visible with the two methods, in figure 4.13(a) and 4.13(b). Nevertheless, they extend further downstream in ZDES. This is due to their high unsteadiness from plane 31% X/C onward, which is dissipated by the URANS approach, and as a consequence, not captured.

The ZDES reveals multiple flow patterns similar to the ones suggested by Bindon [11] on a turbine cascade. The tip clearance flow leaks through channels from the pressure to the suction side of the blade. The flow angle depends on the chordwise position and corresponds to the angle observed within the gap in figure 4.11. Secondary tip-leakage vortices, as the one pointed in figure 4.13(f) migrate from the trailing edge toward the leading edge. Then, once close to the main tip-leakage vortex, their direction changes, they roll up around it due to its high rotational momentum. Finally they disrupt. The secondary tip-leakage vortex which is the closest to the main tip-leakage vortex has a specific behaviour. It does not migrate from the trailing edge and the resulting secondary vortex, pointed in figure 4.13(d), always rolls up from the same position as it can be seen in figures 4.13(b), 4.13(d), 4.13(f) and 4.13(h).

A tip-leakage vortex flutter phenomenon is visible in the present configuration, both in URANS and ZDES. The IGV wake and its tip vortex meet periodically the leading edge of the R1 which leads to this flutter. This arrival is highlighted at section 31% X/C in figure 4.13(g). The interaction between the wake

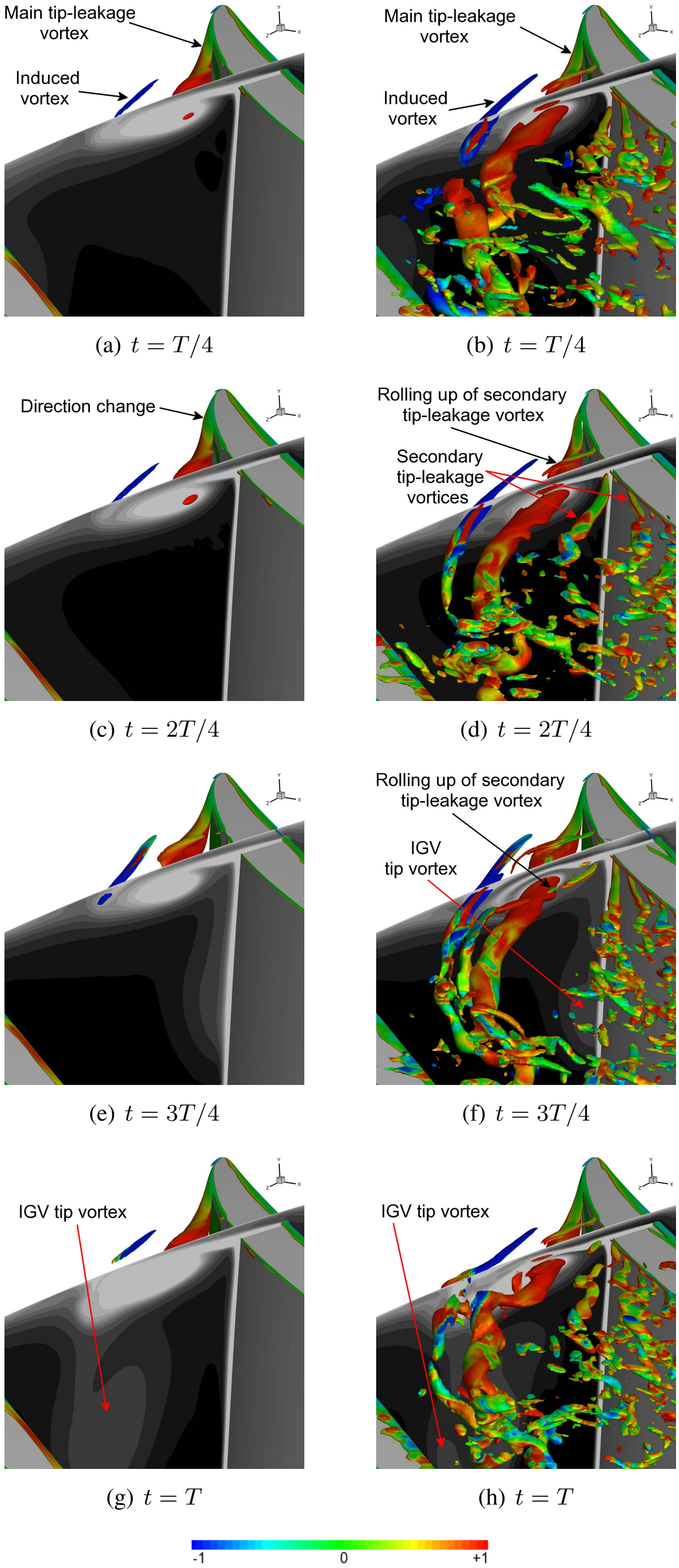

(a) $t = T/4$

(b) $t = T/4$

(c) $t = 2T/4$

(d) $t = 2T/4$

(e) $t = 3T/4$

(f) $t = 3T/4$

(g) $t = T$

(h) $t = T$

Normalized helicity

Figure 4.13 — *Snapshots of Q criterion iso-surface coloured by the normalized helicity and section 31% X/C filled with the entropy (left: URANS, right: ZDES).*

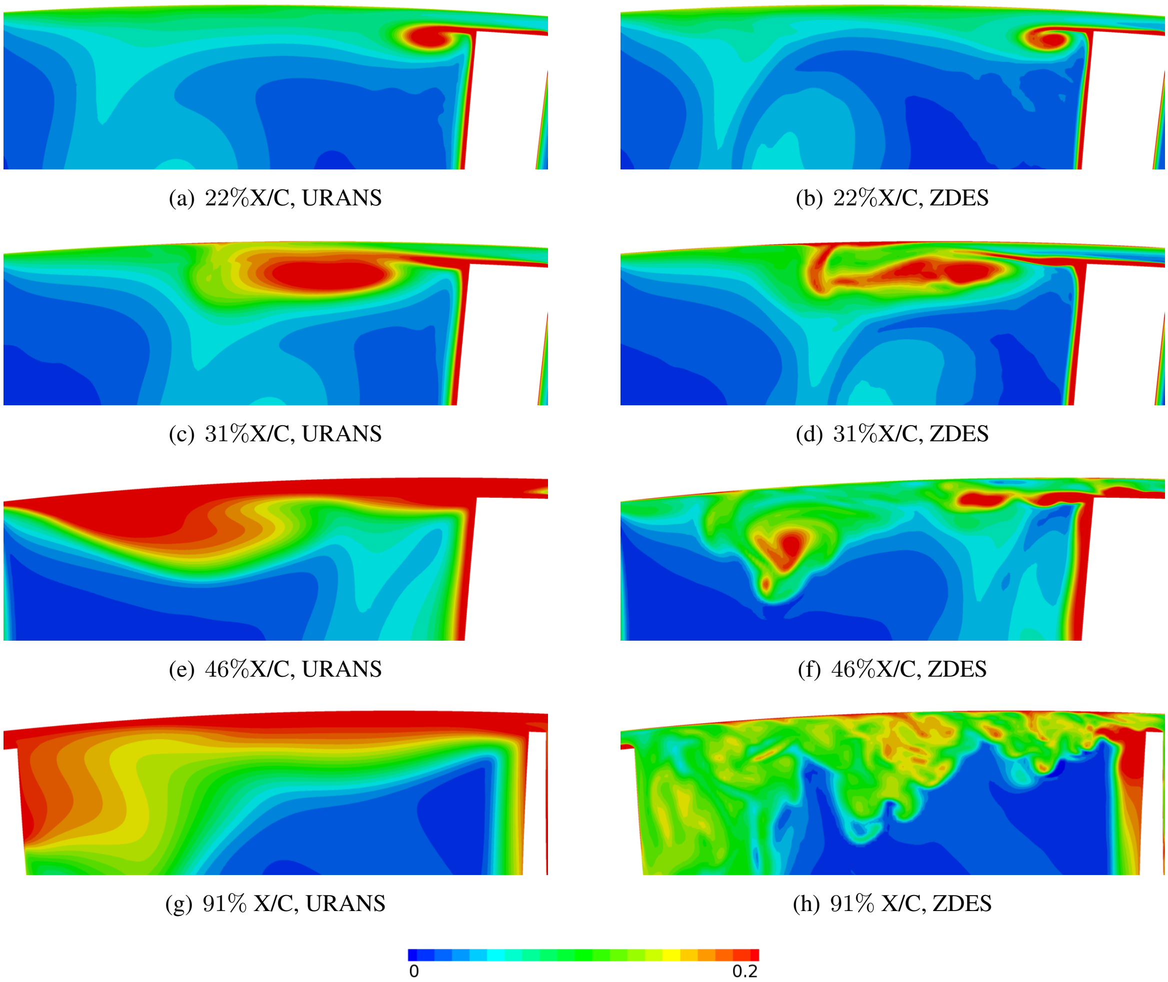

(a) 22%X/C, URANS
(b) 22%X/C, ZDES
(c) 31%X/C, URANS
(d) 31%X/C, ZDES
(e) 46%X/C, URANS
(f) 46%X/C, ZDES
(g) 91% X/C, URANS
(h) 91% X/C, ZDES

Entropy variation

Figure 4.14 — *Entropy planes for four different axial positions at t=3T/4 (left: URANS, right: ZDES).*

and the tip clearance flow, hence this flutter, was already experimentally emphasized by Mailach et al. [109], albeit not with an incoming vortex from the stator as it is the case here. Indeed, only a simple wake was simulated. In CREATE, the velocity deficit in the main flow deflects the leakage flow direction as shown in figures 4.13(c) and 4.13(d). As a consequence, the tip-leakage vortex moves away from the suction side of the blade with a period of T and the axial position of its disruption wanders around 31% X/C.

It must be noticed that the tip-leakage vortex evolution along the chord is different depending on the method used as explained with the time averaged fields seen previously. This is illustrated here by the entropy planes at position 22.3%, 31%, 46% and 91% X/C, for a snapshot at t=3T/4 in figure 4.14. Even if the tip-leakage vortex develops at the leading edge, the boundary layers from both the tip of the blade and its suction side supply the tip-leakage vortex along the chord. The resulting tip-leakage vortices are generated at this shared edge between the blade suction side and the blade tip, this from the leading edge to the trailing edge of the blade, figure 4.14(h). In figures 4.14(a) and 4.14(b), the tip-leakage vortex rolls up and its development is as advanced in RANS as in ZDES. From 31% X/C, the topology differs between the two methods. The vortex coming from the IGV tip stretches periodically the tip-leakage vortex azimuthally and accelerates the casing boundary layer separation seen in the time averaged fields. This is clearly shown by figure 4.14(d) that the IGV wake has not an important role in this stretching, contrary to the IGV vortex. The key element here is the velocity deficit which is more important within the IGV tip vortex. The separation at the casing occurs even when this vortex

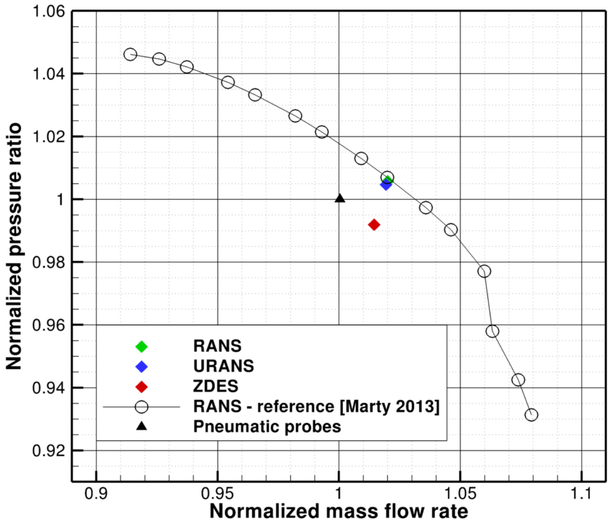

Figure 4.15 — *Pressure ratio versus mass flow rate for RANS, URANS and ZDES, normalized with pneumatic probes data.*

probe values. On the one hand the mass flow average is performed at section 25A, on the other hand, the total pressure ratio corresponds to the ratio of the dynalpic averages at section 25A and 26A. These values are then normalized by the value for the pneumatic probes, and summarized in table 4.1.

First of all, it is important to underscore the fact that the values from pneumatic probes, which are used for reference, have to be considered with caution. Indeed there are important uncertainties for these experimental values since the integration azimuthal period is $9.99°$ instead of $11.25°$ for the R1 periodicity. In addition, and this is the most important uncertainty source, there are no probe values over 95% and below 4% relative height. These zones, near the hub and near the casing are subject to the boundary layer influence and experience a lower total pressure and a lower axial momentum levels. As a consequence, seeing that these values are missing and not totally reliable, using a single value based on integral forces to find the operating point would have led to important errors. This supports the use of the axial momentum radial distribution to define the numerical operating point corresponding to the experimental design point as described in chapter 3. They are nonetheless used as reference here for a better understanding of the computational method effect on the global values.

In order to visualize this effect, the normalized pressure ratio is presented as a function of the normalized mass flow rate in figure 4.15. A reference operating line is given as an example and corresponds to different RANS computations from Marty [113] post processed with the same methodology as the one explained previously. These RANS computations are carried out with elsA 3.4.03 on 48 processors and the averaged inlet cartography from the preliminarily study detailed in chapter 3. The domain is the same as the one for the R1 computation presented in the last chapter, excepted one channel is only modelled. This fine RANS type mesh comprises 4.27 Million points. It is based on a Spalart-Allmaras turbulence model with third order AUSM+P and standard backward Euler. Finally, a radial equilibrium is set as outlet condition with a type 4 valve law, defined in equation II-63. This law is used to define the different working points presented in the figure with circles.

Despite the unsteady aspect of URANS and even the use of a rotating distortion, one can see that its prediction of performance values are close to the ones for RANS. Moreover, the use of a finer grid in this study, based on the ZDES requirements, does not change the operating point when it is compared to the reference RANS cases. All of the computations based on the averaged Navier-Stokes equations overestimate both the pressure ratio and the mass flow rate. Even if similar numerical methods and boundary conditions are used for all the computations of this study, RANS, URANS and ZDES, the global value results differ when considering the ZDES case. Indeed, the ZDES computation overestimates the exper-

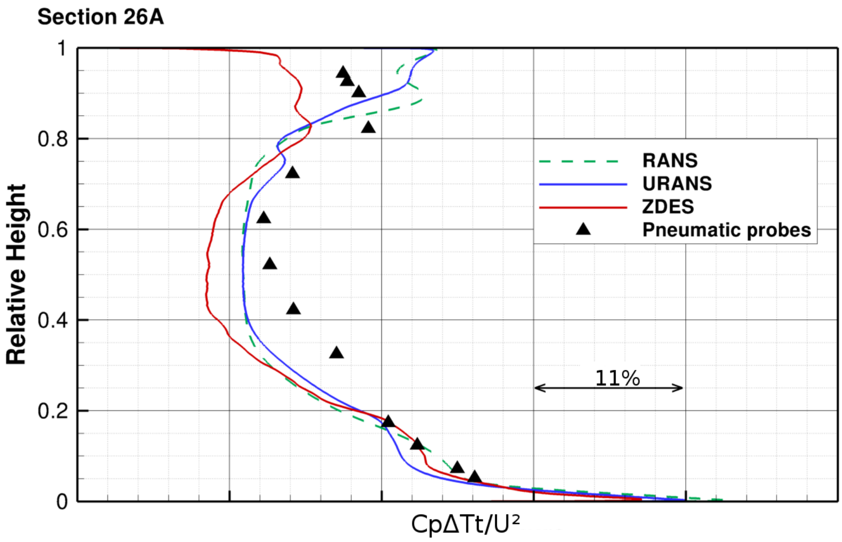

Figure 4.18 — *Radial distribution of time and circumferentially averaged normalized total temperature at section 26A for RANS, URANS, ZDES and experimental probes.*

Navier-Stokes equations for the tip-leakage flow and even at mid span. Nevertheless, at 32% relative height, the computations provide total pressure values which do not match the probes measurements, with an under-estimation of 1% for ZDES and an over estimation of the same order of magnitude for the RANS and URANS methods, depending on the considered probe. A hypothesis for this pressure increase could be that the recirculation from the axial gap upstream from the R1, which can be seen in figure 2.5, modifies the pressure distribution locally at 32% relative height in section 26A. This phenomenon, could not be seen in the configuration set in this paper since no hub recirculation is modelled compared to the configuration studied by Marty and Aupoix [110].

After the axial momentum and the total pressure, another important value informs us on the work of the blade: the total temperature. Figure 4.18 shows the radial distributions at section 26A of the normalized total temperature, $Cp\Delta Tt/U^2$, known as loading coefficient. First, there is a global underestimation of the total temperature value for the computations. This is directly linked to the global overestimation of the axial momentum seen in figure 4.16. This underestimation of the total temperature is amplified for the ZDES which has a value for $Cp\Delta Tt/U^2$ 4% lower than the RANS/URANS cases. Nonetheless, the main difference is visible near the casing where the RANS and URANS computations calculate a $Cp\Delta Tt/U^2$ higher than the probe measurements by 5%. By contrast, the ZDES approach still under predicts the total temperature value which is more consistent with the other values computed below 80% of the span. In order to better understand this difference, a study was carried out by Marty et al. [114] on the same configuration with a different boundary condition at the wall. Marty highlighted that by imposing a temperature, instead of the adiabatic condition, the gradient near the casing can change drastically from the value observed in ZDES to the one in RANS and URANS. Moreover, the boundary condition at the casing wall influences the gradients of temperature above 80% relative height. This is the region where the methods differ here. However, the same adiabatic boundary condition is used for all the computations presented here.

Therefore the difference is due to the method, not the boundary condition. Beyond the absolute value which is directly linked to the operating point, two effects have to be emphasized. The first one is the relative shift between the minimum at mid span and the value near the casing, which is in better agreement with the ZDES. The second one is the inflection point at 82% relative height. This inflection originates from the arrival of the tip-leakage flow. The ZDES captures this inflection. Though the steady RANS captures an inflection, albeit the radial position is overestimated, the unsteady RANS manages to

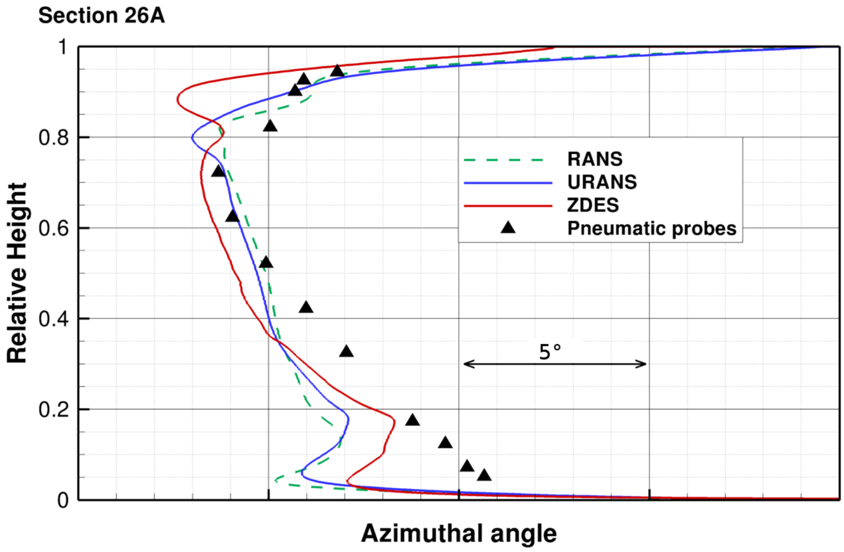

Figure 4.19 — *Radial distribution of time and circumferentially averaged azimuthal angle at section 26A for RANS, URANS, ZDES and experimental probes.*

capture only a light curvature between 90 and 95% and does not capture any inflection. As a consequence, one can see that the ZDES captures more accurately the development stage of the tip-leakage vortex although the operating point of the computation does not match perfectly the experimental one.

The last compared value is the azimuthal angle. The corresponding radial distribution is plotted in figure 4.19. The previous analysis of the axial momentum has shown a work difference between the computations first, and between the computations and the experimental case. This is confirmed by the total temperature distribution. Beyond the main difference with the probes seen along the radius for the different values, there are two zones with different results according to the method used. They are areas where the unsteady aspect of the flow is of major importance: near the casing and near the hub. Moreover, if the angle is changed, the axial momentum changes too. As a result, the same characteristic regions are observed for the axial momentum and the azimuthal angle. The minima of the azimuthal angle are then linked to the maxima of the axial momentum. Indeed, a minimum for the azimuthal angle is encountered at 72% relative height and correctly captured with the ZDES. The ZDES experiences another minimum at 87% which corresponds to the minimum of axial momentum seen in figure 4.16. Even if an inflection can be seen for the probes at 92% relative height, the angle value is clearly underestimated by 2.5° in ZDES. The URANS approach has a similar behaviour but the radial position of its minimum angle is different since it is located at 80%. Besides, there is only one local minimum in URANS contrary to the ZDES. Beyond expectations, the steady RANS reveals to be in better agreement near the casing here.

On the contrary, near the hub, it has the worst results, and the ZDES has the closest angle values to the experimental ones. However, all the computations capture an inflection between 10 and 20% of relative height, which is not measured by the probes. The inflection near the hub is due to the strong corner effect, which is not physical. Many hypothesis can explain this discrepancy with the experimental measurements near the hub. Some are linked to the simplification of the numerical test bench, such as the IGV hub gap modelization, the simplification of the hub surface and platform geometries or the recirculation upstream the R1 which is not taken into account. Other hypothesis are linked to the numerical methods, such as the underlying turbulence model. Indeed, the Spalart-Allmaras model is known for amplifying the separation in turbomachinery as revealed by Marty [112, 111] for the CREATE compressor. The capability of the ZDES to simulate unsteady flows is mainly based on the LES aspect of this method, however, it is important to keep in mind that in the boundary layer, at least with mode = 2, the flow is computed with the unsteady RANS approach. As a consequence, the limitations of the underlying

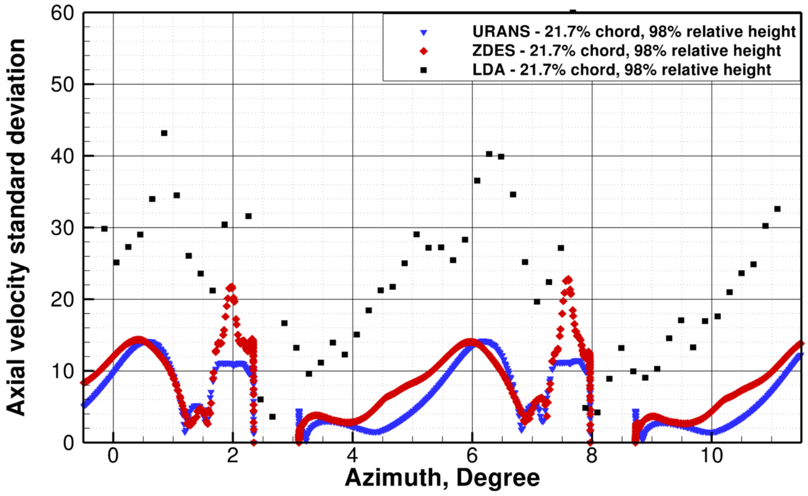

(a) Axial.

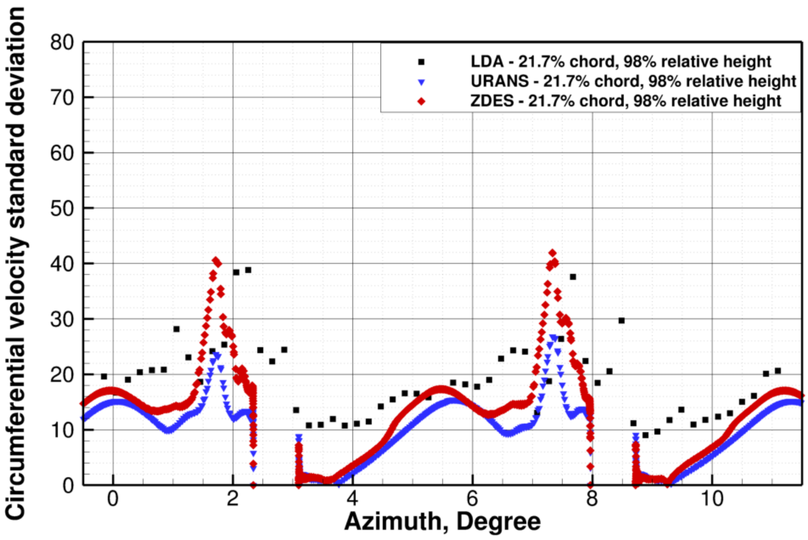

(b) Circumferential.

Figure 4.24 — *Axial and circumferential velocity standard deviations [in $m.s^{-1}$] at 21.7% chord and 98% relative height for RANS, URANS, ZDES and LDA measurements.*

are correctly captured, there is an important underestimation of the standard deviation value for the two computations.

Likewise, the circumferential velocity standard deviation, visible in figure 4.24(b), is underestimated by the computations. In spite of the good agreement for the levels of the normalized circumferential velocity seen in figure 4.20(b), the unsteadiness in the azimuthal direction differs between the computations and the LDA measurements. Indeed, near the pressure side of the blade, at azimuths 3 to 4, it is close to 0 for the computations while it is above $10m.s^{-1}$ for the LDA. The unsteadiness levels for the computations increase in between the blades, up to azimuth 5.5 where it reaches the same levels as the LDA measurements. Then, the levels of the circumferential unsteadiness decrease only for the computations. It only rises again near the suction side of the blade where the levels are in good agreement between the LDA and the computations. At this position, for azimuths 7 to 7.5, there is a peak of unsteadiness corresponding to the position of the main tip-leakage vortex. There is a light improvement for the ZDES with unsteadiness levels closer to the LDA measurements around this peak.

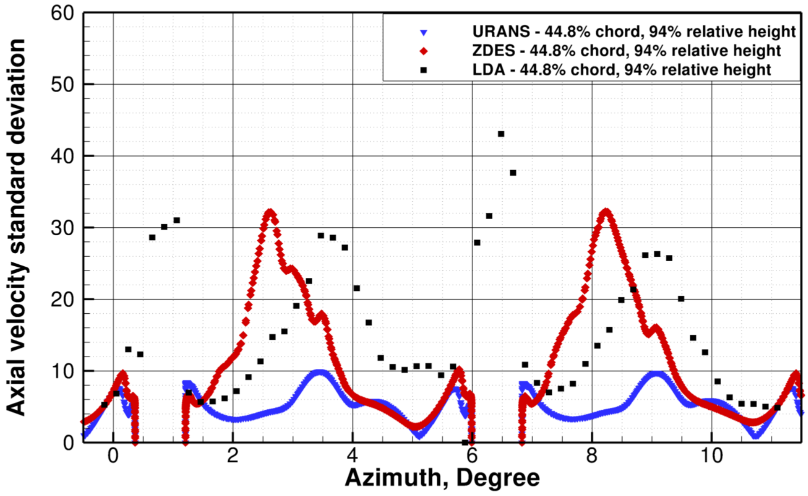

(a) Axial.

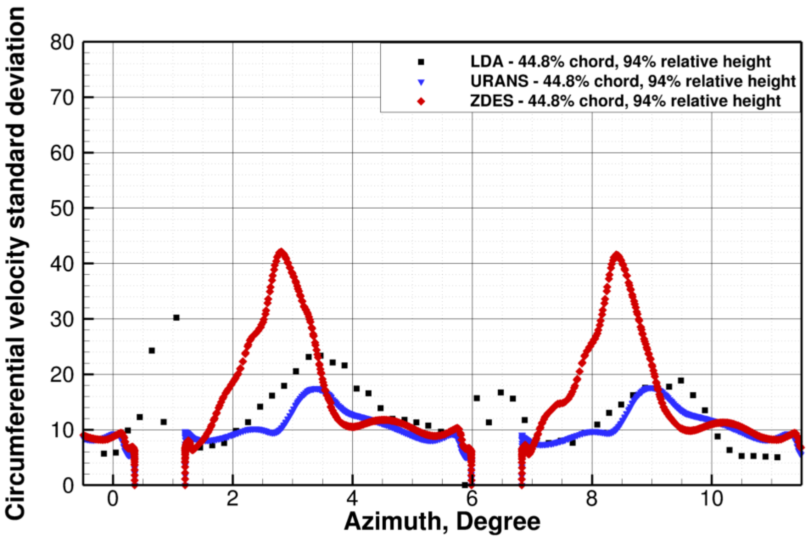

(b) Circumferential.

Figure 4.25 — *Axial and circumferential velocity standard deviations [in $m.s^{-1}$] at 44.8% chord and 94% relative height for RANS, URANS, ZDES and LDA measurements.*

Downstream the shock position, the ZDES capability to capture the axial unsteadiness within the flow outstrips the URANS approach. At the position 44.8% X/C and 94% of relative height, in figure 4.25(a), the levels of axial unsteadiness are correctly captured by the ZDES whereas the URANS barely captures a light unsteady phenomenon. Nevertheless, the azimuthal position has a difference of one degree between the ZDES and the LDA while the position is correct for the URANS. Since the azimuthal position of the tip-leakage vortex is directly correlated to the axial velocity, this confirms the problem of the choice of the operating point for the ZDES. At the same position, the circumferential velocity standard deviation, in figure 4.25(b), highlights an important overestimation for the unsteadiness of the tip-leakage vortex captured by the ZDES which is up to two times higher than what it is experimentally. The same aforementioned position issue is visible for the circumferential velocity standard deviation in ZDES. By contrast, the URANS approach captures correctly the position of the peak at azimuth 3-3.5 and 9. The unsteadiness levels are closer to the ones captured experimentally than what is observed in ZDES. However, there is still an underestimation of the unsteadiness in URANS.

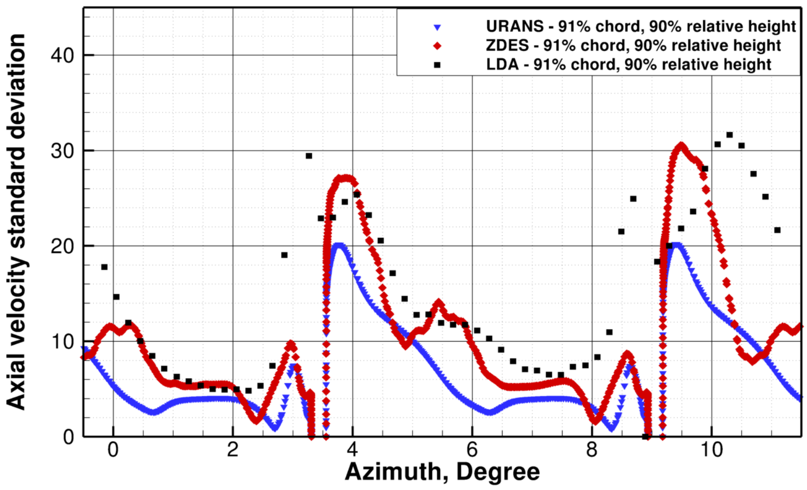

(a) Axial.

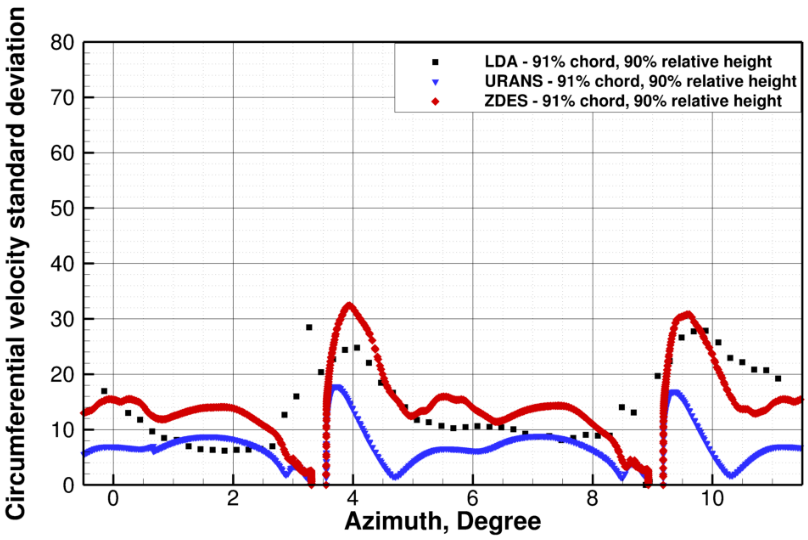

(b) Circumferential.

Figure 4.26 — *Axial and circumferential velocity standard deviations [in $m.s^{-1}$] at 91% chord and 90% relative height for RANS, URANS, ZDES and LDA measurements.*

This trend is confirmed near the trailing edge of the blade, at 91% X/C and 90% of relative height. The axial velocity standard deviation is presented in figure 4.26(a). At this position, the unsteadiness distribution has changed for the computations as well as the measurements. The value is higher near the blade around azimuth 4 and decreases as the azimuth increases up to the other blade. The azimuths 4-6 denote the position of the rim of the main tip-leakage vortex. On the one hand, the intensity and position of this vortex is correctly captured by the ZDES method. On the other hand, the URANS does not capture it at all. Moreover, the levels are lower in URANS with an almost constant 5% discrepancy with the LDA measurements along the azimuth.

Figure 4.26(b) shows similar results for the circumferential velocity standard deviation at the same position. Contrary to what is observed at 44.8% X/C in figure 4.25(b), the ZDES captures unsteadiness levels that suit better the azimuthal distribution observed experimentally than the URANS computation. This confirms that the URANS method underestimates the unsteadiness in both directions downstream the shock position.

The last position to be evaluated is the one corresponding to the upper part of the tip-leakage vortex, in section 26A. Figure 4.27(a) shows the axial velocity standard deviation. The wakes of the R1 are in azimuth 0 and 5.625. Two zones of high unsteadiness in the axial direction are visible on each side of the wake centre, for instance, one at azimuth 5 and one at azimuth 6.5. They have a different level of unsteadiness. This level difference is not captured by the URANS method. Moreover, the URANS computation captures lower levels compared to the LDA measurements. The level difference between the two zones around the wakes is seen by the ZDES, albeit less pronounced than what it is experimentally.

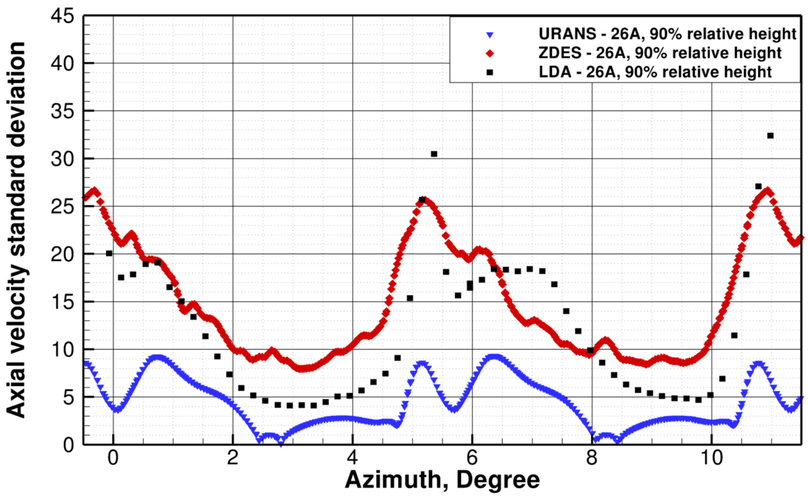

(a) Axial.

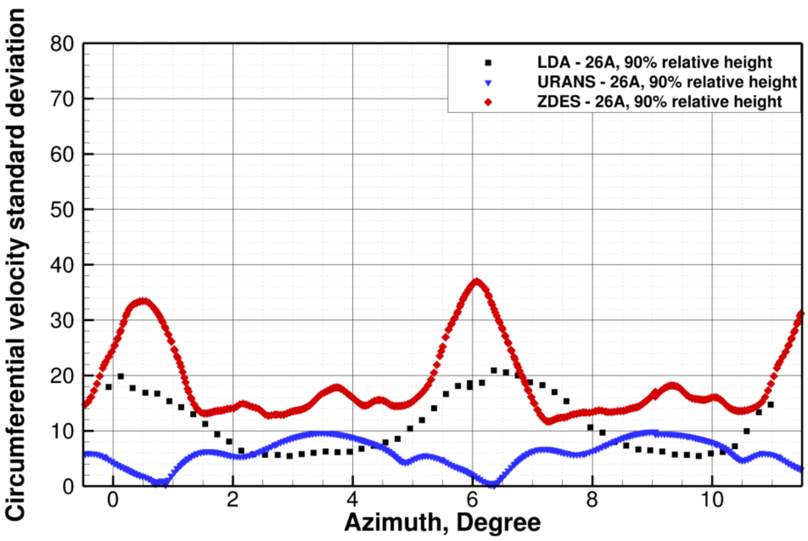

(b) Circumferential.

Figure 4.27 — *Axial and circumferential velocity standard deviations [in $m.s^{-1}$] at section 26A and 90% relative height for RANS, URANS, ZDES and LDA measurements.*

Figure 4.27(b) underlines the difference between the two methods. The circumferential velocity standard deviation is high in ZDES, with values oscillating between 12 and 37 whether there is a wake or not. Conversely, the levels for the URANS method are low and besides, the oscillations have a lower amplitude, from 0 to 10. What is important to notice here, is the level of the LDA measurements. In the zones where there are the wakes, the levels are high and correspond to the peaks seen in the ZDES, albeit the levels in ZDES are almost twice as much as the levels captured experimentally. At these positions,

entropy plane from the ZDES computation. One can see that this position corresponds to the arrival of the tip-leakage vortex too, albeit it is widened and almost dissipated.

The second area is at the casing of section 26A. The same azimuthal position is chosen so that the difference between the probes comes mainly from their distance to the wall, hence their capture of either the inner boundary layer flow or the outer flow.

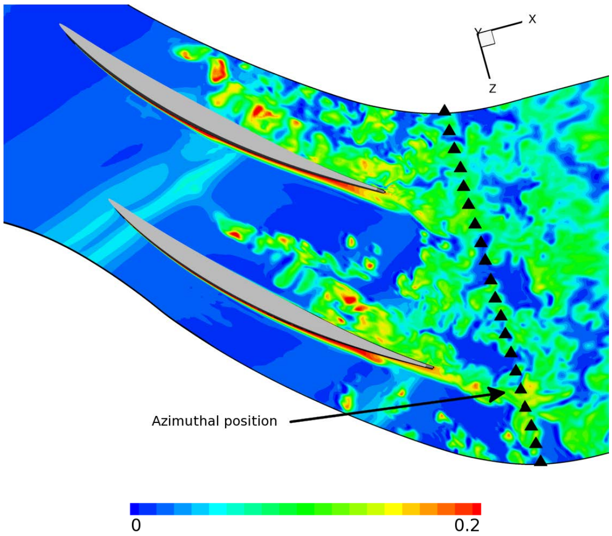

Figure 4.28 — *Probe positions at section 26A. Instantaneous entropy plane at 94% relative height and $t = 3T/4$ from the ZDES computation.*

4.6.2 Power Spectral Density

The spectral analysis is based on the power spectral density (PSD) of the pressure for the aforesaid probes. The PSD is based on the Welch method [172] using an overlap of 50% and ten Hann windows [68] with a linear mean for each. It describes how the root mean squared value of the static pressure is distributed in the frequency spectrum, and thus represents the flow energy. An estimation of the cut-off frequency for the computational results gives $3.2\ 10^5$ Hz. It is based on the cubic root of the cell volume and a characteristic velocity for the turbulent structures defined as $\sqrt{u'^2 + v'^2 + w'^2}$, with u', v' and w' respectively the maximum of the fluctuating velocity in the X, Y and Z directions, as shown in figure 4.28. It is important to keep in mind that the effective cut-off may be at a lower frequency due to the numerous effects that influence it, such as the mesh refinement and the numerical schemes. The value $G_p(f)$ of the static pressure is plotted as a function of the frequency in figure 4.29(a) for the probes at the casing and in figure 4.29(b) for the ones at 94% relative height. For a better understanding, another parameter is displayed : the reduced frequency. It consists in the signal frequency normalized by the IGV blade passing frequency (BPF).

The frequency resolution (FR) is 2000 Hz for the numerical data set arising from a temporal range of 17 T for the ZDES computation and 18 T for the URANS one. This resolution results from the aforementioned minimum number of Hann windows required for the Welch method. By contrast, the resolution for the unsteady probes is of 2 Hz. This is a limiting factor for the comparison of the numerical probes with the experimental ones, especially for the low frequency phenomena. The reason is that the lowest captured frequency is the frequency resolution. Thereby, the phenomena with a characteristic frequency inferior to the frequency resolution of a PSD are not captured. Another effect of the frequency resolution is the level of energy visible in the graphs. Indeed, a small frequency resolution leads to a more

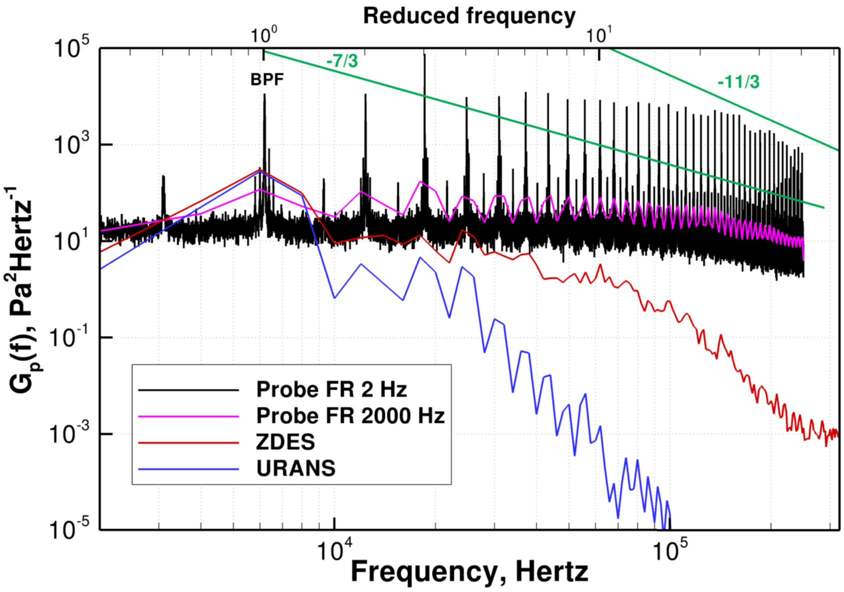

(a) At the casing.

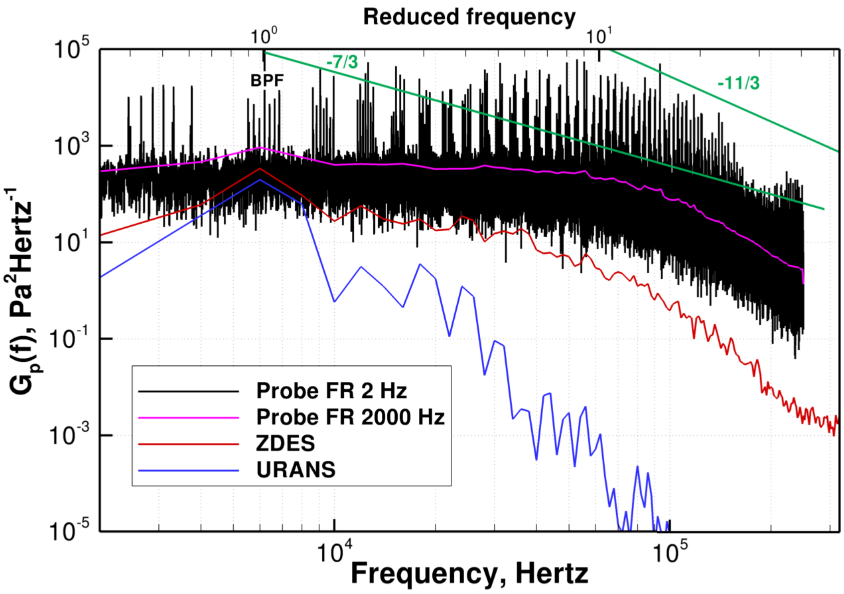

(b) At 94% relative height.

Figure 4.29 — *Power spectral density of pressure at section 26A. URANS, ZDES and experimental unsteady pressure probes (with 2 frequency resolutions).*

accurate capture of the frequency of a phenomenon, denoted by a thin and high peak of energy on the graph. On the contrary, the same phenomenon captured with a higher value for the frequency resolution will result in a wider and shorter peak due to the energy distribution on a wider range of frequency. This effect on the energy level visible is the reason why the PSD for the unsteady probe are displayed with two frequency resolutions. On the one hand, 2 Hz, which is the best available resolution regarding the length of the experimental data set. On the other hand, 2000 Hz, which is the same frequency resolution as the one for the numerical probes from the computations.

One can see in figure 4.29(a) that a low frequency phenomenon is visible for the experimental probe PSD only with the smallest frequency resolution. This phenomenon corresponds to $1/2$ BPF, and is captured neither by the unsteady probe PSD with 2000 Hz of frequency resolution nor by the

from 1 BPF to 10 BPF. In fact, the ZDES approach detects only a light decrease in the energy level for the flow field at 94% of relative height compared to the one at the casing. Therefore, the energy levels are in better agreement for the ZDES, albeit the levels are still at two orders of magnitude lower than the experimental PSD values. Nevertheless, what is important here is that the slope is correctly captured with the ZDES approach. The energy decrease is similar to the unsteady probes, even if there is still the issue with the potential effect of the S1. In other words, the interaction between the mean-shear and the turbulence is correctly captured in the ZDES approach contrary to the URANS method.

In summary, the ZDES brings significant improvements for the simulation of the interactions between the mean-shear and the turbulence. This results in energy levels and an energy decrease which are in better agreement with the experimental ones. Some of these enhancements are visible even in the boundary layer, albeit the ZDES behaves like the URANS method there. This behaviour near the wall prevents nonetheless the ZDES from capturing correctly the turbulence-turbulence interactions.

In the next section, one will compare the energy levels between the two unsteady computational methods so as to understand why there is such a difference for the energy levels when the flow arrives at section 26A.

4.7 Analysis of the energy levels along the tip-leakage vortex

In order to understand why there is such a difference for the energy levels between the URANS and the ZDES approaches at section 26A, a spectral analysis is carried out.

4.7.1 Probe positions along the tip-leakage flow

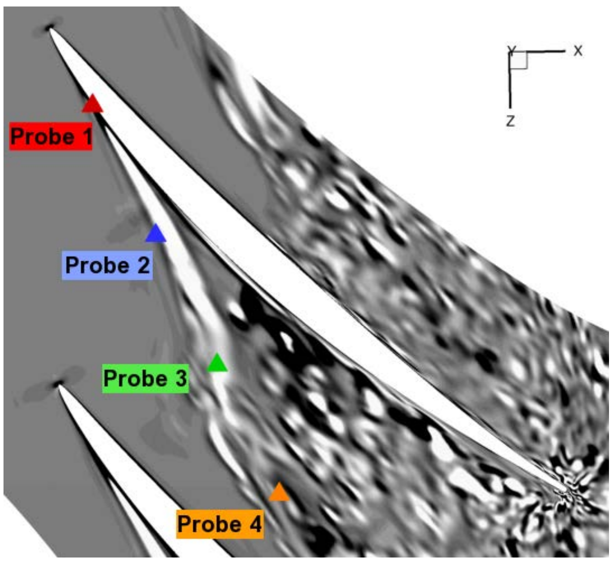

Figure 4.30 — *Probe positions along the main tip-leakage vortex. Instantaneous schlieren at 98% relative height and $T = 3T/4$ from the ZDES computation.*

This analysis aims at understanding how the two methods simulate the tip-leakage vortex development. Thereby, the Power Spectral Density (PSD) function of the static pressure is plotted for four probes within the blade passage. More precisely, they are located at different axial positions along the main tip-leakage vortex core as presented in figure 4.30 with the instantaneous Schlieren at 98% relative height and t=3T/4. The probes 1, in red, and 2, in blue, are located at 11% and 22.5% X/C. The probes

3, in green, and 4, in orange, are located at 33.8% and 45.7% X/C. This means that probes 1 and 2 are upstream the tip-leakage vortex disruption, which occurs after the shock, contrary to probes 3 and 4.

4.7.2 Power Spectral Density along the tip-leakage flow

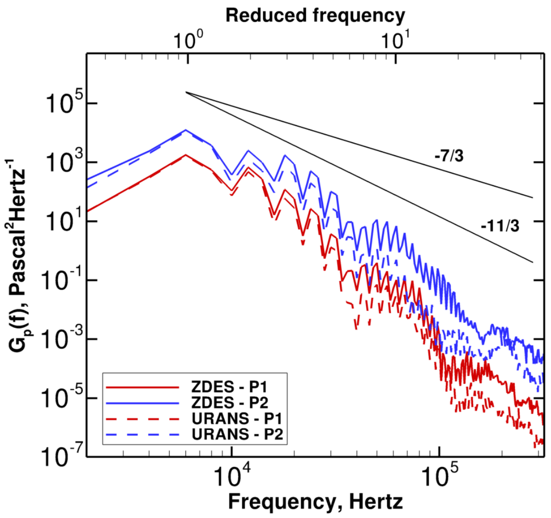

(a) Probes 1 and 2.

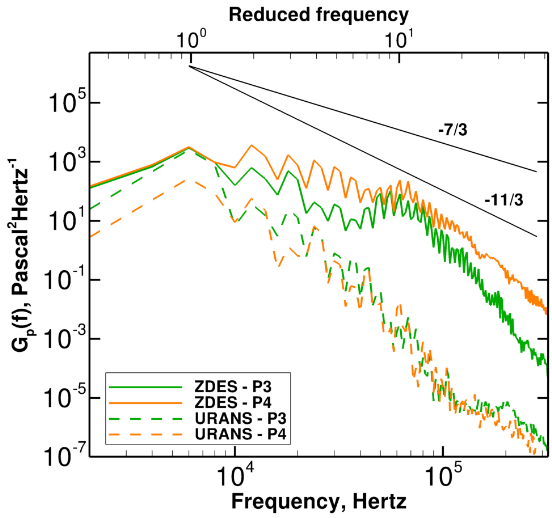

(b) Probes 3 and 4.

Figure 4.31 — *Power spectral density of static pressure for probes along the main tip-leakage vortex. URANS and ZDES.*

The PSD are based on the Welch method [172] using an overlap of 50% and ten Hann windows with a linear mean for each as in the previous section. The same frequency resolution (FR) of 2000 Hz is chosen for both the computations. The PSD functions are plotted for probes 1 and 2 in figure 4.31(a) and for probes 3 and 4, in figure 4.31(b).

The PSD represents the flow energy. For a thorough knowledge of the energy within the flow, the normalized PSD are used too. They are defined by $\frac{f \cdot G_p(f)}{\sigma^2}$ with σ detailed in equation IV-1. The normalized power spectral density shows the contribution to the total energy of the different frequencies. They are plotted for probes 1 and 2 in figure 4.32(a) and for probes 3 and 4, in figure 4.32(b).

$$\sigma^2 = \int_0^\infty G_p(f)df = \int_0^\infty f \cdot G_p(f)d(log(f)) \qquad \text{(IV-1)}$$

Up to section 31% X/C, the energy level increases for every frequency, low, medium and high, and, above all, for both URANS and ZDES in figure 4.31(a). This characterizes a similar evolution of the tip-leakage flow. In addition, the magnitudes for probe 1 are close until 10^5 Hz, except for one peak at 38000 Hz ; then, they diverge. The frequency from which the two methods differ lowers as the probe is downstream. Indeed, for probe 2, it would be around 56000 Hz. The slope of the PSD changes from a steep one at probe 1 to the $k^{-11/3}$ slope which corresponds to a turbulence/mean-shear interaction. However, the ZDES approach is closer to this slope than the URANS method.

From probe 3 onward, figure 4.31(b), the difference in magnitude is important. At probe 3, the two methods match only at the low frequencies: 6000 and 8000 Hz. And finally, at probe 4, the whole spectrum is lower for the URANS approach. Nevertheless, it must be noticed that the 6000 Hz frequency corresponds to the IGV passage frequency (6156 Hz) regarding the PSD frequency resolution. Its harmonics are captured by both methods, although the magnitudes differ. This is clearly seen with

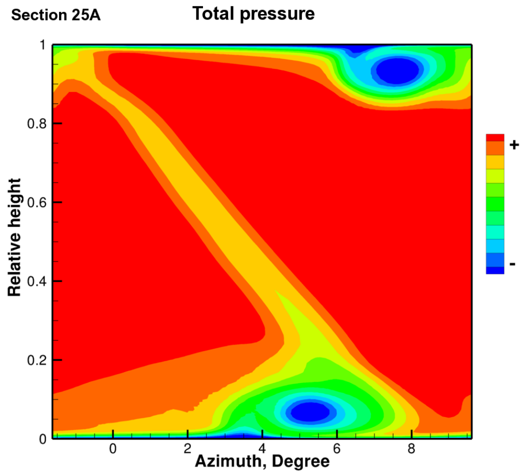

(a) Throttle 1.45. Near surge cartography.

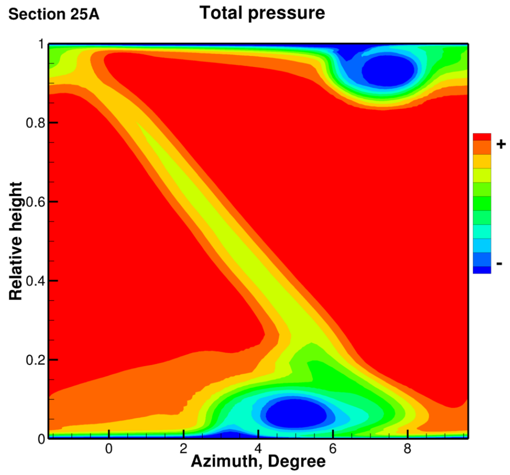

(b) Pivot pressure of 0.93 Pio. Design point cartography.

Figure 5.2 — *Total pressure cartography at section 25A. ZDES computations.*

point for this study and the one retained for the outlet boundary condition.

5.1.2 Inlet cartography definition for the computations on the first rotor near surge

Once the operating point is defined, the flow cartography is extracted at section 25A. The resulting 2D map is then set against the 2D map originating from the design point in the figure 5.2 which shows the total pressure. One can see that the topology of the flows captured is similar between the two operating points. However, the vortices coming from the hub and tip gaps of the IGV are wider at the design point. Besides, they have a lower total pressure in their core. Likewise, the wake is more pronounced at the design point. The azimuthal shift of the tip and hub vortices from the wake position is similar too. That is to say, the vortices development and convection are not drastically changed, despite the change in the axial momentum induced by the change of the operating point.

Notwithstanding these weak differences, it is relevant to use the adapted cartography since the vortex at the tip has changed. This vortex influences the rotor tip-leakage vortex along with the whole flow topology near the casing of the rotor. An insight of this influence was given in chapter 4 and this effect will be further discussed in chapter 6.

5.1.3 Adaptation of the operating point for the computation on the numerical test bench

The same numerical test bench is used for the ZDES computation near surge as the one for the design point. Nonetheless, it is adapted to match the new operating point. Therefore, the unsteady inlet condition known as "rotating distortion" is implemented on the numerical test bench. This time, the rotating distortion is based on the flow cartography near surge previously defined.

The outlet condition is the same type 4 throttle law as the one used for the IGV-R1 preliminary study. The purpose is to be consistent with the methodology followed for the design point. However, the adaptation of the numerical test bench has emphasized a limitation of this throttle law. Indeed, instabilities occur when the type 4 throttle law is used on the numerical test bench defined for this study. It is impossible to achieve a stable operating point, even if the type 4 throttling law was developed originally to avoid instabilities near surge. As far as this issue occurs only with the numerical test bench, which is based on ZDES requirements, and not with the IGV-R1 mesh, the reason seems to be the incompatibility of this boundary with a fine mesh.

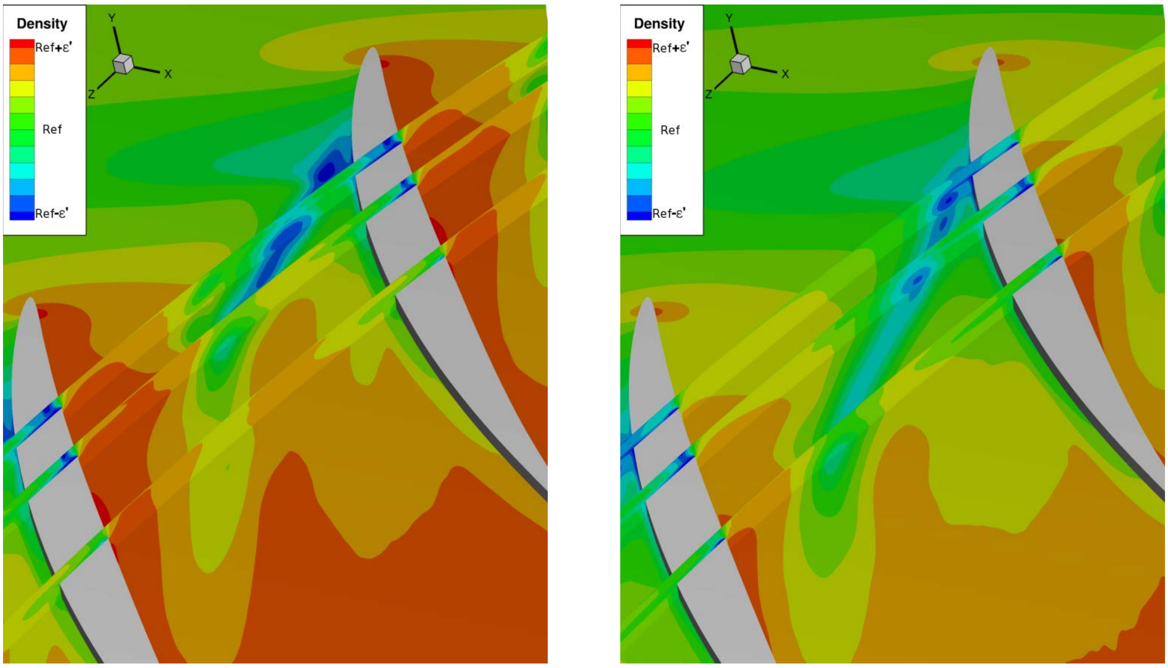

(a) Near surge. (b) Design point.

Figure 5.7 — *Comparison of the time averaged density field for ZDES at two operating points. Density planes at 22%, 31% and 46% chord and 98% relative height.* $\epsilon' = 29\%$ *of the density reference value.*

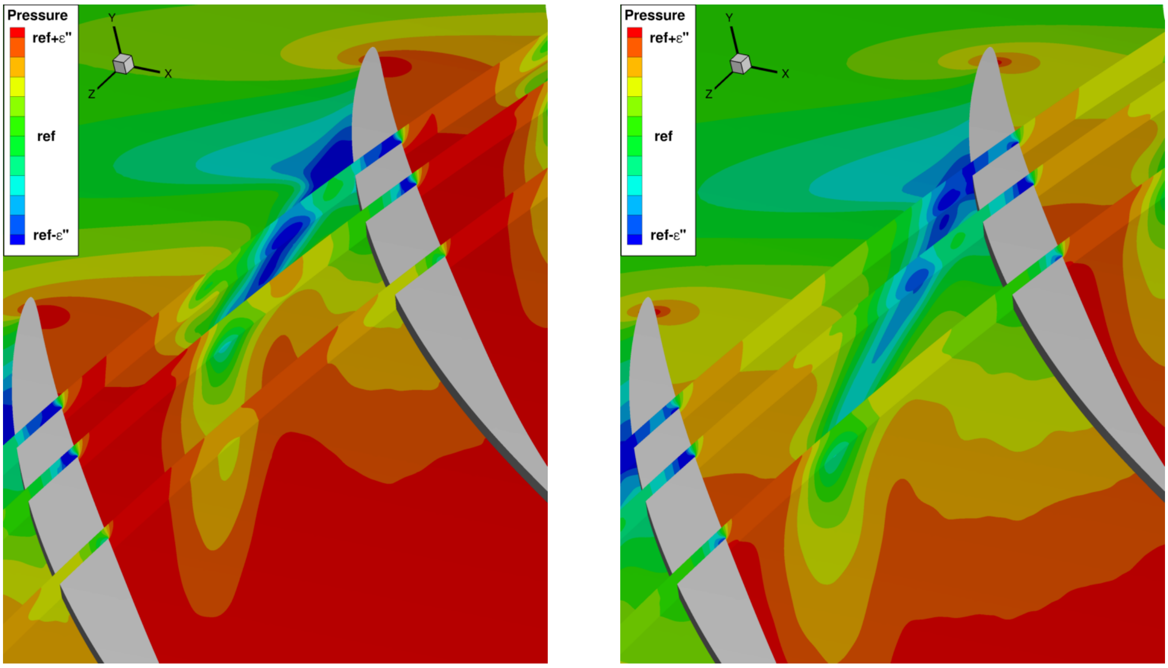

(a) Near surge. (b) Design point.

Figure 5.8 — *Comparison of the time averaged pressure field for ZDES at two operating points. Pressure planes at 22%, 31% and 46% chord and 98% relative height.* $\epsilon'' = 29\%$ *of the pressure reference value.*

Thereby, this confirms the separation at the casing and the importance of the induced vortex in the boundary layer separation.

The deflection of the tip-leakage flow is easily understood when the velocity triangle are considered.

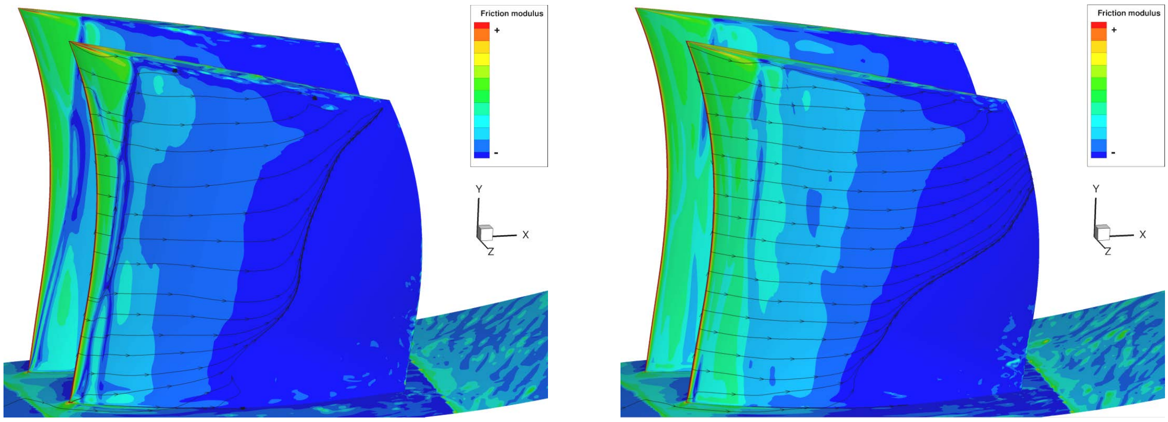

(a) Near surge.

(b) Design point.

Figure 5.9 — *Comparison of the friction lines for the time averaged field for ZDES at two operating points near the hub.*

A decrease of the axial velocity along with the same rotating velocity leads mechanically to an increased angle for the tip-leakage vortex. If the length of the tip-leakage vortex is constant, its disruption occurs earlier axially with a decreased axial velocity. Notwithstanding this effect, there is another phenomenon to be reckoned with: the shock. The analysis of the relative Mach number in figure 5.6 reveals an important difference between the operating points concerning this shock. Indeed, the shock is stronger near surge and the zone of high Mach number is concentrated around the shock which is localized just upstream section 22% X/C. Therefore, it accelerates the vortex disruption. Like the different vortices occurring near the casing, the shock is located closer to the leading edge of the blade near surge. This is coherent with what was observed experimentally by Bergner et al. [9] on a similar configuration.

The effects of the shock are not only visible on the relative Mach number field. Figure 5.7 points out that the drop in the density due to the shock is more important near surge. Although the levels of density are lower near surge at the shock position, near 10% X/C up to just upstream 31% X/C, it must be emphasized that the low density region at 31% X/C, in blue in figure 5.7(b), is not found in figure 5.7(a). Moreover, the density rises again just after section 31%X/C and higher values are found near the trailing edge. In other words, the effects of the shock are localized and centred around its position.

Finally, figure 5.8 corroborates the fact that this is a strong shock compared to the one observed at the design point. Indeed, the gradient is more important near surge. First, there is a rapid decrease of the pressure around 10% X/C with low pressure levels, inferior to the one measured at the same position at the design point. Then, downstream the shock position, there is a rapid rise of the pressure value. Nevertheless, the pressure drop follows the main tip-leakage vortex core, likewise what is noticed with the density.

An interesting effect of the operating point is underscored in figure 5.9, with the skin friction lines [41] and friction modulus at the design point and near the surge line. The area where the friction modulus decreases rapidly near the leading edge is located even closer to this leading edge in the case near surge. The corresponding friction modulus value is inferior too and a distinct line of low friction modulus is emphasized from the tip to the hub of the blade. This line denotes the shock position and its effects throughout the blade height. The friction lines drawn on the suction side of the blade indicate a different behaviour too. The position of the separating line observed at the design point differs. Indeed, it reaches the trailing edge at the tip for the computation near surge. This brings to the fore a massive separation on the suction side for the case near surge. As a consequence, this highlights that the corner effect is amplified near surge. This amplification is however overestimated as already observed for steady RANS computations by Marty et al. [112, 111] and this drawback originates from the Spalart-Allmaras model

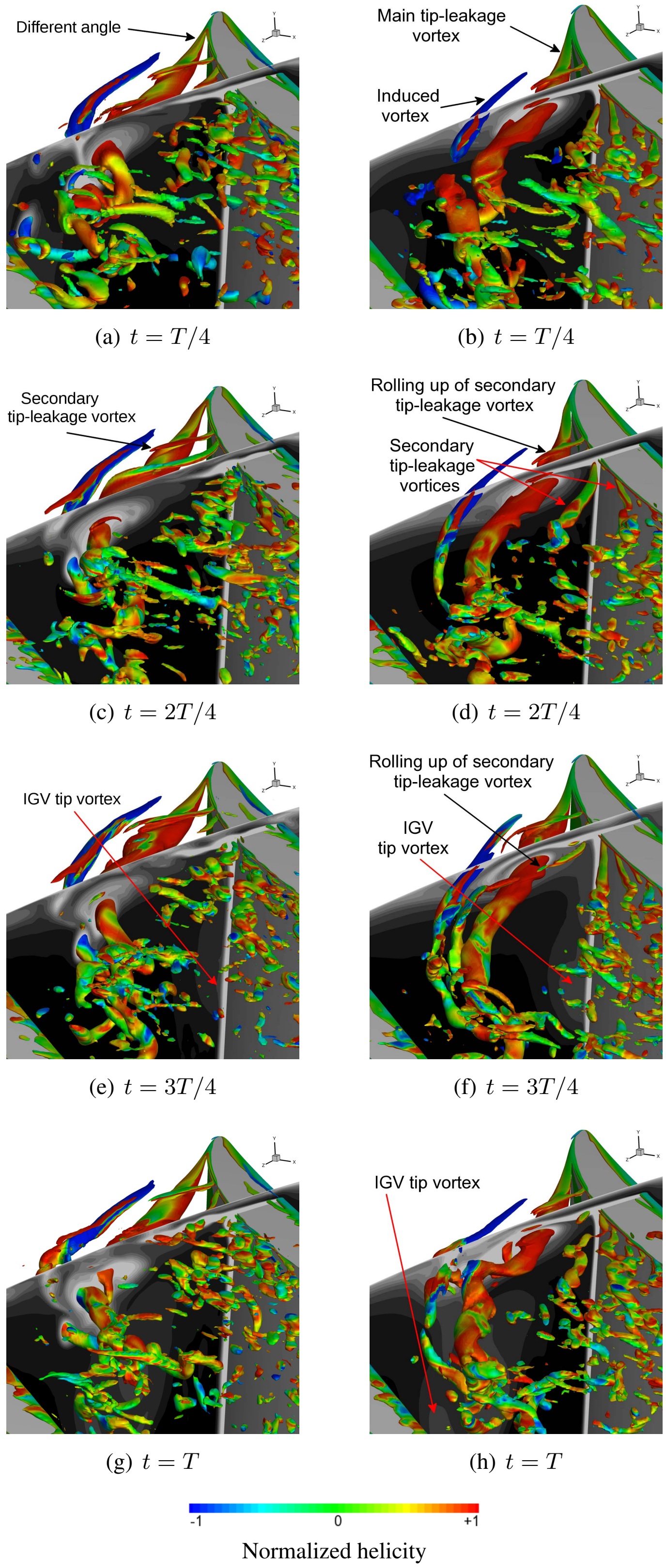

Figure 5.10 — *Snapshots of Q criterion iso-surface coloured by the normalized helicity and section 31% X/C filled with the entropy (left: ZDES near surge, right: ZDES at design point.).*

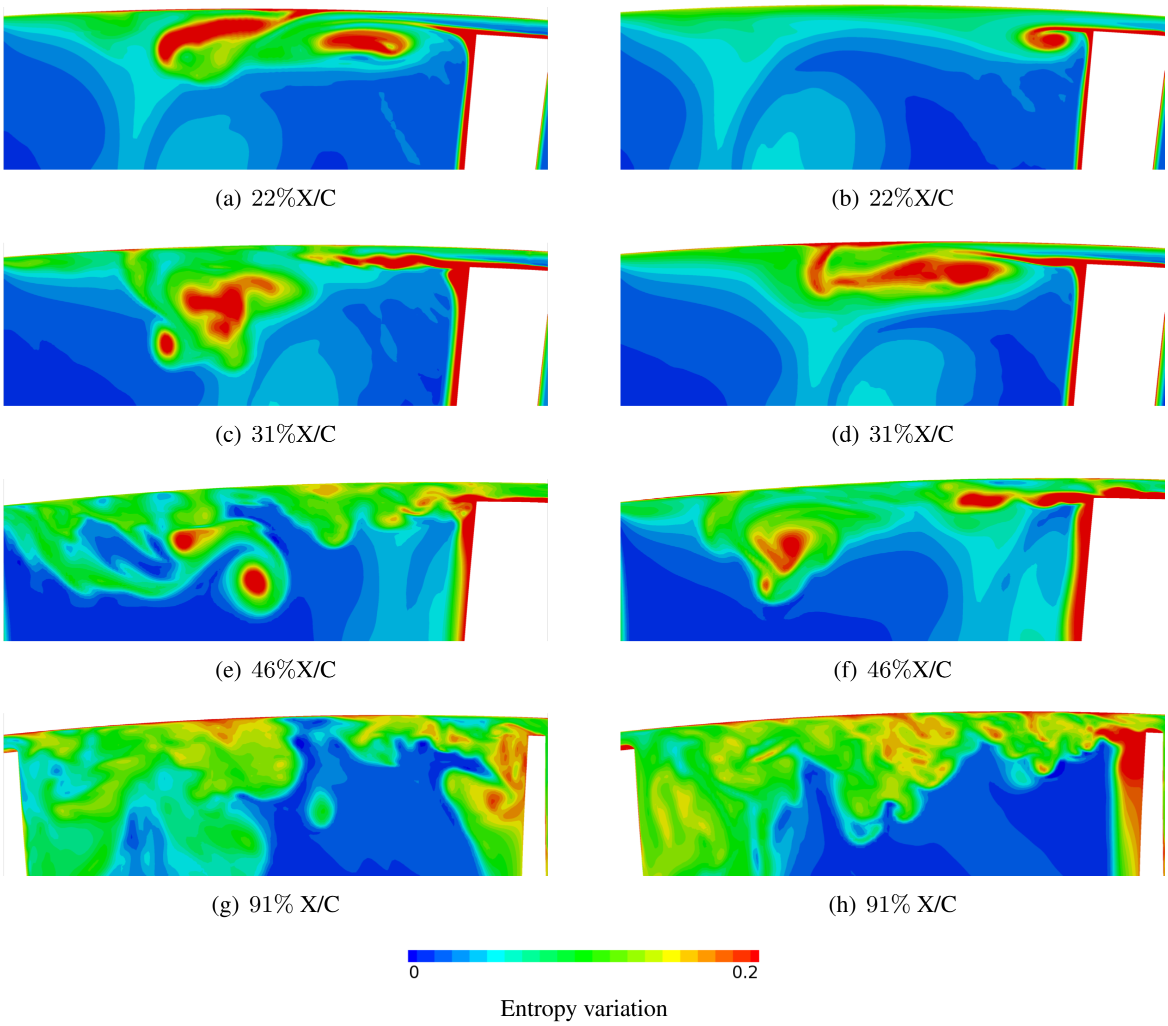

(a) 22%X/C (b) 22%X/C
(c) 31%X/C (d) 31%X/C
(e) 46%X/C (f) 46%X/C
(g) 91% X/C (h) 91% X/C

Figure 5.11 — *Entropy planes for four different axial positions at t=3T/4 (left: ZDES near surge, right: ZDES at design point.).*

with the Q criterion figures, is clearly discernible here by comparing figures 5.11(c) and 5.11(d). This only affects the moment when the IGV tip vortex arrives on the R1 and stretches the tip-leakage vortex azimuthally.

In the next sections, the modifications of the tip-leakage flow when the operating point is close to the surge line will be further discussed with the help of measurements taken on the experimental test bench.

5.3 Effects on performance and 1D distributions

5.3.1 Global values

The first comparison with the experimental data to conduct concerns the global values. The normalized mass flow at section 25A as well as the normalized total pressure ratio between sections 25A and 26A are evaluated for the experiments and the computations. Even if some of the experimental values are missing near the hub and the tip because of the measurement process with the probes, as explained in chapter 4, these global values give an idea of the behaviour of the R1 when the turbomachine gets closer to the surge line. The numerical results along with the experimental ones are summarized in the table

Case	Normalized mass flow	Normalized R1 total pressure ratio
Pneumatic probes - design point	1.000	1.000
Pneumatic probes - near surge	0.927	1.006
ZDES - design point	1.014	0.992
ZDES - near surge	0.948	1.020

Table 5.1 — *Mass flow and total pressure ratio for ZDES at design point and near surge, normalized with the values from the pneumatic probes data at design point.*

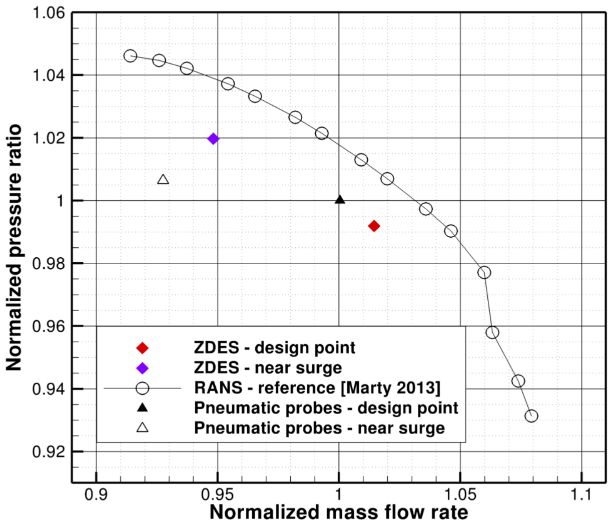

Figure 5.12 — *Pressure ratio versus mass flow rate for ZDES at design point and near surge, normalized with pneumatic probes data at design point.*

5.1. For an easier comparison, they are plotted in figure 5.12 along with the reference computation in RANS from Marty et al. [113]. Details for this reference case are given in chapter 4.

First of all, it must be emphasized that the ZDES underestimates the pressure ratio when it is compared to the reference RANS computations. Therefore, the trend observed in the previous chapter is kept near surge. Nevertheless, and contrary to how it behaves at the design point, the ZDES computation overestimates the pressure ratio compared to experiments. If a line is drawn between the two ZDES computations and the two experimental values, one can distinguish that the slope for the ZDES computations is steeper. However, this slope is similar to the one observed for the reference case, in RANS. Thereby, the same advantage and drawbacks are observed in ZDES as in RANS for this part of the operating line. Notwithstanding the similarity concerning the slopes between the computations, the values are in better agreement in ZDES. This is due to a better capture of the pressure ratio. Moreover, there is still an overestimation by about 2% of the mass flow rate in ZDES near surge, as it is for the design point. This overestimation occurs in spite of the preliminary studies carried out on the IGV-R1 configurations at the design point and near surge that underlined a good agreement of the numerical radial distribution of axial momentum with the probe values at section 25A. This confirms the necessity to rely on radial distributions and not only on global values to choose the appropriate operating point when computations are compared to experiments.

5.3.2 Radial distribution

The radial distributions of different values are plotted at section 26A, which is located downstream R1. Thereby, the phenomena occurring on the blade influence directly these distributions and can be

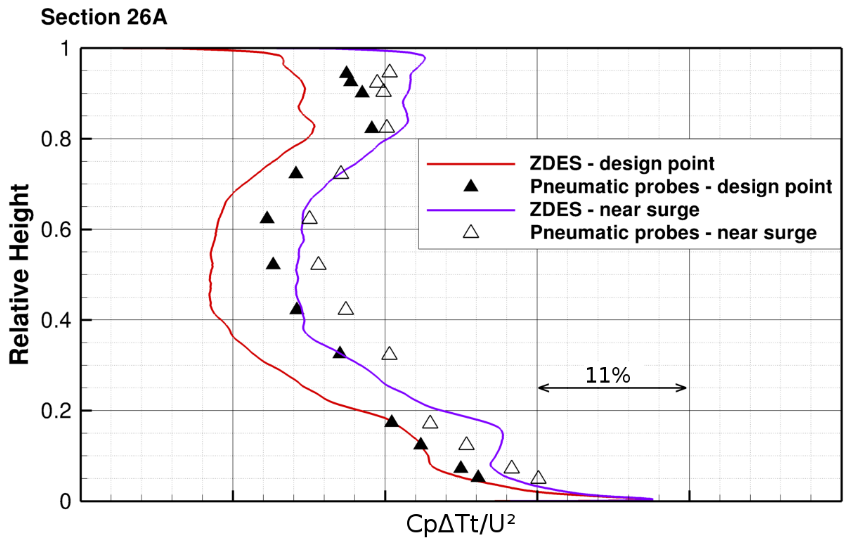

Figure 5.15 — *Radial distribution of time and circumferentially averaged normalized total temperature at section 26A for ZDES at design point and near surge.*

cases at the design point.

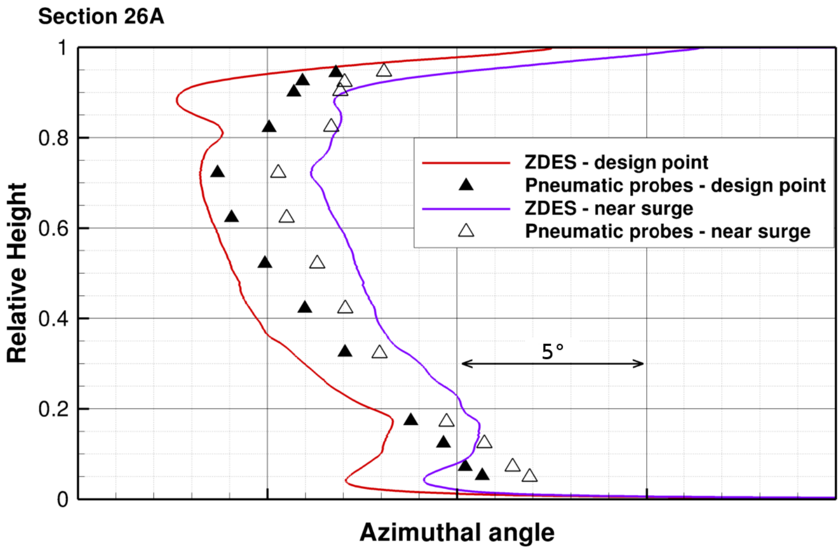

Figure 5.16 — *Radial distribution of time and circumferentially averaged azimuthal angle at section 26A for ZDES at design point and near surge.*

high circumferential velocity areas corresponding to the wakes are accurately located by both ZDES methods. Indeed, the width and the position of the wake is correctly located at around azimuth 5.3 near surge and 5.6 at the design point for both the LDA and the measurements. Nevertheless, the ZDES near surge is more accurate for the capture of the wake width than the ZDES at the design point. The values around azimuth 2.5, which correspond to the tip-leakage vortex, are in better agreement with the LDA for the ZDES near surge. In the other channel, around azimuth 8, the LDA measurements does not see the tip-leakage vortex contrary to the computations. This is linked to the aforementioned non-periodicity of the real test bench.

5.3.4 Azimuthal distribution of the velocity standard deviations

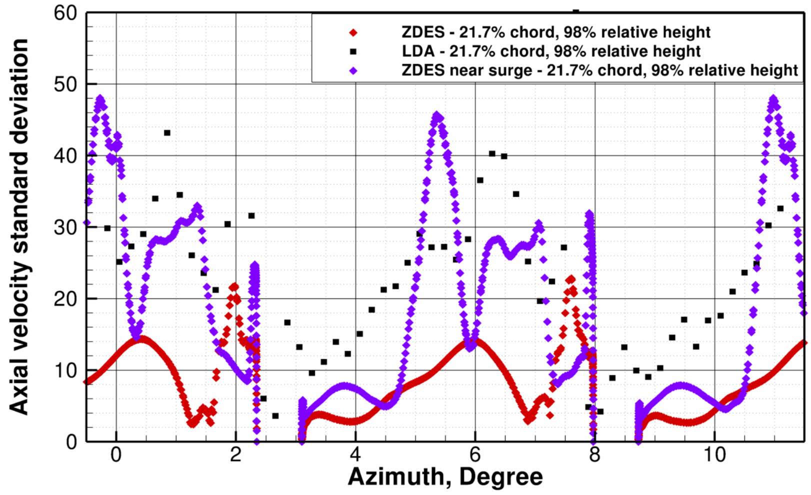

(a) Axial.

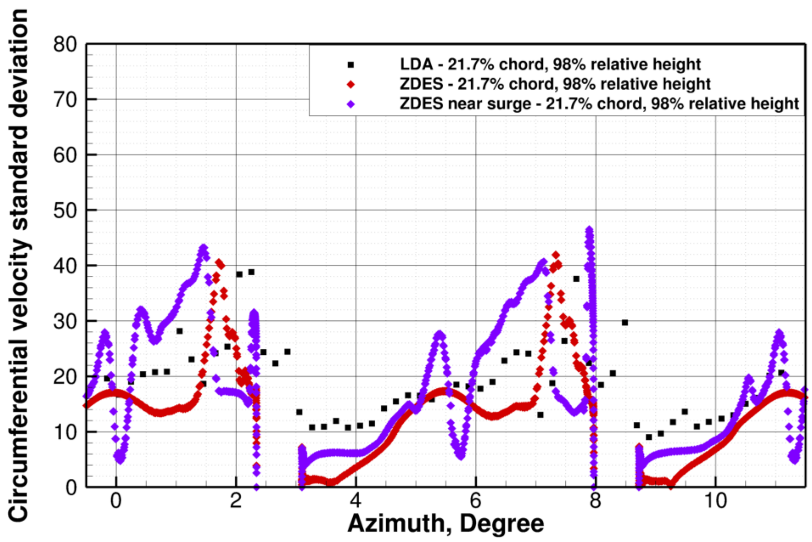

(b) Circumferential.

Figure 5.21 — *Axial and circumferential velocity standard deviations [in $m.s^{-1}$] at 21.7% chord and 98% relative height for ZDES at design point, ZDES near surge and LDA measurements at design point.*

In order to understand the evolution of unsteady phenomena near surge, the standard deviation of the velocities is analysed hereinbelow.

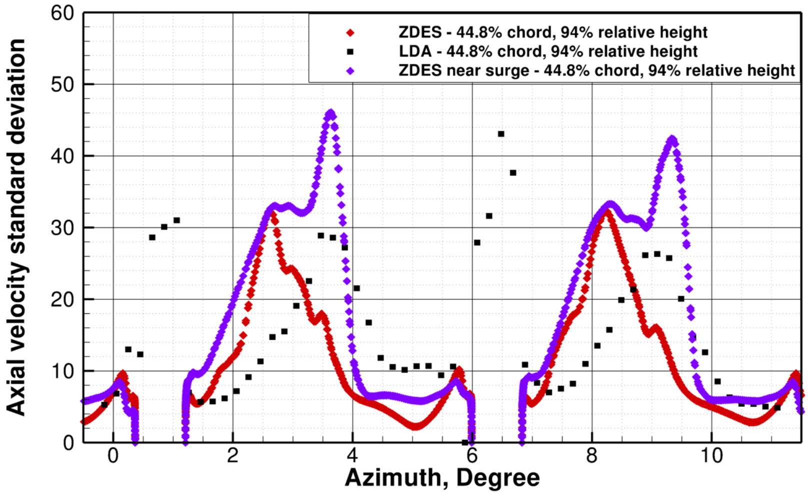

(a) Axial.

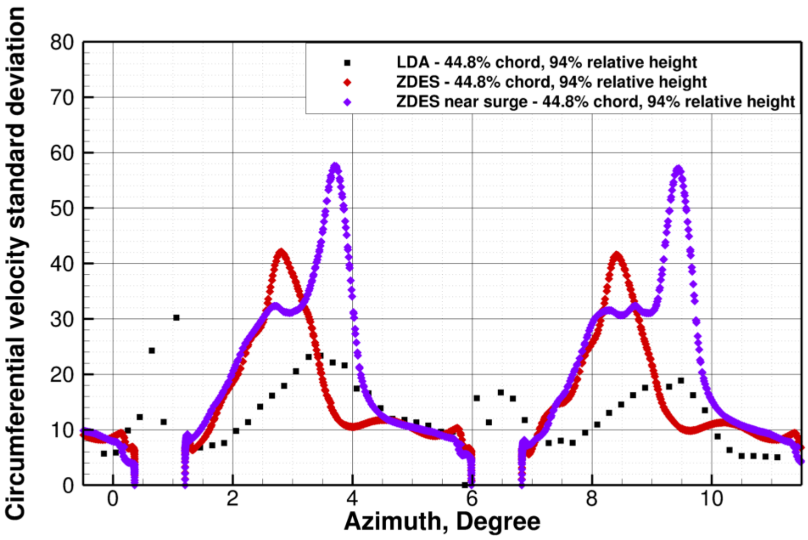

(b) Circumferential.

Figure 5.22 — *Axial and circumferential velocity standard deviations [in $m.s^{-1}$] at 44.8% chord and 94% relative height for ZDES at design point, ZDES near surge and LDA measurements at design point.*

induced vortex that extends further radially from the casing near the surge, due to the boundary layer separation. Since the separation is closer from the leading edge as well as more significant near surge, its influence is captured at 44.8%X/C and 94% of relative height.

Near the trailing edge, at 91% X/C and 90% of relative height, the aforementioned phenomenon of double leakage is clearly highlighted. The axial velocity standard deviation is plotted in figure 5.23(a). At azimuth 4, near the blade, the axial unsteadiness is high with values around $25m.s^{-1}$, whereas the levels of axial velocity standard deviation are between 6 and $14m.s^{-1}$ for the rest of the passage. These values concerns the ZDES near surge. Nonetheless, close levels are captured for the ZDES computation as well as the LDA measurements at the design point. These high unsteadiness levels designate the double leakage phenomenon. At this position, the level of axial unsteadiness near surge is nevertheless lower by $5m.s^{-1}$ compared to the design point.

The position of the tip-leakage vortex rim, located at azimuth 5.5 at the design point for both the nu-

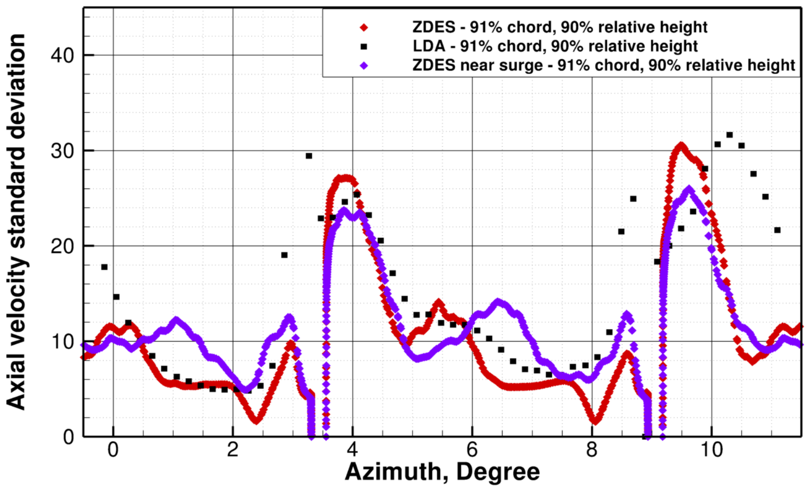

(a) Axial.

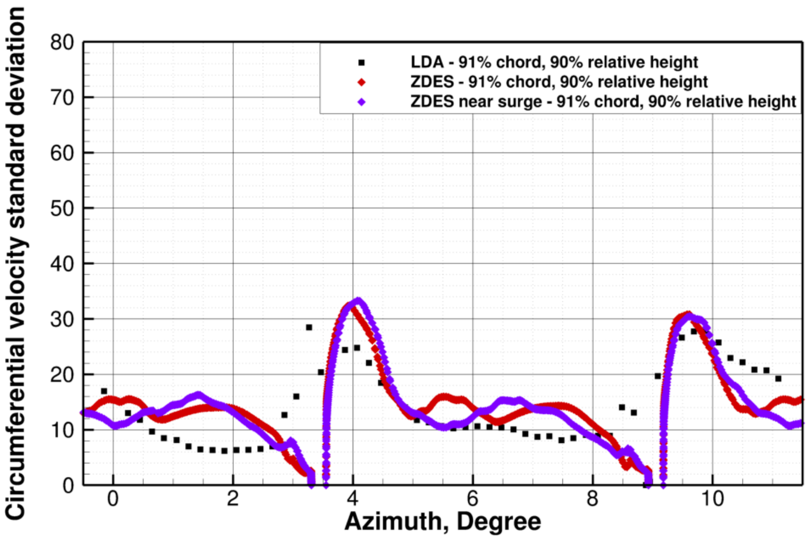

(b) Circumferential.

Figure 5.23 — *Axial and circumferential velocity standard deviations [in $m.s^{-1}$] at 91% chord and 90% relative height for ZDES at design point, ZDES near surge and LDA measurements at design point.*

merical and experimental results, is closer to the blade near surge due to its increased width. Nonetheless, its unsteadiness level is the same as for the design point.

The circumferential velocity standard deviation presented in figure 5.23(b), confirms the double leakage. Although the axial unsteadiness is lower for the double leakage near surge, the levels are similar concerning the circumferential unsteadiness. By contrast, the azimuthal velocity is increased as already seen in figure 5.19(b). Actually, the levels are close throughout the channel. The only exception concerns the position of the peak linked to the rim of the main tip-leakage vortex, as shown at azimuth 6.5 in figure 5.23(b) for the LDA measurements and ZDES near surge. This peak is located at azimuth 5.5 for the ZDES at the design point. This shows that the vortex is wider near surge at this axial position. The ZDES computation near surge is then in better agreement with the LDA measurements, even if this is at the experimental design point.

At section 26A and 90% of relative height, the standard deviation of the velocity is available near

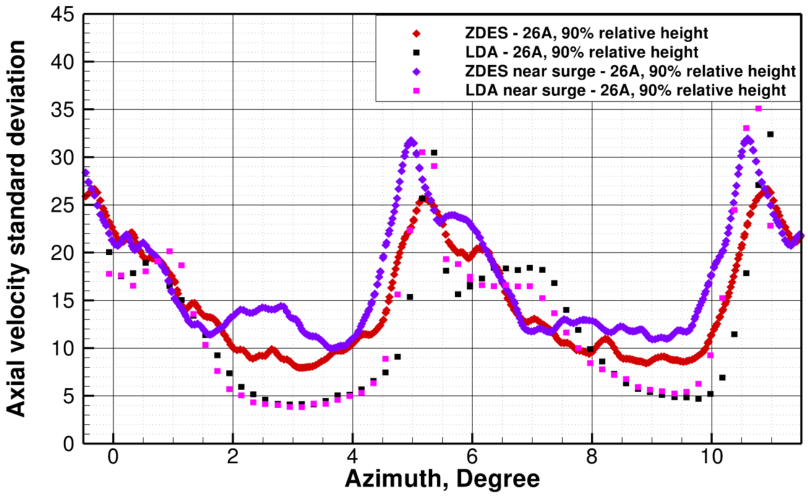

(a) Axial.

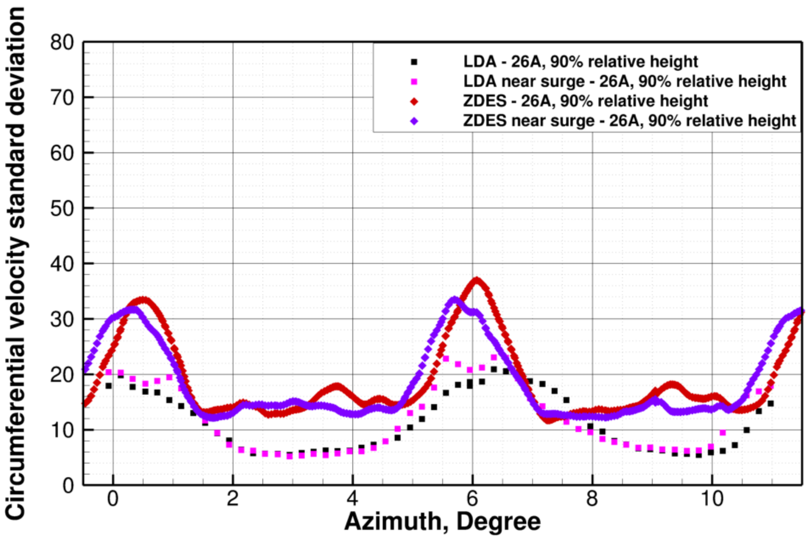

(b) Circumferential.

Figure 5.24 — *Axial and circumferential velocity standard deviations [in $m.s^{-1}$] at section 26A and 90% relative height for ZDES at design point, ZDES near surge and LDA measurements both at design point and near surge.*

surge too. Figure 5.24(a) shows its values for the axial velocity. First, one can see that there is almost no differences between the operating points from the experiments. There is only an azimuthal shift by 0.3 degrees and the maximum level of standard deviation is superior by $3m.s^{-1}$ near surge at azimuth 10.5. This is coherent with the results for the axial velocity seen in figure 5.20(a). Moreover, at the second peak, from azimuth 6 to 7.5, the unsteadiness is higher by 2 $m.s^{-1}$ at the design point than near surge in the experiment. This is the opposite in ZDES for the second maximum peak at azimuth 5.5-6. This shows that some unsteady phenomena occur experimentally and not in the ZDES. This could be explained by potential effects of the stator downstream.

For the computations, at the azimuth 2.5-3 there is a local increase of the unsteadiness due to the tip-leakage vortex. This is clearly amplified near surge with an increase by $5m.s^{-1}$ for the standard deviation. However this is not experienced by the LDA. Actually, the levels captured by the LDA are the same for the two operating points and are twice as small as the values from the ZDES computations.

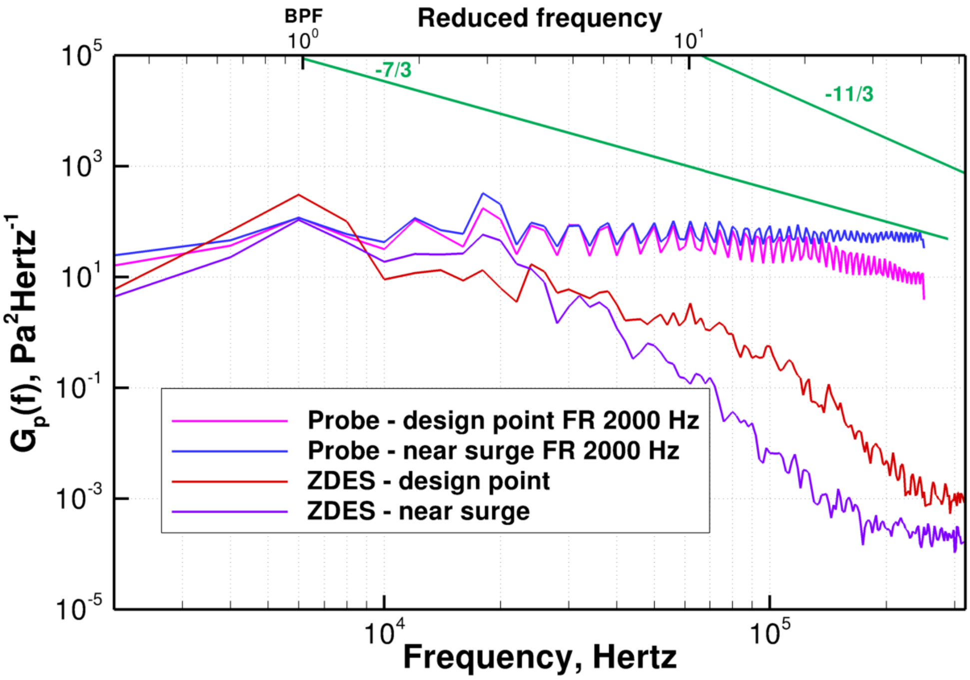

(a) At the casing.

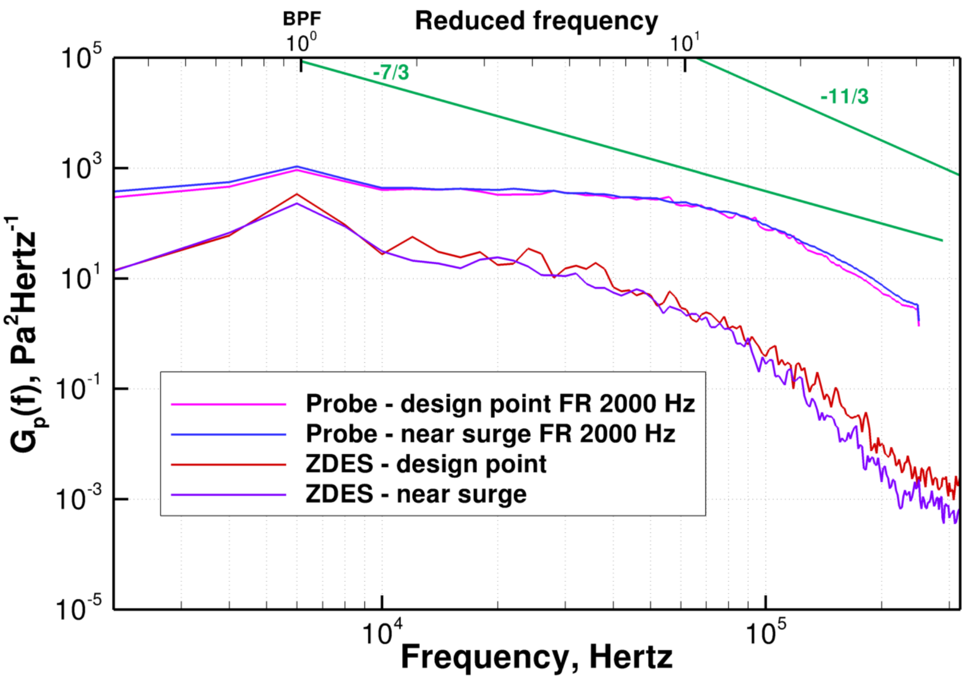

(b) At 94% relative height.

Figure 5.25 — *Power spectral density of pressure at section 26A. ZDES at the design point, ZDES near surge and experimental unsteady pressure probes at the design point.*

design point, at least for some values as shown previously in this chapter. As a result, this proves that the higher energy of the third BPF harmonic comes not only from the potential effect from the first stator (S1) downstream the R1, as it was hypothesized in chapter 4. Otherwise, it would not be captured numerically. Another effect, certainly linked to the surge, seems to participate, along with the potential effect from the S1, to this high energy.

Case	Normalized mass flow	Normalized R1 total pressure ratio
Pneumatic probes	1.000	1.000
ZDES with rotating distortion	1.014	0.992
ZDES with averaged cartography	1.012	0.987

Table 6.1 — *Mass flow and total pressure ratio for ZDES with averaged cartography and with rotating distortion, normalized with the values from the pneumatic probes data.*

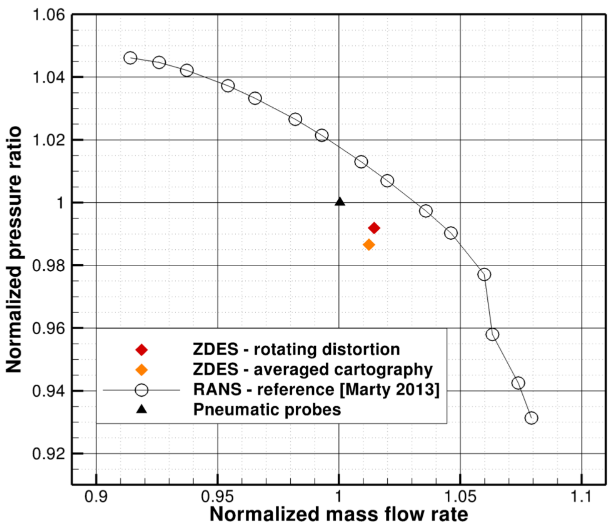

Figure 6.1 — *Pressure ratio versus mass flow rate for ZDES with averaged cartography and with rotating distortion, normalized with pneumatic probes data.*

compressor by Tartousi et al. [166], based on a Fourier decomposition with 60 harmonics, of the two dimensional cartography of the flow. The aim is to capture accurately the phenomena arriving at section 25A from the Inlet Guide Vane (IGV): the IGV wake, the IGV hub vortex and last but not least, the IGV tip vortex. The physical values for stagnation pressure, stagnation enthalpy, primitive turbulence quantity of the model, and direction of the flow are given at each interface of the map. Therefore, with this rotating boundary condition, the unsteady distortion effects induced by the IGV are modelled in the simulation of the flow within the first rotor (R1) of the CREATE compressor. The second one consists in the same two dimensional cartography but azimuthally averaged. There is neither distortion nor rotating inlet map in this case. For each radius, the same physical values are given at each cell of the map. This is the only difference between the two compared ZDES computations. Indeed, the same outlet boundary condition is used for both ZDES computations to comply with the methodology established in chapter 3. Likewise, the same methodology is applied to both the computations to check the convergence. The time range retained for the different analysis of this chapter is 17 T for the ZDES with the averaged cartography, which is the same number of iteration as for the ZDES computation with the rotating distortion.

The fact that the only difference between the computations comes from the inlet condition enables to uncouple the phenomena inherent to the tip-leakage flow from the effects of the IGV wakes on this flow.

6.1.2 The effects on the global values

First of all, table 6.1 summarizes the mass flow at section 25A and the total pressure ratio, between sections 25A and 26A, for the two ZDES fields as well as the experimental values from pneumatic pressure probes. These values are plotted in figure 6.1 for an easier assessment, along with a reference

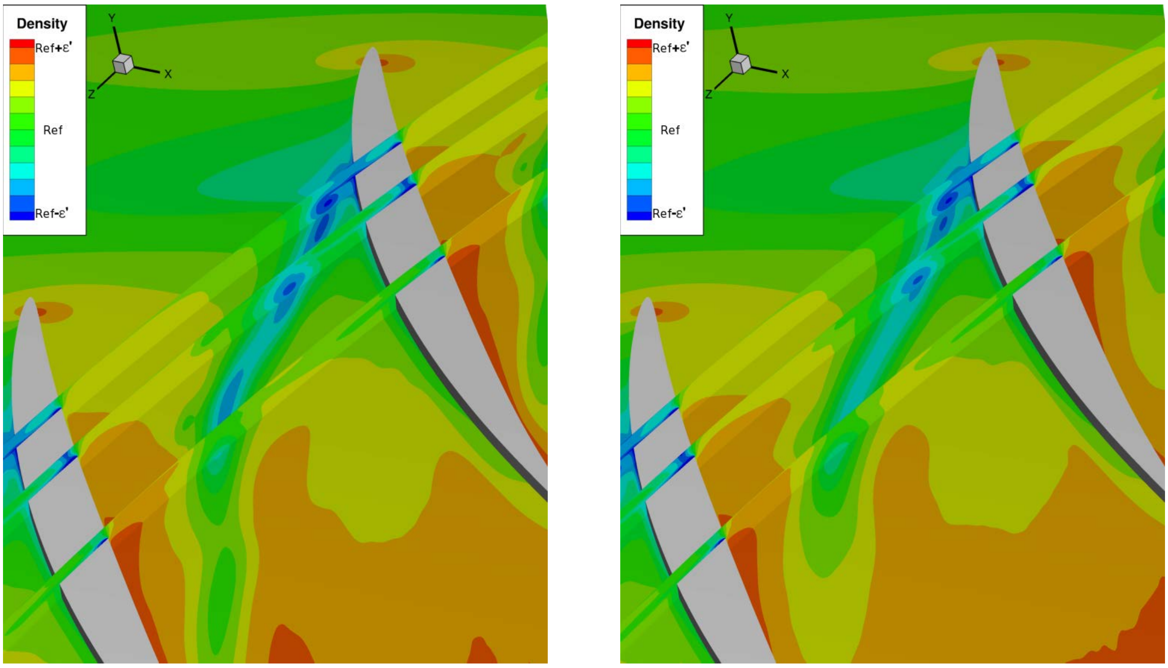

(a) With the averaged cartography.

(b) With the rotating distortion.

Figure 6.5 — *Comparison of the time averaged density field for ZDES with different inlet conditions. Density planes at 22%, 31% and 46% chord and 98% relative height.* $\epsilon' = 29\%$ *of the density reference value.*

rate is mainly focussed near the shock. Nevertheless, a second high entropy area is distinguishable near the pressure side of the adjacent blade in the case with the averaged cartography. Actually, this vortex extends further downstream without the IGV wakes, and then dissipates as it gets closer to the adjacent blade.

The same planes are shown in figure 6.3 for the normalized helicity. The main tip-leakage vortex as well as the induced vortex exhibit a higher rotating intensity highlighted by important zones with a normalized helicity value close to ± 1. Another distinctive effect lies in the amplification of the boundary layer separation at the casing, visible at 31% X/C in figure 6.3(a). Thereby, the effect of the induced vortex is more visible, in blue between the section 31 and 46% X/C in the plane at 98% of relative height. The second zone of high entropy near the pressure side of the adjacent blade is marked by a higher helicity too, albeit less pronounced than the levels upstream section 46% X/C. This clearly strengthens that there is a vortex near the pressure side of the adjacent blade.

Figure 6.4 underscores that the averaged cartography influences the shock on the time averaged field. Indeed, the area with a relative Mach number over 1 is wider. This means that the IGV wakes decrease the shock intensity, at least in average. Besides, a zone of high Mach number, albeit not above 1, extends further downstream along the main tip-leakage vortex up to the section at 46% X/C. This corroborates the fact that the main tip-leakage vortex is more coherent without the wakes.

The analysis of the density field, in figure 6.5 confirms this enhanced coherence of the vortex. The zone of lower density within the vortex core reaches the adjacent blade, whereas the density increases earlier downstream in the case with the IGV wakes. Contrary to the change in operating point detailed in chapter 5, and as expected, the shock does not change drastically without the wakes. The influence of the inlet condition on the shock intensity is nevertheless perceivable, albeit limited.

The pressure field, presented in figure 6.6, validates that the gradients on the time averaged pressure field are similar with or without the arrival of the IGV wakes. Around the shock, there is nothing that

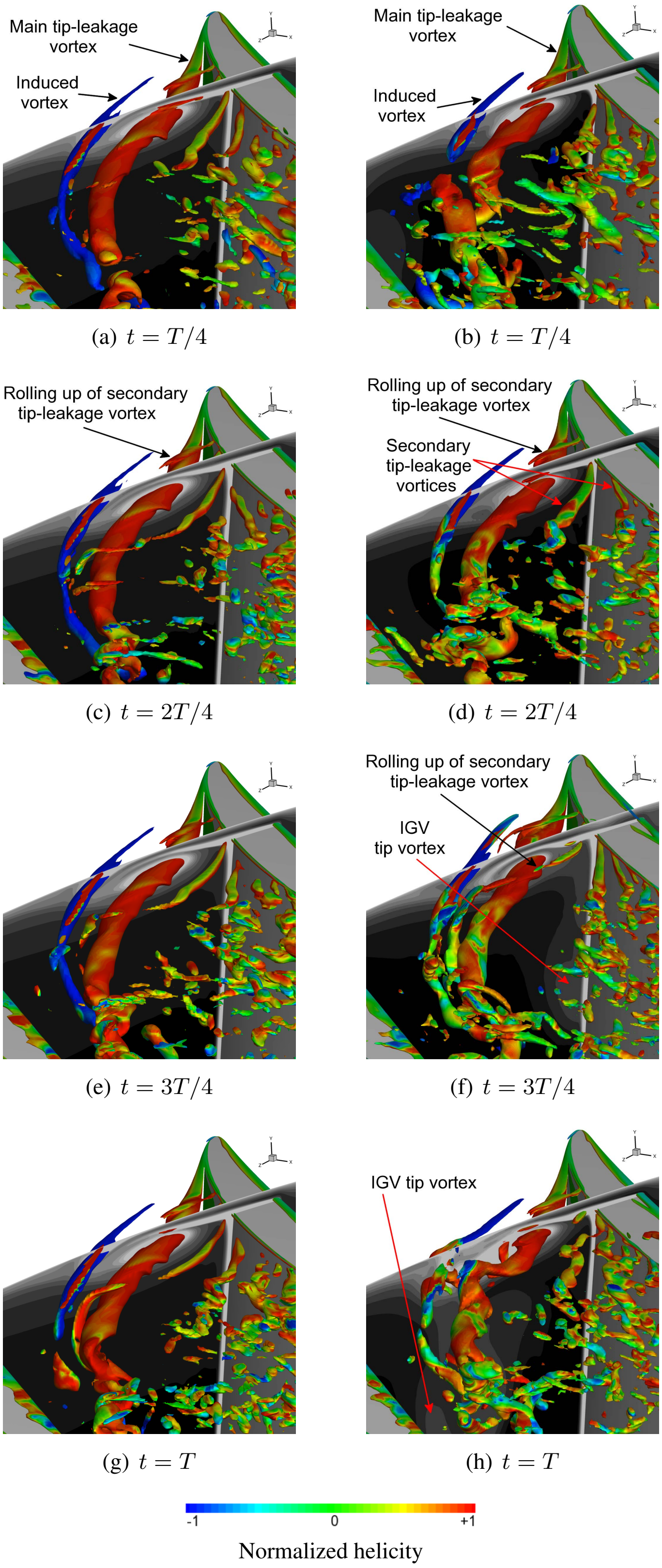

Figure 6.7 — *Snapshots of Q criterion iso-surface coloured by the normalized helicity and section 31% X/C filled with the entropy (left: with averaged cartography, right: with rotating distortion).*

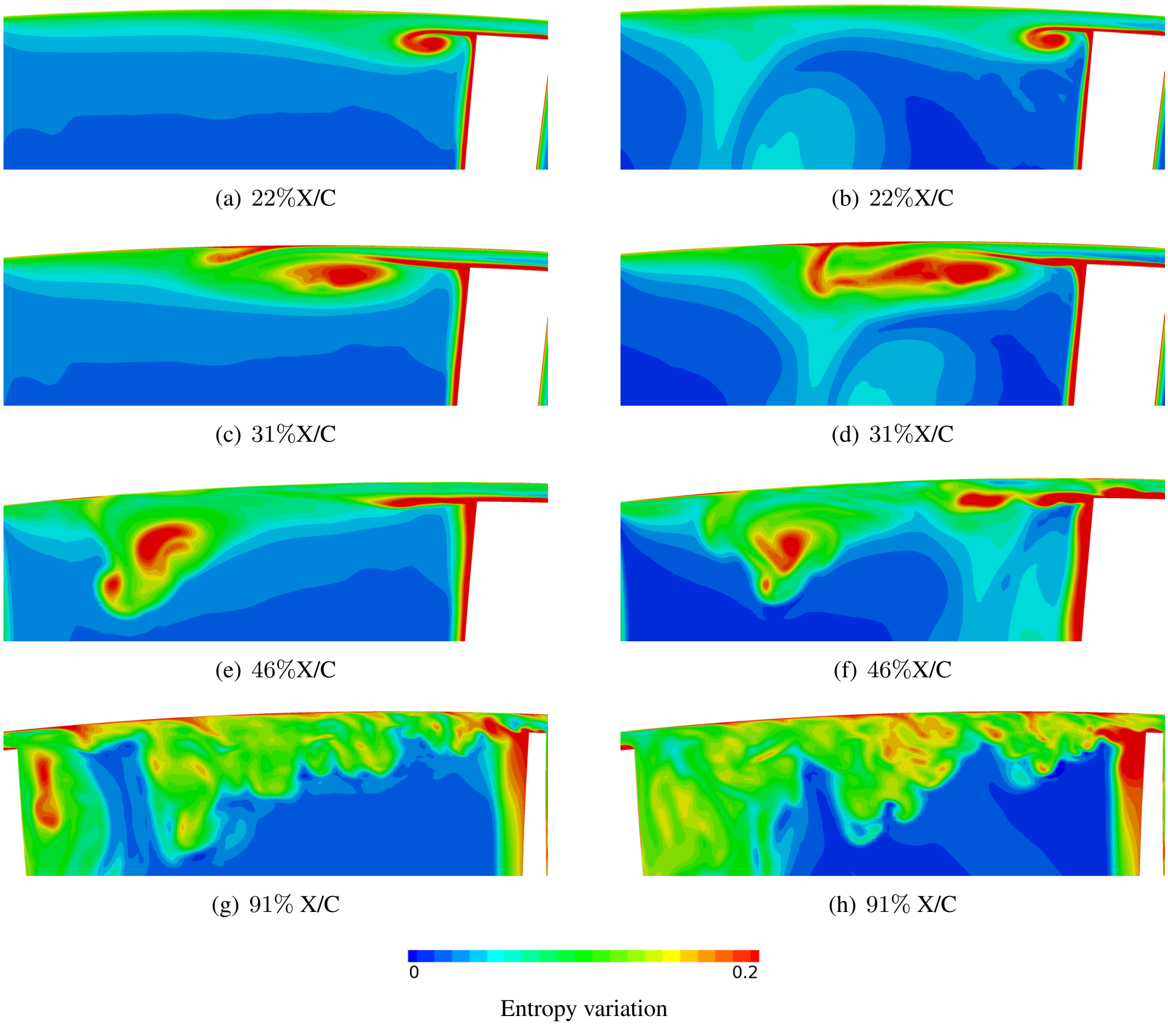

Figure 6.8 — *Entropy planes for four different axial positions at t=3T/4 (left: with averaged cartography, right: with rotating distortion).*

flutter, was already experimentally emphasized in [109], albeit not with an incoming vortex from the stator as it is the case here. In the studied configuration, the IGV tip vortex induces this flutter. The IGV wake, which arrives on the rotor leading edge too has a weak contribution to this phenomenon. The velocity deficit of the main flow deflects the leakage flow direction, from the rotor tip-leakage vortex inception, visible in figure 6.7(d). As a consequence, the rotor tip-leakage vortex moves away from the suction side of the blade with a period of T and it disrupts earlier. The disruption position wanders around 31% X/C. One can see, as already highlighted in chapter 4, that secondary tip-leakage vortices, as the one pointed in figure 6.7(f) migrate from the trailing edge toward the leading edge. This migration originates from this momentum deficit too and is only experienced in the case of the ZDES with the rotating distortion.

Without the arrival of the IGV tip vortex, the rotor vortex topology is at the same development stage as for the case with rotating distortion before its disruption caused by the IGV tip vortex. The closer the origin location of a vortex is from the leading edge, the more stable the vortex. Therefore, the main rotor tip-leakage vortex position remains stable and the induced vortex behaves similarly. There is no direction change in this case. Furthermore, these two vortices have an helicity level increased in absolute value compared to the ZDES with the rotating distortion. This confirms what was seen in figure 6.3(a) with the time averaged helicity planes. As a consequence, these vortices extend further downstream and toward the adjacent blade, which increases the effects of the double leakage.

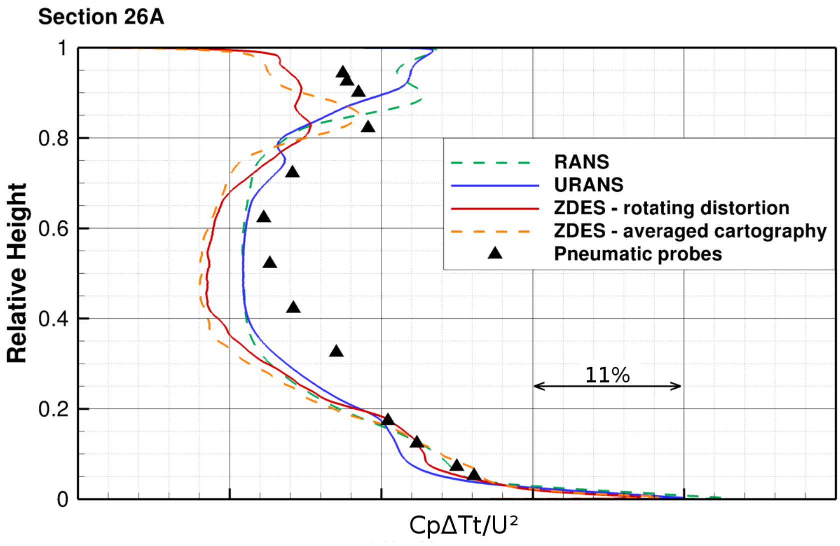

Figure 6.11 — *Radial distribution of time and circumferentially averaged normalized total temperature at section 26A for RANS, URANS, ZDES with rotating distortion, ZDES with averaged cartography and experimental probes.*

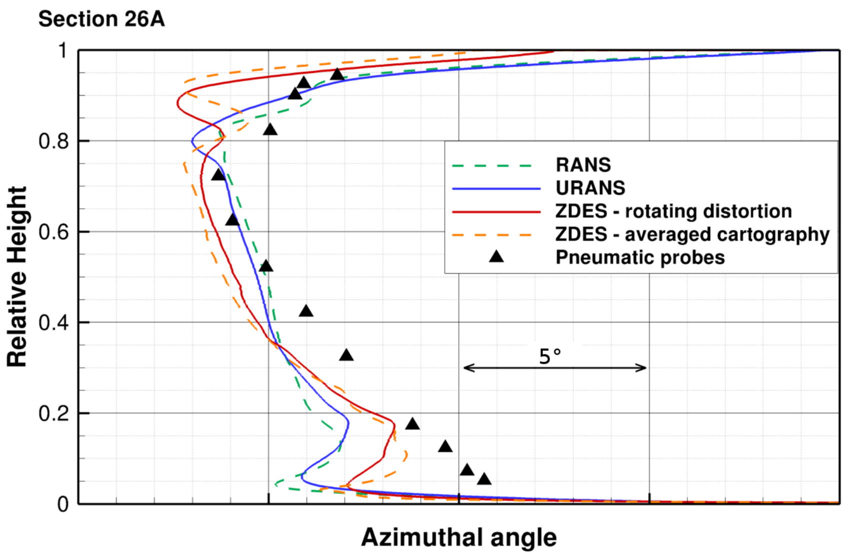

Figure 6.12 — *Radial distribution of time and circumferentially averaged azimuthal angle at section 26A for RANS, URANS, ZDES with rotating distortion, ZDES with averaged cartography and experimental probes.*

the averaged map, corresponds to 0.85% of relative height, which coincides with the maximum for the experimental values. By contrast, this maximum is lower with the rotating distortion. Notwithstanding this apparent advantage of the averaged map for the value at 85% of relative height, the gradient from this radial position to the casing is clearly overestimated. This strengthens the fact the tip-leakage vortex is too coherent with the averaged map compared to what it is in the experiment.

A similar behaviour is captured by the RANS approach. Instead of having just a light curve inflection like in URANS, the use of the averaged cartography enables this steady approach to capture gradients which are in better agreement with the experiments. In other words, the steady RANS approach seems to be more appropriate to simulate the unsteady tip-leakage vortex than the unsteady RANS (URANS) method. This is an unexpected consequence of the use of a less accurate inlet boundary condition.

6.3.3 Azimuthal distribution of the velocity standard deviations

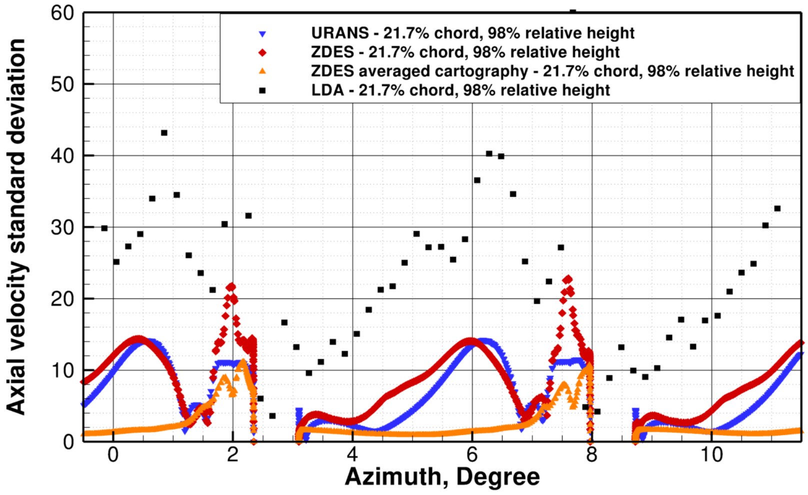

(a) Axial.

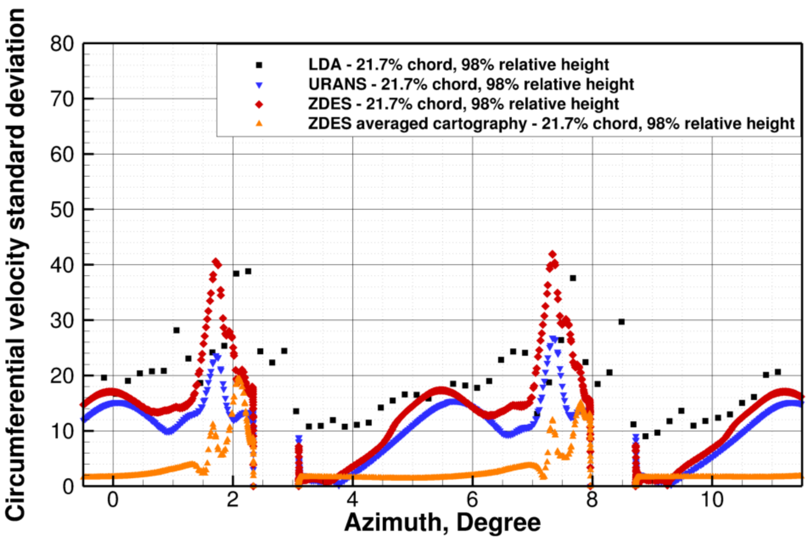

(b) Circumferential.

Figure 6.17 — *Axial and circumferential velocity standard deviations [in $m.s^{-1}$] at 21.7% chord and 98% relative height for URANS, ZDES with rotating distortion, ZDES with averaged cartography and LDA measurements.*

The unsteadiness within the flow is then compared for the same positions with a view to better understand the interactions occurring within the blade passage and downstream. To this end, the azimuthal distributions show the standard deviations of the axial and circumferential velocities. The RANS computation is not displayed within these comparisons, since it is a steady approach.

First of all, the unsteadiness is evaluated near the leading edge of the R1. The axial velocity standard deviation is plotted in figure 6.17(a) for the different azimuthal positions at 21.7% X/C and 98% of relative height. As expected, the case with the averaged cartography has the lower unsteadiness. Nonetheless, the values for the axial unsteadiness are close to $2m.s^{-1}$ from azimuth 4 to azimuth 7. Therefore, there is almost no unsteadiness around azimuth 6 contrary to what is experienced by the LDA, the URANS, and the ZDES with the rotating distortion. As a consequence, the major part of the flow field is stable

without the IGV wakes. However, the unsteadiness rises to reach $10 m.s^{-1}$ at azimuth 8. The area that expends from azimuths 7 to 8 is experienced by the three computations, albeit the unsteadiness is clearly lower with the averaged map. In this zone, the boundary layer on the blade side and the tip-leakage vortex interact, hence this high unsteadiness. Notwithstanding this interaction, the tip-leakage vortex is stable.

The circumferential velocity is shown in figure 6.17(b) for the same position. One can see that there is no unsteadiness in the circumferential direction throughout the whole passage, except close to the blade as it is the case for the axial velocity standard deviation. The unsteadiness levels without the IGV wakes are up to nine times less than with the rotating distortion. This proves that near the leading edge, the instability within the flow close to the shroud originates mainly from the arrival of the IGV tip vortex.

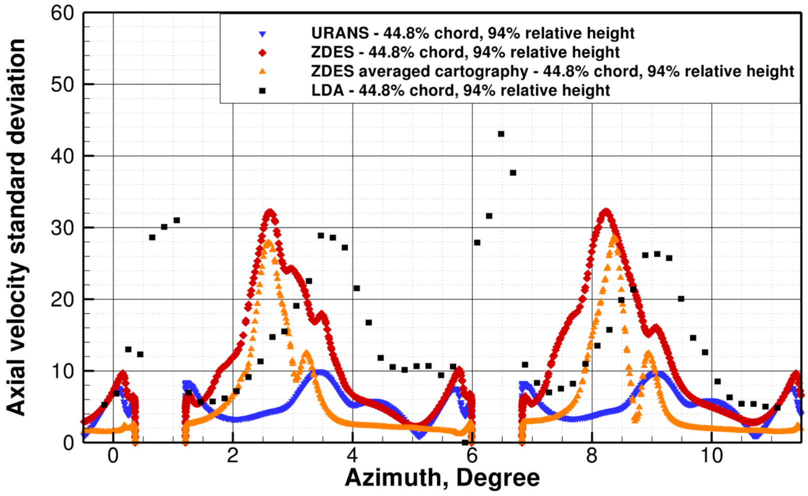

(a) Axial.

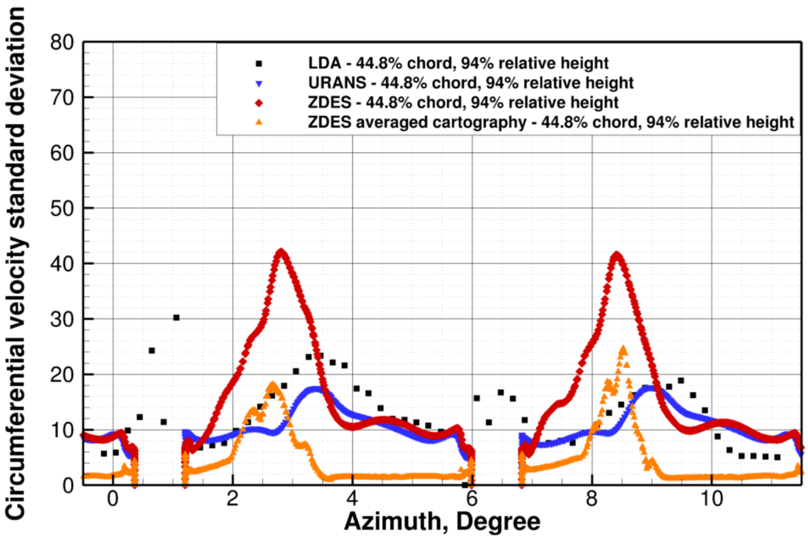

(b) Circumferential.

Figure 6.18 — *Axial and circumferential velocity standard deviations [in $m.s^{-1}$] at 44.8% chord and 94% relative height for URANS, ZDES with rotating distortion, ZDES with averaged cartography and LDA measurements.*

Downstream, at 44.8% X/C and 94% of relative height, the axial velocity standard deviation highlights a more complex pattern, presented in figure 6.18(a). First, without the IGV wakes, the high un-

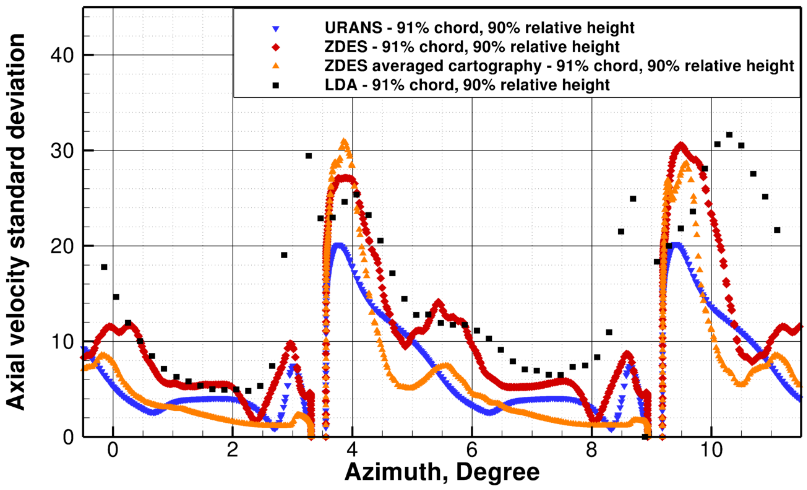

(a) Axial.

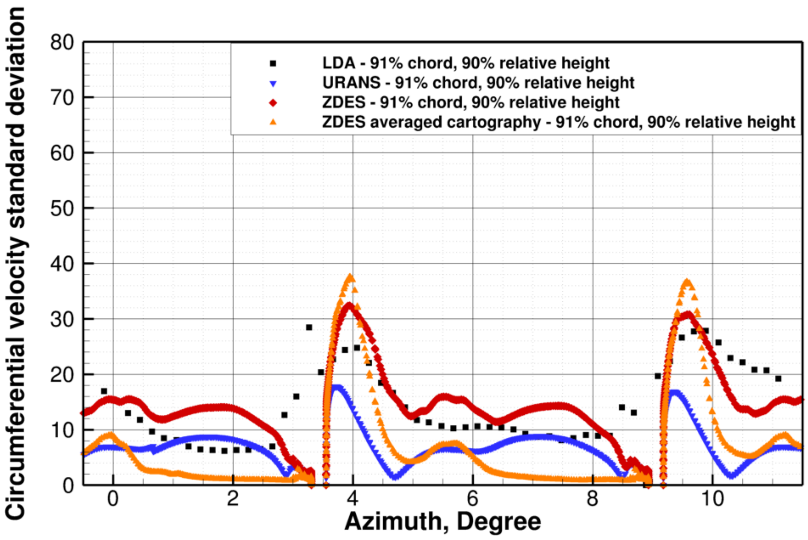

(b) Circumferential.

Figure 6.19 — *Axial and circumferential velocity standard deviations [in $m.s^{-1}$] at 91% chord and 90% relative height for URANS, ZDES with rotating distortion, ZDES with averaged cartography and LDA measurements.*

steadiness area near the blade at azimuth 5.5 is scarcely perceptible contrary to what is seen experimentally and with the two other computations. In the computational cases with the rotating distortion, there is a peak at azimuth 5.5 combined with a rapid and localized drop at azimuth 5. This is not experienced by the LDA that sees a constant and higher value at $10m.s^{-1}$ from azimuths 4.5 to 5.5, that is to say close to the blade. The fact that the experiment captures higher values without this local drop comes from the operating point, as already underlined in chapter 5 in figure 5.22(a).

Second, without the IGV wakes, two peaks are distinguishable. The first one is located at azimuth 2.5, with $28m.s^{-1}$ for its maximum value. The second has a lower unsteadiness value of $12m.s^{-1}$, which shows that it is more stable axially, and is located at azimuth 3.2. They correspond to the main tip-leakage flow and to the induced vortex, or more accurately to the separation of the boundary layer at the casing, visible in figure 6.7(b). Thanks to the averaged cartography, the effects of the vortices stand out from the unsteadiness of the flow. The azimuthal range over which the zone of high unsteadi-

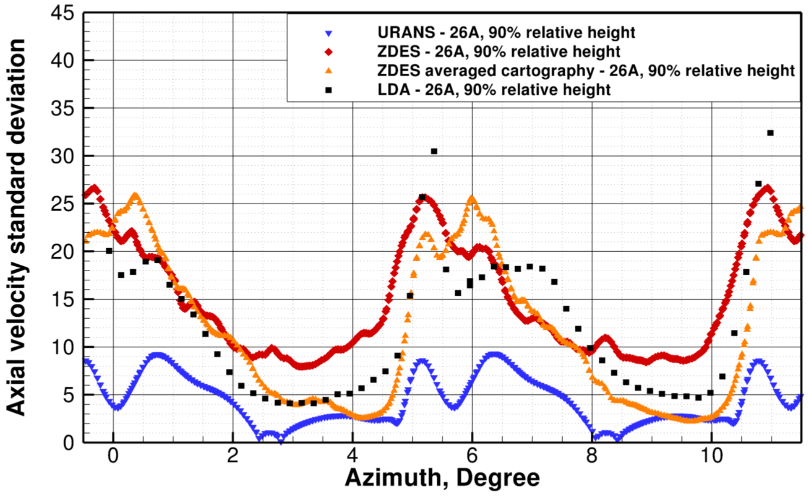

(a) Axial.

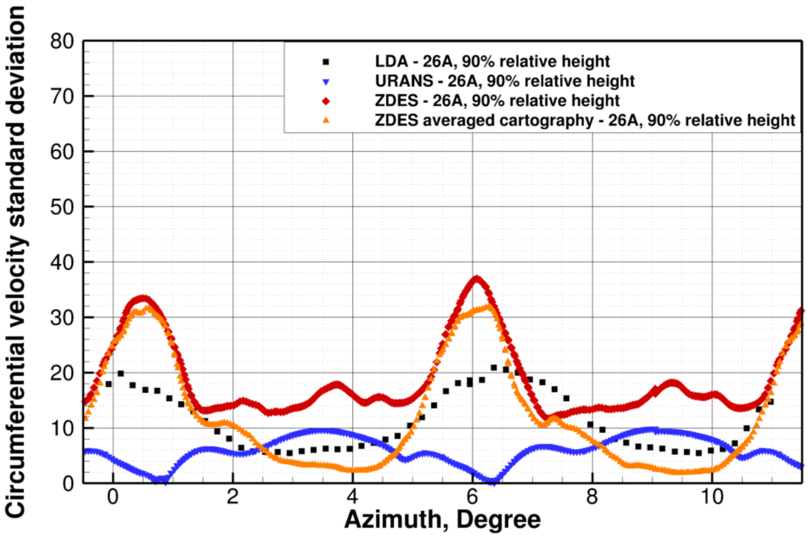

(b) Circumferential.

Figure 6.20 — *Axial and circumferential velocity standard deviations [in $m.s^{-1}$] at section 26A and 90% relative height for URANS, ZDES with rotating distortion, ZDES with averaged cartography and LDA measurements.*

ness spreads is narrower with the averaged map. Besides, this is clearly too narrow compared to the experimental peak. This is expected since there are periodic wakes experimentally. The peak visible on the experimental values is located at a different position : azimuth 3.5. This is due to the difference of operating point underscored in chapter 5. Its value nonetheless corresponds to the one captured by the ZDES computations, either with or without the IGV wakes. The second peak is yet not experienced by the LDA, certainly because of the higher unsteadiness levels throughout the channels.

The circumferential velocity standard deviation, presented in figure 6.18(b) shows the same narrow peak as for the axial velocity standard deviation. Nonetheless, the maximum value is almost halved without the wakes. This proves that the circumferential unsteadiness observed at this axial position comes mainly from the arrival of the wakes from the IGV and their interaction with the flow near the casing. Moreover, the azimuthal position of this peak is more localized, because there is no periodic azimuthal shift due to the arrival of the IGV tip vortex and its stretching of the boundary layer developing

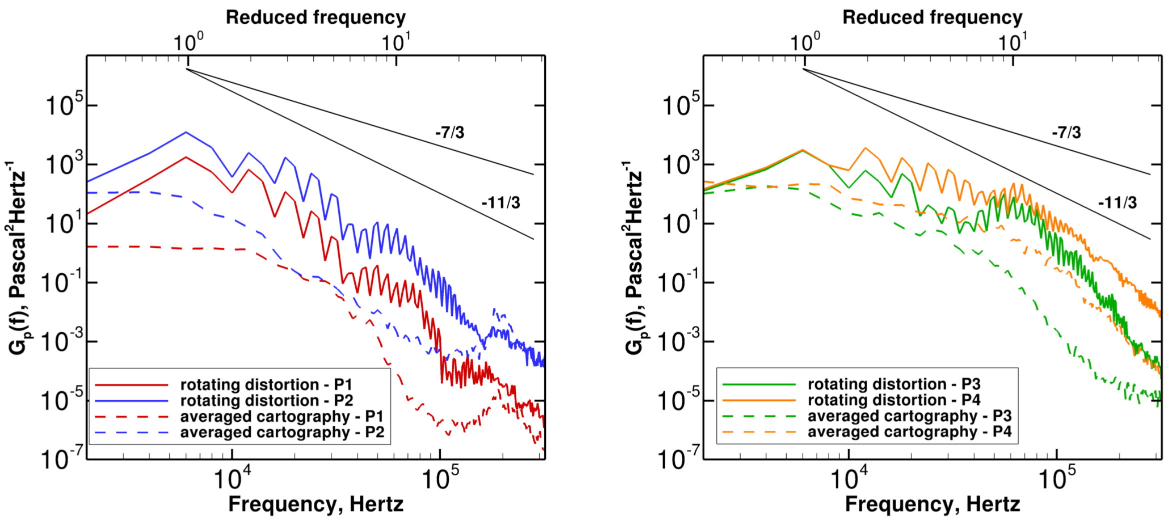

(a) Probes 1 and 2.

(b) [Probes 3 and 4.

Figure 6.21 — *Power spectral density of static pressure for probes along the main tip-leakage vortex. ZDES with the averaged cartography and ZDES with the rotating distortion.*

6.4.1 Influence of the IGV wakes on the energy levels along the tip-leakage vortex

First of all, a spectral analysis is carried out for probes located along the main rotor tip-leakage vortex so as to better understand the physics involved. Only the two ZDES computations at the design point are compared here: the one with the rotating distortion, and the one with the averaged map.

The four probes are located at 98% relative height for different axial positions along the core of the main rotor tip-leakage vortex as presented in chapter 4 in figure 4.30 with the instantaneous Schlieren at 98% relative height and t=3T/4. The probes 1 and 2 are respectively located at 11% and 22.5% X/C. The probes 3 and 4 are located at 33.8% and 45.7% X/C. This means that probes 1 and 2 are upstream the vortex disruption contrary to probes 3 and 4.

The Power Spectral Density (PSD) represents the flow energy distribution. The normalized PSD shows the contribution to the total energy of the different frequencies. Each of them brings a different information on the way the energy is distributed over the frequencies. The PSD functions, $G_p(f)$, are plotted for the probes 1 and 2 in figure 6.21(a) and for 3 and 4, in figure 6.21(b). The normalized PSD functions are plotted for the probes 1 and 2 in figure 6.22(a) and for 3 and 4, in figure 6.22(b).

The main visible difference between the two computations stems from the energy of the IGV tip vortex, which is convected periodically at the IGV Blade Pass Frequency (BPF). Therefore, at the BPF, which is 6156 Hz, and at its harmonics, the whole energy is higher in the case with the rotating distortion as seen in the PSD in figure 6.21. This changes the energy distribution along the frequency bands. Nevertheless, the low frequency phenomena are the limiting factors in the analysis of these computations since the frequency resolution (FR) is 2000 Hz.

The energy level increases for every frequency from probe 1 to probe 2, as highlighted in figure 6.21(a). It arises from the rotor tip-leakage vortex initial development, from a weak jet flow at probe 1 to a full vortex at probe 2. This is the case for both computations. Without the wakes, the slope follows clearly a $k^{-11/3}$ slope at probe 2, which characterizes the interaction between the turbulence and the mean-shear in the inertial subrange [59]. This is distinguishable from the lowest captured frequencies to 20 BPF. However, this interaction does not seem to occur at probe 1 without the IGV wakes, since this slope is not found on the PSD, and the curve can be divided into 3 parts. First, the low frequencies have a lower energy, which is constant up to 2 BPF. Then, the energy level is close to the one for probe

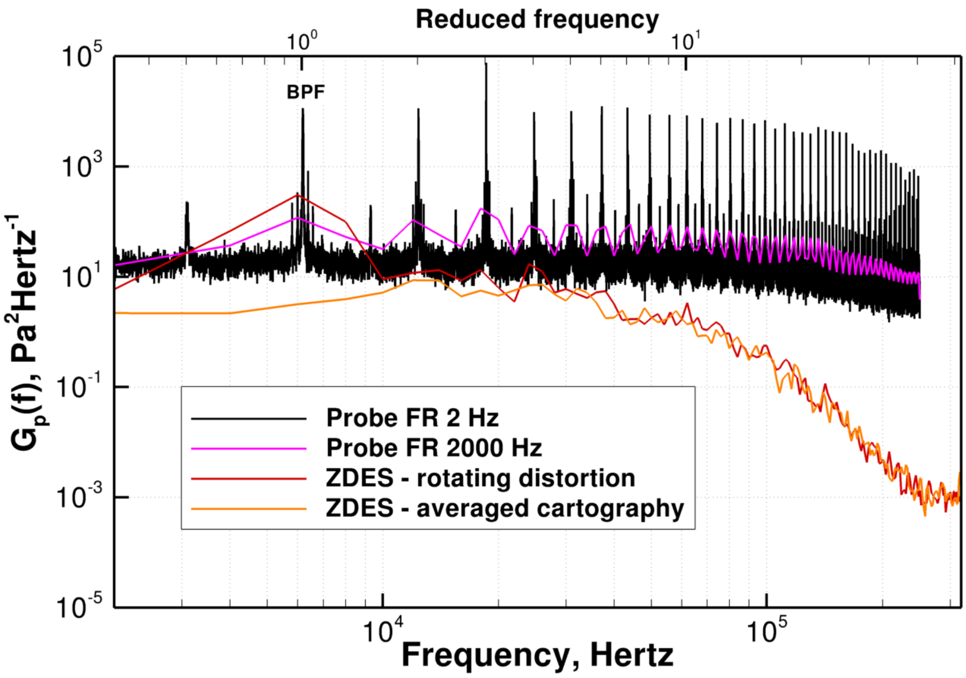

(a) At the casing.

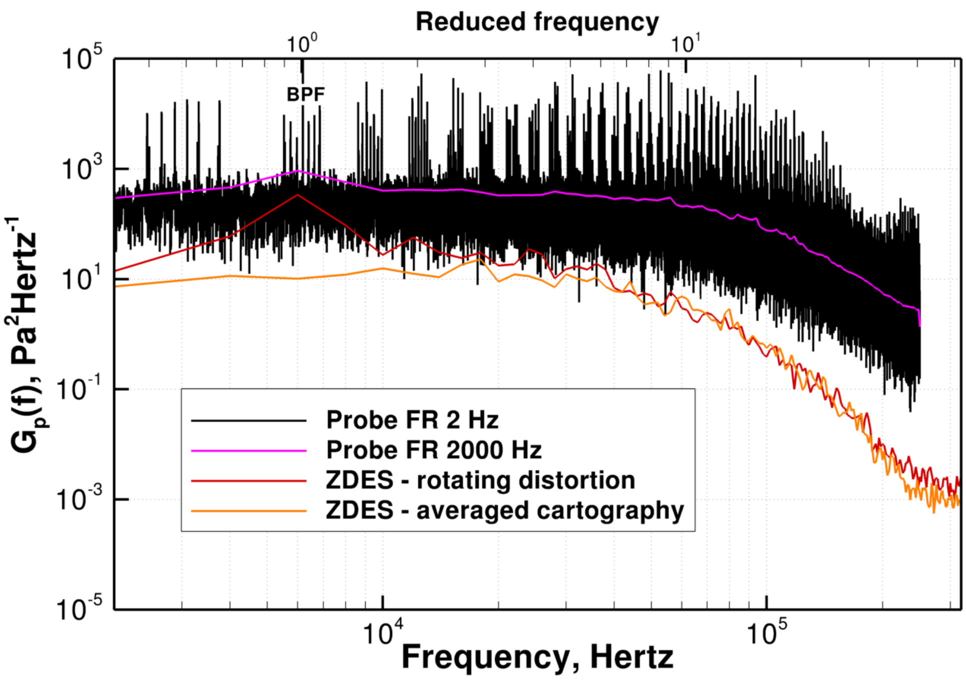

(b) At 94% relative height.

Figure 6.23 — *Power spectral density of pressure at section 26A. ZDES with averaged cartography, ZDES with rotating distortion and data from unsteady probes.*

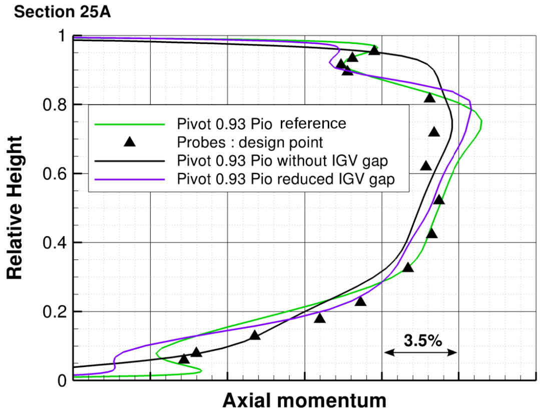

Figure A.1 — *Radial distribution of axial momentum at section 25A for different IGV gaps*

from 2.95% to 1.47% of the hub axial chord. As a result, the gap size is halved and corresponds to a gap configuration smaller than what it is experimentally. The third configuration has neither hub gap nor tip gap for the IGV. These three numerical configurations are compared to the experiment.

A.2 Impact on the radial distributions

First of all, the time and circumferential averaged values are considered through an analysis of the radial distributions at section 25A.

Figure A.1 shows the axial momentum for the three configurations. As expected, the reference configuration is in good agreement with the experimental values from the probes near the hub and near the tip. Indeed, the gradients from the casing down to 80% of relative height are correctly captured, this proves that the IGV tip gap is well taken into account. However, around 70% of relative height, it overestimates the axial momentum value compared to the two other configurations. At this position, the case without any gap tends to be in better agreement. Nevertheless, it does not experience the gradients characterising the IGV tip gap near the casing. This is coherent since this configuration does not model it. Near the hub, this configuration without gap gives relevant results on this averaged radial distribution, since there is no pronounced gradient for the experimental probes. If the configuration with the reduced hub gap is considered, one can clearly observe an underestimation of the axial momentum, both near the hub, and even near the casing. Furthermore, the gradients around 90% of relative height are underestimated too. This proves that a small difference at the hub influences what occurs on the other side of the domain, near the shroud.

The total pressure radial distribution is plotted in figure A.2. Without any gap, the total pressure is clearly overestimated at both hub and tip. By contrast, the configurations with gaps capture a lower total pressure compared to the experimental value. Once more, there is an influence of the modelled hub gap on the flow at the tip, with less pronounced gradients for the IGV tip vortex, around 90% of relative height. The difference is naturally more perceptible near the hub. The gradients are weaker with the reduced hub gap, hence a better agreement with the slope observed experimentally. Nonetheless, there is no shift of the pressure value near the hub toward the value measured by the experimental probe. This highlights two effects. The first one is that the gradient with a "S" form captured by the reference configuration near the hub can be improved by changing the hub gap size. This modifies the vortex width and therefore influences the flow at section 25A. The second noteworthy effect is that the reduced hub gap is not small enough to be in perfect agreement with the experiment. The reduced gap size is nevertheless smaller than the experimental one. Thereby, the total pressure should be higher than what is is experimentally near the hub, and be closer to the configuration with no gap. This shows that the

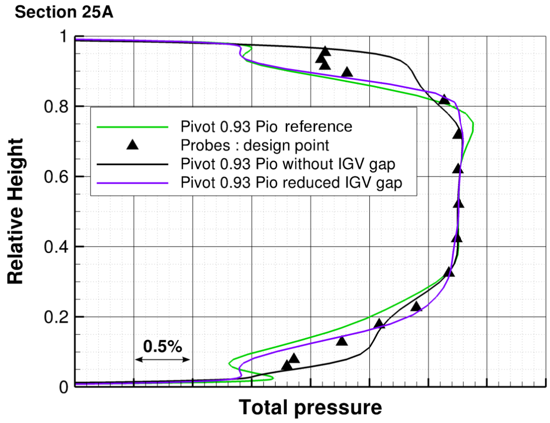

Figure A.2 — *Radial distribution of total pressure at section 25A for different IGV gaps*

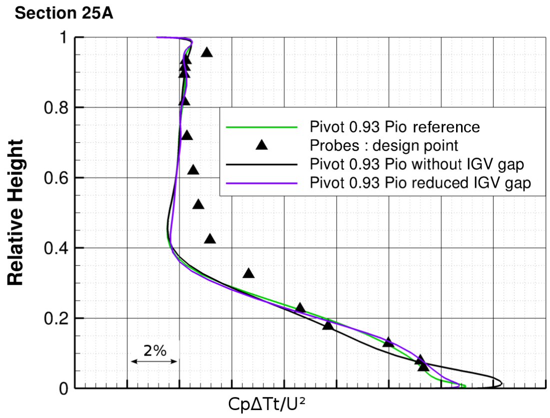

Figure A.3 — *Radial distribution of averaged normalized total temperature at section 25A for different IGV gaps*

Spalart-Allmaras model amplifies the pressure losses. The fact that all the configurations give the same results at mid span strengthens the idea that this drawback of the model is encountered in regions with secondary flows.

Figure A.3 plots the radial distribution of the normalized total temperature, $Cp\Delta Tt/U^2$. There is almost no influence of the gap near the casing, and even at mid span. The simulation of the tip gap influences barely the total temperature. Nevertheless, the figure underlines that even with the smallest hub gap, the simulation is improved compared to the configuration with no gap. However, the gradient around 10% of relative height is captured more accurately in the reference case. This underscores that the corner effect and the hub vortex from the IGV are sensitive to the hub gap size.

The azimuthal angle is plotted in figure A.4. It emphasizes the necessity to take the IGV gaps into account, even with approximations like it is performed in the presented configurations. Indeed, without gap, the angles are overestimated and the gradients not captured at all near the casing and near the hub. This figure reveals that the height corresponding to the gradient of the IGV hub vortex is in better agreement with the experimental measurements in the case of the reduced hub gap. The position of the maximum angle is closer to the hub in this configuration, therefore the curve is similar to what is captured by the probes. By contrast, in the reference case, the angle is underestimated and the position corresponding to the maximum angle value is radial located at a position 5% upper. This highlights that the development stage of the hub vortex, hence its width, is better simulated in the configuration with the reduced gap. However, in this case, the gap size is smaller than what it is in the experiment. This confirms that the numerical schemes and turbulence model used in this study amplify this phenomenon.

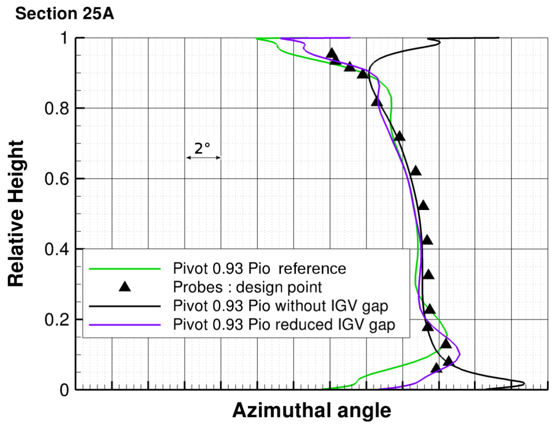

Figure A.4 — *Radial distribution of azimuthal angle at section 25A for different IGV gaps*

A.3 Impact on the captured phenomena in the cartography

This section shows the effects of the IGV gaps on the 2D cartographies of the different configurations. They are presented in figure A.5. The hub gap size influences mainly the azimuthal shift between the IGV hub vortex and the main wake, as visible by comparing the region near 10% of relative height and azimuth 5.5 in figures A.5(a) and A.5(b). This shift originates from the widening of the vortex with a wider gap. Thereby, its azimuthal extension is slower, and there is a delay between the arrival of the main IGV wake and the IGV hub vortex. This phenomenon occurs for the IGV tip vortex too. It results in the IGV tip vortex arriving with an important delay at the leading edge of the R1.

Without gap, some phenomena are experienced too. The cartography captures the IGV main wake and the thickening of the boundary layer on the walls at the hub and casing. Moreover, a corner effect is seen near the hub in figure A.5(c), with a large area of lower total pressure. A similar effect is observed near the tip too. Nevertheless, the effects of the hub and tip vortices are not experienced. It was observed in this thesis that the vortex coming from the IGV tip gap has an important interaction with the tip-leakage vortex of the R1. As a consequence, the simulation of the IGV gaps was necessary in this study in order to accurately capture this interaction.

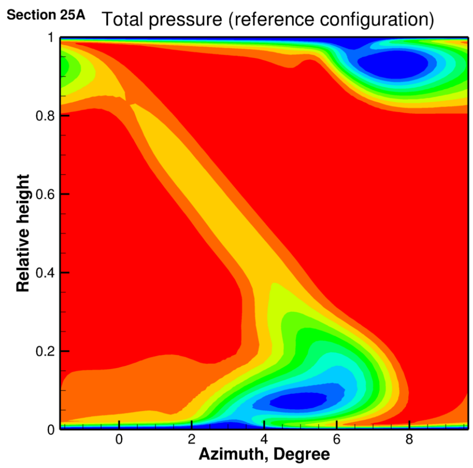

(a) Reference configuration.

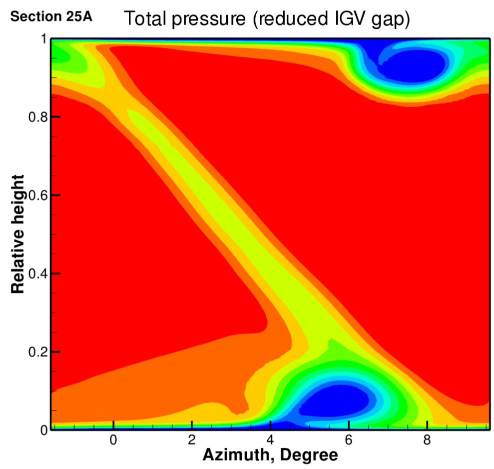

(b) Reduced IGV hub gap configuration.

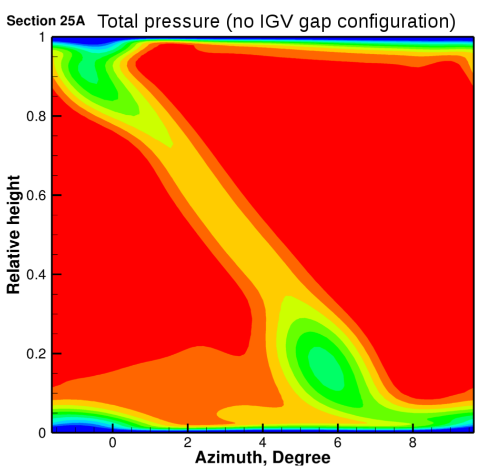

(c) No IGV gap configuration.

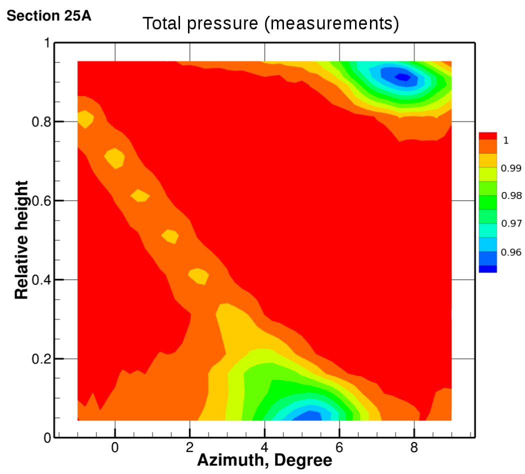

(d) Experimental probes.

Figure A.5 — *Total pressure cartography from the RANS RDE-R1 computations and experimental probes at section 25A. Effects of IGV gaps.*

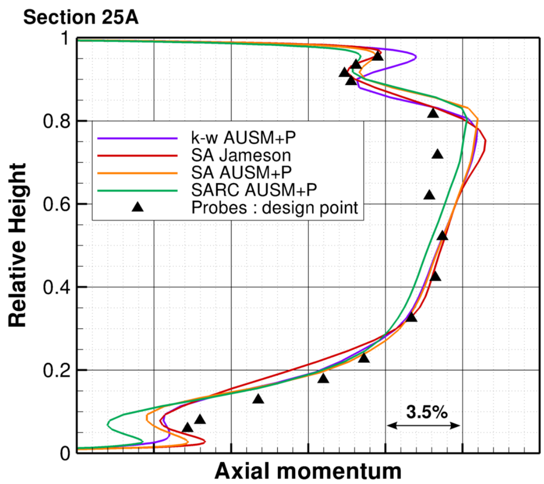

Figure B.1 — *Radial distribution of axial momentum at section 25A for different turbulence models and spatial discretization schemes*

- k-ϵ from Launder and Sharma [103] and the Jameson spatial discretization scheme.

They all converged following the criteria detailed in chapter 3, except both k-ϵ computations. As a consequence they were withdrawn from the following comparison.

B.2 Impact on the radial distributions

The time and circumferential averaged value of axial momentum, total pressure, total temperature, and azimuthal angle are presented below at section 25A.

First of all, figure B.1 shows the radial distribution for the axial momentum. Near the hub, they all underestimate the axial momentum. On the one hand, the AUSM+P scheme tends to increase this discrepancy. On the other hand, it captures more accurately the radial position of the inflection at 80% of relative height. The curvature correction of the Spalart-Allmaras model seems to amplify the effects near the hub. However, it reveals to give relevant results in the area where there is the IGV tip vortex. The k-ω model is the only one to overestimate the axial momentum near the casing. Besides, the captured vortex is further from the casing wall, which shows a major difference in the development stage for the IGV tip vortex with this model. Likewise, near the hub, the gradient with a "S" form captured by all the method is weaker with the k-ω model. As a consequence, it is in better agreement with the measurements.

The total pressure radial distribution is plotted in figure B.2. At mid span, and more accurately from 30% to 80% of relative height, the different computations behave similarly and they all capture the experimental total pressure value. Besides, the deflection at 80% of relative height is correctly experienced by the computations, except the Spalart-Allmaras computation with the Jameson scheme. This computation is the one that underestimates the most the total pressure at the casing, albeit they all underestimate it. This shows the lack of capability of the Jameson scheme to capture the vortex. The k-ω model seems to be the most appropriate to capture both the inflection seen at 90% of relative height and the total pressure level near the casing. As it was observed for the axial momentum, it captures correctly the gradients near the hub.

The normalized total temperature, $Cp\Delta Tt/U^2$, is presented in figure B.3. There is almost no difference between the configurations from 10% of relative height to the casing. The only exception is the area near the hub, where the Spalart-Allmaras computation with the Jameson scheme captures correctly

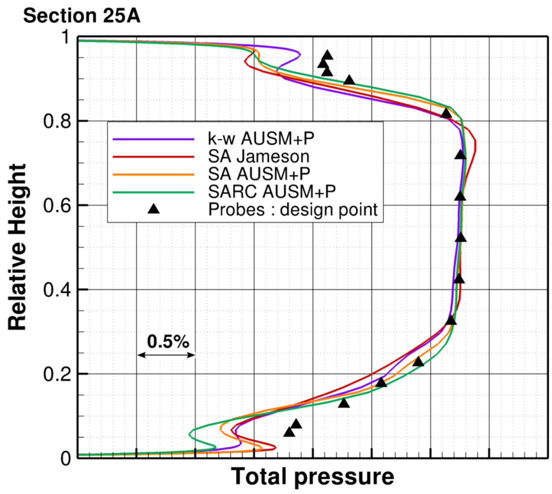

Figure B.2 — *Radial distribution of total pressure at section 25A for different turbulence models and spatial discretization schemes*

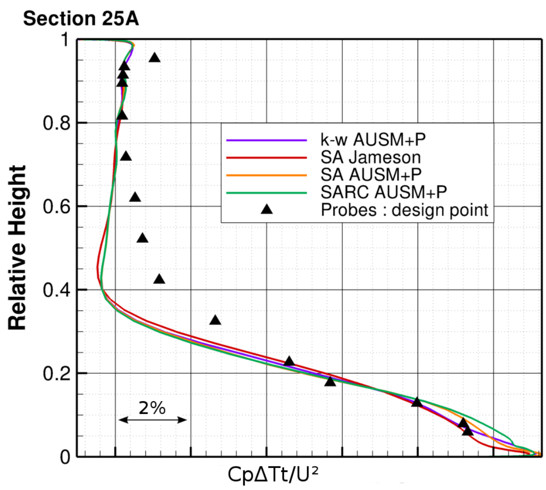

Figure B.3 — *Radial distribution of averaged normalized total temperature at section 25A for different turbulence models and spatial discretization schemes*

the visible inflection. Nevertheless, the other computations experience close results, therefore this is not a key value to consider to appraise the cases.

By contrast, the azimuthal angle, plotted in figure B.4, highlights important discrepancies between the different cases. At the casing, the k-ω model tends to be in better agreement with the experimental values. However, further from the wall, the computations with the Spalart-Allmaras model and the AUSM+P scheme reveal to capture more accurately the inflection induced by the IGV tip vortex, at 90% of relative height. Furthermore, the curvature correction shows better agreement. Moreover, it behaves like the k-ω model above 95% of relative height. Even if all the computations underestimate the angle near the shroud, the Spalart-Allmaras with the Jameson scheme is the configuration with the furthest value from the experiments. Along the span, the results are similar for the methods. Nevertheless, two perceptible effects have to be emphasized. Indeed, two computations stand out from the analysis of this figure. The first one is due to the Jameson scheme, that captures a radial position for the location of the maximum azimuthal angle further from the hub wall compared to the experimental position. This shows that the development stage of the hub vortex is too advanced here. The second is the Spalart-Allmaras with the curvature correction that reveals to be the only one to capture the gradients near the hub for the

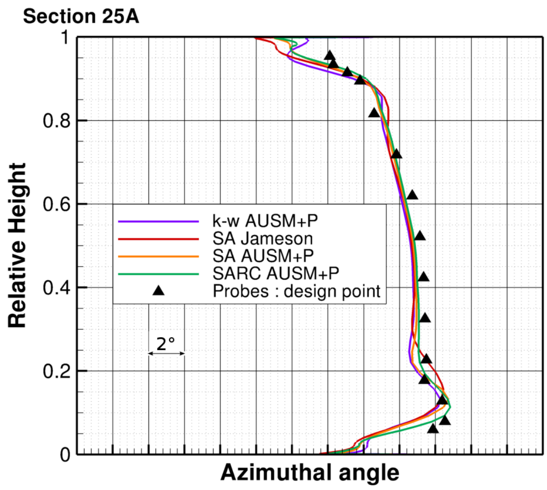

Figure B.4 — *Radial distribution of azimuthal angle at section 25A for different turbulence models and spatial discretization schemes*

azimuthal angle. This is the reason why it was chosen to extract the flow cartography at section 25A, as explained in chapter 3.